Star formation in LITTLE THINGS dwarf galaxies

Dana Ficut-Vicas

A report submitted in partial fulfilment of the requirements of the
University of Hertfordshire for the degree of
Doctor of Philosophy

This programme of research was carried out in the
Centre for Astrophysics Research,
School of Physics, Astronomy and Mathematics,
University of Hertfordshire

May 2015

To Rodi and Vicky, two brilliant minds who have inspired me to follow my dream. Your legacy is safe with me.

To Doru, your love is proof to me that nothing is impossible.

To Mircea, your faith in me has given me strength to go on.

Acknowledgements

My deepest gratitude goes to Prof. Elias Brinks and Prof. Deidre Hunter who have supported and encouraged me to take on this challenge and see it through completion. I would like to thank Prof. Elias Brinks for taking me on as a student, for his endless patience, for his valuable expertise in the field, for his understanding and above all for his efforts (at times misunderstood) to turn me into a researcher. I would like to thank Prof. Deidre Hunter for all the time and expertise she has invested in my project, but most of all for being an inspiration. On her side I learnt I can be myself and still fit in the research community. I would like to thank Michael Rupen for his guidance, for his wonderful ideas and suggestions, for his enthusiasm and for all the encouragement received during my graduate internship at NRAO. I would also like to thank Bruce Elmegreen for ideas and suggestions and very useful discussions. I would like to thank Se–Heon Oh and Hong–Xin Zhang for providing me with essential information for my project. A big thank you goes to all the LITTLE THINGS team for they all contributed to this project.

I would like to also thank my co–supervisors Antonio Usero and Volker Heesen for their availability to help and for their useful suggestions and discussions. A special thanks goes to my collaborator Adam Leroy, for having initiated me in the SF analysis method I am using in this project and for stimulating discussions in this very narrow area of expertise. Most of all I thank him for being a model worthy of following. I am deeply grateful to my husband Doru whose love gave me strength to pursue this project. Sincere thanks also to my family who believed in me and encouraged me. Also, thanks to my friends and colleagues, especially Tom, Yiannis, Antonio, Pierre and Beatriz. Thank you also goes to my friends and colleagues at the Astronomical Observatory Cluj–Napoca for their encouragements and for the interesting discussions.

Finally, I am grateful to the astronomy department of the University of Hertfordshire, for granting me a doctoral scholarship. Also I am grateful to all the people at the National Radio Astronomy Observatory (NRAO) for all their help and support. A special thanks to Eric Greisen who invested time and patience in helping us tune Multi–Scale CLEAN for our project. I would like to also thank Jeff Mangum and his team, and Dale Frail at NRAO for hosting me on an NRAO graduate internship. I thank the National Science Foundation (NSF) for the support that enabled the completion of this project through grant AST-0707563 to Deidre Hunter.

Dwarfs in Lavender

Figure: If you looked through a pair of binoculars and spotted a lavender field could you tell how many butterflies live off it? Could you tell whether there are as many butterflies as there is nectar in this field or whether there is a more fragile and mysterious balance that relates them? Through the eyes of a radiotelescope, I have observed the neutral gas in some dwarf galaxies, combined it with observations of their starlight, in search for the law that dictates at what rate new stars form from the available resources. This concept image is a fusion between a photo I took of one of the 27 antennas of the Very Large Array radiotelescope and two images derived from the astronomical data itself showing the gas distribution (the lavender field) and the young stars in a V band filter optical image (inside the butterfly wings) in the dwarf galaxy DDO133.

Abstract

Dana Ficut-Vicas

Star formation in LITTLE THINGS dwarf galaxies

University of Hertfordshire, 2015

In this thesis we test and expand our current knowledge of Star Formation Laws (SF laws) in the extreme environment of dwarf irregular galaxies. We focus on the SF characteristics of our 18 galaxies sample, extending current investigations of the Schmidt-Kennicutt law to the low luminosity, low metallicity regime.

The H I data used in this project have been observed, calibrated and imaged according to the LITTLE THINGS Survey prescription to which I brought my own contribution as a member of the team. Apart from high resolution, VLA data in B, C and D array configurations, this project makes use of an extensive set of multi–wavelength data (Hα, FUV, 24 μm, 3.6 μm, V–band and K–band). Molecular gas in dwarfs is very difficult to observe, mainly because due to the low metallicity environment, we lose our only molecular tracer, the CO which becomes under luminous. Therefore the gas distribution is represented by H I gas only. We create our Star Formation Rate (SFR) maps mainly based on FUV maps because our analysis shows that FUV is the SF tracer that allows us the most extensive sampling of the SFR surface density (SFRD) and H I surface density relation.

The main results of our study are:

Whereas in spiral galaxies Bigiel et al. (2008) have found a one to one relation between star formation rate and molecular gas and no relation between the SFR and the neutral gas, in a small sample of dwarfs as well as in the outskirts of spiral galaxies Bigiel et al. (2010b) has found that SFRD does correlate with H I surface density. We confirm the existence of the SFRD vs. H I surface density relation in dwarf irregular galaxies and a linear fitting through all our data (all 18 galaxies combined) yields a power law relation $\Sigma_{SFR} \propto \Sigma_{HI}^{1.87\pm0.3}$.

We find that the interiors of H I shells, at 400 pc scales, become resolved and show up in SFRD versus H I surface density plots although within the shell interior we have SFRD values but no H I surface density related to them. Thus, the points originating from those regions contribute significantly to the increase of the scatter

in the plot. We show that by excluding those points the correlation between SFRD and H I surface density improves between 10% and 20%.

Eight of the 18 galaxies in our sample have H I maxima higher than the $10\,M_{\odot}\,pc^{-2}$ value found by Bigiel et al. (2008) for spiral galaxies. Krumholz et al. (2011) predicted that the $10\,M_{\odot}\,pc^{-2}$ threshold is metallicity dependent in galaxies with sub–solar metallicity, however the theoretically predicted values for our galaxies only match the observed H I maxima in one case (DDO 168). We find that metallicity cannot be the only factor setting the H I to H_2 transition. In fact, we find evidence that the higher the interstellar radiation field (ISRF), the higher the H I maximum is, hence we suggest that the ISRF should also be taken into consideration in predicting the H I to H_2 transition threshold.

We find that even tighter than the SFRD vs. H I surface density relation is the SFRD vs. V–band surface density relation. Unlike the SFRD vs. H I surface density relation the SFRD vs. V–band surface density relation follows a power law and can be written as follows: $\Sigma_{SFR} \propto (10^{\mu_V})^{-0.43\pm0.03}$. The SFRD vs. V–band surface density relation suggests that the existing stars also play a role in the formation of the next generation of stars. Within our sample of dwarf galaxies the average pressure per resolution element and the SFRD are in a 1:1 linear relation: $\Sigma_{SFR} \propto P_h^{1.02\pm0.05}$. A similar relation has been found by Blitz & Rosolowsky (2006) for the low–pressure regimes of spiral galaxies.

In conclusion we find that in the extreme environments of dwarf galaxies the metal deficiency and the lack of the classic SF stimulators (spiral arms, shear motions) do not impede the star forming process. In these galaxies, dust–shielding becomes predominantly self–shielding and there is plenty of H I available to achieve this additional task. Existing stars assume the role of pressure enhancers, which in turn will stimulate SF without the need of spiral arms or shear motion.

Contents

Abstract **viii**

1 INTRODUCTION **1**

1.1 **Dwarf Irregular Galaxies** 4

1.2 **Star Formation** 6

1.2.1 How do stars form? 7

1.2.1.1 The Physics of Star Formation 9

1.2.2 Star Formation at larger scales 11

1.2.2.1 Neutral Gas and its transition towards the molecular phase 11

1.2.2.2 Molecular Gas Phase 13

1.2.2.3 Star Formation Tracers 15

1.2.3 Star Formation in Dwarfs vs. Spirals 17

1.2.3.1 Star Formation Histories 17

1.2.3.2 Molecular Gas Phase in Dwarfs 19

1.2.3.3 The Star Formation Tracers in Dwarfs 22

1.2.4 Star Formation Laws 23

1.2.4.1 General SF law 26

1.2.4.2 Molecular SF Law 27

1.2.4.3 Neutral SF Law 28

1.2.4.4 Atomic Hydrogen to Molecular gas transition and the SF Law 28

1.2.4.5 Other aspects of the SF Law 29

1.3 **Motivation** 31

2 DATA PRESENTATION **33**

2.1 **The Data** 34

2.1.1 Subsample Choice . . . 37
2.1.2 Ancillary Data . . . 40
2.2 **H I Observing Strategy and Data reduction** . . . 41
2.2.1 Observing strategy . . . 42
2.2.2 Data calibration and data combining . . . 47
2.3 **Imaging** . . . 49
2.3.1 CLEAN algorithm for LITTLE THINGS sources . . . 49
2.3.2 Alternatives to CLEAN algorithm . . . 51
2.3.3 Multi–Scale Methods . . . 53
2.3.4 Multi–Scale CLEAN for LITTLE THINGS . . . 55
2.4 **Data Display** . . . 68

3 STAR FORMATION ANALYSIS: THE CASE OF DDO 133 AND DDO 168 109
3.1 **Data Presentation** . . . 111
3.1.1 Channel Maps . . . 111
3.1.2 Integrated Properties . . . 112
3.1.3 Gas Distribution in DDO 133 and DDO 168 . . . 113
3.1.4 Kinematical Study of DDO 133 and DDO 168 . . . 120
3.2 **Star Formation Analysis** . . . 125
3.2.1 SF Tracers . . . 125
3.2.2 Internal Extinction . . . 127
3.2.3 The Relation Between Neutral Gas and Star Formation . . . 129
3.2.4 Systematic Effects . . . 134
3.2.4.1 Inclination corrections and their contribution to the SF Plots . . . 134
3.2.4.2 Resolution Effects . . . 135
3.3 **Discussion** . . . 137
3.3.1 The Star Formation Law in the Literature Context . . . 137
3.3.2 Multiple Components in the SF Laws . . . 139
3.3.3 The H I to H_2 Transition . . . 141
3.3.4 The Correlation between SFR and the Stars . . . 144
3.3.5 Molecular Gas Predictions . . . 146

4 STAR FORMATION ANALYSIS: THE ENTIRE SUBSAMPLE 149
4.1 **Methodology** . . . 150

4.1.1 Star Formation tracers . . . 151
4.1.2 Internal Extinction . . . 154
4.2 **Neutral Gas Mass Measurements** . . . 155
4.3 **Neutral Gas and Stars vs. Star Formation Rate and relations therein in individual galaxies** . . . 159
4.4 **Star Formation Law** . . . 181
4.5 **Molecular Gas Mass Predictions** . . . 191
4.6 **Multiple Components in the SF Law** . . . 193
4.7 **The H I to H_2 Transition** . . . 202
4.8 **The Correlation between SFR and the Stars** . . . 210
4.9 **The Relation between SFR and Hydrostatic Pressure** . . . 223

5 CONCLUSIONS 236
5.1 Summary & Conclusions . . . 236
5.2 Implications . . . 241
5.3 Final Act: Have we fulfilled our aims? . . . 243

6 FUTURE PROJECTS 244
6.1 A three dimensional SF analysis where the scale height is accounted for . . . 244
6.2 What drives the scatter in the SFRD vs. H I surface density relation in dwarfs? . . . 245
6.3 The contribution of resolved H I shells to the scatter in the SFRD–H I surface density relation for the entire LITTLE THINGS sample . . . 246
6.4 Does the SFRD vs. V–band surface density relation hold only in dwarf irregular type galaxies? . . . 246
6.5 Understanding the dense H I regime and its relation with the H I to H_2 turnover . . . 247

Bibliography 249

Appendix A Channel Maps 264

Appendix B Internal Extinction Plots 296

List of Figures

1.1 Schematic view of the transition from neutral to molecular gas and then to stars for normal and low metallicity systems 1

1.2 Using a compilation of figures from Gil de Paz et al. (2007); Kennicutt et al. (2003); Walter et al. (2008) we show for comparison the dwarf irregular galaxy M81dwA and the spiral galaxy NGC 5194 (M 51). . . 5

1.3 Using a compilation of figures from Weisz et al. (2008) we show the lifetime SFHs of DDO 63 (Ho I), DDO 165, NGC 2366, DDO 50 (Ho II), and DDO 53. 18

1.4 We show an image from Bolatto et al. (2013) to illustrate the effect of metallicity on CO and H_2 in a spherical clump immersed in a uniform radiation field. 21

1.5 We show an image from Kennicutt (1998) to illustrate the composite star formation law for the normal disk and starburst samples. 25

1.6 We show an image from Bigiel et al. (2008) to illustrate that for spiral galaxies in the THINGS sample atomic hydrogen turns molecular at $10\,M_\odot\,pc^{-2}$. 29

2.1 Composites of the H I map as red, FUV map as blue and V image as green for all galaxies in my thesis subsample 33

2.2 Noise variations as a function of channel for different combinations of baselines 43

2.3 Flux vs. radius for different combinations of scales, different cut–off levels and different α parameters 57

2.4 Integrated Flux density vs. radius in DDO 168 for different noise cut–off combinations 58

2.5 Testing the α parameter in DDO 168. Resolution scale versus major cycle number for α=0, 0.2, 0.4, 0.6, 0.8,1.0 59

2.6 Testing the α parameter in DDO 50. Resolution scale versus major cycle number for α=0, 0.2, 0.4. We used channel 70 for this test. . . . 60
2.7 DDO 168: Comparison between 2σ cut–off level, robust 0, clean maps and residual maps for 15″, 45″, 135″ scale maps for α= 0.2 and α= 0.4. 62
2.8 DDO 133: Comparison between 2σ cut–off level, robust 0, clean maps and residual maps for 15″, 45″, 135″ scale maps for α= 0.2 and α= 0.4 63
2.9 The noise structure inside a line–free channel in a cube with no cleaning compared with the noise histograms in channel 60 of maps cleaned with different α 65
2.10 Surface density maps (H I, FUV, 3.6 μm, Hα) for DDO 168 73
2.11 Moment maps (integrated H I,velocity field, velocity dispersion) and the V–band optical image for DDO 168 74
2.12 Surface density maps (H I, FUV, 3.6 μm, Hα) for DDO 133 75
2.13 Moment maps (integrated H I,velocity field, velocity dispersion) and the V–band optical image for DDO 133 76
2.14 Surface density maps (H I, FUV, 3.6 μm, Hα) for NGC 4214 77
2.15 Moment maps (integrated H I,velocity field, velocity dispersion) and the V–band optical image for NGC 4214 78
2.16 Surface density maps (H I, FUV, 3.6 μm, Hα) for DDO 50 79
2.17 Moment maps (integrated H I,velocity field, velocity dispersion) and the V–band optical image for DDO 50 80
2.18 Surface density maps (H I, FUV, 3.6 μm, Hα) for DDO 216 81
2.19 Moment maps (integrated H I,velocity field, velocity dispersion) and the V–band optical image for DDO 216 82
2.20 Surface density maps (H I, FUV, 3.6 μm, Hα) for NGC 2366 83
2.21 Moment maps (integrated H I,velocity field, velocity dispersion) and the V–band optical image for NGC 2366 84
2.22 Surface density maps (H I, FUV, 3.6 μm, Hα) for WLM 85
2.23 Moment maps (integrated H I,velocity field, velocity dispersion) and the V–band optical image for WLM 86
2.24 Surface density maps (H I, FUV, 3.6 μm, Hα) for DDO 187 87
2.25 Moment maps (integrated H I,velocity field, velocity dispersion) and the V–band optical image for DDO 187 88
2.26 Surface density maps (H I, FUV, 3.6 μm, Hα) for DDO 155 89

2.27 Moment maps (integrated H I,velocity field, velocity dispersion) and the V–band optical image for DDO 155 90
2.28 Surface density maps (H I, FUV, 3.6 μm, Hα) for DDO 165 91
2.29 Moment maps (integrated H I,velocity field, velocity dispersion) and the V–band optical image for DDO 165 92
2.30 Surface density maps (H I, FUV, 3.6 μm, Hα) for IC 1613 93
2.31 Moment maps (integrated H I,velocity field, velocity dispersion) and the V–band optical image for IC 1613 94
2.32 Surface density maps (H I, FUV, 3.6 μm, Hα) for DDO 63 95
2.33 Moment maps (integrated H I,velocity field, velocity dispersion) and the V–band optical image for DDO 63 96
2.34 Surface density maps (H I, FUV, 3.6 μm, Hα) for DDO 53 97
2.35 Moment maps (integrated H I,velocity field, velocity dispersion) and the V–band optical image for DDO 53 98
2.36 Surface density maps (H I, FUV, 3.6 μm, Hα) for DDO 75 99
2.37 Moment maps (integrated H I,velocity field, velocity dispersion) and the V–band optical image for DDO 75 100
2.38 Surface density maps (H I, FUV, 3.6 μm, Hα) for DDO 154 101
2.39 Moment maps (integrated H I,velocity field, velocity dispersion) and the V–band optical image for DDO 154 102
2.40 Surface density maps (H I, FUV, 3.6 μm, Hα) for DDO 69 103
2.41 Moment maps (integrated H I,velocity field, velocity dispersion) and the V–band optical image for DDO 69 104
2.42 Surface density maps (H I, FUV, 3.6 μm, Hα) for M81dwA 105
2.43 Moment maps (integrated H I,velocity field, velocity dispersion) and the V–band optical image for M81dwA 106
2.44 Surface density maps (H I, FUV, 3.6 μm, Hα) for DDO 210 107
2.45 Moment maps (integrated H I,velocity field, velocity dispersion) and the V–band optical image for DDO 210 108

3.1 Artist's Impression inspired by composites of the H I map as blue, FUV map as pink and V image as yellow for DDO 133 and DDO 168 109
3.2 Composites of the H I map as red, FUV map as green and V image as orange for DDO 133 and DDO 168 111
3.3 H I profiles for DDO 133 and DDO 168 112
3.4 Surface density maps (H I, FUV, 3.6 μm, Hα) for DDO 133 114

3.5 Moment maps (integrated H I,velocity field, velocity dispersion) and the V–band optical image for DDO 133 115

3.6 Integrated H I map (moment 0) with optical V–band contours for DDO 133 116

3.7 Integrated H I map (moment 0) with optical V–band contours for DDO 168 117

3.8 Surface density maps (H I, FUV, 3.6 μm, Hα) for DDO 168 118

3.9 Moment maps (integrated H I,velocity field, velocity dispersion) and the V–band optical image for DDO 168 119

3.10 Tilted–ring fit for DDO 133 121

3.11 Tilted–ring fit for DDO 168 123

3.12 SFRD derived from FUV+24 μm vs. SFRD based on FUV only and SFRD from Hα+24 μm vs. SFRD based on Hα for DDO 133 and DDO 168. The MW extinction law is used. Five different internal extinction corrections are considered 128

3.13 SFRD derived from FUV only and Hα only vs. H I surface density for DDO 133 and DDO 168 130

3.14 DDO 133. Density contours of the pixel by pixel distribution of: SFRD surface vs. H I surface density plotted separately for two different SF tracers FUV and Hα and SFE vs H I surface density and vs. stellar surface density (based on the 3.6 μm *Spitzer* map) for FUV as an SF tracer 131

3.15 DDO 168. Density contours of the pixel by pixel distribution of: SFRD surface vs. H I surface density plotted separately for two different SF tracers FUV and Hα and SFE vs H I surface density and vs. stellar surface density (based on the 3.6 μm *Spitzer* map) for FUV as an SF tracer 132

3.16 The effect of different inclination corrections applied to the SFRD vs. H I surface density plot 134

3.17 SFRD vs. H I surface density using three different resolutions for DDO 133 and DDO 168 136

3.18 The left and middle panel show the results published by Bigiel et al. (2010b) for spirals and dIrr galaxies, whereas in the right–most panel we attach our results for comparison: density contours of the pixel by pixel distribution of log SFRD vs. log H I surface density of DDO 133 and DDO 168 138
3.19 In DDO 133 we colour code based on the H I surface density of the region encompassed in one pixel and plot their position on the FUV, H I and Hα maps. Those same pixels are also plotted as SFRD vs. H I surface density, SFE vs. H I surface density, and SFRD vs. V–band surface brightness 140
3.20 Metallicity vs. H I maximum for DDO 133, DDO 168 and the THINGS dwarf sample (DDO 50, DDO 53, DDO 63, DDO 154, NGC 2366, NGC 4214, M81dwA) at 400 pc linear resolution 143
3.21 SFRD vs. optical V–band surface density and SFRD vs. H I surface density for DDO 133 (black) and DDO 168 (red). We also plot SFRD vs. optical and NIR surface densities for the same two galaxies 145

4.1 Skematic view of the transition from the atomic gas phase to the star formation phase 149
4.2 In the case of DDO 133 and NGC 4214 we present a comparison between the SFRD and the H I surface density plots, where the SFRD map is based on four different SF tracers 152
4.3 In the case of DDO 154 and DDO 53 we present a comparison between the SFRD and the H I surface density plots, where the SFRD map is based on four different SF tracers 153
4.4 Colour index E($B-V$) as a function of metallicity 155
4.5 DDO 168; SFRD vs. H I surface density and vs. V–band surface density and SFE vs. H I surface density and vs. stellar surface density. . . 160
4.6 DDO 133; SFRD vs. H I surface density and vs. V–band surface density and SFE vs. H I surface density and vs. stellar surface density. . . 161
4.7 NGC 4214; SFRD vs. H I surface density and vs. V–band surface density and SFE vs. H I surface density and vs. stellar surface density. . . 162
4.8 DDO 50; SFRD vs. H I surface density and vs. V–band surface density and SFE vs. H I surface density and vs. stellar surface density. 163
4.9 DDO 216; SFRD vs. H I surface density and vs. V–band surface density and SFE vs. H I surface density and vs. stellar surface density. . . 164

4.10 NGC 2366; SFRD vs. H I surface density and vs. V–band surface density and SFE vs. H I surface density and vs. stellar surface density. . . 165
4.11 WLM; SFRD vs. H I surface density and vs. V–band surface density and SFE vs. H I surface density and vs. stellar surface density. 166
4.12 DDO 187; SFRD vs. H I surface density and vs. V–band surface density and SFE vs. H I surface density and vs. stellar surface density. . . 167
4.13 DDO 155; SFRD vs. H I surface density and vs. V–band surface density and SFE vs. H I surface density and vs. stellar surface density. . . 168
4.14 DDO 165; SFRD vs. H I surface density and vs. V–band surface density and SFE vs. H I surface density and vs. stellar surface density. . . 169
4.15 IC 1613; SFRD vs. H I surface density and vs. V–band surface density and SFE vs. H I surface density and vs. stellar surface density. 170
4.16 DDO 63; SFRD vs. H I surface density and vs. V–band surface density and SFE vs. H I surface density and vs. stellar surface density. 171
4.17 DDO 53; SFRD vs. H I surface density and vs. V–band surface density and SFE vs. H I surface density and vs. stellar surface density. 172
4.18 DDO 75; SFRD vs. H I surface density and vs. V–band surface density and SFE vs. H I surface density and vs. stellar surface density. 173
4.19 DDO 154; SFRD vs. H I surface density and vs. V–band surface density and SFE vs. H I surface density and vs. stellar surface density. . . 174
4.20 DDO 69; SFRD vs. H I surface density and vs. V–band surface density and SFE vs. H I surface density and vs. stellar surface density. 175
4.21 M81dwA; SFRD vs. H I surface density and vs. V–band surface density and SFE vs. H I surface density and vs. stellar surface density. . . 176
4.22 DDO 210; SFRD vs. H I surface density and vs. V–band surface density and SFE vs. H I surface density and vs. stellar surface density. . . 177
4.23 We plot for each of our galaxies density contours of the pixel–by–pixel distribution of SFRD vs. H I surface density overlaid with their radial profile 179
4.24 All our galaxies with size dependent weights are plotted as density contours of the pixel–by–pixel distribution of SFRD vs. H I surface density and the SFE vs. H I surface density and vs. SFRD. 185
4.25 All our galaxies with equal weights are plotted as density contours of the pixel–by–pixel distribution of SFRD vs. H I surface density and the SFE vs. H I surface density and vs. SFRD. 186

4.26 First two panels, one for THINGS spirals and the other for THINGS dwarfs summarise the results of Bigiel et al. (2010b) whereas in the right–most panel we attach our results for comparison: density contours of the pixel–by–pixel distribution of log SFRD vs. log H I surface density of all galaxies in our subsample 187

4.27 We plot for all galaxies in our subsample, the Spearman correlation coefficient slope between SFRD and H I surface density vs. metallicity, H I mass and M_V 189

4.28 We plot for all galaxies in our subsample, the Spearman correlation coefficient between SFRD and H I surface density vs. log of the integrated SFR over area from FUV and Hα, vs. the molecular fraction and the neutral fraction 190

4.29 Predicted molecular mass related quantities as a function of metallicity 192

4.30 In all the galaxies in our sample, the pixels plotted in previous SFRD vs. H I surface density plots are shown as positions on their corresponding H I maps. 194

4.31 In DDO 133 we colour code based on the H I surface density of the region encompassed in one pixel and plot their position on the FUV, H I and Hα maps. Those same pixels are also plotted as SFRD vs. H I surface density, SFE vs. H I surface density, and SFRD vs. V–band surface brightness 195

4.32 In NGC 4214 we colour code based on the H I surface density of the region encompassed in one pixel and plot their position on the FUV, H I and Hα maps. Those same pixels are also plotted as SFRD vs. H I surface density, SFE vs. H I surface density, and SFRD vs. V–band surface brightness 196

4.33 In DDO 50 we colour code based on the H I surface density of the region encompassed in one pixel and plot their position on the FUV, H I and Hα maps. Those same pixels are also plotted as SFRD vs. H I surface density, SFE vs. H I surface density, and SFRD vs. V–band surface brightness 197

4.34 In IC 1613 we colour code based on the H I surface density of the region encompassed in one pixel and plot their position on the FUV, H I and Hα maps. Those same pixels are also plotted as SFRD vs. H I surface density, SFE vs. H I surface density, and SFRD vs. V–band surface brightness 198
4.35 In DDO 63 we colour code based on the H I surface density of the region encompassed in one pixel and plot their position on the FUV, H I and Hα maps. Those same pixels are also plotted as SFRD vs. H I surface density, SFE vs. H I surface density, and SFRD vs. V–band surface brightness 199
4.36 In DDO 75 we colour code based on the H I surface density of the region encompassed in one pixel and plot their position on the FUV, H I and Hα maps. Those same pixels are also plotted as SFRD vs. H I surface density, SFE vs. H I surface density, and SFRD vs. V–band surface brightness 200
4.37 H I maximum surface density as a function of metallicity, resolution . 203
4.38 H I maximum as a function of metallicity, when the inclination of the galaxies is varied with 10°, 15° or 20° 205
4.39 We present for each galaxy SFRD from FUV–only vs. SFRD based on Hα–only. 206
4.40 We present for three galaxies: NGC 4214, DDO 50 and NGC 2366, SFRD from FUV–only vs. SFRD based on Hα–only compared to SFRD from FUV+24 μm vs. SFRD based on Hα+24 μm. 207
4.41 We plot for all galaxies the ratio of the integrated star formation rates based on Hα and on FUV vs. the H I maximum and the ISRF and the ISRF vs. H I maximum and stellar mass. 209
4.42 We plot for each of our galaxy density contours of the pixel–by–pixel distribution of SFRD based on FUV–only vs. V–band surface density overlaid with their radial profiles 211
4.43 We show the fraction of V–band light contributed by stars formed in the past 10 Myrs and in the past 100 Myrs as a function of the amplitude of the current SFR relative to the average SFR over the lifetime of the galaxy (from Zhang, H., private communication). . . . 214
4.44 We present for each galaxy a scatter plot of V–band and 3.6 μm surface densities vs. SFRD. 217

4.45 All our galaxies, with size dependent weights, are plotted as density contours of the pixel–by–pixel distribution of SFRD vs. stellar surface density and vs. V–band surface density and SFE vs. stellar surface density. 220

4.46 We show for all galaxies with FUV data available the radial profiles in both the SFRD (based on FUV–only) and the V–band surface density maps by comparison with the density contours of the pixel–by–pixel distribution of SFRD vs. V–band surface density. 221

4.47 We plot for all galaxies in our subsample, the Spearman correlation coefficient and the linear fit slope (N) between SFRD and V–band surface density vs. metallicity, H I mass and M_V 222

4.48 We present for each galaxy a scatter plot of the average pressure within the resolution element vs. SFRD. 225

4.49 All our galaxies, with size dependent weights, are plotted as density contours of the pixel–by–pixel distribution of the average pressure vs. SFRD and SFE. 229

4.50 We present for each galaxy a scatter plot of the average pressure within the resolution element vs. V–band surface density. 230

4.51 We plot for all galaxies in our subsample, the linear fit slope (N) between average pressure per resolution element and SFRD vs. metallicity, stellar mass, H I mass and molecular mass. We also compare the index value N of the pressure–SFRD relation with the index values N of the V–band surface density–SFRD relation and of the H I surface density–SFRD relation. 233

A.1 DDO 168. Channel maps based on the robust weighted cube (Resolution: $7\farcs8 \times 5\farcs8$, σ= 6.8 K). The grey scale range is: 0-150.3 K (0 - 11.3 mJy beam^{-1}). All emission channels are shown. The beam is indicated in the bottom left corner of the top left panel. 265

A.2 DDO 133. Channel maps based on the robust weighted cube (Resolution: $12\farcs4 \times 10\farcs8$, σ= 1.7 K). The grey scale range is: 0-51.6 K (0 - 11.3 mJy beam^{-1}). All emission channels are shown. The beam is indicated in the bottom left corner of the top left panel. 267

A.3 NGC 4214. Channel maps based on the robust weighted cube (Resolution: 7.″6 × 6.″4, σ= 9.1 K). The grey scale range is: 0-94.4 K (0 - 7.6 mJy beam^{-1}). All emission channels are shown. The beam is indicated in the bottom left corner of the top left panel. 269

A.4 DDO 50. Channel maps based on the robust weighted cube (Resolution: 7.″0 × 6.″1, σ= 15.2 K). The grey scale range is: 0-132.2 K (0 - 9.3 mJy beam^{-1}). All emission channels are shown. The beam is indicated in the bottom left corner of the top left panel. 271

A.5 DDO 216. Channel maps based on the robust weighted cube (Resolution: 16.″2 × 15.″4, σ= 2.3 K). The grey scale range is: 0-61.1 K (0 - 25.2 mJy beam^{-1}). All emission channels are shown. The beam is indicated in the bottom left corner of the top left panel. 273

A.6 NGC 2366. Channel maps based on the robust weighted cube (Resolution: 6.″9 × 5.″9, σ= 9.4 K). The grey scale range is: 0-135.2 K (0 - 9.1 mJy beam^{-1}). All emission channels are shown. The beam is indicated in the bottom left corner of the top left panel. 275

A.7 WLM. Channel maps based on the robust weighted cube (Resolution: 7.″6 × 5.″1, σ= 12.8 K). The grey scale range is: 0-147.9 K (0 - 9.5 mJy beam^{-1}). All emission channels are shown. The beam is indicated in the bottom left corner of the top left panel. 277

A.8 DDO 187. Channel maps based on the robust weighted cube (Resolution: 6.″2 × 5.″5, σ= 11.0 K). The grey scale range is: 0-104.5 K (0 - 5.879 mJy beam^{-1}). All emission channels are shown. The beam is indicated in the bottom left corner of the top left panel. 279

A.9 DDO 155. Channel maps based on the robust weighted cube (Resolution: 11.″3 × 10.″1, σ= 3.5 K). The grey scale range is: 0-57.8 K (0 - 10.9 mJy beam^{-1}). All emission channels are shown. The beam is indicated in the bottom left corner of the top left panel. 280

A.10 DDO 165. Channel maps based on the robust weighted cube (Resolution: 10.″0 × 7.″6, σ= 5.1 K). The grey scale range is: 0-61.3 K (0 - 7.686 mJy beam^{-1}). All emission channels are shown. The beam is indicated in the bottom left corner of the top left panel. 282

A.11 IC 1613. Channel maps based on the robust weighted cube (Resolution: 7.″7 × 6.″5, σ= 4.5 K). The grey scale range is: 0-124.5 K (0 - 10.3 mJy beam^{-1}). All emission channels are shown. The beam is indicated in the bottom left corner of the top left panel. 284
A.12 DDO 63. Channel maps based on the robust weighted cube (Resolution: 7.″8 × 6.″0, σ= 15.4 K). The grey scale range is: 0-91.8 K (0 - 7.1 mJy beam^{-1}). All emission channels are shown. The beam is indicated in the bottom left corner of the top left panel. 285
A.13 DDO 53. Channel maps based on the robust weighted cube (Resolution: 6.″3 × 5.″7, σ= 10.1 K). The grey scale range is: 0-104.5 K (0 - 6.2 mJy beam^{-1}). All emission channels are shown. The beam is indicated in the bottom left corner of the top left panel. 286
A.14 DDO 75. Channel maps based on the robust weighted cube (Resolution: 7.″6 × 6.″5, σ= 6.3 K). The grey scale range is: 0-146.3 K (0 - 11.9 mJy beam^{-1}). All emission channels are shown. The beam is indicated in the bottom left corner of the top left panel. 287
A.15 DDO 154. Channel maps based on the robust weighted cube (Resolution: 7.″9 × 6.″3, σ= 6.6 K). The grey scale range is: 0-81.1 K (0 - 6.7 mJy beam^{-1}). All emission channels are shown. The beam is indicated in the bottom left corner of the top left panel. 289
A.16 DDO 69. Channel maps based on the robust weighted cube (Resolution: 5.″8 × 5.″4, σ= 12.8 K). The grey scale range is: 0-167.2 K (0 - 8.6 mJy beam^{-1}). All emission channels are shown. The beam is indicated in the bottom left corner of the top left panel. 291
A.17 M81dwA. Channel maps based on the robust weighted cube (Resolution: 7.″8 × 6.″3, σ= 10.4 K). The grey scale range is: 0-63.9 K (0 - 5.2 mJy beam^{-1}). All emission channels are shown. The beam is indicated in the bottom left corner of the top left panel. 292
A.18 DDO 210. Channel maps based on the robust weighted cube (Resolution: 11.″7 × 8.″6, σ= 5.2 K). The grey scale range is: 0-70.2 K (0 - 11.7 mJy beam^{-1}). All emission channels are shown. The beam is indicated in the bottom left corner of the top left panel. 293

B.1 SFRD derived from FUV+24 μm vs. SFRD based on FUV only for all galaxies in our subsample. Two different extinction laws and 5 different internal extinction corrections are considered 296

List of Tables

2.1 General properties of the chosen subsample 36
2.2 Ancillary Data Observation Settings for the chosen subsample 39
2.3 H I observations settings in all arrays for all galaxies in the subsample 46
2.4 Map characteristics for the chosen subsample 67

3.1 Important quantities on DDO 133 and DDO 168 (I) 147
3.2 Important quantities on DDO 133 and DDO 168 (II) 148

4.1 Important quantities for each galaxy in our subsample 157
4.2 We give for each galaxy in our sample the linear fit parameters , rms scatter and the Spearman rank coefficient of the SFRD–H I surface density distribution, where the considered SFR map uses both FUV and Hα–only as SF tracers 183
4.3 We give for each of the six galaxies showing resolved H I shells the linear fit parameters and the Spearman rank coefficient of the SFRD–H I surface density distribution before and after excluding the points that constitute the feature. 201
4.4 We give for each galaxy in our sample observed in FUV the linear fit parameters, the rms scatter and the Spearman rank coefficient of the SFRD–V–band surface density distribution, where the considered SFR map uses both FUV and Hα–only as SF tracers. 216
4.5 We give for each galaxy in our sample observed in FUV the linear fit parameters, the rms scatter and the Spearman rank coefficient of the SFRD–P_h average pressure per resolution element, where the considered SFR map uses both FUV and Hα–only as SF tracers. . . 228

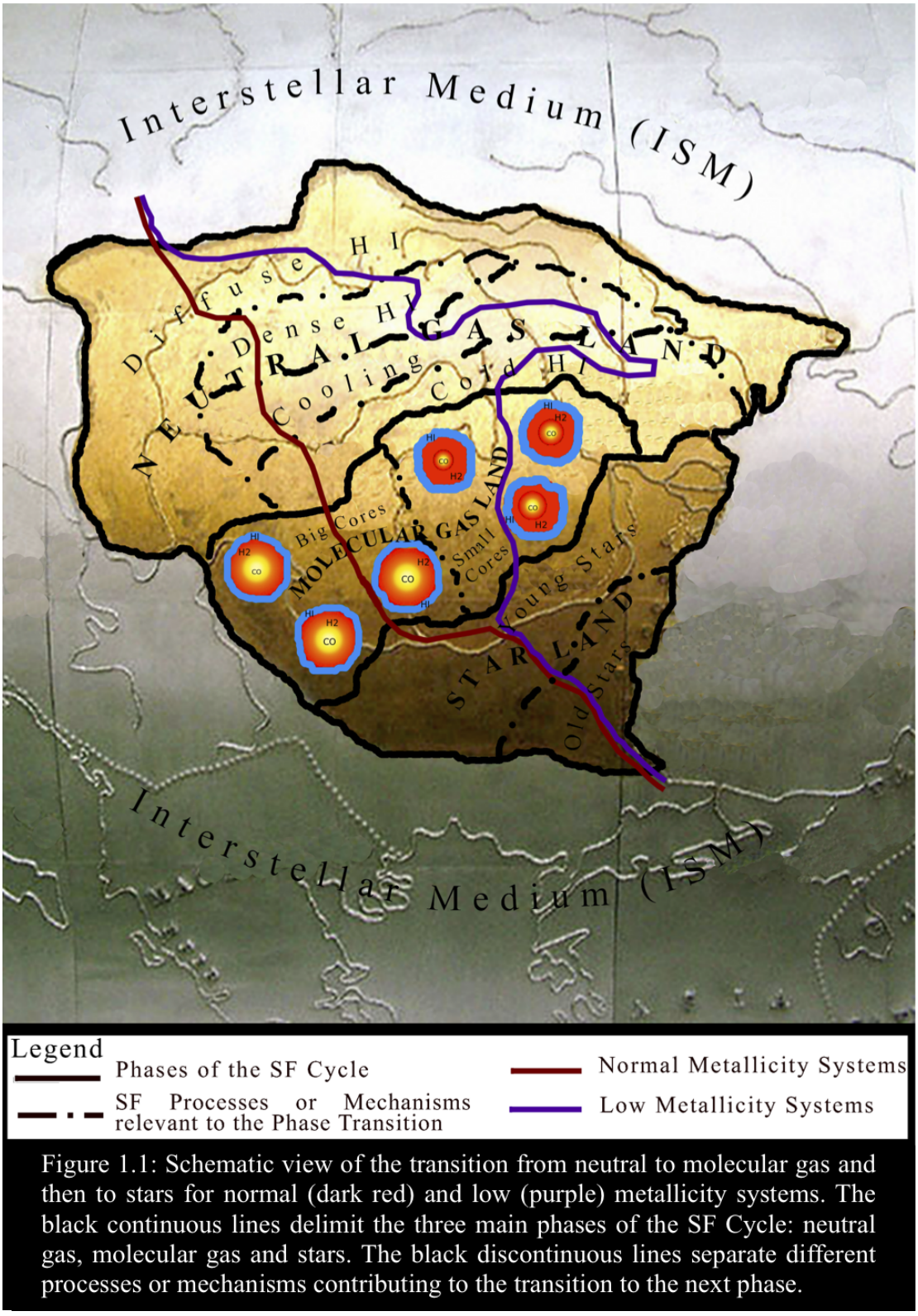

Figure 1.1: Schematic view of the transition from neutral to molecular gas and then to stars for normal (dark red) and low (purple) metallicity systems. The black continuous lines delimit the three main phases of the SF Cycle: neutral gas, molecular gas and stars. The black discontinuous lines separate different processes or mechanisms contributing to the transition to the next phase.

Chapter 1
INTRODUCTION

The architecture of the universe is put in perspective by starlight. This light is propagating through time and space revealing the intricate, yet wonderful, but ever elusive design of the universe. And here we are with our telescopes, our observations, our models and theories, our questions and answers chasing after more whys and hows, striving for the beatitude of understanding how it all came to be. In the end, however, we settle with the answer to a handful of our questions acknowledging that in its greatness the universe seems to always be one question ahead.

We believe that the universe began with The Big Bang. In just one second from the time of the Big Bang, as its temperature was dropping down the universe went through the Planck Epoch where quarks formed and after a period of rapid inflation the Electro Magnetic and Weak Nuclear forces became differentiated and the Particle Cosmology Epoch began where new fundamental particles such as leptons formed and quarks combined to form baryons and mesons. In four minutes from the birth of the universe the light atomic nuclei: hydrogen (one proton), deuterium (one proton and one neutron), helium (two protons and two neutrons), and lithium had already been formed in the Nucleosynthesis phase. Another 3000 years and another drop in temperature (from 10^9 K to 10^5 K) and the universe switched from being radiation dominated to being matter dominated.

Only when the universe was at the age of 380,000 years and a temperature of 3000 K the electrons could no longer overcome the attractive force of atomic nuclei and as they became bound to atoms, the universe became transparent to electromagnetic radiation. The light was set free. This "recombination" process gave rise to the "first light" that reached us in the form of the Cosmic Microwave Background Radiation. Our observations of the Cosmic Microwave Background

(CMB) radiation support the current standard model of cosmology, the Λ Cold Dark Matter (ΛCDM) model (Springel et al., 2006).

Ironically enough, the "first light" set the beginning of the Dark Ages, the period between the time of the emission of the cosmic microwave back–ground radiation and the time when the first stars formed and the evolution of structure based on gravitational collapse of objects started. During the Dark Ages the first molecules of H_2, HD, and LiH formed (Miralda-Escudé, 2003) and most of the existing matter got organised into small dark halos (White & Rees, 1978) and it was inside these halos that the first stars at a redshift of 50 formed and started giving light (Springel et al., 2006). By redshift 15 there were enough first stars to begin a new phase in the life of our universe: reionization. Reionization, known to finish around a redshift of 6, is marking the turnover from a mostly neutral universe to an ionized one, but also encompasses a world of information about the first sources of light in our universe and the star formation mechanisms of its early history.

Theoretically, it is believed that the first stars formed from zero metallicity gas and acted as catalysts in further star formation episodes inside the halo that was hosting them, but also in neighbouring halos (Ricotti et al., 2008). This explains why the first galaxies formed preferentially in chain–like structures, similar to young star clusters at low redshift. In the centre of the dark matter haloes, the gas condensed and cooled and when it reached a sufficiently high density it started to fragment into stars and further gave birth to the first galaxies. The first galaxies were low mass systems, 10^6 times smaller than the Milky Way. Most of their haloes would have merged by now in the larger scale build up (White & Rees, 1978). As the haloes became organised into larger systems and started populating the "cosmic web", groups and clusters of galaxies form. According to White & Rees (1978), as the haloes of the first galaxies became disrupted and merged into larger structures, the residual gas cooled and collapsed forming large central galaxies, explaining in this way the existence of small satellites around big galaxies.

In this scheme of things at least some of the small satellite galaxies (dwarf galaxies) that we see today, sitting inside their cold dark matter haloes may in fact be primordial galaxies. Our knowledge of the history of our universe brings forth the topic of dwarf galaxies as holding essential information not only in confirming our understanding of the present, but also in increasing our knowledge of the past without having to look any further than our own back yard. Dwarfs are the most common type of galaxies, apparently simple, yet with complex star formation histories and

even more exotic star formation mechanisms (Mateo, 1998). Their importance goes beyond solving the dark matter problem. They are able to provide clues on mechanisms acting in low metallicity environments, new constraints on the relationship and interaction models between dwarfs and normal galaxies and last but not least evidence on the structural evolution that enabled the variety of dwarf galaxies we observe today and the possible evolutionary links between them.

1.1 Dwarf Irregular Galaxies

The mystery of the "first star light" is carried through time and space by photons trying to reach us from the Dark Ages and through the reionization. Until they do, there is a treasure of knowledge waiting to be revealed in galaxies still holding on to their "old ways" and forming stars from low metallicity gas just as the first stars in the universe used to. To study the "old ways", the star formation mechanisms at play in low metallicity environments, we focus on dwarf irregular galaxies, where stars still form with only a little (if any at all) aid from metals.

Dwarf galaxies with a mass around 10^6 solar masses and about 1 kpc in size (see Fig. 1.2) can be classified just like the normal galaxies, into ellipticals, spheroidals, spirals and irregulars (Mateo, 1998). They cover a mass range up to that of the Large Magellanic Cloud (LMC) with a size of 8.9 kpc and a mass of $(8.7 \pm 4.3) \times 10^9$ $M_\odot$ (van der Marel et al., 2002).

Gnedin & Kravtsov (2006) suggest that all luminous satellites formed a few stars before reionization, but only the galaxies massive enough (dwarf irregular and dwarf spheroidal types) managed to keep their gas and continue to form stars, while others (fossil dwarf spheroidal galaxies) lost their gas during the epoch of reionization and kept only their, by now, old stellar populations. Other authors, however, suggest that according to observations and theoretical calculations there should be two groups of dwarf galaxies: primordial and tidal dwarf galaxies, easily distinguishable based on their cold dark matter content (Kroupa, 2012). In a follow-up paper Dabringhausen & Kroupa (2013) find that even for a group such as dwarf spheroidals, their properties are best explained as ancient tidal dwarf galaxies rather than primordial dwarfs, raising a question mark to the validity of the ΛCDM model itself. In truth, the ΛCDM model does predict more satellite galaxies than we observe, however there are strong indications that besides the low-mass luminous satellites, dark satellites may also exist even in our Local Group (Simon et al., 2004).

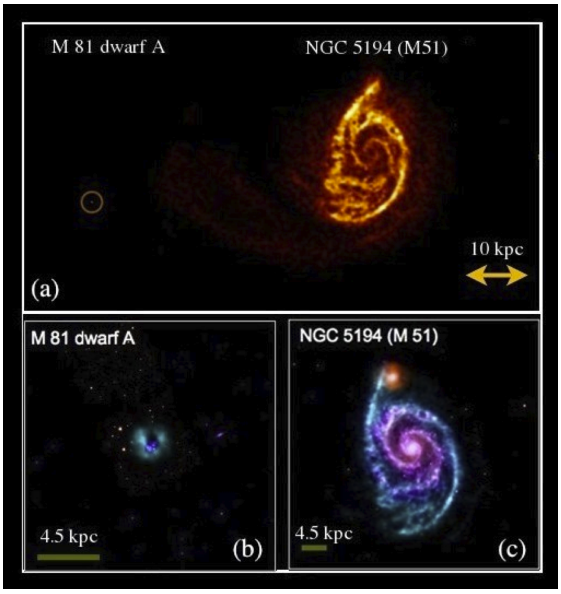

Figure 1.2: We show for comparison the dwarf irregular galaxy M81dwA and the spiral galaxy NGC 5194 (M 51). In panel (a) of this figure we present the H I distribution of the two galaxies at the same linear scale of 10 pc. The image credit for panel (a) goes to Walter et al. (2008). In panels (b) and (c) we show colour coded images of the two galaxies: blue for the atomic hydrogen, orange for the old stars observed with *Spitzer* and magenta for star formation observed with *GALEX* and *Spitzer*. The image credit for panels (b) and (c) goes to Gil de Paz et al. (2007); Kennicutt et al. (2003); Walter et al. (2008) and the scale is given in the bottom left corner of each panel (4.5 pc).

Different types of irregular galaxies share amongst each other properties such as stunted or no spiral arms, no shear motions, slow rotations, low metallicity and large H I content (Hunter et al., 1982; Hunter & Gallagher, 1985b). Irregular galaxies in general, and implicitly dwarf irregulars, are bluer than spirals (Hunter et al., 1982). Morphological peculiarities indicative of past interactions are observed in about one third of them, while 23% of them host stellar bars, which tend to be larger relative to their host galaxy size than in spiral galaxies, at times off–centre and occupying most of the optical disk (de Vaucouleurs & Freeman, 1972; Hunter & Elmegreen, 2006). Dark matter contributes a higher fraction of the total disk mass in irregular galaxies than in spirals (Côté et al., 2000, 1997; Swaters et al., 2011), enhancing in this way the disk instability and allowing the formation of cool H I (Hunter et al., 1998). The lack of spiral arms does not hinder the effectiveness of star formation, hence the wide range of star formation rates observed in these galaxies (Hunter et al., 1982). Due to the low level of shear motions, holes created by massive stars in the ISM will persist longer and implicitly the smoothing of gas will take longer

than in spirals (Bagetakos et al., 2011; Hunter et al., 1998).

Gallagher & Hunter (1984) find that dwarf irregulars, optically tiny galaxies (see Fig. 1.2), show features such as "disconnected blotches of light or plume like features". Some show no rotational motion making any inclination estimation very difficult and have distinct H II regions smaller than those in giant irregulars (according to Gallagher & Hunter (1984); Hunter & Gallagher (1985b) irregular galaxies above a certain surface brightness) suggesting the existence of fewer O stars. They also find that the process of star formation is slower in dwarf irregular galaxies taking of order 10 Hubble times to deplete the current gas supply at the current SFR, ignoring any return of material to the ISM or fresh material falling in (cold flow). In a follow up paper Hunter et al. (1998) suggest that the slowness of the star formation process in dwarf irregulars could be linked to stellar feedback, in other words injecting energy in the interstellar medium enables cloud formation for future star formation events. The longer the star formation cycles, the more pristine and abundant their gas reservoir destined to contribute to future generations of stars, which allows us to observe the star formation mechanisms today in low metallicity environments as they might have been at high redshift.

1.2 Star Formation

It took 400 million years until the birth of the first stars, and for billions of years since, the universe has been continuously forming stars. The neutral gas turns molecular, out of the molecular gas stars form, then stars die and release back into the interstellar medium gas and metals destined to contribute to the life of the following generations of stars. Looking at the small scale star formation mechanisms, one gets the impression that star formation is a complex but very exact process (see Section 1.2.1), yet when looking at larger scales no universal law seems to explain the amazing structural diversity of our universe (see Sections 1.2.2 to 1.2.4). Star formation happens everywhere in the universe, in big spiral galaxies and in small irregular dwarf galaxies, in high and low metallicity gas, in the centre and the outskirts of galaxies. What regulates the star formation process? What law dictates what fraction of the neutral gas will become molecular? Why do stars form where they do? Is star formation self-propagating or does it need an external trigger? Is there a universal star formation law? How does metallicity influence this law? These are just a few of the multitude of star formation related questions still left to be

answered.

1.2.1 How do stars form?

In our Galaxy, observations have shown that stars form from molecular clouds in the interstellar medium. That is why the story of how stars form starts in the interstellar medium, with the transition from the neutral to the molecular medium.

In a large mass of atomic hydrogen two components of very different properties naturally coexist: the warm neutral medium and the cold neutral medium. The warm neutral medium (WNM) with a density of about $0.5\,\mathrm{cm}^{-3}$ and a temperature of $8\times10^3\,K$ is not confined to individual clouds and it has a scale height twice that of the cold neutral medium (CNM) component (Burton et al., 1992). This cold component of the atomic hydrogen is manifested in H I clouds with densities between 10 and $100\,\mathrm{cm}^{-3}$, diameters between 1 and 100 pc and a representative temperature of 80 K. These H I clouds are long lived due to the pressure balance between the confining effect of the warm neutral medium surrounding the cloud and the dispersion by internal thermal motions inside the cloud (Cox & Smith, 1974; McKee & Ostriker, 1977). These cold H I clouds are the parents of molecular clouds.

Ever since the first molecules were observed in diffuse clouds, it has been a challenge to explain the chemistry involved in turning atoms into molecules. If the temperature and density are high enough and the neutral gas is ionized enough to contain some free electrons, the combination of neutral atoms with available electrons, or protons for that matter, can lead to molecular hydrogen formation (Hartquist & Williams, 1995; van Dishoeck & Blake, 1998). A small fraction of the first stars have indeed formed from low temperature, zero metallicity gas clouds, where the molecular hydrogen formation is catalysed by the H^- ion, (Ricotti et al., 2008). This mechanism must have played a key role in the formation of the first stars, but presently a different mechanism is at play. With continuing star formation throughout the life of the universe, the proliferation of metals has opened up a new avenue for molecular hydrogen formation, where two neutral hydrogen atoms can combine on the surface of a dust grain which absorbs the energy released by the atoms in the process without a significant rise in temperature (Hollenbach & Salpeter, 1971). The H_2 molecule is the only one that forms in this way; the formation of other molecules is based on different reactions (the ion–molecule reaction), see Hartquist & Williams (1995); van Dishoeck & Blake (1998).

Cold H I clouds become molecular from the inside out (Goldsmith, 2007). There-

fore, inside the cold H I cloud H_2 molecule formation begins first using the H^- ion as a catalyst until all available electrons are exhausted and then using dust as a catalyst. However no pure H_2 cloud can exist, because all the molecules near the surface are dissociated by ultraviolet photons of 11.2 eV or higher. Therefore even when the whole cloud would have left the neutral phase and joined the molecular phase, where it is known as a Giant Molecular Cloud (GMC), it will still have an atomic envelope. The transition from cold neutral gas to molecular gas implies a drop in temperature from 80 K to 10 K, which can only be achieved through a balance between the heating and cooling mechanisms at play in the molecular environment. The main heating contributors are interstellar cosmic rays and photons (coming from both the diffuse stellar background and the X–rays from pre–main sequence stars), see Glassgold & Langer (1973) and Glassgold et al. (2012) for more details. Cooling on the other hand is achieved mainly through CO trapping, but also through emission of infrared photons mainly from the 63 μm line of [O I] and the 158 μm line of [C II] (Neufeld et al., 1995) and collisional energy transfers from the gas to the dust grains.

Through cooling mechanisms both hydrogen and carbon atoms are turned into molecules. Yet, as long as they are unshielded these molecules will dissociate back into their component atoms under the influence of the heating mechanisms also at play. Shielding the cloud from further dissociation takes place when both the newly formed H_2 molecules and the dust grains present in the cloud will absorb the incoming ultraviolet photons. Consequently these H_2 molecules, the ones involved in the shielding process, will dissociate and the dust will emit at far–infrared (FIR) wavelengths. It is at this depth into the cloud, where the H_2 self-shielding (Hollenbach et al., 1971) mechanism is activated, that the atomic envelope ends and the molecular interior begins.

The self-shielding mechanism active inside the condensing medium of a Giant Molecular Cloud could have induced a degree of clumping inside the gas, where certain regions with higher density (10^3 cm^{-3}) and lower temperatures are surrounded by lower density gas, partly molecular and partly atomic. Morphologically mainly from observations of CO isotopologues we know that a GMC can have either one or more molecular clumps in its composition. One molecular clump is known as an Individual Dark Cloud, while the distribution of multiple molecular clumps is known as a Dark Cloud complex. Both structures have the same temperature of 10 K, however the individual dark cloud has a higher density and a lower mass and

size (Blitz, 1993). Inside the dark clouds we have ten times denser regions called the dense cores (Myers, 1995). It is within these dense cores that the star formation actually takes place. Some of the dense cores we observe via the radio lines of molecules such as NH_3, $^{12}C^{18}O$ and CS and they do have point like infrared sources in their centres, representing their stellar counterparts.

At the centre of a gravitationally collapsing (Bonnor, 1956; Ebert, 1955) dense core a protostar is formed (Bodenheimer & Sweigart, 1968; Shu, 1977) and its mass accretion rate is set by the parent cloud temperature (Boss, 1987). The accretion luminosity while high enough to be optically observed is obstructed by the dust envelope and re–emitted in the infrared. The shock generated by the cloud matter impacting the protostar surface, indirectly ignites deuterium (Stahler, 1988) and turns on convection. In an intermediate–mass protostar the convection will stop, while the deuterium will continue to burn in an inner shell and if accretion continues eventually the ordinary hydrogen will ignite as well (Palla & Stahler, 1991). Although it was believed that a massive star, such as an O or B star cannot form in this manner, but rather arises from the merger of dense cores and previously formed stars, the recent discovery of the massive protostar G35.20-0.74 with SOFIA-FORCAST suggests a unified star formation model after all, for both low– and high–mass stars (Zhang et al., 2013).

1.2.1.1 The Physics of Star Formation

Physically, for star formation to occur gravity has to overcome the resistance of pressure. In the simplest scenario, a nonrotating and unmagnetized cloud of gas is stable against the internal gas pressure of the cloud, as long as the pressure support is sufficient to counterbalance the force of gravity. The British physicist Sir James Jeans, who first considered the scenario of gravitational collapse within a gaseous cloud (Jeans, 1902), showed that, under appropriate conditions, a cloud or part of one would become unstable and begin to collapse for length scale

$$\lambda > \lambda_J \equiv \frac{2\pi}{k_J} = \left(\frac{\pi {c_s}^2}{G\rho_0}\right)^{1/2} \tag{1.1}$$

where ${k_J}^2 \equiv (4\pi G\rho_0)/{c_s}^2$, c_s is the sound speed, G is the gravitational constant and ρ_0 is the initially stationary gas density. The inequality 1.1 is known as **Jeans instability**.

In other words, the gas cloud is stable and gravitational collapse is impeded for

a sufficiently small mass (at a given temperature and radius), known as the Jeans mass:

$$M_J \equiv \frac{4\pi}{3}\rho_0 \left(\frac{\lambda_J}{2}\right)^3 \tag{1.2}$$

However, in deriving the above equations, it has been assumed not only that the cloud is an initial uniform, stationary gas but also that it has vertical gravity equal to zero ($\nabla\phi_0 = 0$). The latter assumption is unphysical, as it implies that $\nabla^2\phi_0 = 0$ and hence $\rho_0 = 0$ so the medium under discussion is a vacuum (Binney & Tremaine, 2008). Still for finite systems, such as molecular clouds, the instability criteria given by more rigorous analyses and the Jeans instability above are close.

Apart from the thermal pressure defined by kinetic theory as the force exerted by molecules or atoms impacting the walls of a container, an additional stabilising force to be considered against the gravitational collapse is the shear force (Safronov, 1960; Toomre, 1964). Hence in the case of a differentially rotating gaseous disk the stability of the disk is given by the **Toomre criterion**, expressed as:

$$\frac{c_s\Omega}{\pi G\Sigma} > 1 \tag{1.3}$$

where c_s is the speed of sound (and measure of the thermal pressure), Ω is the orbital frequency, G is the gravitational constant and Σ is the surface density of the disk.

Because dwarf galaxies are solid body rotators and show no shear forces, the GMCs in these galaxies concentrate into a gravitationally bound system, dense and unique, very likely the precursors of super–star clusters (Weidner et al., 2011). Thus, in the case of dwarf galaxies, the differential rotation is not likely to intervene in achieving the gravitational collapse but magnetic pressure might. If, like Parker (1966), we consider the case of a plane–parallel system with a magnetic field, apart from the gas pressure, we will have to also take in account the magnetic pressure due to the magnetic field and the cosmic ray pressure, due to the cosmic rays "tied" to the magnetic field lines. Parker (1966) finds that perturbing the magnetic field lines in a region, it can have the effect of removing the magnetic and cosmic ray pressure support in that region and thus creating a gravitational instability. This type of instability is known as the **Parker instability**.

Once gravity overcomes pressure, through gravitational collapse the molecular cloud starts clumping, dense cores form inside it and these cores will be able to further collapse into stars only if they have a mass bigger than the **Bonnor–Ebert**

mass, they manage to reduce their magnetic flux by a factor of 3 and are able to lose nearly all of their angular momentum (Draine, 2011). The **Bonnor–Ebert mass** defines the maximum core mass that can be in equilibrium for a given pressure (Bonnor, 1956; Ebert, 1955) and it differs from the Jeans mass by a factor of 1.18 ($M_{BE} \approx 1.18 M_J$). Observations have shown that the magnetic flux of a molecular cloud is much higher than the flux of a young star (Johns-Krull, 2007), which suggests that when cores collapse into stars, they reduce their magnetic flux, most probably through **ambipolar diffusion**. Last but not least the loss of angular momentum can be achieved through two mechanisms: **gravitational torques and magnetic torques**. These dynamical processes remove angular momentum from the inner parts to the outer parts of the clump which now becomes a rotationally supported disk, allowing in this way transfer of matter to the growing star (Draine, 2011). The nuclear fusion will begin within the newly formed star when the central density of the star and its temperature become high enough. From this moment on, with the release of nuclear energy, radiation moving away from the star, exerts a force on atoms, molecules or dust particles, giving birth to radiation pressure. It is this radiation pressure which will now balance out the force of gravity and prevent the star from further gravitational collapse.

1.2.2 Star Formation at larger scales

Star formation is also a global galactic process. Global processes govern the formation of the molecular clouds, for example. Therefore when talking about star formation, apart from understanding how one Individual Dark Cloud or a Dark Cloud complex forms stars, we also need to understand how global the star formation process really is: how many stars form, where do they form, why do they form there and not at some other location and in which way is this star formation process imprinted in the very fabric of our universe. Suddenly the perspective changes and we find ourselves looking at star formation on an individual galaxy level. It is this perspective that makes the subject of this thesis.

1.2.2.1 Neutral Gas and its transition towards the molecular phase

The molecular clouds that form stars form themselves out of neutral hydrogen clouds. Although indirectly, the neutral gas is fuelling the star formation phenomenon. Therefore understanding the transition from neutral to molecular is es-

sential in finding a correlation between gas and star formation, especially in low metallicity environments where the molecular gas becomes difficult to observe.

Abundance of neutral hydrogen is necessary when it comes to star formation, as suggested by the spatial correlation between H I and FUV emissions (Bigiel et al., 2010a). Bigiel et al. (2010a) also find that the large H I reservoir in the outskirts of M 83 is unlikely to be entirely consumed by in situ star formation. In other words neutral hydrogen is necessary but not sufficient for the star forming process. To trace the neutral hydrogen gas we make use of the hydrogen line transition at 21.1 cm (Ewen & Purcell, 1951; van de Hulst, 1945), which is directly proportional to the H I column density. The 21.1 cm transition is due to the hyperfine splitting of the energy levels of the H atom in the ground state. When the spins of the electron and proton change from parallel to anti-parallel, a photon with a wavelength of 21.1 cm is emitted. Although an average of 1×10^7 yr passes between emission events, the large number of available hydrogen atoms produce enough radio signal at 21.1 cm to be detectable (Burton et al., 1992).

Part of the available atomic gas turns molecular. What determines the amount of atomic gas to be turned molecular and what mechanism regulates it are questions dealt with in Section 1.2.2.2 on the molecular gas fraction. In the spiral galaxy M 51, Schuster et al. (2007) find that the ratio between the molecular and the atomic gas surface densities are related with the galactic radius through a power law of index number N=1.5. This relation breaks down at large radii, beyond 6 kpc.

Leroy et al. (2006) argue that the molecular gas fraction is well predicted by pressure, important in enabling the H_2 formation from H I. Since stars play an important role in driving pressure, the Leroy et al. (2006) result sets the stage for the more recent result of Rahman et al. (2012) suggesting that the molecular gas fraction is affected by the stellar potential well, although it cannot influence in any way the rate at which the molecular gas is converted into stars. Pelupessy & Papadopoulos (2009) have incorporated the molecular gas phase in their numerical simulations and find good agreement between their model and observations confirming that the molecular fraction depends on metallicity. Gnedin & Kravtsov (2011) using cosmological simulations conclude that the molecular gas fraction depends on the dust to gas ratio and far ultraviolet (FUV) radiation flux. In other words, the lower the metallicity the lower the dust quantity and hence the dust to gas ratio and the molecular gas fraction since the molecular hydrogen formation mechanism uses dust as a catalyst.

Thus the mechanism involved in turning neutral gas into molecular gas differs based on environment type and implicitly on galaxy type. For more details see Section 1.2.3.

1.2.2.2 Molecular Gas Phase

An in depth knowledge of the properties of GMCs is essential in order to be able to observe star formation at large scales. Bolatto et al. (2008) found GMCs from a wide range of environments are very similar to the ones in our Galaxy: gravitationally bound structures with typical sizes of around 40 pc and a mean surface density of $\approx 1.5 \times 10^{22}\,\mathrm{cm}^{-2}$. Resolution allows us to observe individual GMCs only in our own Galaxy or in very nearby objects. So, to investigate how star formation proceeds in other galaxies we extract from the knowledge we gained from our own Galaxy the signatures that can be seen at low resolution.

Molecular hydrogen, H_2, although it constitutes the largest component of the total molecular gas mass, cannot be traced directly. The H_2 molecule has the smallest moment of inertia, lacks a permanent electric dipole moment and its lowest excited energy levels corresponding to molecular rotation are very difficult to populate. To directly detect it, H_2 has to be observed in environments much warmer than those encountered in GMCs such as clouds shocked by stellar wind. In order to map the molecular gas, observations rely on the detection of CO (Wilson et al., 1970), always present in the molecular interior of the cloud as cores inside an H_2 envelope. The CO molecule is known to have the following isotopologues: $^{12}C^{16}O$, $^{13}C^{16}O$, $^{12}C^{17}O$ and $^{13}C^{18}O$. Inside a molecular core, among the mentioned isotopologues the most abundant one is the CO(1–0) transition of the $^{12}C^{16}O$ isotopologue which corresponds to an emitted photon wavelength of 2.60 mm.

In a spiral galaxy such as NGC 6946, in the central part of the galaxy the total gas surface density is dominated by molecular gas (Crosthwaite & Turner, 2007). Further, outside the nuclear region, the CO emission peaks coincide with high density peaks in H I , Hα and FIR. The correlation between CO and FIR luminosities is a consequence of the fact that the FIR luminosity is dust-reprocessed light coming from young stars that have recently formed out of the molecular gas traced by CO (Leroy et al., 2005).

Unlike the 21 cm emission with respect to the H I column density, the CO luminosity proportionality to the molecular gas surface density depends on local conditions, hence the uncertainties in the CO–to–H_2 conversion factor, also known as the

X_{CO} factor to estimate the molecular H_2 gas mass based on the CO emission. The Galactic X_{CO} factor is $2 \times 10^{20}\,\mathrm{cm^{-2}}$ ($\mathrm{K\,km\,s^{-1}}$). However, the Galactic conversion factor will give correct results only for galaxies which have the same size CO cores as our own galaxy (Bolatto et al., 2008).

Because the dust surface density is spatially correlated with the atomic and molecular gas (Roman-Duval et al., 2010), dust can also be used as a molecular gas tracer. Leroy et al. (2007a) mention among the advantages of using dust as a molecular gas tracer, the dust emission being optically thin in the far infrared, the dust abundance relative to atomic gas being directly measurable outside the GMC cloud and the H_2 molecule and the dust itself in the outer parts of molecular clouds being destroyed in similar quantities (Maloney & Black, 1988). Since dust will be mixed also with the H_2 molecules surrounding the CO cores, it will be able to trace better the extent of the molecular gas disk, beyond the observed edge of the CO disk, which seems rather a detection limit than an actual threshold, at least in NGC 6946 (Crosthwaite & Turner, 2007). Dame et al. (2001) proved that the molecular gas estimate from dust and CO emissions agree well within our own Galaxy.

Another good tracer of molecular gas has proved to be the [C II] line. The available carbon atoms ionised by the ultraviolet photons and turned into C II, through fine structure splitting on impact with ambient hydrogen atoms radiate energy at the 158 μm wavelength, contributing in this way to the gas cooling process. This line was first observed by NASA airborne platforms. The first time this line was observed outside our own Galaxy was in NGC 6946 by Madden et al. (1993) using NASA's Kuiper Airborne Observatory (KAO). They found that the [C II] emission peaks in the centre and follows the spiral arms of the galaxy. In a follow up article, Madden et al. (1997) confirm that the [C II] emission extends beyond the optical disk and the molecular disk traced by CO, while still correlating with high density H I. The [C II] line originates from both neutral and diffuse, partially ionised gas. This emission line has great potential as to shedding light into the mechanisms responsible for triggering star formation. Significant improvements in resolution are already available through the *Herschel* observation campaigns and the coming online of the Stratospheric Observatory For Infrared Astronomy (SOFIA).

Although only part of the neutral gas turns molecular, once molecular, the gas turns into stars at the same depletion time no matter the environment (Krumholz & McKee, 2005). Moreover, Rahman et al. (2012) find that the molecular gas depletion time is independent of both molecular and stellar surface densities and it does not

correlate with either the effective Jeans time or the free fall time in the molecular regions.

1.2.2.3 Star Formation Tracers

Part of our investigation in star formation at larger scales concerns estimating the number of stars resulting in the star formation process, a quantity directly related to the neutral and molecular gas reservoirs available. To assess the rate at which different galaxies form stars we use star formation tracers at wavelengths where young stars emit.

The Hα emission was the first to be used for such a purpose and it traces massive, ionising stars, mainly grouped in OB associations (Kennicutt, 1983, 1988). The conversion from Hα flux to star formation rate (SFR) was further developed by Kennicutt (1998) and more recently by Calzetti et al. (2007). The main caveats of this SF tracer are that it becomes harder to observe in outer disks and that its luminosity is partly affected by internal extinction (Cardelli et al., 1989). Some of the photons that would have otherwise travelled to us as Hα carriers are absorbed by the dust particles along their way out of the galaxy being observed.

To overcome the internal extinction difficulties, a hybrid SF tracer was developed by Calzetti et al. (2007). This hybrid uses Hα luminosity to account for the young star light and correct it for internal extinction by adding to it the mid infrared 24 μm emission representing the obscured light of the young stars re–radiated in the infrared bands.

Another common star formation tracer used today is the FUV emission. The advantage of this tracer over the traditional Hα one and its hybrid flavours resides in the fact that, because it is emitted by slightly lower mass young stars, a greater population than that of O and B stars, it samples star formation over a longer timescale (100 Myr). *GALEX* UV data extend as far as the outskirts of big galaxies and inside the low density regimes, suggesting that SF is active in those environments as well (Boissier, 2008). This result encourages the use of FUV rather than Hα as a star formation tracer. The UV luminosity is dominated by the UV photons originating in the young star atmospheres, thus the star formation rate (SFR) is proportional to the UV flux, as long as the SFR is constant over a timescale of 100 Myr (Iglesias-Páramo et al., 2006).

Similarly, and even more severely than Hα, the FUV emission suffers from internal extinction. Leroy et al. (2008) came up with a hybrid SFR indicator as well, one

where FUV emission is combined with the mid infrared 24 μm emission such that both the obscured and unobscured emission from the young stars are accounted for.

The discovery that obscured light from young stars is traced by infrared emission set the stage for a new category of star formation tracers, one entirely based on mid–infrared band emission. Star formation rate (SFR) correlates with 24 μm emission representing re–processed light from young stars (Calzetti et al., 2005; Pérez-González et al., 2006). On the other hand, 8 μm emission comes from polycyclic aromatic hydrocarbons (PAHs), very small dust grains that, when heated by single UV and optical photons, emit in the mid–infrared. In a more in depth study Calzetti et al. (2007) investigate the accuracy of the mid–infrared bands 24 μm and 8 μm in tracing the star formation rate (SFR) in a sample of 33 nearby galaxies and find that in high metallicity galaxies the 24 μm emission alone is a robust SF tracer even though its correlation with Paα (a near infrared tracer of H II regions only mildly affected by extinction) is not linear, however the 8 μm emission depends strongly on environment, metallicity and star formation history.

The source of radio emission in normal galaxies is mostly the synchrotron emission by Cosmic Ray electrons accelerated in supernova remnants and thermal (free–free) emission of H II regions. According to Condon (1992) and Murphy et al. (2011), both supernova remnants and H II regions are related to massive stars that turn into supernovae or ionise the H II regions. Therefore, the radio emission itself traces massive star formation and implicitly recent star formation activity. The advantages of radio observations are that the emission is largely optically thin, the resolution and the fact that they are not contaminated by the contribution of older populations of stars or "burst" type events with flux intensities proportional to luminosities (Condon, 1992). Adding that radio observations do not suffer from the complications of extinction, the radio emission is one of the most promising SFR tracers (Heesen et al., 2014, 2012). When observing below 3 GHz in frequency, the free–free emission from the H II regions, where massive stars are still ionising their surroundings is very weak. The radio emission is dominated by synchrotron radiation coming from electrons that have outlived the supernova remnants that they originated from. Yet the tight correlation between the FIR and the radio luminosities (de Jong et al., 1985; Helou et al., 1985) provides the necessary constraints for relating radio emission to massive star formation. When observing at higher frequencies, above 10 GHz, the radio emission becomes dominated by free-free emission from H II regions which can be directly related to the ionising photon rate coming from young massive stars

(Condon, 1992). Observing SF in this way has historically been hard in dwarf galaxies because of their faintness, but with the new Jansky Very Large Array (JVLA) instrumentation this has become feasible. Radio emission as a SFR tracer is a recent development in the field and is being explored in dwarfs by Heesen et al. (2014, 2012, 2015); Kitchener et al. (2015).

Another method of determining the SFR with reduced uncertainties due to internal extinction is by measuring the X–ray emission of a galaxy, which according to Fabbiano (2006), preferentially comes from X–ray binaries (XRBs). Within the X–ray binary population, the low mass X–ray binaries (LMBXs) represent the old star population while the high mass X–ray binaries, with lifetimes of $\approx 10^7$ yr, represent the young stellar population and thus can be used as a SF tracer. Apart from the fact that distinguishing between the HMBXs and LMBXs in external galaxies is virtually impossible, what complicates matters even further in the attempt to use this method for determining SFR is the fact that dwarfs are very hard to detect in X–rays (Ott et al., 2005a,b).

1.2.3 Star Formation in Dwarfs vs. Spirals

Does star formation proceed in the same way in all galaxies, no matter their size and type? Spiral galaxies for example, have spiral arms which dictate where most of the star formation sites will be and also re–shuffle gas, in this way increasing the star formation rate locally (Suwannajak et al., 2014). Once it became established that massive star formation rate densities in irregular galaxies can be comparable to those in spirals (Hunter et al., 1982) and spiral density waves are not necessary for forming massive stars (Elmegreen & Elmegreen, 1986), dwarf irregulars came to be seen as interesting environments for investigating star formation mechanisms and triggers. Consequently, a multitude of questions arose such as how giant cloud complexes and stars form at all in low density gas of dwarfs and to what extent different processes contribute to SF in these environments (Boissier, 2008; Kim et al., 2013; Ostriker et al., 2010; Struck & Smith, 1999; Walch et al., 2011).

1.2.3.1 Star Formation Histories

According to Martín-Manjón et al. (2012) three fundamental star formation history (SFH) scenarios can be formulated for dwarf galaxies: **bursting SF**, where stars form in short but intense episodes separated by long quiescent periods (Bradamante

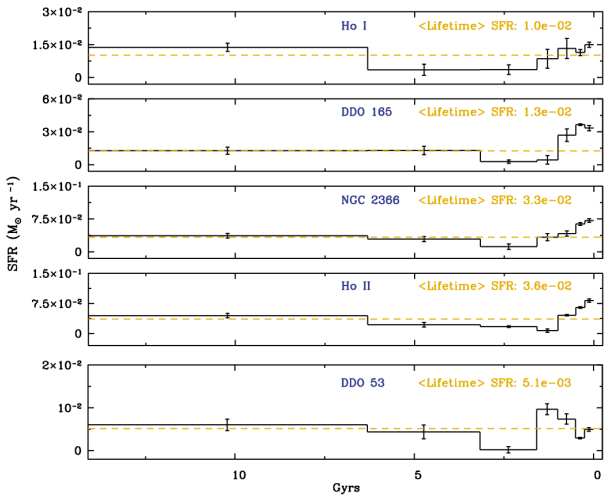

Figure 1.3: Using a compilation of figures from Weisz et al. (2008) we show the lifetime SFHs of DDO 63 (Ho I), DDO 165, NGC 2366, DDO 50 (Ho II), and DDO 53. The time resolution of log(t) is 0.3 Gyr for the most recent SFH. Also, 0 Gyr represents the present, so the time axis is in look–back time.The orange dashed line represents the SFH averaged over the lifetime of the of galaxy. The error bars reflect both systematic and statistical uncertainties. The method employed for measuring the SFH uses a maximum likelihood program which creates synthetic Colour–Magnitude Diagrams (CMDs) for every combination of fixed (IMF, binary fraction, etc) and searchable variables (distance, extinction, SFR and metallicity) which are then compared with the observed CMD. Hence the most likely SFH will be the best fit synthetic CMD.

et al., 1998; Tosi et al., 1991), **gasping SF**, where stars form in long but moderate in intensity episodes separated by short quiescent times (Recchi & Hensler, 2004; Tosi et al., 1991) and finally **continuous SF**, where SF takes place continuously, at low intensity with sporadic small bursts (Legrand et al., 2000). Among these three, dwarf irregular galaxies are best described as having gasping or bursting SF (Gallagher et al., 1996; Tosi et al., 1991), the main difference between these two scenarios being that chemical enrichment of the interstellar medium takes place gradually for the gasping SF scenario and on a time scale of a few tens of millions of years for the bursting SF scenario. To support this scenario in Fig. 1.3, taken from Weisz et al. (2008), we show the lifetime SFHs of DDO 63 (Ho I), DDO 165, NGC 2366, DDO 50 (Ho II), and DDO 53. The lifetime SFH is given by the SFR as a function of time (0-14 Gyr) and metallicity. In practice the SFH is obtained by modelling a synthetic Colour–Magnitude Diagram (CMD) and comparing it with the observed CMD, the best fit CMD yielding the SFH. The correlation between stars age and magnitude (as a stellar population grows older, the magnitude of the brightest stars remaining

on the Main Sequence (MS) gets fainter) on the Main Sequence (MS) is less clear or certain the older the stellar population observed. Hence the oldest reliable age of these CMDs is 5 Gyr. Consequently, the photometry is able to provide only weak constraints for the ancient SFH and with very low time resolution: 6-14 Gyr. In other words, a figure such as Fig. 1.3 can only be used to confirm a SFH scenario related to the recent SF and hence the only bins relevant will be the ones corresponding to the SFH over the past 5 Gyr. The accuracy of the SFH over the past 5 Gyr is in turn affected by the fact that on the MS there are stars of different ages that can have the same colour and magnitude. This effect however can be accounted for at least over the last 1 Gyr by considering along with MS stars also Blue Helium Burner stars (BHeBs), which have distinct magnitudes and colours. The most recent SF episodes are, of course, traced by FUV (10^8 yr timescale) and Hα (10^7 yr resolution).

Boissier (2008) find evidence of a lower star formation efficiency in low surface brightness (LSB) galaxies and favour the idea that the star formation history of these galaxies is most probably characterised by periods of intense bursts in SF followed by longer quiescent phases. For our discussion it is important to note that among the LSB galaxies we find dwarf galaxies along with disk galaxies and even "giant" disk galaxies (with scale lengths larger than 5 kpc and masses comparable to the more massive spirals, such as Malin 1), a wide range of objects assigned to the LSB category because of their low surface brightness (Boissier, 2008). Distinguishing between SF scenarios has the additional difficulty that our observations sample different phases/times in the SF cycle of the targeted galaxies. Martín-Manjón et al. (2012) find evidence that different star formation scenarios correspond in fact to different evolutionary stages of the same star formation cycle.

In galaxies like dwarf irregulars, where there are no spiral density waves it is difficult to pinpoint the regulatory process. The degree of regulation in the global SFR of dwarf irregulars can not be due to environment (Hunter & Elmegreen, 2004), so could only be due to one or more of the following: gas kinematics and distribution, structural properties or feedback processes (Lee et al., 2007). On the other hand, McQuinn et al. (2009) entertain the possibility that star formation propagates through the galaxy independent of any of the above causes.

1.2.3.2 Molecular Gas Phase in Dwarfs

In a study of the molecular gas in the low metallicity dwarf galaxy IC 10, Leroy et al. (2006) find that the GMCs in this galaxy are indistinguishable from those in

spiral galaxies such as M 31 and M 33. They also find that the GMCs in IC 10 are always associated with high density atomic gas suggesting that H I is necessary, but not sufficient, for molecular cloud formation.

Although irregular dwarf galaxies have impressive H I reservoirs, this does not drive the SFRs higher than in spiral galaxies. In other words, the H I emission is not a direct tracer of the molecular gas fraction (Leroy et al., 2006). According to Leroy et al. (2005), the median value of the molecular gas fraction (as inferred from CO luminosity assuming the Galactic conversion factor $X_{CO} = 2 \times 10^{20}\,\mathrm{cm^{-2}}$ $(\mathrm{K\,km\,s^{-1}})^{-1}$) is 0.30 ± 0.05 in dwarf irregulars and 1.5 ± 0.1 in large spirals. Further, they argue that the amount of molecular gas per unit stellar mass is comparable in dwarfs and large spirals and the discrepancy in molecular gas fraction arises from the larger H I reservoirs that are found in dwarfs. When incorporating the molecular gas phase into numerical simulations, Pelupessy et al. (2006) are able to reproduce these molecular fraction values and find that in dwarfs, where CO is often not detected, the upper limit of the molecular hydrogen fraction is 1%. The star formation is more efficient per CO molecule in such systems because the neutral to molecular gas transition takes place at higher densities (n= $100\,\mathrm{cm^{-3}}$) deep within the CNM cloud making up for the reduced dust quantity (Pelupessy & Papadopoulos, 2009; Pelupessy et al., 2006).

In dwarf galaxies, the compact cold cores of the GMCs are surrounded by a large fraction of H_2 gas because H_2 self-shielding is easier to achieve than the shielding of the CO molecule (Maloney & Wolfire, 1997). As illustrated by Bolatto et al. (2013) in Fig. 1.4, as metallicity decreases, the molecular clump does not change its size, but the CO emitting core does and decreases accordingly (Bolatto et al., 2008; Madden et al., 1997). This certainly seems to be the case of NGC 1569 (Hunter et al., 2001b) and IZw18 (Leroy et al., 2007b), both galaxies with active star formation, but low CO content.

Moreover, in dwarf galaxy environments certain epochs of their evolution such as immediately after a burst of star formation, are "CO dark" (Pelupessy & Papadopoulos, 2009). Leroy et al. (2011) found that CO–dark gas becomes an important component of the gas mass in the metallicity range $12+\log(\mathrm{O/H}) \approx 8.2 - 8.4$ and it is expected to be just as important at even lower metallicities since dust extinction is the main parameter influencing the fraction of CO–dark gas (Wolfire, 2010).

Under these circumstances, if in spiral galaxies CO can be used as a tracer for

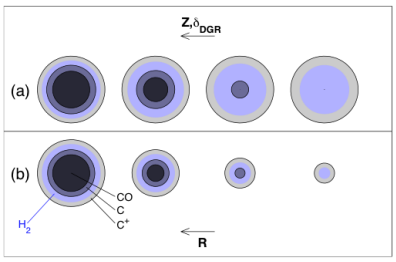

Figure 1.4: We show an image from Bolatto et al. (2013) to illustrate the effect of metallicity on CO and H_2 in a spherical clump immersed in a uniform radiation field. Blue shading indicates the region where the gas is molecular. Increasingly darker shading shows the regions where carbon is found as C^+, C, or CO. The top sequence (a) illustrates the effect of decreasing metallicity and dust-to-gas ratio on the distribution of C^+, CO, and H_2. The bottom sequence (b) illustrates the effect of changing the clump size or column density at a fixed metallicity. Also, metallicity is decreasing from left to right.

molecular gas, in dwarf galaxies this becomes a difficult matter. Not only dearth of CO (as a direct consequence of low metallicity) poses a problem for its detection, but also if observed the conversion of CO luminosity to a molecular gas mass becomes uncertain as it will inevitably depend on metallicity.

It is quite possible that in low metallicity galaxies [C II] or far–infrared emission trace molecular gas better than CO (Madden et al., 1997). Observing the [C II] line in the dwarf irregular IC 10, Madden et al. (1997) find that the [C II] surface density correlates with the H I and CO peaks and that the [C II]/ CO intensity ratio is higher than in solar metallicity galaxies. This higher [C II]/CO intensity ratio has also been observed in the LMC (Poglitsch et al., 1995), SMC (Israel et al., 1996) and a number of other irregular galaxies (Jones et al., 1997). In a low metallicity environment, the dust quantity necessary to ensure the availability of enough carbon atoms to form CO cores, and the dust necessary to maintain the shielding of such cores will control the [C II]–to–CO ratio. Since the CO cores are small, the free carbon atoms will prevail, amounting to a higher contribution in the gas cooling process and also emitting at 158 μm wavelength in the process.

We already know that the molecular hydrogen is more extended than CO, and the dust is mixed in with both the molecular hydrogen and CO dominating regions. Therefore if the dust is warm enough to emit in the far–infrared it will trace molecular gas better than CO (Leroy et al., 2007a). Among the successful attempts of using FIR emission as a proxy for molecular gas maps we remind the reader of the results by Bolatto et al. (2007) and Verdugo et al. (2011) in the Magellanic Clouds.

Also, the excess of FIR emission with respect to the total gas surface density traced by CO and H I indicates the presence of molecular hydrogen not traced by CO in the envelope of the molecular cloud (Roman-Duval et al., 2010). More recent results by Sandstrom et al. (2013) suggest that the dust–to–gas ratio (DGR) is an approximately linear function of metallicity, hence provided that reliable measurements of metallicity gradients are available, the study of DGR becomes a novel way to study the ISM in nearby galaxies. Regarding the conversion factor X_{CO}, studies suggest that in the disk of most galaxies this is mainly constant as a function of radius, despite changes in metallicity, radiation field intensity and star-formation rate surface density and its strongest correlation is with stellar mass surface density (Sandstrom et al., 2013). In fact, the conversion factor depends on temperature and velocity dispersion effects and on the dominance of CO-faint molecular gas at low metallicities (Bolatto et al., 2013).

Furthermore, Leroy et al. (2007a) found that the SMC, for example, emits more at submillimeter and millimeter wavelengths than would be inferred from *Herschel* observations of the FIR emission assuming Galactic dust, suggesting that the most probable cause for this long–wavelength emission is a different grain emissivity law than the Galactic one (Galametz et al., 2011; Galliano et al., 2011; Madden et al., 2012; Rémy-Ruyer et al., 2013). In such a case using FIR emission as a proxy for molecular hydrogen involves added complexity.

In other words, observing molecular gas in low metallicity environments becomes very difficult when we lose confidence in both CO as a tracer and dust–to–gas ratios as means of converting the dust map into a total gas map. In such a context, extending our knowledge from the solar metallicity to the low metallicity regime implies weighing our assumptions very carefully.

1.2.3.3 The Star Formation Tracers in Dwarfs

GMCs turn their masses into stars at a constant rate irrespective of their local environments (Krumholz & McKee, 2005). Both dwarf and spiral galaxies exhibit the same relation between star formation rate and molecular gas surface densities (Leroy et al., 2005).

When it comes to star formation tracers, Lee et al. (2009) find that in low luminosity dwarf galaxies, the total SFR based on Hα as a star formation tracer is lower than the total SFR based on FUV. The authors discuss different possible causes, ruling out metallicity as this would act in the opposite direction than the

observed trend, photon leakage as inhibited by the big H I envelopes of dwarf galaxies and stochasticity in the high mass star formation at low star formation rates as having an effect not large enough to match observations. They conclude that the following two causes are more likely to explain the discrepancy. As dwarf galaxies go through bursts of star formation, the high mass stars will disappear a lot earlier than the low mass ones, so if observed in this post-starburst period a dwarf galaxy would be deficient in Hα compared to FUV. Therefore for current, integrated SFRs lower than $0.01\,M_{\odot}\,yr^{-1}$, FUV as SF tracer rather than Hα is recommended (Lee et al., 2009). At the same time Hα as a star formation indicator relies on highly luminous massive stars, in which case the form of the IMF may also play an important role. Melena et al. (2009) argue that there is no indication of a change in IMF, since dwarfs are just as capable of forming massive star–regions in their outskirts, as they are in their inner parts. The dropout in Hα is not caused by a decrease in the SFR at larger radii, but rather the Hα emission disappears beyond the detectability limit as the ionizing radiation gets spread over a larger and larger volume (Boissier et al., 2007; Melena et al., 2009; Thilker et al., 2007).

When considering alternatives for star formation tracers such as FUV and Hα, we find that decreasing metallicity poses problems also to infrared tracers. Dust properties in dwarf galaxies are distinct from those in spiral galaxies through a combination of factors such as harder radiation fields, more compact structure, different composition, different heating mechanism and different distribution of dust in the interstellar medium (Rosenberg et al., 2008). These authors show that those properties combined with the difference in the shape of the Mid–Infrared continua in dwarfs with respect to spirals complicate using infrared measurements as star formation tracers for measuring the SFR in dwarf galaxies. Also, Calzetti et al. (2010) find indications that the $160\,\mu$m maps are contaminated with dust heated by stellar populations that do not currently participate in the SF process, which confirms the general expectations that as metallicity goes down and galaxies become more transparent, the infrared becomes a poor star formation tracer.

1.2.4 Star Formation Laws

To explain how efficiently gas is turned into stars, Schmidt (1959) assumed explicitly that a power law could describe the relation between the volume density of the interstellar neutral gas in a region of the Galaxy and the number of stars formed there per unit time and volume ($\rho_{SFR} \propto (\rho_{gas})^n$). His assumption was prompted by the

result of van den Bergh (1957) who was first to relate the decrease in interstellar gas density with star formation. In a following paper, Schmidt (1963) stopped regarding the above assumption as a physical law and suggested using the power law simply as a convenient way of parametrizing the relation. From observations, we can only measure projected surface densities, therefore estimating total gas volume densities was not in any way trivial. Schmidt (1959) succeeded estimating the volume densities for a region of the Galaxy, assuming that the distribution of hydrogen is fairly homogeneous, with smooth variations in density and that all stars were formed in a layer of gas with the same distribution in scale height z. He concluded that the power law n was equal to 2.

Over the years other arguments were brought against Schmidt's power law relation. Larson (1977) argues that theoretically SFR cannot depend on gas density alone, even locally. Miller & Scalo (1979) bring forth a whole list of arguments among which only a few are mentioned here: stars form out of molecular gas whereas the correlations are based on neutral gas, theory predicts a relation between gas density and SFR and not between gas density and number of stars, for SF to be proportional to the average gas density, the z dispersion should rather be the dispersion of the gas the stars condense of, when one uses the dispersion in z to rule out particular values of n one implicitly assumes the existence of the power law. These arguments and others not mentioned here have inspired the more recent results in the field, results we present in detail in the following sections.

Other authors, however, looked for observational evidence of this $n = 2$ power law relation in other nearby galaxies: in the SMC (Sanduleak, 1969), in M 31 (Hartwick, 1971), in M 33 (Madore et al., 1974), in the LMC (Tosa & Hamajima, 1975). Also Hamajima & Tosa (1975) looked for the same observational evidence in a sample of seven galaxies (LMC, SMC, M 31, NGC 2403, M 101, M 51, NGC 6949). They all found for n values around 2, although they were all working with surface densities instead of volume densities $\Sigma_{SFR} \propto (\Sigma_{gas})^N$ and assumed that n was equal to N. Guibert et al. (1978) however explains that since $\Sigma \propto \rho z$ the $\Sigma_{SFR} \propto (\Sigma_{gas})^N$ and Schmidt's $\rho_{SFR} \propto (\rho_{gas})^n$ can only be identical if the thickness of the galactic disks corresponding to the gas and the young stars is uniform. It was Kennicutt (1989) who showed that this condition does hold in the disks of spiral galaxies and proved empirically the $\Sigma_{SFR} \propto (\Sigma_{gas})^N$ relation. This relation, illustrated in Fig. 1.5, was called the Star Formation law (SF law) or the Kennicutt-Schmidt law (K–S law), acknowledging the extensive work done by Kennicutt in this field

(Kennicutt & Evans, 2012; Kennicutt, 1983, 1988, 1998; Kennicutt et al., 2007). Although in this field people often use the term SF law or SK-law, they in fact refer to the relation between star formation rate (SFR) and gas content or between star formation rate surface density (SFRD) and gas surface density. Over the years, this area of research has evolved considerably from the traditional study of the SF law as a globally averaged relation (Kennicutt, 1989, 1998), to a more recent direction, investigating the SF law in kpc–size regions within galaxies (Bigiel et al., 2010b, 2008; Leroy et al., 2008, 2012).

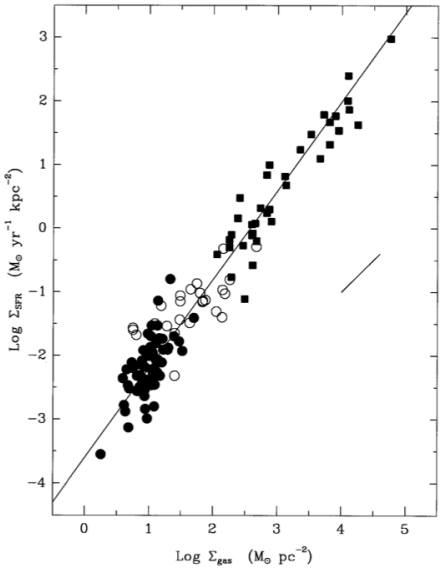

Figure 1.5: We show an image from Kennicutt (1998) to illustrate the composite star formation law for the normal disk (filled circles) and starburst (squares) samples. Open circles show the SFRs and gas densities for the centers of the normal disk galaxies. The line is a least-squares fit with index $N = 1.4$. Modest uncertainties in the linear sizes of the relevant star-forming regions displace the SFR and the gas densities nearly parallel to the Schmidt law itself and the short, diagonal line in the figure shows this effect of changing the scaling radius by a factor of 2 (for a fixed gas mass and total SFR).

Although the power law form of the SF law originated from a logical association between the number of stars observed and the gas, the fuel available for forming them, there are physical reasons to expect such a relation. Coming back to the mathematical formula of the SF law above, let us consider different possibilities to express the gas surface density term and see how the power law index changes. According to Krumholz & McKee (2005), a GMC forms stars from its gas over a free fall time $t_{ff} \propto (\rho_{gas})^{-0.5}$. Therefore, adding to it that the surface density of GMCs is constant, it results that in an individual GMC the power law index is $N \approx$

0.75, whereas for a uniform population of GMCs, where different surface density values represent different number of molecular clouds rather than different physical properties, $N \approx 1$. Theoretically we expect that, if the determining SF process is gravitational instability, the SFR depends on the the free fall time of the total gas so $t_{ff} \propto (\Sigma_{gas})^{-0.5}$, therefore at a constant scale height, $N \approx 1.5$. if, however, the SF process is fundamentally collisional and the scale height is constant, $\rho_{SFR} \propto (\rho_{gas})^2$ and hence $N \approx 2$ (Bigiel et al., 2008). These theoretical expectations are in the range of the observationally derived values.

1.2.4.1 General SF law

Early on, the gas density was represented by atomic gas only. As the technical advances allowed more and more accurate molecular gas observations, the study of the SF law gained perspective as the gas term of the power law could be interpreted as expressing the total gas surface density (let us call this the general SF law), the molecular gas surface density (molecular SF law) or the atomic gas surface density (neutral SF law).

The study of the general SF law was initiated by Robert Kennicutt. Kennicutt (1989), using a sample of disk galaxies, quantified the SFR using Hα as a tracer and related it to a gas density that for the first time also included molecular gas. In this extensive work, Kennicutt (1989, 1998), computed a power law index $N \approx 2.47 \pm 0.39$ for normal spiral galaxies and $N \approx 1.40 \pm 0.15$ for a mixed sample of galaxies (see Fig. 1.5, taken from Kennicutt (1998)). More recently, Crosthwaite & Turner (2007) find evidence in the spiral galaxy NGC 6946, for a closer relation between SFR and total gas surface densities, rather than molecular gas surface density. A similar situation is described by Schuster et al. (2007) in M 51(NGC 5194), where the correlation between SFR and total gas surface densities is strongest and it follows a Schmidt law with an index of $N \approx 1.4 \pm 0.6$.

A low metallicity regime automatically implies a low dust column regime. Therefore, if the turnover where atomic hydrogen becomes molecular is correlated with metallicity as found by Krumholz et al. (2011, 2009), consequently, the K–S law relating SFR and total gas surface densities is dominated by the dust–to–gas ratio (Gnedin & Kravtsov, 2011). They also find that the K–S law shows a less strong dependence on FUV flux. Both the dust–to–gas ratio and the FUV flux play a determining role in the H I to H_2 conversion and it is this role that is reflected in the dependence of the K–S law on these quantities. The higher the dust–to–gas ratio

the more efficiently the H I is turned into molecular gas; the lower the interstellar radiation field and hence the FUV flux, the less likely it is that the newly formed molecules will dissociate.

1.2.4.2 Molecular SF Law

Bigiel et al. (2008), using a large sample of THINGS (The H I In Nearby Galaxies Survey, see Walter et al. (2008)) spiral galaxies, concluded that there is a one to one relation between the SFR surface density and the molecular gas surface density. This relation is now known as the molecular star formation law. In a follow up work, Bigiel et al. (2011b), extend their sample to 30 disk galaxies and confirm previous results which relate the SFR surface density with the molecular gas surface density through a power law with index number $N \approx 1.0$. Using the 24 μm emission in a sample of nearby infrared–bright galaxies as a star formation indicator Rahman et al. (2012) also confirm previous results by computing a power law index for the molecular SF law of $N \approx 0.96 \pm 0.16$. The linearity of the molecular SF law confirms the theoretical scenario of Krumholz & McKee (2005): no matter the environmental parameters the GMCs will turn their masses into stars. Blanc et al. (2009), employs an innovative method of creating a SFR map based on integral field unit (IFU) spectroscopy in NGC 5194 (=M 51) and find that SFR surface density correlates well with molecular gas surface density. Regarding the SF slopes they find agreement with Bigiel et al. (2008), but disagree with Kennicutt et al. (2007). Crosthwaite & Turner (2007) also confirm the molecular star formation law in the spiral galaxy NGC 6946. Still, according to Momose et al. (2013), in the case of 10 spiral galaxies, new CO(J = 1–0) data from the CARMA and NOBEYAMA Nearby-galaxies (CANON) CO survey combined with SFR maps based on Hα and 24 μm yield a super–linear ($N = 1.3$) molecular SF law at scales higher than 500 pc. The super–linear slope of the K–S law is explained as due to non–linear processes enhancing SF in regions of high gas density.

The strength of the correlation between star formation rate and molecular gas surface densities holds throughout the inner and outer parts of big galaxies (Schruba et al., 2011) as well as in dwarfs such as the SMC (Bolatto et al., 2011). Moreover, comparing the general SF law and the molecular SF law, it became obvious that with few exceptions (NGC 6946, M 51), SFR and molecular gas surface densities were more closely correlated than SFR and total gas surface densities (Bigiel et al., 2008; Kennicutt et al., 2007).

1.2.4.3 Neutral SF Law

Regarding the neutral SF law, Kennicutt et al. (2007) and Bigiel et al. (2008) find no strong correlation between SFR and atomic gas surface densities in their spiral galaxies dominated samples. In an extensive study of NGC 5194, Blanc et al. (2009) also find that SFR and atomic gas surface densities are uncorrelated confirming once more the Bigiel et al. (2008) results.

Because star formation occurs almost everywhere H I is observed, the search for a star formation law has also been extended to THINGS dwarfs and the outskirts of spiral galaxies (Bigiel et al., 2010a). In these environments, Bigiel et al. (2010b) find a clear relation between atomic gas and star formation surface densities and compute for this relation a power law index close to 1.7. In a study of star formation in extreme dwarfs, Roychowdhury et al. (2011) also find a clear relation between SFR and atomic gas surface densities.

The relation between the SFRD and H I surface density is different in the outskirts of spirals than in their centres suggesting that the $\Sigma_{SFR} - \Sigma_{gas}$ parameter space is populated differently depending on host environment. The correlation between SFR and atomic gas surface densities switches on in low metallicity regimes only, suggesting that H I surface density plays an important role in driving star formation in the low metallicity environment (Bigiel et al., 2011a).

1.2.4.4 Atomic Hydrogen to Molecular gas transition and the SF Law

Let us define a SF plot as the plot where SFR surface density is represented as a function of gas surface density. Again the gas surface density can be represented by the total gas, molecular or atomic gas surface densities. If both the molecular and neutral gas surface densities are represented in one SF plot, one will notice that there is a clear density limit beyond which the gas is dominantly molecular. Bigiel et al. (2008) find that for spiral galaxies in their sample this transition point where atomic hydrogen turns molecular is always $10\,M_{\odot}\,pc^{-2}$. This is illustrated in Fig. 1.6, a figure taken from the Bigiel et al. (2008) article.

However, dwarf galaxies tend to have higher H I column densities than spirals (Bigiel et al., 2010b) and consequently their turnover has a higher value as well (Leroy et al., 2011; Roychowdhury et al., 2011). In Section 1.2.3, we have already mentioned the result of Leroy et al. (2006) who find that the GMCs in IC 10 are associated with high density H I clouds mostly above $10\,M_{\odot}\,pc^{-2}$. This difference be-

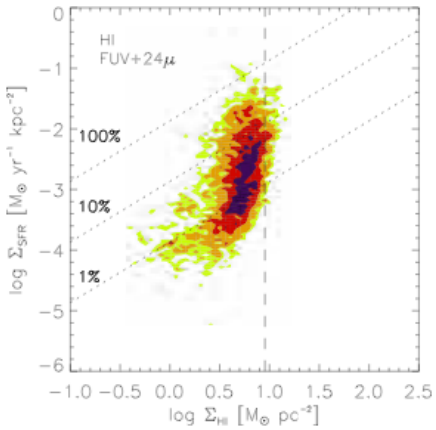

Figure 1.6: We show an image from Bigiel et al. (2008) to illustrate that for spiral galaxies in the THINGS sample atomic hydrogen turns molecular at $10\,M_\odot\,pc^{-2}$ (the vertical dashed line). In the case of seven spiral galaxies plotted together, SFRD as a function of H I surface density is shown at 750 pc resolution. Green, orange, red, and magenta cells show contours of 1, 2, 5, and 10 independent data points, respectively, per 0.05 dex-wide cell. The sensitivity limit of each SF tracer is indicated by a horizontal dotted line. The diagonal dotted lines show lines of constant SFE, indicating the level of SFR needed to consume 1%, 10%, and 100% of the gas reservoir (including helium) in 10^8 years. Thus, the lines also correspond to constant gas depletion times of, from top to bottom, 10^8, 10^9, and 10^{10} yr.

tween spirals and dwarfs is directly linked to their metallicity, which dwarfs have to compensate for by achieving higher atomic gas densities in order to protect molecule formation from photodissociation (Krumholz et al., 2011, 2009). However, the metallicity dependent, high H I densities predicted by theory are higher than the observed H I column densities, an effect attributed to unresolved clumping (Wong et al., 2013).

Roychowdhury et al. (2011), using a sample of 23 dwarf galaxies, find evidence that relates the discrepancies between the Hα based and FUV based SFR surface densities to high neutral gas surface densities. High H I column densities, higher than $10\,M_\odot\,pc^{-2}$, occur in galaxies where the ratio between the Hα based and FUV based SFR surface densities is greater than one, suggesting that massive SF takes place in high column density gas (Roychowdhury et al., 2011).

1.2.4.5 Other aspects of the SF Law

Another way of investigating the K–S law is from the point of view of star formation efficiency (SFE). The definition of star formation efficiency differs depending on the astronomical community discussing the subject. The "GMCs community" defines

at least two different SFEs, the SFE per free fall time defined as the ratio of free fall time t_{ff} to gas depletion time and the SFE of the GMC representing the fraction of H_2 mass of the cloud that is converted into stars over the life time of the cloud (Feldmann & Gnedin, 2011).

Within the "SF law community", SFE is defined as the ratio between the SFRD and gas surface density and it represents a measure of how long it would take for the existing gas to be consumed at the current SFR, assuming no gas return. In a sample of spiral galaxies, Leroy et al. (2008) have found that there is a one to one relation between the SFRD and the molecular gas surface density and consequently the ratio between SFRD and molecular gas surface density is constant: $SFE(H_2)=5.25\times10^{-10}\,yr^{-1}$. The constancy of the $SFE(H_2)$ implies that once molecular the gas will turn into stars within 2 Gyr, no matter the environment surrounding the GMC clouds. In other words the transition from molecular gas to stars is governed only by the microphysics of the GMCs.

Another interesting aspect of the K–S law (SF law) is its correlation with the stellar mass. In a comprehensive study of the relation between SFR and gas surface densities as a function of stellar mass at sub–kpc and kpc scales, Rahman et al. (2012) find that there are no strong correlations between the stellar masses and either the molecular SF law power–law index or the molecular SF law normalization. On the other hand, Shi et al. (2011) find a tight correlation between SFE and stellar mass surface density. They name it the Extended Schmidt Law and interpret it as proof for the important role existing stars play in the SF activity continuity.

Are existing stars a more efficient predictor for star formation (SF) than H I column density thresholds? The mechanism through which stars intervene in the SF scenario is not well understood. Whether they are driving the mid–plane pressure (Leroy et al., 2005), increasing the turbulence to compensate for decreasing metallicity (Walch et al., 2011), inducing star formation by controlling the local gas density and the gas re-shuffling mechanism (Brinks et al., 1990; Dawson et al., 2013; Dolphin & Hunter, 1998; Dopita et al., 1985; Stewart & Walter, 2000; Stewart et al., 2000) or an environment dependent combination of the above, a clear link between the existing stars and the future generations of stars is still elusive. We do know that previous neutral hydrogen (H I) and optical observations of dwarf irregulars showed a better correlation between the star formation rate (SFR) and the V–band surface brightness than any other measure (Hunter & Elmegreen, 2004; Hunter et al., 1998; Shi et al., 2011).

1.3 Motivation

The wonderful legacy of our astronomical community, years of research unfairly crowded in a few sentences and a reference in these pages of our introduction, represents a valuable road map (see Fig. 1.1) in our hands, an indispensible tool we set with on our quest to answer the question of this thesis and earn the privilege of knowledge being built on our shoulders too.

This thesis means to increment the knowledge towards finding the answer to the following question: Is there one universal way of forming stars? Here, by "way of forming stars" we understand a law which governs the star formation process. For historic reasons the SF law relates star formation rate and gas surface and/or volume densities, yet we know that the gas reservoir is not driving star formation on its own, but with the aid of other ingredients such as metallicity, pressure, interstellar radiation field, etc. There are already indications that the first stars in the universe formed differently than the young stars observed in spiral galaxies today suggesting that metallicity plays an important role in star formation. The current studies of SF laws are no longer based on a single ingredient, the gas density. The new direction for this kind of investigations is identifying the key parameters that drive the star formation and assessing their exact contribution, in the hope that once all ingredients are known a universal SF law can be formulated.

The value of a research question's answer lies in the strength and depth of the question itself. Refining a research question by discriminating between knowns and unknowns is an important part of research. We know physically how to form a star and gave an account of this process in Section 1.2.1. We know the ingredients that go into the star formation process at larger scales and described them in Section 1.2.2. We know that the star formation process differs depending on metallicity and that dwarf irregulars are representative for the low metallicity and low gas density regime (see Section 1.2.3). In my opinion, a star formation recipe should be like a cooking recipe, it should tell you what ingredients to put, in what quantities and how to prepare and mix them. So many years of research have been invested in the subject of star formation laws (see Section 1.2.4) and so much knowledge has been gained in the process, however we still do not know the exact quantity of each ingredient and the precise importance of variables such as metallicity, pressure, interstellar radiation field, etc.

This thesis is far from being able to give an expression to the one universal SF

law. It rather tries to assess if a relation between SFR and atomic gas density exists and how this relation changes with metallicity, pressure and interstellar radiation field in a sample of dwarf irregulars. We know that the atomic gas is a prerequisite of any SF recipe, yet it is not the sole ingredient. Atomic gas by itself is not sufficient for SF, however understanding the true nature of the SFR and atomic gas relation implies considering quite a number of additional ingredients and variables, whose importance if quantified will essentially contribute to achieving that one universal SF law.

The work in this field was pioneered by Bigiel et al. (2010a, 2011a, 2010b) who studied the SFR and gas density relation in a small sample of the more massive dwarfs whose high luminosities and high metallicities place them as intermediaries between spirals and dwarfs. We extend their investigation by employing a similar analysis method as Bigiel et al. (2010b, 2008); Leroy et al. (2008) to a larger sample of dwarf irregular galaxies, with a larger range in luminosity, metallicity and total SFR. Extending their investigation became feasible once the technical advances of the last decade made it possible to observe in detail, more dwarf galaxies in our neighbourhood, despite their low luminosities.

The way star formation proceeds in systems such as dwarf irregulars is interesting because it adds new perspectives to the complex picture of star formation put together through observations of spiral galaxies. Dwarfs are able to complement the existing picture with a temporal dimension because in dwarf galaxies stars still form from almost pristine gas just as they used to in the past. Also, dwarfs in their apparent simplicity, no shear or spiral arms, are better case studies for assessing the exact ingredients that enter the SF recipe. The novelty in studying the SFR and gas density relation in dwarf irregulars is in the new flavour that comes with dwarfs: star formation in low metallicity, apparently simpler environments.

In other words, the new direction in star formation studies is to compare and complement the knowledge achieved by investigating star formation in spiral galaxies with the new knowledge on star formation revealed by dwarf galaxies. In this context, this thesis is relevant in the field of star formation because it combines current methods with a larger and better constituted sample ensuring a more general and complete assessment of the laws governing the star formation process in dwarfs. The results presented in this thesis aim to contribute to a better understanding of the way star formation proceeds not only in dwarfs but also universally.

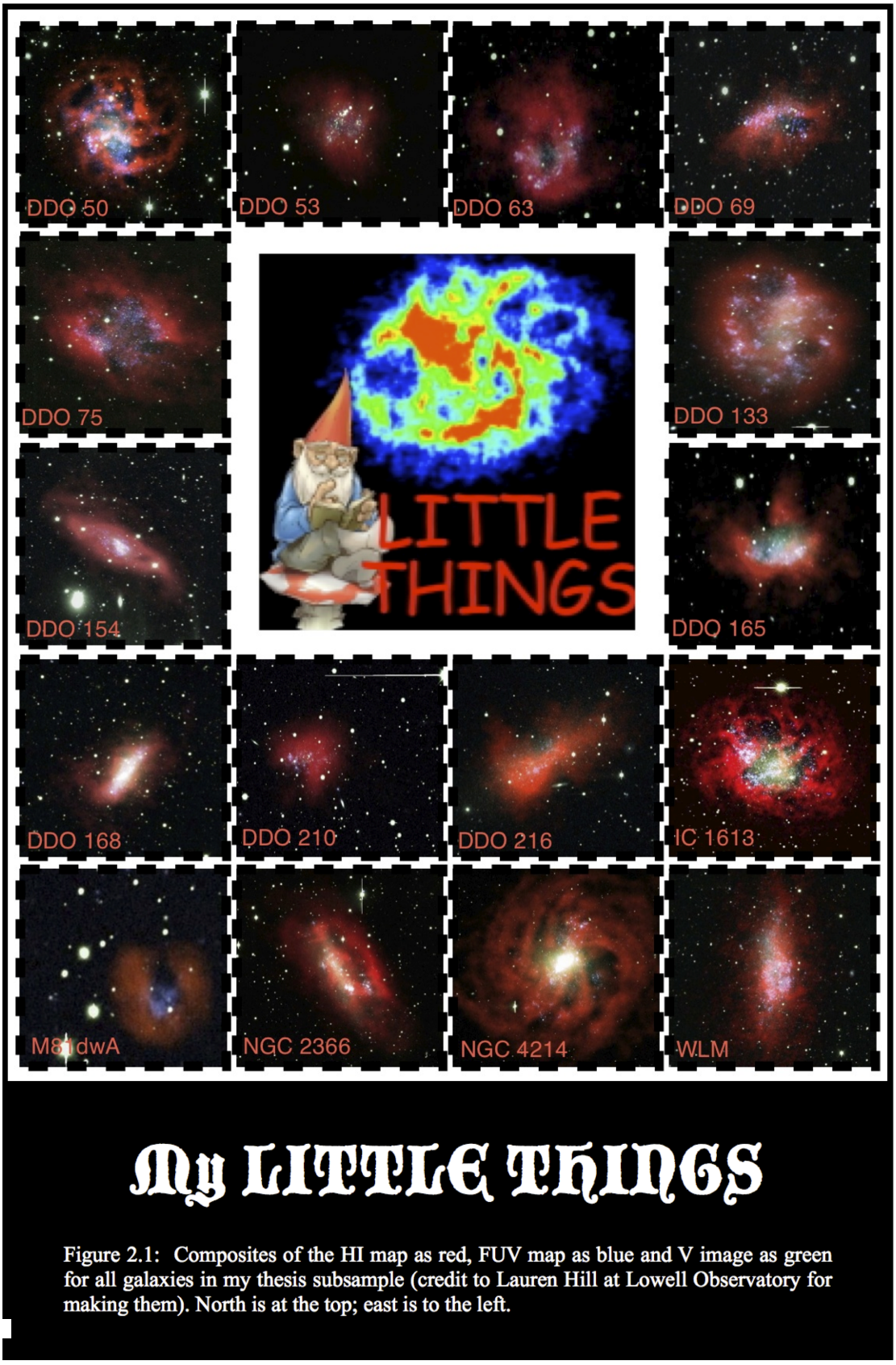

Figure 2.1: Composites of the HI map as red, FUV map as blue and V image as green for all galaxies in my thesis subsample (credit to Lauren Hill at Lowell Observatory for making them). North is at the top; east is to the left.

Chapter 2
DATA PRESENTATION

Substantial elements presented in this Chapter were contributed by me to the paper Little Things by Hunter, D. A., Ficut–Vicas, D., Ashley, T., Brinks, E. et al. 2012, AJ, 144, 134.

2.1 The Data

The data I used for the completion of this thesis project represent 44% of the LITTLE THINGS[1] data (Hunter et al., 2012). The LITTLE THINGS (Local Irregulars That Trace Luminosity Extremes, The H I in Nearby Galaxies Survey) project shifts the interest in objects like nearby spiral galaxies as it was for the THINGS project (Walter et al., 2008) to nearby, relatively normal, gas-rich dwarfs. The LITTLE THINGS[2] Survey uses a multi–wavelength approach to investigate star formation in dwarf galaxies and to shed some light on current topics of interest like what regulates star formation in small, gas rich galaxies, what is the importance of triggered star formation, what happens to star formation in the outskirts of galaxies, etc. The LITTLE THINGS sample is drawn from a larger sample of 94 dwarf irregulars, 24 BCDs (Blue Compact Objects) and 18 Sm galaxies, their observations collected over a 15 year period and investigated at different wavelengths by Hunter & Elmegreen (2004, 2006). The LITTLE THINGS sample is composed of 41 dwarfs: 37 dwarf irregulars and 4 BCDs.

[1]Based on data from the LITTLE THINGS Survey (Hunter et al., 2012), funded in part by the National Science Foundation through grants AST-0707563, AST-0707426, AST-0707468, and AST-0707835 to US-based LITTLE THINGS team members and with generous support from the National Radio Astronomy Observatory.

[2]https://science.nrao.edu/science/surveys/littlethings

Table 2.1. General properties

Name	RA [J2000] (hh mm ss.s)	DEC [J2000] (dd mm ss.s)	D (Mpc)	R_H ($'$)	R_D (kpc)	M_V (mag)	(12+log(O/H))	log (SFR_D) ($M_\odot$ yr^{-1} kpc^{-2})
DDO 168	13 14 27.9	45 55 09.0	4.3	2.32	0.82±0.01	-15.72±0.005	8.29±0.07	-2.04±0.01
DDO 133	12 32 55.4	31 32 14.1	3.5	2.33	1.24±0.09	-14.76±0.01	8.23±0.09	-2.62±0.01
NGC 4214*	12 15 39.2	36 19 38	3.0	4.67	0.75±0.01	-17.63±0.001	8.17±0.06	-1.08±0.01
DDO 50*	08 19 08.7	70 43 25.0	3.4	3.97	1.10±0.05	-16.61±0.003	8.13±0.11	-1.55±0.01
DDO 216	23 28 35.0	14 44 30	1.1	4.00	0.54±0.01	-13.72±0.003	7.93±0.15	-3.21±0.01
NGC 2366*	07 28 48.8	69 12 22.0	3.4	4.72	1.36±0.04	-16.79±0.001	7.91±0.01	-1.66±0.01
WLM	00 01 59.2	-15 27 41	1.0	5.81	0.57±0.03	-14.39±0.004	7.83±0.06	-2.05±0.01
DDO 187	14 15 56.7	23 03 19	2.2	1.06	0.18±0.01	-12.68±0.014	7.69±0.09	-1.98±0.01
DDO 155	12 58 39.8	14 13 10.0	2.2	0.95	0.15±0.01	-12.53±0.015	7.68±0.06	-1.44±0.01**
DDO 165	13 06 25.3	67 42 25.0	4.6	2.14	2.26±0.08	-15.60±0.006	7.63±0.08	-3.67±0.01**

IC 1613	01 04 49.2	02 07 48	0.7	9.10	0.58±0.02	-14.60±0.004	7.62±0.05	-1.99±0.01
DDO 63*	09 40 30.4	71 11 02.0	3.9	2.17	0.68±0.01	-14.79±0.017	7.61±0.11	-1.95±0.00
DDO 53*	08 34 08.0	66 10 37.0	3.6	1.37	0.72±0.06	-13.84±0.008	7.60±0.11	-2.41±0.01
DDO 75	10 10 59.2	-04 41 56	1.3	3.09	0.22±0.01	-13.91±0.008	7.54±0.06	-1.07±0.01
DDO 154*	12 54 06.2	27 09 02	3.7	1.55	0.59±0.03	-14.19±0.015	7.54±0.09	-1.93±0.01
DDO 69	09 59 25.0	30 44 42.0	0.8	2.4	0.19±0.01	-11.67±0.01	7.38±0.10	-2.22±0.01
M81dwA*	08 23 57.2	71 01 51	3.6	...	0.26±0.00	-11.73±0.057	(7.3)	-2.26±0.01
DDO 210	20 46 52.0	-12 50 50.0	0.9	1.31	0.17±0.01	-10.88±0.011	(7.2)	-2.71±0.06

Table 2.1: From left to right the columns represent: Galaxy name, RA, DEC, Distance (Hunter et al., 2012), Holmberg radius measured to a B–band surface brightness of about 26.66 from Hunter & Elmegreen (2006), Disk scale length measured from V–band images R_D (Hunter & Elmegreen, 2006), Absolute V magnitude from Hunter & Elmegreen (2006), Metallicity from Hunter et al. (2012), log of the integrated area normalized SFR from Hunter et al. (2012) determined from *GALEX* FUV fluxes divided by πR_D^2. A double star next to the SFR value indicates a FUV flux was not measured and the SFR value is determined from $L_{H\alpha}$ divided by πR_D^2. A star next to the galaxy name indicates the galaxies are shared between the LITTLE THINGS and the THINGS projects. The galaxies in this table are ordered by metallicity.

The project combines young star tracers: Hα and *GALEX* ultraviolet images; old star tracers: $UBVJHK$ and *Spitzer* 3.6 and 4.5 μm images; dust tracers: *Spitzer* PACS 5.8 and 8.0 μm images, IRS spectra of H II regions, and MIPS 24, 70 and 160 μm images of dust emission. To trace morphological and kinematical structures that are important in star formation, the multi–wavelength domain is completed with H I data. The H I furthermore provides crucial information on the kinematics of the gas. The following subsections give details on how the observations, data calibration, data combination and imaging were done for the LITTLE THINGS galaxies and implicitly for the 18 LITTLE THINGS dwarfs that are part of my thesis subsample. This chapter sums up my detailed contribution to solving the technical challenges of the LITTLE THINGS radio interferometric data set and to implementing a new imaging technique for our data. The main points and results of this technical endeavour are published in the data release paper Hunter, Ficut-Vicas, et. al. 2012, AJ, 144, 134, of which I am a co-author.

2.1.1 Subsample Choice

The aim of this thesis is to study the star formation laws in extreme environments such as the ones in dwarf galaxies. To achieve this purpose the choice of which galaxies are part of the investigated subsample is not trivial. We guided our choice partly on the availability of ancillary data and mainly on sampling broadly three main dimensions of our parameter space: metallicity, luminosity and integrated star formation rates.

In Table 2.1 is illustrated how our sample of 18 galaxies spans in metallicity (12+log(O/H)) from 7.2 for DDO 210 to 8.29 for DDO 168. According to the latest measurement by Pereira et al. (2009) the solar metallicity has a (12+log(O/H)) value of 8.69 ± 0.05. We expect metallicity to play a very important role in our sample and to influence the star formation mechanisms, therefore the subsample galaxies appear ordered by metallicity in all tables and plots. In terms of luminosity, the absolute V–band magnitude of the galaxies in our subsample ranges from -10.9 mag for DDO 210 to -17.6 mag for NGC4214. We notice that lower metallicity does not necessarily mean lower luminosity, nor lower integrated star formation rate (SFR). The integrated SFR in our sample is based on FUV fluxes for all except two (DDO 155, DDO 165) galaxies, where FUV data were not available. The log of the integrated area normalized SFR ranges from -1.07 $M_\odot$ yr^{-1} kpc^{-2} for DDO 75 to -3.67 $M_\odot$ yr^{-1} kpc^{-2} for DDO 165, this latter value being based on the Hα flux.

Table 2.2. Ancillary Data Observation Settings

Name	Alt. Name	Optical & NIR UBVJHK	Telescope (UBVJHK)	Instrument (FUV)	Instrument (3.6 μm, 24 μm)	Telescope (Hα)
DDO 168	PCG 46039	UBV	HT	*GALEX*	*Spitzer*	PT, FP
	UGC 8320	JHK	PT			NCCD
DDO 133	PCG 41636	UBV	HT	*GALEX*	*Spitzer*	PT, FP
	UGC 7698	J	PT			NCCD
NGC 4214	PCG 39225, UGC 7278	UBV	KPNO4m	*GALEX*	*Spitzer*	PT, 4:1
	PCG 39225, UGC 7278	JHK	PT			NOTI
DDO 50	PCG 23324, UGC 4305	UBV	HT	*GALEX*	*Spitzer*	PT, 4:1
	Holmberg II, VIIZw 223	...	...			NOTI
DDO 216	PGC 71538, UGC 12613	UBV	KPNO4m	*GALEX*	*Spitzer*	PT, 4:1
	Peg DIG, Pegasus Dwarf	...	...			NOTI
NGC 2366	PGC 21102	UBV	KPNO4m	*GALEX*	*Spitzer*	PT, FP
	UGC 3851, DDO 42	JHK	PT			NCCD
WLM	PGC 143, UGCA 444, DDO 221	UBV	HT	*GALEX*	*Spitzer*	PT, FP
	Wolf-Lundmark-Melott	...	...			NCCD
DDO 187	PGC 50961	UBV	HT	*GALEX*	*Spitzer*	PT, FP
	UGC 9128	J	PT			NCCD
DDO 155	PGC 44491, UGC 8091	UBV	HT	...	*Spitzer*	PT, 4:1
	LSBC D646-07, GR 8	J	PT			NCCD
DDO 165	PGC 45372, UGC 8201	UBV	HT	...	*Spitzer*	PT, FP

	IIZw 499, Mailyan 82	J	PT			NCCD
IC 1613	PGC 3844	UBV	CTIOs	*GALEX*	*Spitzer*	PT, FP
	UGC 668, DDO 8	...	...			NCCD
DDO 63	PGC 27605, UGC 5139	UBV	HT	*GALEX*	*Spitzer*	HT, 2048
	Holmberg I , Mailyan 044	...	...			
DDO 53	PGC 24050	UBV	KPNO4m	*GALEX*	*Spitzer*	PT, FP
	UGC 4459, VIIZw 238	JH	PT			NCCD
DDO 75	PGC 29653	UBV	CTIO0.9m	*GALEX*	*Spitzer*	PT, FP
	UGCA 205, Sextans A	...	...			NCCD
DDO 154	PGC 43869, UGC 8024	UBV	HT	*GALEX*	*Spitzer*	PT, 4:1
	NGC 4789A	...	...			NCCD
DDO 69	PCG 28868	UBV	HT	*GALEX*	*Spitzer*	PT, FP
	UGC 5364, Leo A	...	...			NCCD
M81dwA	PGC 23521	UBV	HT	*GALEX*	*Spitzer*	HT, 2048
DDO 210	PGC 65367, Aquarius Dwarf	UBV	KPNO4m	*GALEX*	*Spitzer*	KPNO4m, HT
		...	...			Mos, 2048

Table 2.2: From left to right the columns represent: Galaxy name, Other names, Optical and near IR bands observed, Instruments used for the optical and near IR bands, Instrument used for the FUV observations, Instrument used for the 3.6 μm, 24 μm observations , Instrument used for the Hα observations. The telescope codes are the following: HT= 1.1–m Hall telescope at Lowell Observatory, PT= 1.8–m diameter Perkins telescope at Lowell Observatory, FP= Ohio State University Fabry-Perot used as a simple 3:1 reducer, 4:1= 4:1 focal reducer, KPNO4m= Kitt Peak National Observatory 4–m telescope, Mos= KPNO mosaic camera, 2048= SITe 2048×2048 CCD, NCCD= a TI 800×800 CCD provided to the Lowell Observatory by the National Science Foundation, NOTI= a TI 800×800 CCD on loan to the Lowell Observatory from the US Naval Observatory, Flagstaff station, CTIOs= Schmidt telescope at Cerro Tololo Inter-American Observatory, CTIO0.9m= 0.9–m telescope at Cerro Tololo Inter-American Observatory. The galaxies in this table are ordered by decreasing metallicity.

The galaxies in our subsample (see Fig. 2.1) are no further than 4.6 Mpc away (DDO 165) and no closer than 0.7 Mpc (IC 1613). Table 2.2 illustrates the range of wavelengths and consequently instruments, we used in our attempt to get as complete a picture as possible on what governs star formation in dwarf galaxies. The ancillary data and their provenance are discussed in Section 2.1.2. To ensure continuity between our study and previous studies in this field (e.g. Bigiel et al., 2010b; Leroy et al., 2008) and to ease the comparison of our results with the literature we overlapped our sample with the THINGS sample. Therefore, seven of the THINGS galaxies (DDO 50, DDO 53, DDO 63, DDO 154, M81dwA, NGC 2366, NGC 4214), passed on to the LITTLE THINGS project were selected.

2.1.2 Ancillary Data

The UBV optical data of our subsample were obtained with five different telescopes: the 1.1–m Hall telescope at Lowell Observatory, the 1.8–m Perkins telescope, the Kitt Peak National Observatory 4–m telescope, the Schmidt telescope at Cerro Tololo Inter-American Observatory, and the 0.9–m telescope at Cerro Tololo Inter-American Observatory, from 1993 to 2002 (see Table 2.2).

We have $K-$band observations available for only three galaxies in our subsample: DDO 168, NGC 4214, and NGC 2366. These were obtained from 1996 to 1998 again at Lowell Observatory with the 1.8–m Perkins telescope. More details on the instrumental setup and data processing can be found in Hunter & Elmegreen (2006), where these data have been published.

The Hα data were observed from 1988 to 1998 in a large campaign dedicated to irregular galaxies. Details of that campaign and its results can be found in Hunter & Elmegreen (2004). In Table 2.2 we only list the telescope names used for the Hα observations of each galaxy in our subsample. Two members of our subsample M81dwA and DDO 210 show no emission in Hα.

The FUV images used in this thesis have been obtained by the Galaxy Evolution Explorer satellite (*GALEX*) which images simultaneously in two channels FUV (bandpass of 1350-1750 Å and resolution of 4″) and NUV (bandpass of 1750-2800 Å and resolution of 5.″6). The *GALEX* data processing details and analysis are presented in Hunter et al. (2010). Out of the 18 dwarf galaxy members of our subsample two, DDO 155 and DDO 165, were not observed in FUV.

The *Spitzer* data have been acquired as part of large surveys such as the Spitzer Nearby Galaxies Survey (SINGS; Kennicutt et al., 2003) and the Local Volume

Legacy Survey (LVL; Dale et al., 2009), which together made significant libraries of data on nearby galaxies in a multitude of bands available to the astronomical community of which we use the 3.6 μm and 24 μm bands.

2.2 H I Observing Strategy and Data reduction

With the ancillary data at hand, the LITTLE THINGS team was awarded 376 hours of neutral hydrogen observations in a sample of 42 dwarfs with the NRAO[3] Jansky Very Large Array (VLA[4]). In the case of all these galaxies we combined observations from the VLA archives where available with new observations where necessary in order to achieve complete sets of B–, C– and D–array data. We used 1.3 or 2.6 km s^{-1} channel separation to resolve kinematic structures. To probe high resolution structures as well as extended emission each complete set of B–, C– and D–array data summed up approximately 20 hours of observations, 12 hours in B–array, 6 hours in C–array and 2 hours in D–array. Among the galaxies in our sample, DDO 216 is the only one for which no observations in the B–array configuration were performed. Still the spatial resolution achieved for this galaxy (DDO 216) has not been compromised since it is situated at a distance of only 1.1 Mpc from us. In the case of the galaxies inherited from the THINGS project (DDO 50, DDO 53, DDO 63, DDO 154, M81dwA, NGC 4214, NGC 2366) we have used the THINGS' team calibrations and data combination and we have only changed the imaging technique, using Multi–Scale CLEAN (see Section 2.3) instead of the residual rescaling imaging technique used by Walter et al. (2008). In my subsample of 18 galaxies, three data sets for the galaxies DDO 168, DDO 187 and DDO 155 are composed of completely new observations, the one on DDO 168 being discussed in detail in Chapter 3.

The new observations were scheduled while the VLA was going through its upgrade to EVLA: the old VLA front–end and back–ends being replaced with new EVLA ones. Until the new correlator came online, to continue functioning the telescope relied on hardware to convert the digital signals from the EVLA front–end into analog signals to be fed into the VLA correlator. This conversion however caused extra power to be aliased into the bottom 0.7 MHz of the baseband, being strongest

[3]The National Radio Astronomy Observatory is a facility of the National Science Foundation operated under cooperative agreement by Associated Universities, Inc.

[4]These data were taken during the upgrade of the VLA to the Expanded VLA or EVLA. In this paper we refer to the instrument as the VLA, the retrofitted antennae as EVLA antennae, and non-retrofitted antennae as VLA antennae. This emphasizes the hybrid nature of the instrument and distinguishes it from the far more powerful Jansky VLA or JVLA it has become since 2012.

at the lowest frequencies and dropping off rapidly with frequency. The aliased signal manifests itself on EVLA–EVLA baselines as a noise increase, the correlator power entering with a quasi–random phase, thus scattering this aliased signal across the map. On VLA–EVLA baselines the signals are largely uncorrelated, leading to only a marginal noise increase. As the upgrade progressed however, the number of EVLA–EVLA baselines increased, leaving fewer reliable baselines to work with.

2.2.1 Observing strategy

Signal being aliased into the first 0.7 MHz of the baseband has a serious impact on observing, especially when observing in narrow bands as it affects all fields that contain continuum emission. In spectral line mode the actual line emission may not suffer from aliasing if the bandwidth used is at least 1.5 MHz and the spectral line is narrow, falling beyond the affected 0.7 MHz. The phase and bandpass calibrators are continuum sources, hence they are affected. In most cases, for the galaxies, the field of view will contain both line and continuum emission and removing the continuum requires extra care. In all cases noise is aliased into the band and will decrease the effective sensitivity, with the channels closest to the baseband edge being most affected. This is most noticeable on EVLA–EVLA baselines, and to a lesser extent on EVLA–VLA baselines; VLA–VLA baselines are not affected (see Fig. 2.2).

We observed without Doppler tracking, at a fixed frequency, to avoid phase jumps on EVLA–VLA baselines. We added a dummy scan to make sure the antennas start observing at the same time from the very start of our observing session. We selected our calibrators to be strong sources, to ease the calibration process and added extra calibrator scans bracketing the source whenever there was a need for a change in frequency, in order to track phase jumps due to the frequency changes.

In our observations we had a number of sources which were being observed through Galactic H I. The standard approach in these cases is observing both primary and secondary calibrators offset from the Galactic H I contaminated zone of the band. In our observing campaign, however, we observed only the primary calibrator with a plus and minus offset, avoiding in this way changes in frequency when looking at the secondary calibrator, changes that could easily cause compromising phase jumps.

To make up for the loss in sensitivity due to the aliasing problem, the LITTLE THINGS team was granted extra observing time, which was dynamically scheduled,

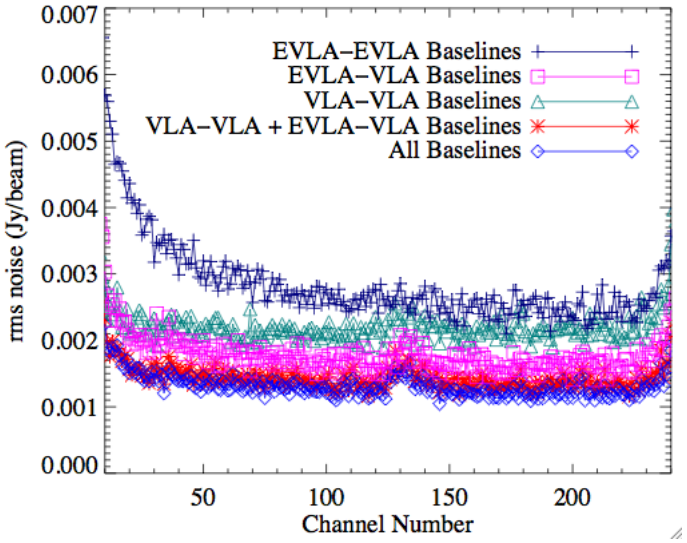

Figure 2.2: Noise level(left) and flux intensity of the secondary calibrator(right) as a function of channel number for data obtained observing with 26 antennas and 12 of them EVLA ones, during the EVLA–VLA transition period for different combination of baselines: all baselines (open blue diamonds), VLA–EVLA baselines (open magenta squares), VLA–VLA baselines (open green triangles), EVLA–EVLA baselines (navy plusses) and VLA–VLA plus VLA–EVLA baselines (red stars).

in short 2–3 hour blocks. Without an exact time allocation and without Doppler tracking, the dynamically scheduled observations required careful planning to ensure that the observing frequency was the appropriate one for the aimed source at the time of observation. The sensitivity loss compensation came also at the price of more data reduction and more efforts in combining the different array data sets into a final one.

All new observations were made by us from late 2007 through to 2008. While the archival observations were done in 2IF mode with online Hanning smoothing and 128 channels, for the new observations, taken during the VLA to EVLA transition, we did not use online Hanning smoothing due to bandwidth considerations related to the special observing setup imposed by the EVLA–VLA transition. Any Hanning smoothing applied to the new data was done as part of the data reduction. To account for variations across the bandpass and overall flux calibration, for all 18 galaxies in the subsample, we used as a flux density and bandpass calibrator one of the following three: 3C286, 3C48, 3C147. The choice of bandpass calibrator (primary calibrator) was based on which of the three was above the horizon at the time of observation.

Table 2.3. VLA Observation Settings

Name	Array Config.	Observing Date yy-mm-dd	TOS (min)	Secondary Calibrator	BW (MHz)	Han.	Chan. No.
DDO 168	D	08-Jul-07	120	1227+365	1.56	N	256
	C	08-Mar-27, 08-Apr-22	355	1227+365	1.56	N	256
	B	08-Jan-20, 08-Feb-01, 08-Feb-06	675	1313+549	1.56	N	256
DDO 133	D	04-Jun-21, 04-Aug-21/22	483	1221+282	1.56	Y	128
	C	08-Mar-22, 08-Jun-3	355	1227+365	1.56	N	256
	B	07-Dec-24, 08-Jan-11, 08-Feb-02	520	1227+365	1.56	N	256
NGC 4214*	D	94-Jan-27	135	1227+365	0.78	Y	128
	C	93-Aug-09	240	1227+365	0.78	Y	128
	B	94-Jun-30, 94-Jul-1	345	1227+365	0.781	Y	128
DDO 50*	D	91-Mar-07	105	0836+710	1.56	Y	128
	C	90-Dec-02	135	0836+710	1.56	Y	128
	B	90-Aug-10	330	0859+681	1.56	Y	128
DDO 216	D	08-Mar-22, Jun-3	122	2255+132	0.78	Y	128
	C	95-Mar-13	380	2255+132	0.78	Y	128
NGC 2366*	D	04-Jul-02	90	0614+607	1.56	Y	128
	C	04-Feb-23	120	0614+607	1.56	Y	128
	B	03-Dec-03	330	0614+607	1.56	Y	128
WLM	D	01-Oct-19	20	2321-163	1.56	Y	128
	C	00-Mar-31	312	2321-163	1.56	Y	128

	B	02-Jul-9, 02-Jul-12	504	2357-114	1.56	Y	128
DDO 187	D	08-Jul-11, 08-Aug-05, 08-Aug-06, 08-Aug-16	186	1330+251	1.56	Y	128
	C	08-Mar-28, 08-May-30	228	1330+251	1.56	Y	128
	CnB	08-Feb-10, 08-Feb-12	108	1330+251	1.56	Y	128
	B	07-Nov-17	474	1330+251	1.56	Y	128
DDO 155	D	08-Aug-17, 08-Aug-02	158	1347+122, 1254+116	0.78	N	256
	C	08-Jul-13, 08-Aug-02	300	1347+122	0.78	N	256
	B	07-Nov-17, 08-Feb-10	554	1254+116, 1347+122	0.78	N	256
DDO 165	D	08-Jul-06, 08-Jul-31	106	1313+675	1.56	N	256
	C	08-Mar-23, 08-Apr-14, 91-Jan-16	555	1313+675, 1358+624	1.56	N	256
	B	08-Jan-25 , 08-Feb-03, 08-Feb-09	540	1313+675	1.56	N	256
IC 1613	D	95-Apr-14	216	0106+013	1.56	Y	128
	C	96-Feb-11	354	0106+013	1.56	Y	128
	B	95-Dec-16, 95-Dec-18	726	0106+013	1.56	Y	128
DDO 63*	D	91-Mar-07	105	0836+710	1.56	Y	128
	C	90-Dec-02	135	0836+710	1.56	Y	128
	B	90-Jul-23	360	0917+624	1.56	Y	128
DDO 53*	D	04-Jul-09	90	0834+555	1.56	Y	128
	C	04-Feb-23	120	0834+555	1.56	Y	128
	B	03-Dec-22	360	0834+555	1.56	Y	128
DDO 75	D	92-Jul-13	90	0941-080	1.56	Y	128
	C	92-May-09, 04-May-14, 08-Mar-16	546	0941-080, 0943-083	1.56	Y	128
	B	05-May-09, 05-May-10, 07-Nov-21	306	0943-083	1.56	Y	128

	AB	94-Jun-17	42	0941-080	1.56	Y	128
DDO 154*	D	04-Jul-05	90	1330+251	1.56	Y	128
	C	04-Apr-28	150	1330+251	1.56	Y	128
	B	05-May-06	375	1330+251	1.56	Y	128
DDO 69	D	92-Jul-19	110	1003+351	0.78	N	256
	C	92-Apr-20 to Apr-21	250	1003+351	0.78	N	256
	B	95-Dec-02	420	1003+351	0.78	N	256
M81dwA*	D	01-Dec-10	195	0841+708	0.78	Y	128
	C	02-Nov-03	135	0841+708	0.78	Y	128
	B	03-Dec-16	345	0921+622	0.78	Y	128
DDO 210	D	02-Nov-01	186	2047-026	0.78	Y	128
	CD	95-Jan-20	122	2011-067	0.78	Y	128
	C	99-Jan-25	304	2011-067	0.78	Y	128
	B	02-Aug-02 , 02-Aug-09, 02-Aug-19	389	2011-067	0.78	Y	128

Table 2.3: From left to right the columns represent: Galaxy name, VLA Array configuration, Observing Date, Time on source (TOS) in minutes, the secondary Calibrator, Bandwidth in MHz, Hanning smoothing: Y or N, and Number of Channels. A star next to the galaxy name indicates the galaxies that are shared between the LITTLE THINGS and the THINGS projects. The galaxies in this table are ordered by decreasing metallicity.

The secondary calibrators, for each galaxy in our subsample track changes in phase and amplitude with time and are listed in Table 2.3 along with other observational settings. In general, each secondary calibrator was chosen on the basis of brightness and proximity to the source, all falling within about 12 degrees of the target galaxy. They were observed in scans of typically 4 minutes, alternating with 20 minutes on source.

2.2.2 Data calibration and data combining

For the data calibration and reduction we used the AIPS[5] package (version 31DEC08). Standard routines were used, although extra steps were necessary to deal with the problems brought on by the VLA upgrade. To better understand the aliasing effect, we imaged separately different combinations of baselines and measured the noise in each channel of each resulting dataset, see Fig. 2.2. The navy plusses indicate the behaviour of the EVLA–EVLA baselines which are most affected by the aliasing effect.

In our tests, we have also found that due to the aliasing effect, the EVLA–EVLA baselines contribute a considerable noise increase to the overall dataset, so much so that the noise within the data set containing all baselines (blue open diamonds) and the noise within the data set without the EVLA–EVLA baselines (red stars) are at the same level. This means that even if it were possible to rescue the EVLA–EVLA baselines it would not improve the signal–to–noise level.

At this point our only remaining concern is whether the EVLA–EVLA baselines are invaluable in terms of *uv*–coverage. After further tests we find that, as the EVLA antennas were spread quasi–randomly across the array, our *uv*–coverage was complete enough to make do without the EVLA–EVLA baselines. Therefore one of the first steps that we took in the calibration of the data was to discard all EVLA–EVLA baselines.

We will present the data reduction and recipes used for combining our data, by mentioning only the most relevant steps taken to obtain high quality data and to attenuate the effects of the above mentioned observing setup difficulties. When loading data into AIPS, with FILLM, we allow channel/IF dependent weights and by doing so we get the true weight of all visibilities just as observed. The true weights represent valuable and accurate information on the IFs and antenna performance at

[5]The Astronomical Image Processing System is a software package provided by the National Radio Astronomy Observatory.

the time of observation and when properly used can increase the sensitivity of the final image. After running task FILLM we will end up with two files, the Channel 0 file representing a continuum data base obtained by averaging the inner 75% of the channel range of the spectral line observations and the actual Line file. Because of the aliasing effect, the automatically created Chanel 0 file is inaccurate so unlike standard spectral line calibration proceedings, we first work on the Line file applying some necessary corrections and only after that we manually recreate the Channel 0 as follows.

Once the data are loaded into the AIPS package, we remove 8% of the channels, 4% on each side of the band, using UVCOP. We choose to discard them at the very beginning because the increased noise at the edges affects the bandpass calibration, which is one of the first issues to deal with during the calibration. We run task SETJY to provide the flux density of the primary calibrators. After removing the EVLA–EVLA baselines, flagging of other bad data, and correcting for the position of the antennas with VLANT we proceed with the bandpass calibration (the correction for channel to channel sensitivity variations), using task BPASS. This step removes VLA–EVLA closure errors, due to non–matched bandpass shapes between VLA and EVLA antennas.

By correcting the bandpass, we can then proceed to reconstruct the Channel 0 using AVSPEC. It is this Channel 0 that we then further calibrate in a fairly standard manner. We copy over the FG table, a table containing a list of all the bad data points and baselines, from the line data (*uv* visibilities as a function of all channels) to the new Channel 0 and execute task CALIB, which generates the SN table containing the complex gain solutions. Next GETJY calculates the flux density of the secondary calibrator and sets the SN table amplitude gains to reflect a common flux density scale. CLCAL creates from the SN table through interpolation a new version of the CL table, containing the complex gain corrections at all time intervals which, applied to the data, completes the calibration process. We then check our calibrated Channel 0 in TVFLG, and image the data. We subsequently transferred the SN table from the Channel 0 to the line data and ran CLCAL on the line data.

At crucial points in our calibration recipe we run a number of tests to check the quality of the calibration to detect any possible problems. These tests involve checking the weights of the data using ANBPL, checking the amplitudes and phases versus *uv*–distance with UVPLT for calibrators and the target galaxy, checking vec-

tor averages of all data for each calibrator and the target with POSSM, making dirty images of the secondary calibrator and the source from the calibrated new channel 0, as well as making dirty cubes of the galaxy at the end of the line calibration.

For the LITTLE THINGS galaxies we have radio interferometric data for all galaxies in three different array configurations B, C and D, that are combined into one dataset. Some of the data in the LITTLE THINGS sample is from the archive, while the rest is recently observed. The archival data, such as the D array data on DDO 133, are Hanning smoothed while the new data are not. Once calibrated, we run CVEL to correct the frequencies from scan to scan as well as to align the dynamically scheduled observations with the regular ones. If Hanning smoothing is necessary, it can be applied to the data within CVEL. Although CVEL applies Hanning smoothing, it does not remove every other channel, which is what was done with the archival data; for that we use task UVDEC. Once the data sets have the same frequency resolution and sampling, are aligned in velocity and precessed to the same J2000 epoch, we use task DBCON to merge them into the final dataset. Because we opted not to use the EVLA–EVLA baselines, the continuum subtraction becomes a matter of simply linear–fitting using the channels without emission on either side of the line profile. We use UVLSF, and a linear baseline, to extract the continuum based on channels free from line emission identified in a dirty cube of all data combined. Once the data are combined and continuum subtracted, we make a standard IMAGR data cube to check for calibration and array combination errors. Continuum maps were also created by averaging all line–free channels.

2.3 Imaging

In the radio domain, to achieve high angular resolution, we make use of interferometers which measure the Fourier transform of the sky intensity distribution. However, interferometric data are affected by incomplete coverage of the aperture plane: unmeasured short–baseline information, missing baselines, missing or deleted hour angle ranges. To remove these effects, deconvolution algorithms are needed and so the CLEAN method (Högbom, 1974) was developed.

2.3.1 CLEAN algorithm for LITTLE THINGS sources

In order to improve the quality of our maps we invested effort in understanding the shortcomings of using CLEAN for low signal to noise extended sources such as the

dwarf galaxies. The disadvantages of CLEAN are:

- In cases of low signal to noise, CLEAN may find clean components in places where only noise spikes are present. (Solution: If sources of known structure, windowing to limit the search area, speeds up the algorithm and makes it more reliable. Normally the flux of a clean component is set to a 10% of the peak flux of the residual map, a percentage also known as the loop gain. Lowering the value of the loop gain is also a solution to the above mentioned problem. However, it increases the computation time, by requiring a greater number of clean components).

- In the case of extended sources, the contribution to the integrated flux from an extended, low-level intensity distribution can be substantial, even if the brightness in each pixel is below the level down to which the map is cleaned, which means that CLEAN has to go to very low levels to recover all signal. However, it is difficult to do so, as CLEAN tends to diverge when reaching levels of less than a sigma. (Solution: Smoothing the map to a lower resolution improves the signal to noise ratio per pixel for extended sources. However, it also loses information on small scale structure, the very information one was trying to obtain by means of attaining higher angular resolution).

- When the synthesized beam has strong side-lobes, CLEAN can introduce corrugation, parallel stripes in the clean map. These stripes are artificially created, when clean components are found at the position of spurious peaks resulting from side-lobes of a dirty beam subtracted at a nearby position. Such a map will be consistent with the data, but it will not be a realistic brightness distribution (Schwarz, 1984).

- Interferometry is physically limited when it comes to the shortest spacings available. Because the antennas of an interferometer can only be so close to each other, the shortest possible distance between them gives the largest angular size measurable. The interferometer will not measure anything more extended than this largest angular size, hence the missing short spacings problem. CLEAN or any other deconvolution algorithm cannot be discredited because it cannot recover flux that has not been measured, however the effects of

the missing short spacings in the map plane and the ability of CLEAN to deal with such effects is important to ensure that the data actually measured is not contaminated with artefacts. CLEAN is in difficulty when trying to deal with missing short spacing for extended sources, because in their case a large part of the signal is in the short baselines and only a small part of their Fourier Transform is sampled. Another effect of the missing short spacings is the variation of the zero level, also known as "the negative bowl". If we consider a source with a box-like intensity, its FT will be a sinc^2 function. The centre part however is missing from the observation; therefore in the map plane the Fourier Transform of a box-like function with a missing central part will be a sinc^2 function with the central part subtracted resulting in a large depression in the map. (Solution: Obtaining single dish data to fill in the short spacings void, while a useful solution, is not a trivial one, since it involves obtaining matched single dish observations.)

2.3.2 Alternatives to CLEAN algorithm

Since the 1980s, as the above mentioned disadvantages became clearer, different attempts have been made to improve CLEAN, either by using practical solutions such as windowing or a different loop gain, in combination with CLEAN, or by looking into alternatives to the CLEAN method itself. Here are some of the alternatives to CLEAN that have been proposed over the years:

- **Cornwell (1983)** modifies CLEAN by adding a delta function to the beam, an improvement not suitable to very extended sources.

- **Braun & Walterbos (1985)** provide a way to extrapolate the data in the *uv*–plane, however this method is not able to remove the side-lobes.

- **Steer et al. (1984)** define a component as an area in which the intensities are above a certain cut–off and convolve the data in that area with the beam.

- **Brinks & Shane (1984)** suggest a way to use CLEAN to deconvolve a smooth dirty map and still keep the original resolution; they call it "multi-

resolution CLEAN". This method has the disadvantage that it first finds the clean components at the highest resolution, subtracts them and then moves down to the lower resolutions and by doing so it potentially contaminates the lower resolution residual maps with artefacts produced when cleaning the high resolutions.

- **Wakker & Schwarz (1988)** follow on to the concept of multi-resolution CLEAN and add to it. Their multi-resolution CLEAN does not modify the basic CLEAN but instead separates the process into several steps, each step a simple CLEAN with optimised parameters. It creates two intermediary maps, the smoothed map, which has the advantage of making extended structures more compact (point like) and the difference map, obtained by subtracting the smoothed map from the original data, which if also cleaned, makes it possible to retain the original resolution. The disadvantage of this method is that the algorithm works sequentially on all considered scales, which might cause a scale size to be frozen in.

Whereas CLEAN deconvolution normally works by modelling the image as a collection of point sources and it is optimised for sources which are not vastly extended compared to the size of the synthesised beam, Multi–Resolution CLEAN uses smoothing of the map and the dirty beam to decrease the number of clean components and to go down to lower flux levels (Wakker & Schwarz, 1988). A standard CLEAN map consists of a sum of two maps: one containing the restored clean components and the other containing the residual map.

Usually the fluxes are determined on the combined map assuming that the clean beam is the correct one for the entire map, an assumption which fails on extended structures (Jörsäter & van Moorsel, 1995). In reality the flux is calculated correctly only for the cleaned part of the map, for the residual map it is overestimated by a factor equal to the ratio between the dirty and clean beam (for more details, see Walter et al., 2008). For this reason, a standard IMAGR cleaned image for extended structure can overestimate the flux by as much as 50% as shown in Fig. 2.3, bottom left panel, where the red line represents the flux versus radius for a standard IMAGR data cube. The THINGS project dealt with this effect by working with two sets of cubes, one with rescaled fluxes, represented in green in Fig. 2.3, bottom

left panel, which shows the correct fluxes and one without rescaling which preserves the original noise characteristics, (Walter et al., 2008).

Whereas the rescaling deals with overestimating flux, it does not deal with the intrinsic difficulty CLEAN has in dealing with missing short spacings. This is evident from Fig. 2.3 (bottom left panel), where one sees that the flux recovered by standard CLEAN (red line) gradually drops when increasing the radius from 200″ to 800″, reflecting a large scale depression in this radius range and beyond.

2.3.3 Multi–Scale Methods

To address the difficulties that the CLEAN algorithm has with extended emission, Wakker & Schwarz (1988) developed an algorithm, that solves sequentially, in the image plane, for point components and set size Gaussians. The idea of recovering an object by modelling it as a composition of various different scale sizes, rather than a collection of points has opened up a new direction in the field of imaging techniques: the Multi–Scale methods. These methods differ in the way the reconstruction algorithm tries to quantify the strength of the various contributing scales (Cornwell, 2008). We recognise the following approaches:

- **Multi–Resolution Clean**: a special version of CLEAN, which concentrates on the large–scale emission first followed by cleaning at higher resolution. The dirty image and point spread function are smoothed to emphasize the broad emission. The resulting image is then used as an initial model for a CLEAN deconvolution of the full resolution image.

- **Multi–Scale Maximum Entropy**: The image is reconstructed by estimating pixels in the combined space such that the convolution equation is satisfied, after setting a hierarchy of scale sizes. The performance of this algorithm can be improved by decomposing the image to be estimated into several channels of different resolutions (Starck et al., 2002). The disadvantages of this method are the following: it cannot recover simultaneously both compact and extended sources, results depend on the background level, the entropy functions give poor results for negative structures embedded in the background, and spatial correlation in the images is not taken into account.

- **Wavelets**: This type of algorithm searches for clean components not in the dirty image but in the multi-resolution wavelet transform of the dirty image based on the dirty beam. When the signal presents localized features, such as singularities or edges, these features can no longer be well represented by Fourier functions, which extend to the whole spatial domain. Other functions, such as wavelets are better suited for a wide range of signals. Wavelets provide an ideal way to incorporate noise modelling and regularization in the deconvolution methods (Slezak et al., 1990; Starck et al., 2002). Disadvantage: Wavelet Clean is only available for images which do not contain large-scale structures.

- **Pixons**: This method estimates the pixel strengths along with an associated scale size, iteratively decomposing an image into a collection of locally best-fit kernels (usually Gaussians). The combination of strength and scale size is called "a pixon". It has been reported to have a very good performance, however it is not applicable to synthesis observations, because the assumptions that the PSF is compact and that the noise is independent and additive, are not true for Fourier Synthesis (Pina & Puetter, 1993; Puetter, 1995).

- **Adaptive Scale Pixels (ASP)**: This algorithm estimates the best Asp (=a simple functional form defined by specifying the Amplitude, Location and Scale), at the location of the peak in the residual image at each iteration. While the pixon method exploits the locality of the effects of the PSF to limit the dimensionality of the search space, Multi–Resolution Clean explicitly limits the dimensionality of the space by decomposing the image into a fixed set of scales. Both mentioned methods work with a fixed set which remains unchanged from iteration to iteration and does not admit any other scales than those in the fixed set. ASP does not impose a fixed set, but allows changes at each iteration. Due to the inherent coupling of pixels in the true image as well as due to the extent of the PSF, only a sub-set of Asps changes significantly at each iteration, a sub-set which is referred to as an "active-set" and is to be determined at each iteration. Since the members of the sub-set are determined on the fly, the set of scales used at each iteration potentially changes from iteration to iteration and all possible scales are admissible (Bhatnagar &

Cornwell, 2004). Disadvantage: Although it is known to have a good deconvolution performance, it is computationally very expensive.

2.3.4 Multi–Scale CLEAN for LITTLE THINGS

From the methods mentioned above, only the Multi–Resolution CLEAN category can be applied to our data. In this category fall extensions of the Wakker and Schwarz algorithm, which have been implemented independently in CASA by Tim Cornwell: Multi–Scale CLEAN (Cornwell et al., 1999; Cornwell, 2008) and in AIPS by Eric Greisen: Multi–resolution CLEAN (Greisen et al., 2009). Advances in computing have made it possible to solve for different size components simultaneously. Both the AIPS and CASA implementations belong to the Multi–Scale methods category, one of the main differences between them being that whereas the CASA implementation operates in the map plane, the AIPS implementation subtracts the clean components in the *uv*–plane and re–images at each major cycle (Rich et al., 2008). To obtain our final data cubes we opted for the Multi–Resolution CLEAN (Greisen et al., 2009) within IMAGR in AIPS. From here on, although referring to the AIPS implementation we will use the term of Multi–Scale CLEAN.

Multi–Scale CLEAN deals with extended structure by using *a priori* knowledge of the strengths and weaknesses of the CLEAN algorithm and the advantages of smoothing. CLEAN is optimised for sources less extended compared to the size of the synthesised beam. At the same time, when smoothing, the ratio of the source size to beam size improves which means that what was extended in the original resolution is small scale in a smoothed map. More than that, the signal to noise in a smoothed map improves as well as long as the structure in the map remains resolved, allowing a much deeper clean and therefore ensuring that most of the flux is recovered. However, if one were to clean only the smoothed map, that will result in loss of interesting information on small scale structure. To ensure that information on all scales is retrieved, in the AIPS implementation of Multi–Scale CLEAN, the user can choose the model components to be used by specifying the number (up to a maximum of 10) and the widths of circular Gaussians that converted into tapers will be used to make beam and data images at each scale. The 0th scale ensures the recovery of small scale structure as well as dealing with unresolved objects.

To implement the Multi–Scale CLEAN, AIPS uses the multi facets approach available in IMAGR for wide–field imaging. As the sky is a sphere, approximating

it to a two dimensional flat patch only holds for small enough patches of sky, called facets. In wide–field astronomy the imaging is done by imaging facets and putting them together in one image.

While for the wide–field astronomer IMAGR is creating a final map as a composition of imaged adjacent facets, for the Multi–Scale CLEAN user IMAGR creates a map out of overlapping facets over the same area of the sky, each facet representing a different resolution scale. At each major cycle, it selects one of the facets (i.e. spatial scale), re–images that facet with the current residual *uv* data, finds clean components for that facet using minor cycles, subtracts those components from the data and continues until it reaches one of the stopping criteria, prompting clean to go through the next major cycle. The selection of which resolution should be cleaned is done by establishing which resolution has the highest peak flux. The algorithm stops when the flux level in all facets is below the user–defined flux cut–offs. Then, the clean components for all resolutions, each with their corresponding clean beam are restored to the image made at the finest resolution (Greisen et al., 2009). In more recent versions of AIPS (31DEC10 and 31DEC11) the clean components are restored to all facets resulting in cleaned maps for each resolution considered. In this way the AIPS implementation of the Multi–Scale CLEAN, works in both the image plane during the minor cycles and *uv*–plane during the major cycles.

It should be stressed that the parameter choice must be carefully tuned to the data set to be imaged. The Multi–Scale algorithm available under IMAGR in AIPS uses a number of steering parameters. The first two of them are NGAUS and WGAUS representing the number of scales to clean simultaneously and the approximate width of the scales used, in arcseconds. In the literature the AIPS Multi–Scale clean has been mainly applied to data sets from a single array configuration and typically 3-4 gaussians have been used. We apply the algorithm to a B–, C–, and D– configurations combined data set and after several tests (see Fig. 2.3, top left panel) we decided on four gaussians of widths $0''$, $15''$, $45''$, $135''$.

Another important steering parameter is FGAUS which allows the user to impose a stopping criterion for each resolution. In our tests, we established our rms noise threshold by measuring the noise in each of the four resolutions (fields) of a dirty, line–free channel, imaged with Multi–Scale CLEAN. Consequently, we have four different noise levels to work with, one for each field. The four cut–off levels to be set in FGAUS are not independent, being different smoothed versions of the same dataset (see Schwarz 1988).

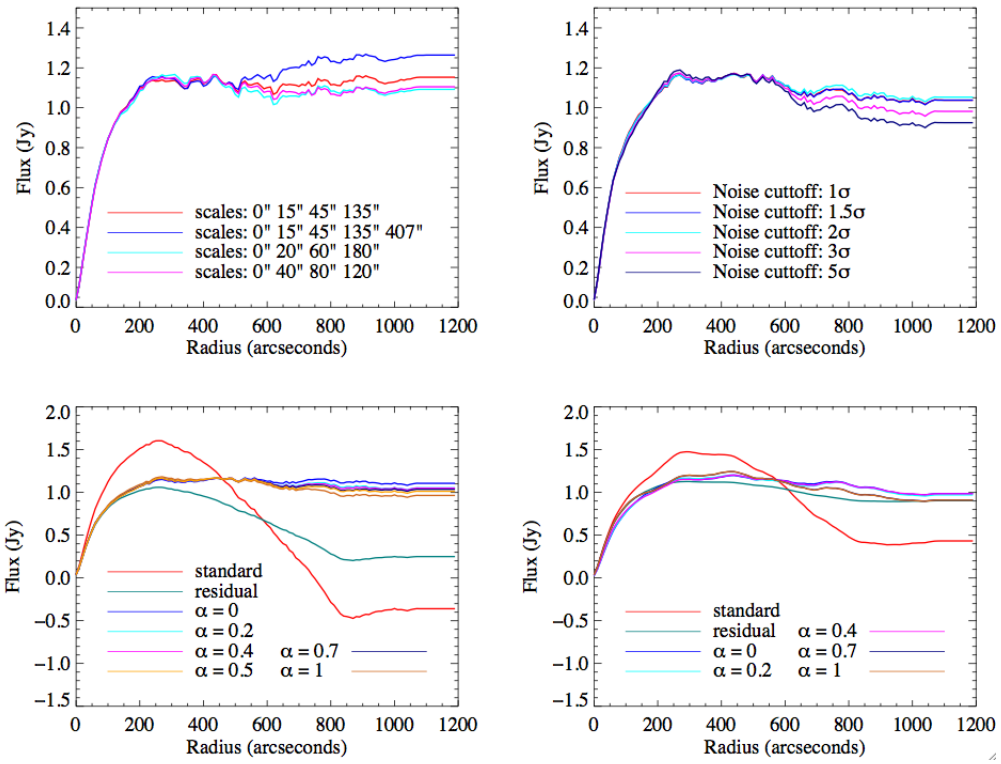

Figure 2.3: *Top Left*: Integrated Flux density vs. radius in DDO 168; with $\alpha = 0.2$, robust= 0, different combinations of scales (red: 0 15 45 135, green: 0 15 45 135 407, blue: 0 20 60 180, magenta: 0 40 80 120). *Top Right*: Flux vs. radius in DDO 168; with $\alpha = 0.2$, robust = 0, variable flux cut–off (red: 1σ , green: 1.5σ , blue: 2σ, magenta: 3σ, cyan: 5σ). *Bottom Left*: Flux vs. radius in DDO 168; cleaned to 2σ level, robust 0, α parameter variable (red: standard CLEAN, green: residuals scaled standard CLEAN, blue: $\alpha = 0$, magenta: $\alpha = 0.2$, navy blue: $\alpha = 0.4$, cyan: $\alpha = 0.5$, orange: $\alpha = 0.7$, yellow: $\alpha = 1$). *Bottom Right*: Flux vs. radius in DDO 168; cleaned to 2σ level, natural weighting, α parameter variable (red: standard CLEAN, green: residuals scaled standard CLEAN, blue: $\alpha = 0$, magenta: $\alpha = 0.2$, cyan: $\alpha = 0.4$, orange: $\alpha = 0.7$, yellow: $\alpha = 1$). In all these plots we look at one emission channel (channel 60).

We tested the FGAUS parameter by setting different flux cut–offs: we tried deeper cleaning, down to 1σ and 1.5σ and more superficial cleaning to 3σ and 5σ. We plotted the integrated flux as a function of radius (see Fig. 2.3, top right panel), in order to understand how the cut–off cleaning level affects recovering of all emission and to find the optimum cut–off level. It should be high enough, for Multi–Scale CLEAN not to diverge but it has to be low enough to retrieve all flux.

Generally, problems arise when the extended nature of the source has it so that large visibility amplitudes are in the exact region, around the origin of the *uv*–plane, where the interferometer cannot probe. This problem, known as the "missing short

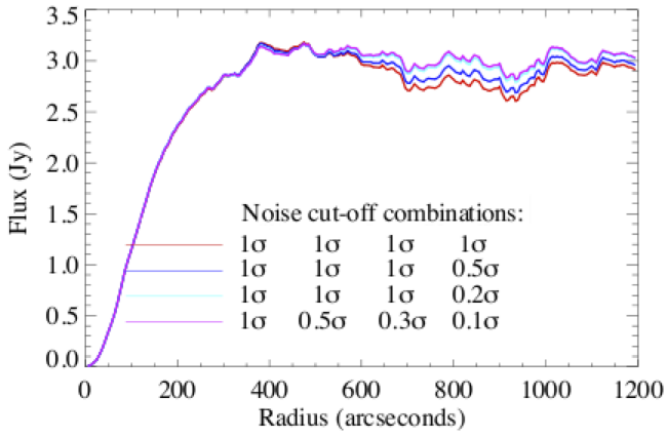

Figure 2.4: Integrated Flux density vs. radius in DDO 168 for different noise cut–off combinations (red: 1σ in all four fields; blue: 1σ in field 1 (highest resolution), 1σ in field 2, 1σ in field 3, 0.5σ in field 4 (lowest resolution); cyan: 1σ in field 1 (highest resolution), 1σ in field 2, 1σ in field 3, 0.2σ in field 4 (lowest resolution); magenta: 1σ in field 1 (highest resolution), 0.5σ in field 2, 0.3σ in field 3, 0.1σ in field 4 (lowest resolution)). The same channel 60 is used as in Fig. 2.3.

spacings" reflects itself in the map plane through the presence of negative intensity regions or depressions, in the areas where the large scale structure has been filtered out by the instrument. With Multi–Scale CLEAN we find that cleaning down to 3 or 5σ is not sufficient; because we are not retrieving all the flux, there remains a small depression at large radii. Cleaning down to 1, 1.5 or 2σ shows a levelling of integrated flux density at larger radii. Cleaning down to 1 or 1.5σ does not retrieve more flux than cleaning down to 2σ; however, clean artefacts such as holes the size of the synthesized beam start to become obvious in the final map. This actually means that we do not need to go any deeper than 2σ to retrieve all flux. Therefore for our LITTLE THINGS dwarf galaxies we are using as cut–off levels 2σ for the robust weighted cubes and 2.5σ for the natural weighted cubes.

Along the same line we have also tested how changing the cleaning cut–off level in each field improves the imaging process (see Fig. 2.4). We found that the changes are minimal, however cleaning to a lower cut–off level in the lowest resolution fields than in the highest resolution one results in a flatter behaviour at large radii. It is important to note that such a per field differential cleaning implies knowing your source well enough to predict what the cut–off level should be in each field and most likely it will be galaxy dependent.

Lastly, there is a steering parameter, IMAGRPRM(11). Naively one would look

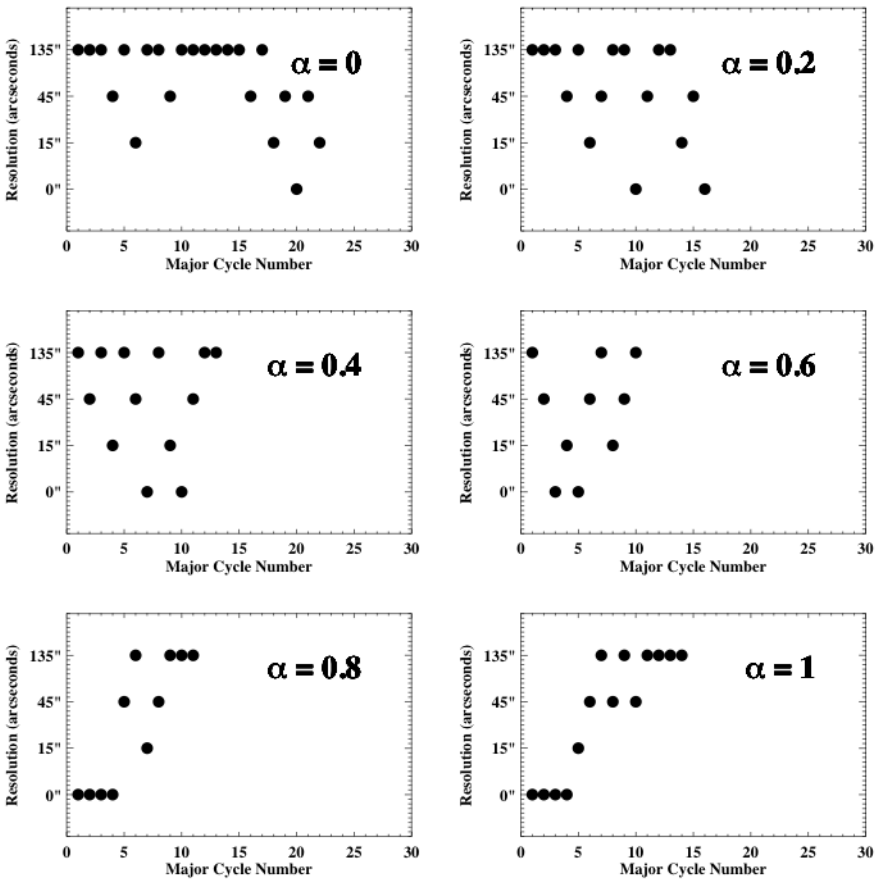

Figure 2.5: Testing the α parameter in DDO 168. Resolution scale versus major cycle number for α=0, 0.2, 0.4, 0.6, 0.8,1.0

for the peak residual at any resolution, and choose the next clean component. However, in this way, since the lowest resolution always shows more flux as the beam area is larger, the algorithm will be biased towards the largest scales (Greisen et al., 2009). Biasing towards or against a certain size structure is done by weighting the peak fluxes in each field by a factor of 1/[(field beam area/minimum beam area)$^{\mathrm{IMAGRPRM(11)}}$]; in other words by controlling the IMAGRPRM(11) parameter, hereafter called the α parameter. This parameter gives one control over which resolution is going to be chosen next. If α=0, than the peak fluxes at each resolution are seen for what they are, hence the natural bias towards the largest scale as explained above becomes obvious. If α=1, the peak flux at the highest resolution will be the true peak flux, while the peak flux at all other resolutions will be adjusted to its smallest value, which is a factor of the current beam over the highest beam, smaller than the true peak flux at that resolution.

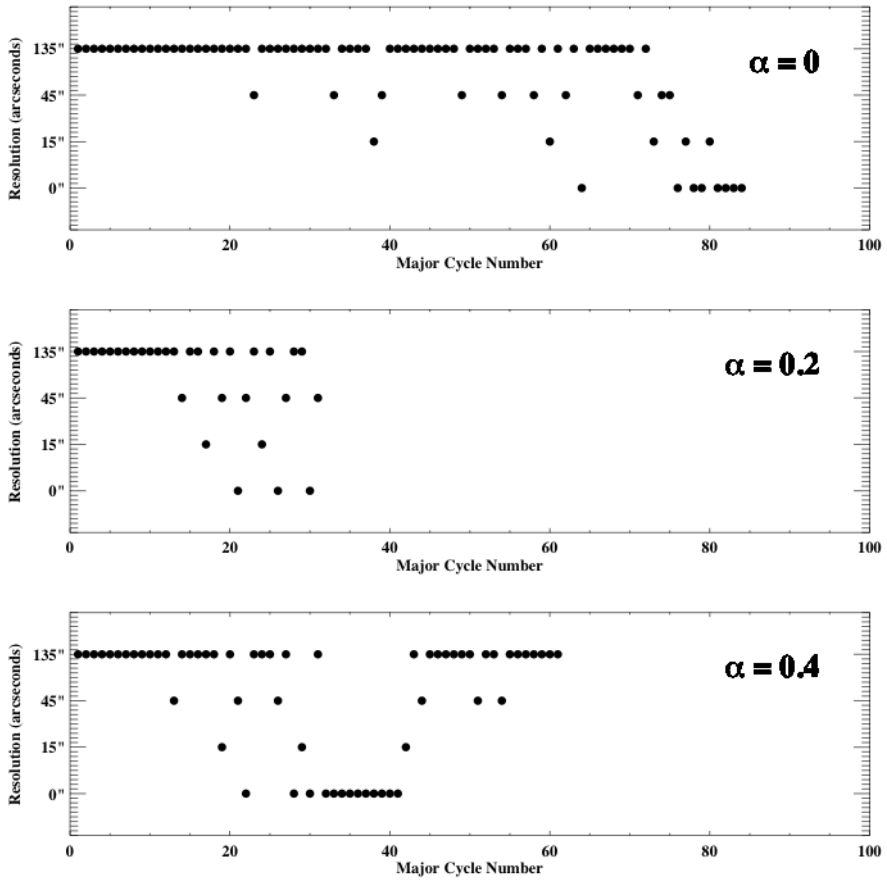

Figure 2.6: Testing the α parameter in DDO 50. Resolution scale versus major cycle number for α=0, 0.2, 0.4. We used channel 70 for this test.

Thus, the highest resolution will be selected first and then the others successively. To further understand how the biasing works we plot the choice of resolution in each major cycle when cleaning one channel with the AIPS Multi–Scale CLEAN (Fig. 2.5 and Fig. 2.6). Fig. 2.5 shows the resolution scale as a function of the major cycle number in DDO 168 for a wide range of α values (0, 0.2, 0.4, 0.6, 0.8,1.0). This plot illustrates that the α value works as intended, it biases towards choosing the lowest resolution scale when α=0.0 and the highest when α=1.0. Although in Fig. 2.5 for α values ranging from 0.2 to 0.6 the choice of scales is in all cases equilibrated, in Fig. 2.6 plotting the resolution scale vs. the major cycle number in DDO 50 for α values ranging from 0.0 to 0.4, the choice of scales is less equilibrated for α=0.4. Therefore, α=0.2 in both DDO 168 and DDO 50 is the parameter which best meets our need for a steering parameter that neither biases towards the lowest, nor towards the highest resolution scales and makes the imaging algorithm spend an equilibrated amount of

time cleaning with each resolution scale.

A balance between small and large scale structure components needs to be found, a balance that is dependent on the kind of object to be imaged. We have made tests on the appropriate choice of α and we find all different α maps have a very similar amount of total flux, which means that no matter which α one chooses, the algorithm is able to converge. Still, choosing the α parameter is in no way trivial. If we subtract too many small scale components (α =1), we will create holes which will be taken by the larger scales as real emission and converted to cleaned flux. On the other hand if we clean too many components on the largest scale (α =0), we start converting noise to clean flux density and the algorithm may even diverge (see Fig. 2.3, bottom panels). In this same Figure, we can see that different α values, although finding similar values in total flux, do behave differently at larger radii. When α=0, the algorithm finds the highest level of total flux (blue line). Most of the time the α=0.2 line follows it very closely. In Fig. 2.3, however, at very large radii the difference between the α=0 line and the rest is more obvious probably because in the case of the particular structure of the object, DDO 168, having been biased towards using points as model components, it starts interpreting smoothed noise as real emission and so to increase artificially the overall flux found in the map. On the other hand, when α= 1 (yellow line), we are imposing on IMAGR a model which says the source is very extended, so IMAGR will spend more time looking for extended components and what remains may not be picked up by the higher resolution within the clean cut–offs imposed. The α = 0.0, 0.2 and 0.4 flatten at large radii and are almost indistinguishable from one another.

The differences between 0.2 and 0.4 as choices for α become more evident when looking at the final and residual maps resulting from applying Multi–Scale CLEAN to a line emission channel for two different structured sources (see Fig. 2.7 and Fig. 2.8). When looking at a source such as DDO 168 the differences between α= 0.2 and 0.4 are hard to distinguish, but when looking at a more complicated source such as DDO 133, things become more obvious.

While for α=0.2 the 15″, 45″ and 135″ residual fields look flat, for α=0.4 one can start seeing signs of over–cleaning (see Fig. 2.8). When comparing Fig. 2.7 and Fig. 2.8, one should also realise how much the choice of the α parameter actually depends on the complexity of the source to be imaged.

When investigating how different α values behave in the natural weighting regime, we find that the residual scaled standard clean follows extremely well the Multi–

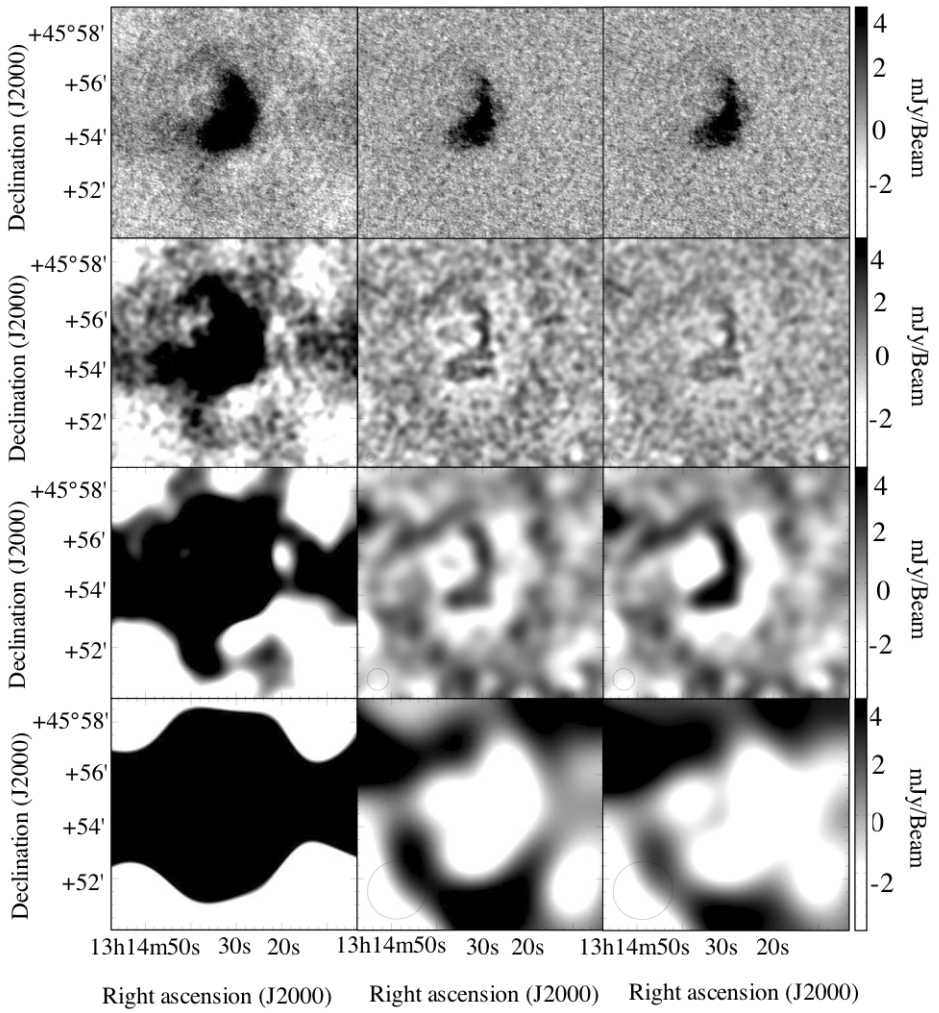

Figure 2.7: DDO 168: Comparison between 2σ cut–off level, robust 0, clean maps (top) and residual maps for $15''$ scale map (second row), $45''$ scale map (third row) and $135''$ scale map (fourth row) for α= 0.2 (middle column) and α= 0.4 (right column). The beam size is shown in the bottom left corner of each figure of the middle and right columns. In the left column we show as a reference the uncleaned map for each field. All panels of the figure use the same grey scale, shown on the right hand side.The same channel 60 is used as in Fig. 2.3.

Scale CLEAN results even at larger radii, which was not the case for the robust=0 case (see Fig. 2.3, bottom right panel). This is not an effect of the Multi–Scale CLEAN, but rather a consequence of the different sampling density in the centre of the *uv*–plane for a natural weighted compared to a robust weighted map.

Regarding our final choice of α, since the LITTLE THINGS project is dealing with extended emission, we started on the premise that an α which balances the time

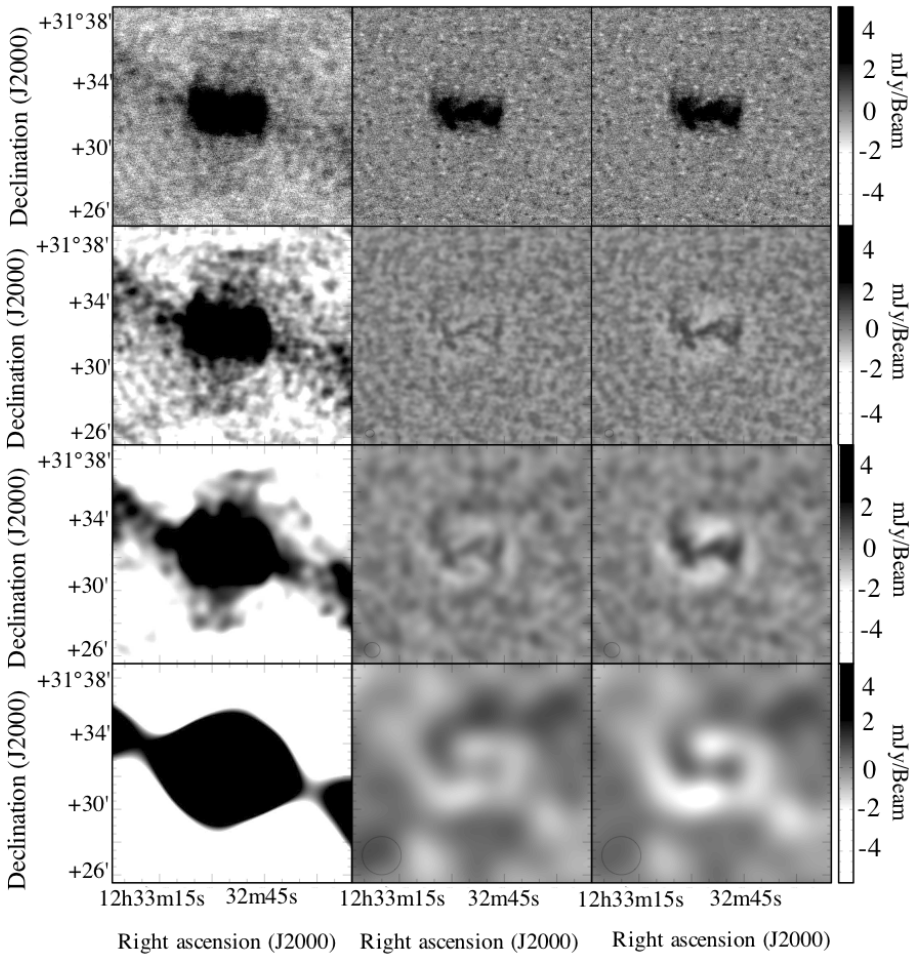

Figure 2.8: DDO 133: Comparison between 2σ cut–off level, robust 0, clean maps (top) and residual maps for $15''$ scale map (second row), $45''$ scale map (third row) and $135''$ scale map (fourth row) for α= 0.2 (left column) and α= 0.4 (right column). The beam size is shown in the bottom left corner of each figure of the middle and right columns. In the left column we show as a reference the uncleaned map for each field. All panels of the figure use the same grey scale, shown on the right hand side.We used channel 58 for this test.

spent on large scales and on low scales would be best. As a result of our imaging tests, we decided to use $\alpha = 0.2$.

There are another two steering parameters, IMAGRPRM(13) and IMAGRPRM(14) useful in cases where the lower resolution fields become easily over–cleaned. They allow the user to either lower the loop gain for a certain resolution (IMAGRPRM(13)), or decrease the cut–off level in each major cycle for a certain resolution by a factor equal to IMAGRPRM(14). These two parameters have been used with their default

values by the LITTLE THINGS team.

If we compare Multi–Scale CLEAN with traditional imaging methods on one of our maps we find that standard CLEAN has a peak flux density which is 40% higher than Multi–Scale CLEAN or the residual scaled one (see Fig. 2.3, bottom left panel). This shows that Multi–Scale CLEAN, unlike standard CLEAN, properly addresses the residual flux problem. At the same time Multi–Scale CLEAN also deals with the missing short spacings better than standard CLEAN, reducing considerably the negative bowl problem in extended sources. It is important to stress that multi–scale CLEAN, although it manages largely to reduce the negative bowl which is the signature of there being emission in the field that is more extended than the largest scale that can be measured, does not retrieve that emission. Any such extended emission is simply not represented in the data.

We know that one can deal with the flux overestimation also by rescaling the map, a process in which the noise characteristics of the map are compromised (for more details, see Walter et al., 2008). This knowledge has prompted us to look into more detail at the noise characteristics of the Multi–Scale CLEAN and investigate whether this algorithm may be superior from this point of view as well. In Fig. 2.9 we present noise histograms for different choices of α corresponding to the cleaned maps and the $15''$ and $45''$ residual maps to show how the noise characteristics are being preserved to a major extent, meaning that when dealing with extended structure using Multi–Scale CLEAN leaves one with a single final cube where the flux and noise characteristics are in no way seriously affected by the implementation of the applied algorithm.

For the LITTLE THINGS galaxies, we are combining data from three array configurations so we chose to work with 4 scales: $0''$ (innate resolution of the data), $15''$, $45''$ and $135''$ resolution. We first determine the noise at each resolution by imaging a line–free channel. This value is further used in computing the cut–off level set with FGAUSS. As cut–offs, we use for each scale, a 2σ level for the robust cubes and a 2.5σ level for the natural cubes. We use IMAGRPRM(11)= 0.2 to ensure we are removing all the emission, which mostly is large scale structure. IMAGRPRM(11) works like a bias, it is steering the algorithm towards spending more time at the smaller scales when close to 1 and at larger scales when closer to 0. The mapping details of the natural and robust weighted data cubes for all the 18 galaxies of my subsample, are available in Table 2.4.

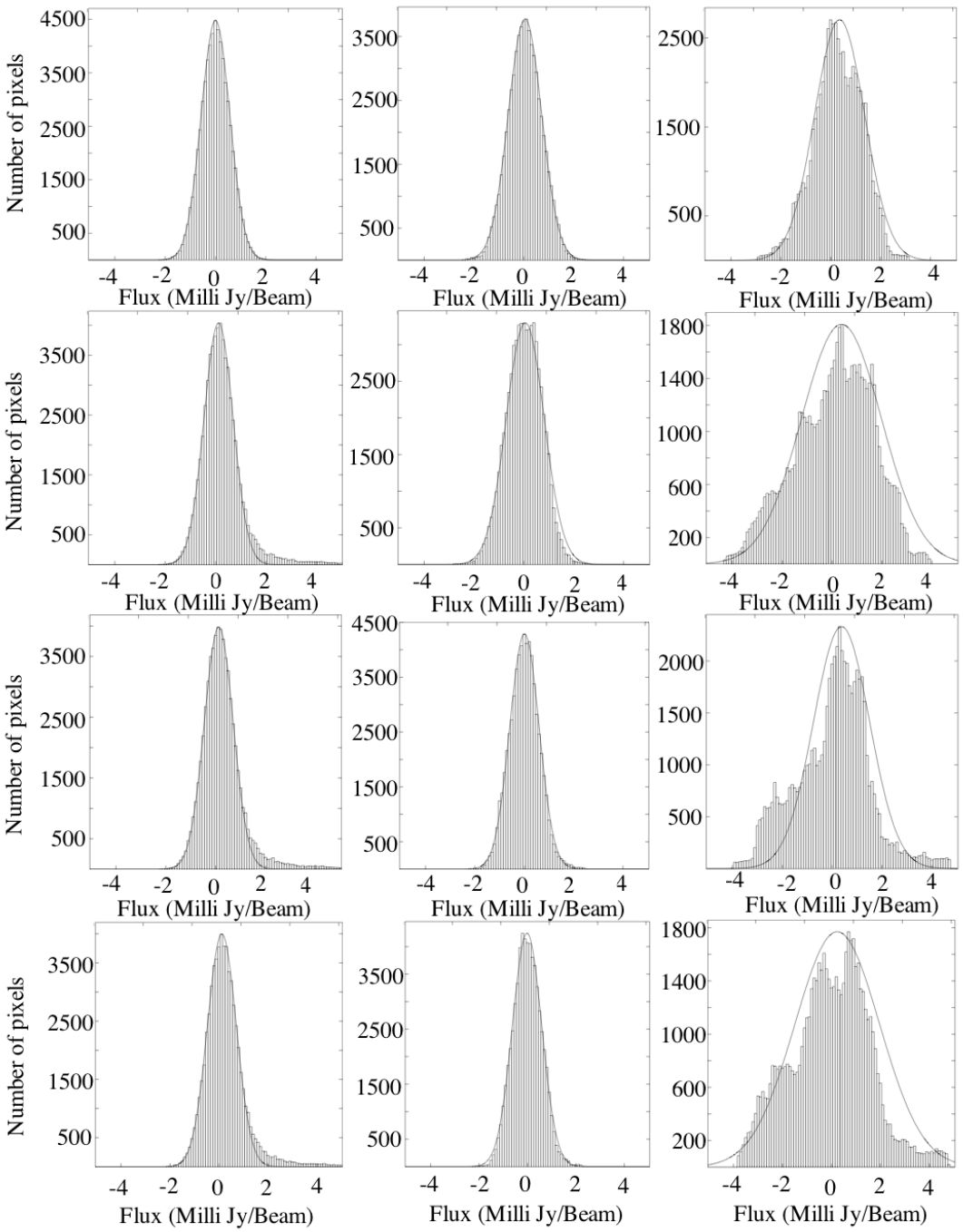

Figure 2.9: The row at the top is put as reference and it represents the noise structure inside a line–free channel in a cube with no cleaning. Rows 2, 3, 4 are the noise histograms in channel 60 of maps cleaned with different α : from top to bottom α= 0, α= 0.2, α= 0.4. Each column is a different map: first column corresponds to the cleaned maps, second column to the 15″ residual map and the third column to the 45″ residual map.

Table 2.4. Map characteristics

Name	Weighting	Bmaj (″)	Bmin (″)	BPA (°)	Noise (mJy beam^{-1})	Galaxy Size [pixels]	Pixel Size (″)	No. Chan.	Chan. Width (km s^{-1})
DDO 168	NA	12.6	11.2	63.2	0.47	1024	1.5	103	2.6
	RO	7.8	5.8	67.5	0.51				
DDO 133	NA	19.2	18.1	-84.0	0.33	1024	1.5	102	2.6
	RO	12.4	10.8	-87.9	0.37				
NGC 4214*	NA	14.7	13.9	-48.2	0.66	2048	1.5	108	1.3
	RO	7.6	6.4	89.8	0.73				
DDO 50*	NA	13.7	12.6	-40.1	1.02	2048	1.5	108	2.6
	RO	7.0	6.1	-32.9	1.07				
DDO 216	NA	20.0	18.9	55.2	0.88	1024	1.5	107	1.3
	RO	16.2	15.4	69.8	0.96				
NGC 2366*	NA	13.0	11.8	-1.6	0.61	1024	1.5	108	2.6
	RO	6.9	5.9	20.1	0.63				
WLM	NA	10.6	7.4	-14.2	0.76	1024	1.5	107	2.6
	RO	7.6	5.1	-3.4	0.82				
DDO187	NA	12.4	11.0	-88.8	0.54	1024	1.5	99	2.6
	RO	6.2	5.5	62.9	0.62				
DDO 155	NA	16.2	15.2	-52.9	0.60	1024	1.5	95	1.3
	RO	11.3	10.1	-84.6	0.65				
DDO 165	NA	14.8	12.9	78.1	0.62	1024	1.5	101	2.6

	RO	10.0	7.6	67.1	0.64				
IC1613	NA	13.2	11.0	-5.0	0.37	2048	1.5	107	2.6
	RO	7.7	6.5	6.7	0.40				
DDO 63*	NA	14.7	12.7	-41.6	1.06	1024	1.5	108	2.6
	RO	7.8	6.0	-71.5	1.19				
DDO 53*	NA	11.8	9.5	-6.0	0.56	1024	1.5	108	2.6
	RO	6.3	5.7	2.59	0.60				
DDO 75	NA	11.9	10.0	4.2	0.45	2048	1.5	104	2.6
	RO	7.6	6.5	13.7	0.51				
DDO 154*	NA	14.1	12.6	-58.1	0.52	1024	1.5	108	2.6
	RO	7.9	6.3	-87.2	0.54				
DDO 69	NA	8.3	7.7	70.8	0.62	1024	1.5	107	1.3
	RO	5.8	5.4	89.3	0.66				
M81dwA*	NA	15.9	14.2	10.2	0.74	1024	1.5	108	1.3
	RO	7.8	6.3	4.5	0.84				
DDO 210	NA	16.6	14.1	-4.0	0.80	1024	1.5	107	1.3
	RO	11.7	8.6	-6.78	0.87				

Table 2.4: From left to right the columns represent: Galaxy name, Weighting function used, Major axis of the synthesized beam in arcseconds, Minor axis of the synthesized beam in arcseconds, Position angle of the synthesized beam in degrees, Noise level in one channel map in mJy beam^{-1}, Size of the map in pixels, Pixel size in arcseconds, Number of channels, and Channel width in km s^{-1}. A star next to the galaxy name indicates the galaxies that are shared between the LITTLE THINGS and the THINGS projects. The galaxies in this table are ordered by decreasing metallicity.

We have used extensively in this thesis the term of "data cube" and here we would like to state the obvious and explain the origin of the term. The H I data and spectral line data in general come as three dimensional measurements of right ascension, declination and frequency or velocity; hence the term of data cube. The image obtained through mapping algorithms described above, is a representation of the sky multiplied by the primary beam response of the antennas. The primary beam is the Fourier transform of the aperture, hence an indication of the sensitivity of our instrument as a function of direction.

At the mapping stage one may choose the appropriate density weighting function that may compensate for the clumping of data in the *uv*–plane. If all points within the *uv*–plane are treated alike, then natural weighting is achieved as well as the best signal to noise ratio for detecting weak sources. If the weighting function is designed as a tradeoff between beam resolution and weighting noise, then we are dealing with robust weighting. A robust parameter of 0.5 has been determined as most appropriate for the galaxies in the LITTLE THINGS sample. The moment maps are obtained by collapsing the data cube from three dimensional into two dimensional images of the information of interest which can be the integrated emission known as moment 0, the intensity–weighted mean velocity known as moment 1 or velocity field and the intensity–weighted velocity dispersion known as moment 2. Although conceptually simple, creating the moment maps requires some care to avoid adding in unwanted noise which we were able to overcome by using interactive blanking (see the following paragraph).

Once the galaxies were imaged we put them through a by now standard blanking process (Walter et al., 2008), where we discriminate against any regions which do not show emission above a set level in at least three consecutive channels. We create a master blanking cube based on the smoothed to 25″ natural weighted maps blanked at 2σ or 2.5σ, which we further apply to all our cubes. Only then do we create the moment maps using the AIPS task XMOM. All moment 0 maps used in this paper are primary beam corrected using task PBCOR.

2.4 Data Display

In this section we would like to put on display all the galaxies in our subsample in a gallery of ancillary data maps combined with moment maps. The purpose of such a display is to understand these galaxies better and visualise the maps that are later

used in the SF analysis. In a subsample of 18 galaxies we can still easily talk about individual galaxies with their dust, gas and star distributions and their kinematical characteristics. We will only briefly comment on the maps presented here. Figures and descriptions of each galaxy in the subsample are ordered by metallicity. The channel maps for all members of our subsample are presented in Appendix A.

- **DDO 168.** Qualified by Broeils & van Woerden (1994) as kinematically peculiar, this dwarf galaxy is compact, with the high density gas concentrated in the centre along with the FUV and Hα emission (see Fig. 2.10). The kinematical peculiarity may be due to a bar which was confirmed in the V–band by Hunter & Elmegreen (2006) (see Fig. 2.11). More details on this particular galaxy can be found in Chapter 3 since it represents one of the two galaxies that made the subject of our pilot study, which is fully described in the above mentioned chapter.

- **DDO 133.** At the first glance there is nothing unusual about this galaxy (see Fig. 2.12). It has a typical solid body rotation with an extended H I distribution, disturbed only by the existence of a few, quite large H I shells (see Fig. 2.13). In V–band this galaxy has features to indicate that it has a bar, however the existence of this bar has not been kinematically confirmed. DDO 133 is the second galaxy of our pilot study therefore its full description can be found in Chapter 3.

- **NGC 4214.** This galaxy is one of the galaxies inherited from the THINGS project, which places it in the category of galaxies with intermediate features between spirals and dwarfs. As can be seen in Fig. 2.14, it has an extended H I disk whereas the old stars traced by 3.6 μm and the young stars as traced by FUV and Hα emission are confined to the centre of the galaxy. In Fig. 2.15, we see again a dwarf galaxy in regular rotation which allows the kinematical determination of quantities such as the inclination.

- **DDO 50.** This galaxy is also a member of the THINGS sample and a dwarf galaxy with a size and metallicity worthy of an intermediary between spirals and dwarfs. Its gas distribution is similar in aspect to NGC 4214, although the presence of H I shells becomes more noticeable in this galaxy. The stars are less centrally confined, although the younger stars traced by Hα are concentrated in a few compact blotches of emission (see Fig. 2.16). DDO 50 shows an

underlying, regular rotation pattern. Some of the excursions that can be seen in Fig. 2.17, in the isovelocity contours of DDO 50 are due to H I associated with the many expanding shells which causes local deviations from regular rotation.The line of sight through these same expanding shells often shows two peaks, well separated in velocity which leads to localised areas with higher values in the moment 2 map.

- **DDO 216.** With this galaxy we start to really sample the dwarf galaxy realm. The H I disk is no longer regular in shape but rather peculiarly compact in the centre (see Fig. 2.18). The Hα emission in this galaxy is scarce, which suggests that this galaxy is not forming stars at present. Yet stars do exist in this galaxy as indicated by the V–band image in Fig. 2.19. The velocity field presented in this same figure indicates that the gas distribution aligns with the stellar distribution. Towards the south there is abundant H I without any optical counterpart. This is where the velocities show almost a reversal, the kinematical major axis turning sharply towards the South.

- **NGC 2366.** One of the larger dwarf galaxies from the THINGS sample. This galaxy has an inclination of over 60 °which gives it the appearance of an almost edge–on galaxy. It has an unusual gas distribution with a ring like distribution of high gas density areas associated with FUV and Hα emission (Fig. 2.20). It also contains two super–giant H II regions and a large embedded star–forming region. With a metallicity lower than that of DDO 216 for example, this galaxy impresses with the regularity of its velocity field (see Fig. 2.21). This galaxy was investigated in detail by Hunter et al. (2001a).

- **WLM.** This galaxy (see Fig. 2.22) is one of the five galaxies in our sample at a distance of around 1 Mpc. Its proximity has made it subject of many studies in the literature. We will only point out that we are dealing with an inclined disk, similar to NGC 2366. The velocity field (see Fig. 2.23) is regular, in fact remarkably so for such a low–mass system.

- **DDO 187.** This galaxy looks like a blob of gas with a central compact region where dense H I, dense FUV, Hα and V–band emissions coincide. Figures Fig. 2.24 and Fig. 2.25 show a misalignment between the V–band and the H I disks, a feature not at all uncommon in dwarf galaxies (Hunter & Elmegreen, 2006). DDO 187 shows an almost constant velocity across its face. This can be due

to either it being nearly face–on or it having intrinsically little rotation as it is at the extreme low–mass end of dIrr scale. In these kinds of galaxies we rely for inclination estimates on optical measurements alone.

- **DDO 155.** Another dIrr galaxy, much like DDO 187, with a compact H I distribution and little in terms of rotation (see Fig. 2.26 and Fig. 2.27). Although a fascinating subject, we were not able to take full advantage of this galaxy's presence in our sample because we have no FUV observations in this galaxy. The Hα data we present in Fig. 2.26 show that SF is currently taking place just to the side of each of the three H I density peaks.

- **DDO 165.** Another irregular distribution of gas where the H I is concentrated in an incomplete ring–like feature. The central part of the galaxy is almost devoid of H I gas suggesting that the SF sites have moved outward. The right side of the ring is associated with Hα emission, see Fig. 2.28 for more details. Also for this galaxy no FUV observations were available and no velocity gradient was observed. The velocity field is fairly regular (see Fig. 2.29). The large gaps correspond to the locations of H I supershells.

- **IC 1613.** One of the most impressive galaxies in our sample is IC 1613. Its round regular distribution reminds us of galaxies such as NGC 4214 or DDO 50, yet the intricate network of H I shells in the centre make it unique (see Fig. 2.30). In this central part of the galaxy, as shown in Fig. 2.31 associated with the H I shells is the V–band emission located.

- **DDO 63.** This is an irregular dwarf galaxy also part of the THINGS sample, where the H I is distributed in a distorted ring–like structure. The centre of this ring coincides with the V–band centre represented by a plus in Fig. 2.32. The H I peaks along the bottom half of the ring structure and the high density H I in this arc is obviously associated with FUV and Hα emission suggesting that recent star formation has taken place in this region. The H I in the upper half of the ring however has no optical counterpart (see Fig. 2.32 and Fig. 2.33).

- **DDO 53.** The H I distribution in this galaxy is quite irregular. As shown in Fig. 2.34, the H I peaks to the North and South of the centre. Bright FUV and V–band emission coincide broadly with the H I, but bracket the centre on to the East and West forming, together with the H I a complete ring or doughnut. There is a hint of rotation (see Fig. 2.35).

- **DDO 75.** This galaxy seems to be a larger version (in angular size, at least) of the just described DDO 53. Again the H I gas peaks in two semi–arcs coinciding with the peaks in both Hα and FUV (see Fig. 2.36). Star formation is active inside both arcs. Like DDO 53, this galaxy shows a modest velocity gradient (see Fig. 2.37).

- **DDO 154.** The gas is distributed in a disk like structure, with the H I peaks concentrated near the centre. Star formation seems to currently take place in the centre of the galaxy, as the H I high density blobs coincide with the Hα and FUV peaks (see Fig. 2.38). Despite its low metallicity this galaxy has a regular velocity field (see Fig. 2.39).

- **DDO 69.** The H I in this galaxy is distributed in a doughnut shape. The highest H I densities are located in the northern, especially north western arc of the H I distribution and they coincide with the peaks in FUV and Hα (see Fig. 2.40). From the quantity of Hα emission it seems that this galaxy has gone through past SF episodes and is currently going through a more quiescent state. This galaxy is one of the lowest metallicity galaxies in our sample. The velocity field of this galaxy shows little to no rotation (see Fig. 2.41).

- **M81dwA.** Here we are almost at the extreme of our metallicity range. The gas distribution is again an incomplete ring–like structure (see Fig. 2.42). The FUV emission comes from the southern part inside the ring structure and partly coincides with the margin of the ring structure. The H I peaks do not coincide with peaks in FUV emission. No Hα has been detected in this galaxy, suggesting that star formation hasn't occurred here in the past 10 Myr. This shows that star formation in dwarf galaxies is episodic, rather than continuous. This galaxy also lacks a velocity gradient (see Fig. 2.43).

- **DDO 210.** The galaxy with the lowest metallicity in our sample has its H I distributed in a half moon structure (see Fig. 2.44). The centre of the V–band image lies on the edge of the H I gas distribution. The FUV emission suggests SF has taken place in the past, but the distribution of the FUV emission although it coincides with the H I gas is not uniformly distributed within this gas distribution. Like in M81dwA, in this galaxy, no Hα has been detected and no significant rotation either (see Fig. 2.45).

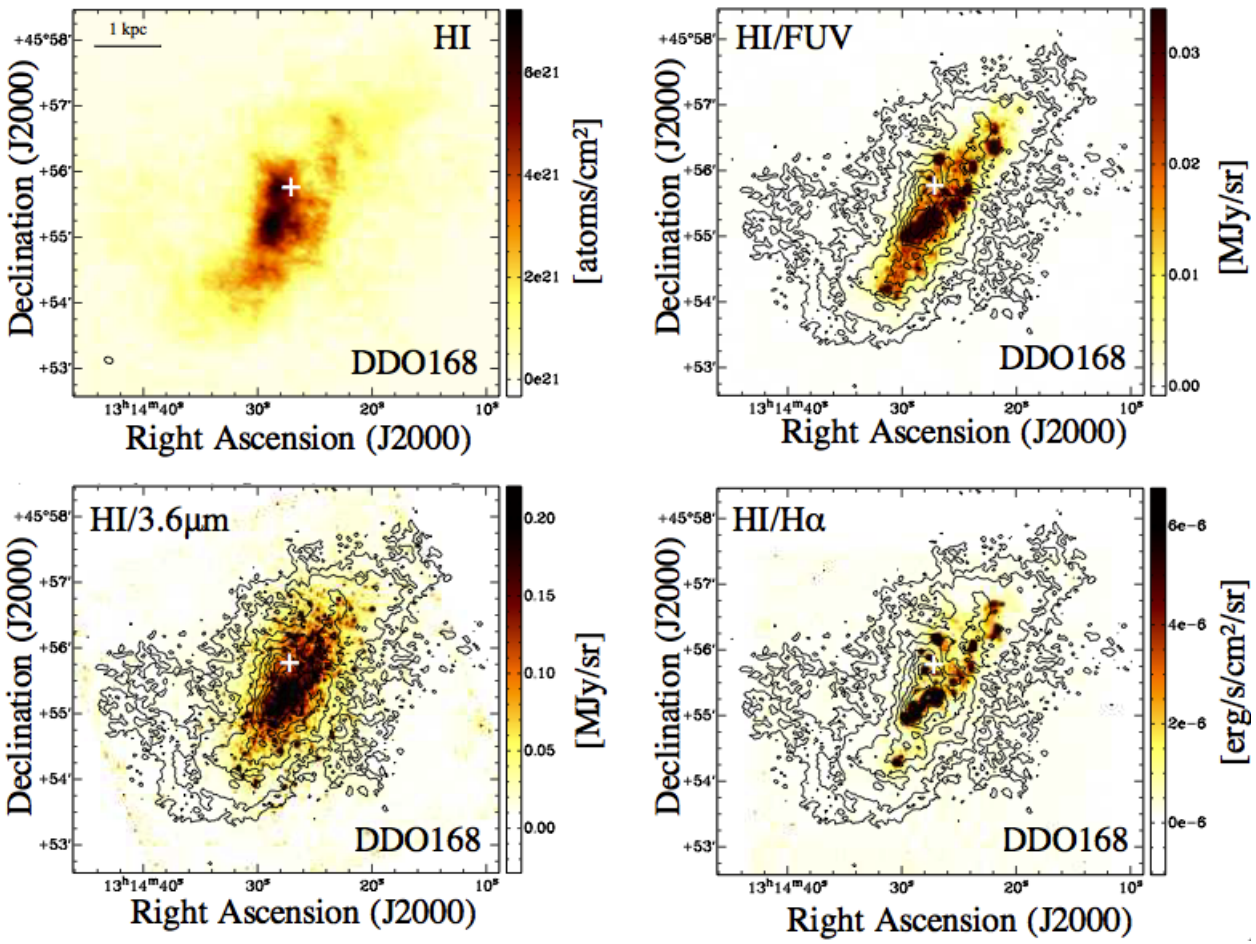

Figure 2.10: Surface density maps for DDO 168. *Top Left*: Integrated H I map (resolution: $7\farcs8 \times 5\farcs8$, lowest confidence level (2.5σ over 3 channels): 2.4×10^{20} atoms cm^{-2}, colour scale: 0 - 6×10^{21} atoms cm^{-2}). *Top Right*: H I contours overlaid on the FUV image (colour scale: 0 - 3×10^{-2} MJy sr^{-1}). *Bottom Left*: H I contours overlaid on the *Spitzer* 3.6 μm image (colour scale: 0 - 0.2 MJy sr^{-1}). *Bottom Right*: H I contours overlaid on the Hα map (colour scale: 0 - 6×10^{-6} ergs s^{-1} cm^{-2} sr^{-1}). The H I contours are at (0.35, 0.5, 1, 2, 4, 6)$\times 10^{21}$ atoms cm^{-2}. In all panels the plus represents the kinematic and the V–band centre of the galaxy. The H I map beam size is indicated in the bottom left corner of the top left panel.

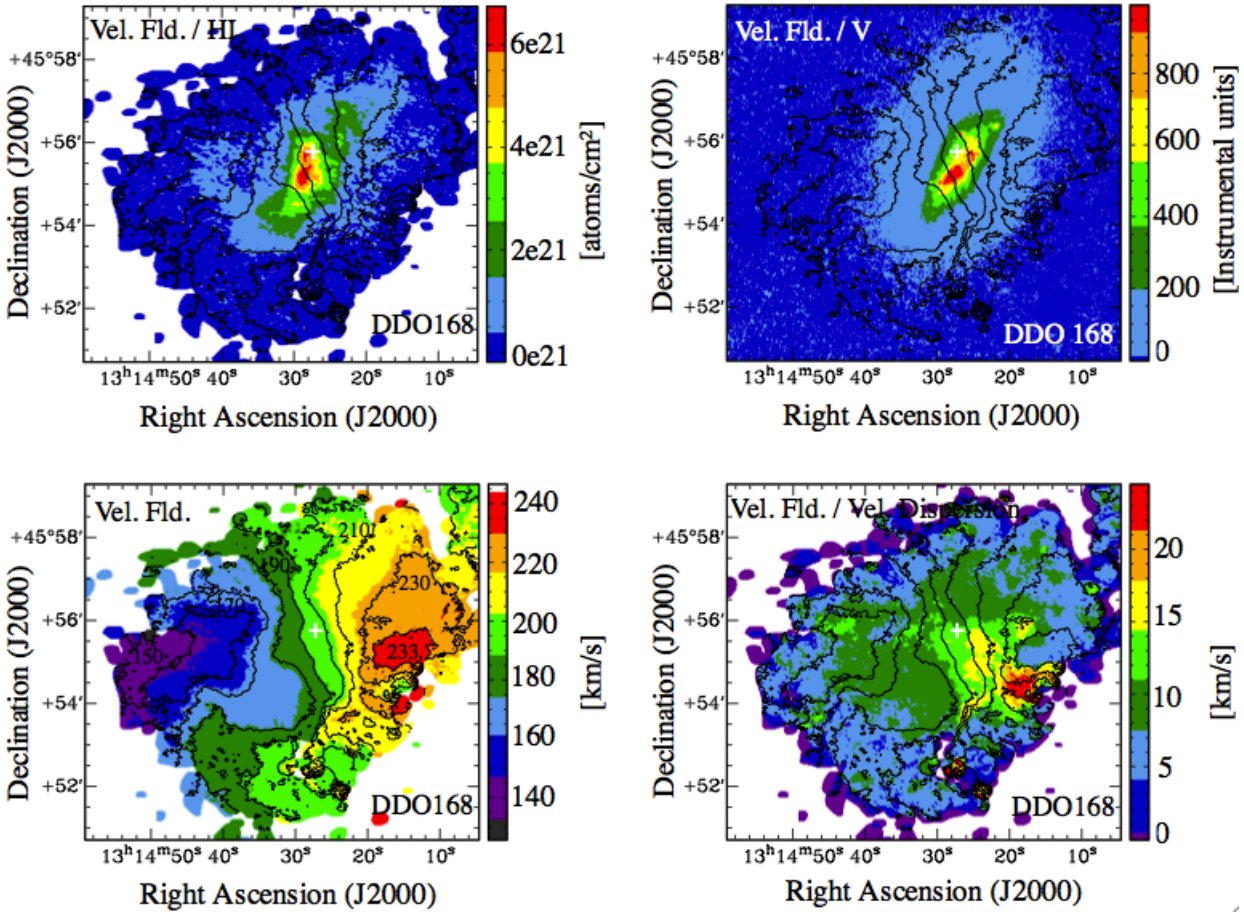

Figure 2.11: Moment maps for DDO 168. *Top Left*: Integrated H I map (moment 0) with velocity field contours. *Top Right*: velocity field contours overlaid on the V–band optical image (colour scale: 0 - 800 instrumental units). *Bottom Left*: Contoured Velocity Field (colour scale: 150 - 250 km s^{-1}). *Bottom Right*: Velocity contours overlaid on the velocity dispersion map (colour scale: 0 - 25 km s^{-1}). The velocity field contours are at (150, 170, 180, 190, 200, 210, 220, 230, 233) km s^{-1}. In all panels the plus represents the kinematic and the V–band centre of the galaxy.

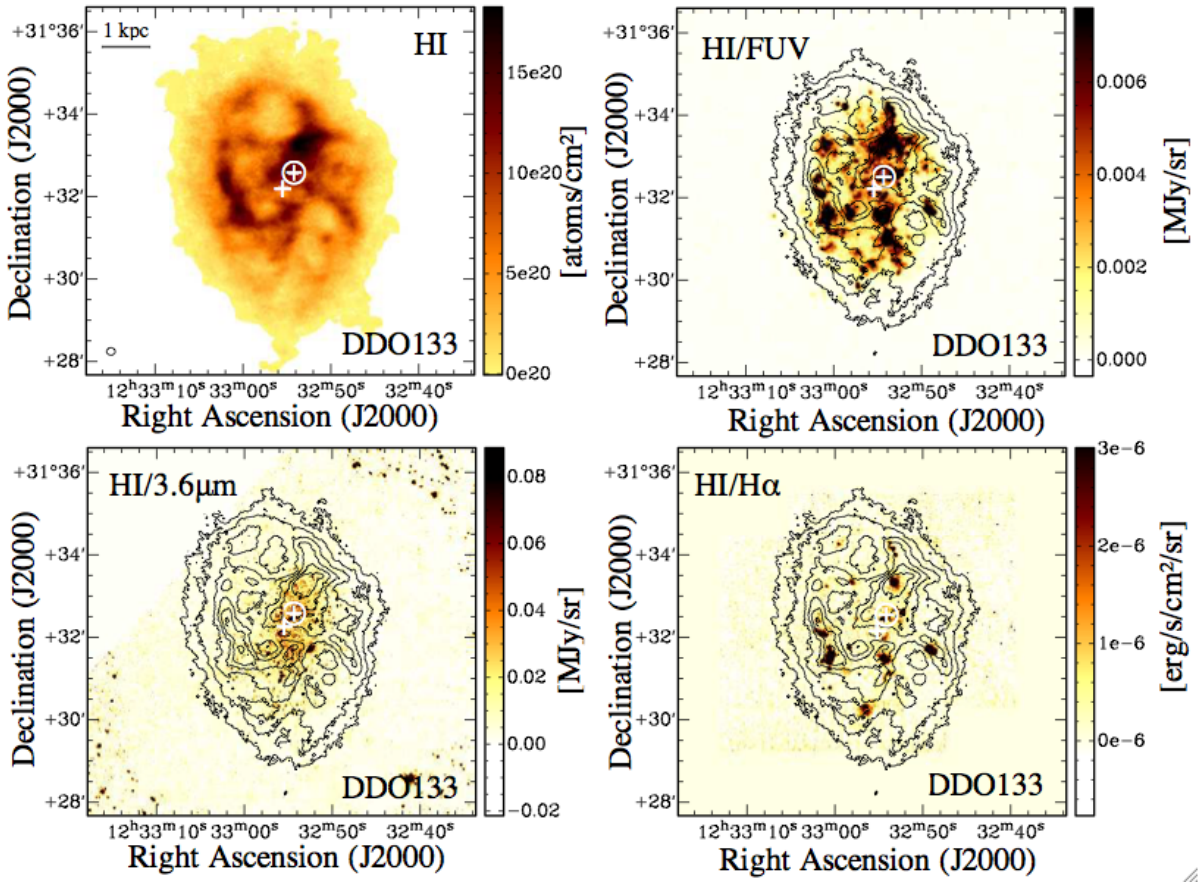

Figure 2.12: Surface density maps for DDO 133. *Top Left*: Integrated H I map (resolution: $12\farcs4 \times 10\farcs8$, lowest confidence level 2.5σ over 3 channels: 0.61×10^{20} atoms cm^{-2}, colour scale: 0 - 1.5×10^{21} atoms cm^{-2}). *Top Right*: H I contours overlaid on the FUV image (colour scale: 0 - 8×10^{-3} MJy sr^{-1}). *Bottom Left*: H I contours overlaid on the *Spitzer* 3.6 μm image (colour scale: 0 - 0.2 MJy sr^{-1}). *Bottom Right*: H I contours overlaid on the Hα map (colour scale: 0 - 1×10^{-7} ergs s^{-1} cm^{-2} sr^{-1}). The H I contours are at (0.1, 0.3, 0.6, 0.9, 1.2, 1.5)$\times 10^{21}$ atoms cm^{-2}. In all panels the plus represents the V–band and the kinematic centre of the galaxy, whereas the circled plus represents the centre of the bar. The H I map beam size is indicated in the bottom left corner of the top left panel.

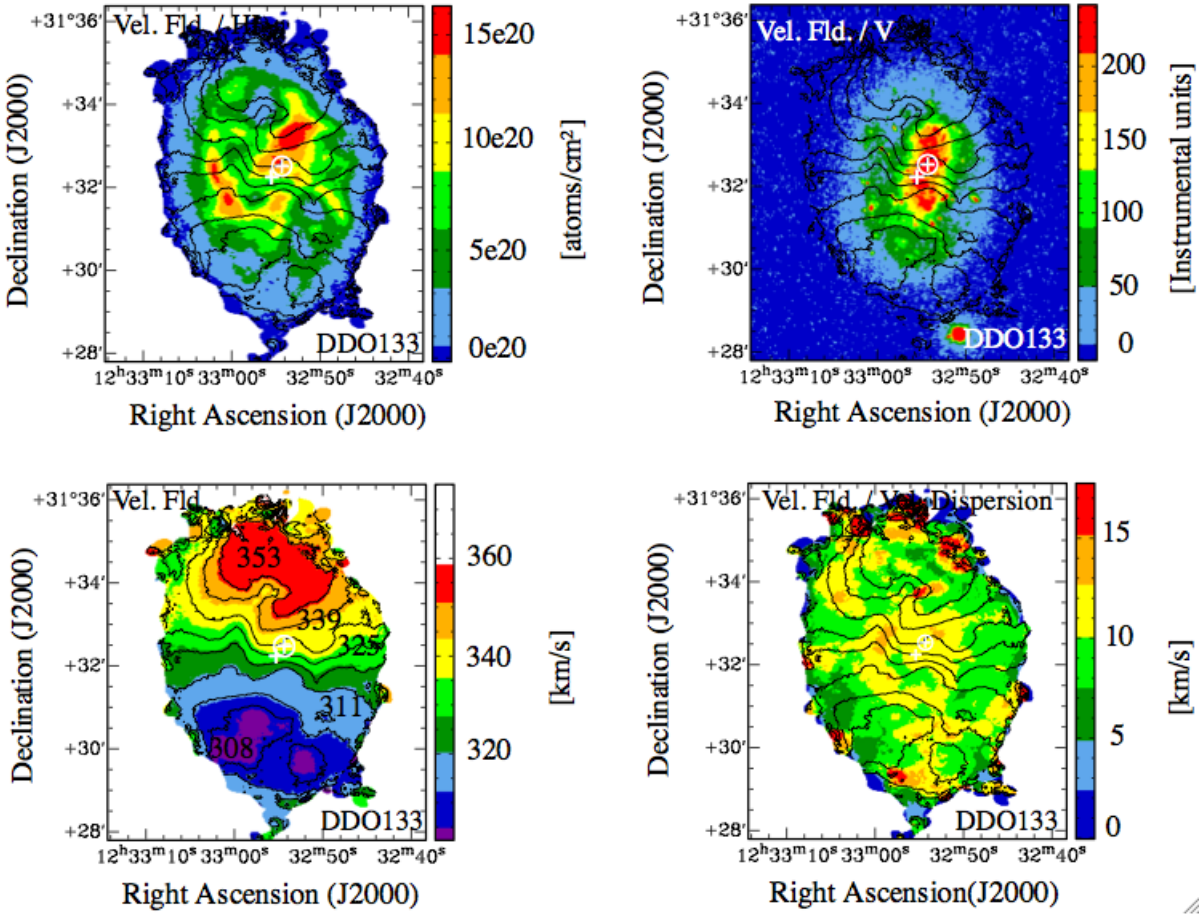

Figure 2.13: Moment maps for DDO 133. *Top Left*: Integrated H I map (moment 0) with velocity field contours. *Top Right*: velocity field contours overlaid on the V–band optical image (colour scale: 0 - 800 instrumental units). *Bottom Left*: Contoured Velocity Field (colour scale: 300 - 360 $\mathrm{km\,s^{-1}}$). *Bottom Right* : Velocity contours overlaid on the velocity dispersion map (colour scale: 0 - 25 $\mathrm{km\,s^{-1}}$). The velocity field contours are at (308, 311, 318, 325, 332, 339, 346, 353) $\mathrm{km\,s^{-1}}$. In all panels the plus represents the V–band and the kinematic centre of the galaxy, whereas the circled plus represents the centre of the bar.

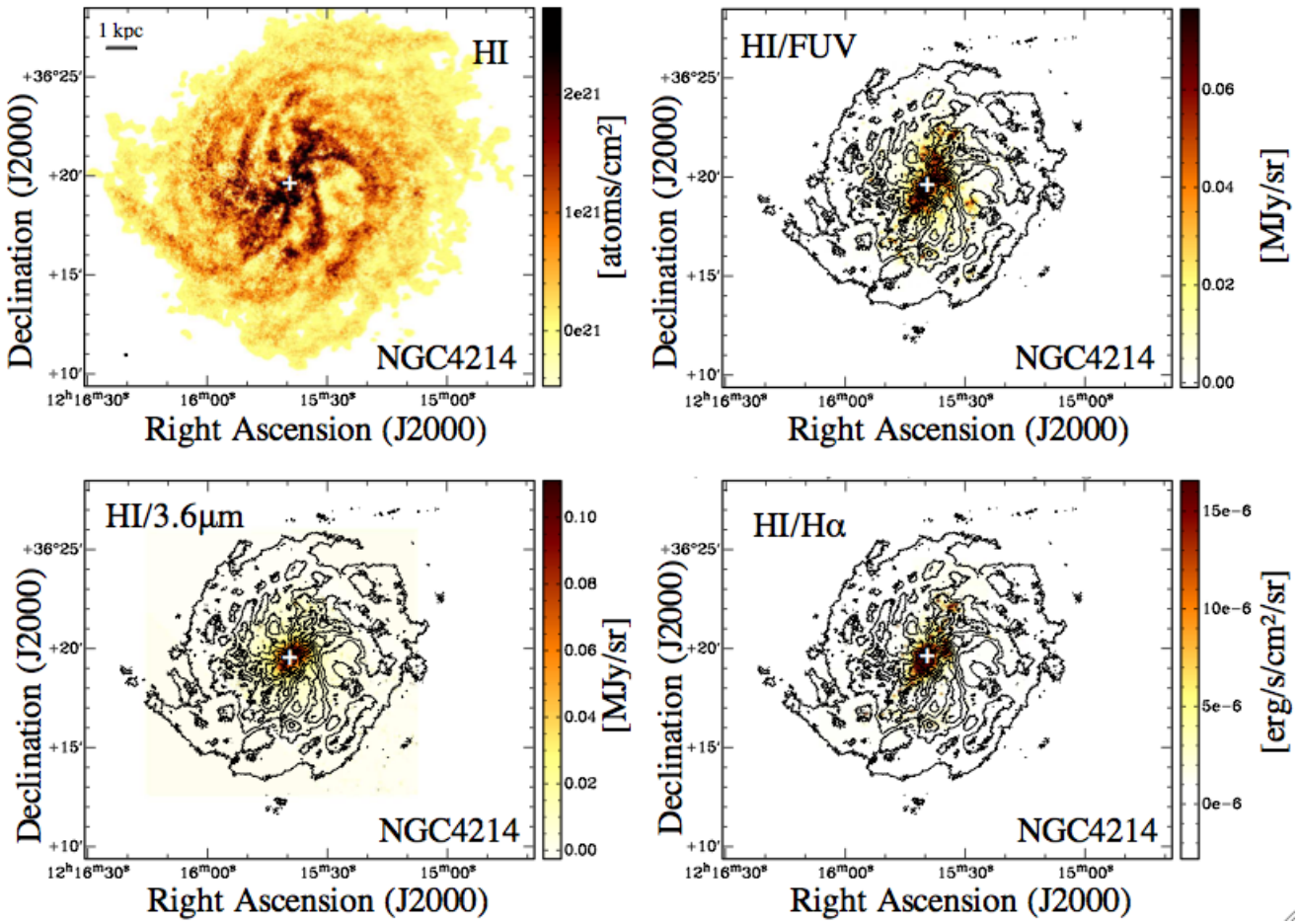

Figure 2.14: Surface density maps for NGC 4214. *Top Left*: Integrated H I map (resolution: $7\farcs6 \times 6\farcs4$, lowest confidence level (2.5σ over 3 channels): 1.6×10^{20} atoms cm^{-2}, colour scale: 0 - 2×10^{21} atoms cm^{-2}). *Top Right*: H I contours overlaid on the FUV image (colour scale: 0 - 6×10^{-2} MJy sr^{-1}). *Bottom Left*: H I contours overlaid on the *Spitzer* 3.6 μm image (colour scale: 0 - 0.1 MJy sr^{-1}). *Bottom Right*: H I contours overlaid on the Hα map (colour scale: 0 - 15×10^{-6} ergs s^{-1} cm^{-2} sr^{-1}). The H I contours are at (0.2, 1, 2)$\times 10^{21}$ atoms cm^{-2}. In all panels the plus represents the V–band centre of the galaxy. The H I map beam size is indicated in the bottom left corner of the top left panel.

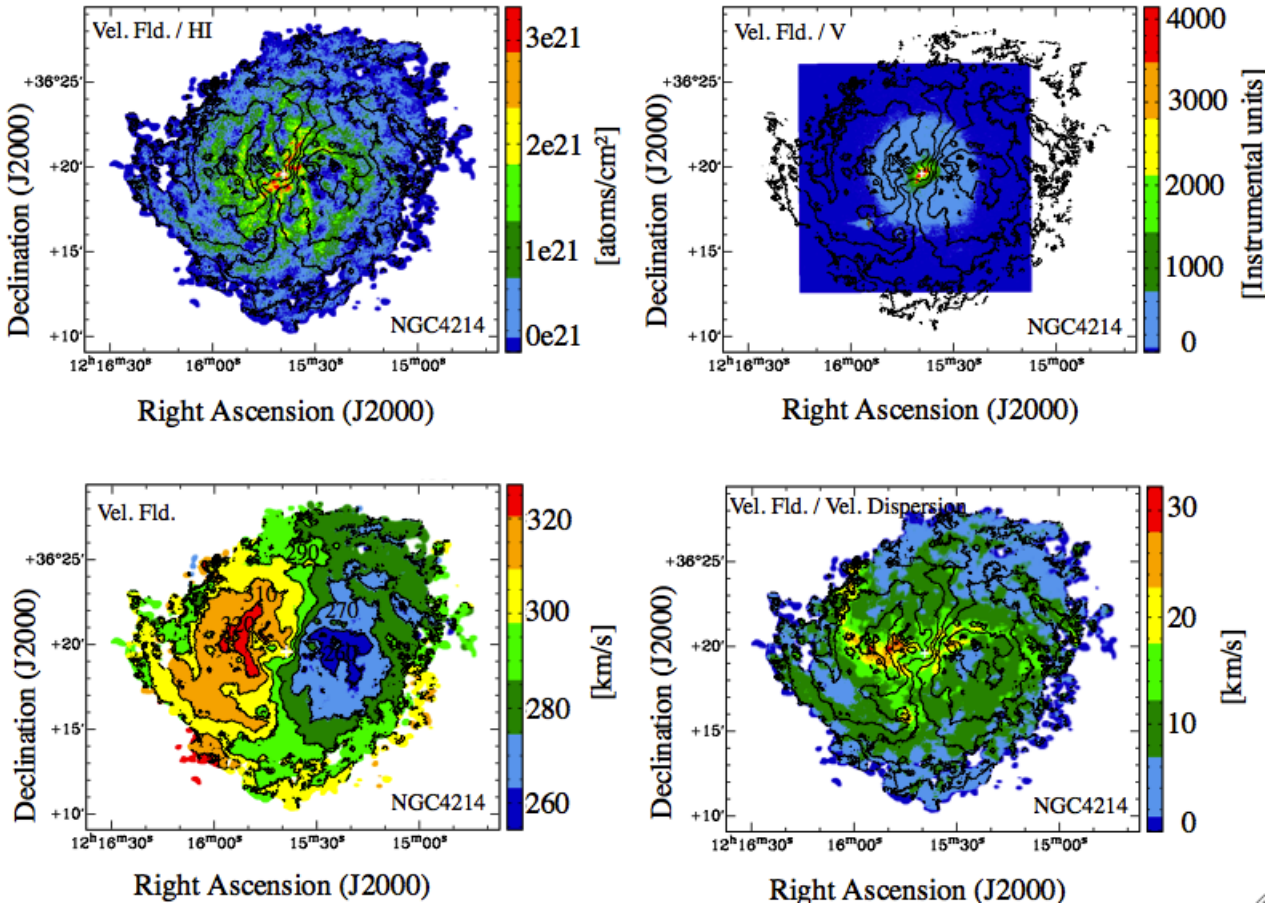

Figure 2.15: Moment maps for NGC 4214. *Top Left*: Integrated H I map (moment 0) with velocity field contours. *Top Right*: velocity field contours overlaid on the V–band optical image (colour scale: 0 - 1500 instrumental units). *Bottom Left*: Contoured Velocity Field (colour scale: 240 - 360 km s^{-1}). *Bottom Right* : Velocity contours overlaid on the velocity dispersion map (colour scale: 0 - 30 km s^{-1}). The velocity field contours are at (260, 270, 280, 290, 300, 310, 320) km s^{-1}. In all panels the plus represents the V–band centre of the galaxy.

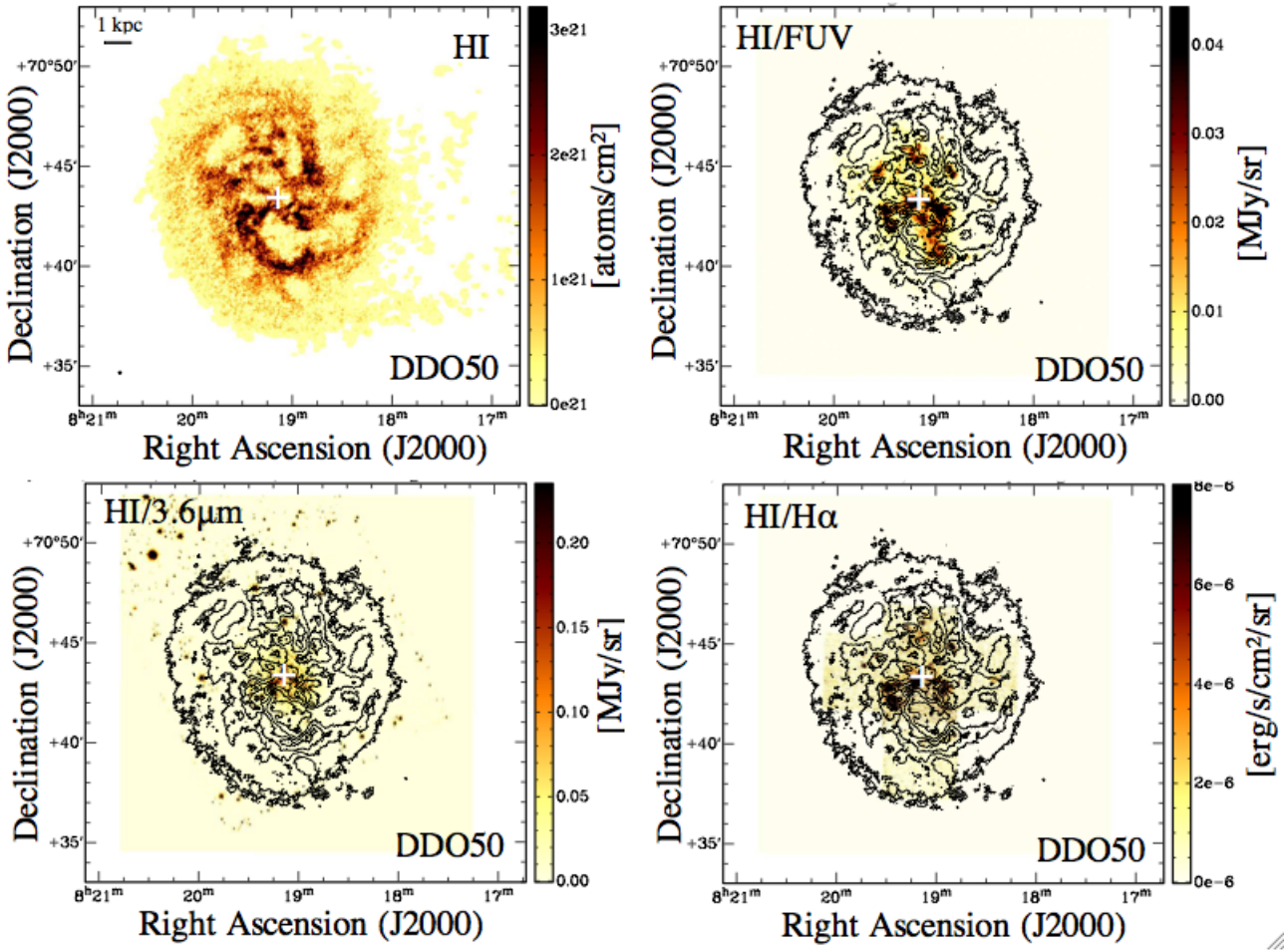

Figure 2.16: Surface density maps for DDO 50. *Top Left*: Integrated H I map (resolution: $7\farcs0 \times 6\farcs1$, lowest confidence level (2.5σ over 3 channels): 5.4×10^{20} atoms cm^{-2}, colour scale: 0 - 3×10^{21} atoms cm^{-2}). *Top Right*: H I contours overlaid on the FUV image (colour scale: 0 - 4×10^{-2} MJy sr^{-1}). *Bottom Left*: H I contours overlaid on the *Spitzer* 3.6 μm image (colour scale: 0 - 0.2 MJy sr^{-1}). *Bottom Right*: H I contours overlaid on the Hα map (colour scale: 0 - 8×10^{-6} ergs s^{-1} cm^{-2} sr^{-1}). The H I contours are at (0.1, 1, 2)$\times 10^{21}$ atoms cm^{-2}. In all panels the plus represents the V–band centre of the galaxy. The H I map beam size is indicated in the bottom left corner of the top left panel.

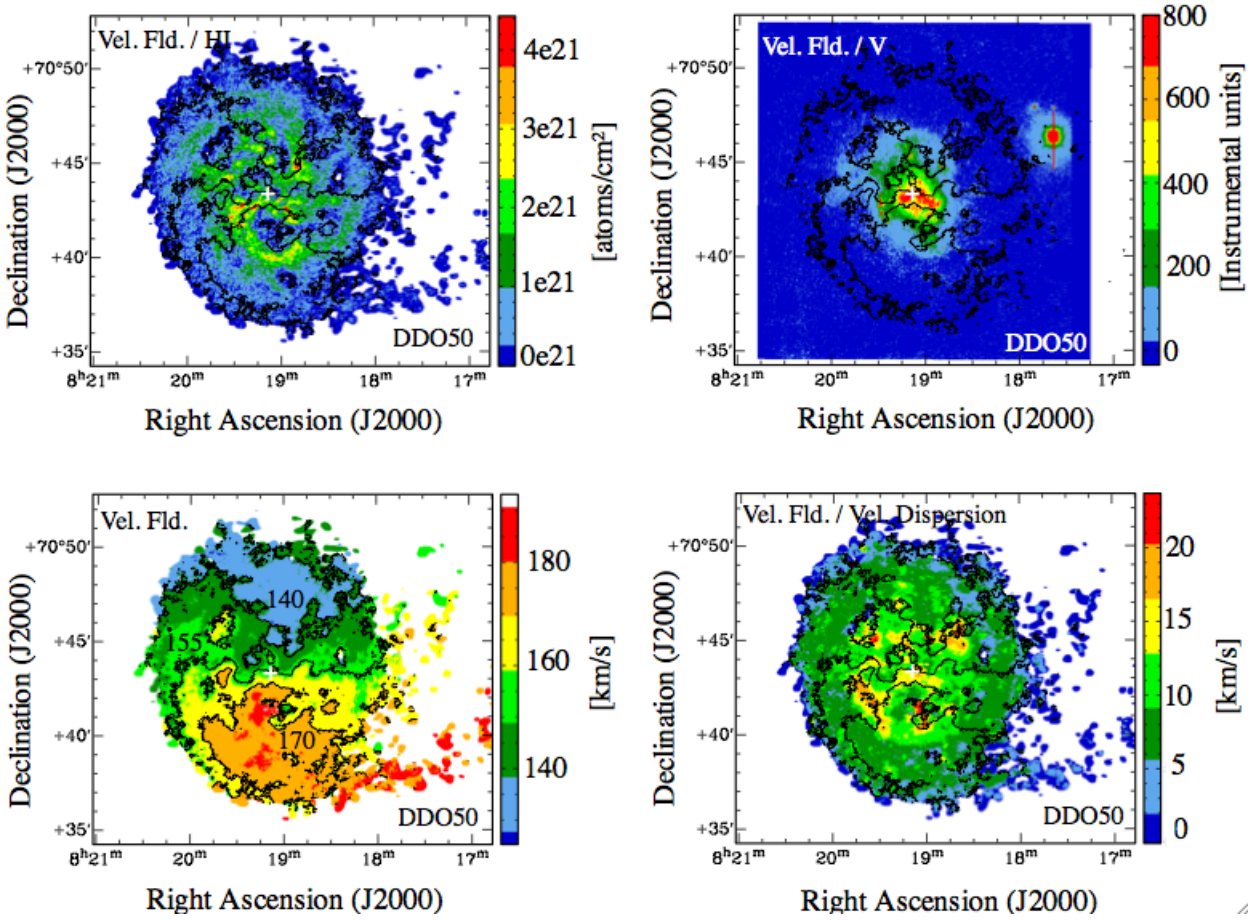

Figure 2.17: Moment maps for DDO 50. *Top Left*: Integrated H I map (moment 0) with velocity field contours. *Top Right*: velocity field contours overlaid on the V–band optical image (colour scale: 0 - 600 instrumental units). *Bottom Left*: Contoured Velocity Field (colour scale: 100 - 300 $\mathrm{km\,s^{-1}}$). *Bottom Right*: Velocity contours overlaid on the velocity dispersion map (colour scale: 0 - 25 $\mathrm{km\,s^{-1}}$). The velocity field contours are at (140, 155, 170) $\mathrm{km\,s^{-1}}$. In all panels the plus represents the V–band centre of the galaxy.

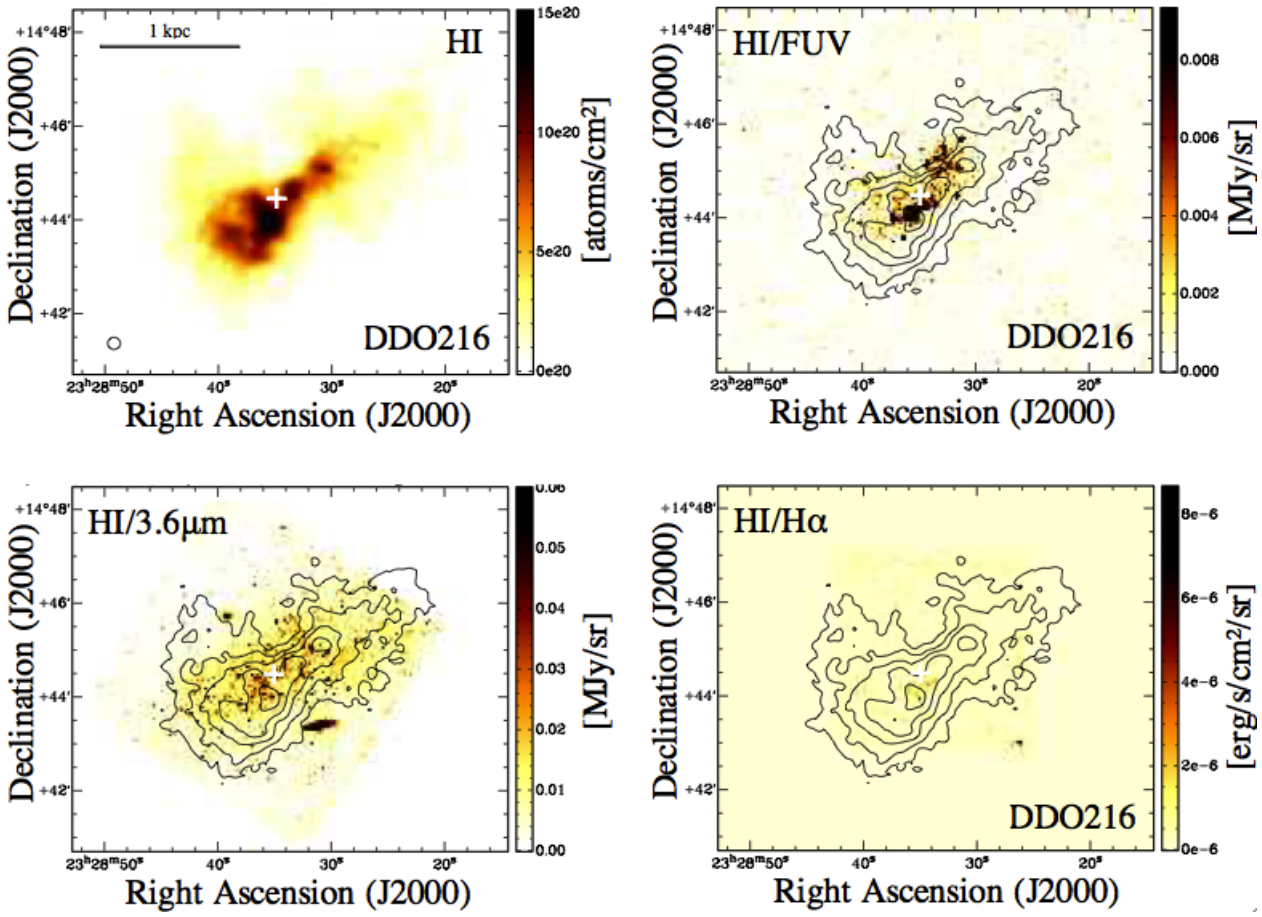

Figure 2.18: Surface density maps for DDO 216. *Top Left*: Integrated H I map (resolution: $16\farcs2 \times 15\farcs4$, lowest confidence level 2.5σ over 3 channels: 0.41×10^{20} atoms cm^{-2}, colour scale: 0 - 1.5×10^{21} atoms cm^{-2}). *Top Right*: H I contours overlaid on the FUV image (colour scale: 0 - 8×10^{-3} MJy sr^{-1}). *Bottom Left*: H I contours overlaid on the *Spitzer* 3.6 μm image (colour scale: 0 - 0.06 MJy sr^{-1}). *Bottom Right*: H I contours overlaid on the Hα map (colour scale: 0 - 8×10^{-6} ergs s^{-1} cm^{-2} sr^{-1}). The H I contours are at (1.5, 3, 5, 8, 12)$\times 10^{20}$ atoms cm^{-2}. In all panels the plus represents the V–band centre of the galaxy. The H I map beam size is indicated in the bottom left corner of the top left panel.

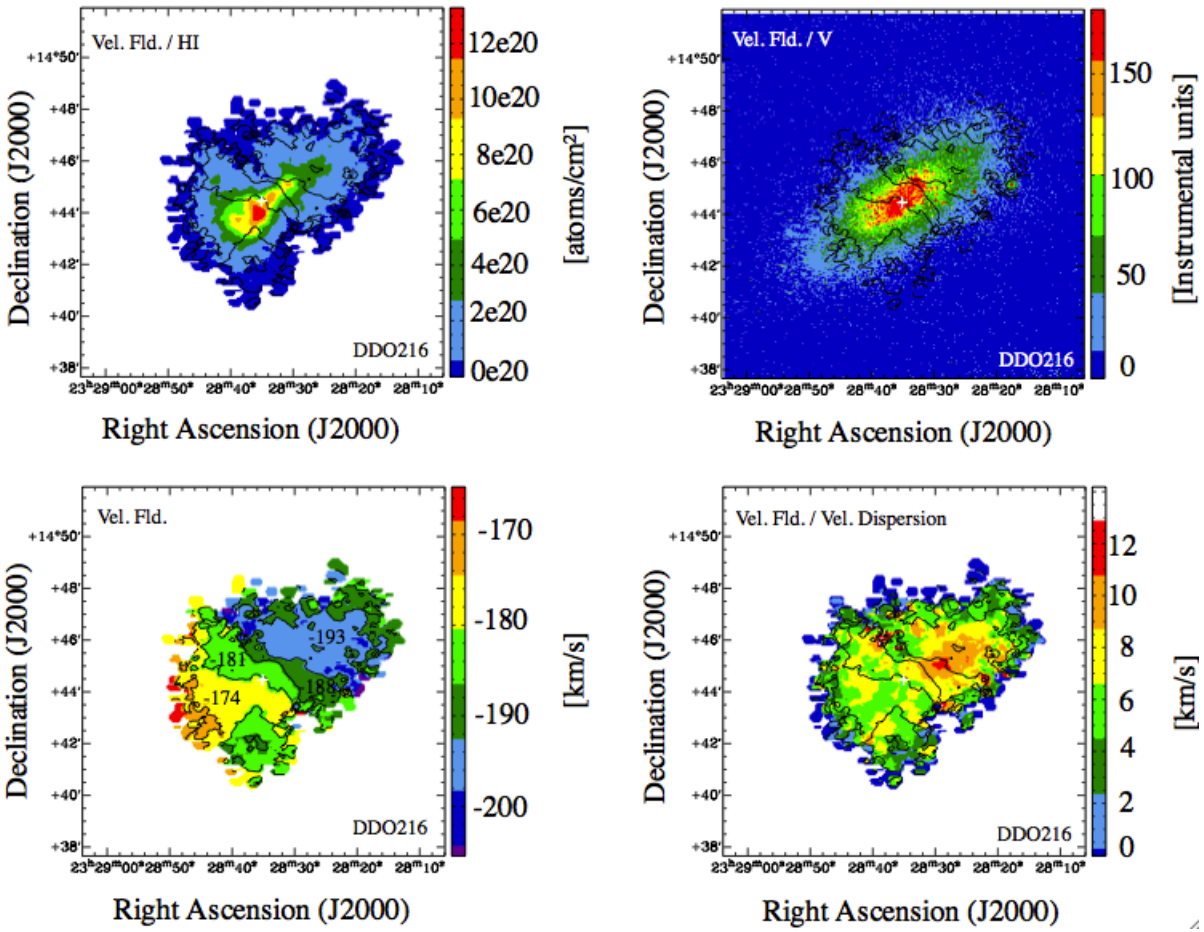

Figure 2.19: Moment maps for DDO 216. *Top Left*: Integrated H I map (moment 0) with velocity field contours. *Top Right*: Velocity field contours overlaid on the V–band optical image (colour scale: 0 - 250 instrumental units). *Bottom Left*: Contoured Velocity Field (colour scale: -210 to - 170 $\mathrm{km\,s^{-1}}$). *Bottom Right*: Velocity field contours overlaid on the velocity dispersion map (colour scale: 0 - 14 $\mathrm{km\,s^{-1}}$). The velocity field contours are at (-193, -188, -181, -174) $\mathrm{km\,s^{-1}}$. In all panels the plus represents the V–band centre of the galaxy.

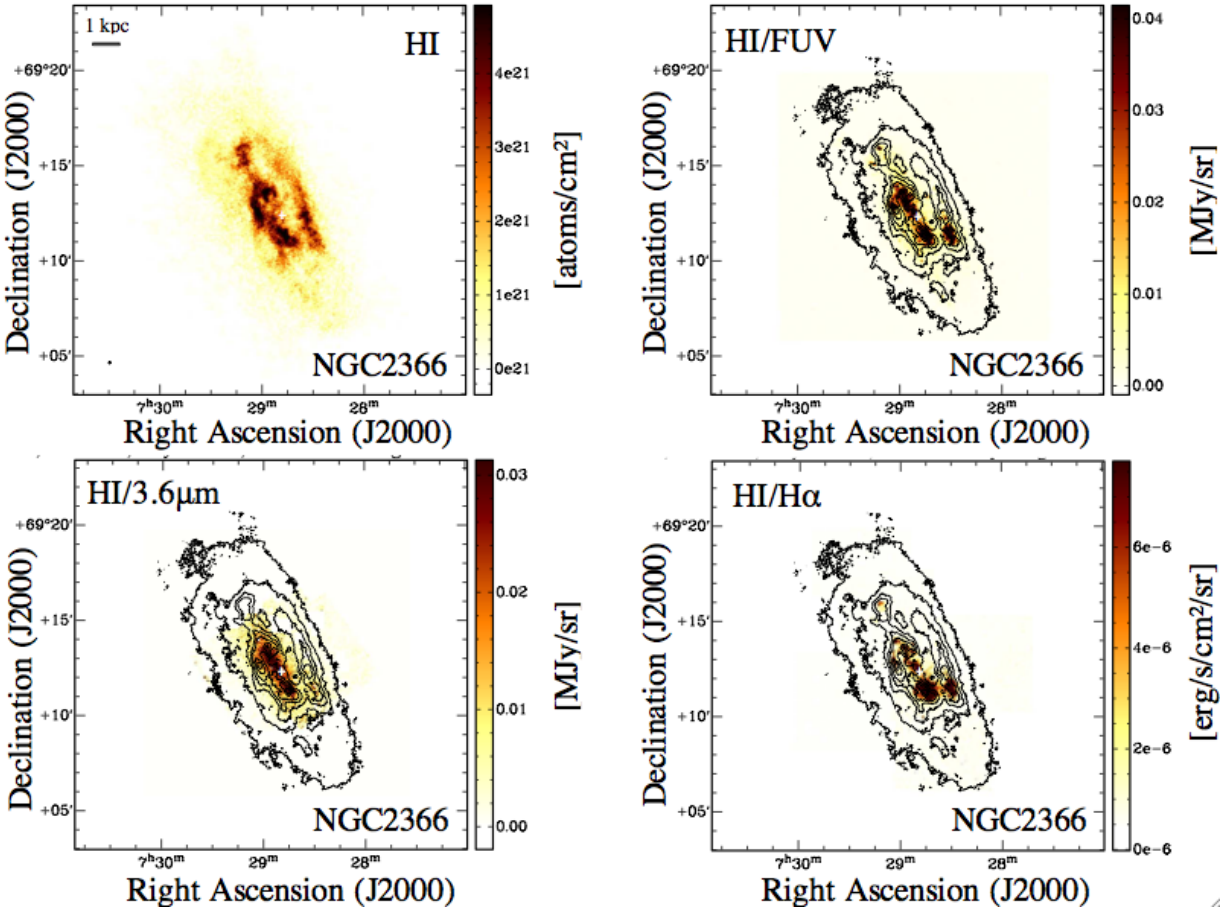

Figure 2.20: Surface density maps for NGC 2366. *Top Left*: Integrated H I map (resolution: $6\farcs9 \times 5\farcs9$, lowest confidence level (2.5σ over 3 channels): 3.3×10^{20} atoms cm^{-2}, colour scale: 0 - 4×10^{21} atoms cm^{-2}). *Top Right*: H I contours overlaid on the FUV image (colour scale: 0 - 4×10^{-2} MJy sr^{-1}). *Bottom Left*: H I contours overlaid on the *Spitzer* 3.6 μm image (colour scale: 0 - 0.3 MJy sr^{-1}). *Bottom Right*: H I contours overlaid on the Hα map (colour scale: 0 - 6×10^{-6} ergs s^{-1} cm^{-2} sr^{-1}). The H I contours are at (0.1, 1, 2, 3, 4)$\times 10^{21}$ atoms cm^{-2}. In all panels the plus represents the V–band centre of the galaxy. The H I map beam size is indicated in the bottom left corner of the top left panel.

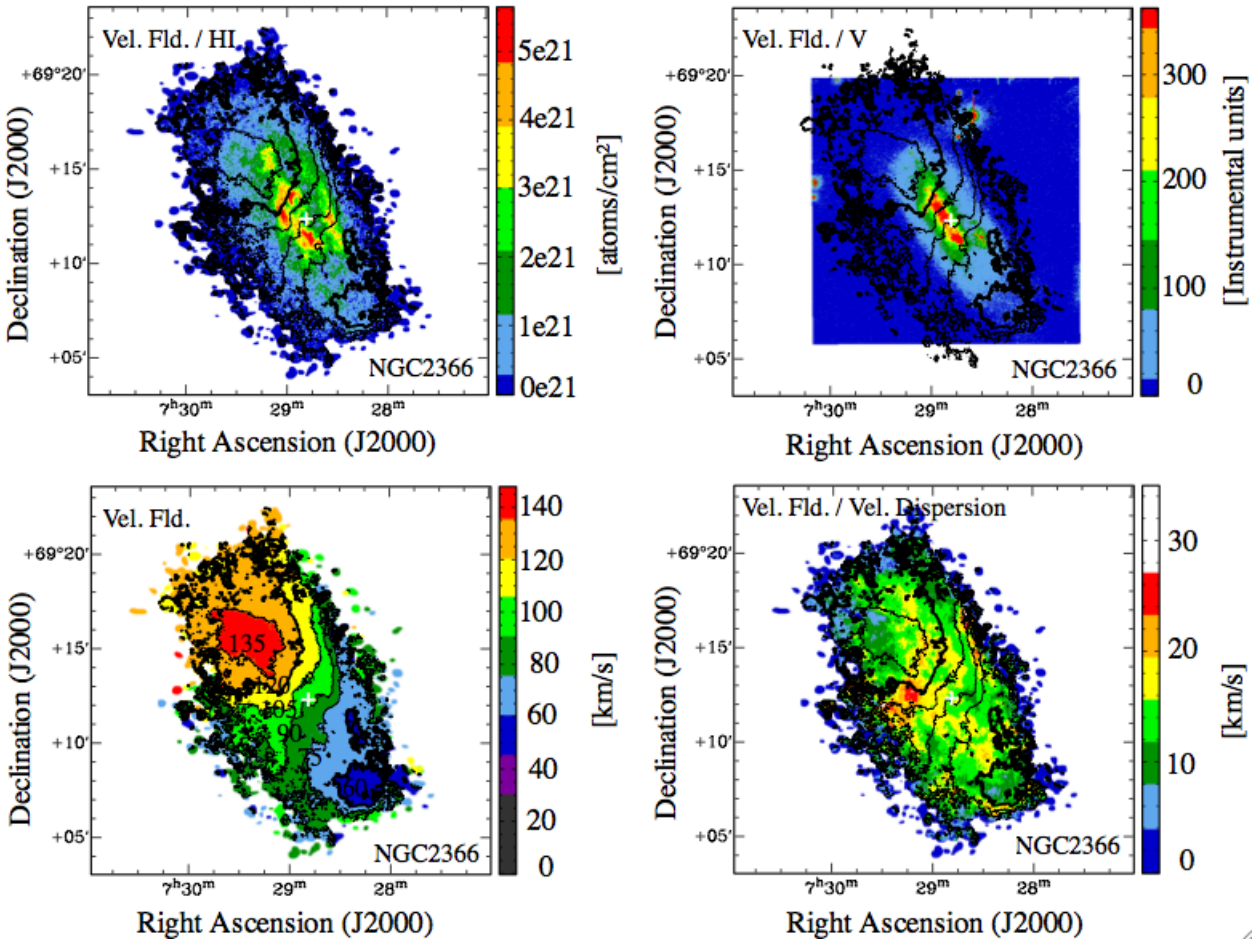

Figure 2.21: Moment maps for NGC 2366. *Top Left*: Integrated H I map (moment 0) with velocity field contours. *Top Right*: Velocity field contours overlaid on the V–band optical image (colour scale: 0 - 400 instrumental units). *Bottom Left*: Contoured Velocity Field (colour scale: 60 - 140 km s^{-1}). *Bottom Right*: Velocity field contours overlaid on the velocity dispersion map (colour scale: 0 - 40 km s^{-1}). The velocity field contours are at (60, 75, 90, 105, 120, 135) km s^{-1}. In all panels the plus represents the V–band centre of the galaxy.

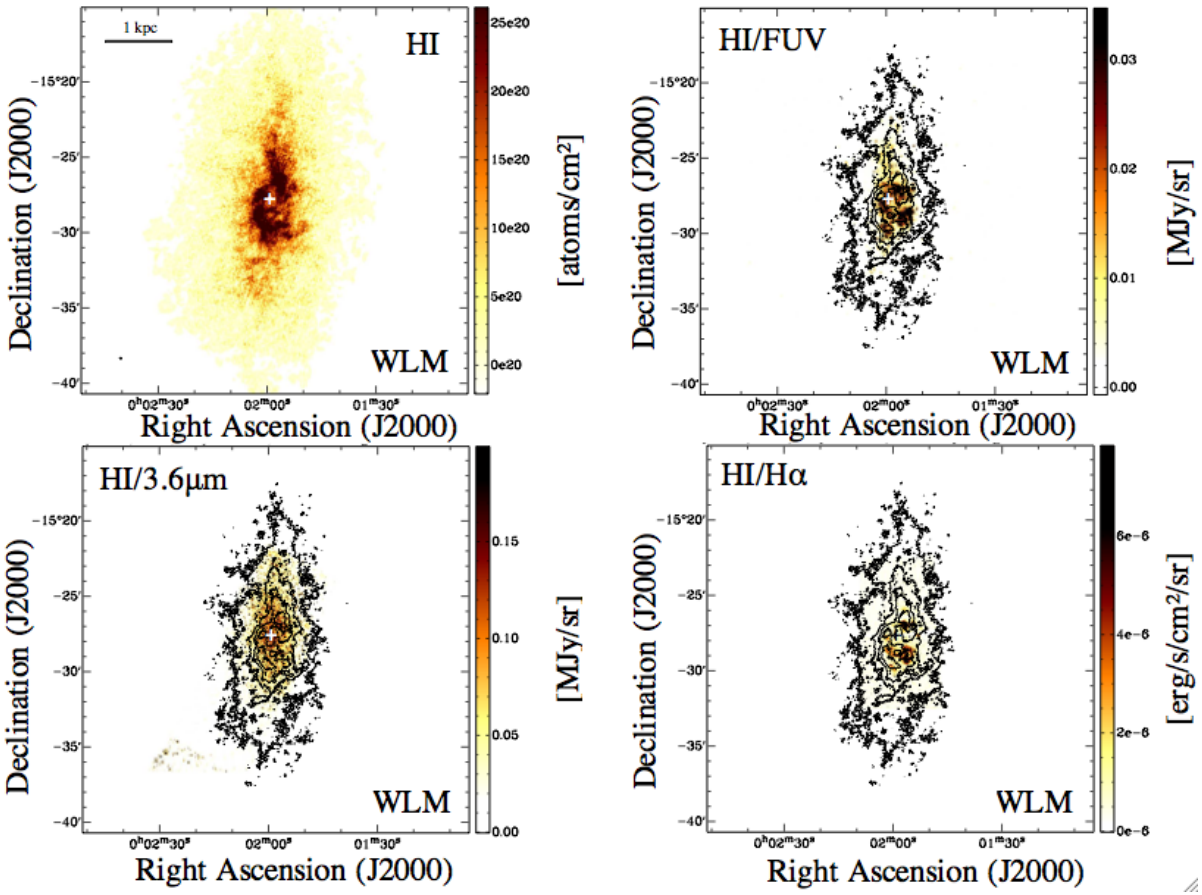

Figure 2.22: Surface density maps for WLM. *Top Left*: Integrated H I map (resolution: $7\farcs6 \times 5\farcs1$, lowest confidence level 2.5σ over 3 channels: 4.6×10^{20} atoms cm^{-2}, colour scale: 0 - 2.5×10^{21} atoms cm^{-2}). *Top Right*: H I contours overlaid on the FUV image (colour scale: 0 - 3×10^{-2} MJy sr^{-1}). *Bottom Left*: H I contours overlaid on the *Spitzer* 3.6 μm image (colour scale: 0 - 0.15 MJy sr^{-1}). *Bottom Right:* H I contours overlaid on the Hα map (colour scale: 0 - 6×10^{-6} ergs s^{-1} cm^{-2} sr^{-1}). The H I contours are at (5, 12, 19, 26)$\times 10^{20}$ atoms cm^{-2}. In all panels the plus represents the V–band centre of the galaxy. The H I map beam size is indicated in the bottom left corner of the top left panel.

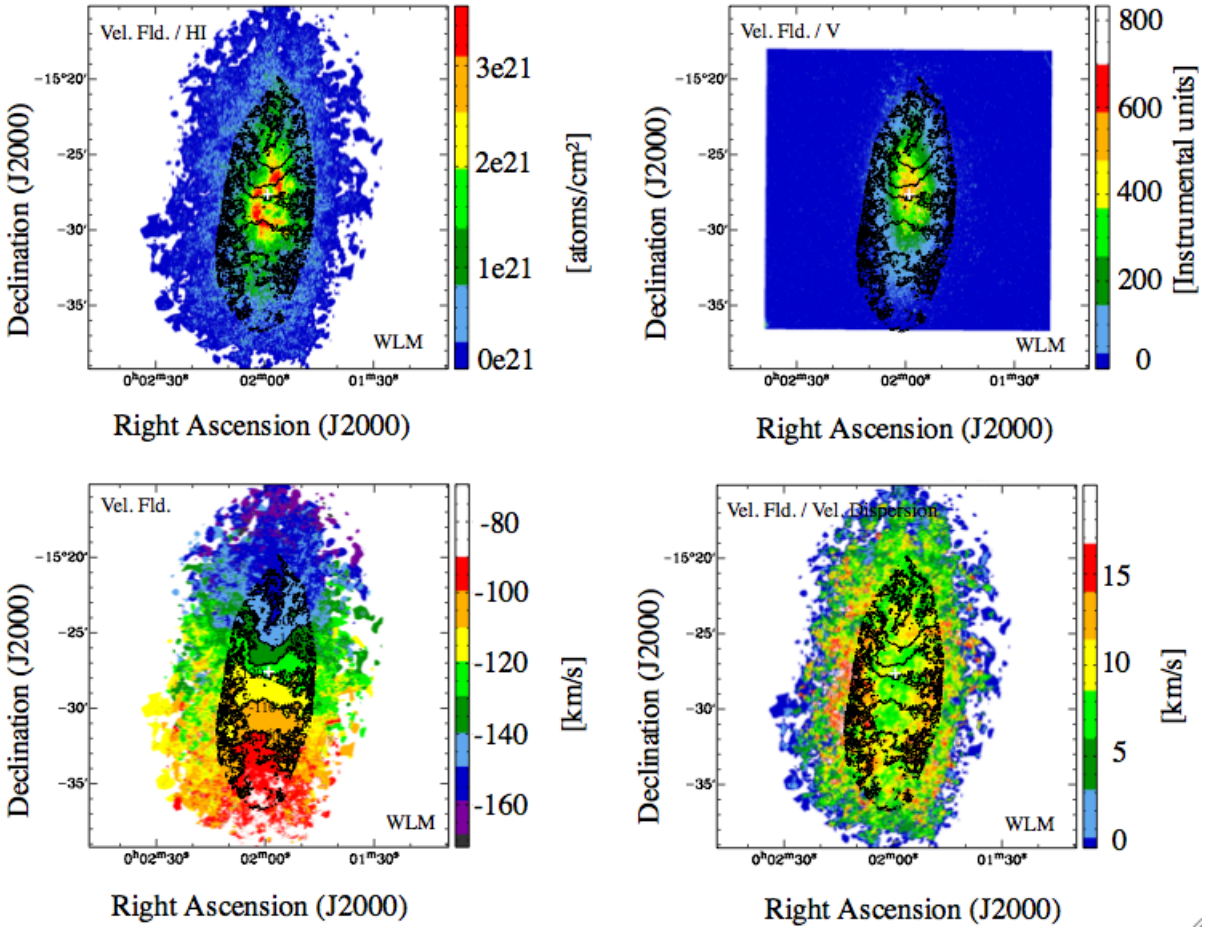

Figure 2.23: Moment maps for WLM. *Top Left*: Integrated H I map (moment 0) with velocity field contours. *Top Right*: Velocity field contours overlaid on the *V*–band optical image (colour scale: 0 - 500 instrumental units). *Bottom Left*: Contoured Velocity Field (colour scale: -160 to - 80 $\mathrm{km\,s^{-1}}$). *Bottom Right*: Velocity field contours overlaid on the velocity dispersion map (colour scale: 0 - 20 $\mathrm{km\,s^{-1}}$). The velocity field contours are at (100, 110, 120, 130, 140, 150) $\mathrm{km\,s^{-1}}$. In all panels the plus represents the *V*–band centre of the galaxy.

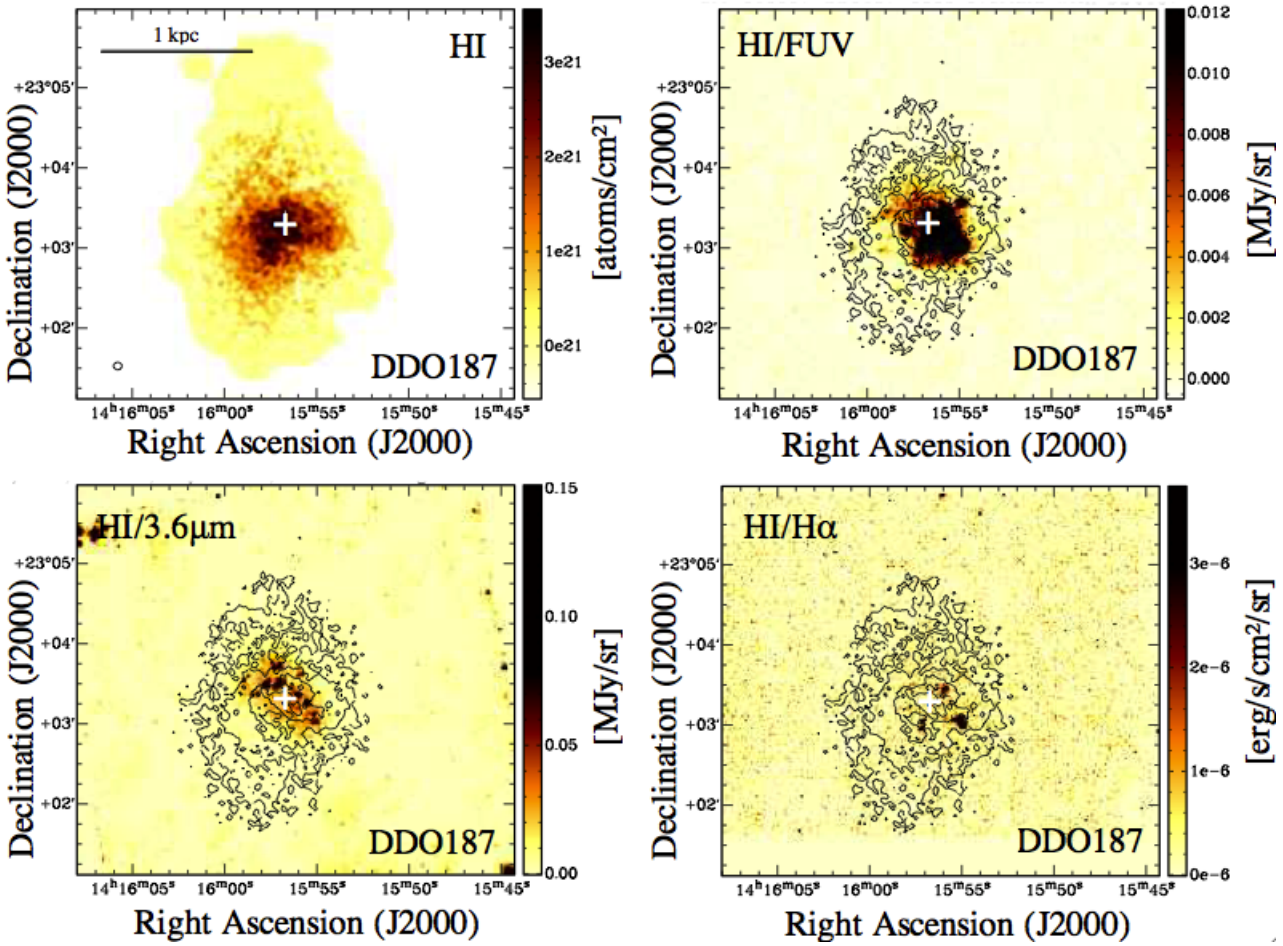

Figure 2.24: Surface density maps for DDO 187. *Top Left*: Integrated H I map (resolution: $6\farcs2 \times 5\farcs5$, lowest confidence level (2.5σ over 3 channels): 3.9×10^{20} atoms cm^{-2}, colour scale: 0 - 3×10^{21} atoms cm^{-2}). *Top Right*: H I contours overlaid on the FUV image (colour scale: 0 - 1×10^{-2} MJy sr^{-1}). *Bottom Left*: H I contours overlaid on the *Spitzer* 3.6 μm image (colour scale: 0 - 0.15 MJy sr^{-1}). *Bottom Right*: H I contours overlaid on the Hα map (colour scale: 0 - 3×10^{-6} ergs s^{-1} cm^{-2} sr^{-1}). The H I contours are at (0.3, 1, 2, 2.8)$\times 10^{21}$ atoms cm^{-2}. In all panels the plus represents the V–band centre of the galaxy. The H I map beam size is indicated in the bottom left corner of the top left panel.

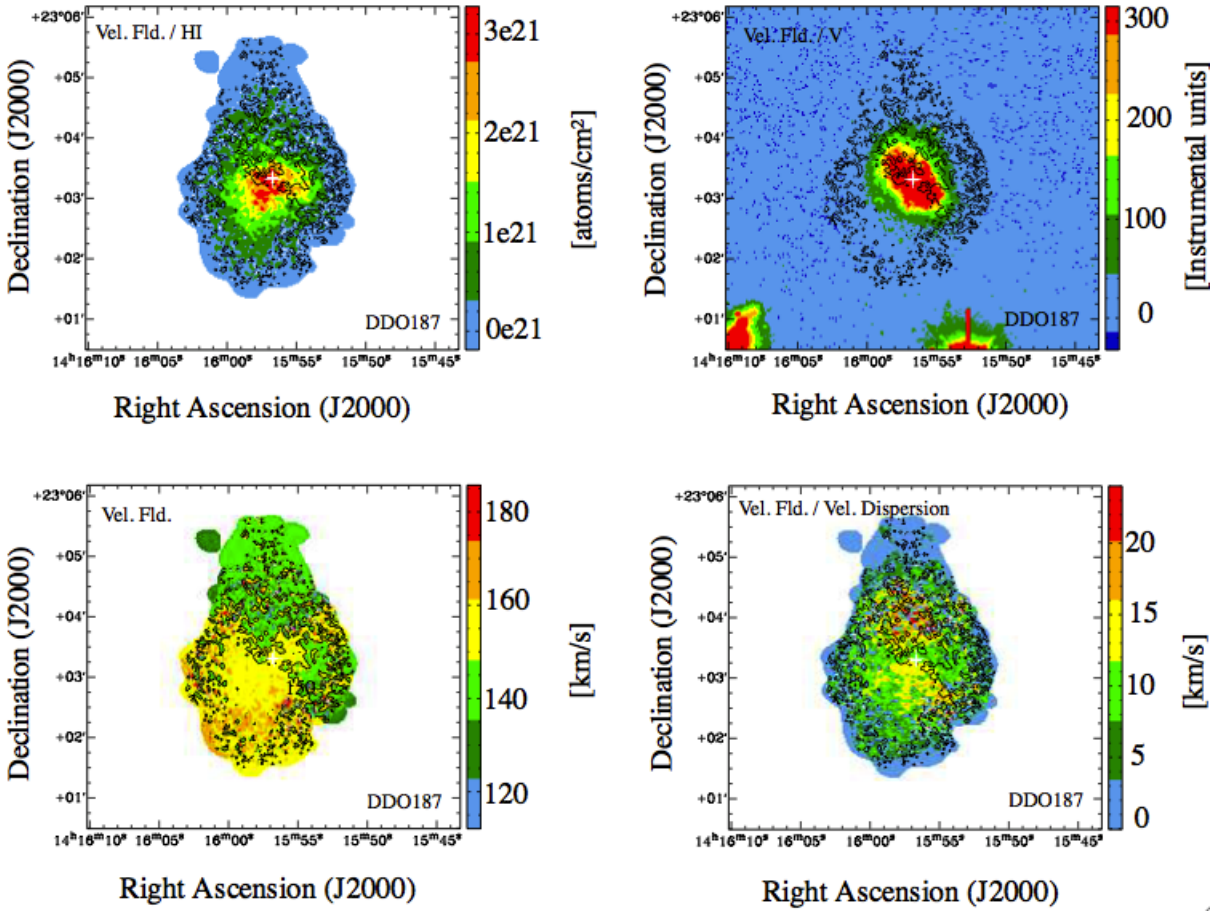

Figure 2.25: Moment maps for DDO 187. *Top Left*: Integrated H I map (moment 0) with velocity field contours. *Top Right*: Velocity field contours overlaid on the V–band optical image (colour scale: 0 - 300 instrumental units). *Bottom Left*: Contoured Velocity Field (colour scale: 130 - 160 km s^{-1}). *Bottom Right*: Velocity field contours overlaid on the velocity dispersion map (colour scale: 0 - 80 km s^{-1}). The velocity field contours are at (150) km s^{-1}. In all panels the plus represents the V–band centre of the galaxy.

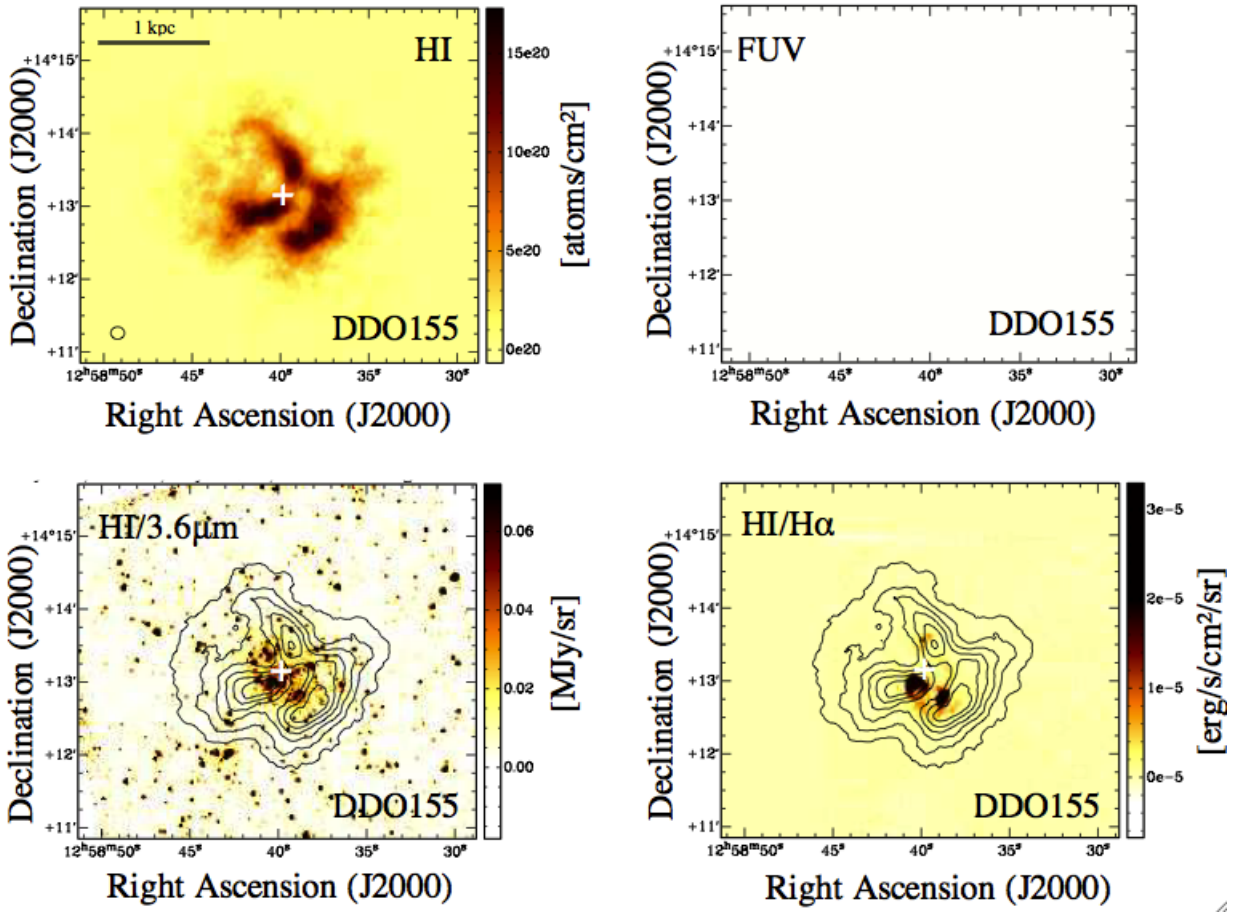

Figure 2.26: Surface density maps for DDO 155. *Top Left*: Integrated H I map for DDO 155 (resolution: $11\farcs3 \times 10\farcs1$, lowest confidence level (2.5σ over 3 channels): 0.61×10^{20} atoms cm^{-2}, colour scale: 0 - 1.5×10^{21} atoms cm^{-2}). *Top Right*: the empty panel illustrates the lack of ancillary data in FUV. *Bottom Left*: H I contours overlaid on the *Spitzer* 3.6 μm image (colour scale: 0 - 0.06 MJy sr^{-1}). *Bottom Right*: H I contours overlaid on the Hα map (colour scale: 0 - 3×10^{-5} ergs s^{-1} cm^{-2} sr^{-1}). The H I contours are at (0.1, 2.5, 5, 7.5, 10, 12.5)$\times 10^{20}$ atoms cm^{-2}. In all panels the plus represents the V–band centre of the galaxy. The H I map beam size is indicated in the bottom left corner of the top left panel.

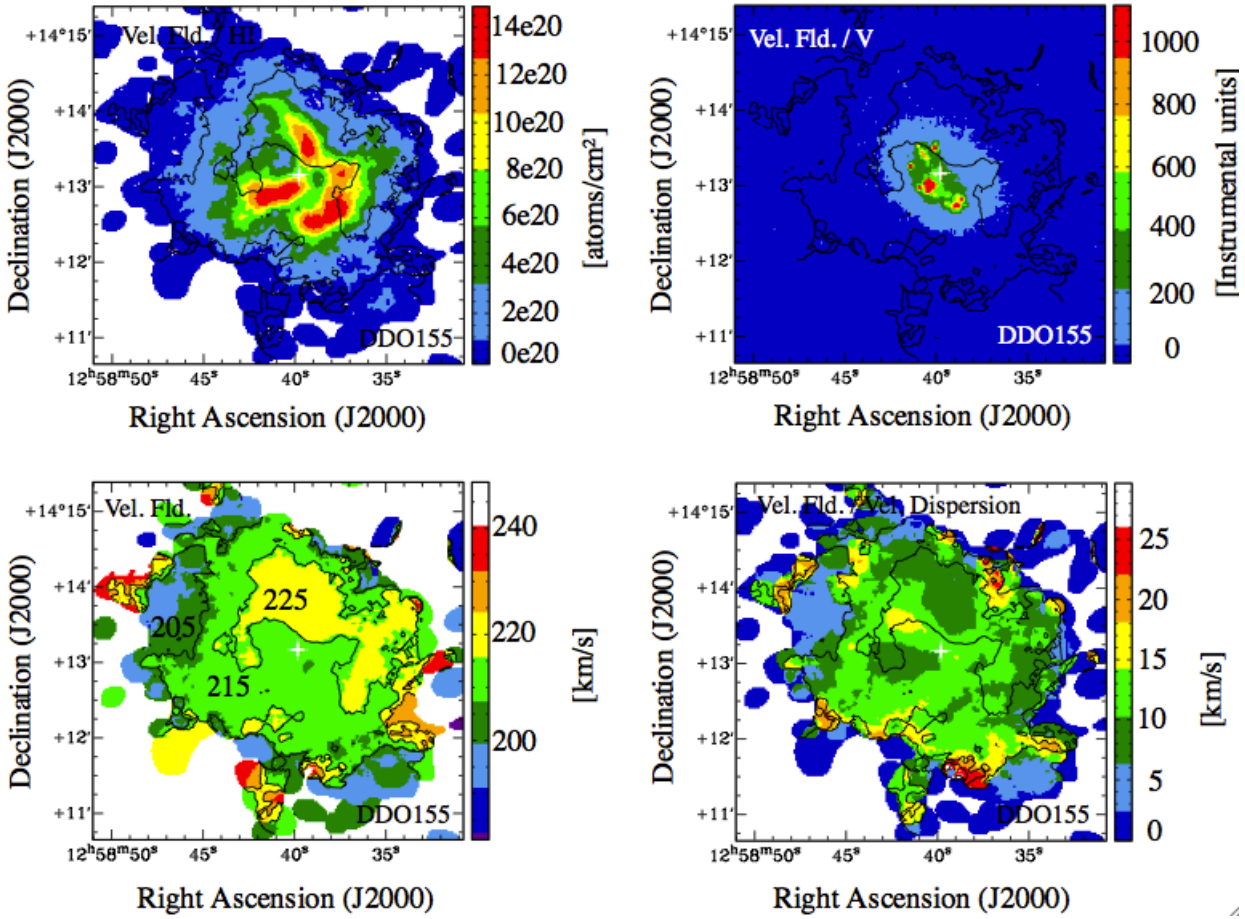

Figure 2.27: Moment maps for DDO 155. *Top Left*: Integrated H I map (moment 0) with velocity field contours. *Top Right*: Velocity field contours overlaid on the V–band optical image (colour scale: 0 - 1000 instrumental units). *Bottom Left*: Contoured Velocity Field (colour scale: 160 - 260 $\mathrm{km\,s^{-1}}$). *Bottom Right*: Velocity field contours overlaid on the velocity dispersion map (colour scale: 0 - 50 $\mathrm{km\,s^{-1}}$). The velocity field contours are at (205, 215, 225) $\mathrm{km\,s^{-1}}$. In all panels the plus represents the V–band centre of the galaxy.

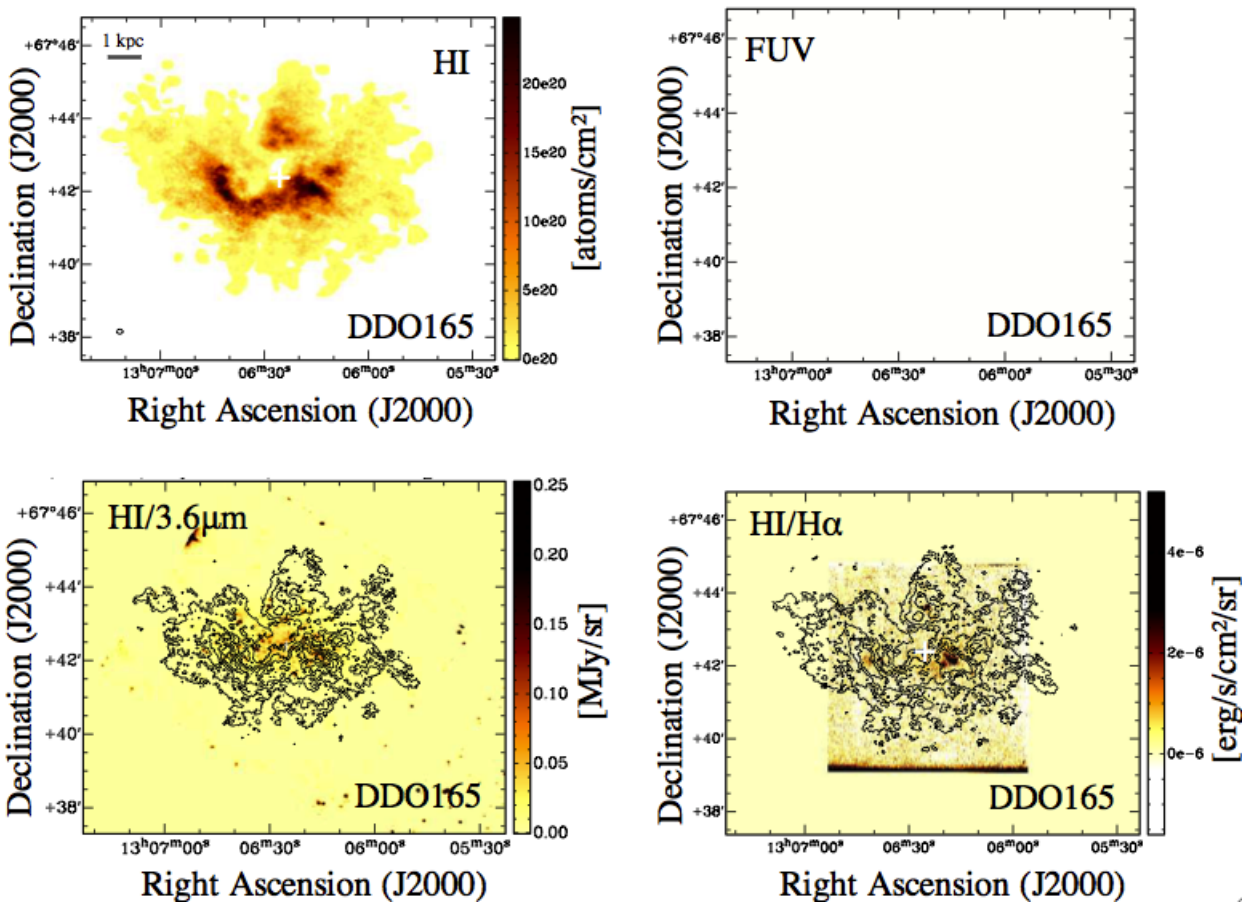

Figure 2.28: Surface density maps for DDO 165. *Top Left*: Integrated H I map (resolution: $10\farcs0 \times 7\farcs6$, lowest confidence level (2.5σ over 3 channels): 1.8×10^{20} atoms cm^{-2}, colour scale: 0 - 2×10^{21} atoms cm^{-2}). *Top Right*: the empty panel illustrates the lack of ancillary data in FUV. *Bottom Left*: H I contours overlaid on the *Spitzer* 3.6 μm image (colour scale: 0 - 0.25 MJy sr^{-1}). *Bottom Right*: H I contours overlaid on the Hα map for DDO 165 (colour scale: 0 - 4×10^{-5} ergs s^{-1} cm^{-2} sr^{-1}). The H I contours are at (0.1, 1, 2)$\times 10^{21}$ atoms cm^{-2}. In all panels the plus represents the V–band centre of the galaxy. The H I map beam size is indicated in the bottom left corner of the top left panel.

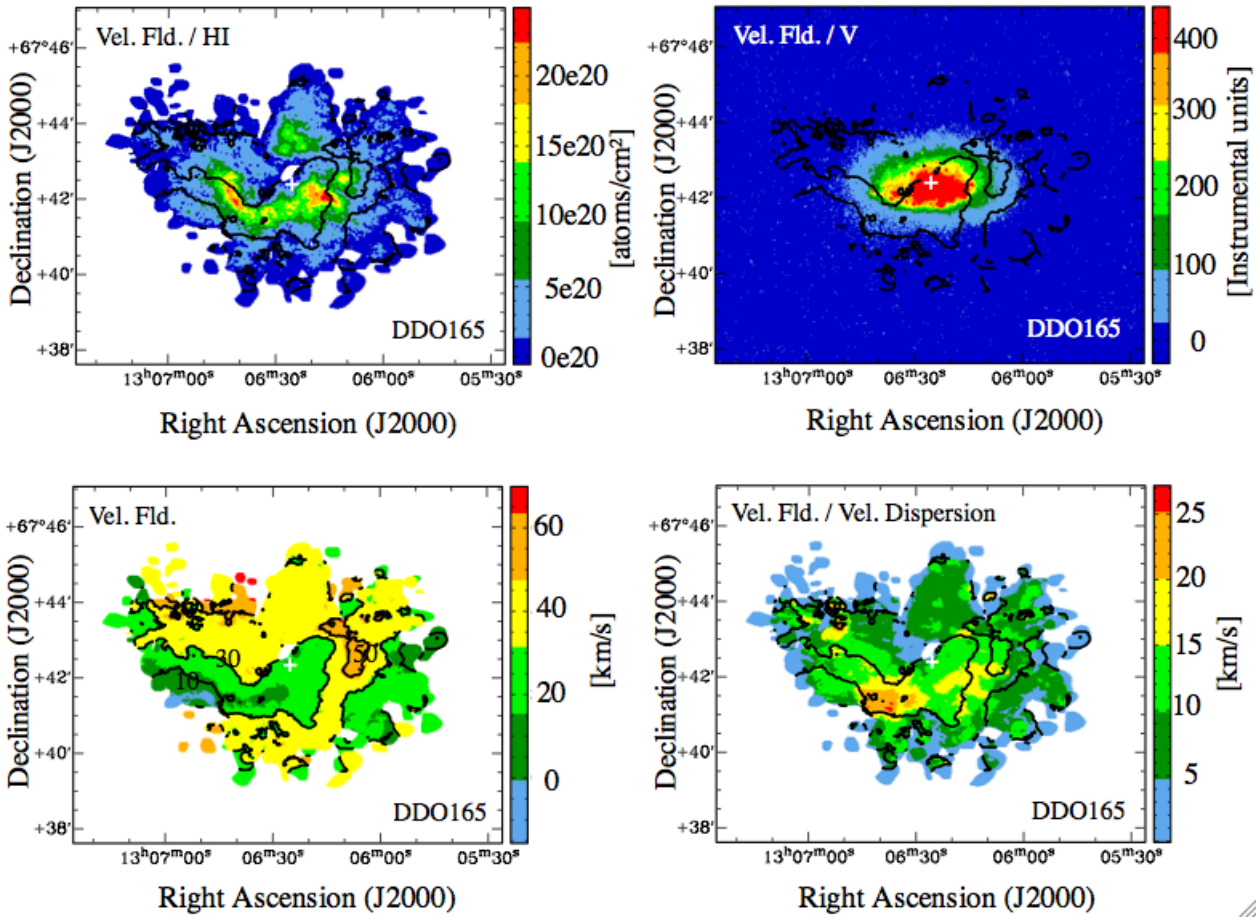

Figure 2.29: Moment maps for DDO 165. *Top Left*: Integrated H I map (moment 0) with velocity field contours. *Top Right*: Velocity field contours overlaid on the V–band optical image (colour scale: 0 - 300 instrumental units). *Bottom Left*: Contoured Velocity Field (colour scale: 0 - 60 km s^{-1}). *Bottom Right*: Velocity field contours overlaid on the velocity dispersion map (colour scale: 0 - 100 km s^{-1}). The velocity field contours are at (10, 30, 50) km s^{-1}. In all panels the plus represents the V–band centre of the galaxy.

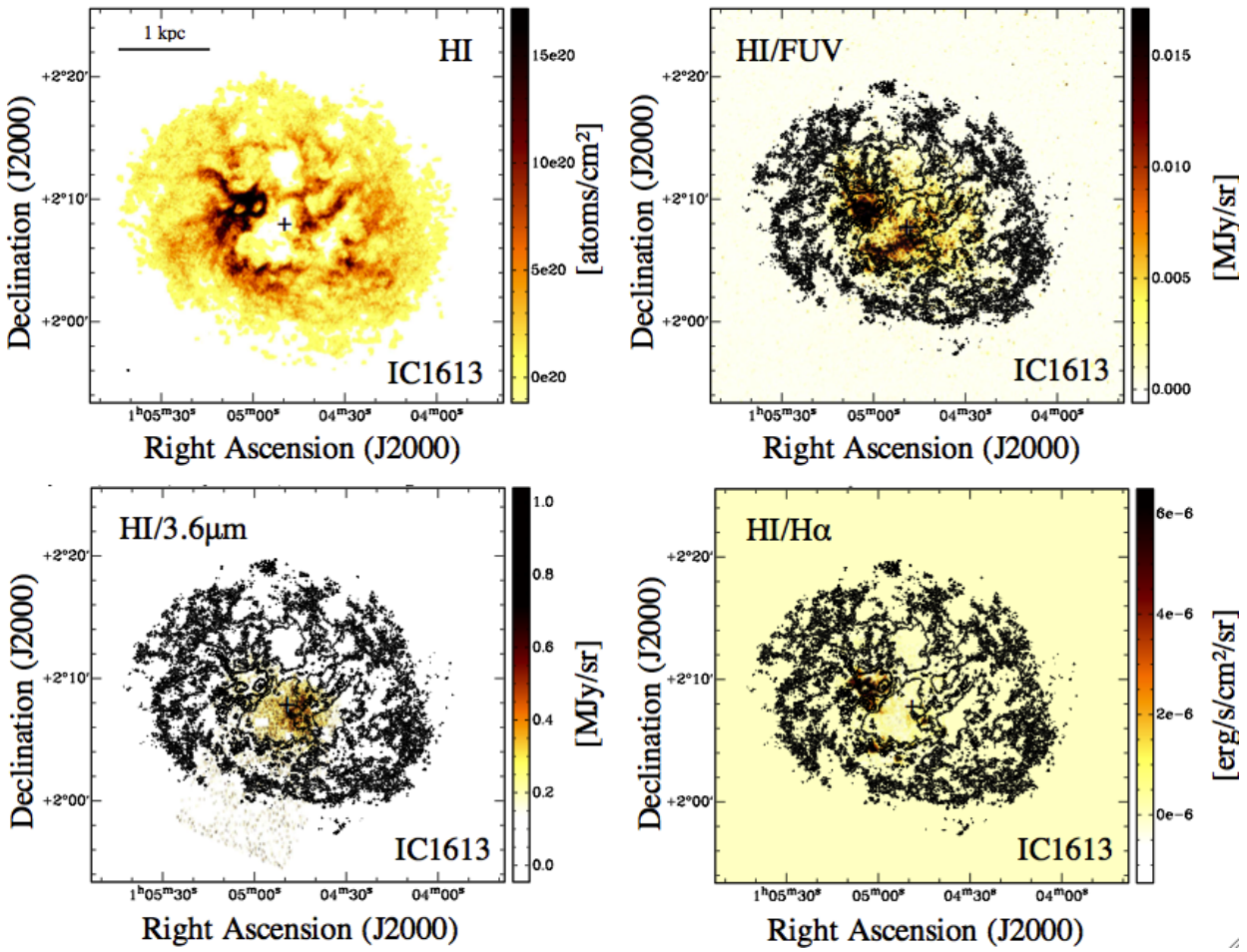

Figure 2.30: Surface density maps for IC 1613. *Top Left*: Integrated H I map (resolution: $7\farcs7 \times 6\farcs5$, lowest confidence level (2.5σ over 3 channels): 1.7×10^{20} atoms cm^{-2}, colour scale: 0 - 1.5×10^{21} atoms cm^{-2}). *Top Right*: H I contours overlaid on the FUV image (colour scale: 0 - 1.5×10^{-2} MJy sr^{-1}). *Bottom Left*: H I contours overlaid on the *Spitzer* 3.6 μm image (colour scale: 0 - 1.0 MJy sr^{-1}). *Bottom Right*: H I contours overlaid on the Hα map (colour scale: 0 - 6×10^{-6} ergs s^{-1} cm^{-2} sr^{-1}). The H I contours are at (2, 10, 14)$\times 10^{20}$ atoms cm^{-2}. In all panels the plus represents the V–band centre of the galaxy. The H I map beam size is indicated in the bottom left corner of the top left panel.

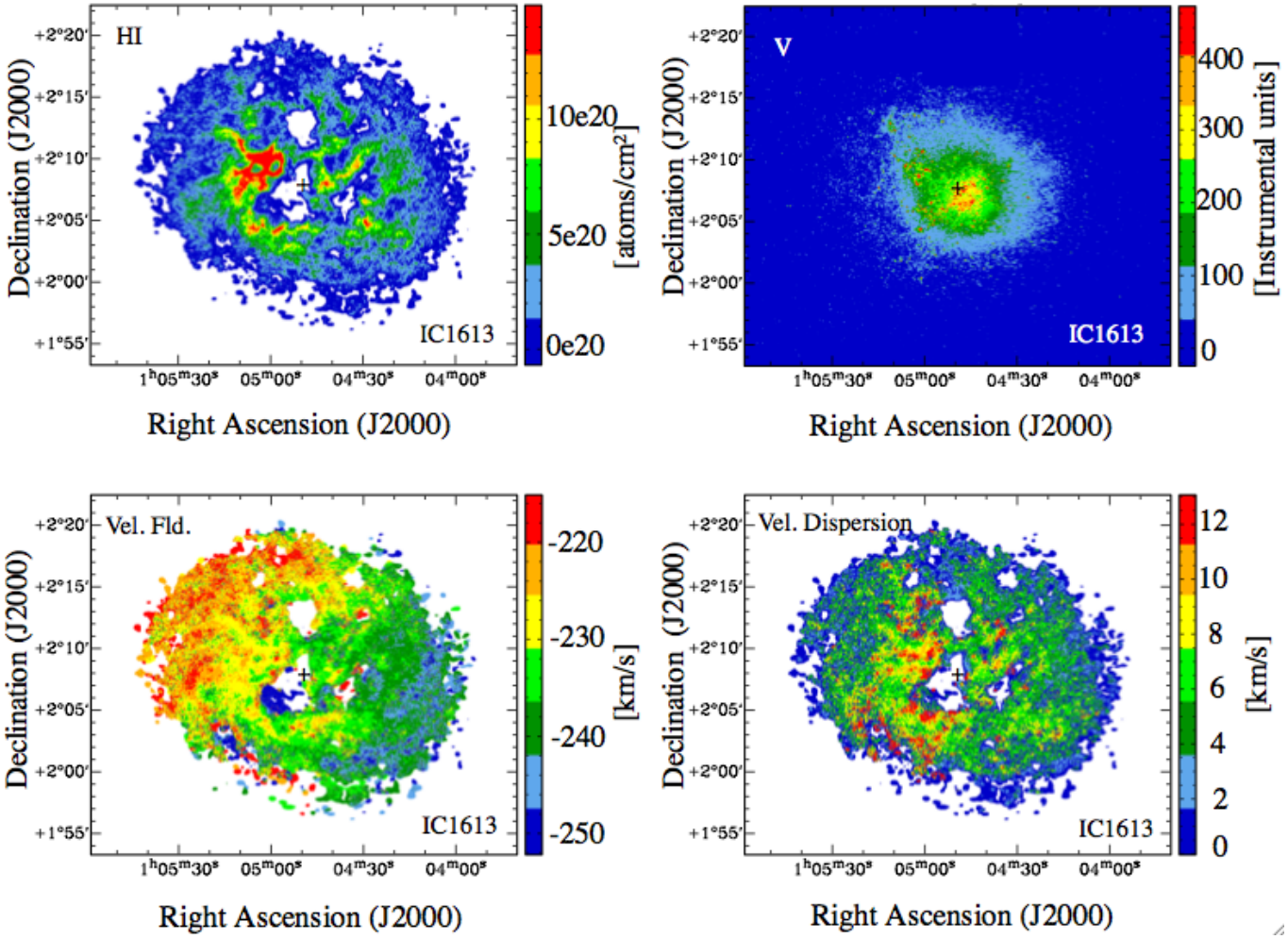

Figure 2.31: Moment maps for IC 1613. *Top Left*: Integrated H I map (moment 0). *Top Right*: V–band optical image (colour scale: 0 - 400 instrumental units). *Bottom Left*: Velocity Field (colour scale: -260 to - 220 $\mathrm{km\,s^{-1}}$). *Bottom Right*: Velocity dispersion map (colour scale: 0 - 15 $\mathrm{km\,s^{-1}}$). In all panels the plus represents the V–band centre of the galaxy.

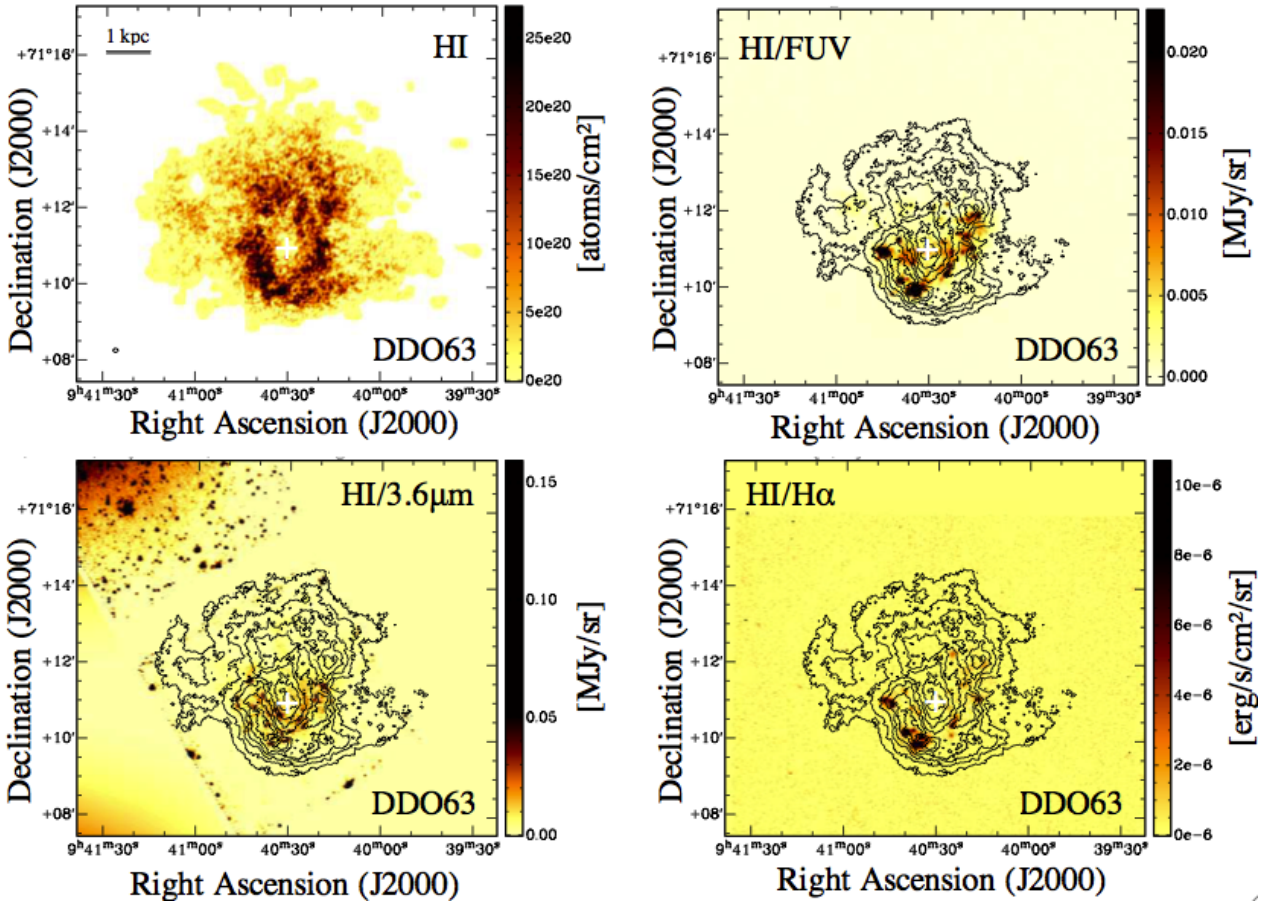

Figure 2.32: Surface density maps for DDO 63. *Top Left*: Integrated H I map (resolution: $7\farcs8 \times 6\farcs0$, lowest confidence level (2.5σ over 3 channels): 5.5×10^{20} atoms cm^{-2}, colour scale: 0 - 2.5×10^{21} atoms cm^{-2}). *Top Right*: H I contours overlaid on the FUV image (colour scale: 0 - 2×10^{-2} MJy sr^{-1}). *Bottom Left*: H I contours overlaid on the *Spitzer* 3.6 μm image (colour scale: 0 - 0.15 MJy sr^{-1}). *Bottom Right*: H I contours overlaid on the Hα map (colour scale: 0 - 10×10^{-6} ergs s^{-1} cm^{-2} sr^{-1}). The H I contours are at (0.1, 1, 2)$\times 10^{21}$ atoms cm^{-2}. In all panels the plus represents the V–band centre of the galaxy. The H I map beam size is indicated in the bottom left corner of the top left panel.

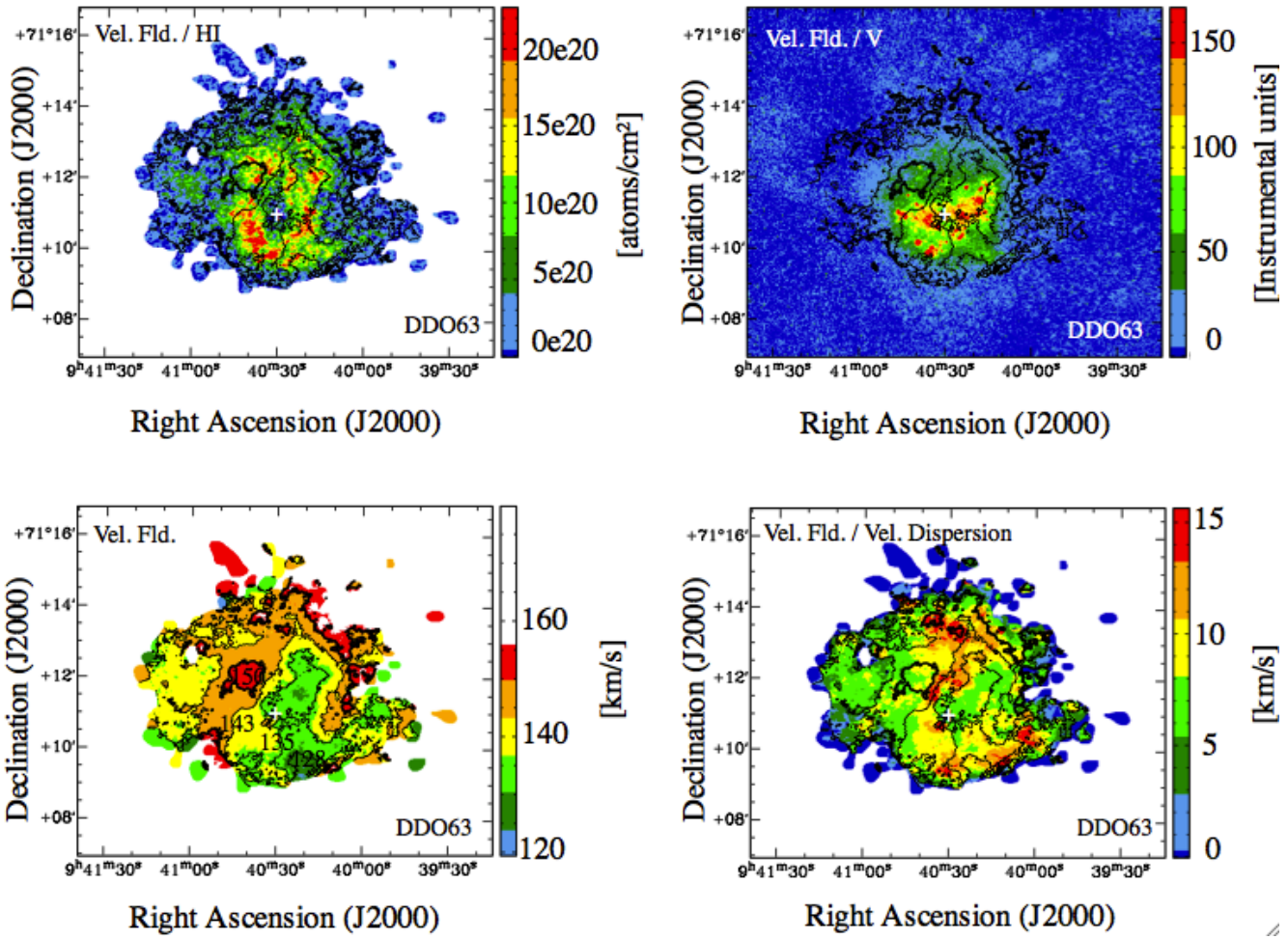

Figure 2.33: Moment maps for DDO 63. *Top Left*: Integrated H I map (moment 0) with velocity field contours. *Top Right*: Velocity field contours overlaid on the V–band optical image (colour scale: 0 - 100 instrumental units). *Bottom Left*: Contoured Velocity Field (colour scale: 0 - 170 km s^{-1}). *Bottom Right*: Velocity field contours overlaid on the velocity dispersion map (colour scale: 0 - 25 km s^{-1}). The velocity field contours are at (128, 135, 143, 150) km s^{-1}. In all panels the plus represents the V–band centre of the galaxy.

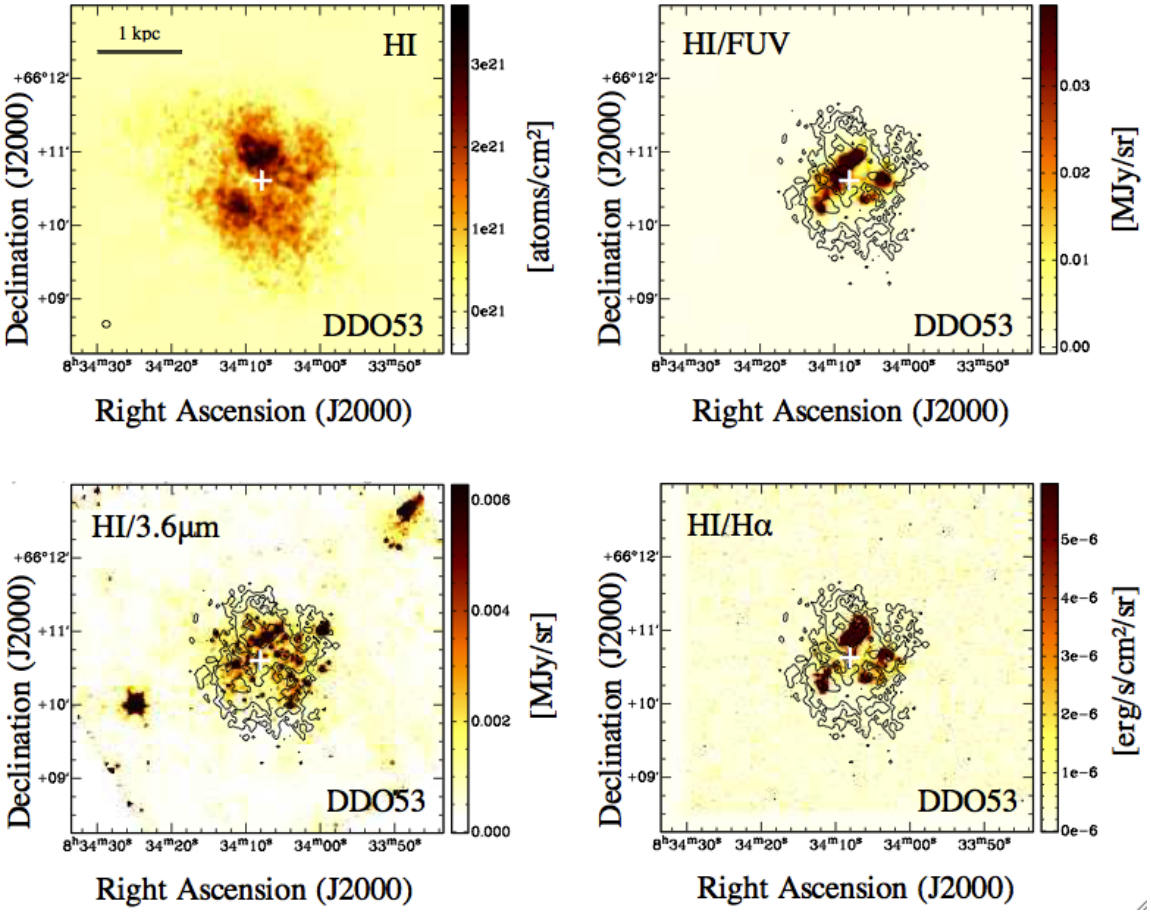

Figure 2.34: Surface density maps for DDO 53. *Top Left*: Integrated H I map (resolution: $6\farcs3 \times 5\farcs7$, lowest confidence level (2.5σ over 3 channels): 3.6×10^{20} atoms cm^{-2}, colour scale: 0 - 3×10^{21} atoms cm^{-2}). *Top Right*: H I contours overlaid on the FUV image (colour scale: 0 - 6×10^{-2} MJy sr^{-1}). *Bottom Left*: H I contours overlaid on the *Spitzer* 3.6 μm image (colour scale: 0 - 6×10^{-3} MJy sr^{-1}). *Bottom Right*: H I contours overlaid on the Hα map (colour scale: 0 - 5×10^{-6} ergs s^{-1} cm^{-2} sr^{-1}). The H I contours are at (1, 1.5, 2.5)$\times 10^{21}$ atoms cm^{-2}. In all panels the plus represents the V–band centre of the galaxy. The H I map beam size is indicated in the bottom left corner of the top left panel.

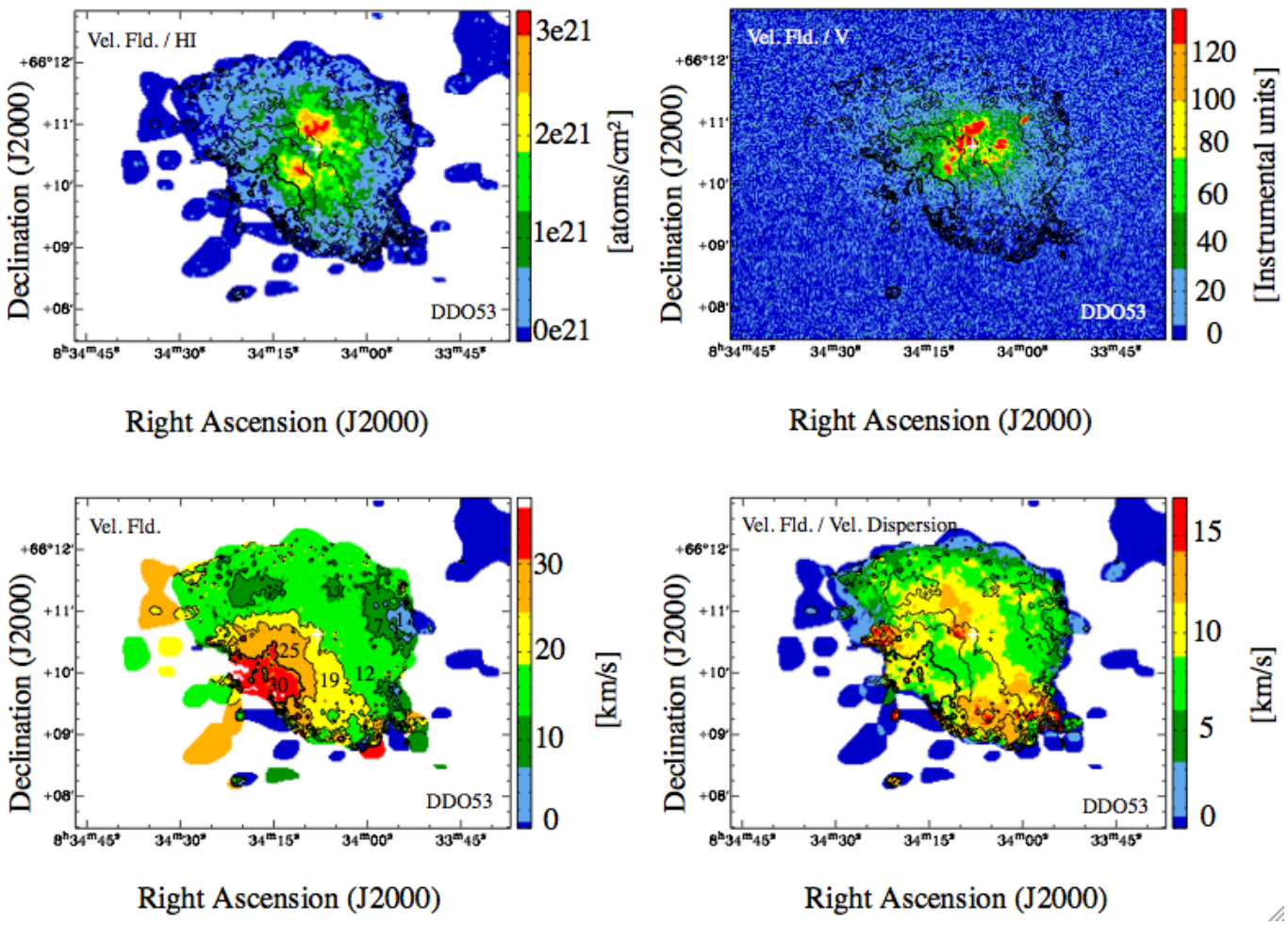

Figure 2.35: Moment maps for DDO 53. *Top Left*: Integrated H I map (moment 0) with velocity field contours. *Top Right*: Velocity field contours overlaid on the V–band optical image (colour scale: 0 - 120 instrumental units). *Bottom Left*: Contoured Velocity Field (colour scale: 0 - 30 km s^{-1}). *Bottom Right*: Velocity field contours overlaid on the velocity dispersion map (colour scale: 0 - 15 km s^{-1}). The velocity field contours are at (1, 7, 12, 19, 25, 30) km s^{-1}. In all panels the plus represents the V–band centre of the galaxy.

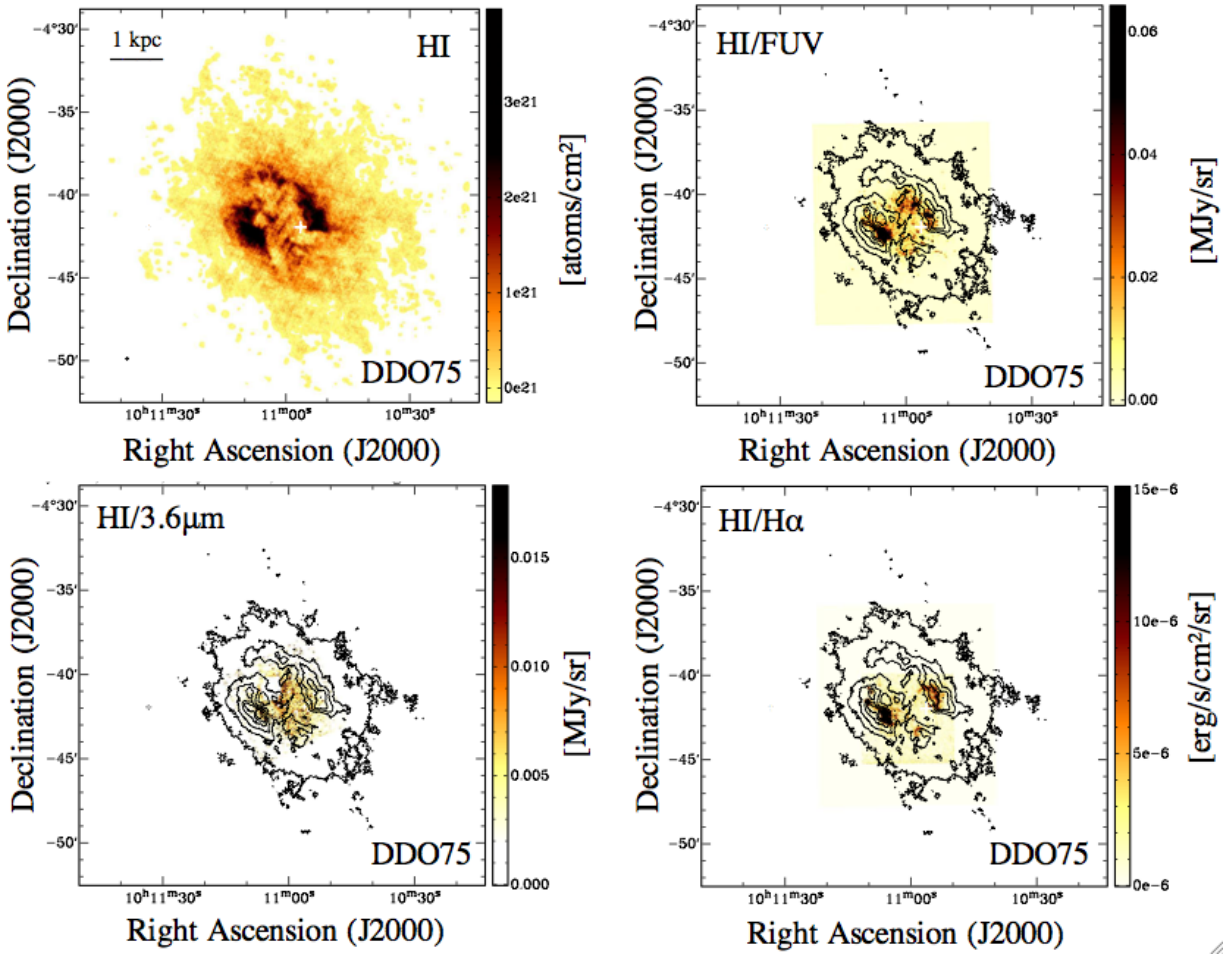

Figure 2.36: Surface density maps for DDO 75. *Top Left*: Integrated H I map (resolution: $7\farcs6 \times 6\farcs5$, lowest confidence level (2.5σ over 3 channels): 2.2×10^{20} atoms cm^{-2}, colour scale: 0 - 3×10^{21} atoms cm^{-2}). *Top Right*: H I contours overlaid on the FUV image (colour scale: 0 - 6×10^{-2} MJy sr^{-1}). *Bottom Left*: H I contours overlaid on the *Spitzer* 3.6 μm image (colour scale: 0 - 1.5×10^{-2} MJy sr^{-1}). *Bottom Right*: H I contours overlaid on the Hα map (colour scale: 0 - 15×10^{-6} ergs s^{-1} cm^{-2} sr^{-1}). The H I contours are at (0.2, 1, 2, 3)$\times 10^{21}$ atoms cm^{-2}. In all panels the plus represents the V–band centre of the galaxy. The H I map beam size is indicated in the bottom left corner of the top left panel.

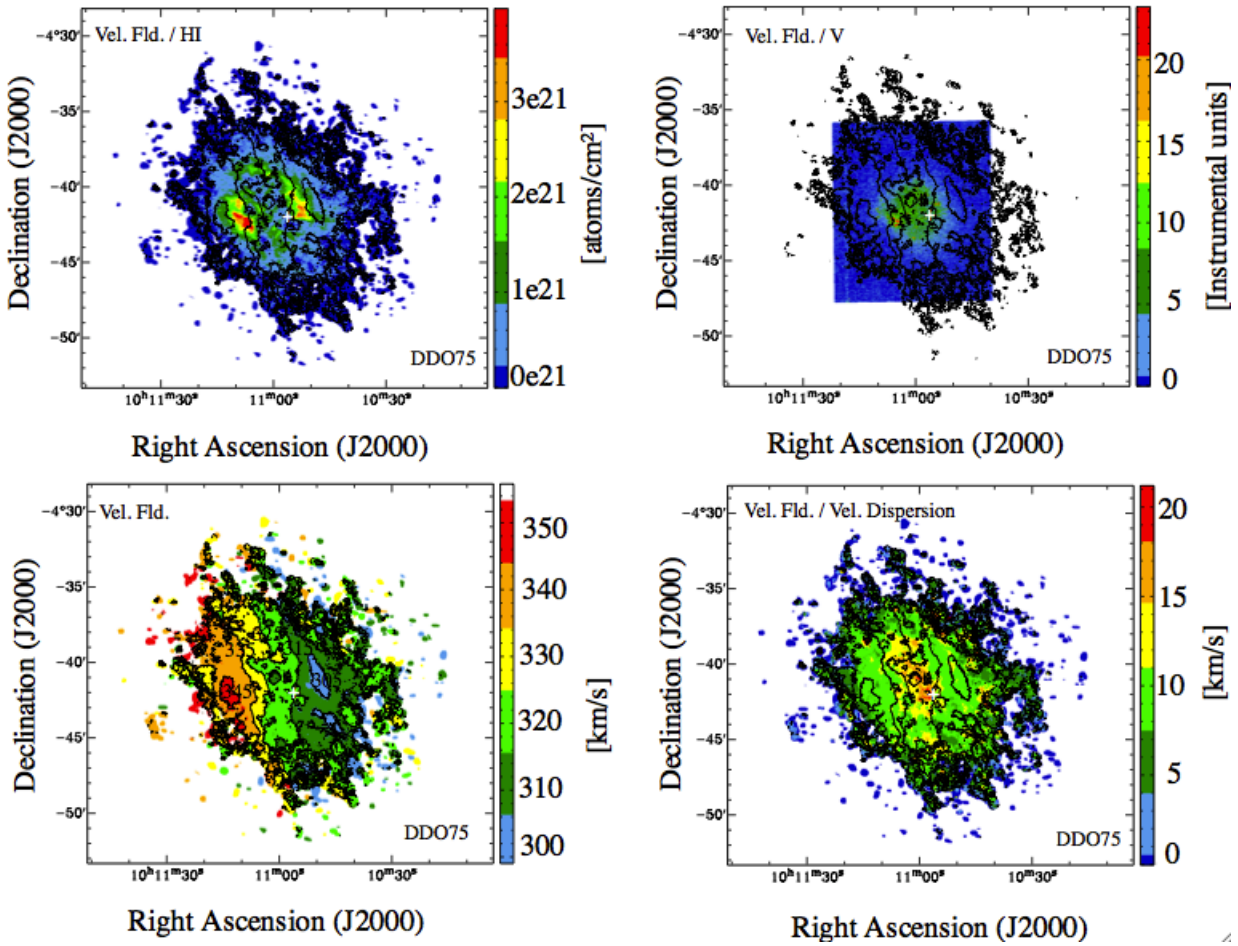

Figure 2.37: Moment maps for DDO 75. *Top Left*: Integrated H I map (moment 0) with velocity field contours. *Top Right*: Velocity field contours overlaid on the V–band optical image (colour scale: 0 - 6 instrumental units). *Bottom Left*: Contoured Velocity Field (colour scale: 300 - 360 $\mathrm{km\,s^{-1}}$). *Bottom Right*: Velocity field contours overlaid on the velocity dispersion map (colour scale: 0 - 20 $\mathrm{km\,s^{-1}}$). The velocity field contours are at (305, 315, 325, 335, 345) $\mathrm{km\,s^{-1}}$. In all panels the plus represents the V–band centre of the galaxy.

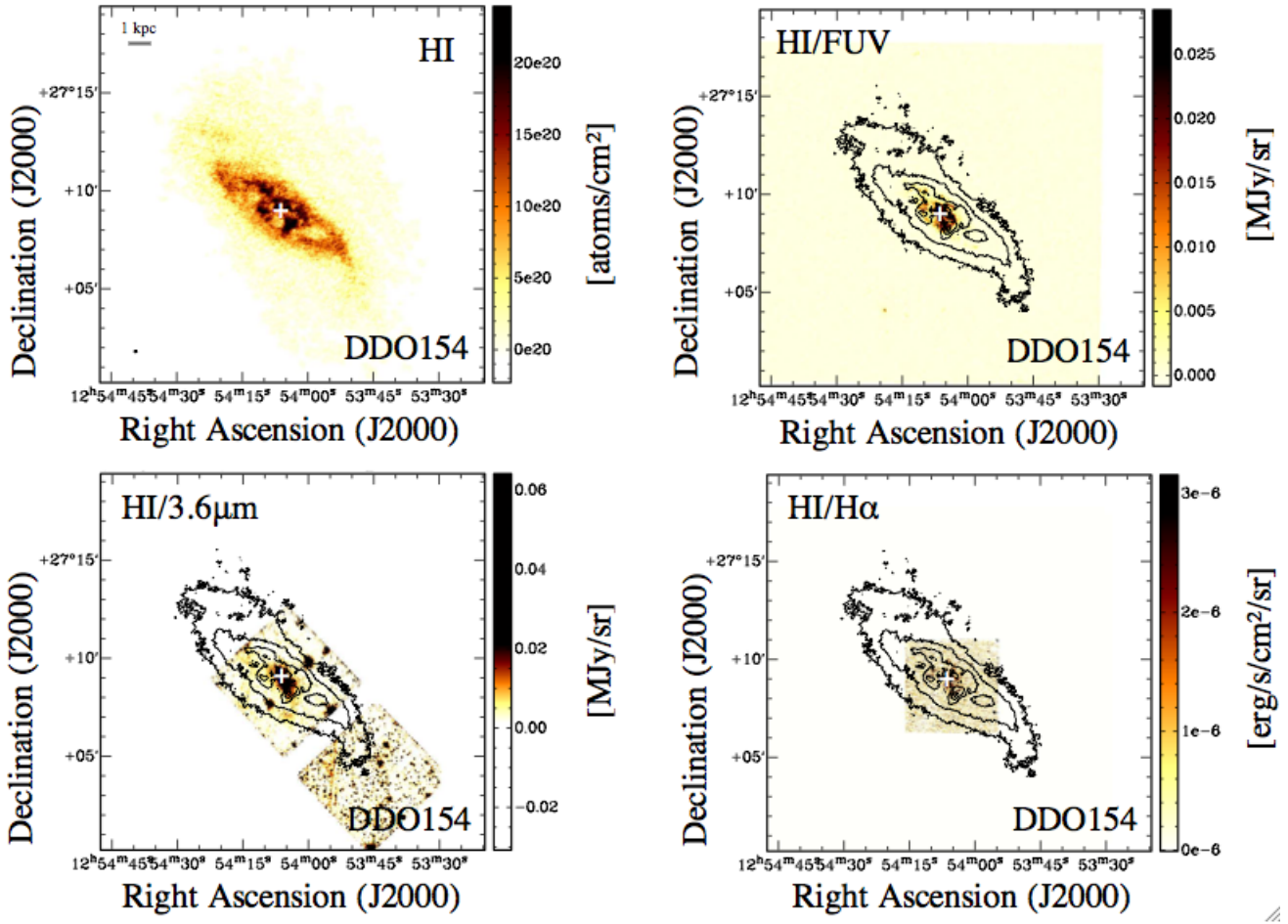

Figure 2.38: Surface density maps for DDO 154. *Top Left*: Integrated H I map (resolution: $7\farcs9 \times 6\farcs3$, lowest confidence level 2.5σ over 3 channels: 2.3×10^{20} atoms cm^{-2}, colour scale: 0 - 2×10^{21} atoms cm^{-2}). *Top Right*: H I contours overlaid on the FUV image (colour scale: 0 - 2.5×10^{-2} MJy sr^{-1}). *Bottom Left*: H I contours overlaid on the *Spitzer* 3.6 μm image (colour scale: 0 - 0.06 MJy sr^{-1}). *Bottom Right*: H I contours overlaid on the Hα map (colour scale: 0 - 3×10^{-6} ergs s^{-1} cm^{-2} sr^{-1}). The H I contours are at (2, 5, 10, 15)$\times 10^{20}$ atoms cm^{-2}. In all panels the plus represents the V–band centre of the galaxy. The H I map beam size is indicated in the bottom left corner of the top left panel.

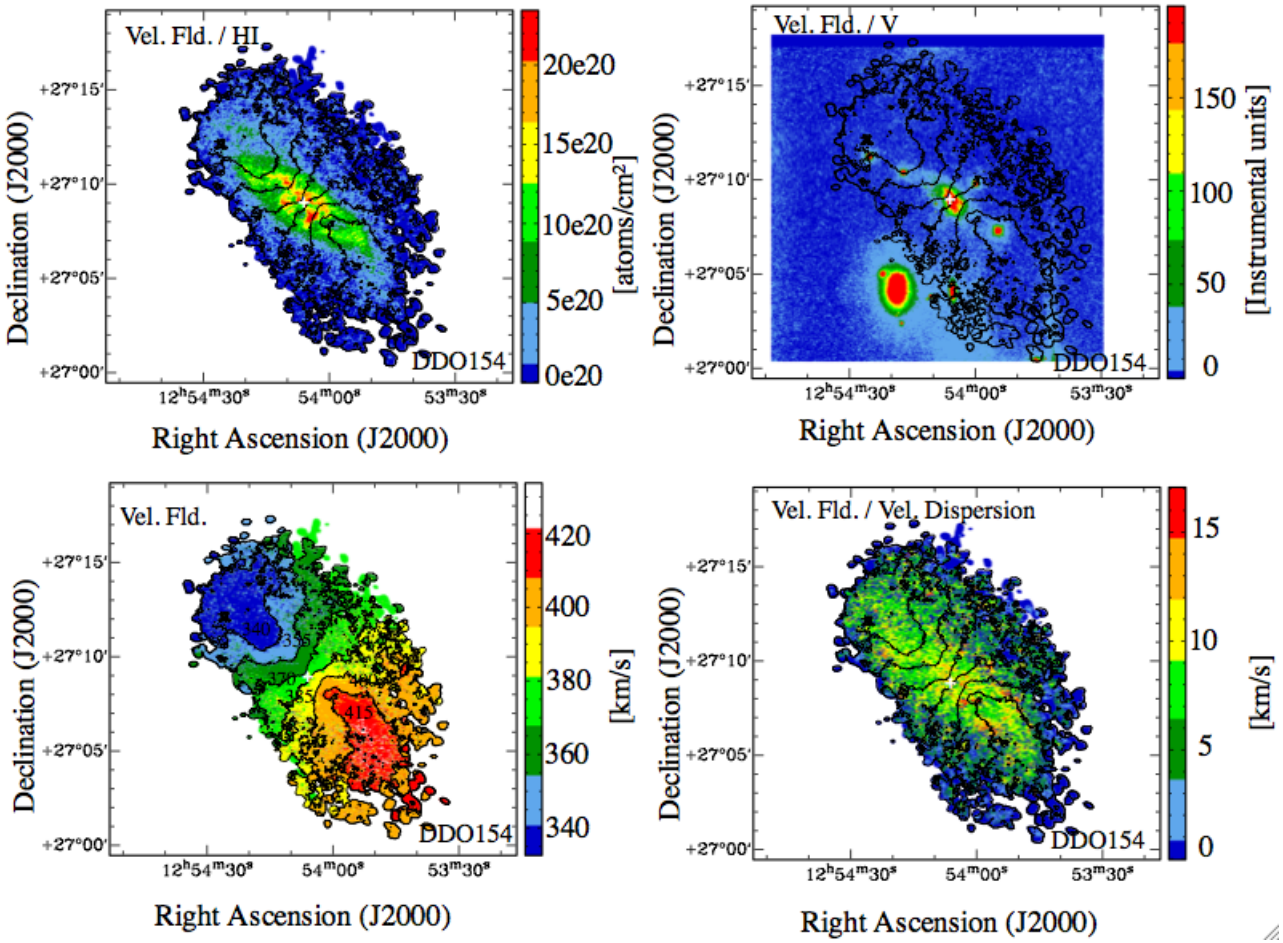

Figure 2.39: Moment maps for DDO 154. *Top Left*: Integrated H I map (moment 0) with velocity field contours. *Top Right*: Velocity field contours overlaid on the V–band optical image (colour scale: 0 - 300 instrumental units). *Bottom Left*: Contoured Velocity Field (colour scale: 340 - 420 km s^{-1}). *Bottom Right*: Velocity field contours overlaid on the velocity dispersion map (colour scale: 0 - 15 km s^{-1}). The velocity field contours are at (340, 355, 370, 385, 400, 415) km s^{-1}. In all panels the plus represents the V–band centre of the galaxy.

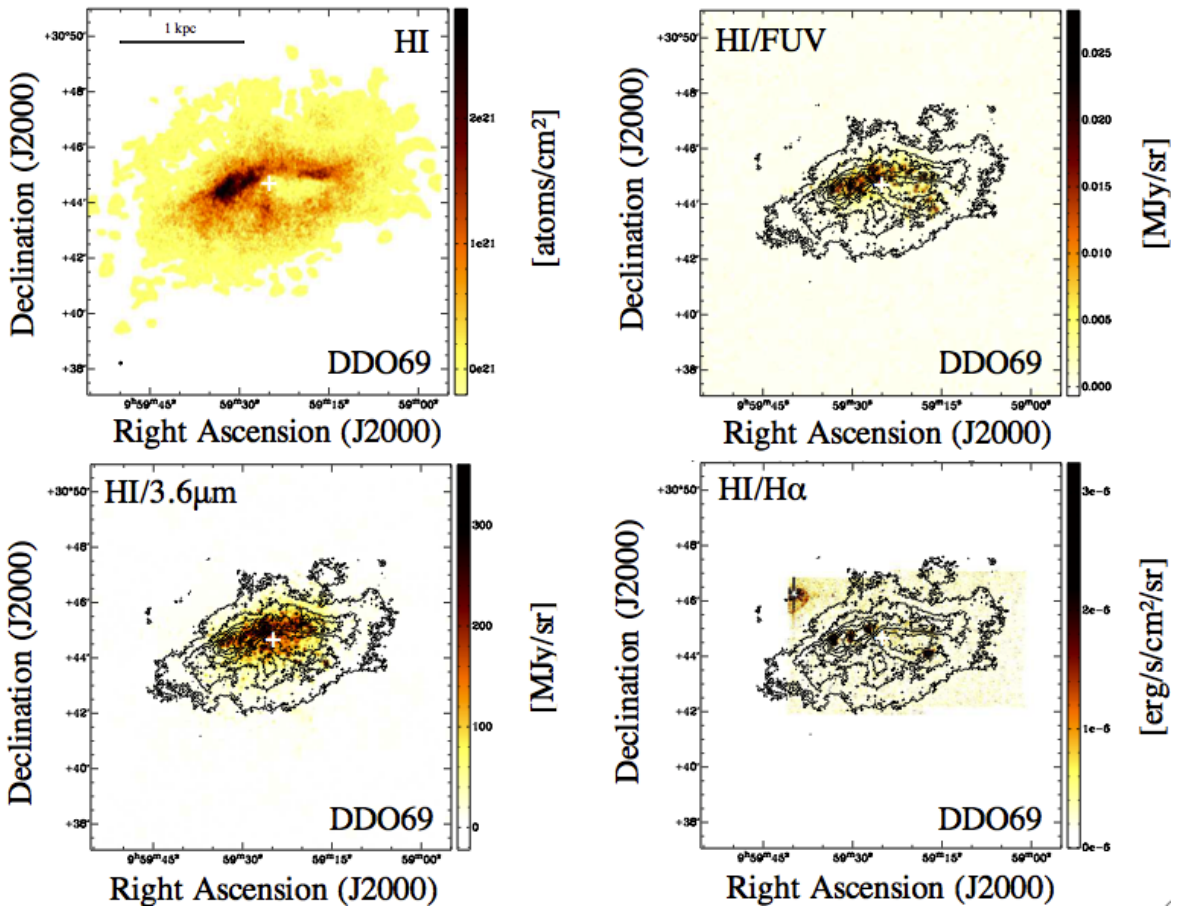

Figure 2.40: Surface density maps for DDO 69. *Top Left*: Integrated H I map (resolution: $5\farcs8 \times 5\farcs4$, lowest confidence level (2.5σ over 3 channels): 2.3×10^{20} atoms cm^{-2}, colour scale: 0 - 2×10^{21} atoms cm^{-2}). *Top Right*: H I contours overlaid on the FUV image (colour scale: 0 - 2.5×10^{-2} MJy sr^{-1}). *Bottom Left*: H I contours overlaid on the *Spitzer* 3.6 μm image (colour scale: 0 - 300 MJy sr^{-1}). *Bottom Right*: H I contours overlaid on the Hα map (colour scale: 0 - 3×10^{-6} ergs s^{-1} cm^{-2} sr^{-1}). The H I contours are at (0.14, 0.5, 1, 1.5, 2)$\times 10^{21}$ atoms cm^{-2}. In all panels the plus represents the V–band centre of the galaxy. The H I map beam size is indicated in the bottom left corner of the top left panel.

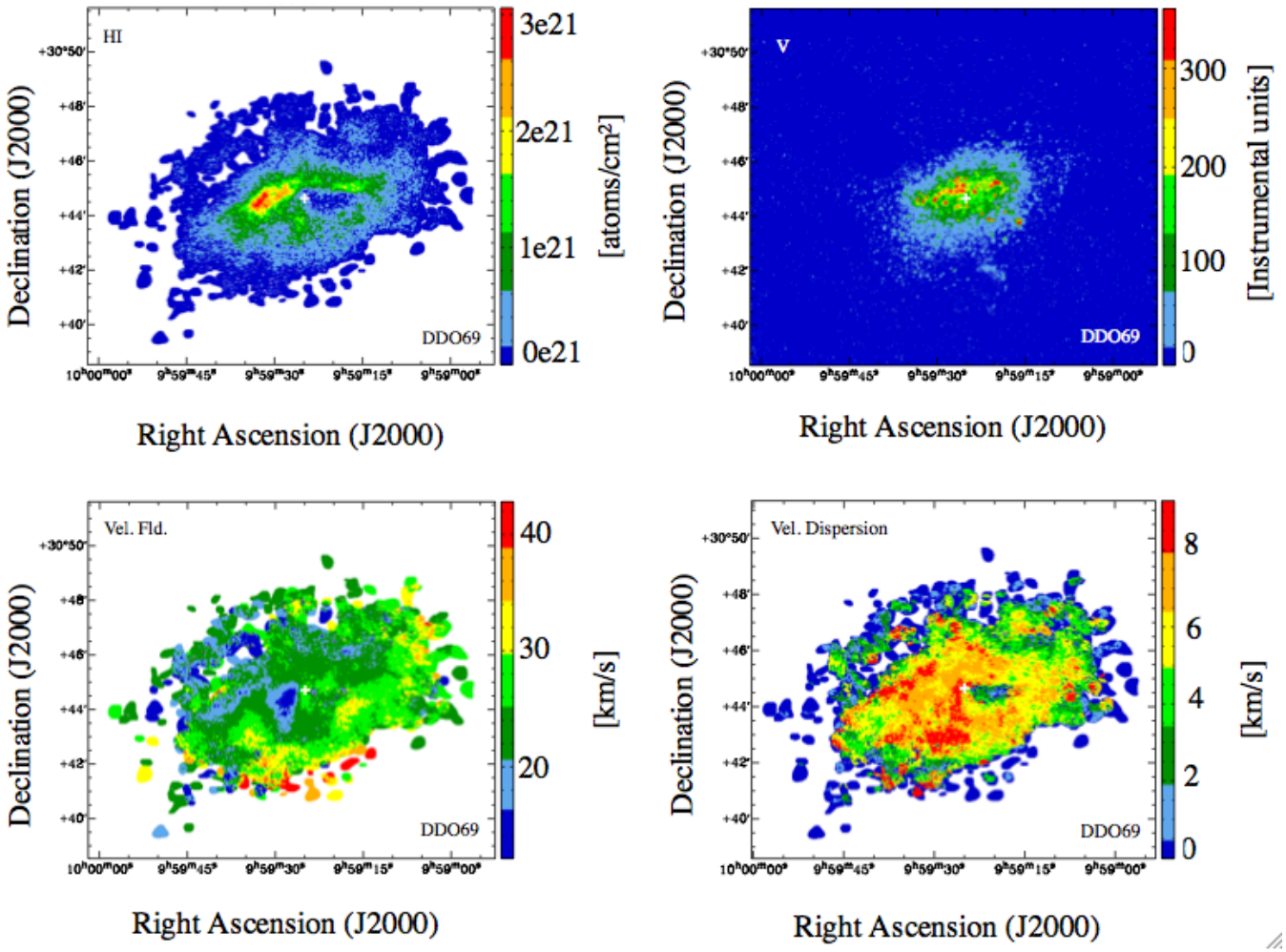

Figure 2.41: Moment maps for DDO 69. *Top Left*: Integrated H I map (moment 0). *Top Right*: V–band optical image (colour scale: 0 - 200 instrumental units). *Bottom Left*: Velocity Field (colour scale: 0 - 40 km s^{-1}). *Bottom Right*: Velocity dispersion map (colour scale: 0 - 15 km s^{-1}). In all panels the plus represents the V–band centre of the galaxy.

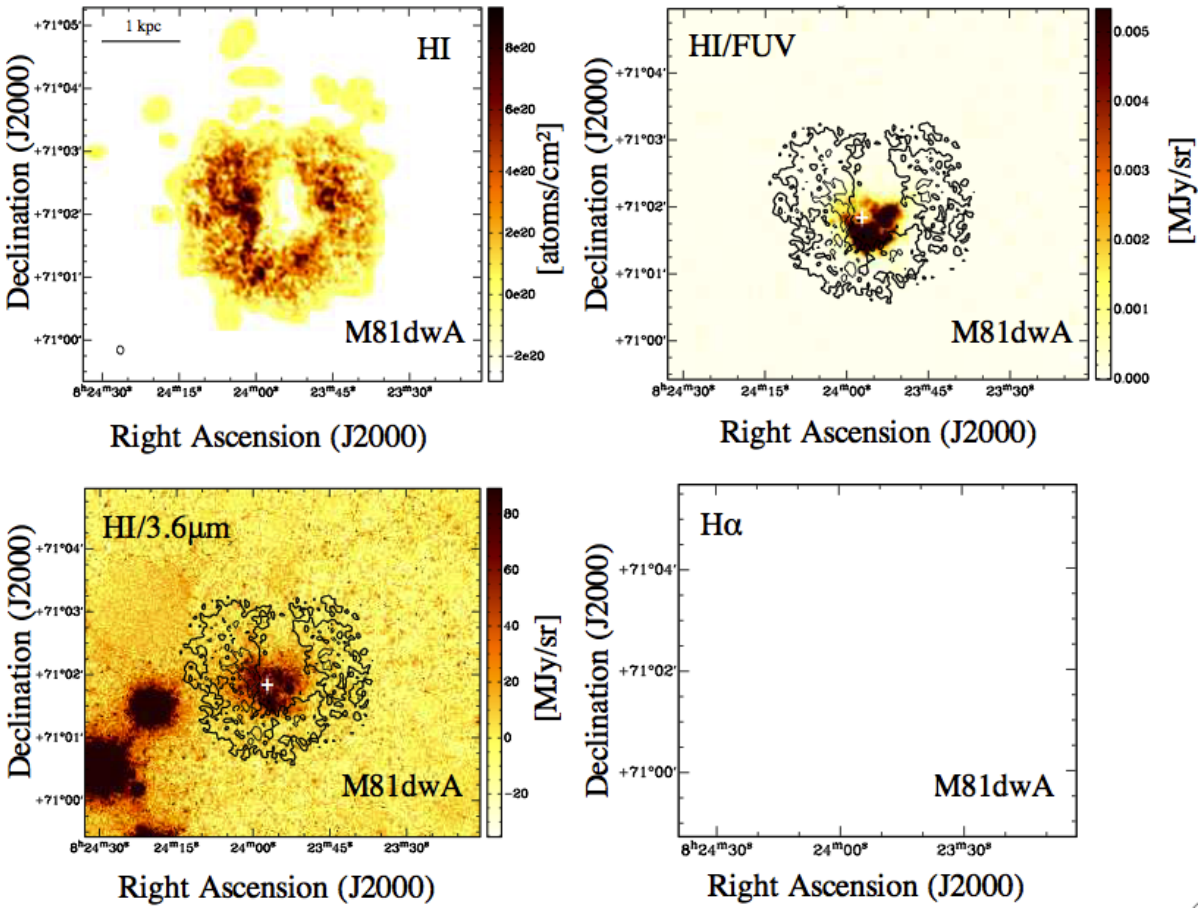

Figure 2.42: Surface density maps for M81dwA. *Top Left*: Integrated H I map for M81dwA (resolution: $7\farcs8 \times 6\farcs3$, lowest confidence level (2.5σ over 3 channels): 1.8×10^{20} atoms cm^{-2}, colour scale: 0 - 0.8×10^{20} atoms cm^{-2}). *Top Right*: H I contours overlaid on the FUV image for M81dwA (colour scale: 0 - 0.5×10^{-2} MJy sr^{-1}). *Bottom Left*: H I contours overlaid on the *Spitzer* 3.6 μm image (colour scale: 0 - 80 MJy sr^{-1}). *Bottom Right*: the empty panel illustrates the lack of Hα emission. The H I contours are at (2, 6.5)$\times10^{20}$ atoms cm^{-2}. In all panels the plus represents the V–band centre of the galaxy. The H I map beam size is indicated in the bottom left corner of the top left panel.

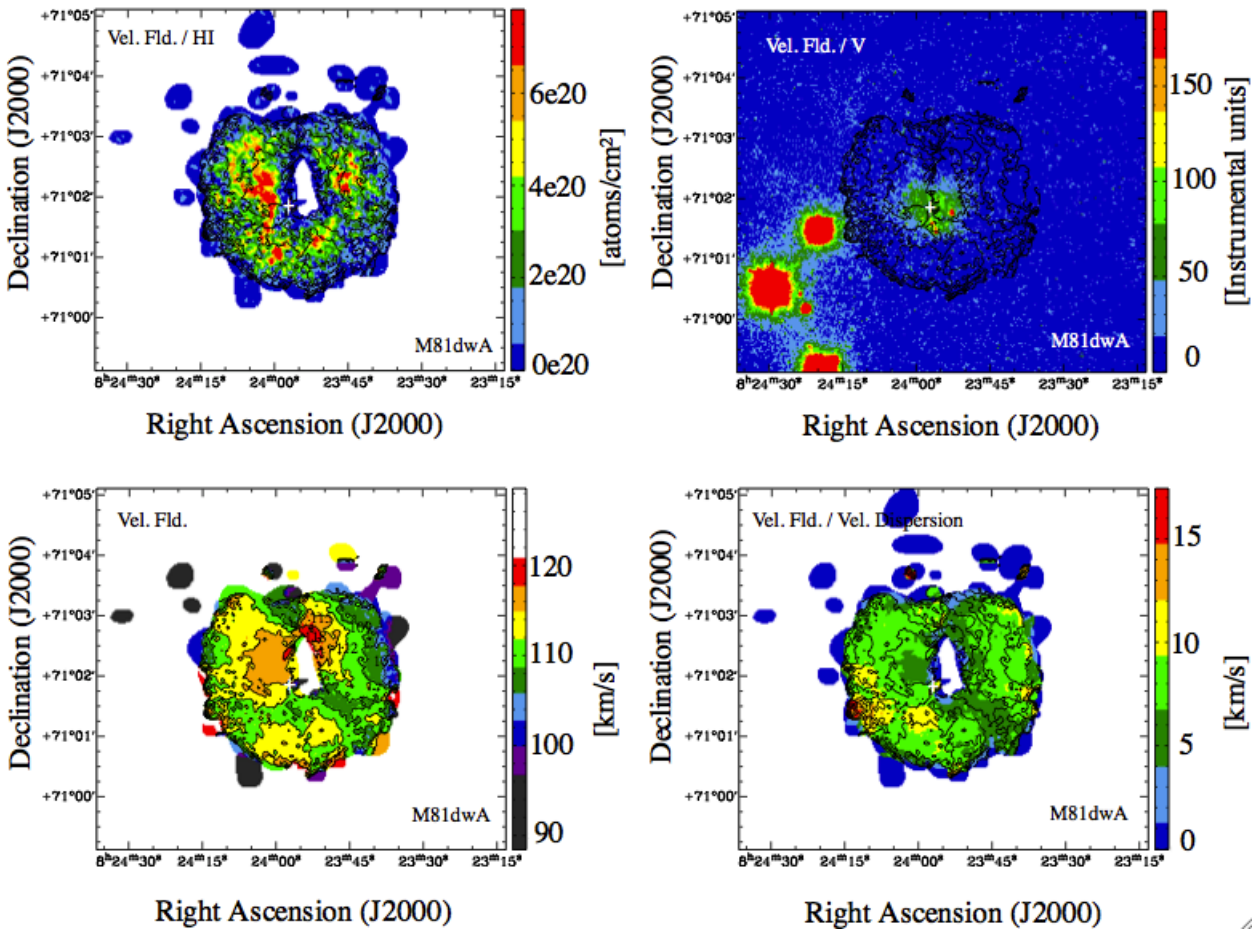

Figure 2.43: Moment maps for M81dwA. *Top Left*: Integrated H I map (moment 0) with velocity field contours. *Top Right*: Velocity field contours overlaid on the V–band optical image (colour scale: 0 - 150 instrumental units). *Bottom Left*: Contoured Velocity Field (colour scale: 90 - 120 $\mathrm{km\,s^{-1}}$). *Bottom Right*: Velocity field contours overlaid on the velocity dispersion map (colour scale: 0 - 30 $\mathrm{km\,s^{-1}}$). The velocity field contours are at (105, 109, 112, 115, 118) $\mathrm{km\,s^{-1}}$. In all panels the plus represents the V–band centre of the galaxy.

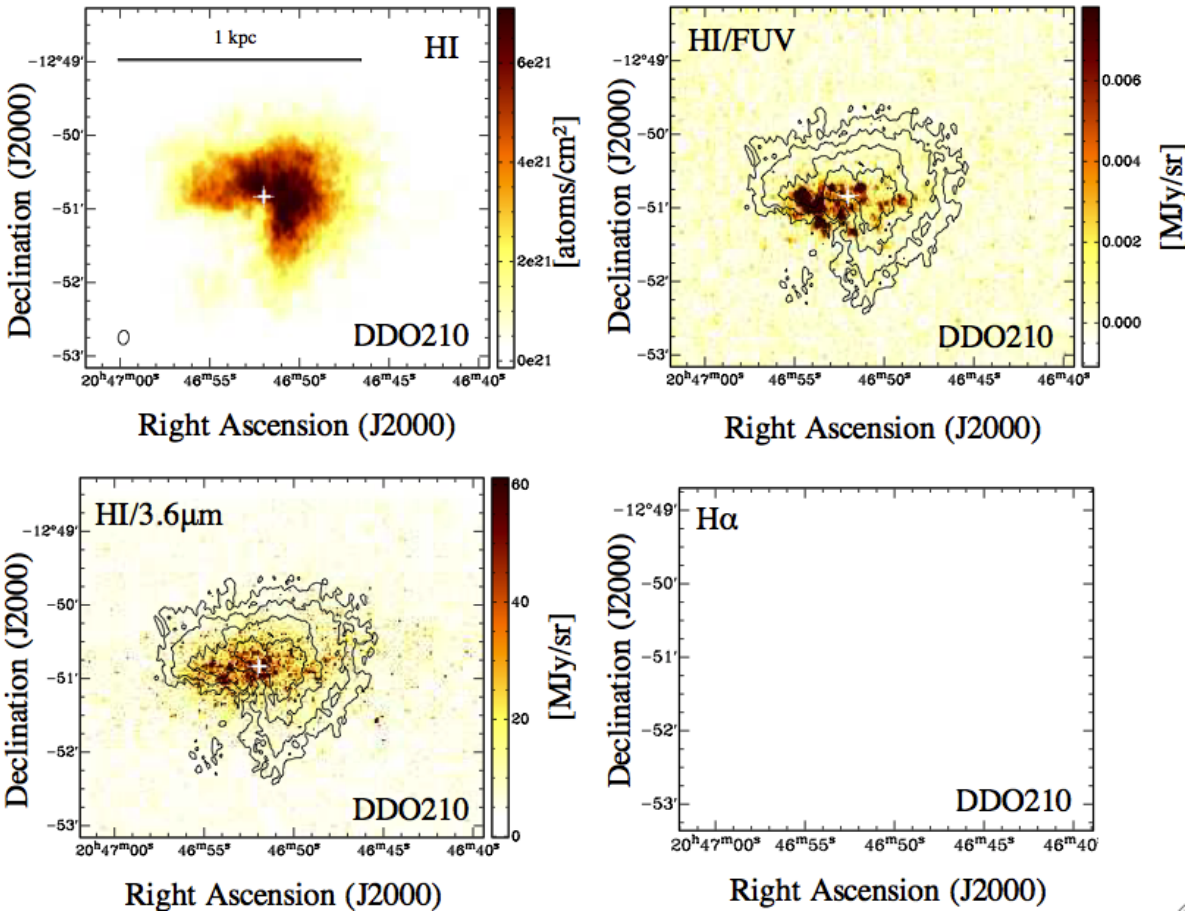

Figure 2.44: Surface density maps for DDO 210. *Top Left*: Integrated H I map for DDO 210 (resolution: $11\farcs7 \times 8\farcs6$, lowest confidence level (2.5σ over 3 channels): 0.93×10^{20} atoms cm^{-2}, colour scale: 0 - 6×10^{21} atoms cm^{-2}). *Top Right*: H I contours overlaid on the FUV image (colour scale: 0 - 6×10^{-3} MJy sr^{-1}). *Bottom Left*: H I contours overlaid on the *Spitzer* 3.6 μm image (colour scale: 0 - 60 MJy sr^{-1}). *Bottom Right*: the empty panel illustrates the lack of Hα emission. The H I contours are at (1, 2, 4, 6)$\times 10^{21}$ atoms cm^{-2}. In all panels the plus represents the V–band centre of the galaxy. The H I map beam size is indicated in the bottom left corner of the top left panel.

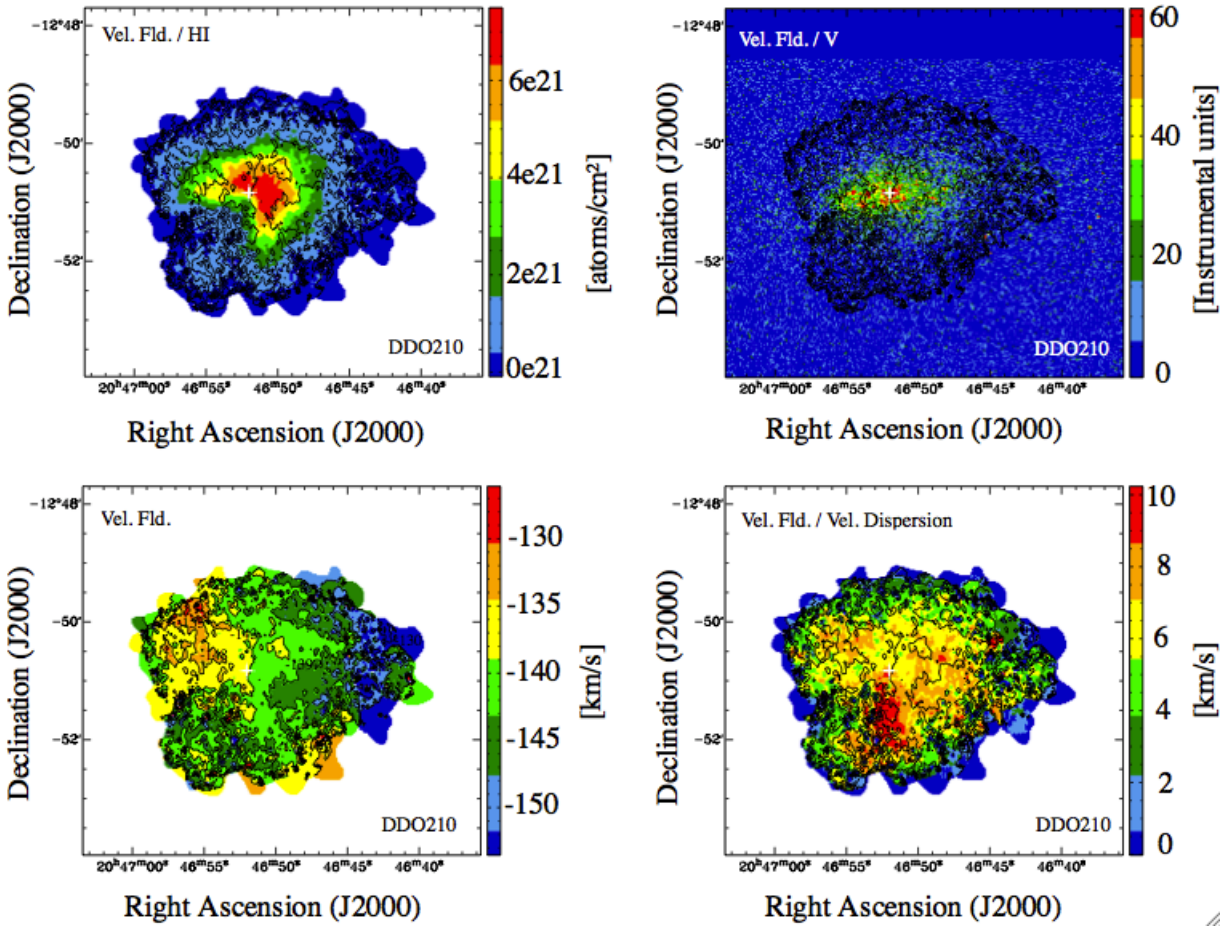

Figure 2.45: Moment maps for DDO 210. *Top Left*: Integrated H I map (moment 0) with velocity field contours. *Top Right*: Velocity field contours overlaid on the *V*–band optical image (colour scale: 0 - 30 instrumental units). *Bottom Left*: Contoured Velocity Field (colour scale: -150 to - 130 $\mathrm{km\,s^{-1}}$). *Bottom Right*: Velocity field contours overlaid on the velocity dispersion map (colour scale: 0 - 12 $\mathrm{km\,s^{-1}}$). The velocity field contours are at (-130, -135, -139, -143, -148, -153) $\mathrm{km\,s^{-1}}$. In all panels the plus represents the *V*–band centre of the galaxy.

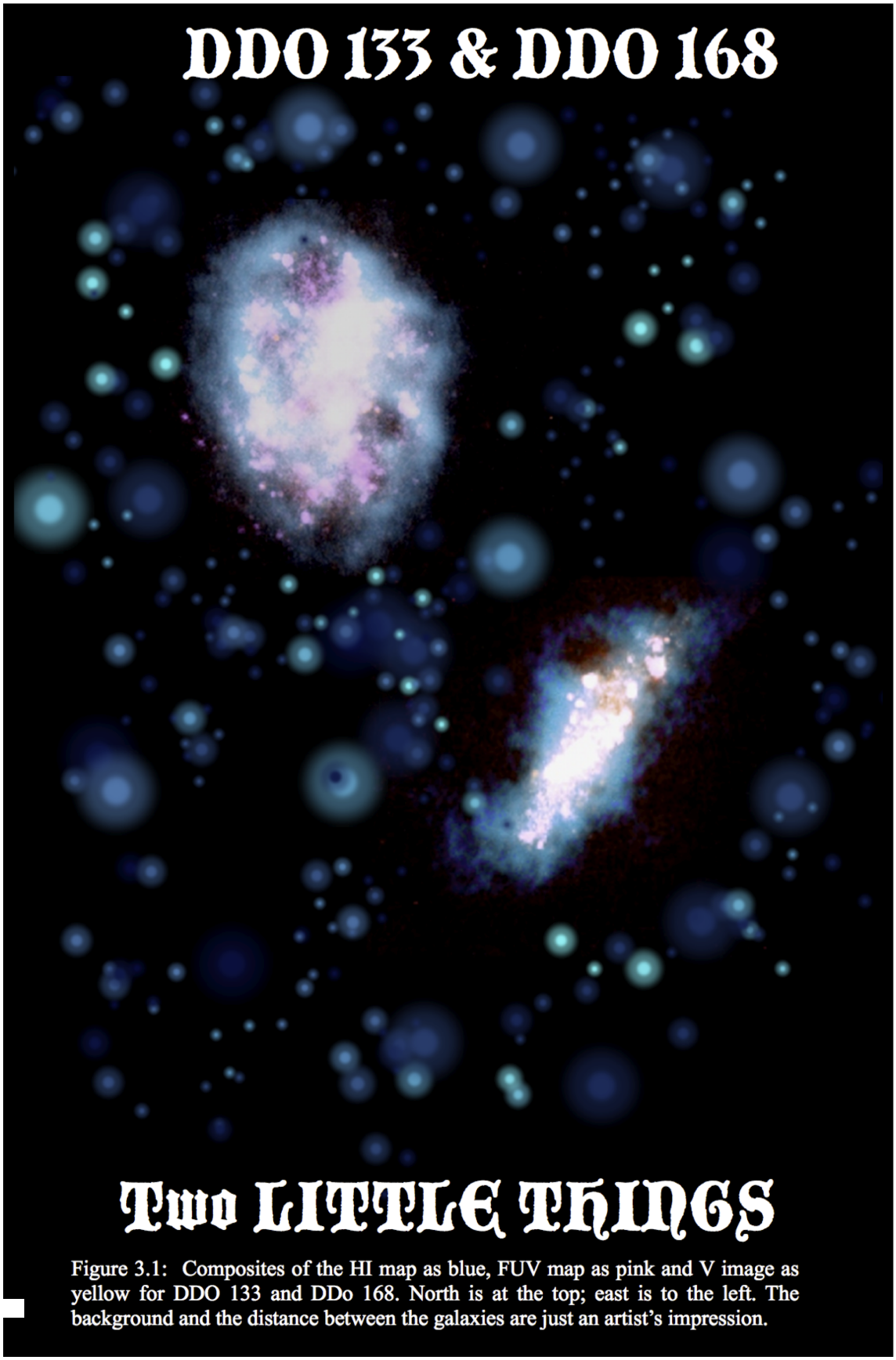

Figure 3.1: Composites of the HI map as blue, FUV map as pink and V image as yellow for DDO 133 and DDo 168. North is at the top; east is to the left. The background and the distance between the galaxies are just an artist's impression.

Chapter 3
STAR FORMATION ANALYSIS: THE CASE OF DDO 133 AND DDO 168

In this chapter, we present our star formation analysis method applied to a case study of two LITTLE THINGS galaxies DDO 133 and DDO 168 (see Fig. 3.1 and Fig. 3.2). The two galaxies have similar metallicities, a difference in V–band brightness of only one magnitude and also similar integrated star formation rates (see Table 2.1). These two dwarf galaxies have been observed at ultraviolet (Hunter et al., 2010), Hα (Hunter & Elmegreen, 2004) and optical wavelengths (Hunter & Elmegreen, 2006; Hunter et al., 1982; Kennicutt et al., 2008). DDO 133 is peculiar in the sense that whereas most of the major axis V–band profiles of dwarf galaxies are exponential (Herrmann et al., 2013; Hunter & Elmegreen, 2006), this galaxy's profile is flat. DDO 133 also hosts a bar (Hunter & Elmegreen, 2006). Neutral hydrogen in DDO 133 has been observed previously only with VLA D configuration but the data were never published. DDO 168, is described as peculiar and noted to have a significant position angle difference between the optical and the H I attributed to a possible past disturbance. Its gas surface density drops a factor of 10 over the radius of the optical galaxy, but there is no reflection of such a drastic change in the optical colours. Broeils & van Woerden (1994) used the Westerbork Telescope for a short 2–hour observation of DDO 168. The peculiar H I spatial morphology of DDO 168 prompted deeper observations (Broeils & Rhee, 1997), yet not at the angular resolution we are providing here. These new observations enabled them to describe DDO 168 as having a "symmetric distribution with a strong condensation

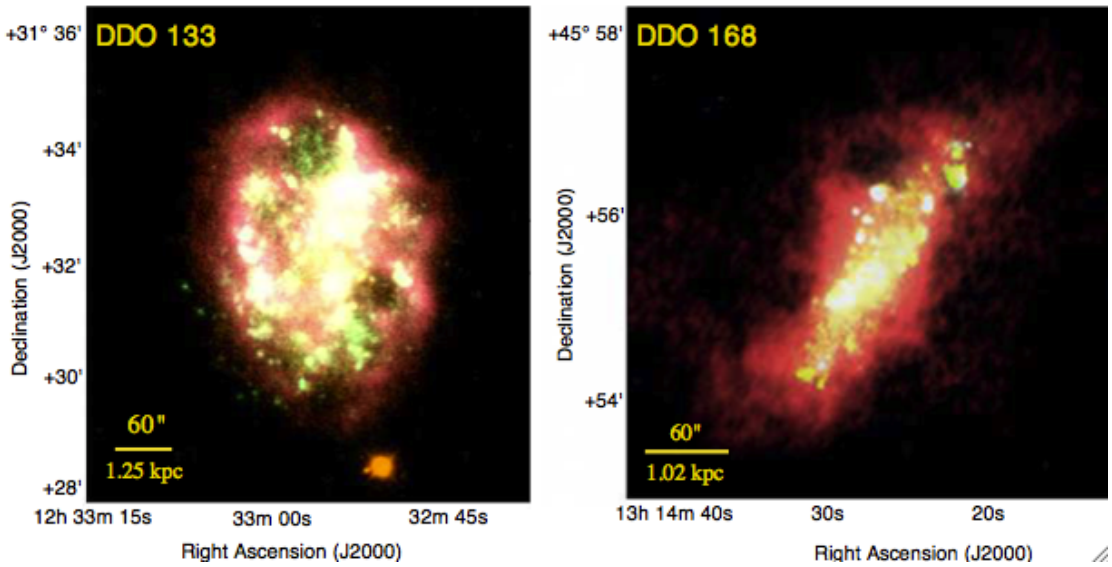

Figure 3.2: Composites of the H I map as red, FUV map as green and V–band image as orange for DDO 133 (left) and DDO 168 (right). North is at the top; east is to the left.

towards the centre".

We begin this chapter with a detailed presentation of the two galaxies in Section 3.1, continue with Section 3.2 on star formation analysis fundamentals, methods used and preliminary results on the two dwarfs. Then, in Section 3.3, we delve deeper into the subject of star formation in DDO 133 and DDO 168 and discuss in detail our pilot study involving the above mentioned two galaxies.

3.1 Data Presentation

3.1.1 Channel Maps

We combined the B–, C–, and D–array configuration VLA data into a final data set which probes high resolution structures as well as extended emission. We created both robust and natural weighted cubes, see Table 2.4 for mapping characteristics. In this thesis, we only show and use the robust=0 cubes because although their noise level is comparable to the natural weighted cubes' noise level, their resolution ($12\farcs4 \times 10\farcs8$ for DDO 133 and $7\farcs8 \times 5\farcs8$ for DDO 168) is higher. The asymmetrical uv–coverage (as a result of eliminating baselines between EVLA antennas) affects the natural weighted cube more, resulting in only a mild improvement in signal to

noise compared to the robust=0 cubes, at the cost of a loss in resolution.

The channel maps of DDO 168 and DDO 133 are available in Appendix A, Fig. A.1 and Fig. A.2, respectively. All emission channels are shown and the beam sizes are indicated in the bottom left corner of the top left panel. These channel maps are not primary beam corrected.

3.1.2 Integrated Properties

We present the integrated H I spectra of DDO 133 and DDO 168 in Fig. 3.3. These were obtained by integrating the channel maps over the area of the source after subtracting the continuum background. The flux is given in Jansky and the channel separation for our data (which is also the velocity resolution) is 2.6 km s^{-1}. In Fig. 3.3, the continuous line represents our robust weighted data cubes. The dashed line represents published single dish data from Springob et al. (2005) for DDO 133 and from Hunter & Gallagher (1985a) for DDO 168. Both DDO 133 and DDO 168 single dish observations were taken with the NRAO 43 m Green Bank telescope. The single dish data on DDO 168 were in units of brightness temperature, which we converted into flux measurements using a telescope gain of 3.3 Jy K^{-1} as given by van Zee et al. (1997).

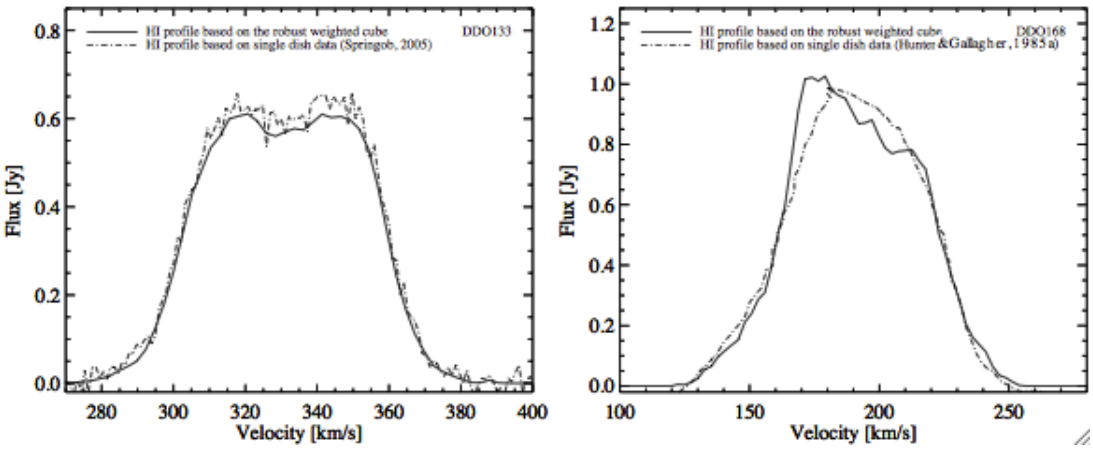

Figure 3.3: H I profiles of the calibrated, combined B–, C–, and D–array configuration VLA data for DDO 133 (left) and DDO 168 (right). The profiles are based on the robust weighted maps (full line) and are compared with published single dish profiles (dashed line).

On a channel by channel basis the robust intensity–velocity plots of both galaxies agree with the single dish measurements to within 10%, see Table 3.1. In DDO

168, there is some systematic difference with the single-dish profile between 165-210 km s^{-1}. The discrepancy is most probably due to baseline ripples that did not subtract properly in the single dish data (Hunter et al., 2012).

The galaxy DDO 133 has an inferred systemic velocity of 331 ± 2 km s^{-1}. The total integrated flux is 36.4 Jy km s^{-1} corresponding to an H I mass of $(1.1 \pm 0.2) \times 10^8$ M$_\odot$ (adopting a distance of 3.5 Mpc, see Table 3.1). We find this value to be in good agreement with a single dish measurement of 1.2×10^8 M$_\odot$ made with the NRAO 43 m Green Bank telescope (Fisher & Tully, 1981). We are also within 10% agreement with the more recent single dish measurement from Springob et al. (2005).

The measured systemic velocity for DDO 168 is 192 ± 3 km s^{-1}. The total integrated flux is 64 Jy km s^{-1} corresponding to an H I mass of $(2.8 \pm 0.4) \times 10^8$ M$_\odot$, (adopting a distance of 4.3 Mpc, see Table 3.2). We again find this value smaller, yet in fair agreement with the single dish measurement of 77 Jy km s^{-1} made with the NRAO 43 m telescope (Hunter & Gallagher, 1985a) or the 76.5 Jy km s^{-1} value found by Huchtmeier & Richter (1986) with the WSRT.

3.1.3 Gas Distribution in DDO 133 and DDO 168

The H I in DDO 133 is organised in an extended moderately inclined disk with a number of readily identifiable holes (Fig. 3.4). When we further investigate the integrated H I distribution map (see Fig. 3.5, top left), we find in close proximity to some of the holes two areas with dense H I. Neither of the two areas is central to the galaxy and in both areas the velocity dispersion is high (see Fig. 3.5, bottom right).

The H I gas is asymmetrical with respect to the optical disk. However the kinematical centre agrees well with the centre (plus symbol in all panels of Fig. 3.4) indicated by the stars traced by the *Spitzer* 3.6 μm map and the optical data centre given by Hunter & Elmegreen (2006). From V–band imaging, these authors find the galaxy to be barred, with the bar centre (RA: $12^h\ 32^m\ 54\overset{s}{.}3$ and DEC: $31^\circ\ 32'\ 32''$) offset from the galaxy centre (RA: $12^h\ 32^m\ 55\overset{s}{.}4$ and DEC: $31^\circ\ 32'\ 14''$). All coordinates are in J2000.0. There is a position angle difference of 8 °between the bar and the host galaxy; the bar has a semi–major radius of 2.48 kpc, as determined by Hunter & Elmegreen (2006). We have marked the center of the bar with a circled plus symbol in Figs. 3.4 – 3.6.

In Fig. 3.6 we plot V–band contours on top of the H I distribution map showing the twisting of the optical contours at the position of the proposed bar. The tip of the bar coincides with one of the high H I density areas previously mentioned.

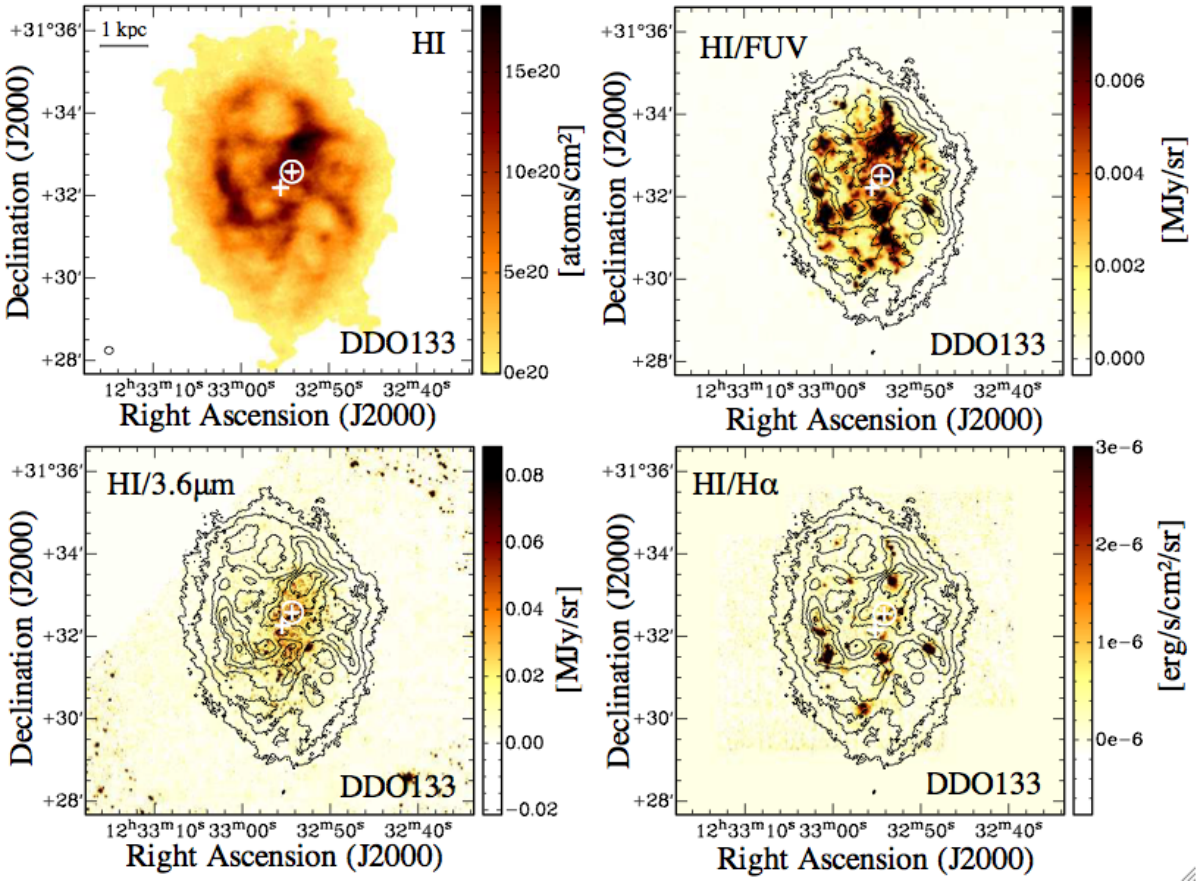

Figure 3.4: Surface density maps for DDO 133. *Top Left*: Integrated H I map (resolution: $12\farcs4 \times 10\farcs8$, lowest confidence level 2.5σ over 3 channels: 0.61×10^{20} atoms cm^{-2}, colour scale: 0 - 1.5×10^{21} atoms cm^{-2}). *Top Right*: H I contours overlaid on the FUV image (colour scale: 0 - 8×10^{-3} MJy sr^{-1}). *Bottom Left*: H I contours overlaid on the *Spitzer* 3.6 μm image (colour scale: 0 - 0.2 MJy sr^{-1}). *Bottom Right*: H I contours overlaid on the Hα map (colour scale: 0 - 1×10^{-7} ergs s^{-1} cm^{-2} sr^{-1}). The H I contours are at (0.1, 0.3, 0.6, 0.9, 1.2, 1.5)$\times 10^{21}$ atoms cm^{-2}. In all panels the plus represents the V–band and the kinematic centre of the galaxy, whereas the circled plus represents the centre of the bar. The H I map beam size is indicated in the bottom left corner of the top left panel.

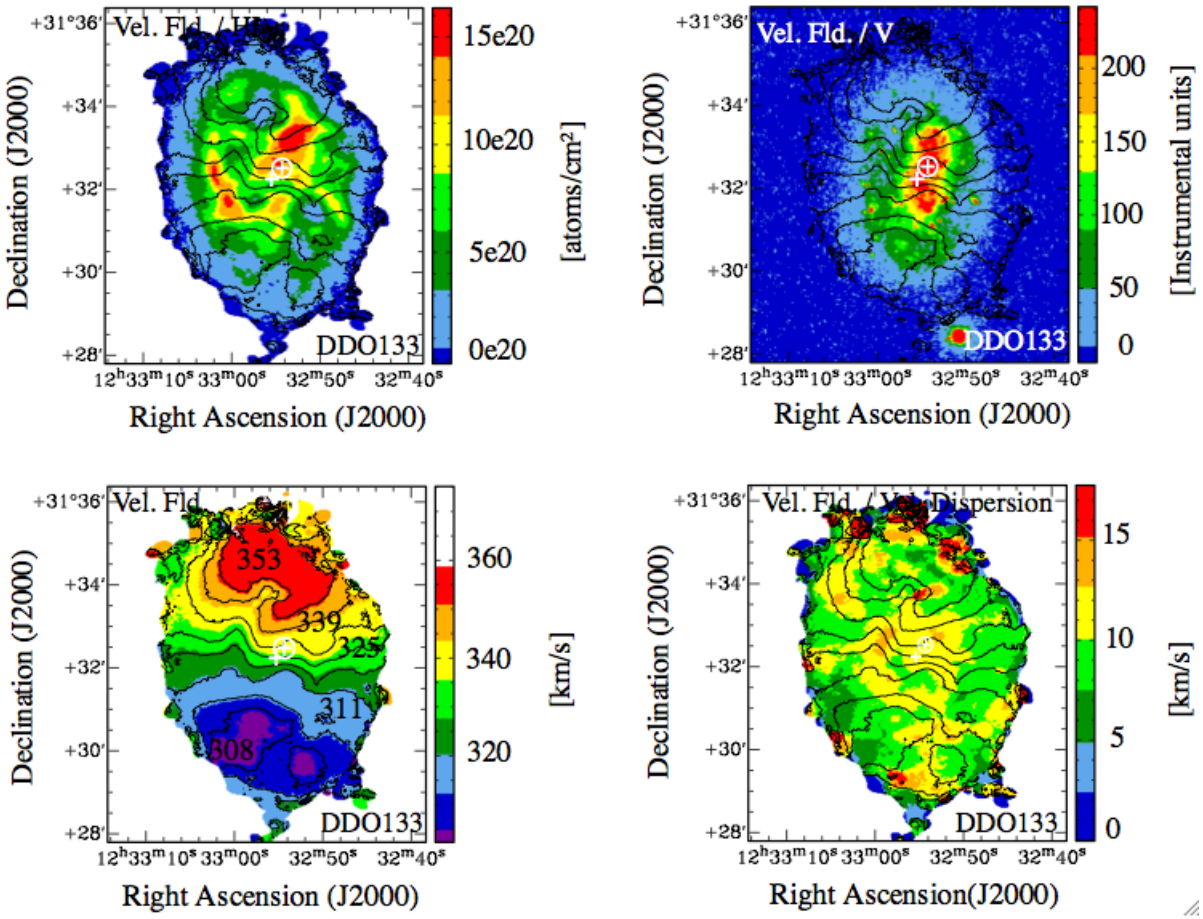

Figure 3.5: Moment maps for DDO 133. *Top Left*: Integrated H I map (moment 0) with velocity field contours. *Top Right*: velocity field contours overlaid on the V–band optical image (colour scale: 0 - 800 instrumental units). *Bottom Left*: Contoured Velocity Field (colour scale: 300 - 360 $\mathrm{km\,s^{-1}}$). *Bottom Right* : Velocity contours overlaid on the velocity dispersion map (colour scale: 0 - 25 $\mathrm{km\,s^{-1}}$). The velocity field contours are at (308, 311, 318, 325, 332, 339, 346, 353) $\mathrm{km\,s^{-1}}$. In all panels the plus represents the V–band and the kinematic centre of the galaxy, whereas the circled plus represents the centre of the bar.

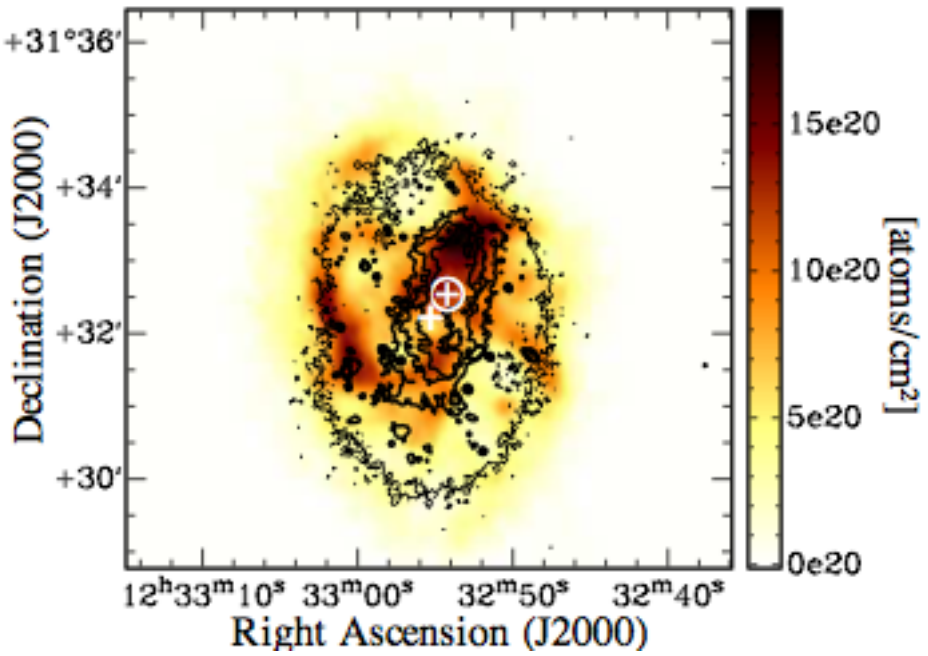

Figure 3.6: DDO 133: Integrated H I map (moment 0) with optical V–band contours. The V–band contours are at (25.8, 24.6, 24.2, 23.9) mag arcsec^{-2}. The plus represents the V–band and the kinematic centre of the galaxy, whereas the circled plus represents the centre of the bar.

The star formation regions as seen in the FUV and Hα images (Fig. 3.4) follow the H I gas concentrations. Strong FUV and Hα emission is associated not only with the dense H I structures, but also with the rims of the most important H I holes. Compact FUV emission is found close to the edge of the H I holes, suggestive of supernova explosions not just creating a hole in H I and pushing material outwards, but triggering new star formation there as well (Dopita et al., 1985; Opik, 1953; van Dyk et al., 1998).

DDO 168 has a peculiar H I distribution confirming the results of Broeils & van Woerden (1994). The highest concentrations of H I lie in the centre of the galaxy but at a different orientation with respect to the brightest emission in the optical. In Fig. 3.7 we plot V–band contours on top of the H I distribution. The centre of the optical disk, in J2000.0 coordinates, RA: $13^{\rm h}\ 14^{\rm m}\ 27\overset{\rm s}{.}2$ and DEC: $45^\circ\ 55'\ 46''$ (marked with a plus in each panel of Fig. 3.8), given by Hunter & Elmegreen (2006), coincides with the *Spitzer* 3.6 μm image and the kinematical centre of the H I. The velocity field (Fig. 3.9) of the H I gas also shows twisted isovelocity contours in the central part of the galaxy characteristic of a bar presence, which, however, has not

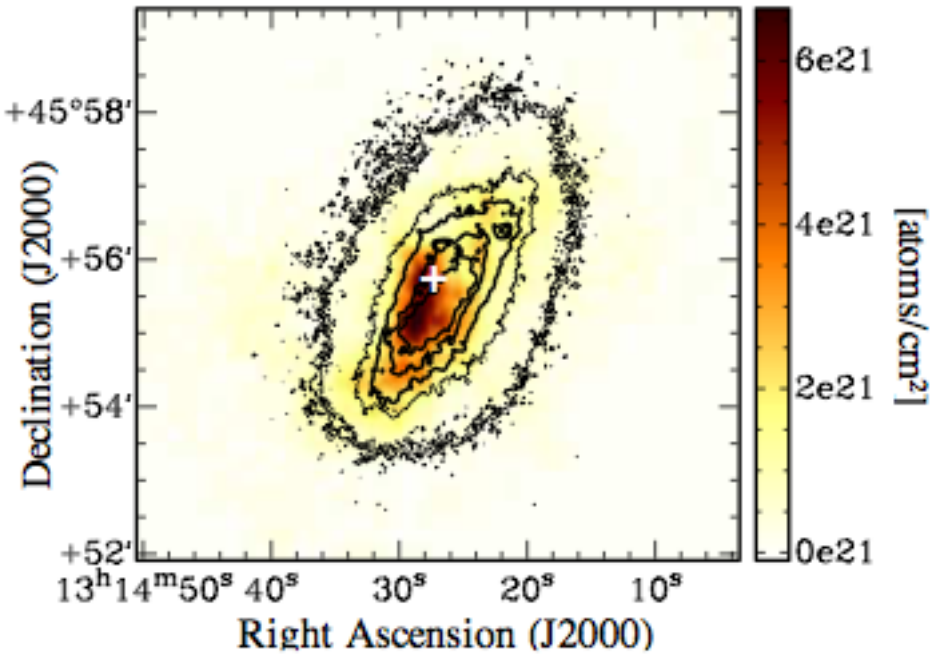

Figure 3.7: DDO 168: Integrated H I map (moment 0) with optical V–band contours. The V–band contours are at (25.9, 25.0, 24.0, 23.3, 22.8) mag arcsec^{-2}. The plus represents the V–band and the kinematic centre of the galaxy.

been confirmed in the V–band (Hunter & Elmegreen, 2006). We come back to this in the following section.

In the case of DDO 168, the H I distribution is fairly symmetrical with respect to the optical images. Whereas the optical data suggest an inclined disk, where old stars and new stars coexist, the central neutral gas traced by the H I maps is obviously misaligned with respect to the optical disk. Furthermore, another peculiarity of this system is a higher velocity dispersion compared to DDO 133. The velocity dispersion is at its maximum (15 km s^{-1}) in the southwest part of the galaxy as indicated in the velocity dispersion map (see bottom right panel of Fig. 3.9). The higher velocity dispersion region spreads out over two different regimes: one described as dense H I correlated with emission peaks in optical bands and the second characterised by low density gas and stars. A similar feature was also found in another dwarf galaxy, NGC 2366 (Hunter et al., 2001a).

Although not coincident, the densest H I region in the centre of the galaxy is also where the Hα and FUV emissions peak (see Fig. 3.8), indicating recent SF in that area.

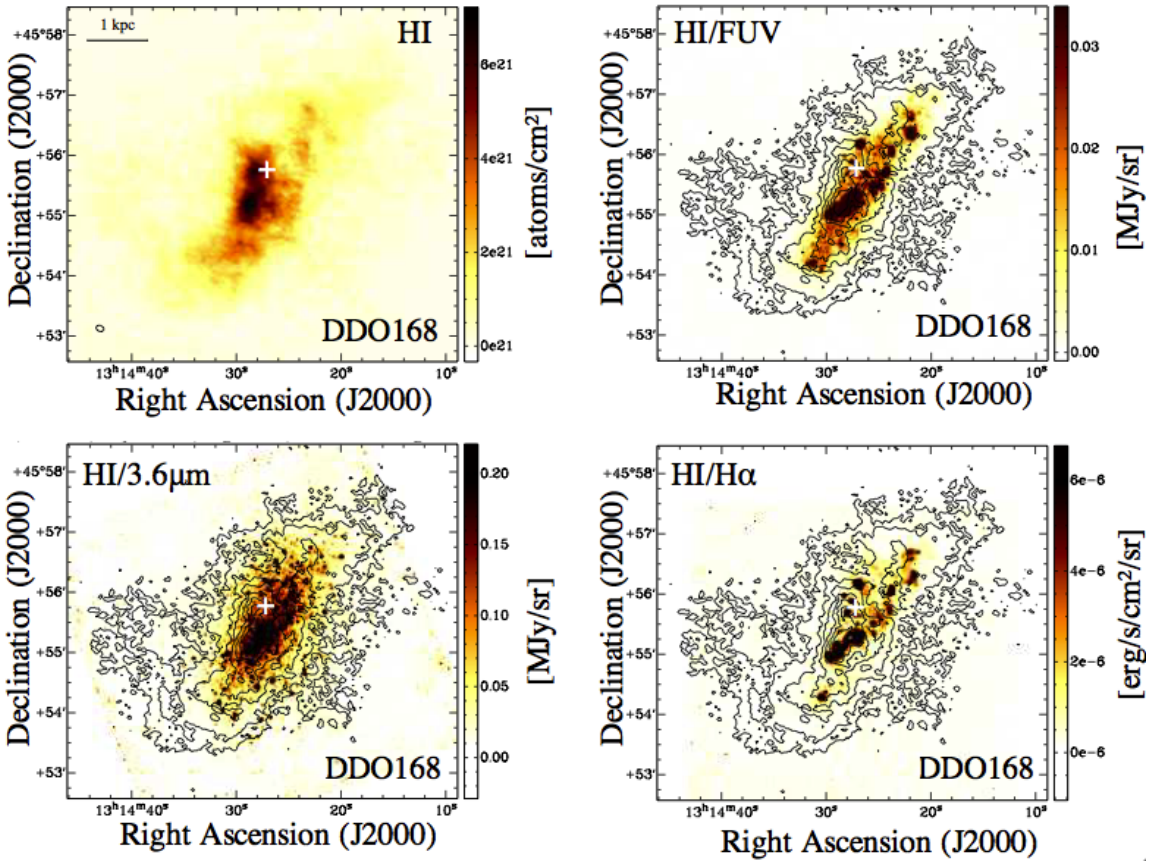

Figure 3.8: Surface density maps for DDO 168. *Top Left*: Integrated H I map (resolution: $7\farcs8 \times 5\farcs8$, lowest confidence level (2.5σ over 3 channels): 2.4×10^{20} atoms cm^{-2}, colour scale: 0 - 6×10^{21} atoms cm^{-2}). *Top Right*: H I contours overlaid on the FUV image (colour scale: 0 - 3×10^{-2} MJy sr^{-1}). *Bottom Left*: H I contours overlaid on the *Spitzer* 3.6 μm image (colour scale: 0 - 0.2 MJy sr^{-1}). *Bottom Right*: H I contours overlaid on the Hα map (colour scale: 0 - 6×10^{-6} ergs s^{-1} cm^{-2} sr^{-1}). The H I contours are at (0.35, 0.5, 1, 2, 4, 6)$\times 10^{21}$ atoms cm^{-2}. In all panels the plus represents the kinematic and the V–band centre of the galaxy. The H I map beam size is indicated in the bottom left corner of the top left panel.

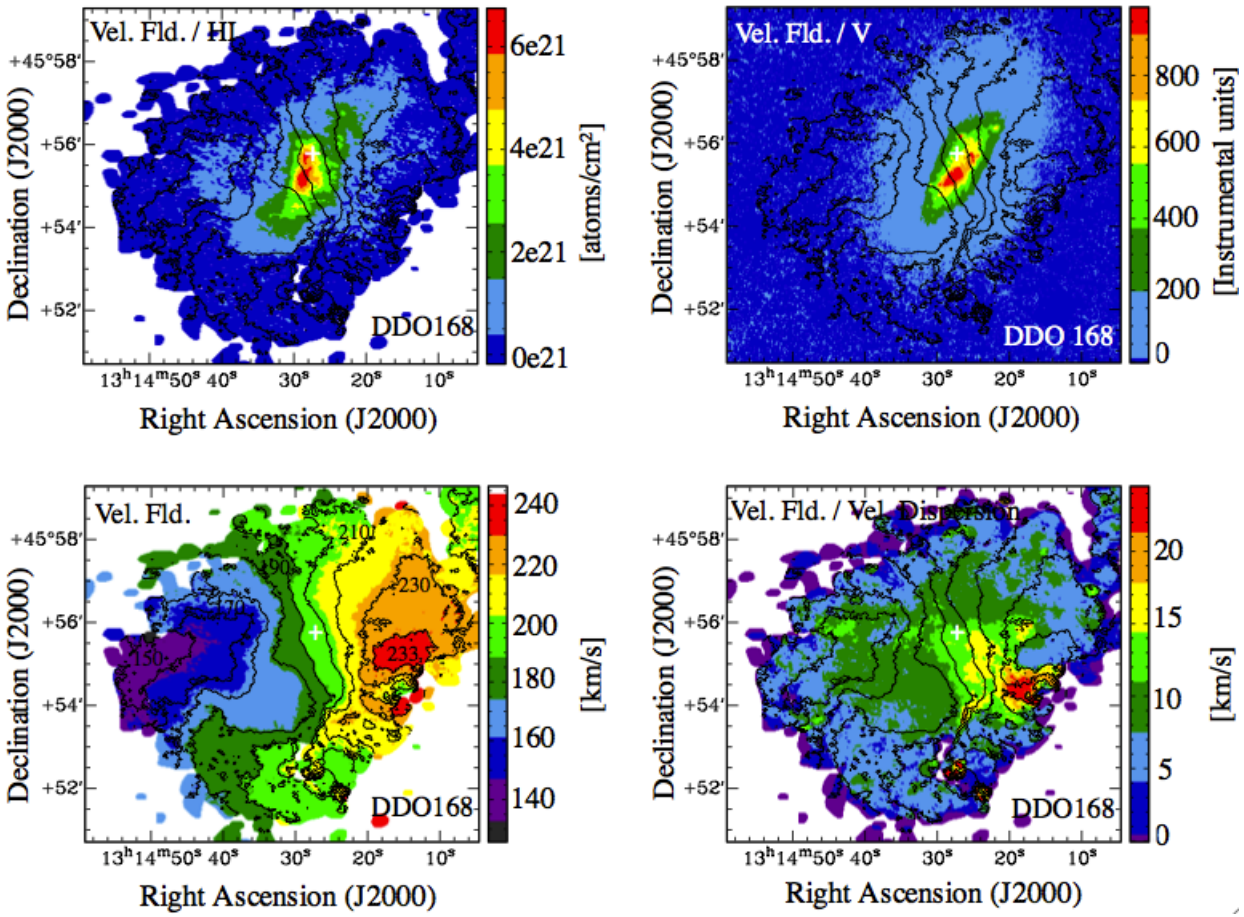

Figure 3.9: Moment maps for DDO 168. *Top Left*: Integrated H I map (moment 0) with velocity field contours. *Top Right*: velocity field contours overlaid on the V–band optical image (colour scale: 0 - 800 instrumental units). *Bottom Left*: Contoured Velocity Field (colour scale: 150 - 250 km s^{-1}). *Bottom Right*: Velocity contours overlaid on the velocity dispersion map (colour scale: 0 - 25 km s^{-1}). The velocity field contours are at (150, 170, 180, 190, 200, 210, 220, 230, 233) km s^{-1}. In all panels the plus represents the kinematic and the V–band centre of the galaxy.

3.1.4 Kinematical Study of DDO 133 and DDO 168

Our SF analysis requires knowing the inclination of a galaxy. We derive this from their H I kinematics. We first extract the velocity fields of the galaxies from the natural–weighted cubes, using various methods for determining the bulk motion of the gas at each spatial pixel: the intensity–weighted mean (IWM), fitting the intensity-velocity profile with a single Gaussian, and fitting the profile with a hermite h_3 function. Compared to the other types of velocity field determinations, the hermite h_3 velocity field using a Gauss–Hermite polynomial is able to model the skewness of a non–Gaussian velocity profile that is usually caused by multiple velocity components (van der Marel & Franx, 1993). For this reason, the velocity field determined using hermite h_3 fits to the velocity profiles was adopted as the standard method for the kinematic analyses of the THINGS galaxies sample (de Blok et al., 2008). We refer to Oh et al. (2011a, 2008) for more details and discussions.

The iso–velocity contours of the velocity fields (see Fig. 3.5 and Fig. 3.9) are distorted in some regions, which indicates the presence of non–circular motions in the galaxies. In general the small–scale distortions are mainly due to supernova–driven gas outflows or stellar winds in star–forming regions (Oh et al., 2011b). However, despite the distorted velocity fields, the circular rotation of the galaxies dominates the non–circular motions as shown by the overall rotation pattern in the velocity fields.

We derive the rotation curves of DDO 133 and DDO 168 by fitting a set of concentric tilted–rings to the hermite h_3 velocity fields of the galaxies, by means of the task ROTCUR in GIPSY (Begeman, 1989). Each tilted–ring is characterised by six ring parameters: kinematic center (XPOS, YPOS), inclination INCL, position angle PA, systemic velocity VSYS, and rotation velocity VROT (Begeman, 1989). PA is measured counter–clockwise from the major axis of the receding half of a galaxy.

We derive the rotation curves of DDO 133 and DDO 168 as shown in the lower panels of Fig. 3.10 and Fig. 3.11. In the top two rows of both Fig. 3.10 and 3.11, the solid lines indicate the derived tilted–ring parameters that best describe the velocity fields. In addition, for reference, we also show the results (open circles) derived keeping all ring parameters free.

The resulting rotation velocities show a typical behavior: linearly increasing in the inner regions (solid–body) and flattening in the outer regions. The maximum rotation velocities of DDO 133 and DDO 168 are $\sim$40 km s^{-1} at a radius of $\sim$4.0 kpc and $\sim$50 km s^{-1} at a radius of $\sim$2.5 kpc, respectively. In general, the shape of the

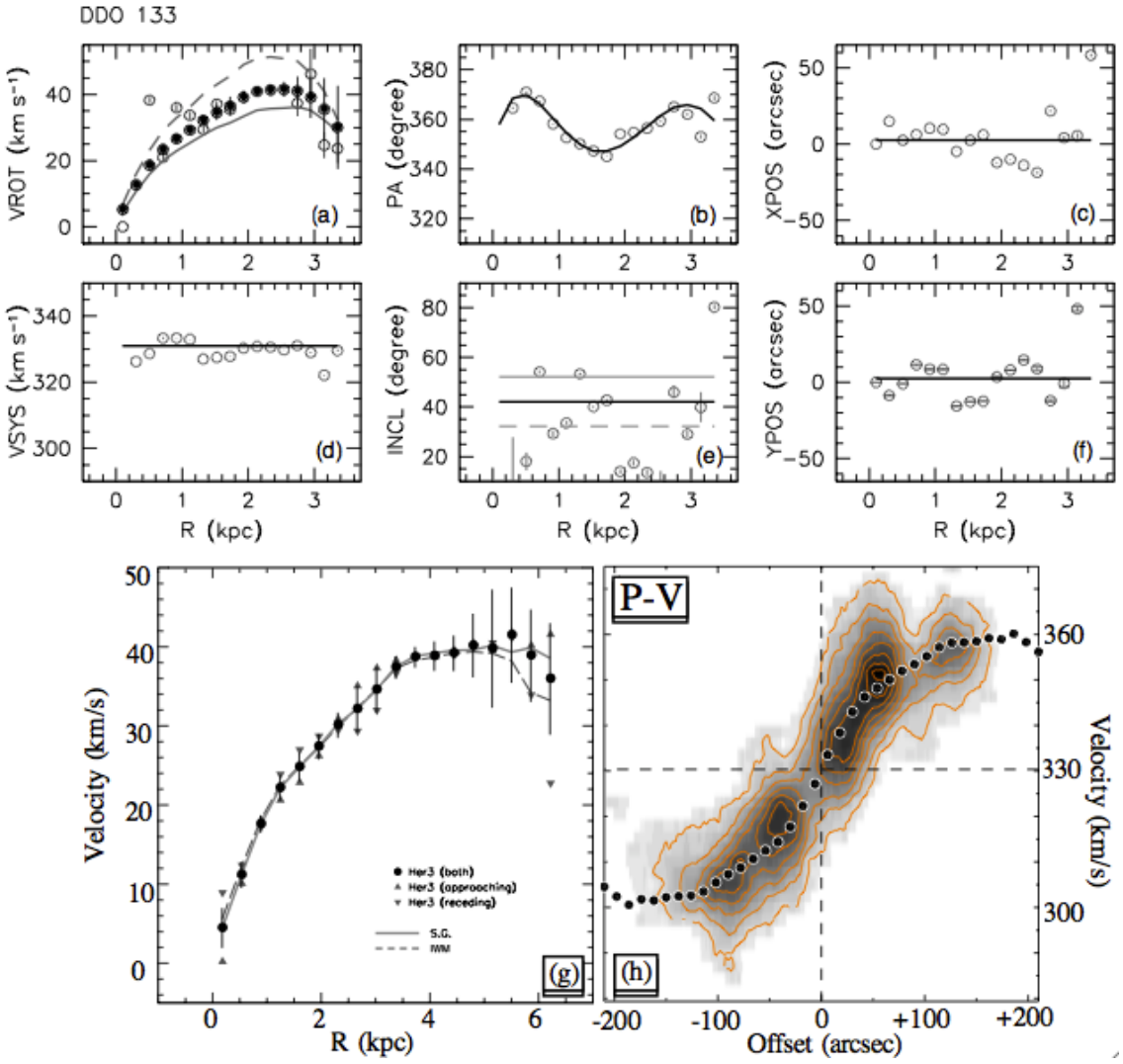

Figure 3.10: Tilted–ring fit for DDO 133: (a) Rotational velocity (the grey curves indicate rotation curves derived by using variations in inclination of $+10°$ – the solid grey line and $-10°$ – the dashed grey line), (b) Position angle, (c) Position offset of the kinematic centre on the X axis with respect to the X coordinate of the GIPSY centre of the map, (d) Systemic velocity, (e) Inclination (the horizontal lines indicate variations in inclination by $+10°$ – the solid grey line and $-10°$ – the dashed grey line), (f) Position offset of the kinematic centre on the Y axis with respect to the Y coordinate of the GIPSY centre of the map, (g) Rotation curve fitting and (h) – Rotation curve over-plotted on the position–velocity diagram taken along the kinematical major axis. The black solid lines in panels (b)–(f) represent the tilted–ring parameters that best describe the velocity fields considered. Open circles trace the results derived from keeping all parameters free. In panel (g) we show three rotation curves derived using the different velocity fields: IWM (dashed grey line), single Gaussian function (continuous grey line) and Gauss–Hermite h_3 polynomial (black filled circles).

rotation curves resembles those of THINGS dwarf galaxies with near–solid–body rotation in Oh et al. (2011a). As discussed in Bureau & Carignan (2002), a correction for asymmetric drift is required for galaxies whose velocity dispersions are significant compared to their maximum rotation velocities. However, as shown in Fig. 3.5 and Fig. 3.9, the velocity dispersion maps of DDO 133 and DDO 168 show globally small velocity dispersions ($\sim$7 km s^{-1}) compared to their maximum rotation velocities ($\sim$40 km s^{-1} and $\sim$50 km s^{-1}), respectively. This implies that the pressure support in the disk is insignificant with respect to their circular rotation. And since we explore the kinematics mainly for estimating the inclination, we therefore apply no asymmetric drift corrections for DDO 133 and DDO 168.

Although most ring parameters are well constrained, the inclination of DDO 133 shows a large scatter as a function of radius. We therefore examine the sensitivity of the rotation curves to the exact value of the inclination by varying the inclination by $+10°$ and $-10°$ as shown in panel (e) of Fig. 3.10. The rotation curves derived using these inclinations while keeping other ring parameters the same are indicated by the grey solid (for 10°inclination) and dashed (for $-10°$ inclination) lines in Fig. 3.10(a). Despite large variations of the inclinations, the deviations of the resulting rotation velocities are insignificant ($\sim$5 km s^{-1}) with respect to the ones with the best–fit inclinations (i.e., black dots in the VROT panels of Fig. 3.10).

Applying the same ring parameters derived using the hermite h_3 velocity fields to the IWM and single Gaussian fit velocity fields, we also derive the IWM and single Gaussian fit rotation curves of the galaxies and compare them with the hermite h_3 rotation curves. As shown in Fig. 3.10(g) of DDO 133, the rotation curves derived using the different velocity fields agree well within the uncertainties, suggesting that small–scale random non–circular motions in the galaxies are insignificant.

When taking a closer look at the velocity field of DDO 133 one notices twisted iso–velocity contours which can be associated with the region hosting a bar according to V–band studies (Hunter & Elmegreen, 2006) although some velocity twists can also be connected to the position of the H I holes in the neutral gas distribution map (see top left panel in Fig. 3.5). There is not enough kinematical evidence to confirm any effect of the bar on the H I gas kinematics.

In DDO 168, the derived PA shows a gradual decrease towards the outer regions (see Fig. 3.11(b)) and this might be due to the presence of a mild bar. The evidence of a bar in the gas kinematics is related to non-circular motions associated with large scale symmetric deviations, where there is a major axis change in the inner parts

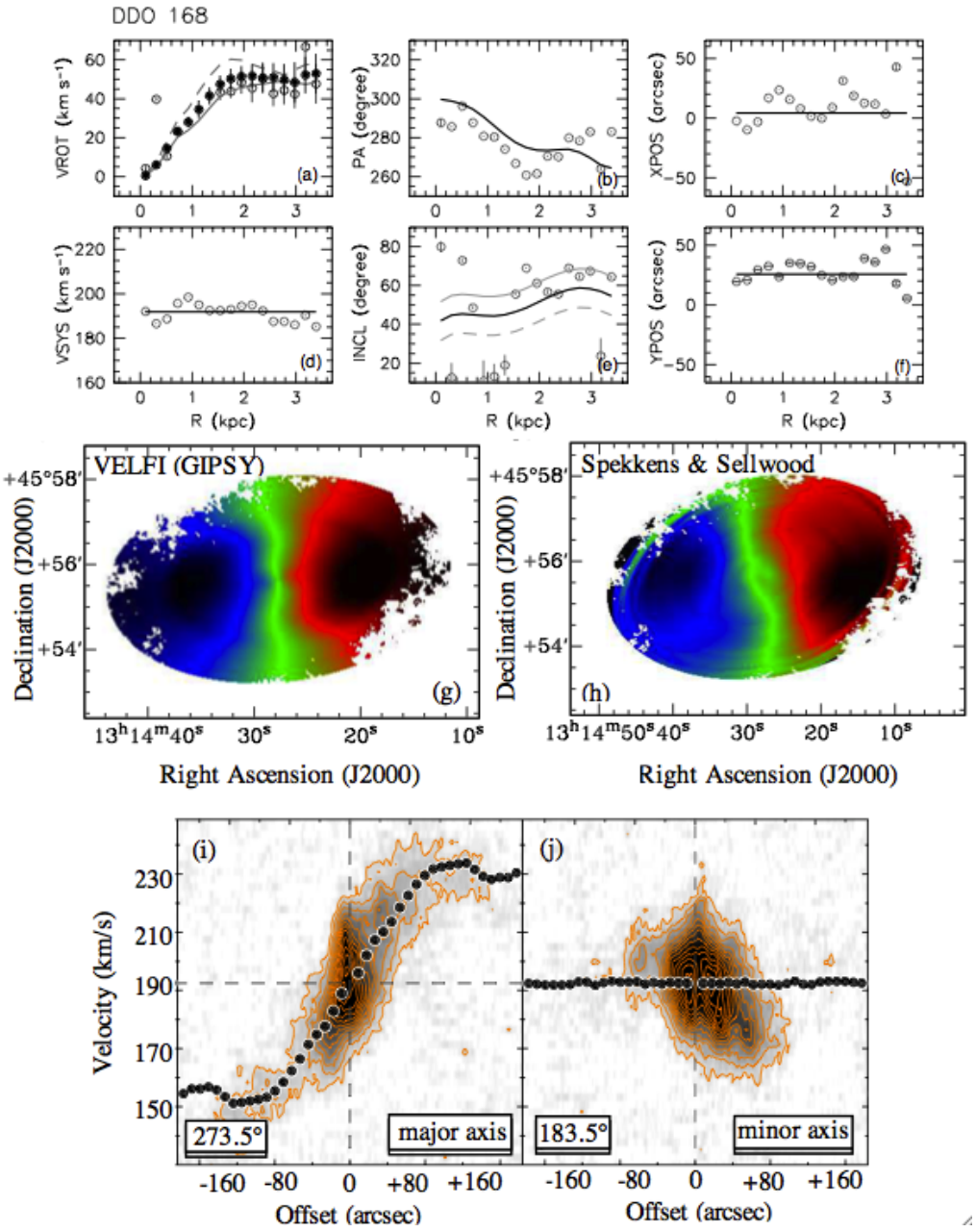

Figure 3.11: Tilted–ring fit for DDO 168: (a) Rotational velocity (the grey curves indicate rotation curves derived by using variations in inclination of $+10°$ – the solid grey line and $-10°$ – the dashed grey line), (b) Position angle, (c) Position offset of the kinematic centre on the X axis with respect to the X coordinate of the GIPSY centre of the map, (d) Systemic velocity, (e) Inclination (the horizontal lines indicate variations in inclination by $+10°$ –the solid grey line and $-10°$ – the dashed grey line), (f) Position offset of the kinematic centre on the Y axis with respect to the Y coordinate of the GIPSY centre of the map, (g) Standard VELFI (GIPSY) model velocity field, (h) Spekkens & Sellwood (2007) VELFIT model velocity field, (i) Rotation curve derived from the Gauss–Hermite h_3 polynomial velocity field over-plotted on the position–velocity diagram along the kinematical major axis, and (j) expected velocities over-plotted on the position–velocity diagram along the kinematical minor axis.

(Bosma, 1978, 1981). Such a major axis change will manifest itself in a position angle change with radius, misalignments of the major axis with other structures seen in the optical and non orthogonality of the major axis relative to the minor axis (Bosma, 1981, 1996).

A bar feature in a dwarf galaxy is not uncommon. However bars are difficult to identify in irregular galaxies (Hunter & Elmegreen, 2006), and even more so when taking in account that, for these kind of galaxies, the bar may be offset to one side, as in the LMC (de Vaucouleurs & Freeman, 1972). In addition, the optical and gas kinematics may not give a consistent story, like the case of DDO 133 above and the case of NGC 2366 where the optical morphology suggest the presence of a bar, yet the the H I observations do not provide strong support for its existence (Hunter et al., 2001a). Alternatively, a bar seen end-on could be present but hidden in regular kinematics, as in the center of NGC 6503 (Kuzio de Naray et al., 2012).

Besides the PA change with radius mentioned earlier, DDO 168 clearly exhibits also a misalignment between the brightest emission in the optical and the radio data (see Fig. 3.8). Looking at Fig. 3.9, one immediately sees that the kinematical major and minor axes are non–orthogonal, a sign of non-circular motions due to a bar potential. In order to examine kinematically the possibility of the bar, we fit a flat disk model which includes a bar–like potential with a different PA but with the same inclination as the fit to the data. Using VELFIT, a code developed by Spekkens & Sellwood (2007) for modelling non-circular motions in disk galaxy velocity fields, we fit such a disk model to the hermite h_3 velocity field of DDO 168. The best fit of the model (see Fig. 3.11(h)) describes the disk of DDO 168 as a combination of a flat disk and a bar with the same inclination of $53\overset{\circ}{.}4$ as our original fit to the data, but different PAs of 261°and 327°, respectively. The best fit model fits the data well and supports the idea that DDO 168 is better described by a model with a bar–like potential. As shown in panels (g) and (h) of Fig. 3.11, the best–fit bisymmetric model for DDO 168 shows considerable amounts of m = 2 perturbations that induce a larger ($\sim 10\,\mathrm{km\,s^{-1}}$) circular rotation velocity of the disk than that of the tilted–ring model. When inspecting the position–velocity diagram (PVD) along the major axis (see Fig. 3.11(i)) we find H I gas that deviates from the fitted rotational velocity, gas that we ascribe to the bar. The PVD along the minor axis (see Fig. 3.11(j)) shows that the minor axis derived from the tilted ring model deviates appreciably from the kinematical minor axis, fact consistent with the bar scenario. More details on the kinematics of DDO 168 can be found in Oh et al. (2015).

3.2 Star Formation Analysis

At this stage we have all the necessary data to investigate the relation between star formation rate surface density (SFRD) and H I surface density.

We can only speak of a SF law as long as we do not resolve individual star forming structures, but each galaxy region we are considering is large enough to contain more than one phase of the star forming cycle (Becerra & Escala, 2014; Onodera et al., 2010; Schruba et al., 2010). The working linear resolution we chose is 400 pc. This resolution takes into account the small size of dwarf galaxies, ensuring enough independent regions to be studied without reaching the anti–correlation scale where we find Giant Molecular Clouds (GMC) and no SF activity or SF regions and no GMCs. This resolution also allows a comparison to be made between the two galaxies presented here and with results in the literature. Both the FUV and the Hα maps have been corrected for foreground extinction using the Cardelli et al. (1989) extinction law and the Schlegel et al. (1998) colour index values. All plotted data are corrected for inclination given in Table 3.2.

We begin this section with a summary of commonly used star formation tracers, describing what arguments and formulae have been employed in obtaining the SFRD maps (see Section 3.2.1). Then we discuss how considerations regarding internal extinction (see Section 3.2.2) affect our SF plots. In Section 3.2.3 we compare the performance of the different tracers considered in the environment of the two chosen dwarfs and present some preliminary results. We describe their systematic effects in Section 3.2.4 where we explain in some detail the effects of inclination uncertainties on our results (see Section 3.2.4.1) and the effect of resolution on the SF plots (see Section 3.2.4.2).

3.2.1 SF Tracers

The traditional star formation tracer is Hα, which is directly proportional to current massive SF. The Hα emission traces massive, ionising stars, mainly grouped in OB associations. The conversion from Hα fluxes to SFRs was initially given by Kennicutt (1983, 1988). Later, Kennicutt (1998) improved on this relation and recently, Calzetti et al. (2007) reconsidered the IMF and the stellar population assumptions (model of a 100 Myr constant SFR versus the infinite age case assumed

by Kennicutt, 1998) and converged on the following relation:

$$\mathrm{SFR}[\mathrm{M}_\odot\,\mathrm{yr}^{-1}] = 5.3 \times 10^{-42}\, L^*_{H\alpha}[\mathrm{erg\ s}^{-1}] \tag{3.1}$$

where $L^*_{H\alpha}$ is the extinction corrected Hα luminosity. Throughout this section the asterisk denotes that the luminosity or the flux has been corrected for internal extinction.

Eq. 3.1 can be converted to SFRD as follows:

$$\Sigma_{\mathrm{SFR}}[\mathrm{M}_\odot\,\mathrm{yr}^{-1}\mathrm{kpc}^{-2}] = 6.34 \times 10^2\, I^*_{H\alpha}[\mathrm{erg\ s}^{-1}\ \mathrm{cm}^{-2}\ \mathrm{sr}^{-1}] \tag{3.2}$$

where $I^*_{H\alpha}$ is the extinction corrected flux density of the Hα emission.

The Hα emission however is to some extent affected by internal extinction. Internal extinction, even in nearby galaxies, cannot be measured directly. Thus, estimates on internal extinction are based on measurements inside the Milky Way and more recently in the LMC and SMC (Gordon et al., 2003). A way around this problem is by using dust measurements to estimate the obscured emission fraction. The dust heated by hot, massive stars emits at mid–infrared wavelengths such as that being observed by Spitzer at 24 μm and 8 μm. Whereas the 8 μm emission is sensitive to metallicity and star formation history, the 24 μm (in the absence of an AGN) is less affected by metallicity and the contribution of non–ionizing regions, and can be used in combination with Hα to account for the dust obscured emission (Kennicutt et al., 2007). Calzetti et al. (2007) find a correlation between extinction–corrected Paα and 24 μm emission which they used to correct Hα for dust extinction according to:

$$\mathrm{SFR}[\mathrm{M}_\odot\,\mathrm{yr}^{-1}] = 5.3 \times 10^{-42}\,(L_{H\alpha}[\mathrm{erg\,s}^{-1}] + (0.031 \pm 0.006)\, L_{24\,\mu m}[\mathrm{erg\,s}^{-1}]) \tag{3.3}$$

Again expressed in units of surface density, this can be written as:

$$\Sigma_{\mathrm{SFR}}[\mathrm{M}_\odot\mathrm{yr}^{-1}\,\mathrm{kpc}^{-2}] = 6.34{\times}10^2\, I_{H\alpha}[\mathrm{erg\,s}^{-1}\,\mathrm{cm}^{-2}\,\mathrm{sr}^{-1}]{+}0.246{\times}10^{-2}\, I_{24\,\mu m}[\mathrm{MJy\,sr}^{-1}] \tag{3.4}$$

Salim et al. (2007), using a sample of 50 000 optically selected galaxies in the local universe ranging from gas–rich dwarfs to massive ellipticals, find that for the star forming galaxies the SFRs obtained from UV–observations agree well with those obtained from measuring the Hα emission lines. Therefore Salim et al. propose a

SF tracer based on the FUV emission, which operates on a timescale of 100 Myr and directly probes the contribution of young, massive stars. Unfortunately, the FUV emission is heavily affected by internal extinction, but as long as one is able to correct for that, the FUV is a better SF tracer than Hα in the sense that it can probe further out radially in the galaxy than Hα (Meurer et al., 2004). Salim et al. empirically infer the conversion factor for a Salpeter IMF from stellar population modeling to the obscured SED of their galaxy sample combined with a transformation between Chabrier and Salpeter IMFs based on the Bruzual & Charlot (2003) models and find:

$$\mathrm{SFR}[\mathrm{M}_\odot\,\mathrm{yr}^{-1}] = 1.08 \times 10^{-28}\, L^*_{FUV}[\mathrm{erg\,s^{-1}\,Hz^{-1}}] \tag{3.5}$$

where L^*_{FUV} represents the dust–corrected FUV luminosity. Expressed in terms of surface density this becomes:

$$\Sigma_{\mathrm{SFR}}[\mathrm{M}_\odot\,\mathrm{yr}^{-1}\,\mathrm{kpc}^{-2}] = 8.1 \times 10^{-2}\, I^*_{FUV}[\mathrm{MJy\,sr^{-1}}] \tag{3.6}$$

where I^*_{FUV} is the extinction corrected FUV intensity.

Both Eq. 3.6 and Eq. 3.7 are derived based on the Salim et al. (2007) empirically inferred conversion factor which in turn implies a certain above mentioned assumption regarding the IMF, an assumption we carry on with also in this thesis.

Leroy et al. (2008) try to overcome the effect extinction has on the FUV emission by using 24 μm to infer the dust obscured component, in the same manner as Calzetti et al. (2007) had done for the Hα SFR calibration. They use the Salim et al. (2007) result, and take Eq. 3.6 as the unobscured FUV emission component and calibrate the second term which accounts for the dust obscured emission in two ways: by extrapolation from the term derived for Hα by Calzetti et al. and through direct estimates from comparing total SFR with FUV emission. They find:

$$\Sigma_{\mathrm{SFR}}[\mathrm{M}_\odot\,\mathrm{yr}^{-1}\,\mathrm{kpc}^{-2}] = 8.1\times10^{-2}\, I_{FUV}[\mathrm{MJy\,sr^{-1}}]+3.2\times10^{-3}\, I_{24\,\mu m}[\mathrm{MJy\,sr^{-1}}] \tag{3.7}$$

3.2.2 Internal Extinction

The above mentioned formulae are well established in spiral galaxies. However as we move to the lower metallicity regime the 24 μm emission becomes weaker, reflecting a lower dust content, and the FUV+24 μm and Hα+24 μm SF tracers become dominated by the noise in the 24 μm maps.

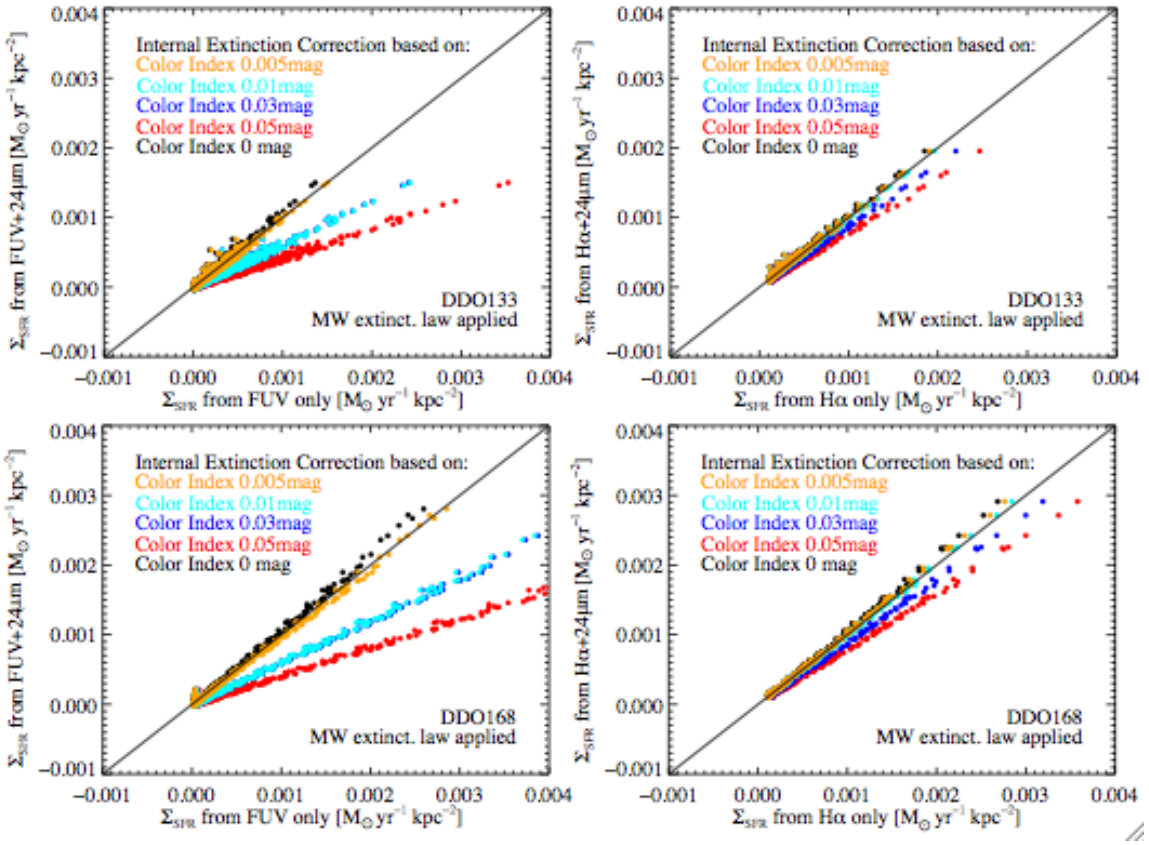

Figure 3.12: DDO 133 (top) and DDO 168 (bottom), we present SFRD derived from FUV+24 μm vs. SFRD based on FUV only (left) and SFRD from Hα+24 μm vs SFRD based on Hα (right). Different colours represent internal extinction corrections of different colour index E($B-V$) numbers: 0.05 mag (red), 0.03 mag (blue), 0.01 mag (cyan), 0.005 mag (orange) and 0 mag (black). The MW extinction law is assumed. The black continuous line represents a 1:1 relation between the x and y axis.

Hunter & Hoffman (1999) measured the Balmer decrement in H_2 regions in a sample of 39 dwarf irregular galaxies and find that the internal reddening correction in these regions is of the order of 0.1 mag. They take half of this value to represent the reddening of the stars, thus an internal extinction colour index of 0.05 mag.

If we adopt the Milky Way extinction law with $A_{H\alpha}$=2.5E($B-V$) from Cardelli et al. (1989) and A_{FUV}=8.24E($B-V$) from Wyder et al. (2007), the contribution to the SFRD of the internal extinction correction we apply to the FUV and Hα maps to account for the obscured emission should be equal to the contribution to the SFRD of the 24 μm emission we have measured. On this principle, in Fig. 3.12 we plot for both DDO 133 (top) and DDO 168 (bottom), SFRD based on FUV

only points against SFRD based on FUV+24 μm (left) and SFRD based on Hα only points against SFRD based on Hα+24 μm (left), using the formulae in the previous section, each colour representing a different internal extinction correction applied based on different colour index values. In red we represent the internal extinction colour index E($B-V$) of 0.05 mag used in the literature for dwarfs. The black continuous line marks a 1:1 relation between the two plotted quantities. The points with no internal extinction correction applied, in black, lie slightly above the continuous line, indicating that the 24 μm contribution to the SFRD map is minimal and that internal extinction is low. In this way we find that the best agreement with the 24 μm emission is obtained for internal FUV and Hα extinction corrections at the 1% level, both 10 times lower than the internal reddening correction given by Hunter & Hoffman (1999).

However, recent studies (Gordon & Clayton, 1998; Gordon et al., 2003) have shown that the extinction in metal poor environments such as the LMC and SMC is different from that found in the Milky Way. Within the LMC, the reddening parameter $R_V = A_V/E(B-V)$ varies by 25% between the LMC average and the LMC2 supershell (Gordon et al., 2003). In the metal poor SMC, Gordon & Clayton (1998), have shown that the UV extinction curves in the actively star forming bar are linear with wavelength, rising more steeply than in the Milky Way. Since the choice of UV extinction laws is limited at the moment to either Milky Way or SMC extinction law, we did also test the effect applying the SMC extinction law would have on our analysis and found it to be small. And since the small dust contribution we found in our two dwarf galaxies does not confirm the need for a more radical UV extinction law, we chose in the end to rely on the Milky Way extinction law and to apply no internal extinction correction to our data.

3.2.3 The Relation Between Neutral Gas and Star Formation

In our SF analysis we take a spatially resolved approach and use a diverse set of multi–wavelength data. We adopted the 400 pc linear resolution. Our approach follows closely the Bigiel et al. (2008) and Leroy et al. (2008) working method, including the use of the same sampling method (hexagonal spacing).

Prior to the analysis we prepare our maps to ensure they have the proper physical units, they are aligned and are at the same resolution. We use the H I data as a

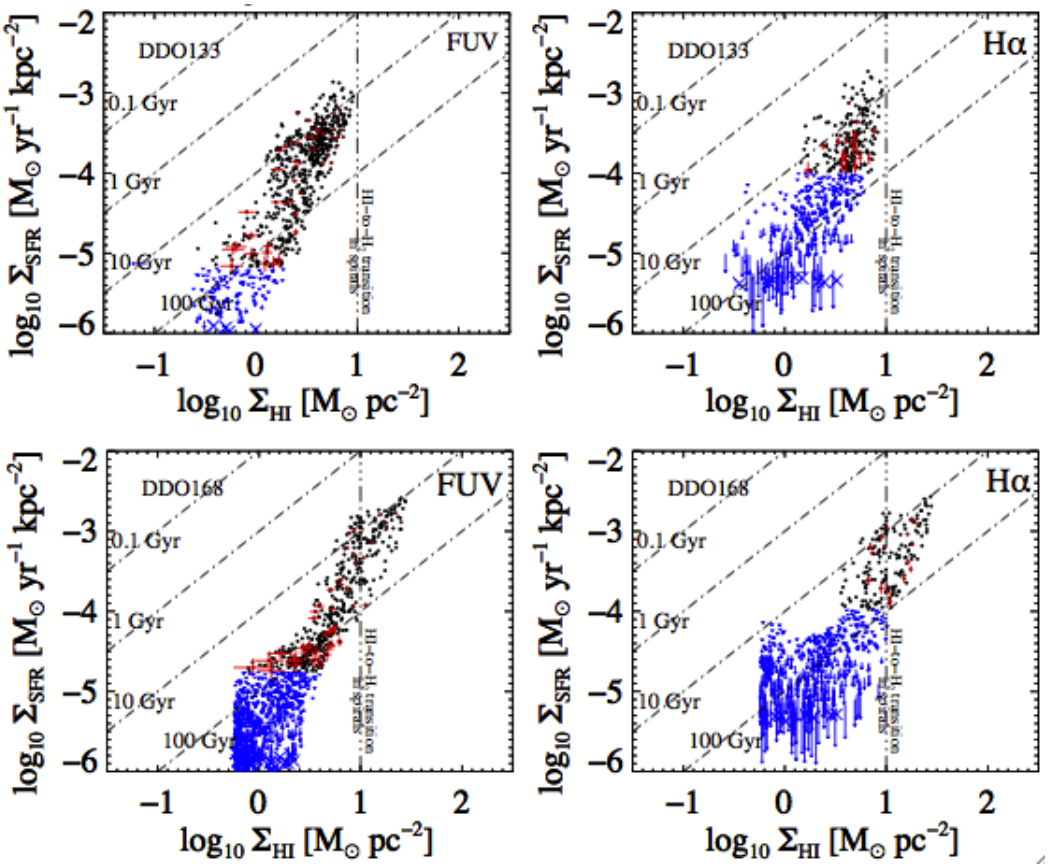

Figure 3.13: SFRD derived from FUV only (left) and Hα only (right) vs. H I surface density for DDO 133 (top) and DDO 168 (bottom). All points are independent and above a 5σ cutoff level in SFR. In red we display error bars for every 10$^{\text{th}}$ point in the plot. With blue arrows we represent the upper limits. The vertical dashed line represents an H I surface density of 10 $M_\odot$ pc^{-2}. The four diagonal dashed lines represent constant depletion times of 0.1 Gyr, 1 Gyr, 10 Gyr, and 100 Gyr.

reference for the alignment and convolution, because the H I data have the lowest resolution among the considered wavelengths. The H I maps have resolutions of 12.″5 for DDO 133 and 8″ for DDO 168 while the 24 μm maps have 6″, FUV maps have 4″ and the optical and near-IR data are all better than 3.″5.

In all our SF plots we use a sensitivity cutoff as follows: 5σ in SFRD maps, 3σ in 3.6 μm images, 2σ in V–band and 2σ in H I. The sensitivity cutoffs are chosen to ensure that only scientifically meaningful data points are considered. The σ in H I represents the σ of the H I distribution map (moment 0 map) which is estimated as 2.5 (the level used in the blanking stage) times the H I data cube σ at full resolution (given in Table 2.4) taking into account the fact that the moment 0 map is an

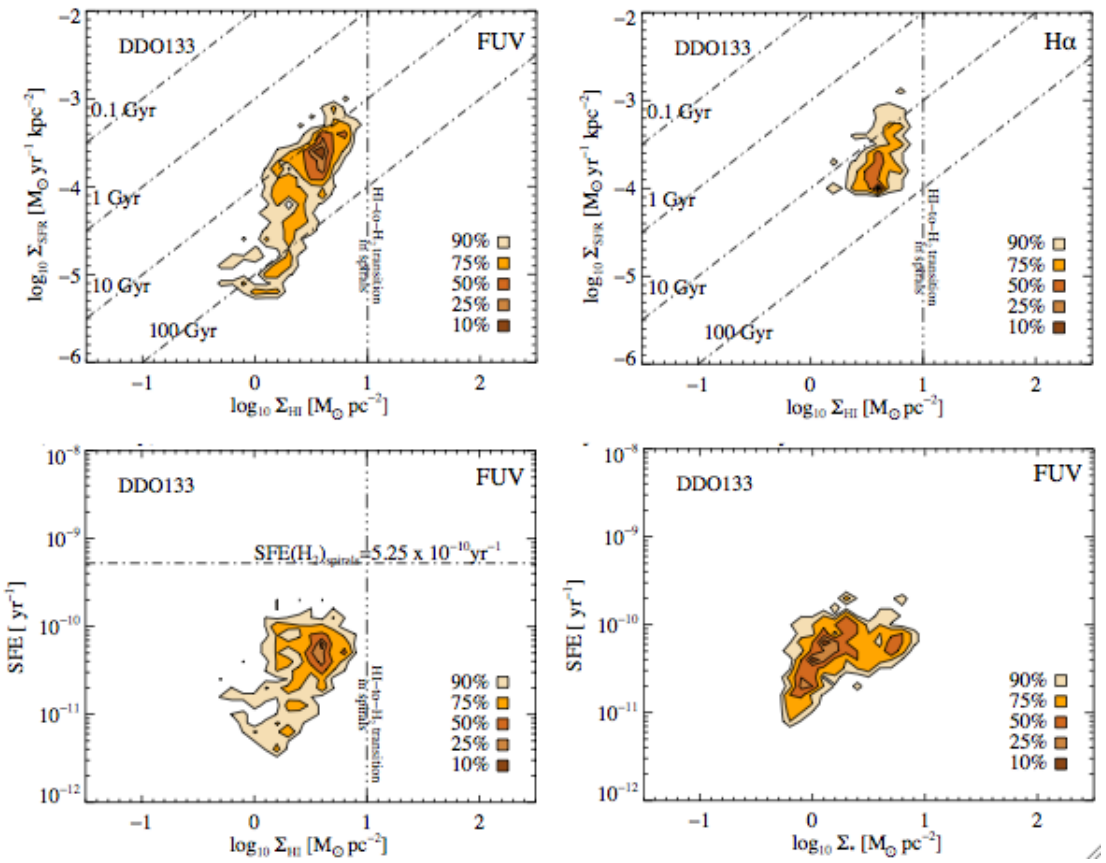

Figure 3.14: DDO 133. Density contours at 10%, 25%, 50%, 75% and 90% of the pixel by pixel distribution of: SFRD surface vs. H I surface density plotted separately for two different SF tracers FUV (top left) and Hα (top right) and SFE vs. H I surface density (bottom left) and vs. stellar surface density (based on the 3.6 μm *Spitzer* map) for FUV as an SF tracer (bottom right). All maps used for the above plots have the same linear resolution of 400 pc. All data points used are independent and above a 5σ cutoff level in SFR. The vertical dashed line represents an H I surface density of 10 $M_\odot$ pc^{-2}. The horizontal dashed line represents a constant molecular gas SFE of 5.25×10^{-10} yr^{-1}. The four diagonal dashed lines in the top row represent gas constant depletion times of 0.1 Gyr, 1 Gyr, 10 Gyr, and 100 Gyr.

integration over all frequency channels of the data cube. The σ in SFRDs, 3.6 μm and V–band are measured using Gaussian statistics on the grounds that when working with conservative cutoffs such as we are here the Gaussian and Poissonian statistics agree.

As explained in Section 3.2.2 we chose to work with the FUV–only and the Hα–only SF tracers. In Fig. 3.13, the panels display SFRD vs. H I surface density for both DDO 133 (top panels) and DDO 168 (bottom panels), where the SFRD is

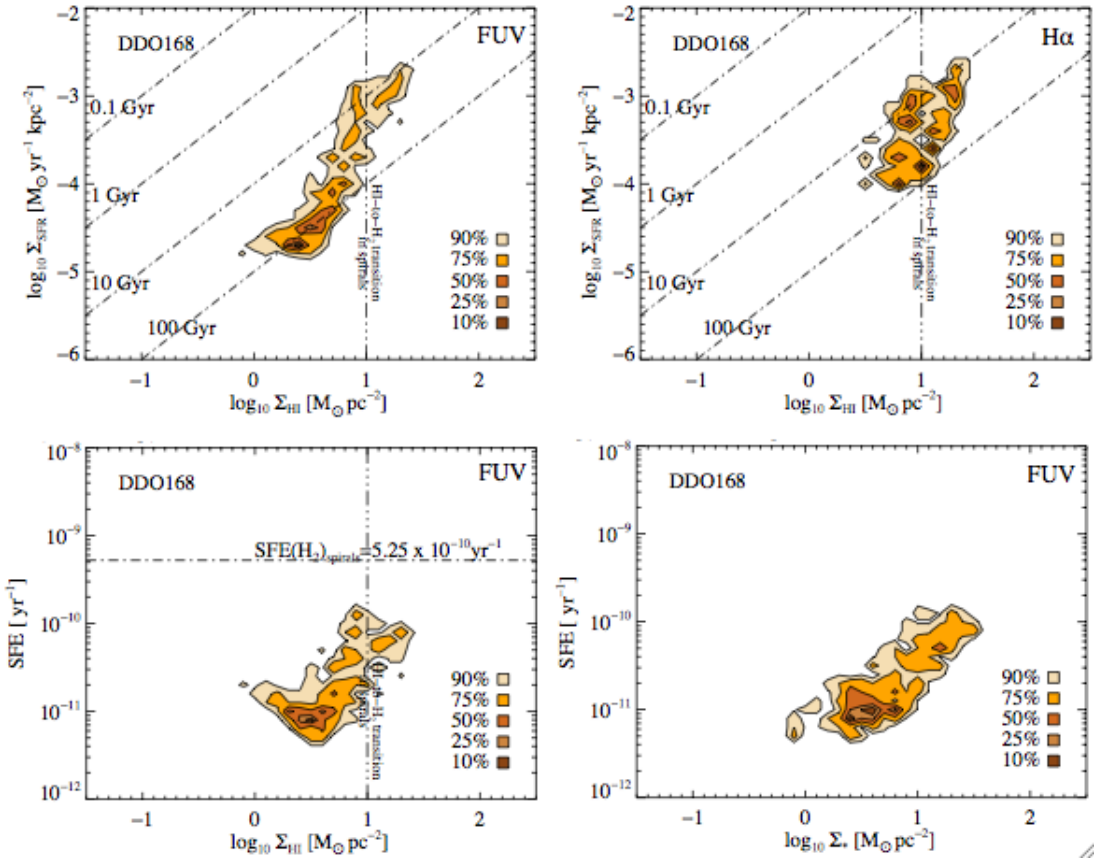

Figure 3.15: DDO 168. Density contours at 10%, 25%, 50%, 75% and 90% of the pixel by pixel distribution of: SFRD vs. H I surface density plotted separately for two different SF tracers FUV (top left) and Hα (top right) and SFE vs. H I surface density (bottom left) and vs stellar surface density (based on the 3.6 μm *Spitzer* map) for FUV as an SF tracer (bottom right). All maps used for the above plots have the same linear resolution of 400 pc. All points are independent and above a 5σ cutoff level in SFR. The vertical dashed line represents an H I surface density of 10 $M_{\odot}$ pc^{-2}. The horizontal dashed line represents a constant molecular gas SFE of 5.25×10^{-10} yr^{-1}. The four diagonal dashed lines in the top row represent constant gas depletion times of 0.1 Gyr, 1 Gyr, 10 Gyr, and 100 Gyr.

derived from two different tracers, FUV–only (left) and Hα–only (right). As we can see in Fig. 3.13, the two chosen tracers agree well with each other in both galaxies. This agreement is expected since we are measuring the same quantity, the SFR, by involving two independent methods each tracing different timescales: Hα 10 Myrs, FUV 100-200 Myrs. The FUV–only tracer has good signal–to–noise which allows us to probe not only the higher end of the SF law but also the lower density regions (Lee et al., 2009). The Hα–only tracer, although only sampling the higher end of

the SF law, is used for comparison.

The top panels in Figs. 3.14 and 3.15 show SFRD vs. H I surface density, where the SFRD is derived from two different tracers, FUV–only (top left) and Hα–only (top right). We plot as a reference four dashed diagonal lines representing gas depletion times[1] of 0.1 Gyr, 1 Gyr, 10 Gyr, and 100 Gyr. The vertical dashed line indicates the H I threshold of 10 $M_{\odot}$ pc^{-2} beyond which the neutral gas turns molecular in solar metallicity galaxies (Bigiel et al., 2008). In all panels we plot density contours, representing 10%, 25%, 50%, 75% and 90% levels of the peak density of points as the colour coding used gets lighter in tone.

Both galaxies show an increasing SFRD with increasing H I gas density and for both galaxies the amount of time needed to exhaust their H I reservoir at the current SFR ranges between 10 and 100 Gyr. When comparing the contour densities of the two galaxies we find that in DDO 133 the highest density of points is aligned with the 10 Gyr depletion line whereas in DDO 168 the highest density of points is aligned with the 100 Gyr depletion line.

The bottom panels of Figs. 3.14 and 3.15 show the star formation efficiency (SFE) as a function of atomic gas surface density (bottom left) and stellar surface density as inferred from the 3.6 μm map using the method described in Leroy et al. (2008) (bottom right). We remind the reader here, that star formation efficiency (SFE), defined as the ratio between the SFRD and gas surface density, is a measure of how long it would take for the existing gas to be consumed at the current SFR, assuming no gas return. We also remind the reader that in a sample of spiral galaxies, Leroy et al. (2008) have found that the ratio between SFRD and molecular gas surface density is constant: SFE(H_2)=5.25×10^{-10} yr^{-1}. The horizontal line in these bottom panels gives as a reference this constant line of SFE(H_2).

In the ideal case for the computation of the SFE, the gas surface density would be represented by the total gas surface density incorporating both the neutral and the molecular component. In spiral galaxies, a plot of SFE vs. total gas surface density shows an increasing trend in the H I dominated areas and a plateau of constant SFE in the H_2 dominated regions (Leroy et al., 2008). Unfortunately molecular gas observations are not available for these two dwarfs, so we calculate SFE based on the assumption that in dwarf galaxies the H I dominates so overwhelmingly that the molecular gas contribution to the total gas is insignificant.

[1]the gas depletion time is defined as the time it would take to consume the current gas content at the current SFR, and assuming no gas is being returned to the ISM

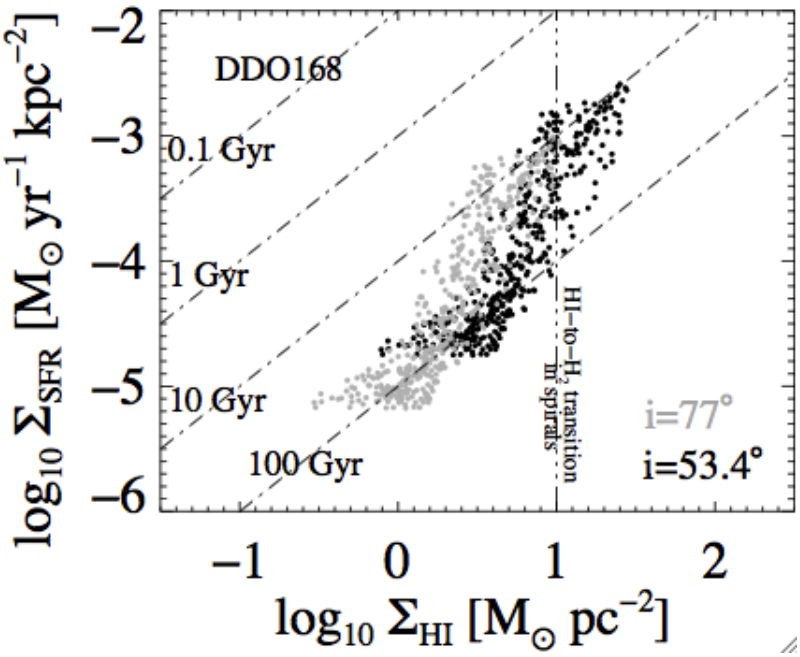

Figure 3.16: The effect of different inclination corrections applied to the SFRD vs. H I surface density plot. Black points are corrected for an inclination of 77°, whereas the grey points are corrected for an inclination of 53.°4. The four diagonal dashed lines represent constant gas depletion times of 0.1 Gyr, 1 Gyr, 10 Gyr, and 100 Gyr.

3.2.4 Systematic Effects

3.2.4.1 Inclination corrections and their contribution to the SF Plots

Attempts have been made to determine the intrinsic shape of dwarf galaxies, to find out whether they have an oblate spheroidal shape like in spiral galaxies or a triaxial shape, by using the ratio between the optical minor and major axes (Hodge & Hitchcock, 1966). Whereas van den Bergh (1988) argues that dwarfs are oblate spheroids with a thick disk (b/a=0.6) there are other authors who argue that triaxiality is needed to describe the shape of dwarf irregulars and Blue Compact Dwarfs (BCDs) (Binggeli & Popescu, 1995). Another way to settle this argument is by measuring the ratio between the rotational velocity and the velocity dispersion of the stars. Ratios of V/σ in spiral galaxies range from 2 to 5 (Bottema, 1993) implying a thin cold disk. The ratio of the LMC (van der Marel et al., 2002) equals 3, which lies within the range of spiral galaxies. There are not many measurements of stellar kinematics in dwarfs (Johnson et al., 2012), and those which exist sample the higher luminosity end of dwarf galaxies, so this result might not be generally true for all

dwarf irregulars (Hunter et al., 2005).

Adding to the difficult problem of establishing the true shape of our targets, more complications arise from the fact that in the dwarf regime the thin disk assumption does not necessarily apply and one must also consider that the HI disk may be thicker than the disk of stars. In this context de–projection becomes more challenging. In addition to the H I disk thickness, Banerjee et al. (2011) using a small sample of four dwarf galaxies in which gas and stars gravitationally dominate the disk, found that most dwarf galaxies exhibit H I flaring with radius. In other words there is an exponential increase of the scale height with radius.

Even for the increased scale height typically found in dwarfs as shown by Banerjee et al. (2011), lines of sight, even for quite inclined disks, will probe the H I within the immediate neighbourhood of where SF originates. As one of the factors in the formation of molecular clouds is self–shielding by a sufficiently large column of gas, to first order we can ignore variations in scale height and only consider for de–projection the inclination corrections. The inclination is derived through kinematical studies, explained in detail in paragraph 3.1.3.

However, we considered how uncertainty in the inclination affects our SF analysis. In Fig. 3.16, we plot SFRD vs. H I surface density for DDO 168 with two different inclination corrections applied. A higher inclination correction, grey points, moves all points in the plot downward and leftward. Although the positions of the points in the plot change with different inclination corrections the relation between them remains the same. It is that relation that constitutes the SF law we are interested in investigating, thus inclination uncertainties do not affect our conclusions.

3.2.4.2 Resolution Effects

Our radio interferometric data have the largest beam size of the data used which limits the smallest linear scale at which we can analyse the relation between SFRD and gas surface density. We plot in Fig. 3.17 the SFRD against the H I surface density of DDO 133 and DDO 168 at three spatial resolutions: native H I resolution (210 pc for DDO 133 and 170 pc for DDO 168), 400 pc, and 750 pc. As a general trend we can see that a decrease in resolution moves the points of the SF plot downwards and leftwards to lower SFRD and lower H I surface density. This trend can be explained as the effect of the resolution degradation combined with the distribution of the finer scale structure.

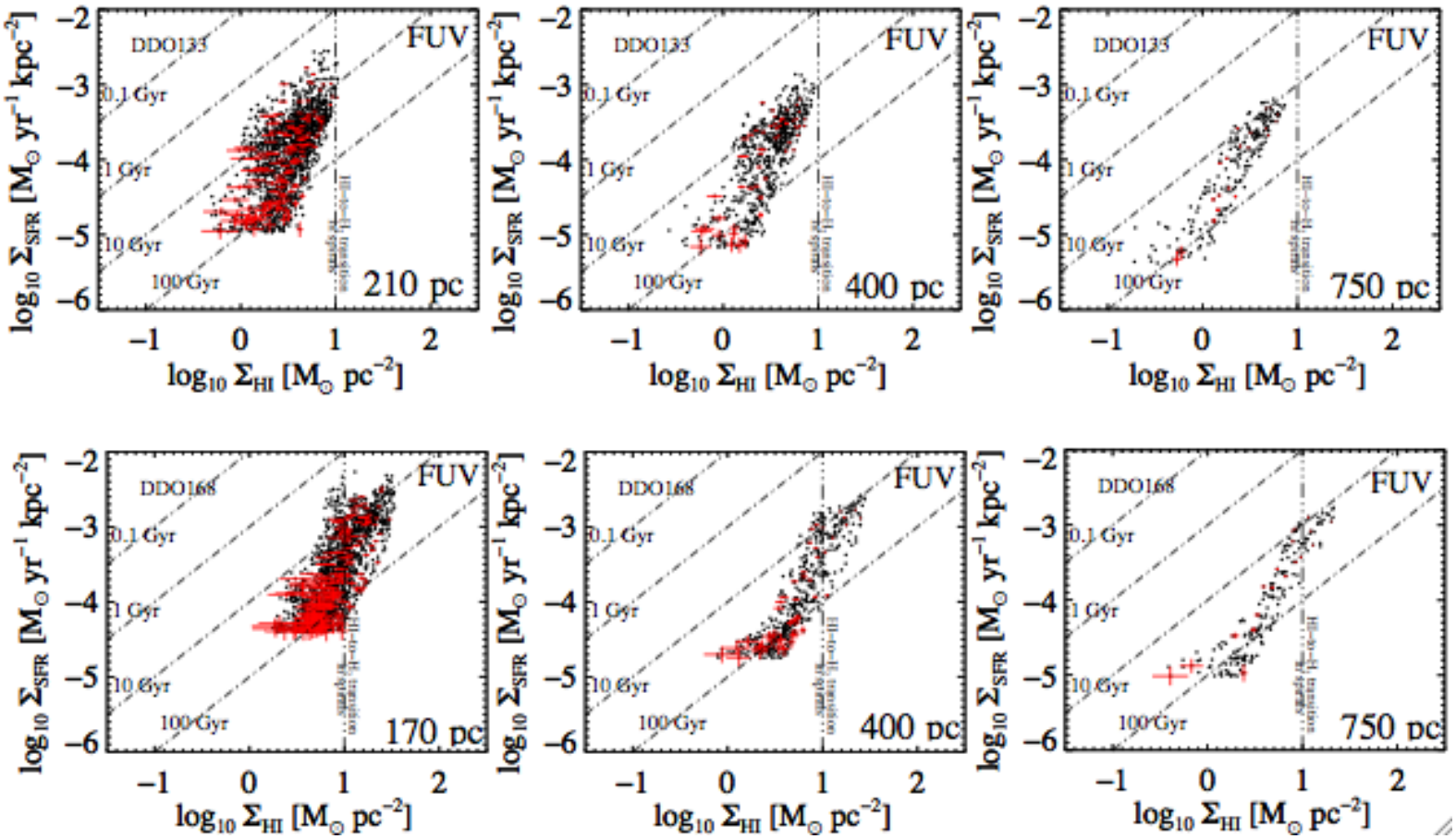

Figure 3.17: DDO 133 on the top row and DDO 168 on the bottom row, from left to right we show SFRD vs. H I surface density using three different resolutions: the finest linear resolution (210 pc for DDO 133 and 170 pc for DDO 168), 400 pc linear resolution and 750 pc linear resolution. The SFRD is based on FUV only as a star formation tracer. All points are independent and above a 5σ cutoff level in SFR. In red we display error bars for every 10^{th} point in the plot. The vertical dashed line represents an H I surface density of $10\,M_\odot\,pc^{-2}$. The four diagonal dashed lines represent constant gas depletion times of 0.1 Gyr, 1 Gyr, 10 Gyr, and 100 Gyr.

When one smooths the data, the way the total flux is spread out in the map changes and the flux peak inside a beam element becomes smaller proportionally with the beam size increase. However, if the H I gas is smooth and without any fine scale structure to begin with, the resolution degradation will not change the average surface density. Consequently, the presence of small scale structure in our data results in lowering the average surface density with resolution. Thus, the change in resolution has an effect on the scatter, on the number of points, and on the position of points in the SF plot.

We adopted a common linear resolution of 400 pc, which is a compromise between having high enough resolution to be able to do a meaningful spatially resolved study of dwarf galaxies, and a sufficiently high signal to noise to reduce the scatter in the relations probed. A resolution of 400 pc allows us to make direct comparisons with similar studies of other galaxies in the literature (Bigiel et al., 2010b, 2008; Leroy et al., 2008).

3.3 Discussion

3.3.1 The Star Formation Law in the Literature Context

Bigiel et al. (2010b) found that the SF characteristics of THINGS dwarfs are indistinguishable from those in the outskirts of spiral galaxies. They show that in the outskirts of nearby spiral galaxies unlike in their centres, although with a large scatter, there is a relation between H I and star formation. The correlation between SFR and atomic gas surface densities switches on in low metallicity regimes only, suggesting that H I surface density plays an important role in driving star formation in the low metallicity environment (Bigiel et al., 2011a).

In Fig. 3.18, right-most panel, we show the relation between SFRD and H I surface density for DDO 133 and DDO 168. The SFRD increases with increasing H I gas density, yet not without scatter (one order of magnitude). This scatter reminds us that H I gas density is not deterministic in this relation and this is understandable because only part of the H I gas density is transformed into molecular gas and then turned into stars. In other words there is neutral hydrogen unrelated with SF, which might be responsible for the scatter in the relation between H I surface density and SFRD. To quantify this correlation we use the Spearman's rank correlation coefficient. Whereas, for Bigiel et al. (2008) the H I used to infer the

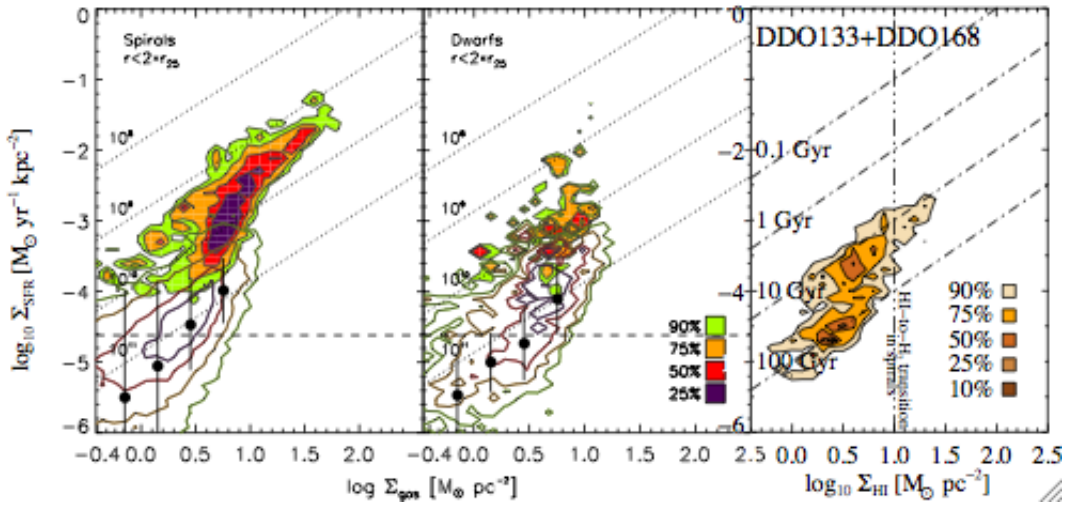

Figure 3.18: The left and middle panel show the results published by Bigiel et al. (2010b) for spirals and dIrr galaxies, respectively, taken from THINGS. The filled colour contours show the pixel by pixel distribution of FUV converted to SFRD as a function of gas surface density inside r_{25}, whereas the empty contours show the same but beyond r_{25}. The horizontal dashed line indicates the 3σ sensitivity level of the FUV measurements. The black filled circles represent their best fit through the data. In the right–most panel we attach our results for comparison: density contours at 10%, 25%, 50%, 75% and 90% of the pixel by pixel distribution of log SFRD vs. log H I surface density of DDO 133 and DDO 168. All points are independent and above a 5σ cutoff level in SFR. The vertical dashed line represents an H I surface density of 10 $M_\odot$ pc^{-2}. In all three panels the four dashed lines represent constant gas depletion times of 0.1 Gyr, 1 Gyr, 10 Gyr, and 100 Gyr.

gas surface density map and the FUV used as a SF tracer to obtain the SFRD map have a Spearman's correlation rank of 0.7, we find that the same correlation rank for DDO 133 and DDO 168 is 0.78 and 0.91 respectively, indicating a strong correlation between the SFRD and H I surface density. The correlation is stronger in DDO 168 than in DDO 133, because in DDO 133 we have a group of points that follow a rather different trend. We will talk more about those regions in Section 3.3.2.

We compare in Fig. 3.18 our results with those from the THINGS survey published by Bigiel et al. (2010b, 2008). It is important to point out here that in Bigiel's figure the x–axis is gas surface density while in our figure is H I surface density. In both dwarfs and outskirts of spirals (the empty contours in Bigiel's figure) the H I and gas surface densities are quite similar, however for the filled contours of the left most panel of Fig. 3.18 representing the SFRD–gas surface density distribution within r_{25} of the THINGS spirals, the gas surface density includes also the molecular gas surface density. The narrow tip of the filled contours (gas surface densities above 10 $M_\odot$ pc^{-2}) is due to the dominating contribution of the molecular gas sur-

face density to the gas surface density in these regions, and hence it shows the 1:1 relation between SFRD and gas in the molecular regime. As the gas surface density decreases so does the contribution of the molecular gas surface density and the SFRD–gas surface density relation widens as the unrelated H I contributes to the plot in a larger measure. By comparing different radial regimes of spiral galaxies with the colour density contours of the SFRD–H I surface density distribution of a small sample of dwarfs, Bigiel et al. (2008) establishes that the contours of spirals at radii beyond $0.75\,r_{25}$ overlap with those of dwarfs. This explains why in the left most panel of Fig. 3.18 there is an overlap between the empty and the filled contours and also defines the term outskirts of spirals.

Our colour density contours show the galaxies in their entirety without the segregation based on r_{25} used by Bigiel et al. (2010b). For both our galaxies, DDO 133 especially, we have deep observations in the FUV which explains why even with a more conservative cutoff of 5σ we are able to go deeper than the 3σ FUV sensitivity level represented by the horizontal dashed line in the Bigiel et al. (2010b) plots.

We find that the H I correlates with the FUV and can be approximated by a power law relation. We use the ordinary least squares (OLS) Bisector, as recommended by Isobe et al. (1990). We find that $\Sigma_{SFR} \propto (\Sigma_{HI})^{1.8\pm0.3}$, which agrees within the error bars with the 1.7 value found by Bigiel et al. (2010b). The neutral gas depletion times, the inverse of the star formation efficiency, for both DDO 133 and DDO 168 range between 10^{10} yr and 3×10^{11} yr (see Fig. 3.14 and Fig. 3.15, bottom left panels), again similar to the Bigiel et al. (2010b) result of order $\sim 10^{11}$ yr.

3.3.2 Multiple Components in the SF Laws

We return to the SFRD–H I surface density relation in DDO 133. In Fig. 3.19, we correlate features in the H I-SFRD plots with their physical location in the integrated H I maps. We colour coded different significant regions in the neutral gas distribution map: red for H I holes (shell interior regime), orange for high H I surface density regions and blue for the outskirts. In Fig. 3.19, using this colour code, we plot the position of the points on top of the highest resolution FUV (top right), H I (middle right) and Hα (bottom right) maps as well as display them in plots presenting SFRD or SFE vs. H I surface density and SFRD vs. V–band emission.

We find that the points (in red) that represent regions within H I shells in the SFRD vs. H I gas surface density plot, cluster within the same general area which seems to indicate too high a SFR for the column density of gas detected along the

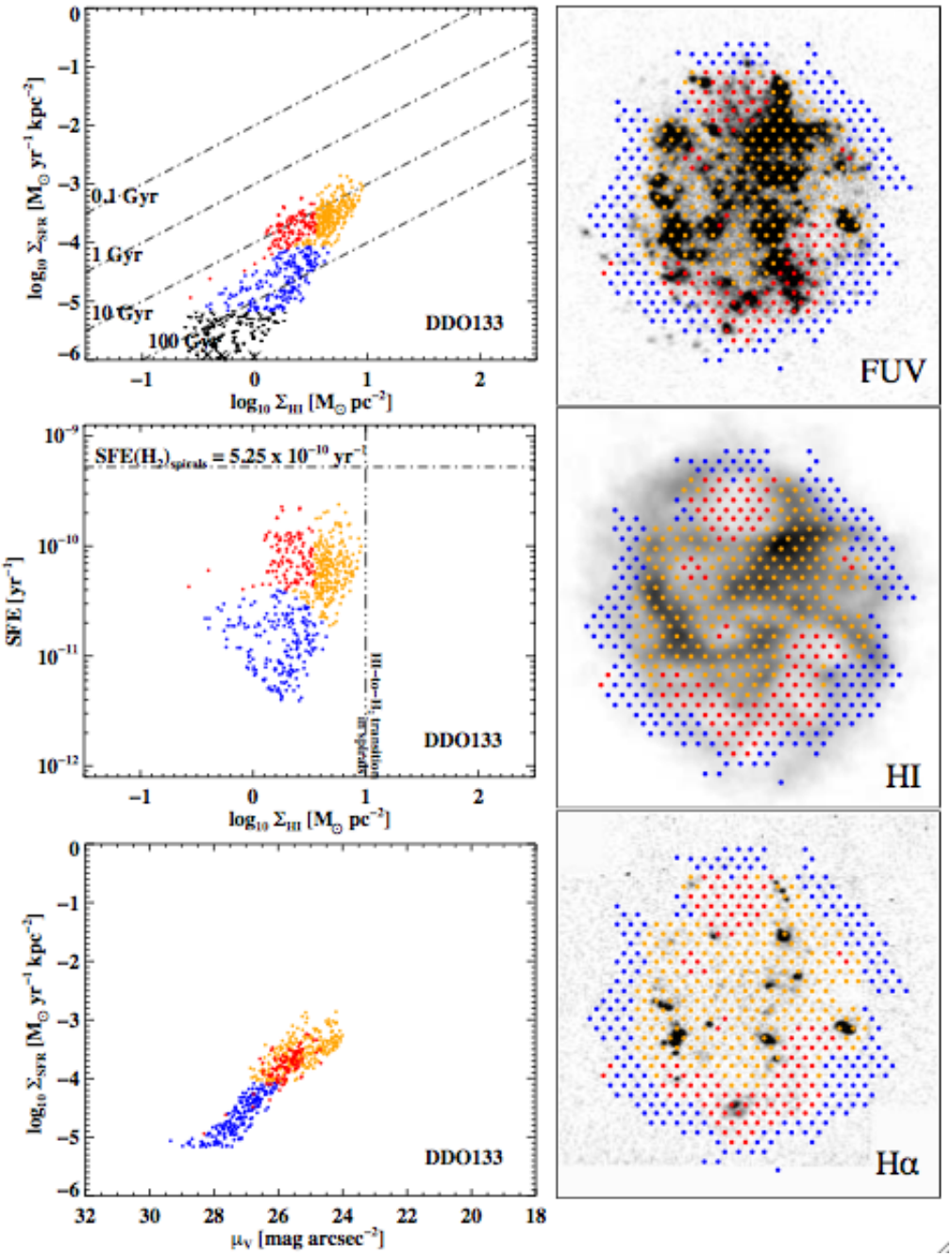

Figure 3.19: DDO 133: In an in depth study of the SF Law, based on the H I distribution map we separate the galaxy into three regions: red for H I shell interiors, orange for high H I surface density regions and blue for the outskirts. Their positions are plotted on the FUV (top right), H I (middle right) and Hα (bottom right) maps. We plot the same pixels as in the panels to the right as a SFRD vs. H I surface density plot (top left), SFE vs. H I surface density (middle left), and SFRD vs. V–band surface brightness (bottom left). All points are independent and above a 5σ cutoff level in SFR. The vertical dashed line represents an H I surface density of $10\,M_\odot\,pc^{-2}$. The horizontal dashed line represents constant molecular gas SFE of $5.25\times10^{-10}\,yr^{-1}$. The four diagonal dashed lines in the top left panel represent constant gas depletion times of 0.1 Gyr, 1 Gyr, 10 Gyr, and 100 Gyr.

line of sight. Most studies (Bagetakos et al., 2011; Brinks & Bajaja, 1986) explain the creation of H I shells through star formation and their results are backed by a correlation between small shells and OB associations. In a dwarf galaxy environment with no shear or spiral arms, the lifespan of an H I hole is longer (Brinks & Walter, 1998), so one cannot rule out the possibility of the H I hole outliving the star formation tracers that could have testified to that past SF event.

In our case, the smaller shells, in the central part of the galaxy are also associated with higher velocity components and higher Hα and FUV emission. The presence of Hα emission, the clumpy distribution of the FUV emission and the shell size suggest a rather recent SF event in these regions. However the bigger northern H I shell is only associated with diffuse FUV emission, testifying to a considerably older SF episode. If we look at the bottom left panel of Fig. 3.19, we see that there is V–band light in these regions, which betrays the presence of main sequence stars and to some extent a contribution from red giants. The stars that now contribute to the V–band, FUV and Hα emission have created the H I shells. The 400 pc resolution element is able to pick up this fine detail in the SF cycle and it appears as a distinct feature in the SFRD vs. H I surface density plot (SF plot). If one looks at Fig. 3.17 where we compare these plots at different resolutions one finds that the larger the value of the resolution element, the smaller the number of points representing the shell interior region and the more diminished its effect on the overall trend of the SF plot. If we remove the red points from the distribution of points considered in the Spearman's rank correlation computation for DDO 133, this coefficient changes its value from $r_s = 0.78$ to $r_s = 0.89$, a value closely matching the value we find in DDO 168.

As long as SF inside the H I shell is not second generation SF and the H I shell size is bigger than the resolution element, we will see this effect in the SF law, corresponding to the H I shell interior regions is not a true trend, but one artificially induced by the fact that in the chosen resolution element we have SF activity but no neutral gas to continue the SF cycle. Supernovae push the neutral hydrogen around and create H I holes inside which the SF law cannot be studied because the neutral gas phase and the SF phase do not coexist within the chosen resolution element.

3.3.3 The H I to H_2 Transition

One striking feature of the H I vs. SFR relation is the high H I surface density of $\sim 28\,M_\odot\,pc^{-2}$ found in DDO 168, which goes beyond $10\,M_\odot\,pc^{-2}$, the empirical limit

above which the H I turns molecular in solar metallicity galaxies (Bigiel et al., 2008; Krumholz et al., 2011). This is not a systematic effect due to either resolution or inclination uncertainties. Only an extreme, unrealistic inclination correction could bring the H I surface density value maximum in DDO 168 below $10\,M_{\odot}\,pc^{-2}$ (see Fig. 3.16). The thickness of the H I layer can also play a role. If the H I disk is much thicker than the SF disk, than along the line of sight the H I above and below the mid-plane of the disk where SF is taking place would add up to the total column density although it does not participate in the SF process. In this way, the H I surface density can be higher than the $10\,M_{\odot}\,pc^{-2}$ limit. However, according to this scenario, we expect this effect to be more prominent in the outskirts of galaxies if the gas density as a function of height follows an exponential distribution (Banerjee et al., 2011). In such a case DDO 133, where there are strong indications that the SF activity has moved from the centre towards the outskirts, should be more affected by this effect than DDO 168, where the high H I surface densities are in the centre and the H I and SF layers are thought to be comparable in thickness.

Similar, yet more extreme ($\Sigma_{HI} \sim 100\,M_{\odot}\,pc^{-2}$) behaviour has been noted in the SMC by Bolatto et al. (2011). The magnitude of the effect in the SMC is attributed to the complex geometry of the source, which if accounted for, decreases its value by a factor of 1.5 – 2. But even a geometry corrected value is still significantly higher than the $10\,M_{\odot}\,pc^{-2}$ limit. According to theoretical predictions the $10\,M_{\odot}\,pc^{-2}$ limit is inversely proportional with metallicity (Fumagalli et al., 2010; Krumholz et al., 2011). Such a relation would explain the geometry corrected value of the Σ_{HI} upper limit found for SMC and would predict for DDO 168, based on a metallicity of 12+log(O/H) = 8.29, a Σ_{HI} upper limit of $\sim 29\,M_{\odot}\,pc^{-2}$, in excellent agreement with the observed value. DDO 133, however, with a metallicity 12+log(O/H) = 8.23 only slightly lower than that of DDO 168 does not break the $10\,M_{\odot}\,pc^{-2}$ Σ_{HI} upper limit. When considering the THINGS dwarfs, we find that at 400 pc linear resolution there are several THINGS dwarfs such as DDO 63, DDO 53, DDO 50, NGC 2366, NGC 4214 which exceed the $10\,M_{\odot}\,pc^{-2}$ limit. Comparing our data on DDO 133 and DDO 168 with the THINGS data on seven dwarfs we do not find any strong evidence for the predicted trend with metallicity (see Fig. 3.20). Consequently, there must be more parameters influencing the Σ_{HI} upper limit, than metallicity alone and a better understanding of what drives the peak H I column density will require a similar study to the one done here but on a larger sample.

Krumholz et al. (2009) shows that besides metallicity, the degree of clumping

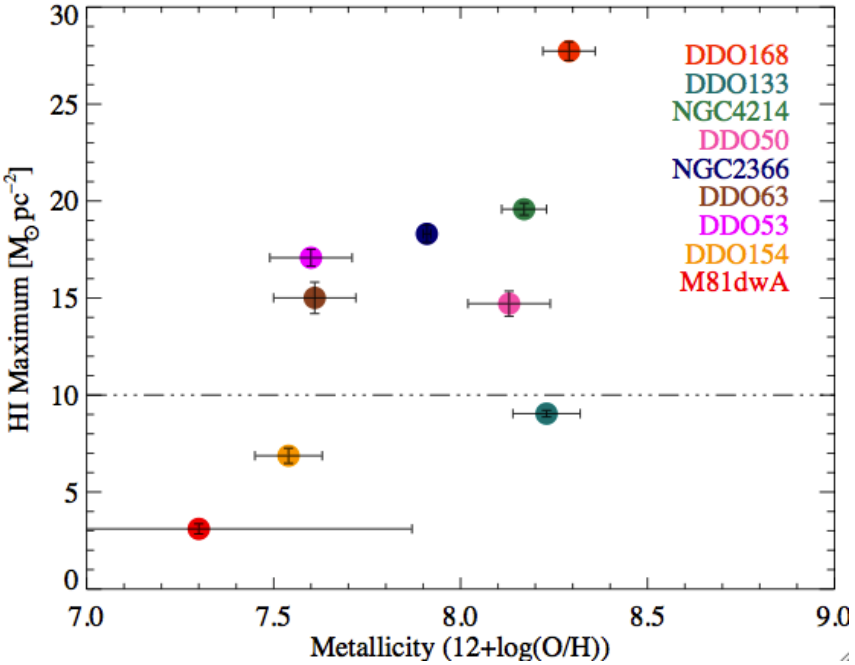

Figure 3.20: Metallicity vs. H I Maximum for DDO 133, DDO 168 and the THINGS dwarf sample (DDO 50, DDO 53, DDO 63, DDO 154, NGC 2366, NGC 4214, M81dwA) at 400 pc linear resolution. The vertical dashed line represents an H I surface density of 10 $M_\odot$ pc^{-2}. The metallicity values and error bars are taken from Hunter et al. (2012), as the above mentioned THINGS dwarfs are also part of the LITTLE THINGS sample.

in the gas also plays a role in the value of the H I maximum and one can imagine that the variation from dwarf to dwarf could also be due to the particular phase of the star formation cycle that the dwarf galaxy is going through at the moment of observation since dwarfs, being tiny, are more affected by stochastic SF than large spirals. Both DDO 133 and DDO 168 have extended FUV emission throughout the galaxy, however the Hα emission follows the FUV emission contours with more fidelity in DDO 168 than in DDO 133 (see Fig. 3.4 and Fig. 3.8). This suggests that DDO 133 is entering a post–starburst phase. Massive star formation, such as traced by Hα is more likely to happen in gas with high column densities. Roychowdhury et al. (2011), based on a sample of 23 extreme dwarfs, find that the higher the $\Sigma_{SFR(H\alpha)}/\Sigma_{SFR(FUV)}$ ratio the more likely it is to find gas with a column density higher than the 10 $M_\odot$ pc^{-2} limit, a result we confirm here. The $\Sigma_{SFR(H\alpha)}/\Sigma_{SFR(FUV)}$ ratio tells us whether we are currently actively forming stars. A different suggestion is that higher $\Sigma_{SFR(H\alpha)}/\Sigma_{SFR(FUV)}$ ratio indicates a larger interstellar radiation field (ISRF). In other words the reason why in DDO 168 we see a higher than 10 $M_\odot$ pc^{-2}

column densities and in DDO 133 not is related to the intensity of the ISRF in each galaxy. Often V–band emission can be used as a proxy for the ISRF intensity (Elmegreen, 1993), so if we look at the top right panel of Fig. 3.21 we find higher values of V– band surface densities in DDO 168 than in DDO 133 suggesting that the ISRF is more intense in DDO 168 than in DDO 133. A more intense ISRF implies the need for greater self-shielding hence the higher H I column densities.

It may very well be that in a scenario where as metallicity goes down and dust–shielding loses its dominating role (Bolatto et al., 2011), we should see more dense H I envelopes, which coexist with the molecular phase. Their gas has the density necessary to turn molecular, but cannot cool due to the interstellar radiation field. If we were to detect such envelopes, the H I maximum would no longer coincide with the H I to H_2 turning point, but rather be a representation of the molecular phase itself and the shielding mechanisms of low metallicity dwarf galaxies.

3.3.4 The Correlation between SFR and the Stars

Dwarf irregulars show a better correlation between the integrated SFR and V–band emission than any other measure (Hunter & Elmegreen, 2004; Hunter et al., 1998). We confirm this result existent in the literature and show that this relation holds not only when it comes to global averages over an entire galaxy but also on smaller scales such as the 400 pc resolution element we work with here. We plot in Fig. 3.21 the SFRD vs. V–band emission (top right) for DDO 133 (black) and DDO 168 (red) and we find that the relation between the two quantities is tighter (less scatter) than the relation between SFRD and H I gas density (top left). To assess the strength of the correlation between SFRD and V–band surface density we compute the Spearman's rank correlation coefficient and find: $r_s = 0.90$ for DDO 133 and $r_s = 0.92$ for DDO 168, in other words they are highly correlated, more so than the SFRD–H I surface density relation.

In the same figure, Fig. 3.21 we also plot SFRD vs. V–band emission (in red) and 3.6 μm emission (navy) for DDO 133 (bottom left) and SFRD vs. V–band emission (in red), K–band emission (orange) and 3.6 μm emission (navy) for DDO 168 (bottom right), to explore the relation of the SFR with different stellar populations. Whereas the V–band is dominated by main sequence (MS) stars with a considerable contribution from red giants, the K–band is dominated by K giant stars and older stars. We only have K–band data available for DDO 168. When K–band maps are unavailable, 3.6 μm can be used as a proxy for the old stellar populations (Oh et al.,

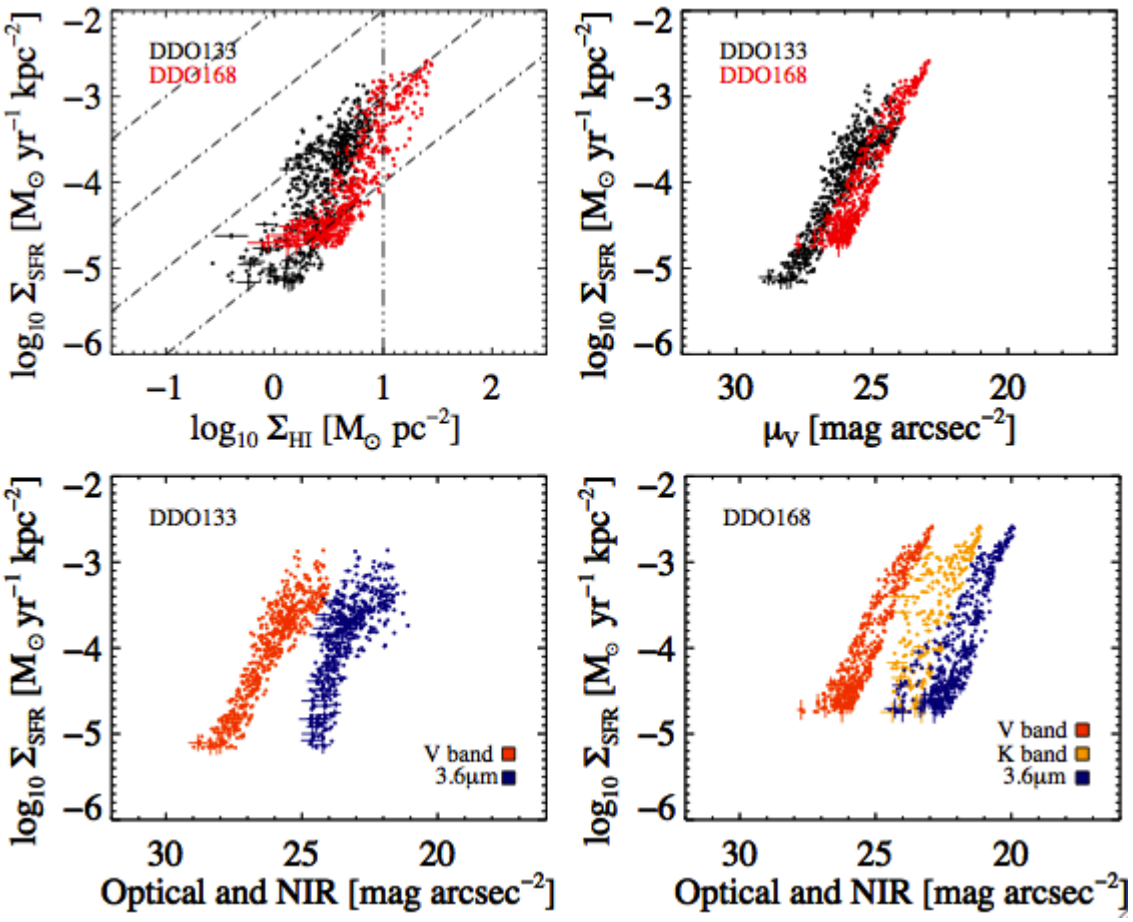

Figure 3.21: In the top right panel we represent the SFRD vs. optical V–band surface density for DDO 133 (black) and DDO 168 (red). Using the same symbols we give as a reference in the top left panel the SFRD vs. H I surface density. The vertical dashed line represents an H I surface density of $10\,M_{\odot}\,pc^{-2}$. We also show for DDO 133 (bottom left) and DDO 168 (bottom right), SFRD vs. optical and NIR surface densities: $3.6\,\mu$m (navy), K–band (yellow) and V–band (orange). Note that there were no K–band observations available for DDO 133. We also display error bars for every $10^{\rm th}$ point in all the panels of the plot. All points are independent and above a 5σ cutoff level in SFR and 3σ cutoff level in the optical and NIR bands.

2008), yet we caution the reader that even the $3.6\,\mu$m band is not sampling solely the old stars contribution. The relation persists at all considered wavelengths, but the relation to the V–band remains tightest. In DDO 133 the correlation between SFR and the $3.6\,\mu$m emission ($r_s = 0.78$) is as tight as the one between SFRD and H I surface density. In DDO 168 the correlations between SFRD and the $3.6\,\mu$m emission ($r_s = 0.86$) and the K–band ($r_s = 0.78$) are both weaker than the one between SFRD and H I surface density. The optical and NIR bands follow each other closely.

Since they trace such different populations of stars, and since different mixtures of contributions from different populations are present in both optical and NIR bands, their agreement is even more puzzling and difficult to explain as due to a certain population of stars. Consequently it seems that in dwarfs such as DDO 133 and DDO 168 the V–band map traces the stellar surface density with the same fidelity as K–band or 3.6 μm maps. Thus the observed relation of the SFRD and the V–band surface density is driven by the gravitational potential well provided by the stars. Gas collects there, enhancing the local gas density, leading to molecular cloud and subsequent star formation. In other words, where stars were formed in the not too distant past (100 Myr - 1 Gyr), new stars will form again simply because here is where the baryonic matter has accumulated and reached conditions conducive of SF.

This scenario is supported by the relation between molecular gas mass and K–band luminosity found by Leroy et al. (2005): the larger the K–band luminosity, that is the higher the stellar mass density, the higher the midplane hydrostatic pressures leading to higher gas densities and more efficient molecular gas formation.

Shi et al. (2011) find a correlation between SFE and stellar mass density, by looking at the dependence of Σ_{SFR} on Σ_{gas} and Σ_{star}. In terms of SFE, DDO 168 shows, as expected an increasing trend with the increase of stellar surface density (see Fig. 3.15, bottom right panel), whereas DDO 133 is rather ambiguous (see Fig. 3.14, bottom right panel). This may be due to the weakness of the 3.6 μm emission. Further, Shi et al. (2011) explain this correlation as an indication of the critical role played by existing stellar populations in the current SF events.

3.3.5 Molecular Gas Predictions

Stars form out of molecular gas. Therefore relating the SFRD to the H I surface density is valuable only in the sense of studying the transition of atomic gas into molecular gas. In fact, Bigiel et al. (2010b) have shown that a relation between SFRD and H I surface density exists only in dwarfs and the outskirts of spirals. This indirect relation between the star formation process and the neutral gas behaviour has became more interesting since Bigiel et al. (2008) have shown that the SFRD follows the molecules. Leroy et al. (2008) have investigated this relation further and found the SFE of the molecular gas to be a constant: $\mathrm{SFE}(H_2) = 5.25 \times 10^{-10}\,\mathrm{yr}^{-1}$. This result, based on CO observations of THINGS spiral and gas-rich dwarf galaxies, can be used to predict the molecular gas quantity in galaxies where CO observations

are not available.

We cannot directly observe H_2. We can only infer this quantity from CO observations (Leroy et al., 2007b; Schuster et al., 2007) and more recently from gas–to–dust ratios (Leroy et al., 2007a, 2011). Dwarf galaxies are low metallicity environments, where the CO molecules are under–abundant and thus cannot easily be used as proxies for molecular gas mass determinations (Bolatto et al., 2008; Leroy et al., 2007b).

TABLE 3.1. Important quantities on DDO 133 and DDO 168 (I)

Name	$(S_{HI})^{s}$ (Jy km s^{-1})	S_{HI} (Jy km s^{-1})	log $(M_{H\,I})^{s}$ (log($M_\odot$))	log $(M_{H\,I})$ (log($M_\odot$))	log (M_{H2}) (log($M_\odot$))	r_{max} (kpc)
DDO 133	40.98 ± 1.6	36.42	8.09	8.02	7.03	6.2
DDO 168	76.50 ± 4.5	64.00	8.51	8.45	7.26	4.2

Table 3.1: We give for DDO 133 and DDO 168 the single dish H I flux from Springob et al. (2005) and Huchtmeier & Richter (1986) respectively, the LITTLE THINGS H I flux, the single dish H I mass from Fisher & Tully (1981) and Hunter & Gallagher (1985a) respectively, measured LITTLE THINGS H I mass, inferred H_2 mass and the maximum radius based on H I. Note that the total uncertainty in our H I flux calculation is dominated by the accuracy of the flux calibration (of order 5%), whereas the uncertainty in our H I mass calculation (of order 15%) is due to the uncertainty in the flux measurement and the assumption that H I is optically thin (self–absorption underestimates the derived H I masses by up to 10% according to Zwaan et al. (1997)).

If we assume that metallicity does not influence the quantity of H_2 (Krumholz et al., 2011, 2009), we can use the SFE value by Leroy et al. (2008) to infer the molecular gas mass. We find a predicted amount of molecular gas of $1 \times 10^7\,M_\odot$ for DDO 133 and $2 \times 10^7\,M_\odot$ for DDO 168 (see Table 3.1). Leroy et al. (2007a) found the H_2 mass in the SMC, which has a metallicity that is similar to that of DDO 133 and DDO 168, to be $3.2 \times 10^7\,M_\odot$, a value which shows that our predicted values are reasonable compared to values estimated from CO and dust observations.

With a molecular gas estimate at hand, in order to derive the total gas mass, and correcting by a factor of 1.34 to take into account the helium fraction and we obtain a value of $1.5{\times}10^8\,M_\odot$ for DDO 133 and $4.2{\times}10^8\,M_\odot$ for DDO 168. We use an empirical conversion to transform the 3.6 μm map intensity to K–band intensity and from there using the K–band mass to light ratio we obtain the stellar density map (Leroy et al., 2008). We then use this stellar density map to compute the stellar mass of DDO 133: $M_* = 0.5 \times 10^8\,M_\odot$ and of DDO 168: $M_* = 0.8 \times 10^8\,M_\odot$. In DDO 133, the mass of stars combined to the total gas mass yields a total baryonic mass of $2.1 \times 10^8\,M_\odot$,

TABLE 3.2. Important quantities on DDO 133 and DDO 168 (II)

Name	M_* ($M_\odot$)	$M_{baryonic}$ ($M_\odot$)	M_{dyn} ($M_\odot$)	W_{20} ($km\,s^{-1}$)	v_{rot} ($km\,s^{-1}$)	Incl. (°)
DDO 133	0.5×10^8	2.05×10^8	2.3×10^9	83	40 ± 5	46 ± 5
DDO 168	0.8×10^8	4.99×10^8	2.44×10^9	87	50 ± 7	53 ± 8

Table 3.2: We give for DDO 133 and DDO 168 the stellar mass, the baryonic mass, the dynamical mass, the H I profile width at 20% of the peak intensity, the kinematically determined rotational velocity and the inclination determined from kinematical studies.

amounting to 1/11 of the dynamical mass $M_{dyn} = 2.3 \times 10^9\,M_\odot$ (v_{max}=40 $km\,s^{-1}$, and r_{max}=6.2 kpc). In turn, for DDO 168, the mass of stars combined to the total gas mass yields a total baryonic mass of $5.0 \times 10^8\,M_\odot$, amounting to 1/5 of the dynamical mass $M_{dyn} = 2.44 \times 10^9\,M_\odot$ (v_{max}=50 $km\,s^{-1}$, and r_{max}=4.2 kpc). All the above mentioned quantities are given in Table 3.1 and Table 3.2.

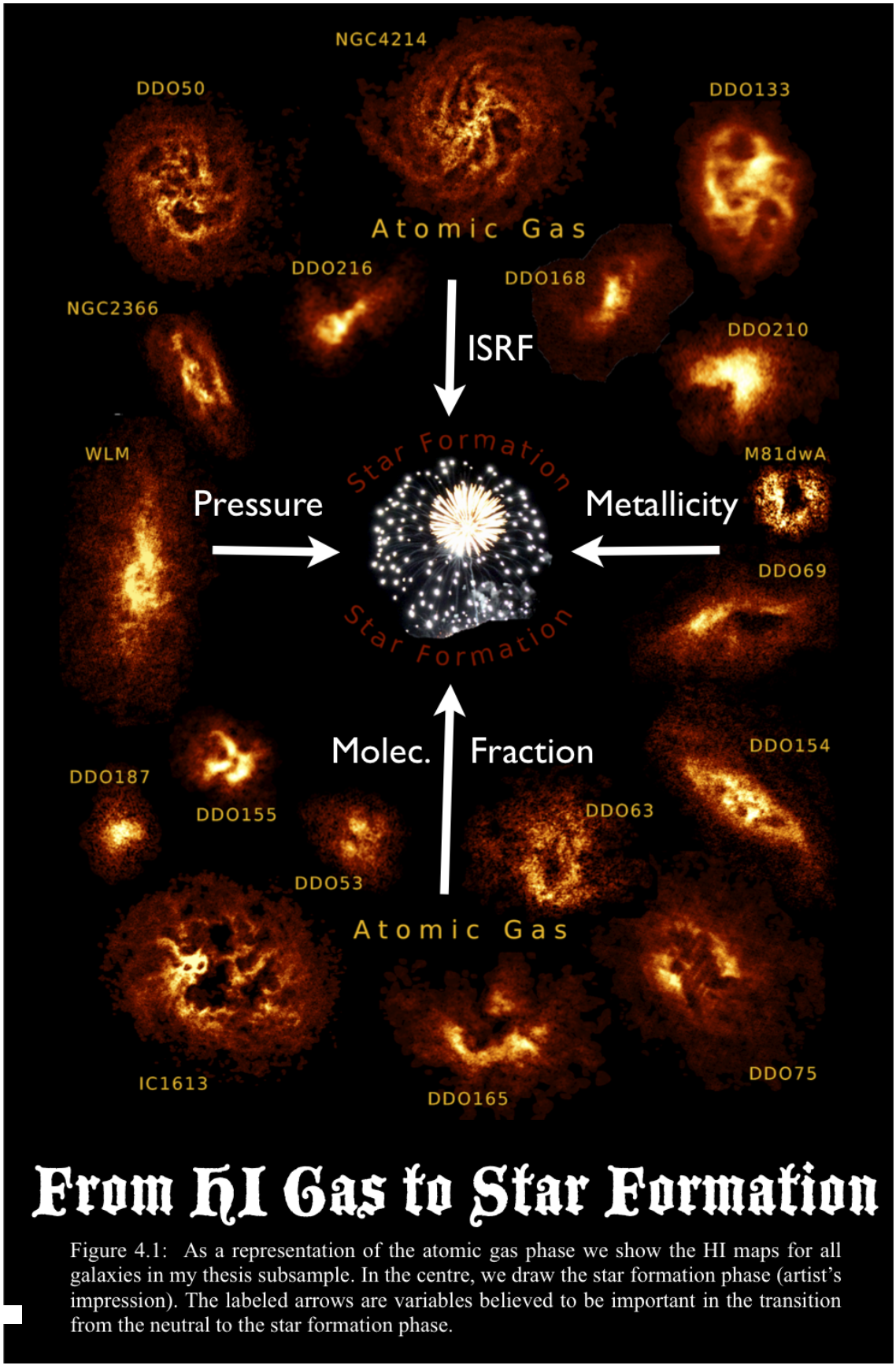

Figure 4.1: As a representation of the atomic gas phase we show the HI maps for all galaxies in my thesis subsample. In the centre, we draw the star formation phase (artist's impression). The labeled arrows are variables believed to be important in the transition from the neutral to the star formation phase.

Chapter 4
STAR FORMATION ANALYSIS: THE ENTIRE SUBSAMPLE

4.1 Methodology

After testing our method on two galaxies we have extended its use to a subsample. The gas surface density maps rely on H I observations only, as obtaining molecular gas observations pose serious problems once we move into the low luminosity regime of dwarf galaxies. From the H I gas kinematics we derived inclination estimates for most of the galaxies in our subsample. These values along with the optical derived values for inclination are all listed in Table 4.1. The kinematically and the optically derived values for inclination are, in general, consistent with each other within 10 °. However there is one galaxy, DDO 53, where the kinematically derived inclination differs from the optically derived one by almost 40 °, but as the kinematics provide a better handle on the orientation of the disk, we use the kinematically derived inclination. Galaxies such as DDO 155, DDO 165, M81dwA, DDO 75, DDO 187 and DDO 69 show no dominant circular rotation, so the inclination could not be estimated in this way. We have used for these galaxies the inclination derived from the ratio of the minor to major axis of each galaxy in the V–band (Hunter & Elmegreen, 2006). We apply the inclination correction to both the H I surface density and the SFRD maps.

To create our star formation rate maps we have used four different tracers based on FUV, Hα emissions and their combinations with 24 μm emission. We extend our discussion on the efficiency of these tracers in the next section (see Section 4.1.1).

We remind the reader that our subsample contains two galaxies (DDO 155 and DDO 165) not observed in FUV and two galaxies (M81dwA and DDO 210) showing no emission in Hα. Based on the findings presented in the previous chapter, we apply no internal extinction correction when using tracers such as FUV and Hα on their own. We check, however, if the low level of internal extinction holds also for the other galaxies in our subsample and discuss our findings in Section 4.1.2. We do not consider any other corrections, leaving considerations regarding the three–dimensional shape of the galaxies, the H I flaring and the H I scale height for further refinement in future projects.

4.1.1 Star Formation tracers

As previously mentioned, we have considered four different SF tracers: FUV–only, Hα–only, FUV+24 μm and Hα+24 μm. In Chapter 3, Section 3.2.1 we explain in detail the formulae used to construct the SFRD maps from each of these four tracers. In Section 3.2.2 we argue for using the FUV–only as a SF tracer since Hα emission is detected at sufficient signal-to-noise in the central parts only. Also a correction for internal extinction was deemed not necessary. With a larger sample at hand and to further test our approach, we compare the SFRD vs. H I surface density plots obtained based on different SF tracers and combinations thereof. We present in Fig. 4.2 and Fig. 4.3 four galaxies DDO 133, NGC 4214, DDO 154 and DDO 53, ordered by metallicity. These four were chosen for being representative of the entire metallicity range of our sample. Analysing Fig. 4.2 and Fig. 4.3, we conclude that indeed an SFRD map based on FUV–only as a tracer is able to describe the outskirts of the galaxies as well as their centres, whereas the SF tracers Hα–only and other hybrids based on combinations with 24 μm emission can only be used to describe the higher end of the SFRD. The S/N at 24 μm, in most of our dwarf galaxies is very low such that the contribution by 24 μm dominates the error bars of the FUV+24 μm maps. NGC 4214 is an exception. The 24 μm emission in this galaxy is significant enough that the FUV–only based SFRD and the FUV+24 μm based SFRD are consistent and the noise in the 24 μm no longer causes truncation of the SFRD, the FUV–only tracer gives an SFRD map with only slightly lower values than those of the other three tracers. For a more exact estimate of the discrepancy in the SFRD for FUV–only as the SF tracer as opposed to FUV+24 μm as a SF tracer in NGC4214, we refer the reader to the next section where we estimate the internal extinction based on the 24 μm emission in each galaxy of our sample.

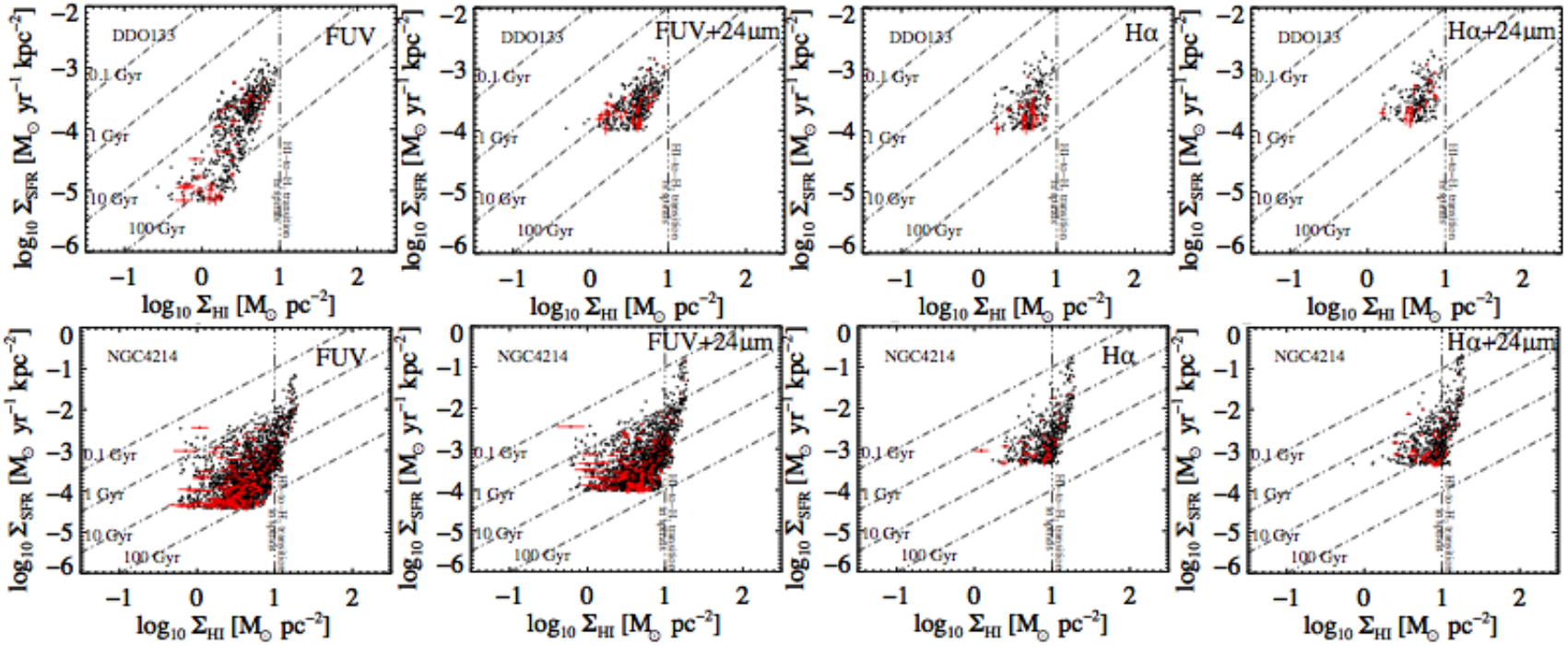

Figure 4.2: In the case of DDO 133 and NGC 4214 we present a comparison between the SFRD and the H I surface density plots, where the SFRD map is based on four different SF tracers: FUV, FUV+24 μm, Hα and Hα+24 μm. Each row of plots represents a distinct galaxy and each column a different SF tracer. All maps used for the above plots have the same linear resolution of 400 pc. All points are independent and above a 5σ cutoff level. In red we display error bars for every 10^{th} point in the plot. The vertical dashed line represents an H I surface density of 10 $M_\odot$ pc^{-2}. The other four dashed lines represent constant gas depletion times of 0.1 Gyr, 1 Gyr, 10 Gyr and 100 Gyr.

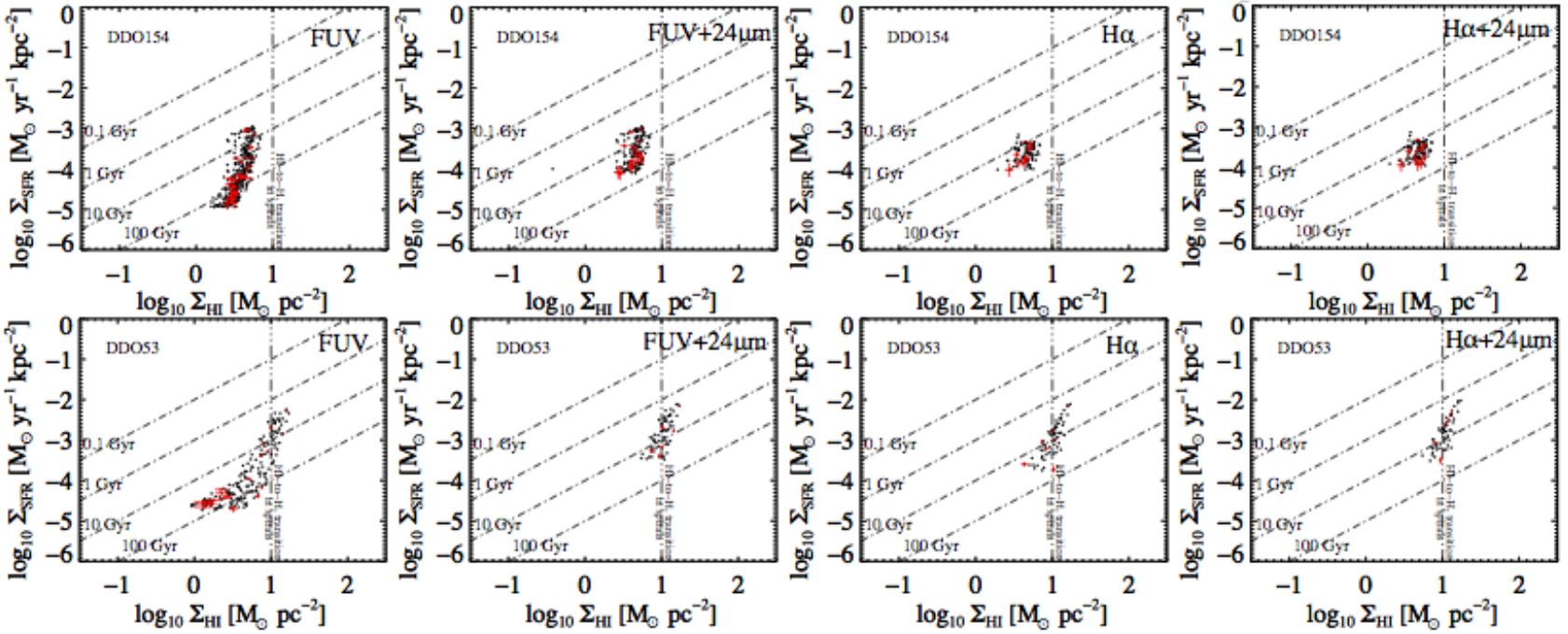

Figure 4.3: In the case of DDO 154 and DDO 53 we present a comparison between the SFRD and the H I surface density plots, where the SFRD map is based on four different SF tracers: FUV, FUV+24 μm, Hα and Hα+24 μm. Each row of plots represents a distinct galaxy and each column a different SF tracer. All maps used for the above plots have the same linear resolution of 400 pc. All points are independent and above a 5σ cutoff level. In red we display error bars for every 10$^{\text{th}}$ point in the plot. The vertical dashed line represents an H I surface density of 10 $M_\odot$ pc^{-2}. The other four dashed lines represent constant gas depletion times of 0.1 Gyr, 1 Gyr, 10 Gyr and 100 Gyr.

4.1.2 Internal Extinction

Just as we have already mentioned in Section 3.2.2, we estimate the contribution of internal extinction to our SFR maps by comparing different star formation tracers and assessing what colour index value E($B-V$) corresponds to the 24 μm emission. We remind the reader that at 24 μm we observe the obscured light, which is re–processed through dust and re–radiates at infrared wavelengths (Calzetti et al., 2007, 2010). Our method implies a series of assumptions: the extinction law used in deriving the colour index value E($B-V$) from the estimated internal extinction correction is appropriate, and the factors defining the amount of obscured and unobscured light (see Equation 3.3 and Equation 3.4) hold true also in the low metallicity environment of dwarfs.

In the previous chapter we concluded that weak 24 μm emission suggests low dust content and hence a more transparent medium where internal extinction is at such low levels that no correction is necessary. Here, however we would like to take advantage of the larger sample available to us at this stage and extend that study. In Appendix B, Fig. B.1 we present for each individual galaxy the comparison between SFR maps using FUV+24 μm as a tracer and FUV–only as a tracer assuming both the Milky Way (left) and the SMC (right) extinction laws. In the Fig. B.1, to match the 24 μm emission with the appropriate internal extinction correction, we use different colours for different colour index E($B-V$) values, ranging between 0 and 0.05 mag. We look for the value that is closest to the 1:1 black continuous line in the figure. That is, we look for the mean, galaxy–wide extinction value that brings the SFR derived from FUV+24 μm and the SFR determined from FUV–only into closest agreement.

The colour index E($B-V$) values found in the above described manner are shown as a function of metallicity in Fig. 4.4. We find that the colour index values are low, confirming our preliminary conclusion based on DDO 168 and DDO 133, that no internal extinction correction is necessary. This is to be expected in the low metallicity regime, where the dust abundance is low as reflected by the weak 24 μm emission and hence the medium is more transparent. This conclusion alone is enough, for the immediate requirements of our project. However, we cannot refrain from exploring this subject a little bit further.

At the beginning of this section we mentioned a few assumptions we made and now we return to them and discuss what impact they in fact have on our results. In Fig. 4.4 we differentiate based on the extinction law assumed (Milky Way or

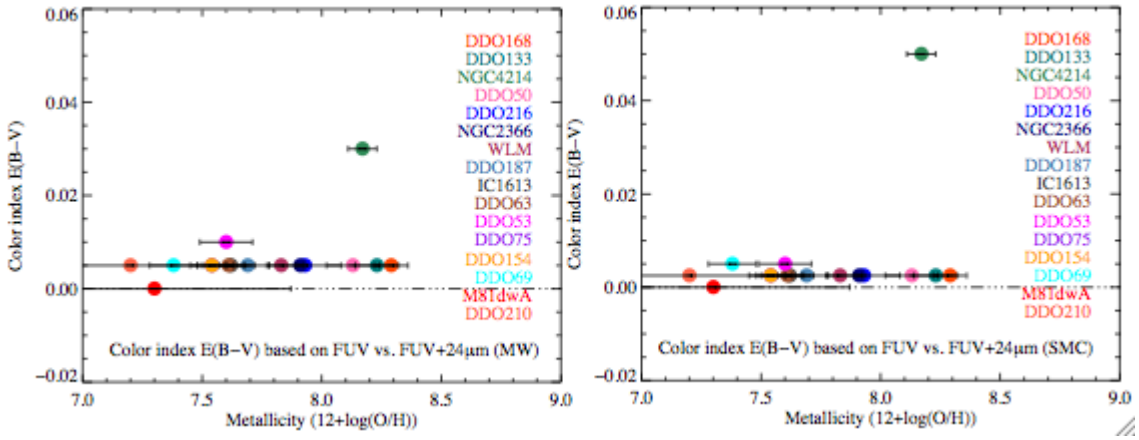

Figure 4.4: We present for all galaxies in our subsample with appropriate ancillary data available, the colour index E($B-V$) as a function of metallicity. The colour index E($B-V$) values have been inferred from comparing SFRD from FUV–only and FUV+24 μm based on the Milky Way extinction law (left) and SMC extinction law (right).

SMC) and find that for FUV as a SF tracer, when assuming the SMC extinction law instead of the Milky Way one, the estimated colour index E($B-V$) value shows no or minimal change for 94% of our subsample. Exceptions are DDO 53 with a decrease in estimated colour index E($B-V$) value of 0.005 mag and NGC 4214 with an increase in estimated colour index E($B-V$) value of 0.02 mag.

In our method of estimating the internal extinction we have used the same factors to combine FUV and 24 μm as were used for spiral, i.e., higher metallicity galaxies. We found that if we amend the factors according to the Calzetti et al. (2010) recipe, by lowering the contribution of the 24 μm luminosity from 0.031 (see Equation 3.3) to 0.020, the value of the colour index value shows no noticeable change for FUV as a SF tracer.

4.2 Neutral Gas Mass Measurements

We calculated for the galaxies in our subsample, the integrated H I mass (see Table 4.1). The uncertainty in the H I masses follows from the uncertainty in the flux measurement (of order 5%) combined with the effect of underestimating self–absorption (Zwaan et al., 1997). We also collected from the literature the available single dish measurements of the H I mass in our galaxies of interest and compared these values to the ones measured by us. As shown in Table 4.1, we find in general good agreement (within 20%) between the single dish and our measured values.

Table 4.1. General Properties

Name	$S_{H\,I}$ (Jy km s^{-1}) *(Observed)*	log ($M_{H\,I}$) (log($M_\odot$)) *(Observed)*	log ($M_{H\,I}$) (log($M_\odot$)) *(Single Dish)*	Ratio $M_{H\,I}{}^{Sing.\ Dish}/M_{H\,I}{}^{Obs.}$	log (M_{H2}) (log($M_\odot$)) *(Predicted)*	Inclination (°) *(Opt.)*	Inclination (°) *(Kin.)*	(12+log(O/H))	θ_{LAS} ($''$)
DDO 168	6.17	8.47	8.51	1.09	7.26	54	53.4	8.29±0.07	269
DDO 133	6.39	8.02	8.09	1.17	7.02	49.4	46.2	8.23±0.09	354
NGC 4214*	6.82	8.76	8.78	1.05	7.18	25.8	16.3	8.17±0.06	605
DDO 50*	6.75	8.85	8.92	1.17	8.04	46.7	49.0	8.13±0.11	649
DDO 216	5.65	6.75	6.84	1.23	5.91	69.4	56.8	7.93±0.15	356
NGC 2366*	6.72	8.84	8.90	1.15	8.02	72.1	63.0	7.91±0.01	710
WLM	6.76	7.85	7.84	0.98	6.95	70.3	75.2	7.83±0.06	928
DDO 187	5.30	7.12	7.16	1.09	6.06	39.0	...	7.69±0.09	169
DDO 155	5.70	7.00	6.98	0.95	...	47.6	...	7.68±0.06	197

DDO 165	6.01	8.13	8.18	1.12	...	61.9	...	7.63±0.08	359
IC 1613	6.86	7.53	7.74	1.62	6.93	37.9	42.0	7.62±0.05	949
DDO 63*	6.01	8.19	8.21	1.05	7.30	0	13.0	7.61±0.11	307
DDO 53*	5.49	7.72	8.39	4.68	6.92	64.4	27.0	7.60±0.11	126
DDO 75	6.65	7.86	7.85	0.98	7.18	33.5	...	7.54±0.06	793
DDO 154*	6.35	8.46	8.43	0.93	7.01	65.2	66.0	7.54±0.09	596
DDO 69	5.86	6.84	7.00	1.45	5.84	60.3	...	7.38±0.10	541
M81dwA*	5.09	7.18	7.12	0.87	5.82	45.8	...	(7.3)	138
DDO 210	5.72	6.30	6.38	1.20	5.26	66.9	67.3	(7.2)	229

Table 4.1: From left to right the columns represent: Galaxy name, Observed Integrated H I Flux, Observed H I Mass, Single dish values of the H I Mass from Huchtmeier & Richter (1986), Ratio of the single dish and the observed H I masses, M_{H2} predicted from the SFR map (details in Leroy et al. (2008)), Inclination determined from the b/a ratio in Hunter & Elmegreen (2006) under the assumption that $(b/a)_0 = 0.3$ and from gas kinematics, Metallicity and the largest angular size measured ($\theta_{LAS} = x/D$, where D is the distance to the galaxy and x is its linear size from our H I maps). For reference, the largest angular scale that can be measured with the VLA, in D configuration array (shortest baselines available), in L band (21cm) is $970''$. Also note that the total uncertainty in our H I flux calculation is dominated by the accuracy of the flux calibration (of order 5%), whereas the uncertainty in our H I mass calculation (of order 15%) is due to the uncertainty in the flux measurement and the assumption that H I is optically thin (Zwaan et al., 1997).

The nature of this agreement is discussed in Hunter et al. (2012) and, therefore here we simply note that most of the gas in the galaxies in our subsample is included in our maps. Table 4.1 also shows that DDO 53 is exceptional, with a considerably larger single dish value compared to our observed one. This, however, is due to the single dish measurement in this particular galaxy being affected by Galactic confusion.

The last column of Table 4.1 shows for each galaxy in our sample the largest angular scale measured. When comparing these values with the largest angular scale measurable with the VLA in D array configuration at L band ($970''$) we find that most of our galaxies are considerably smaller than the instrumental limitation, indicating that these galaxies are not affected by missing short spacings.

However, two of the galaxies in our sample, WLM and IC 1613, have θ_{LAS} values close to $970''$. These two galaxies are not the biggest in size in our sample but they are at less than 1 Mpc away. WLM shows good agreement between the single dish and our measured values, hence clearing any doubts regarding missing short spacings in our observations of this galaxy.

In the case of IC 1613, however, the VLA measured flux is one third lower than the single dish one. Hunter et al. (2012) attribute this discrepancy to "surface brightness sensitivity compounded over the galaxys large area", yet the high θ_{LAS} value suggests this galaxy has emission extended beyond what our instrument can measure. IC 1613 is the only galaxy in our sample which may suffer from missing short spacings.

Assuming that the 30% missing emission is localised in an extended disk with a radius of about 2.5 kpc, hence a total area of $\pi(2.5)^2\,\mathrm{kpc}^2$ distributed uniformly such that the extra emission contributes equally to each sampled pixel representing an area of $0.25\,\mathrm{kpc}^2$, a back of the envelope calculus yields that the extra flux distributed over the entire area of the galaxy is in fact less than 0.4% per pixel. With such a small contribution per pixel, missing short spacings in IC 1613 has no consequence upon our science, because in our pixel–by–pixel analysis the extra flux contribution per pixel is lower than our error bars.

Even for a considerably higher extra flux contribution per pixel, as long as the distribution of the extended, missing emission is uniform, each pixel would be underestimated by the same factor along the H I axis, so our SF plots will be shifted on the H I axis however the relation between SFRD and H I surface density would remain the same.

4.3 Neutral Gas and Stars vs. Star Formation Rate and relations therein in individual galaxies

One of the main results of the study of DDO 133 and DDO 168 presented in the previous chapter is the clear emergence of two trends, one between SFRD and H I surface density and the other between SFRD and V–band surface density. Here we extend that study to a larger sample of 18 galaxies. In Figs. 4.5 to 4.22, we present for each galaxy in our subsample a composite of six panels where we explore the relation between SFRD (traced by both FUV and Hα) and H I surface density, between SFE and neutral gas surface density, between SFE and stellar surface density as traced by 3.6 μm emission and between SFRD (traced by both FUV and Hα) and V–band surface density.

In all panels of the plots in Figs. 4.5 to 4.22, the error bars in both directions are shown in red, and in the top panels we identify upper limits in blue, areas where either there is gas above the cutoff level but no SFRD above 5σ or there is SFRD above the cutoff level but no gas above 2σ. The length of any of the blue arrows represents a 1/5th of σ (the error bar at that point) and the blue crosses indicate values that qualify as upper limits but whose error bars extend beyond the plot margins. Each point in these plots represents a resolution element of 400 pc.

An important trend present in all the galaxies of the subsample is that between SFRD and H I surface density, the denser the H I the higher the SFR. We plot this relation using both the FUV and the Hα as SF tracers for each individual galaxy and find that in general the two tracers agree, yet the relation relying on Hα as a SF tracer exhibits more scatter and samples only the high end of the relation. With the exception of DDO 187 suffering low number statistics as mentioned above, all galaxies in the subsample show increasing SFE with higher H I surface density.

If we consider the SFR per unit gas, in other words the star formation efficiency, in relation to the stellar surface density as traced by 3.6 μm (see Section 3.2.3 and also Leroy et al. (2008) and references therein for explanations on how the stellar map is derived), we find that the higher the stellar density the more efficient the star formation process is in most of the galaxies in our sample. Exceptions are DDO 133 and DDO 154, that have large error bars inherited from a poorer quality 3.6 μm map, and DDO 187, M81dwA and DDO 210 where the relation is difficult to probe due to low number statistics. Also in the SFE vs. stellar surface density plot, DDO 50 stands out again with two distinct groups of points one following an

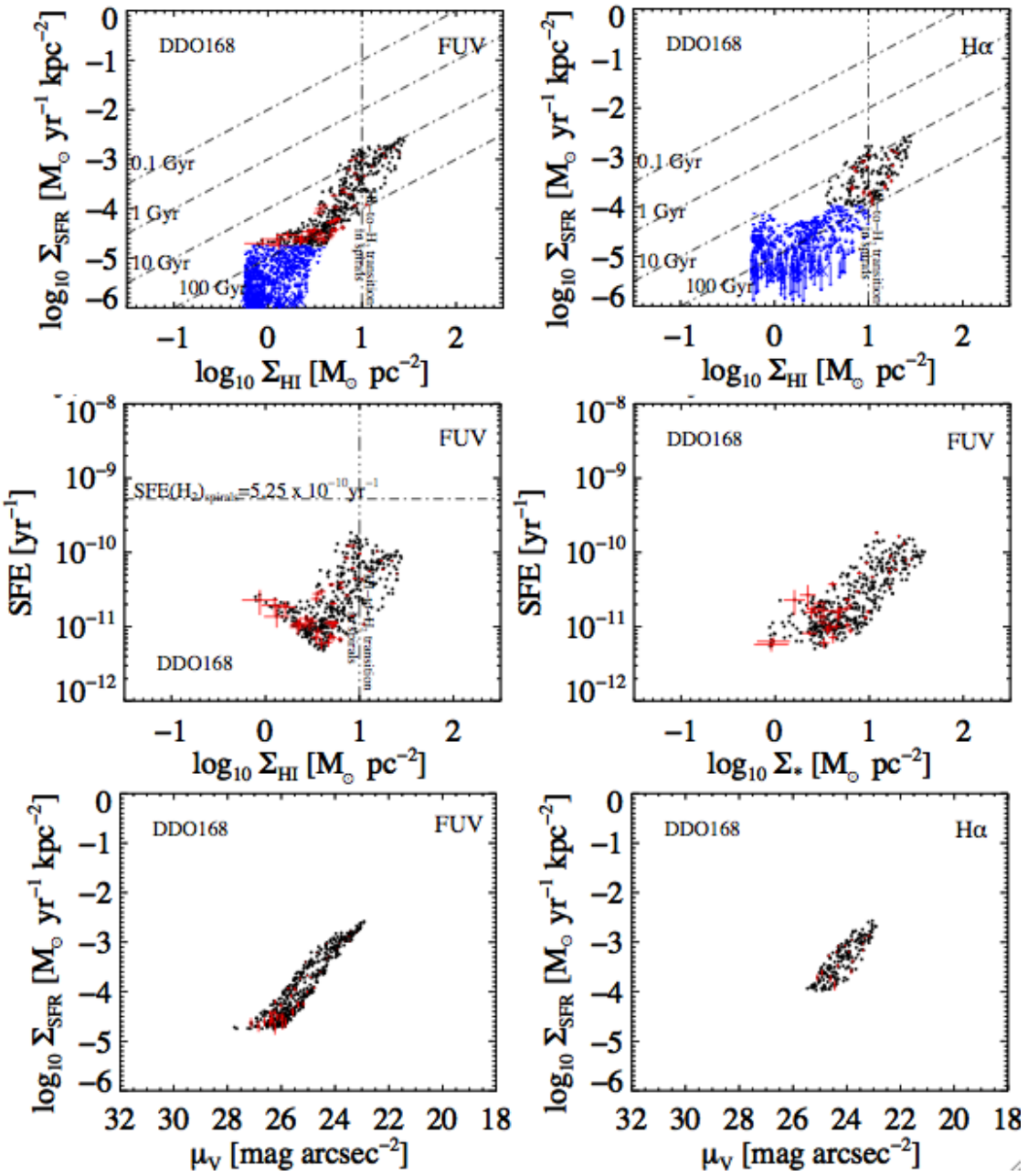

Figure 4.5: DDO 168; SFRD vs. H I surface density plotted separately for two different SF tracers, FUV (top left) and Hα (top right) and SFE vs. H I surface density (middle left) and vs. stellar surface density (based on the 3.6 μm *Spitzer* map) for FUV as an SF tracer (middle right). We also plot SFRD vs. V–band surface density plotted separately for two different SF tracers, FUV (bottom left) and Hα (bottom right). All maps used for the above plots have the same linear resolution of 400 pc. All points are independent and above a 5σ cutoff level. In red we display error bars for every 10^{th} point in the plot. With blue arrows and crosses we represent upper limits. The vertical dashed line represents an H I surface density of 10 $M_\odot$ pc^{-2}. The horizontal dashed line represents constant molecular gas SFE of 5.25×10^{-10} yr^{-1}. The other four dashed lines in the top row represent constant gas depletion times of 0.1 Gyr, 1 Gyr, 10 Gyr and 100 Gyr.

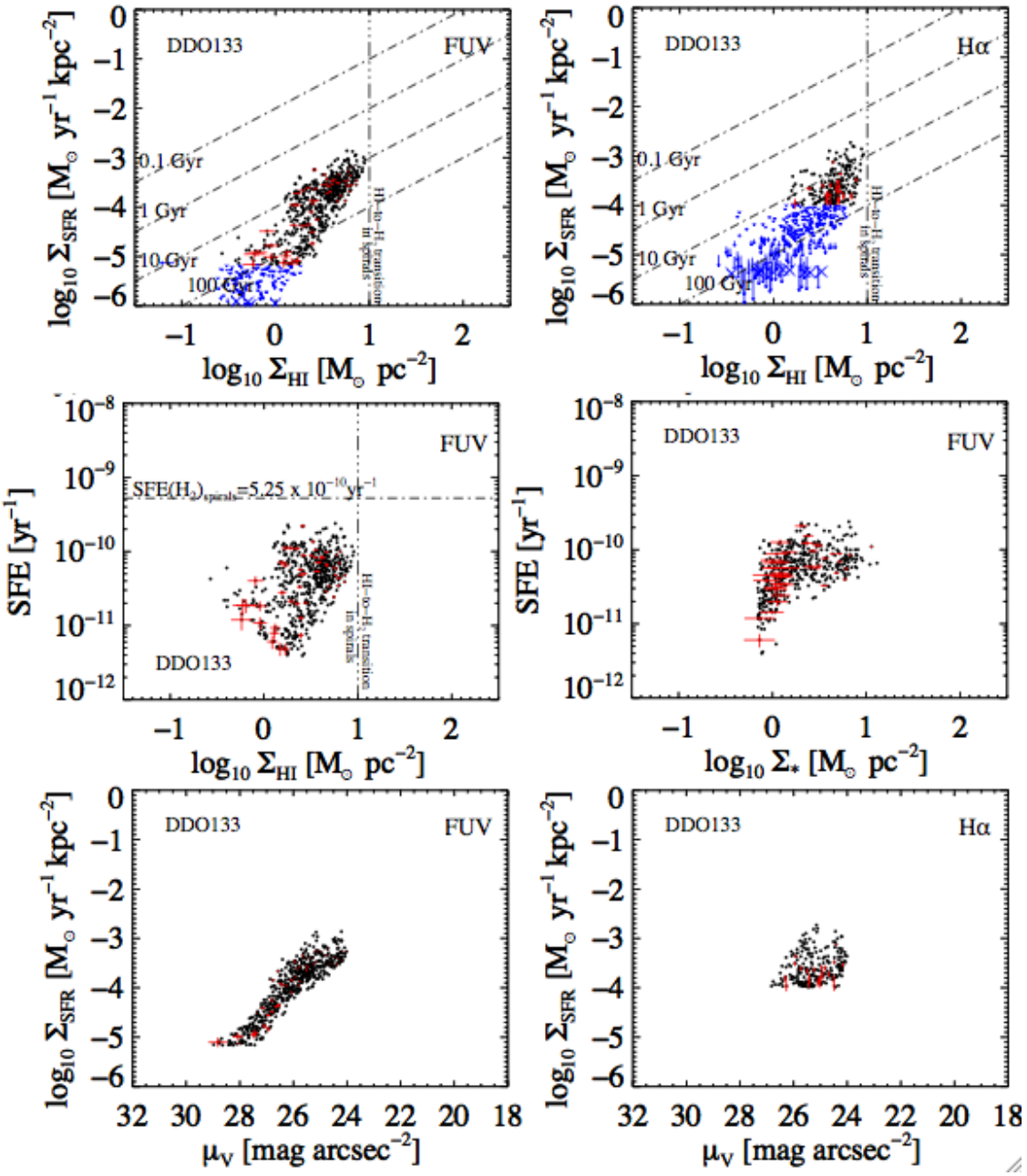

Figure 4.6: DDO 133; SFRD vs. H I surface density plotted separately for two different SF tracers, FUV (top left) and Hα (top right), and SFE vs. H I surface density (middle left) and vs. stellar surface density (based on the 3.6 μm *Spitzer* map) for FUV as an SF tracer (middle right). We also plot SFRD vs. V–band surface density plotted separately for two different SF tracers, FUV (bottom left) and Hα (bottom right). All maps used for the above plots have the same linear resolution of 400 pc. All points are independent and above a 5σ cutoff level. In red we display error bars for every 10$^{\rm th}$ point in the plot. With blue arrows and crosses we represent upper limits. The vertical dashed line represents an H I surface density of 10 $M_\odot$ pc^{-2}. The horizontal dashed line represents constant molecular gas SFE of 5.25×10^{-10} yr^{-1}. The other four dashed lines in the top row represent constant gas depletion times of 0.1 Gyr, 1 Gyr, 10 Gyr and 100 Gyr.

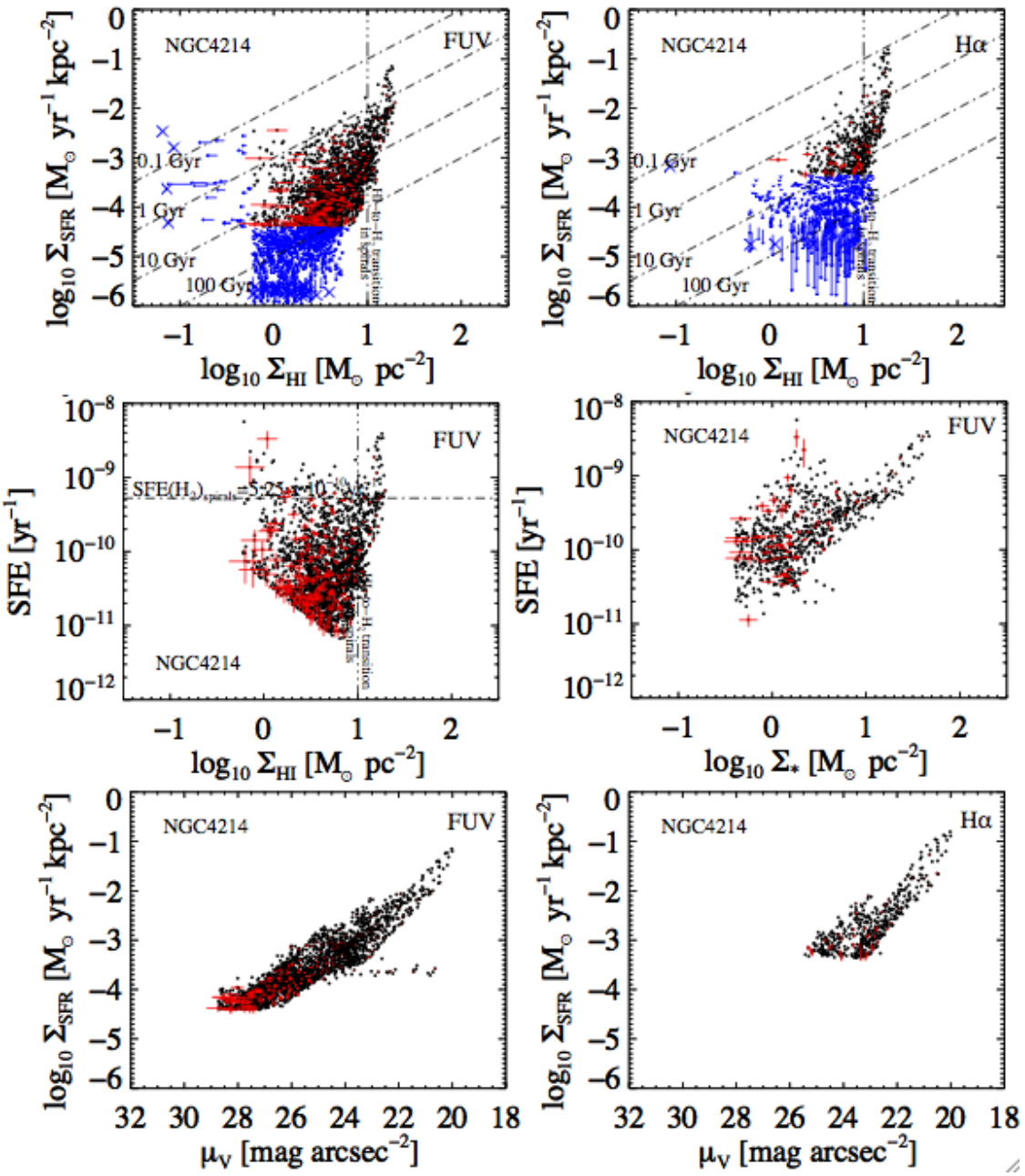

Figure 4.7: NGC 4214; SFRD vs. H I surface density plotted separately for two different SF tracers, FUV (top left) and Hα (top right), and SFE vs. H I surface density (middle left) and vs. stellar surface density (based on the 3.6 μm *Spitzer* map) for FUV as an SF tracer (middle right). We also plot SFRD vs. V–band surface density plotted separately for two different SF tracers, FUV (bottom left) and Hα (bottom right). All maps used for the above plots have the same linear resolution of 400 pc. All points are independent and above a 5σ cutoff level. In red we display error bars for every 10$^{\rm th}$ point in the plot. With blue arrows and crosses we represent upper limits. The vertical dashed line represents an H I surface density of 10 $M_\odot$ pc^{-2}. The horizontal dashed line represents constant molecular gas SFE of 5.25×10^{-10} yr^{-1}. The other four dashed lines in the top row represent constant gas depletion times of 0.1 Gyr, 1 Gyr, 10 Gyr and 100 Gyr.

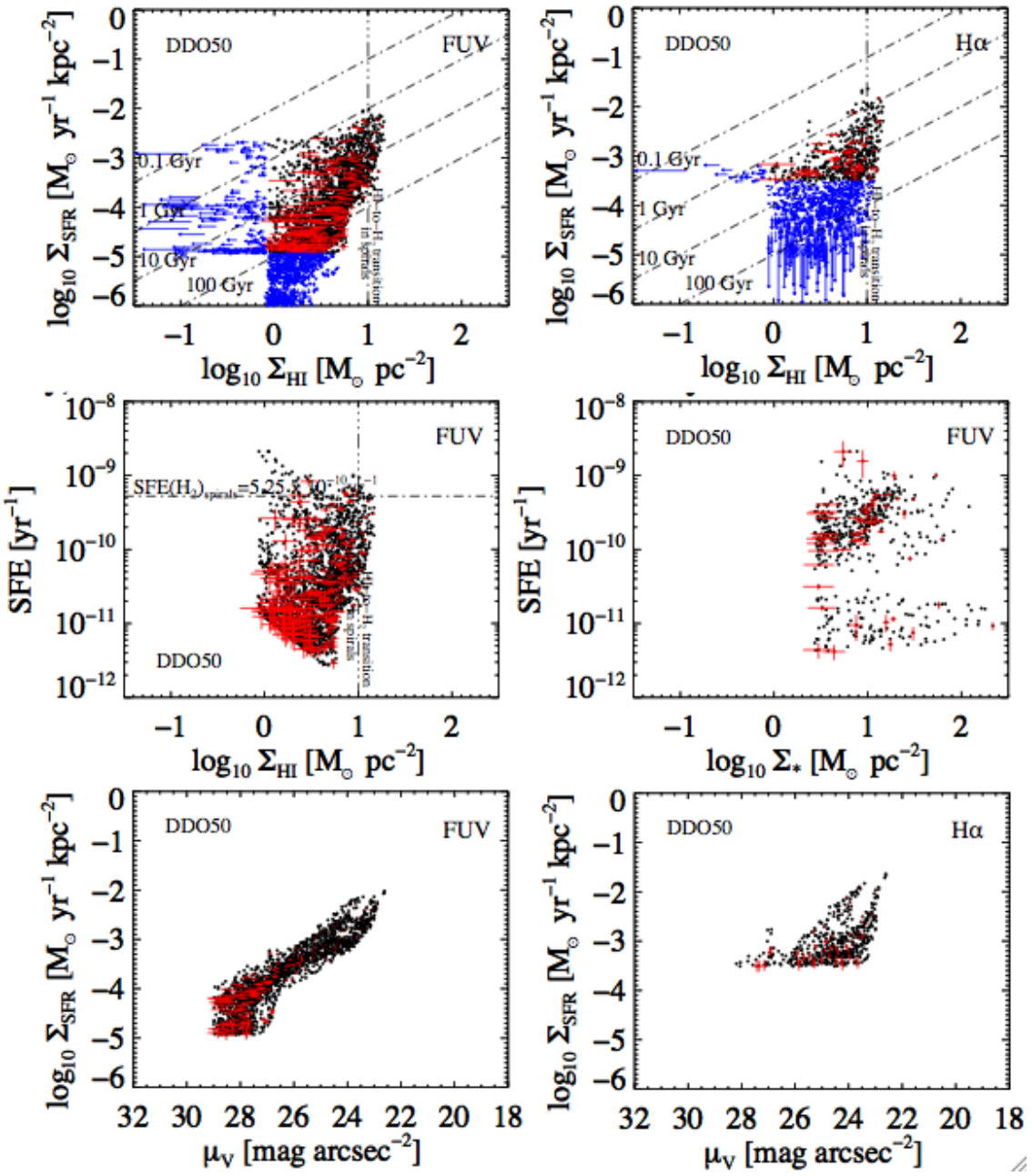

Figure 4.8: DDO 50; SFRD vs. H I surface density plotted separately for two different SF tracers, FUV (top left) and Hα (top right), and SFE vs. H I surface density (middle left) and vs. stellar surface density (based on the 3.6 μm *Spitzer* map) for FUV as an SF tracer (middle right). We also plot SFRD vs. V–band surface density plotted separately for two different SF tracers, FUV (bottom left) and Hα (bottom right). All maps used for the above plots have the same linear resolution of 400 pc. All points are independent and above a 5σ cutoff level. In red we display error bars for every 10$^{\rm th}$ point in the plot. With blue arrows and crosses we represent upper limits. The vertical dashed line represents an H I surface density of 10 $M_\odot$ pc^{-2}. The horizontal dashed line represents constant molecular gas SFE of 5.25×10^{-10} yr^{-1}. The other four dashed lines in the top row represent constant gas depletion times of 0.1 Gyr, 1 Gyr, 10 Gyr and 100 Gyr.

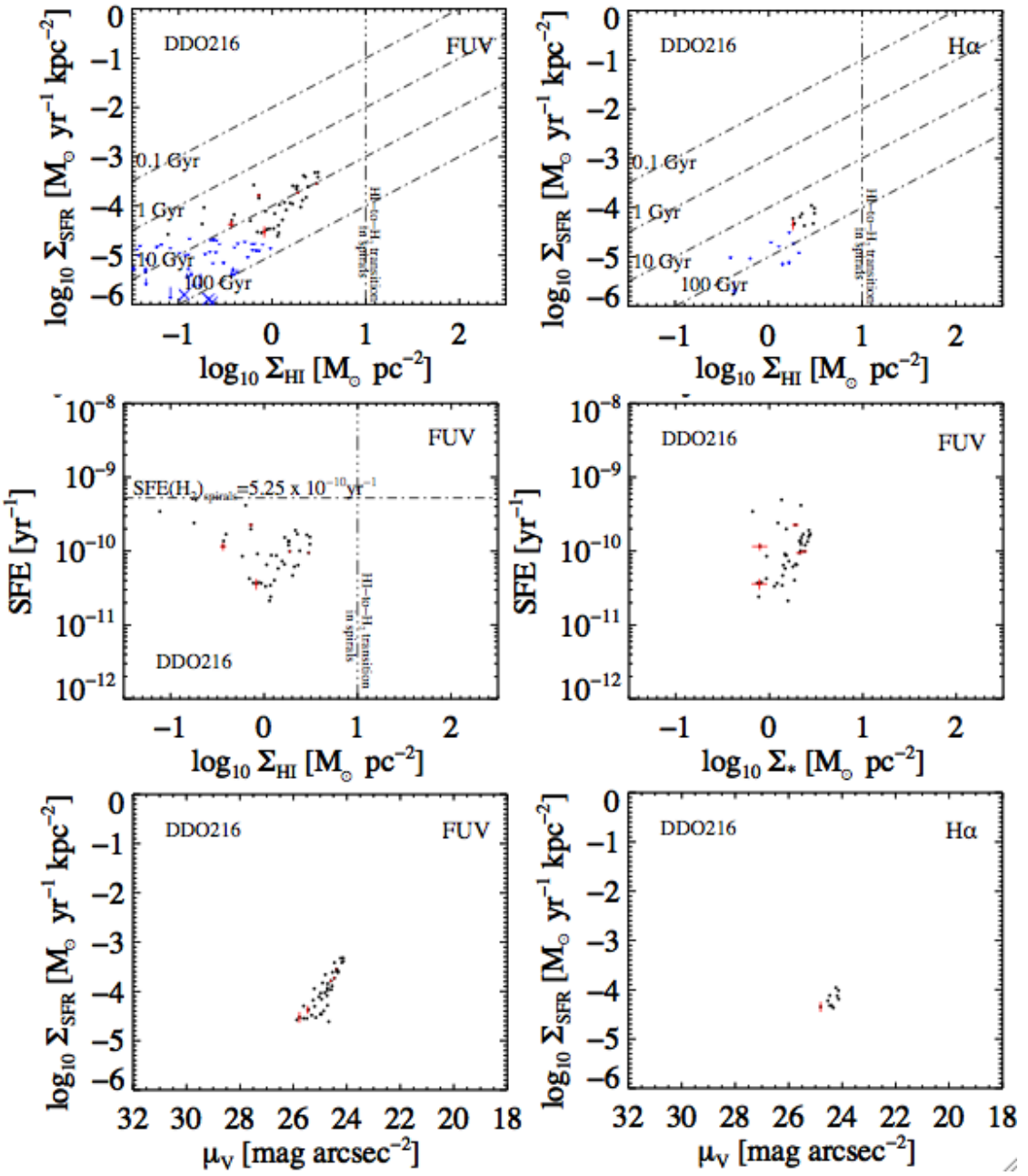

Figure 4.9: DDO 216; SFRD vs. H I surface density plotted separately for two different SF tracers, FUV (top left) and Hα (top right), and SFE vs. H I surface density (middle left) and vs. stellar surface density (based on the 3.6 μm *Spitzer* map) for FUV as an SF tracer (middle right). We also plot SFRD vs. V–band surface density plotted separately for two different SF tracers, FUV (bottom left) and Hα (bottom right). All maps used for the above plots have the same linear resolution of 400 pc. All points are independent and above a 5σ cutoff level. In red we display error bars for every $10^{\rm th}$ point in the plot. With blue arrows and crosses we represent upper limits. The vertical dashed line represents an H I surface density of 10 $M_\odot$ pc^{-2}. The horizontal dashed line represents constant molecular gas SFE of 5.25×10^{-10} yr^{-1}. The other four dashed lines in the top row represent constant gas depletion times of 0.1 Gyr, 1 Gyr, 10 Gyr and 100 Gyr.

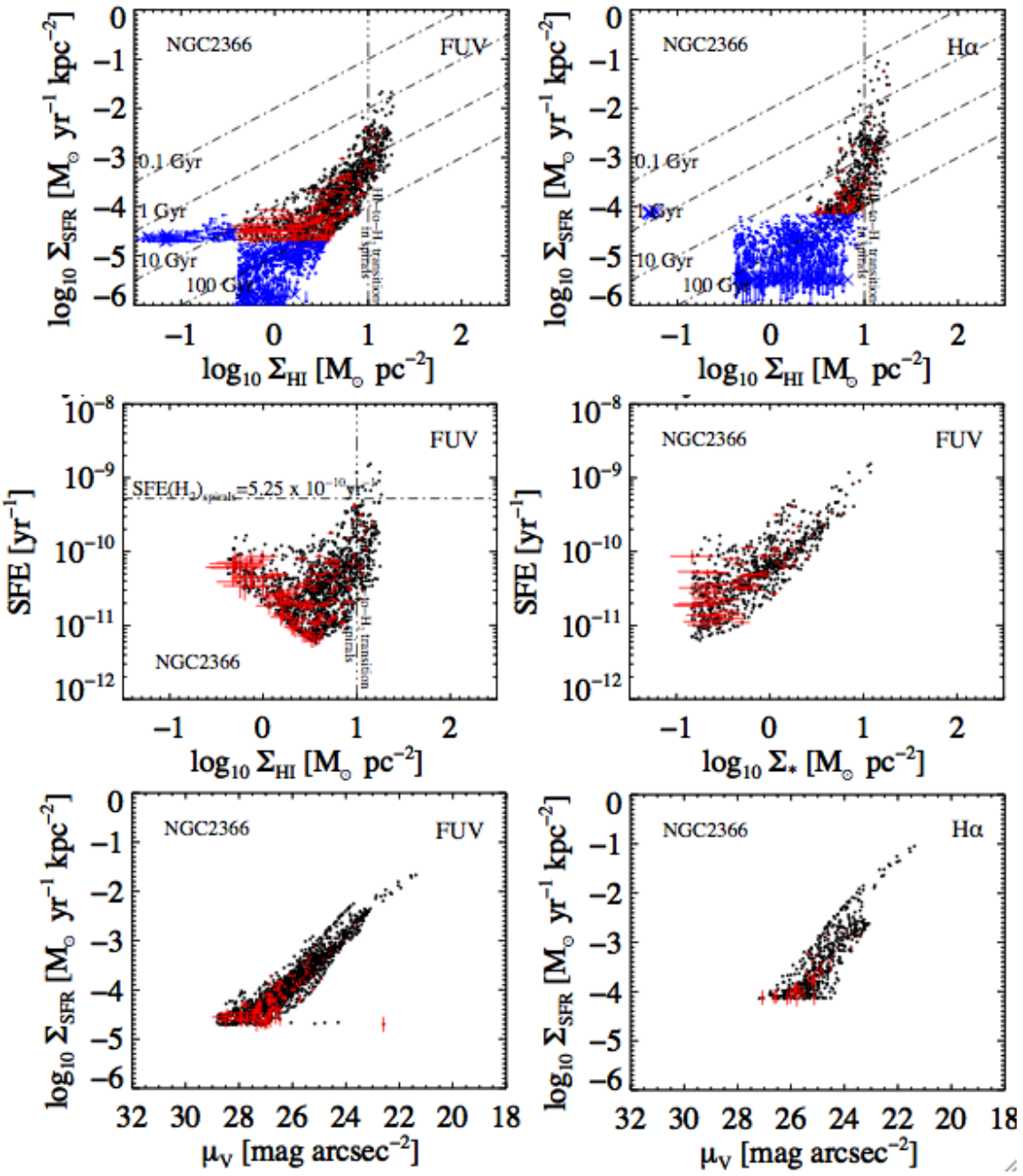

Figure 4.10: NGC 2366; SFRD vs. H I surface density plotted separately for two different SF tracers, FUV (top left) and Hα (top right), and SFE vs. H I surface density (middle left) and vs. stellar surface density (based on the 3.6 μm *Spitzer* map) for FUV as an SF tracer (middle right). We also plot SFRD vs. *V*–band surface density plotted separately for two different SF tracers, FUV (bottom left) and Hα (bottom right). All maps used for the above plots have the same linear resolution of 400 pc. All points are independent and above a 5σ cutoff level. In red we display error bars for every 10$^{\rm th}$ point in the plot. With blue arrows and crosses we represent upper limits. The vertical dashed line represents an H I surface density of 10 $M_\odot$ pc^{-2}. The horizontal dashed line represents constant molecular gas SFE of 5.25×10^{-10} yr^{-1}. The other four dashed lines in the top row represent constant gas depletion times of 0.1 Gyr, 1 Gyr, 10 Gyr and 100 Gyr.

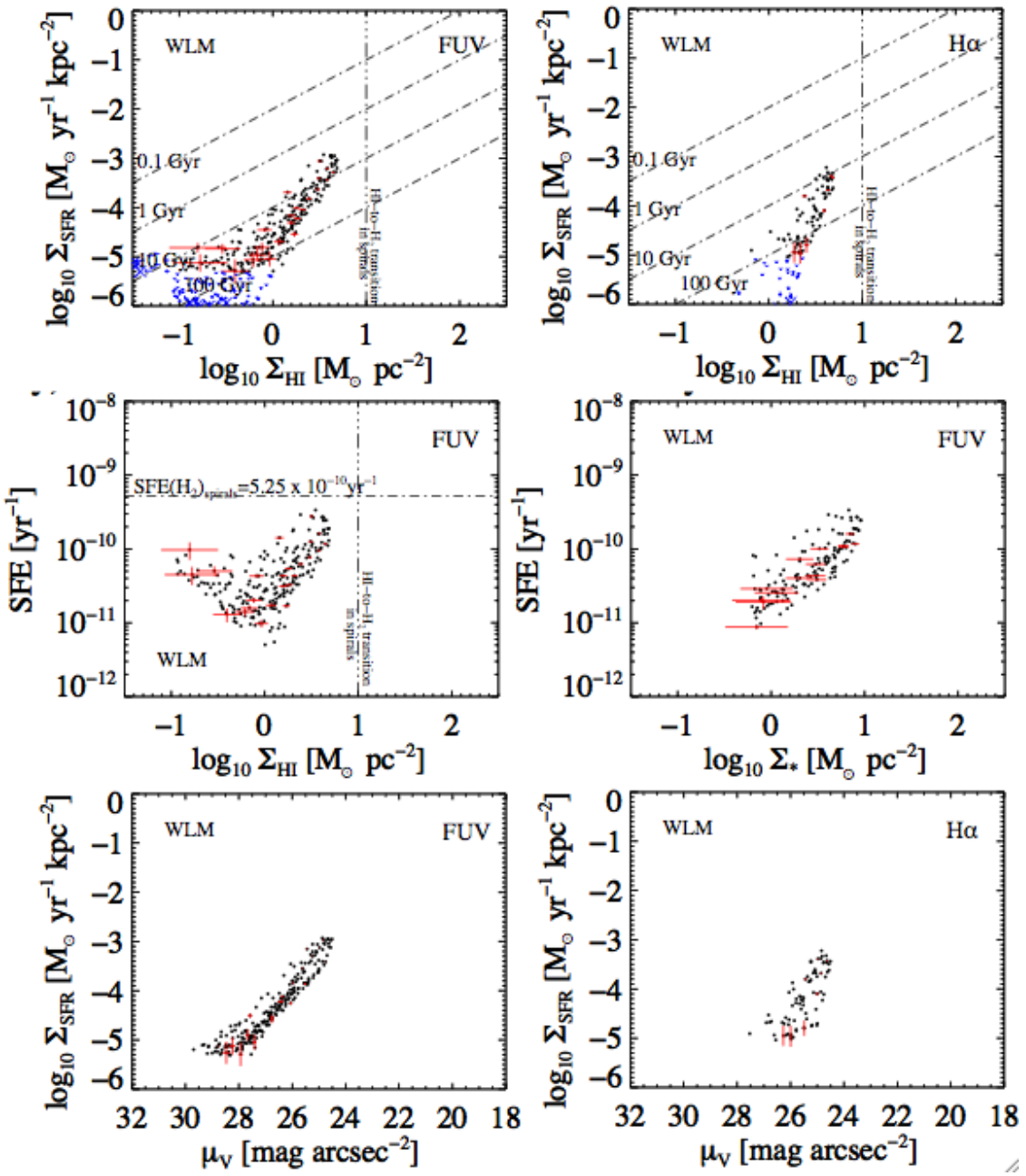

Figure 4.11: WLM; SFRD vs. H I surface density plotted separately for two different SF tracers, FUV (top left) and Hα (top right), and SFE vs. H I surface density (middle left) and vs. stellar surface density (based on the 3.6 μm *Spitzer* map) for FUV as an SF tracer (middle right). We also plot SFRD vs. V–band surface density plotted separately for two different SF tracers, FUV (bottom left) and Hα (bottom right). All maps used for the above plots have the same linear resolution of 400 pc. All points are independent and above a 5σ cutoff level. In red we display error bars for every 10^{th} point in the plot. With blue arrows and crosses we represent upper limits. The vertical dashed line represents an H I surface density of 10 $M_\odot$ pc^{-2}. The horizontal dashed line represents constant molecular gas SFE of 5.25×10^{-10} yr^{-1}. The other four dashed lines in the top row represent constant gas depletion times of 0.1 Gyr, 1 Gyr, 10 Gyr and 100 Gyr.

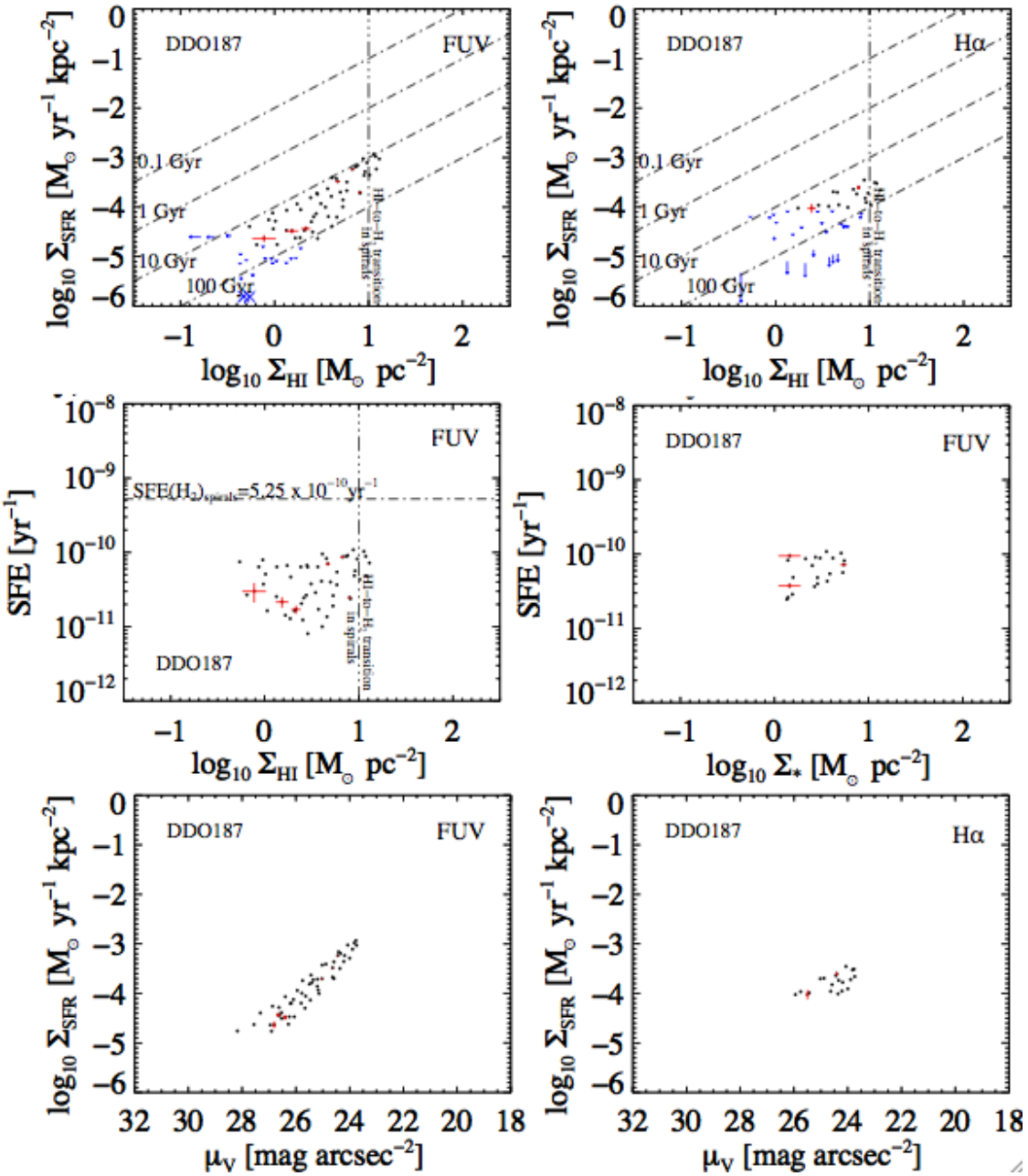

Figure 4.12: DDO 187; SFRD vs. H I surface density plotted separately for two different SF tracers, FUV (top left) and Hα (top right), and SFE vs. H I surface density (middle left) and vs. stellar surface density (based on the 3.6 μm *Spitzer* map) for FUV as an SF tracer (middle right). We also plot SFRD vs. *V*–band surface density plotted separately for two different SF tracers, FUV (bottom left) and Hα (bottom right). All maps used for the above plots have the same linear resolution of 400 pc. All points are independent and above a 5σ cutoff level. In red we display error bars for every 10^{th} point in the plot. With blue arrows and crosses we represent upper limits. The vertical dashed line represents an H I surface density of 10 $M_\odot$ pc^{-2}. The horizontal dashed line represents constant molecular gas SFE of 5.25×10^{-10} yr^{-1}. The other four dashed lines in the top row represent constant gas depletion times of 0.1 Gyr, 1 Gyr, 10 Gyr and 100 Gyr.

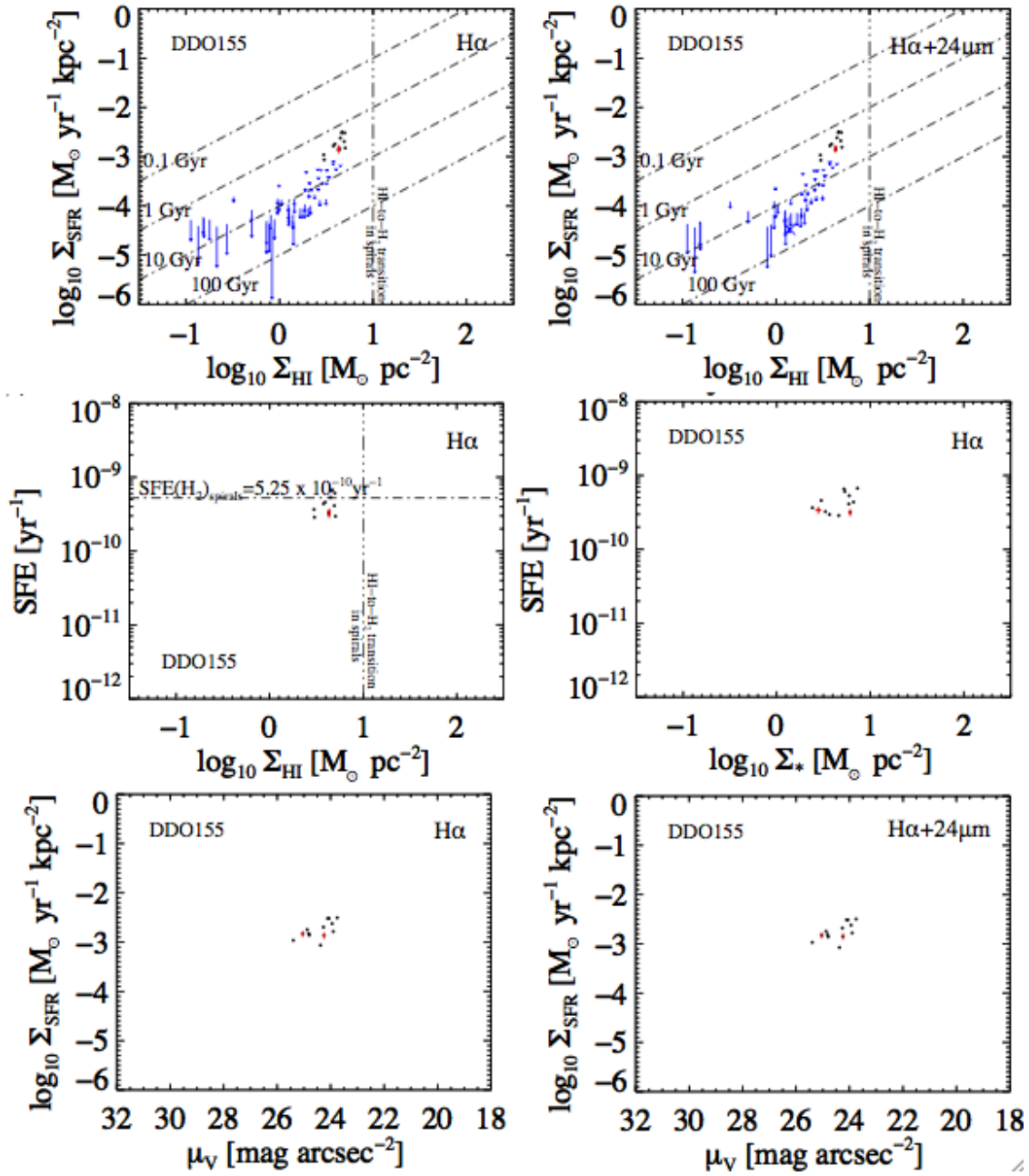

Figure 4.13: DDO 155; SFRD vs. H I surface density plotted separately for two different SF tracers, Hα (top left) and Hα+24 μm (top right), and SFE vs. H I surface density (middle left) and vs. stellar surface density (based on the 3.6 μm *Spitzer* map) for Hα as an SF tracer (middle right). We also plot SFRD vs. V–band surface density plotted separately for two different SF tracers, Hα (bottom left) and Hα+24 μm (bottom right). All maps used for the above plots have the same linear resolution of 400 pc. All points are independent and above a 5σ cutoff level. In red we display error bars for every 10$^{\rm th}$ point in the plot. With blue arrows and crosses we represent upper limits.The vertical dashed line represents an H I surface density of 10 $M_\odot$ pc^{-2}. The horizontal dashed line represents constant molecular gas SFE of 5.25×10^{-10} yr^{-1}. The other four dashed lines in the top row represent constant gas depletion times of 0.1 Gyr, 1 Gyr, 10 Gyr and 100 Gyr.

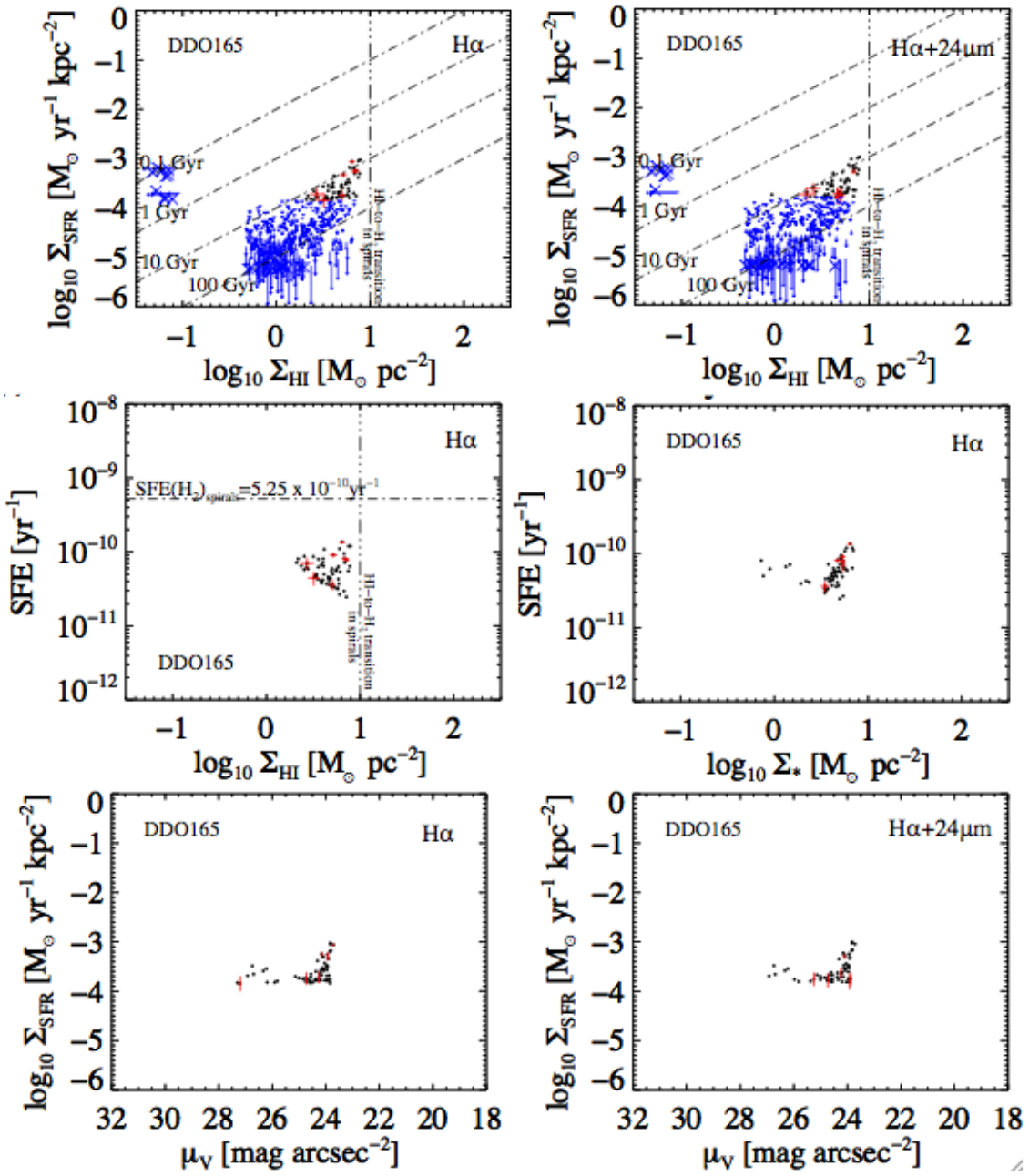

Figure 4.14: DDO 165; SFRD vs. H I surface density plotted separately for two different SF tracers, Hα (top left) and Hα+24 μm (top right), and SFE vs. H I surface density (middle left) and vs. stellar surface density (based on the 3.6 μm *Spitzer* map) for Hα as an SF tracer (middle right). We also plot SFRD vs. V–band surface density plotted separately for two different SF tracers, Hα (bottom left) and Hα+24 μm (bottom right). All maps used for the above plots have the same linear resolution of 400 pc. All points are independent and above a 5σ cutoff level. In red we display error bars for every 10$^{\rm th}$ point in the plot. With blue arrows and crosses we represent upper limits.The vertical dashed line represents an H I surface density of 10 $M_\odot$ pc^{-2}. The horizontal dashed line represents constant molecular gas SFE of 5.25×10^{-10} yr^{-1}. The other four dashed lines in the top row represent constant gas depletion times of 0.1 Gyr, 1 Gyr, 10 Gyr and 100 Gyr.

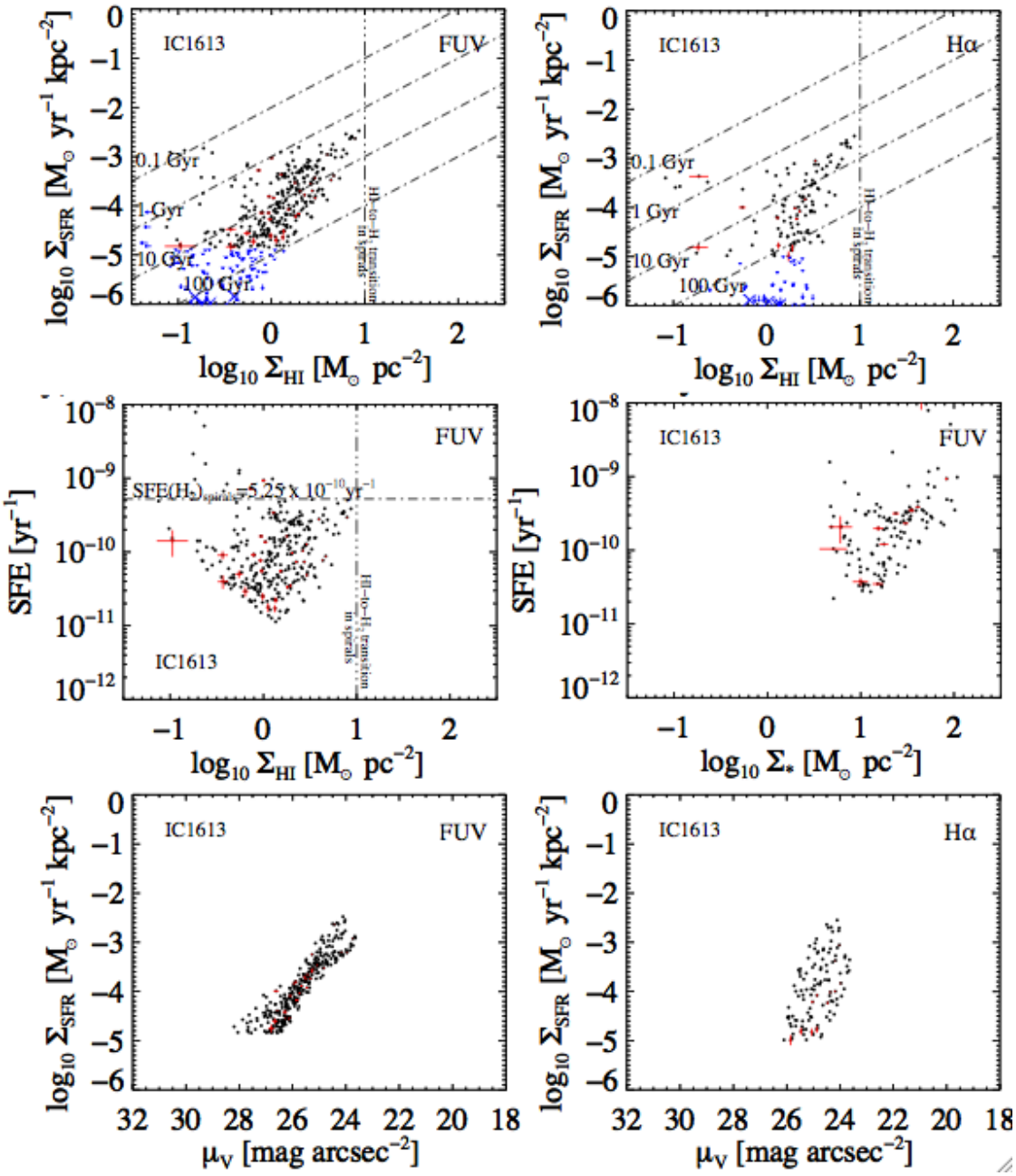

Figure 4.15: IC 1613; SFRD vs. H I surface density plotted separately for two different SF tracers, FUV (top left) and Hα (top right), and SFE vs. H I surface density (middle left) and vs. stellar surface density (based on the 3.6 μm *Spitzer* map) for FUV as an SF tracer (middle right). We also plot SFRD vs. V–band surface density plotted separately for two different SF tracers, FUV (bottom left) and Hα (bottom right). All maps used for the above plots have the same linear resolution of 400 pc. All points are independent and above a 5σ cutoff level. In red we display error bars for every $10^{\rm th}$ point in the plot. With blue arrows and crosses we represent upper limits. The vertical dashed line represents an H I surface density of 10 $M_\odot$ pc^{-2}. The horizontal dashed line represents constant molecular gas SFE of 5.25×10^{-10} yr^{-1}. The other four dashed lines in the top row represent constant gas depletion times of 0.1 Gyr, 1 Gyr, 10 Gyr and 100 Gyr.

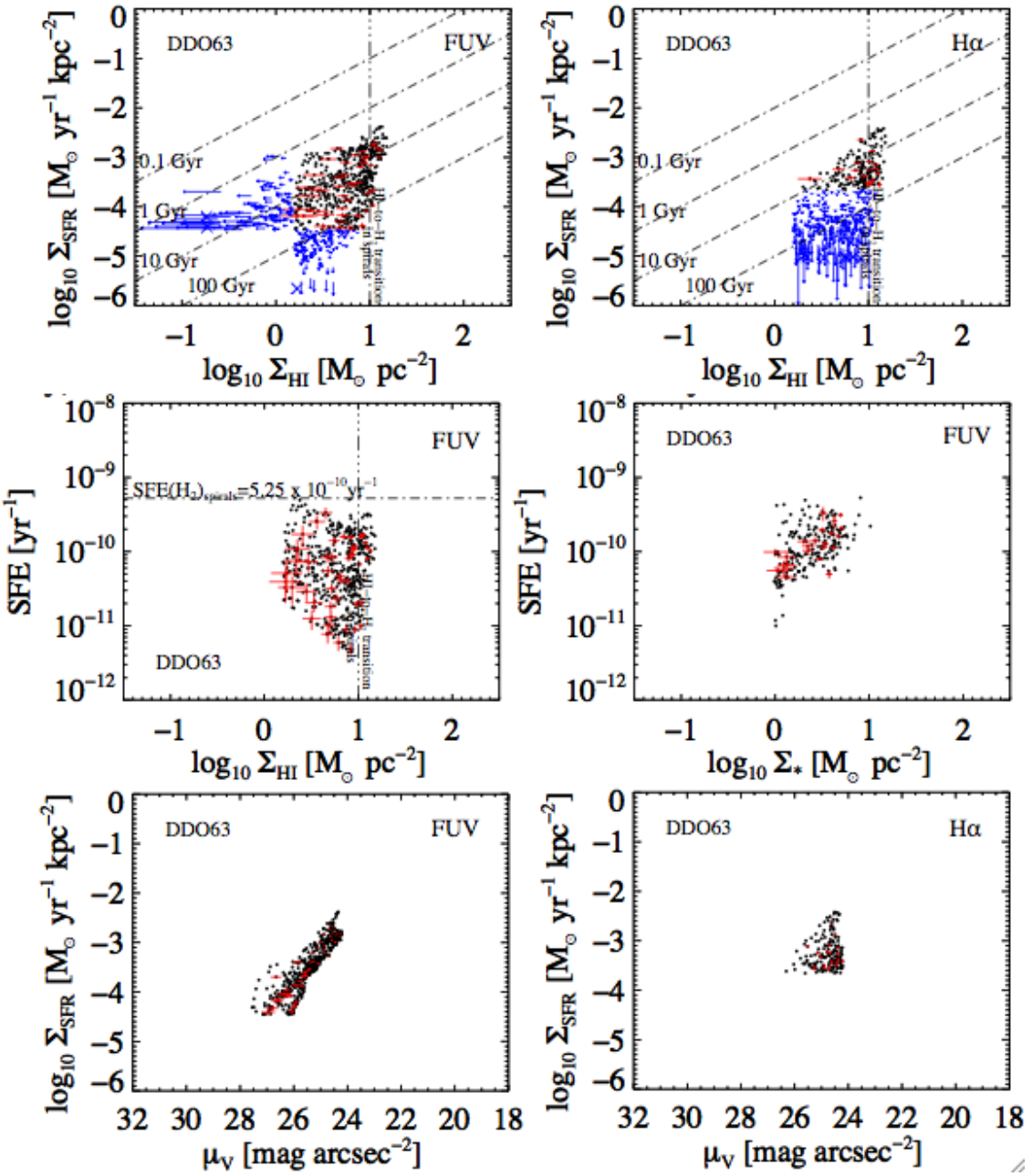

Figure 4.16: DDO 63; SFRD vs. H I surface density plotted separately for two different SF tracers, FUV (top left) and Hα (top right), and SFE vs. H I surface density (middle left) and vs. stellar surface density (based on the 3.6 μm *Spitzer* map) for FUV as an SF tracer (middle right). We also plot SFRD vs. V–band surface density plotted separately for two different SF tracers, FUV (bottom left) and Hα (bottom right). All maps used for the above plots have the same linear resolution of 400 pc. All points are independent and above a 5σ cutoff level. In red we display error bars for every 10$^{\rm th}$ point in the plot. With blue arrows and crosses we represent upper limits. The vertical dashed line represents an H I surface density of 10 $M_\odot$ pc^{-2}. The horizontal dashed line represents constant molecular gas SFE of 5.25×10^{-10} yr^{-1}. The other four dashed lines in the top row represent constant gas depletion times of 0.1 Gyr, 1 Gyr, 10 Gyr and 100 Gyr.

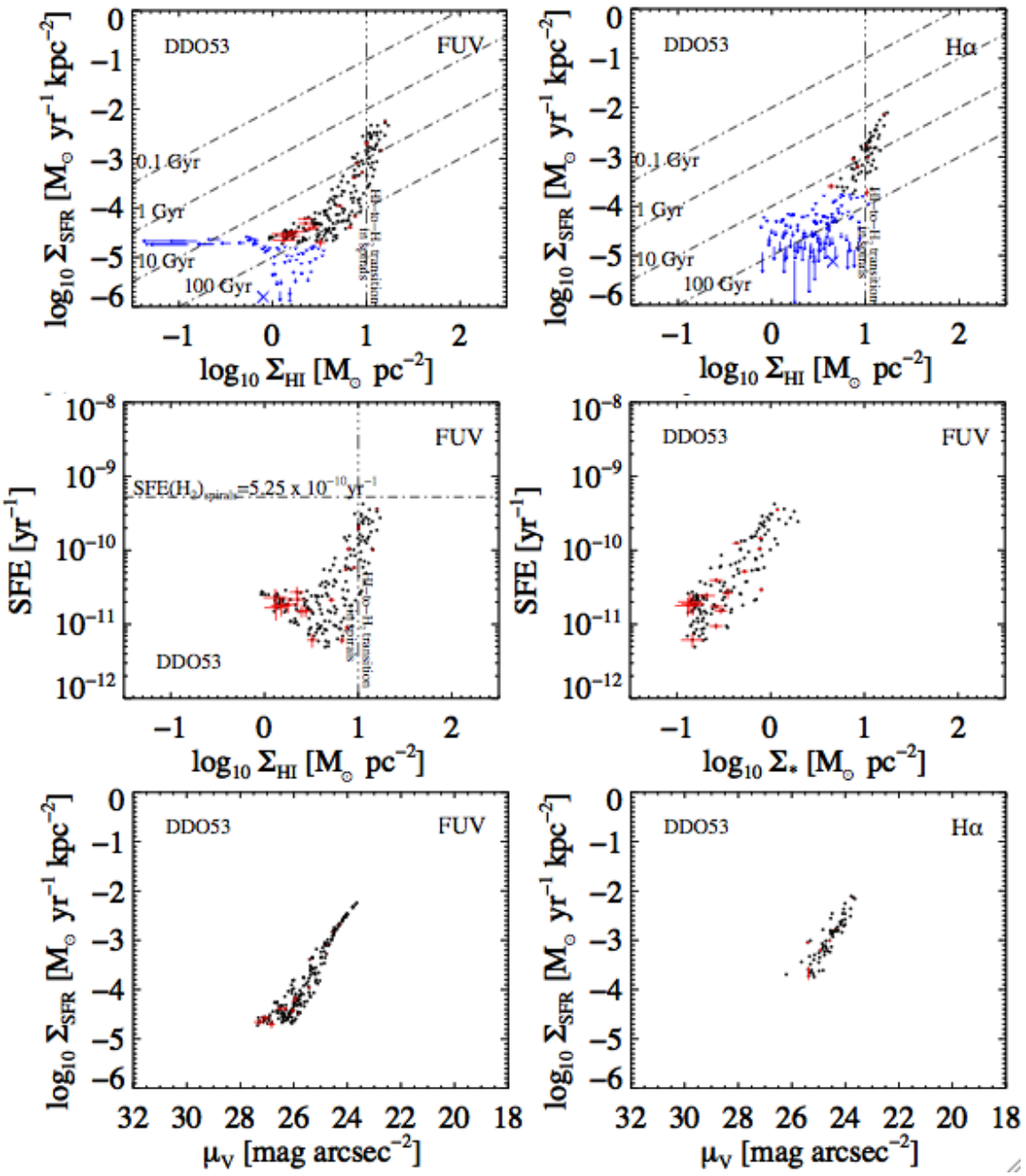

Figure 4.17: DDO 53; SFRD vs. H I surface density plotted separately for two different SF tracers, FUV (top left) and Hα (top right), and SFE vs. H I surface density (middle left) and vs. stellar surface density (based on the 3.6 μm *Spitzer* map) for FUV as an SF tracer (middle right). We also plot SFRD vs. V–band surface density plotted separately for two different SF tracers, FUV (bottom left) and Hα (bottom right). All maps used for the above plots have the same linear resolution of 400 pc. All points are independent and above a 5σ cutoff level. In red we display error bars for every $10^{\rm th}$ point in the plot. With blue arrows and crosses we represent upper limits. The vertical dashed line represents an H I surface density of 10 $M_\odot$ pc^{-2}. The horizontal dashed line represents constant molecular gas SFE of 5.25×10^{-10} yr^{-1}. The other four dashed lines in the top row represent constant gas depletion times of 0.1 Gyr, 1 Gyr, 10 Gyr and 100 Gyr.

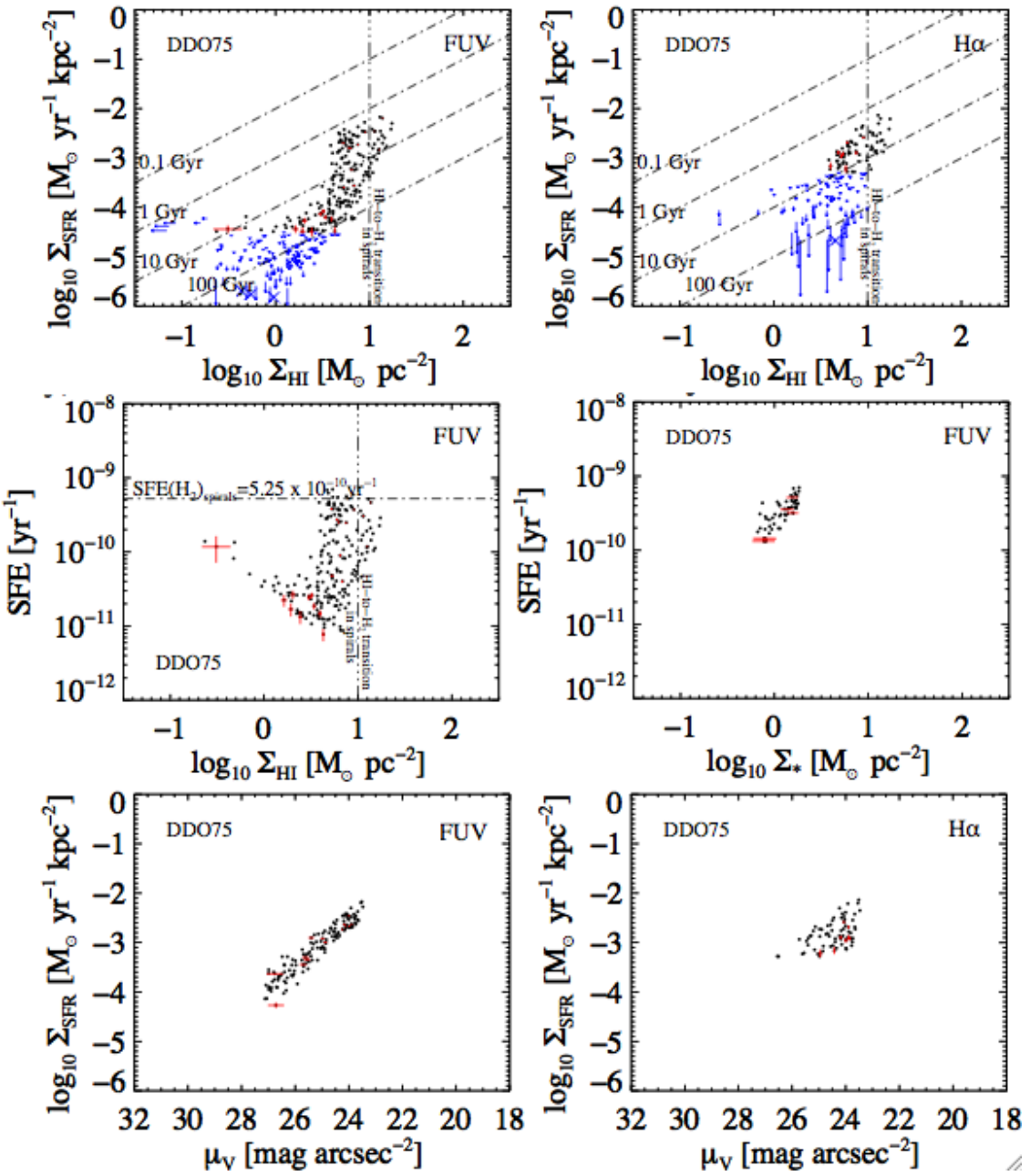

Figure 4.18: DDO 75; SFRD vs. H I surface density plotted separately for two different SF tracers, FUV (top left) and Hα (top right), and SFE vs. H I surface density (middle left) and vs. stellar surface density (based on the 3.6 μm *Spitzer* map) for FUV as an SF tracer (middle right). We also plot SFRD vs. *V*–band surface density plotted separately for two different SF tracers, FUV (bottom left) and Hα (bottom right). All maps used for the above plots have the same linear resolution of 400 pc. All points are independent and above a 5σ cutoff level. In red we display error bars for every 10$^{\rm th}$ point in the plot. With blue arrows and crosses we represent upper limits. The vertical dashed line represents an H I surface density of 10 $M_\odot$ pc^{-2}. The horizontal dashed line represents constant molecular gas SFE of 5.25×10^{-10} yr^{-1}. The other four dashed lines in the top row represent constant gas depletion times of 0.1 Gyr, 1 Gyr, 10 Gyr and 100 Gyr.

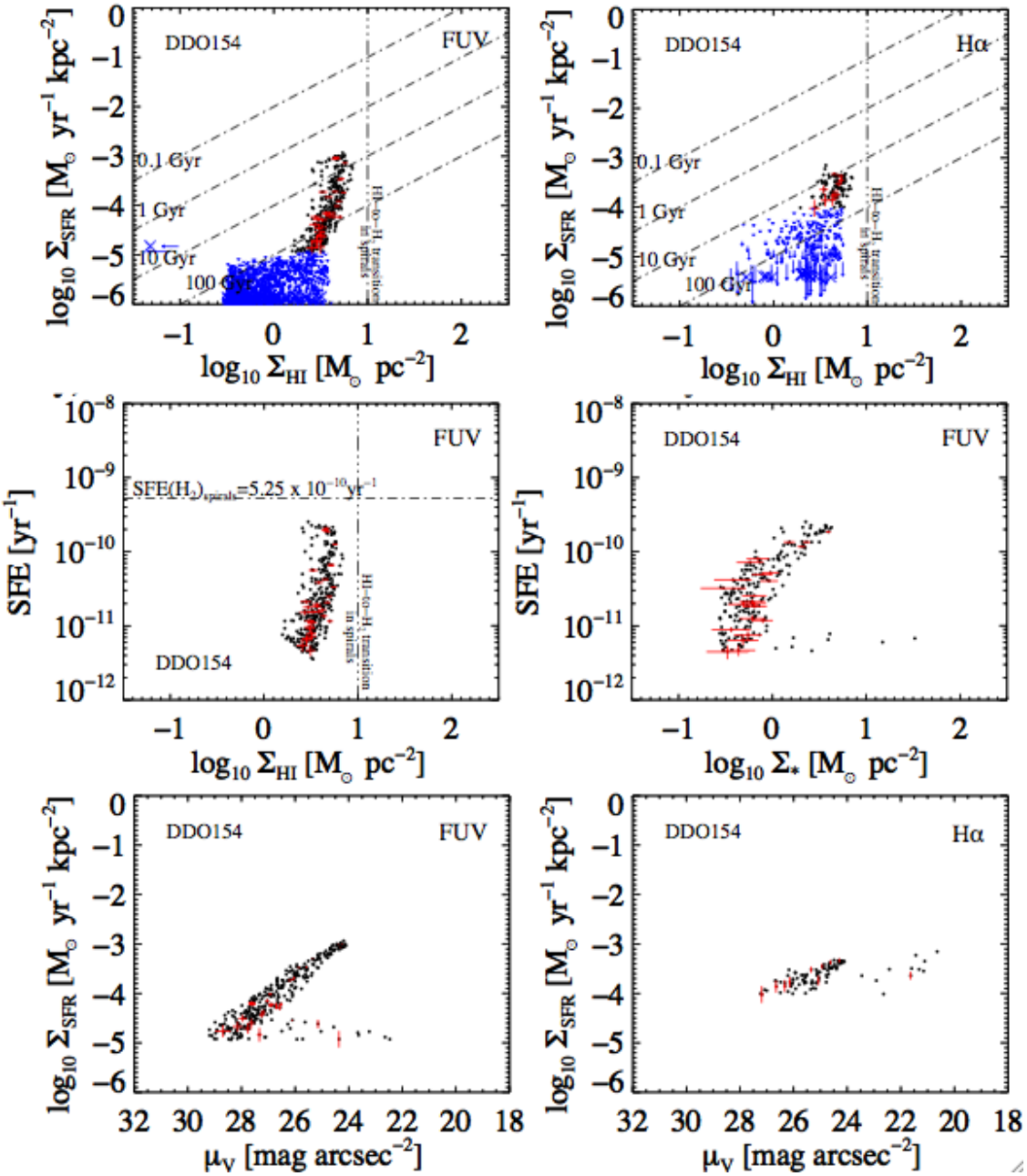

Figure 4.19: DDO 154; SFRD vs. H I surface density plotted separately for two different SF tracers, FUV (top left) and Hα (top right), and SFE vs. H I surface density (middle left) and vs. stellar surface density (based on the 3.6 μm *Spitzer* map) for FUV as an SF tracer (middle right). We also plot SFRD vs. V–band surface density plotted separately for two different SF tracers, FUV (bottom left) and Hα (bottom right). All maps used for the above plots have the same linear resolution of 400 pc. All points are independent and above a 5σ cutoff level. In red we display error bars for every 10$^{\rm th}$ point in the plot. With blue arrows and crosses we represent upper limits. The vertical dashed line represents an H I surface density of 10 $M_\odot$ pc^{-2}. The horizontal dashed line represents constant molecular gas SFE of 5.25×10^{-10} yr^{-1}. The other four dashed lines in the top row represent constant gas depletion times of 0.1 Gyr, 1 Gyr, 10 Gyr and 100 Gyr.

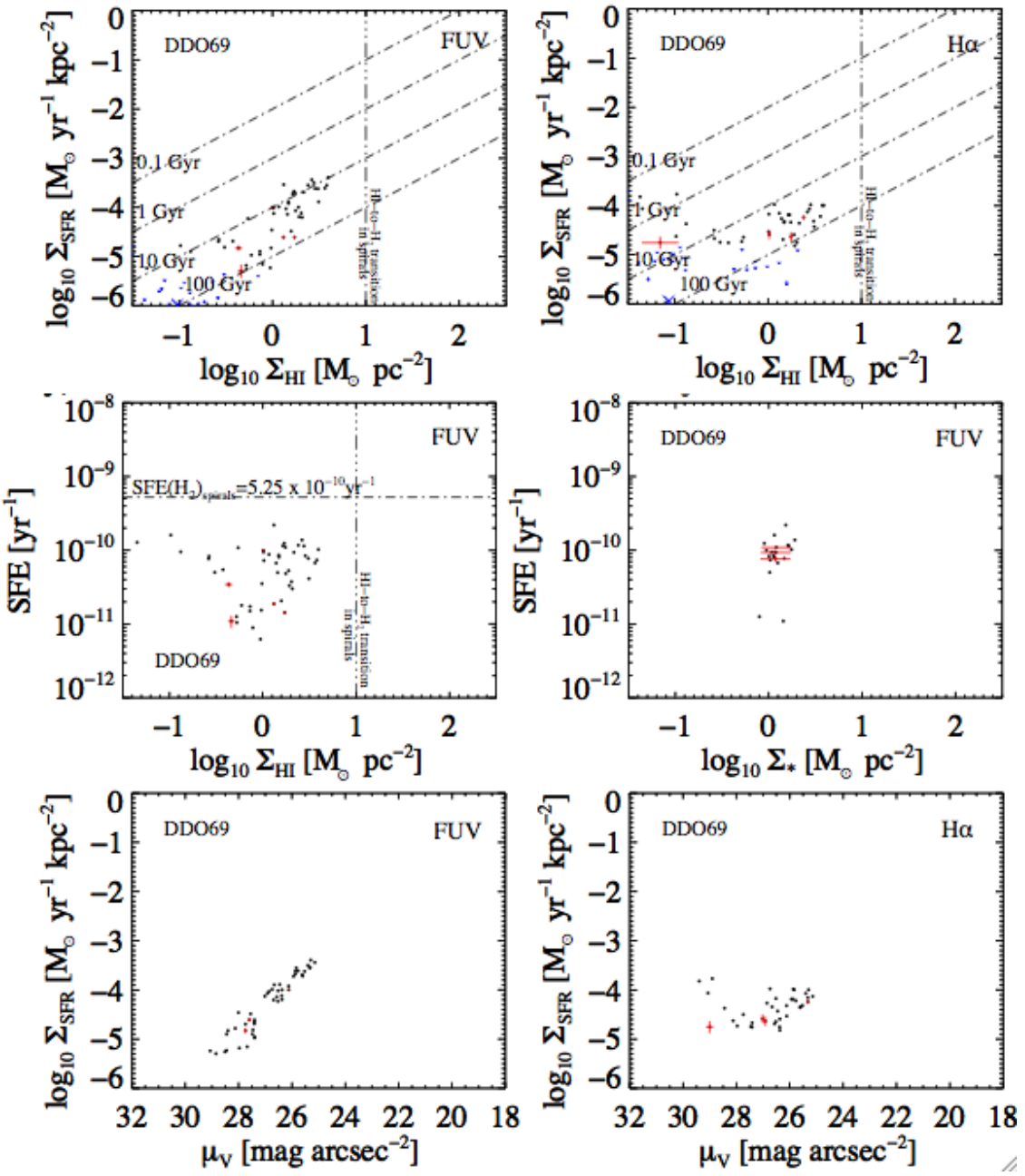

Figure 4.20: DDO 69; SFRD vs. H I surface density plotted separately for two different SF tracers, FUV (top left) and Hα (top right), and SFE vs. H I surface density (middle left) and vs. stellar surface density (based on the 3.6 μm *Spitzer* map) for FUV as an SF tracer (middle right). We also plot SFRD vs. *V*–band surface density plotted separately for two different SF tracers, FUV (bottom left) and Hα (bottom right). All maps used for the above plots have the same linear resolution of 400 pc. All points are independent and above a 5σ cutoff level. In red we display error bars for every 10$^{\rm th}$ point in the plot. With blue arrows and crosses we represent upper limits. The vertical dashed line represents an H I surface density of 10 $M_\odot$ pc^{-2}. The horizontal dashed line represents constant molecular gas SFE of 5.25×10^{-10} yr^{-1}. The other four dashed lines in the top row represent constant gas depletion times of 0.1 Gyr, 1 Gyr, 10 Gyr and 100 Gyr.

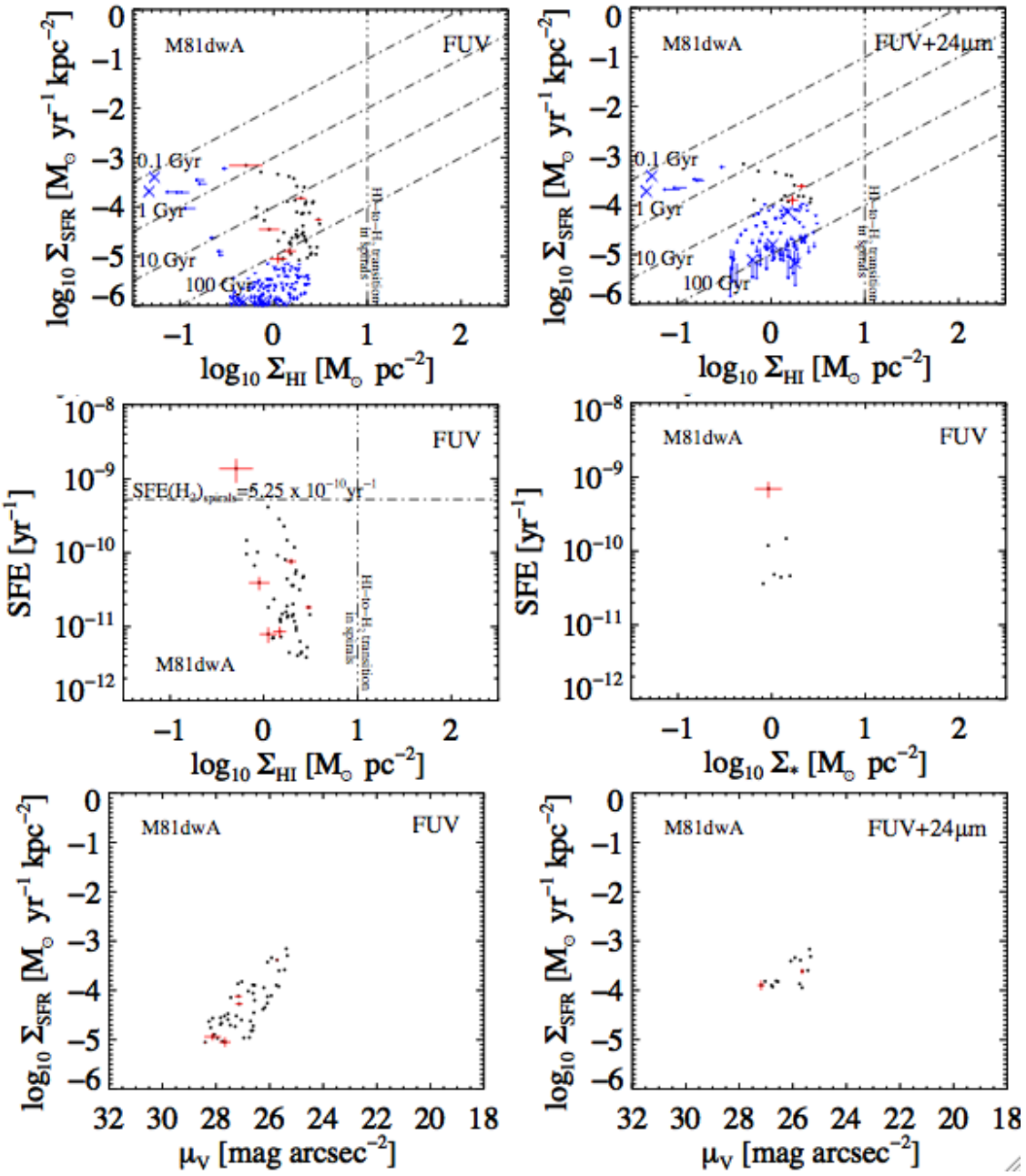

Figure 4.21: M81dwA; SFRD vs. H I surface density plotted separately for two different SF tracers, FUV (top left) and FUV+24 μm (top right), and SFE vs. H I surface density (middle left) and vs. stellar surface density (based on the 3.6 μm *Spitzer* map) for FUV as an SF tracer (middle right). We also plot SFRD vs. V–band surface density plotted separately for two different SF tracers, FUV (bottom left) and FUV+24 μm (bottom right). All maps used for the above plots have the same linear resolution of 400 pc. All points are independent and above a 5σ cutoff level. In red we display error bars for every 10^{th} point in the plot. With blue arrows and crosses we represent upper limits.The vertical dashed line represents an H I surface density of 10 $M_\odot$ pc^{-2}. The horizontal dashed line represents constant molecular gas SFE of 5.25×10^{-10} yr^{-1}. The other four dashed lines in the top row represent constant gas depletion times of 0.1 Gyr, 1 Gyr, 10 Gyr and 100 Gyr.

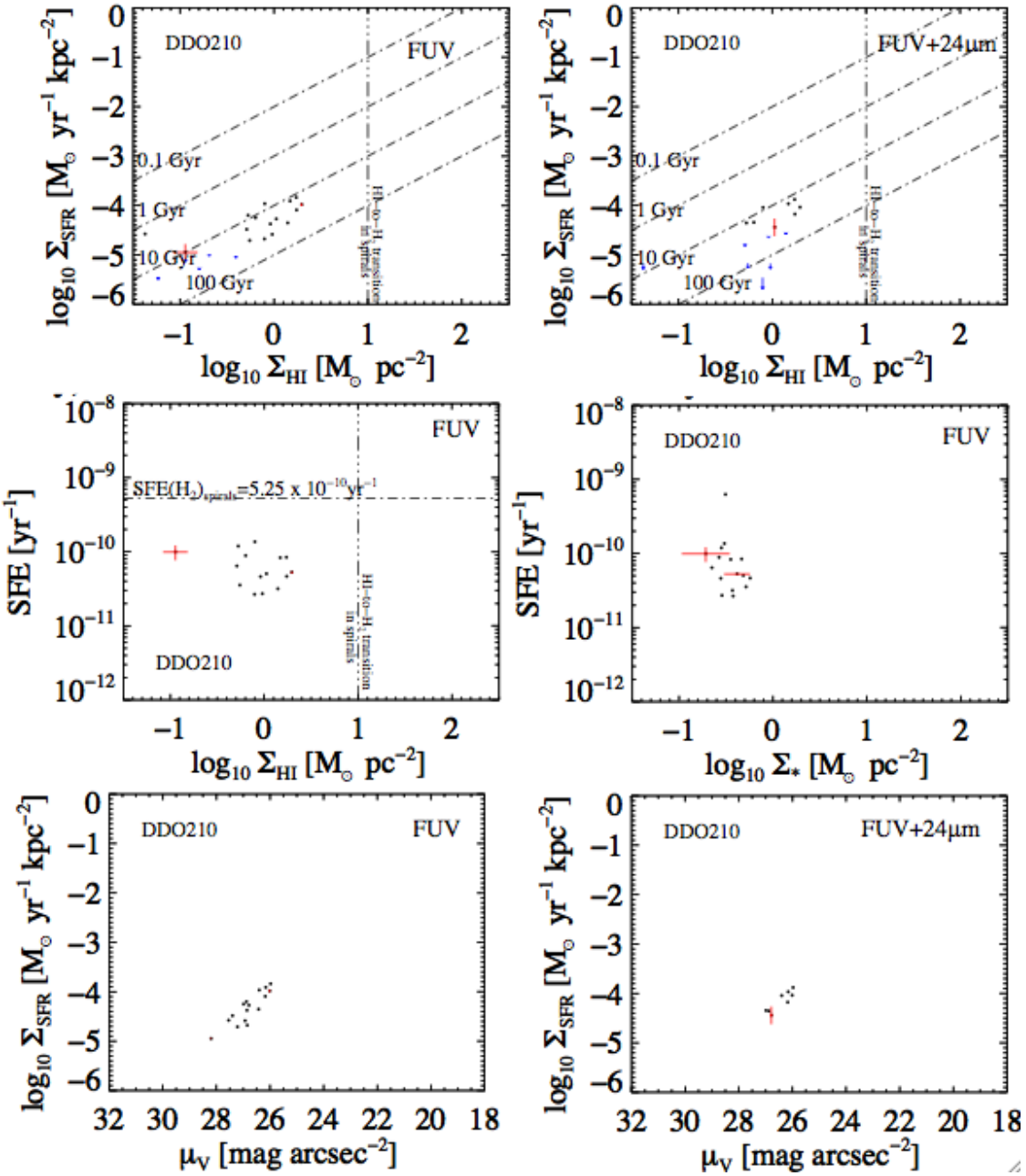

Figure 4.22: DDO 210; SFRD vs. H I surface density plotted separately for two different SF tracers, FUV (top left) and FUV+24 μm (top right), and SFE vs. H I surface density (middle left) and vs. stellar surface density (based on the 3.6 μm *Spitzer* map) for FUV as an SF tracer (middle right). We also plot SFRD vs. *V*–band surface density plotted separately for two different SF tracers, FUV (bottom left) and FUV+24 μm (bottom right). All maps used for the above plots have the same linear resolution of 400 pc. All points are independent and above a 5σ cutoff level. In red we display error bars for every 10$^{\text{th}}$ point in the plot. With blue arrows and crosses we represent upper limits.The vertical dashed line represents an H I surface density of 10 $M_\odot$ pc^{-2}. The horizontal dashed line represents constant molecular gas SFE of 5.25×10^{-10} yr^{-1}. The other four dashed lines in the top row represent constant gas depletion times of 0.1 Gyr, 1 Gyr, 10 Gyr and 100 Gyr.

ascending trend and the other showing a constant SFE.

In all of the galaxies in our subsample we confirm the existence of a tight relation between SFRD and V–band surface density, a relation which will be discussed in Section 4.8. If we further discriminate between SFRD based on FUV and based on Hα, we find that in general the two tracers agree. However, six out of 14 galaxies observed in both FUV and Hα show larger scatter in the SFRD vs. V–band surface density relation when SFR is traced by Hα rather than FUV.

The case of DDO 154 and DDO 69 also stand out as having a different slope in their relation depending on the SF tracer used in creating the SFR map. Also exceptional is the case of DDO 50, where the SFRD vs. V–band surface density relation at the high SFR end of the distribution splits into two distinct and parallel groups of points.

To further investigate the relation between the SFRD and H I surface density we plot in Fig. 4.23 for each galaxy in our sample the density contours at 10%, 25%, 50%, 75% and 90% of the pixel–by–pixel distributions. On top of the contours we overlay filled circles (black dots with coloured centres) representing azimuthal averages in both the SFRD and the H I surface density direction. Each point represents the average within circular annuli with a width of the H I beam, which ensures that all the averages shown are derived from independent data points. The coloured centres are a visual aid for distinguishing between the different radii in the galaxy as given by the legend in the figure. The black continuous line represents the linear fit through the pixel–by–pixel distribution.

We find a trend much like that found in spiral and the most luminous dwarf irregular galaxies (Bigiel et al., 2010b, 2008) in the sense that at large galactocentric radius both the SFRD and the H I surface density are low, and that both increase towards the centres of the dwarfs. In some targets there is a conspicuous absence of H I emission which can affect the innermost annuli.

The choice of the working resolution has been fully explained in the previous chapter so we will not return to this subject here. We will, however, mention that imposing a unique resolution element to the entire subsample of galaxies has the consequence that some galaxies (DDO 216, DDO 187, DDO 155, DDO 165, DDO 69, M81dwA and DDO 210) end up being represented by less than 60 points. With such low number statistics one cannot draw any firm conclusions on the individual characteristics of these galaxies.

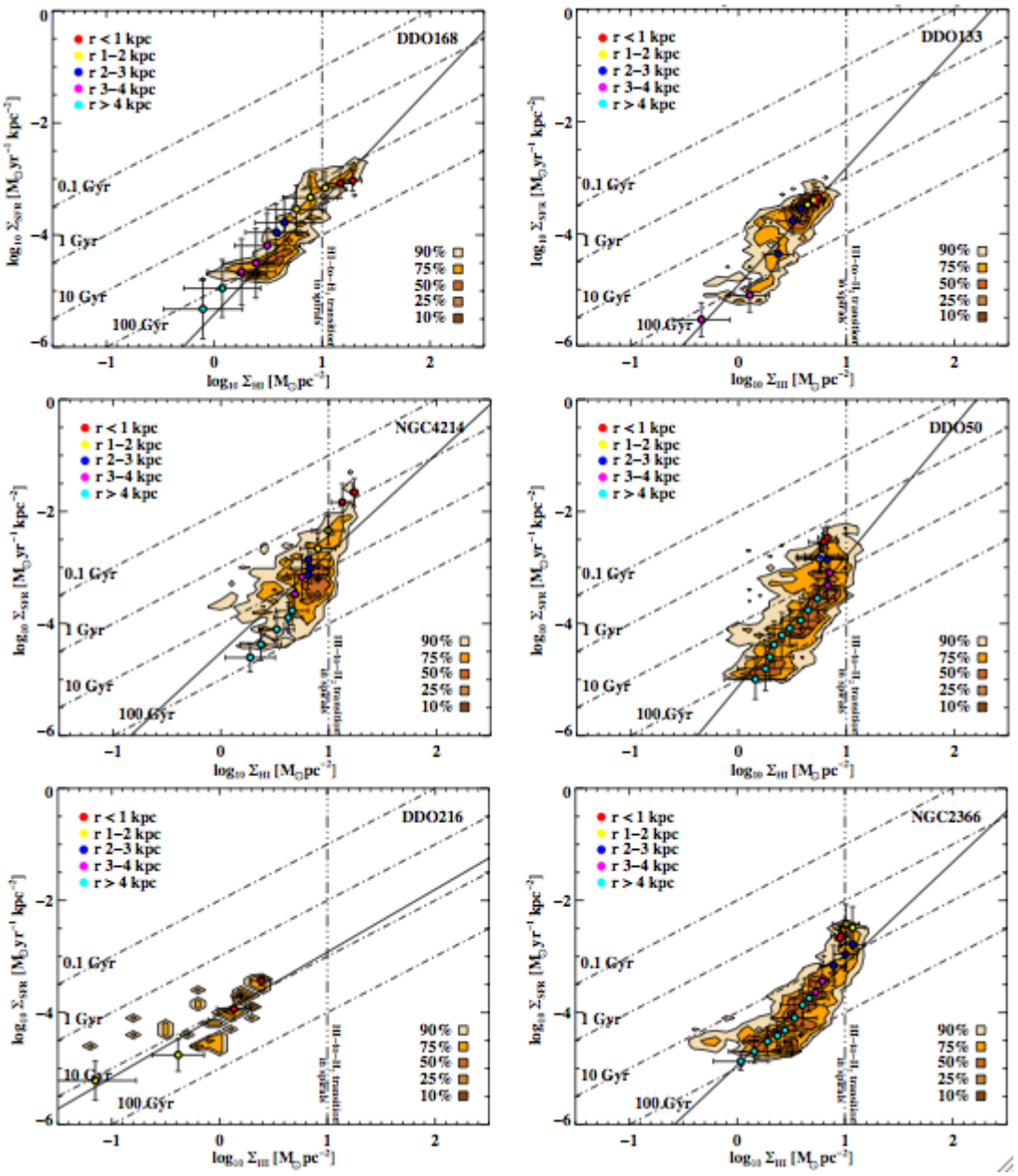

Figure 4.23: We plot for all galaxies in our subsample observed in FUV, density contours at 10%, 25%, 50%, 75% and 90% of the pixel–by–pixel distribution of SFR based on FUV–only surface density vs. H I surface density. The filled circles show the data plotted in radial bins the width of a beam size, and their coloured cores represent different radii: red cores for smaller than 1 kpc, yellow cores from 1 to 2 kpc, blue cores from 2 to 3 kpc, magenta cores from 3 to 4 kpc and cyan cores for larger than 4 kpc. All maps used for the above plots have the same linear resolution of 400 pc. All points are independent and above a 5σ cutoff level. The vertical dashed line represents an H I surface density of $10\,M_{\odot}\,pc^{-2}$. The other four dashed lines in the top row represent constant gas depletion times of 0.1 Gyr, 1 Gyr, 10 Gyr and 100 Gyr. The black continuous line represents for each galaxy, the fitted power law through the pixel–by–pixel distribution. The power law parameters are given in Table 4.2

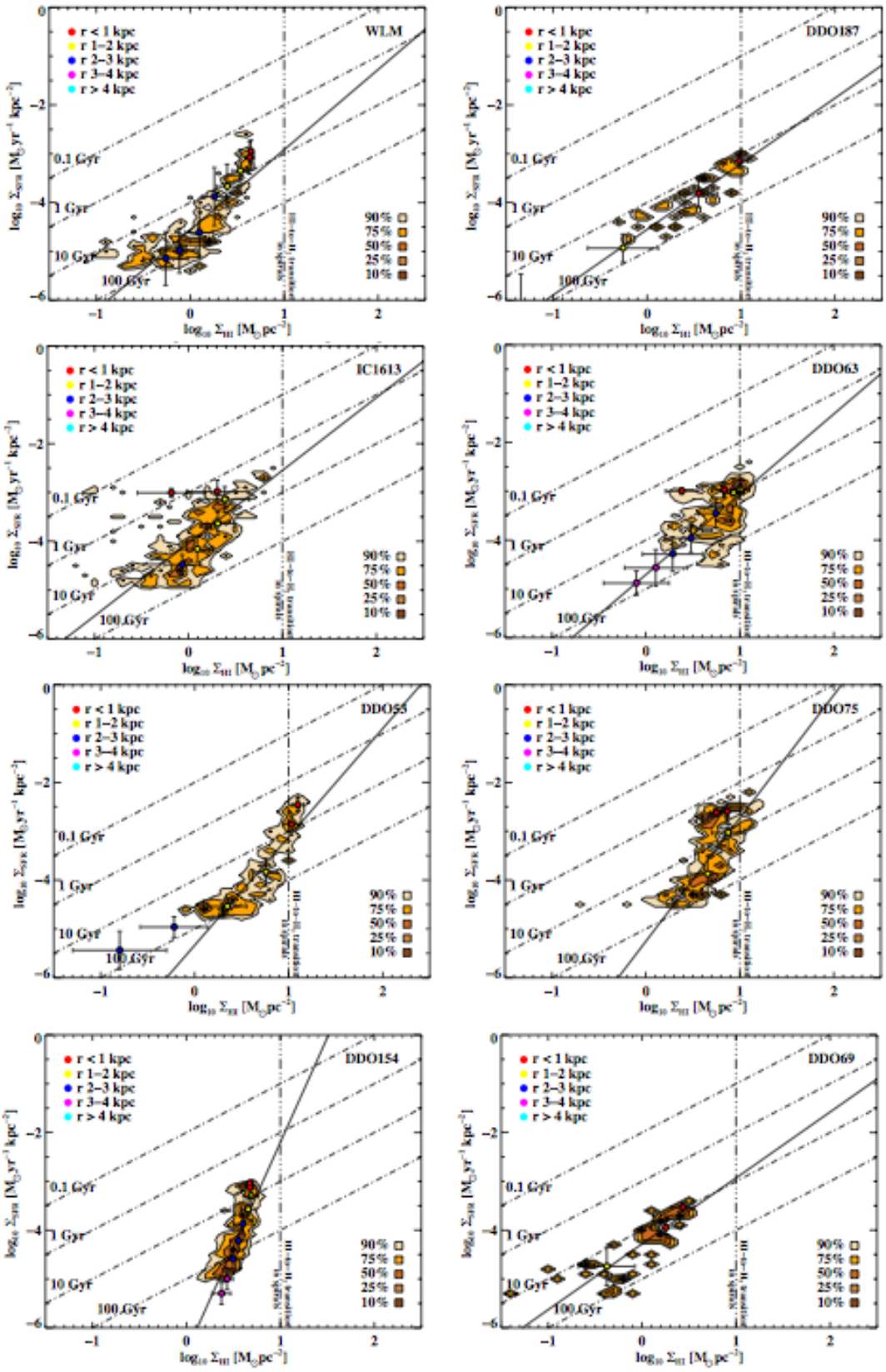

Fig. 4.23 continues ...

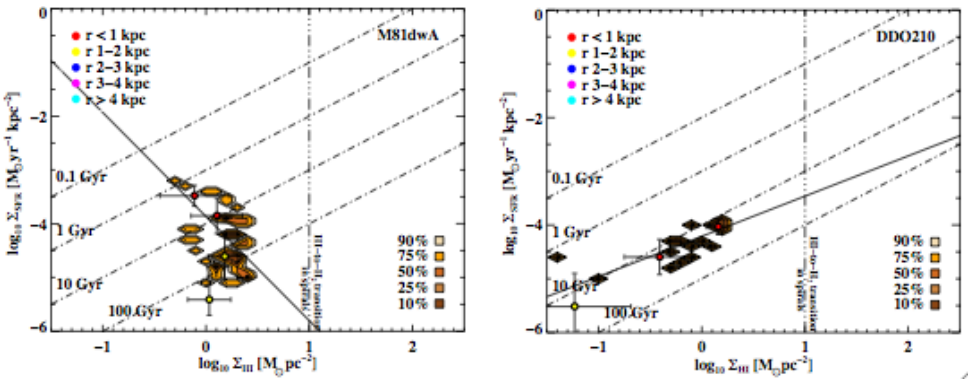

Fig. 4.23 continues ...

4.4 Star Formation Law

The Star Formation law relates the star formation rate and the gas density and follows a power law (Kennicutt & Evans, 2012; Kennicutt, 1998; Schmidt, 1959). In the previous section we have shown that in each galaxy of our dwarf sample there exists a relation between the SFRD and the H I surface density. If this relation would have the same characteristics in all galaxies studied as illustrated in Fig. 4.1, it could be passed as a SF law in the neutral gas regime. Already in the literature there are results suggesting a SF law in the neutral regime for low metallicity galaxies and the outskirts of spirals (Bigiel et al., 2011a, 2010b).

As for DDO 133 and DDO 168, we performed for each galaxy a linear regression using the ordinary least squares (OLS) Bisector method (Isobe et al., 1990) and the parameters of this linear fitting, the index number N and the coefficient A which in fact represents the SFRD at an H I surface density of $1\,M_{\odot}$ pc^{-2} are shown in Table 4.2. We found for the galaxies not affected by low number statistics, that the power law index ranges from 1.4 ± 0.3 in DDO 187 to 2.4 ± 0.6 in DDO 50. These error bars reflect the rms scatter rather than the much smaller error of the fit. The rms scatter is computed in the SFRD direction as the root–mean–square deviation of the measured SFRD with respect to the SFRD predicted by the linear regression (see Table 4.2).

The large range of power law index values needed to accommodate our galaxies suggests that the SFRD and H I surface density relation is not a straightforward one. Because stars form out of molecular gas, relating star formation to neutral gas even conceptually is indirect, which may very well explain both the scatter of the relation and the variations of this relation in each galaxy.

Table 4.2. Fitted Power-Law Parameters at 400 pc Resolution (Σ_{SFR}–Σ_{HI})

	FUV as SF tracer				Hα as SF tracer			
Name	Coef. (A)	Index (N)	Cor. coef. (r_s)	rms scatter	Coef. (A)	Index (N)	Cor. coef. (r_s)	rms scatter
DDO 168	−5.4	2.02	0.91	0.3	−5.1	1.72	0.55	0.3
DDO 133	−4.9	2.10	0.78	0.4	−4.6	1.52	0.43	0.3
NGC 4214*	−4.8	1.93	0.55	0.6	−4.9	2.35	0.61	0.5
DDO 50*	−5.2	2.39	0.66	0.6	−4.1	1.39	0.46	0.4
DDO 216	−4.0	1.12	0.69	0.3	−4.7	1.42	0.47	0.1
NGC 2366*	−4.9	1.77	0.82	0.4	−6.5	3.35	0.69	0.5
WLM	−4.6	1.64	0.79	0.5	−5.6	3.06	0.83	0.3
DDO 187	−4.6	1.44	0.85	0.3	−4.4	0.76	0.58	0.2
DDO 155	...	...	...	...	−4.2	2.25	0.66	0.1

DDO 165	...	...	...	...	−4.5	1.44	0.66	0.2
IC 1613	−4.0	1.49	0.61	0.6	−4.3	1.35	0.45	0.7
DDO 63*	−4.8	1.74	0.49	0.5	−4.6	1.50	0.44	0.3
DDO 53*	−5.3	2.22	0.88	0.4	−6.3	3.35	0.75	0.3
DDO 75	−5.0	2.23	0.74	0.5	−4.2	1.52	0.62	0.2
DDO 154*	−6.5	4.33	0.77	0.4	−4.6	1.44	0.25	0.2
DDO 69	−4.3	1.38	0.82	0.4	−4.31	0.89	0.22	0.6
M81dwA*	−3.9	−1.84	−0.16	0.5	...	...	...	...
DDO 210	−4.2	0.74	6.38	0.3	...	...	...	...
All	-4.88 ± 0.6	1.87±0.3	0.67	...	-4.8 ± 0.6	1.90±0.3	0.58	...

Table 4.2: We give for each galaxy in our sample the linear fit parameters A and N ($\Sigma_{SFR} = A\Sigma_{HI}^{N}$) , rms scatter in SFRD direction and the Spearman rank coefficient (r_s) of the SFRD–H I surface density distribution, where the considered SFR map uses both FUV (columns 2 to 5) and Hα (columns 6 to 9) only as SF tracers

We know that not all the neutral gas available is turned into molecular gas, so when searching for a direct relation between H I gas and star formation, one would do better to differentiate between the neutral gas that will turn molecular and the part that does not (de Blok & Walter, 2006; Young et al., 2003). For this reason Warren et al. (2012) isolate the cold component of the neutral medium and find that, contrary to expectations, the cold H I regions do not coincide with density peaks in the H I overall distribution, which most frequently coincide with current SF sites.

One could imagine that a dwarf galaxy caught in the act of turning its molecular gas into stars would shield its molecular cores in very dense envelopes of H I gas. These envelopes are predominantly neutral, where the ultraviolet photons govern the heating and the chemistry of the region, and are known as photodissociation regions or PDRs (Hollenbach & Tielens, 1999). Allen et al. (2004) have shown that, both 21 cm H I observations and 2.6 mm CO observations can provide important clues when investigating the physical conditions in PDRs. The challenge with H I observations of PDRs lies, of course, in attaining the high resolution images (100 pc scales) that show the PDR signature morphology and in differentiating between the emission from the PDR and the unrelated H I along the line of sight. At the 400 pc linear scale we are using for this investigation the PDRs remain unresolved so they cannot solely drive the SFRD and H I surface density relation.

Rather than comparing the relation amongst galaxies like we have done in the previous section, another way of looking at the relation within the sample is by presenting all independent points in all galaxies in one plot. To make sure that the galaxies with a smaller number of points participate in the plot with equal importance, when constructing the total distribution we weight the data points from each galaxy by the total number of contributing points from that particular galaxy. In this way we obtain Fig. 4.24, with weighting applied. In Fig. 4.25, no weighting is applied so the contours are smoother but are dominated by the larger galaxies. Coming back to Fig. 4.24, where we present colour density contours of the distribution of SFRD vs. H I surface density, SFE vs. H I surface density and SFE vs. SFRD for both Hα and FUV as SF tracers, we find agreement between the relations sampled with different SF tracers. We also find evidence for increasing SFE with SFRD and no clear relation between SFE and H I surface density.

To compare the SFRD vs. H I surface density relation with similar results in the literature, we show in Fig. 4.26 side by side the results of Bigiel et al. (2010b) in the first two panels and our results in the third panel which presents the same

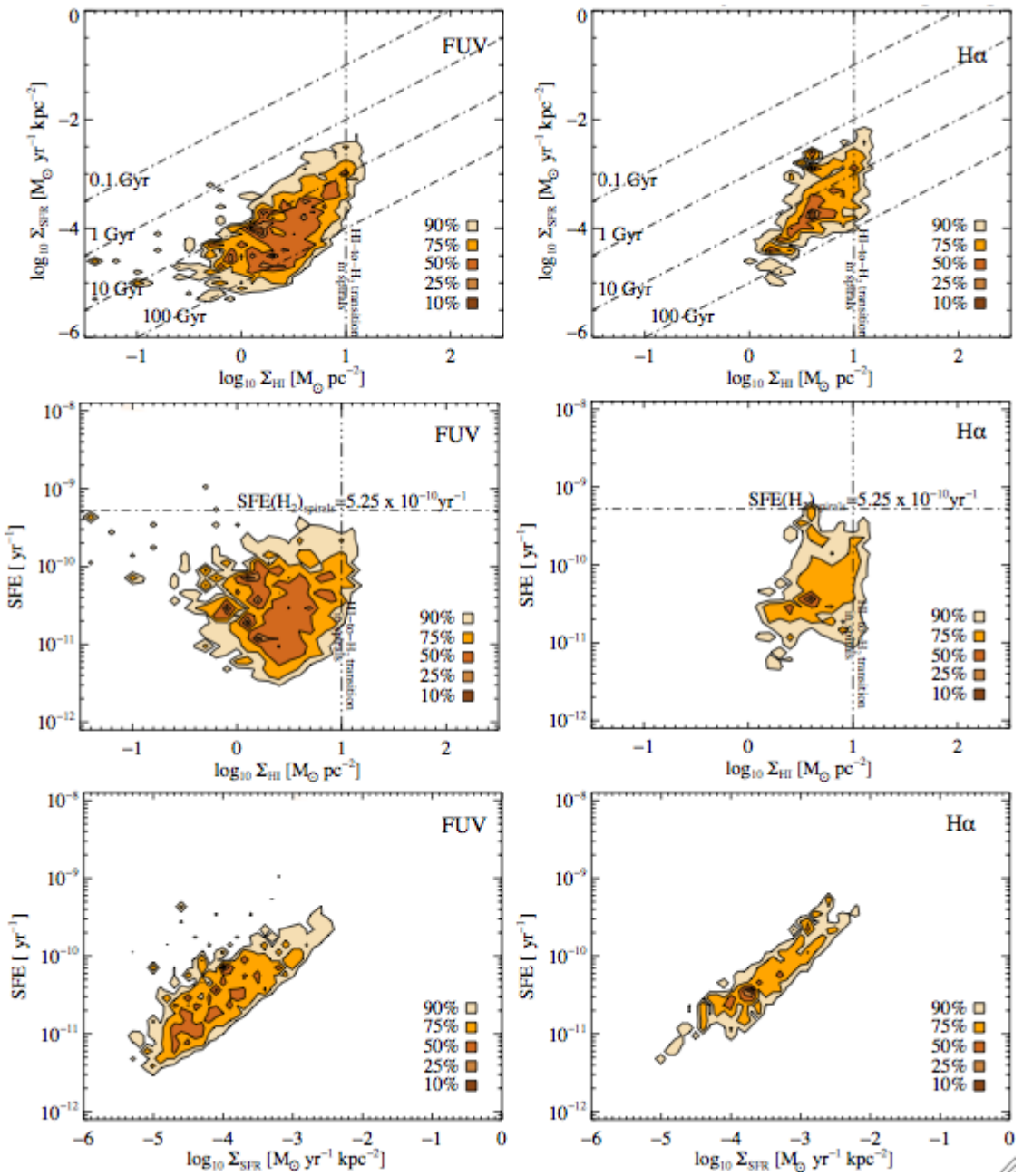

Figure 4.24: We plot for all galaxies in our subsample observed in FUV and Hα respectively, density contours at 10%, 25%, 50%, 75% and 90% of the pixel–by–pixel distribution of: SFRD vs. H I surface density (top), SFE vs. H I surface density (middle) and SFE vs. SFRD (bottom) plotted separately for two different SF tracers FUV (left) and Hα (right). All maps used for the above plots have the same linear resolution of 400 pc. All points are independent and above a 5σ cutoff level. *We weight the data points from each galaxy by the total number of contributing points for that particular galaxy.* The vertical dashed line represents an H I surface density of $10\,M_{\odot}\,pc^{-2}$. The horizontal dashed line represents constant molecular gas SFE of $5.25\times10^{-10}\,yr^{-1}$. The other four dashed lines in the top row represent constant gas depletion times of 0.1 Gyr, 1 Gyr, 10 Gyr and 100 Gyr.

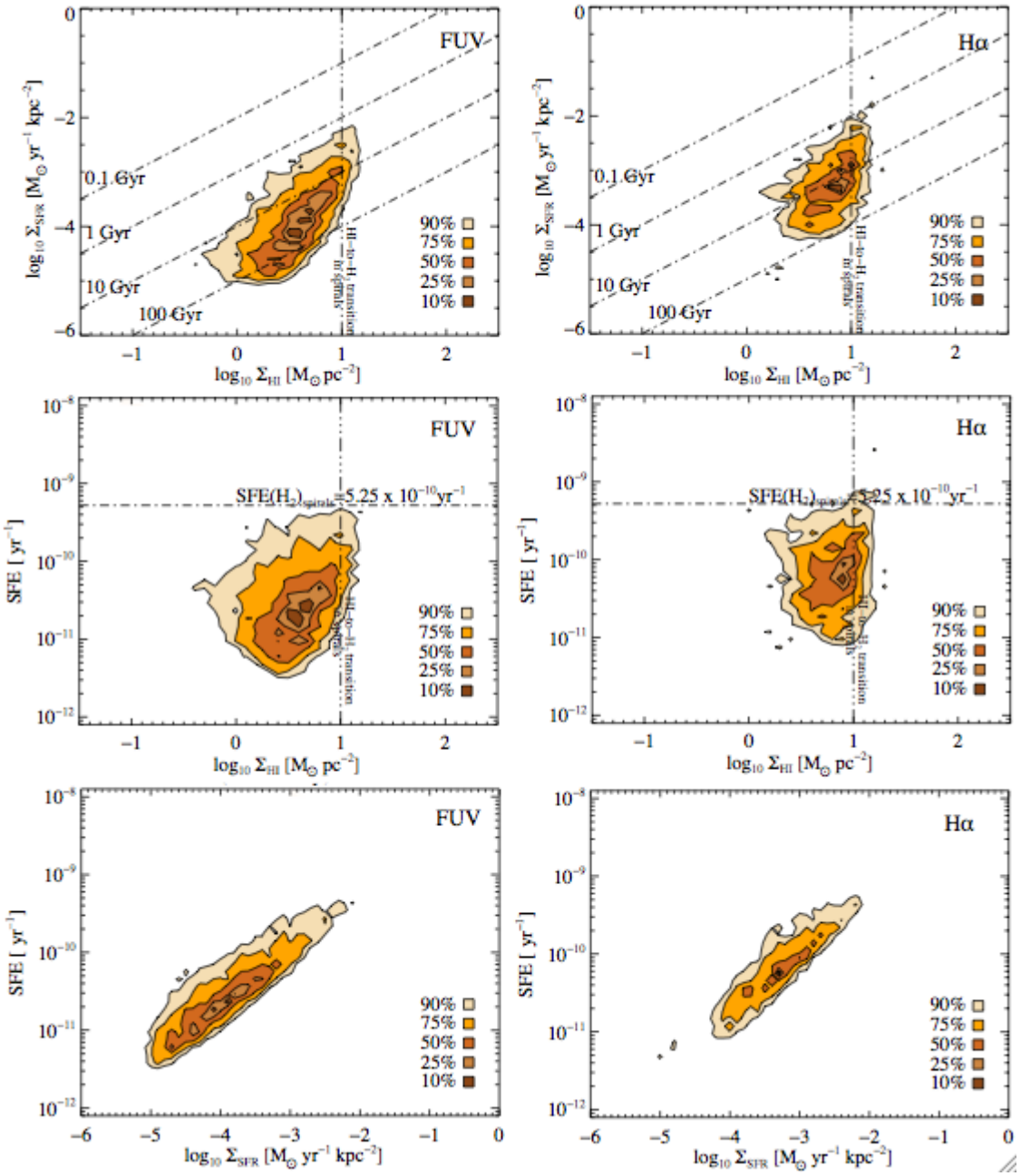

Figure 4.25: We plot for all galaxies in our subsample observed in FUV and Hα respectively, density contours at 10%, 25%, 50%, 75% and 90% of the pixel–by–pixel distribution of: SFRD vs. H I surface density (top), SFE vs. H I surface density (middle) and SFE vs. SFRD (bottom) plotted separately for two different SF tracers FUV (left) and Hα (right). All maps used for the above plots have the same linear resolution of 400 pc. All points are independent and above a 5σ cutoff level. *All points have equal weights no matter the number of points with which each galaxy contributes to the plot.* The vertical dashed line represents an H I surface density of $10\,M_{\odot}\,pc^{-2}$. The horizontal dashed line represents constant molecular gas SFE of $5.25\times10^{-10}\,yr^{-1}$. The other four dashed lines in the top row represent constant gas depletion times of 0.1 Gyr, 1 Gyr, 10 Gyr and 100 Gyr.

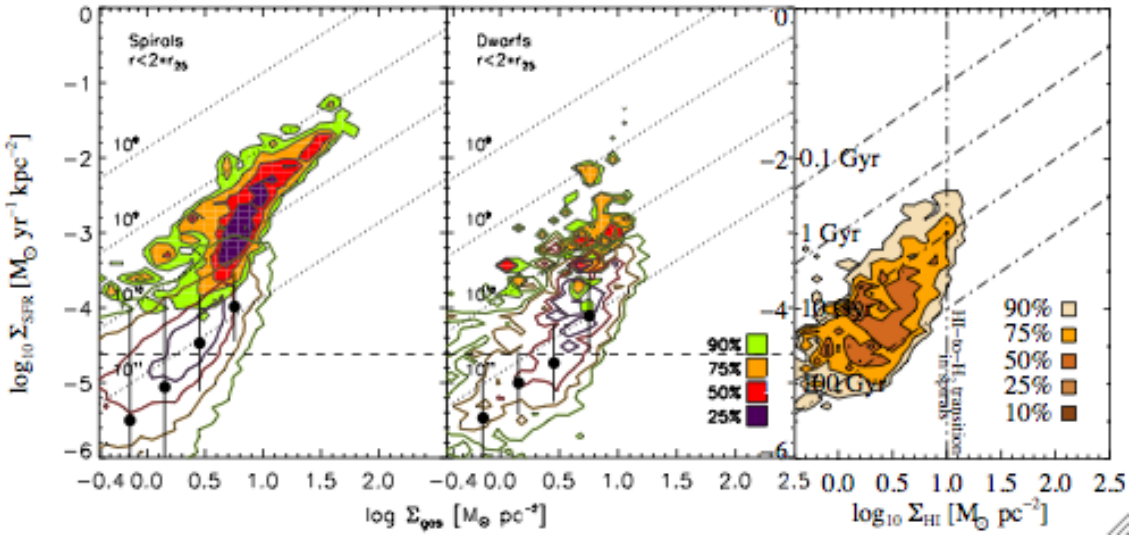

Figure 4.26: First two panels, one for THINGS spirals and the other for THINGS dwarfs summarise the results of Bigiel et al. (2010b). The filled colour contours show the pixel–by–pixel distribution of FUV converted to SFRD as a function of gas surface density inside r_{25}, whereas the empty contours show the same but beyond r_{25}. The horizontal dashed line indicates the 3σ sensitivity level of the FUV measurements. *In all panels the data points from each galaxy are weighted by the total number of contributing points for that particular galaxy.* The black filled circles represent their best fit through the data. In the right–most panel we attach our results for comparison: density contours at 10%, 25%, 50%, 75% and 90% of the pixel–by–pixel distribution of log SFRD vs. log H I surface density of all galaxies in our subsample. All points are independent and above a 5σ cutoff level in SFR. The vertical dashed line represents an H I surface density of $10\,M_\odot$ pc^{-2}. In all three panels the four dashed lines represent constant gas depletion times of 0.1 Gyr, 1 Gyr, 10 Gyr, and 100 Gyr.

data as already shown in the top left panel of Fig. 4.24. Our plot shows density contours of a distribution of points from each galaxy of our sample irrespective of where they are located within the dwarf irregular. The THINGS results displayed in the first two panels of Fig. 4.26 show the pixel–by–pixel distribution of FUV converted to SFRD as a function of gas surface density inside (with filled contours) and outside (with empty contours) r_{25} for the THINGS spirals in the left panel and the THINGS dwarfs in the middle panel. We remind the reader that the THINGS figures show gas surface density on the x–axis, whereas we show H I surface density on the x–axis. As explained in the previous chapter the two surface densities are different only in the left most panel where for the filled contours the total gas surface density also includes the molecular gas surface density. The higher the SFRD, the more dominating is the contribution of the molecular surface density to the total

gas surface density. In the case of the SFRD–gas surface density distribution of the dwarfs and the outskirts of spirals (the empty contours) the gas surface density does not differ from H I surface density. In fact, we use these contours to compare our data with theirs.

In all three panels weighting is used to ensure that each galaxy contributing to the plot is given equal importance. In Fig. 4.26, when comparing the THINGS results with ours, we observe that the SFRD vs. H I surface density relation in our sample of galaxies matches very well the shape of the SFRD vs. H I surface density relation found in THINGS dwarfs. Our total distribution of points has a similar range in SFRD as the THINGS dwarfs. However, our distribution shows a different range in H I surface density than the THINGS result, especially at the higher density end where our sample seems to have more galaxies crossing the $10\,M_{\odot}\,pc^{-2}$ threshold.

Although any individual dwarf irregular galaxy in our sample shows that with increasing HI surface density there is a corresponding increase in SFRD, there is a large variation from galaxy to galaxy in the rate of this increase. To explore if there is any underlying mechanism, we investigate the relation between the degree of correlation between SFRD and H I surface density and parameters such as metallicity, H I mass, integrated SFR, and others. In Fig. 4.27, we find that the degree of correlation between SFRD and H I surface density does not depend on either metallicity, H I mass or absolute V–band magnitude. Neither does it depend on quantities such as the Integrated SFR/area from FUV or Hα (see Fig. 4.28). Also shown here, in Fig. 4.28, is the fact that the correlation is not driven by the molecular or neutral gas fractions either. We would like to mention here that the molecular gas fraction is based on the molecular gas mass prediction explained in Section 4.5.

However, the degree of correlation between SFRD and H I surface density does not tell us anything about how the galaxies in our sample correlate with each other in terms of a common SF law. For this purpose we also studied the parameters derived for each galaxy in the linear regression, the index values N and the coefficient A normalized at Σ_{HI}=1 $M_{\odot}\,pc^{-2}$ in relation with parameters such as metallicity, H I mass, integrated SFR, and others. No conclusive results were found either, therefore the plots obtained are not shown.

To quantify the power law index number N which best describes the total distribution of points, we use linear regression, more specifically the ordinary least squares (OLS) Bisector method (Isobe et al., 1990) and find $\Sigma_{SFR} \propto \Sigma_{HI}^{1.87\pm0.3}$. Here and throughout this chapter, the error bars given for the SF laws of the whole

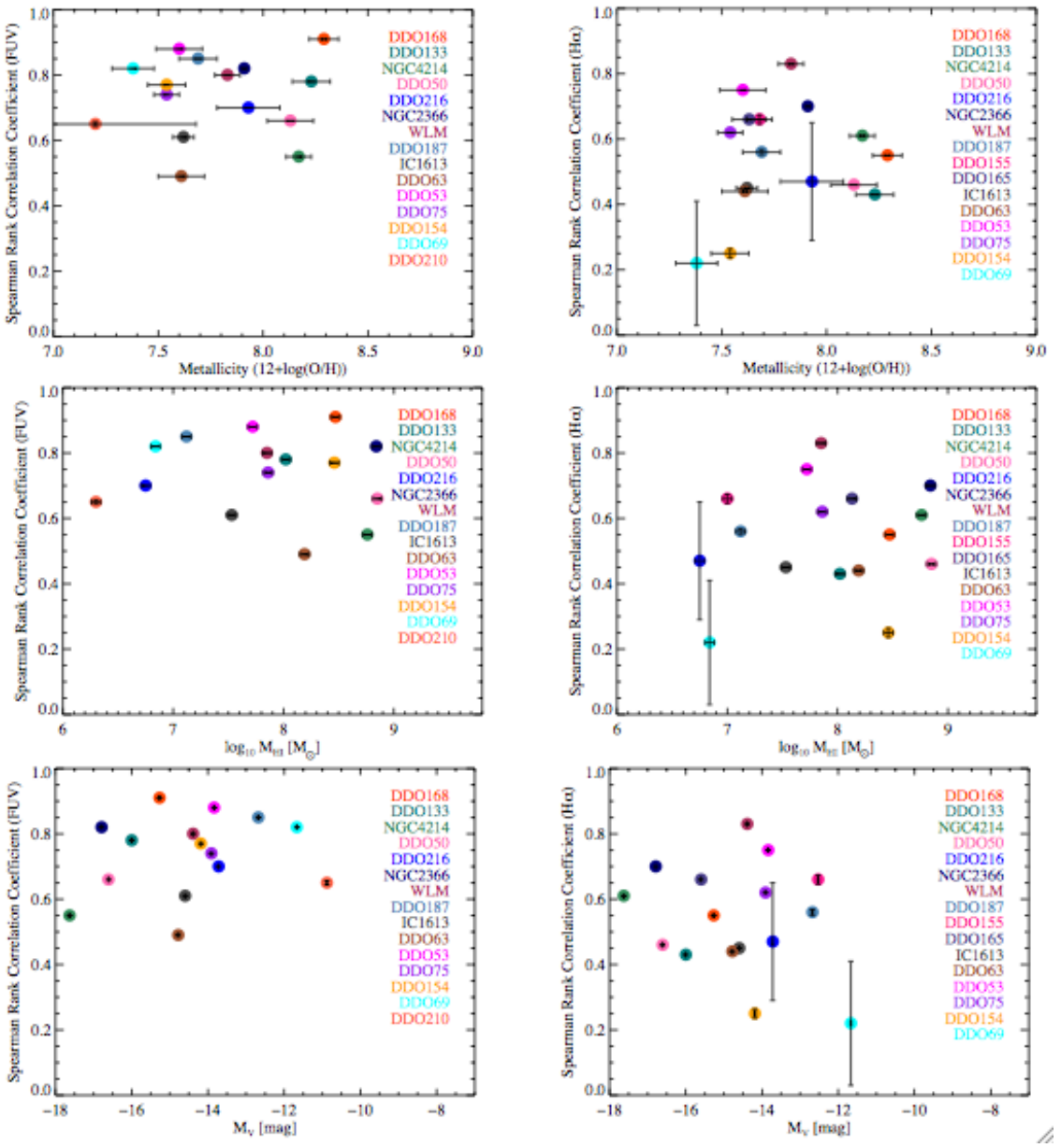

Figure 4.27: We plot for all galaxies in our subsample, the Spearman correlation coefficient slope between SFRD and H I surface density vs. metallicity (top), H I mass (middle) and M_V (bottom), plotted separately for two different SF tracers FUV (left) and Hα (right).

sample include apart from the error of the fit, which is solely depending on the number of participating data points, also the average rms scatter representing the root–mean–square deviation of the measured values with respect to the regression line.

Our index value is close to the value of 1.8 found for DDO 168 and DDO 133 in the previous chapter and also to the value of 1.7 found by Bigiel et al. (2010b)

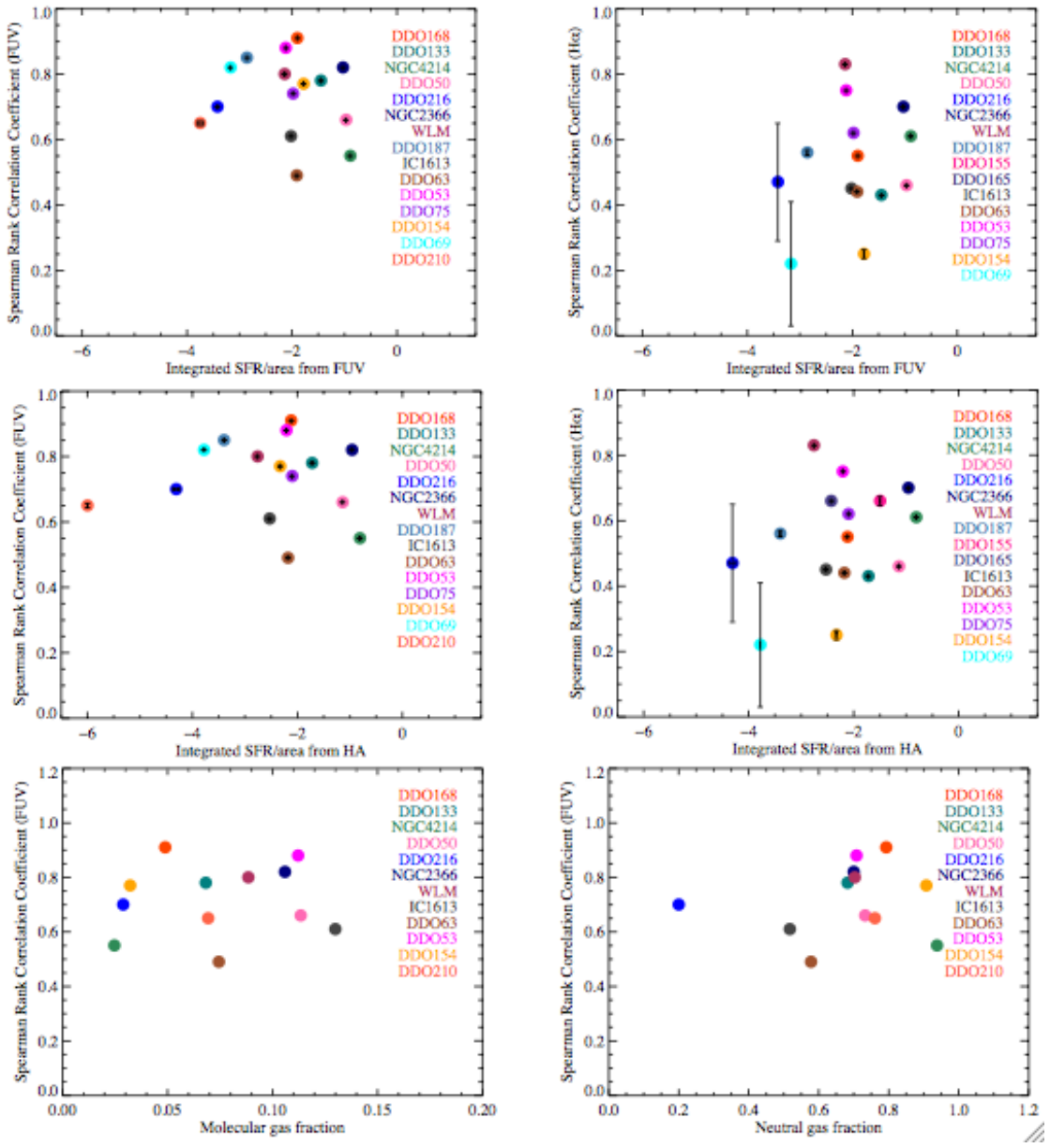

Figure 4.28: We plot for all galaxies in our subsample, the Spearman correlation coefficient between SFRD and H I surface density vs. log of the integrated SFR over area from FUV (top) and Hα (middle). In the bottom panels we plot the Spearman correlation coefficient between SFRD and H I surface density vs. the molecular fraction (left) and neutral fraction (right).

for a sample of five dwarf galaxies and the outskirts of 17 spiral galaxies. We also compute a Spearman rank correlation coefficient of 0.67, indicating a good degree of correlation among the points of the distribution.

4.5 Molecular Gas Mass Predictions

In the study of SF laws an important quantity is the gas surface density consisting of neutral, including helium, and molecular gas. However in the low metallicity environment of dwarfs several complications prevent us from being able to measure the molecular gas quantity. Due to low metallicity, the CO cores are smaller and underluminous (Bolatto et al., 2007), so we lose that molecular gas tracer. Apart from the dearth of CO molecules, the H_2 mass estimation is further complicated by the uncertainties in the conversion factor X_{CO}. We remind the reader that the commonly used conversion factor is derived from observations of the Milky Way. However, there are strong indications that in low metallicity environments this conversion factor has a different value (Bolatto et al., 2008; Leroy et al., 2011; Sandstrom et al., 2013). Current lines of study use dust as a proxy for molecular gas measurements. However, since the discovery that the dust properties in dwarf galaxies are different than in spirals (Galametz et al., 2011; Galliano et al., 2011; O'Halloran et al., 2010; Rosenberg et al., 2008), using dust as a tracer for molecular gas in dwarfs is a method that still needs refinement. Although difficult to obtain, an estimate of the molecular gas quantity in dwarf galaxies would be very useful.

As it turns out we can estimate it based on the SFR map. As prescribed by Leroy et al. (2008), knowing that molecular gas surface density and SFRD are connected through a 1:1 relation and hence that the corresponding SFE defined as the ratio between the SFRD and gas surface density (in this case molecular gas surface density), is constant and equal to $5.25\times10^{-10}\,\mathrm{yr}^{-1}$, one can use this to predict the molecular gas mass. We have computed for each of our galaxies an integrated value and we present it in Table 4.1. Although H_2 is difficult to observe in dwarfs, its presence is hinted at, by the presence of star formation. Even if star formation could occur in H I instead, as suggested by Krumholz (2012), such an occurrence would take place at metallicities of a few percent of Solar, where clouds are able to cool and form stars before the molecules form because the free fall time has a value between the thermal and the chemical timescales. This phenomenon would cause the breaking of the relation between H_2 and star formation and consequently our approach of predicting molecular gas mass would become invalid.

According to Bigiel et al. (2008), in spiral galaxies the highest H I densities (but not necessarily corresponding to the highest SFRDs) constitute a turnover point beyond which molecular gas becomes dominant. Provided that the slope of the SFRD

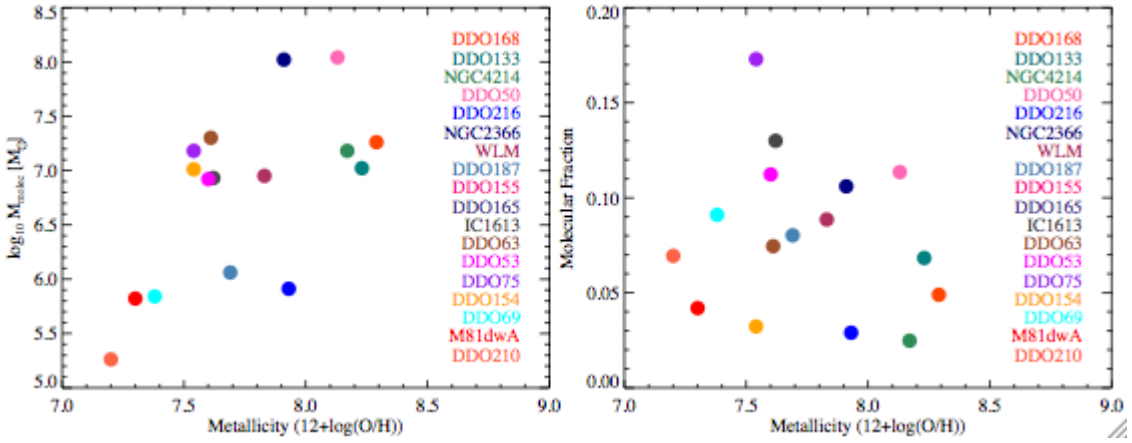

Figure 4.29: We plot for all galaxies the predicted molecular mass and molecular gas fraction against metallicity.

and H I surface density trend is higher than unity, at the highest H I densities, one would expect to reach the highest SFE which in the molecular gas regime continues as a constant at this same level. The constant SFE of $5.25\times10^{-10}\,\mathrm{yr}^{,-1}$, governing the molecular gas regime is determined by the microphysics of the GMCs, hence the SFE in the molecular gas regime should be $5.25\times10^{-10}\,\mathrm{yr}^{,-1}$ no matter the environment. Moreover, in a recent study of the resolved SF law in an unlensed, $z = 4$ galaxy, Hodge et al. (2015) found evidence to support a power law slope of $N = 2.1 \pm 0.1$ and hence a fixed SFE per free–fall time on kiloparsec scales confirming once more that the molecular SF law does not evolve with redshift either. However, a fixed SFE conclusion has not been observationally probed in dwarfs, most probably due to the uncertainties in the conversion factor X_{CO}.

The SFE defined as the ratio of SFRD and H I surface density is determined by the macrophysics of the H I to H_2 transition, hence the H I to H_2 transition varies with metallicity. Walch et al. (2011) argue that metallicity plays an important role in the molecular core formation, yet it does not seem to influence the molecular gas mass as shown in Fig. 4.29. Neither does metallicity influence the molecular gas fraction (see Fig. 4.29) calculated as the ratio between the molecular gas mass and the total baryonic mass which includes neutral and molecular gas mass with corrections for helium and the stellar mass.

Since we do not have any molecular gas observations, we assume in our prediction that beyond that turnover point the SFE is indeed $5.25\times10^{-10}\,\mathrm{yr}^{,-1}$ and calculate the molecular mass accordingly.

4.6 Multiple Components in the SF Law

In Chapter 3, Section 3.3.2, we have shown that in DDO 133, the H I shell interiors become resolved at 400 pc scales and appear as a distinct feature in the SFRD–H I surface density relation. There we use colour coding to identify the physical location of each point of the SFRD vs. H I surface density plot in the H I, FUV and Hα maps.

We find that, because the H I shells in dwarfs are larger than in spirals at 400 pc resolution, the shell interiors are represented by multiple points which occupy a particular region in the SFRD–H I surface density plot. We showed that the SFRD–H I surface density relation improves significantly if these points are excluded.

In this section of the thesis we bring more evidence for this effect. In our galaxy subsample we find apart from DDO 133, another 5 galaxies which show resolved H I shells at 400 pc scales: NGC 4214, DDO 50, IC1613, DDO 63 and DDO 75. We open the discussion on this subject with Fig. 4.30, which shows for all the galaxies in our sample, all the pixels plotted in previous SFRD vs. H I surface density plots as positions on their corresponding H I maps. In magenta are shown the galaxies that do not have resolved H I shells at 400 pc, whereas the six above mentioned galaxies are shown using the following colour code: red for H I shell interiors, orange for high H I surface density regions and blue for the outskirts.

We show here Fig. 4.31 to remind the reader of the results presented in the previous chapter. Applying the same colour coding method we obtain figures Fig. 4.32 to Fig. 4.36. These figures show that the H I shell interiors correspond to a lack of gas, but do contain FUV emission to a varying degree. Depending on the age of the shell and the time of the last SF event that created the H I shell in that region, we then find points in the SFRD–H I surface density plots that have excess SF for the amount of H I sampled along the line of sight.

Another feature to note in Figs. 4.31–4.36 is that for five out of six galaxies the red points representing the H I shell interiors and the orange points representing the high H I density regions are well mixed in the SFRD vs. V–band surface density plot suggesting that the stars which emit in V–band are present in both types of regions.

DDO 75 represents the exception to the rule because the points representing the H I shell interiors are grouped separately from the high H I surface density points, with a distinctive lower SFRD, although sharing the same range in V–band surface densities. In fact in DDO 75 the distribution of red points suggests more of a low H I density region caused by gas being concentrated in the two adjacent high density

regions, rather than a classical H I shell.

As can be seen in Table 4.3, the correlation coefficient for the relation between the SFRD and H I surface density for these six galaxies ranges from 0.49 for DDO 63 to 0.78 for DDO 133.

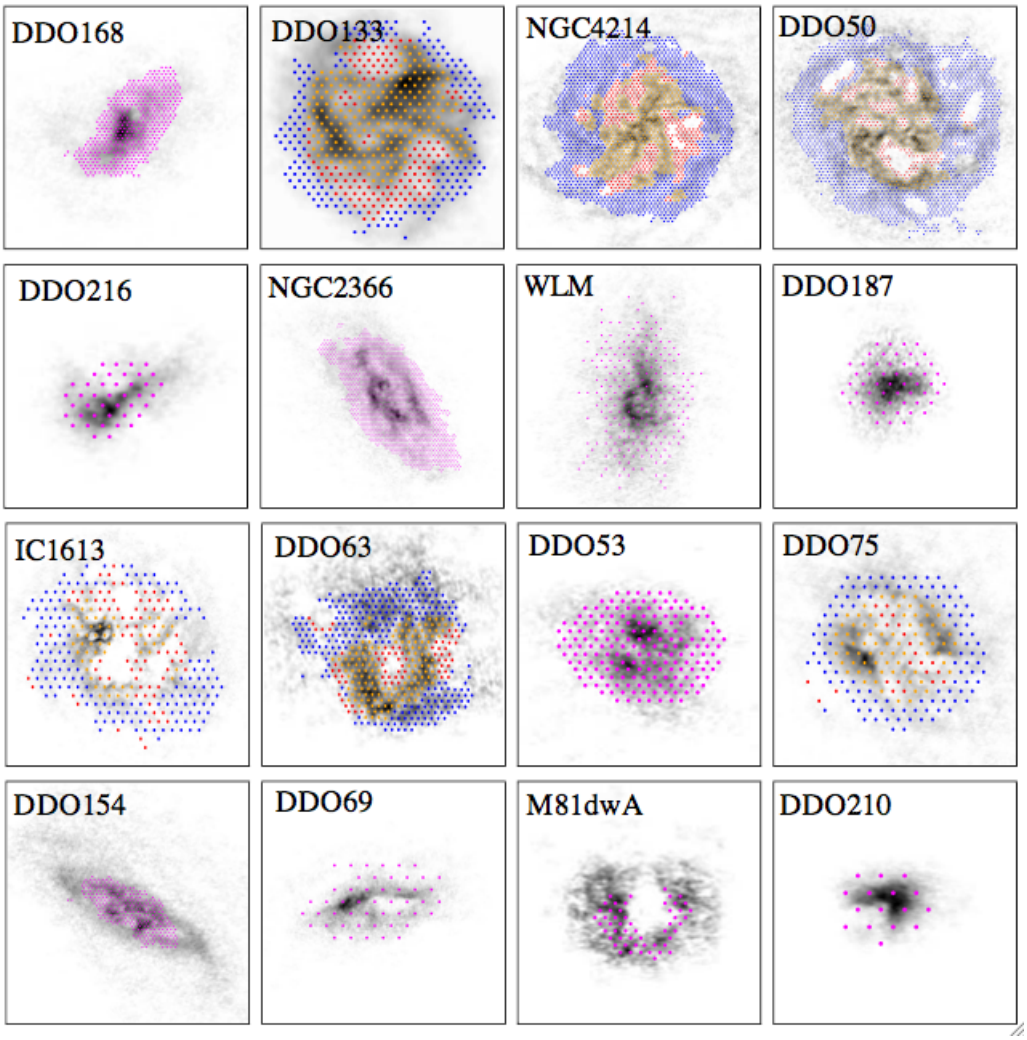

Figure 4.30: In an in depth study of the SF Law, based on the H I distribution map, for each galaxy of our sample we plot the position of the pixels previously shown in SFRD vs. H I surface density plots overlaid on their corresponding H I maps. In magenta are shown the galaxies which do not have resolved H I shells, whereas for galaxies with resolved H I shells, such as DDO 133, NGC 4214, DDO 50, IC 1613, DDO 63 and DDO 75, based on the H I distribution map we separate the galaxies into three regions: red for H I shell interiors, orange for high H I surface density regions and blue for the outskirts. All points are independent and above a 5σ cutoff level in SFR.

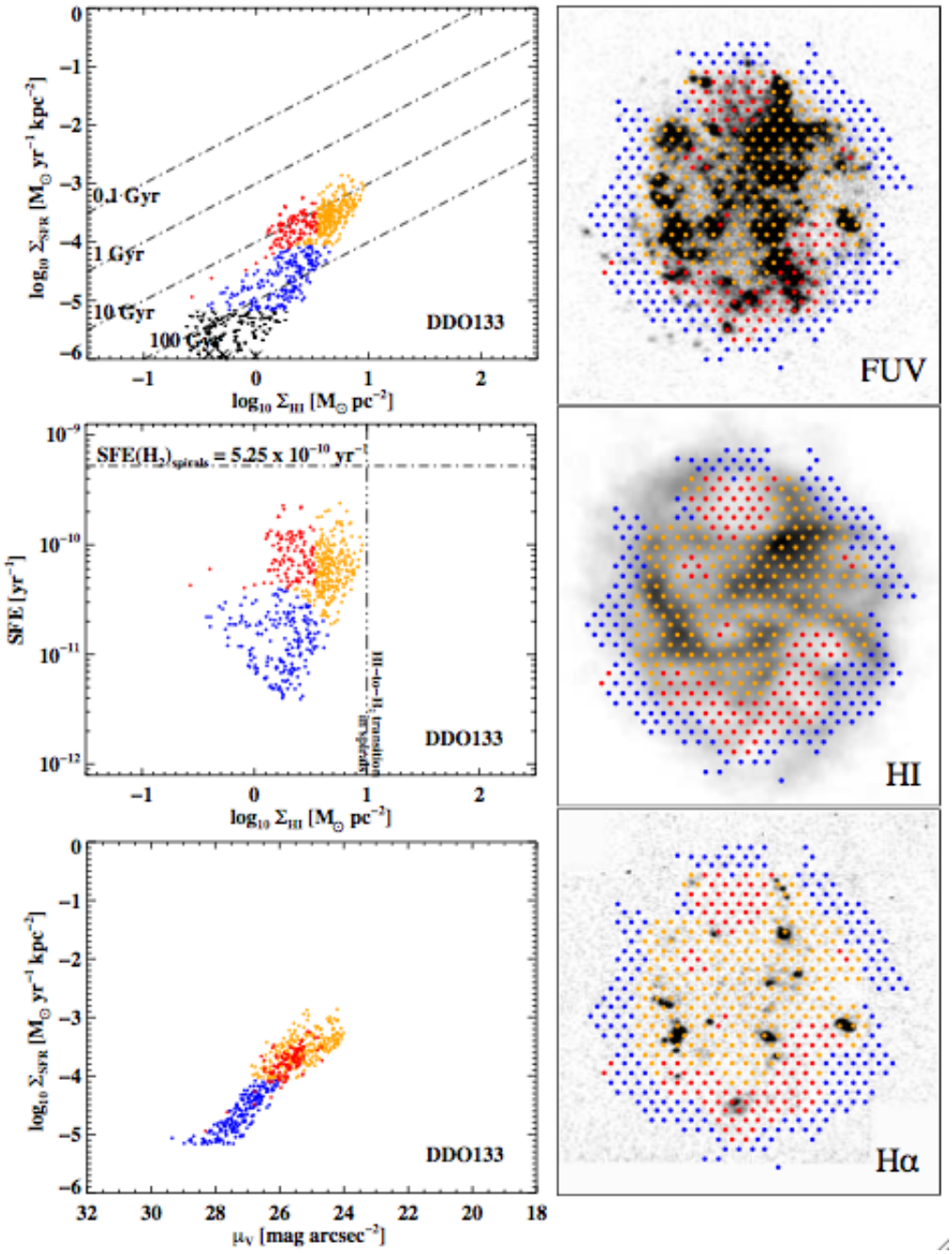

Figure 4.31: DDO 133: In an in depth study of the SF Law, based on the H I distribution map we separate the galaxy into three regions: red for H I shell interiors, orange for high H I surface density regions and blue for the outskirts. Their position is plotted on the FUV (top right), H I (middle right) and Hα (bottom right) maps. We plot the same pixels as in the panels to the right as a SFRD vs. H I surface density plot (top left), SFE vs. H I surface density (middle left), and SFRD vs. V–band surface brightness (bottom left). All points are independent and above a 5σ cutoff level in SFR. The vertical dashed line represents an H I surface density of $10\,M_\odot\,pc^{-2}$. The horizontal dashed line represents constant molecular gas SFE of $5.25\times10^{-10}\,yr^{-1}$. The four diagonal dashed lines in the top left panel represent constant gas depletion times of 0.1 Gyr, 1 Gyr, 10 Gyr, and 100 Gyr.

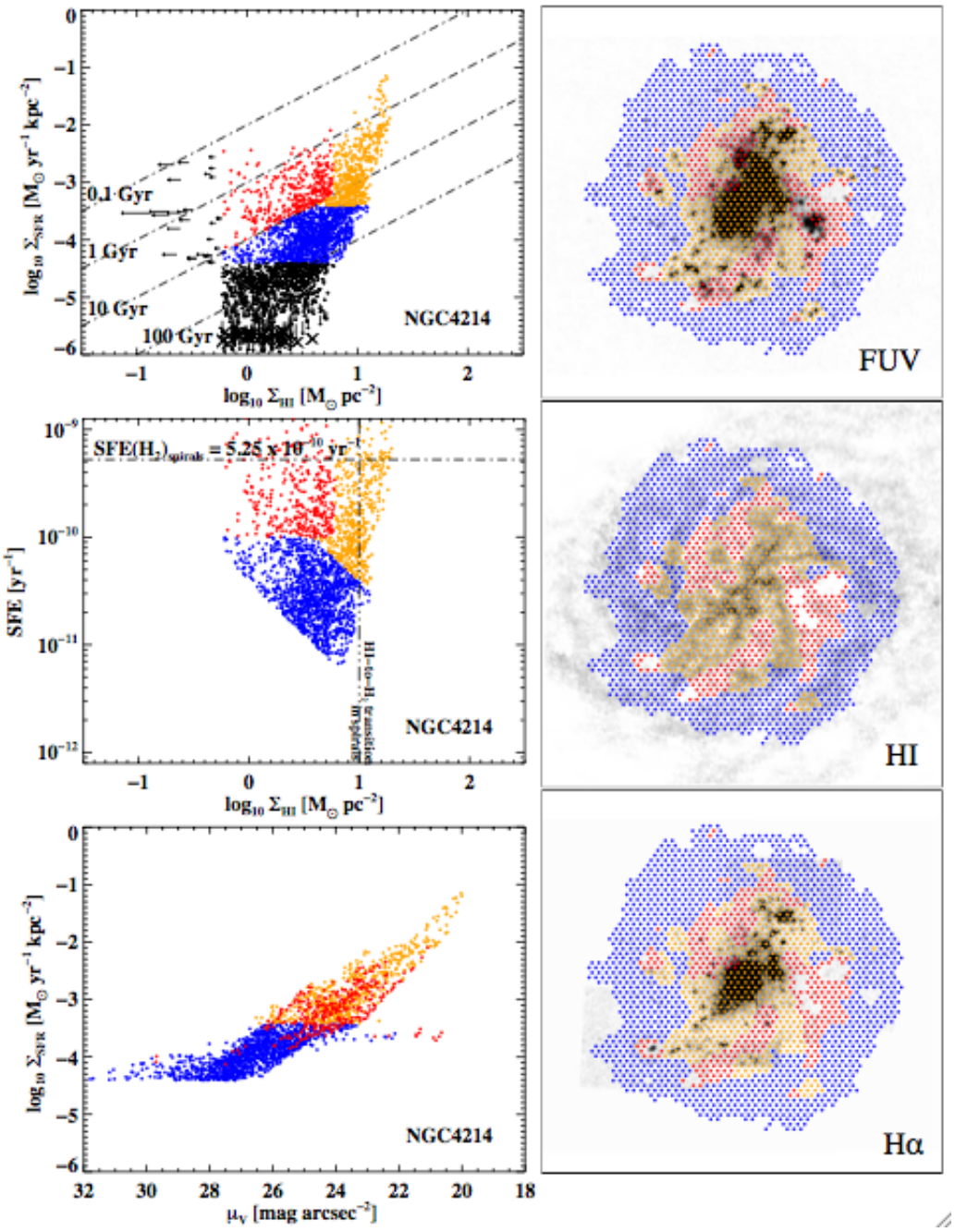

Figure 4.32: NGC 4214: In an in depth study of the SF Law, based on the H I distribution map we separate the galaxy into three regions: red for H I shell interiors, orange for high H I surface density regions and blue for the outskirts. Their position is plotted on the FUV (top right), H I (middle right) and Hα (bottom right) maps. We plot the same pixels as in the panels to the right as a SFRD vs. H I surface density plot (top left), SFE vs. H I surface density (middle left), and SFRD vs. V–band surface brightness (bottom left). All points are independent and above a 5σ cutoff level in SFR. The vertical dashed line represents an H I surface density of $10\,M_\odot\,pc^{-2}$. The horizontal dashed line represents constant molecular gas SFE of $5.25\times10^{-10}\,yr^{-1}$. The four diagonal dashed lines in the top left panel represent constant gas depletion times of 0.1 Gyr, 1 Gyr, 10 Gyr, and 100 Gyr.

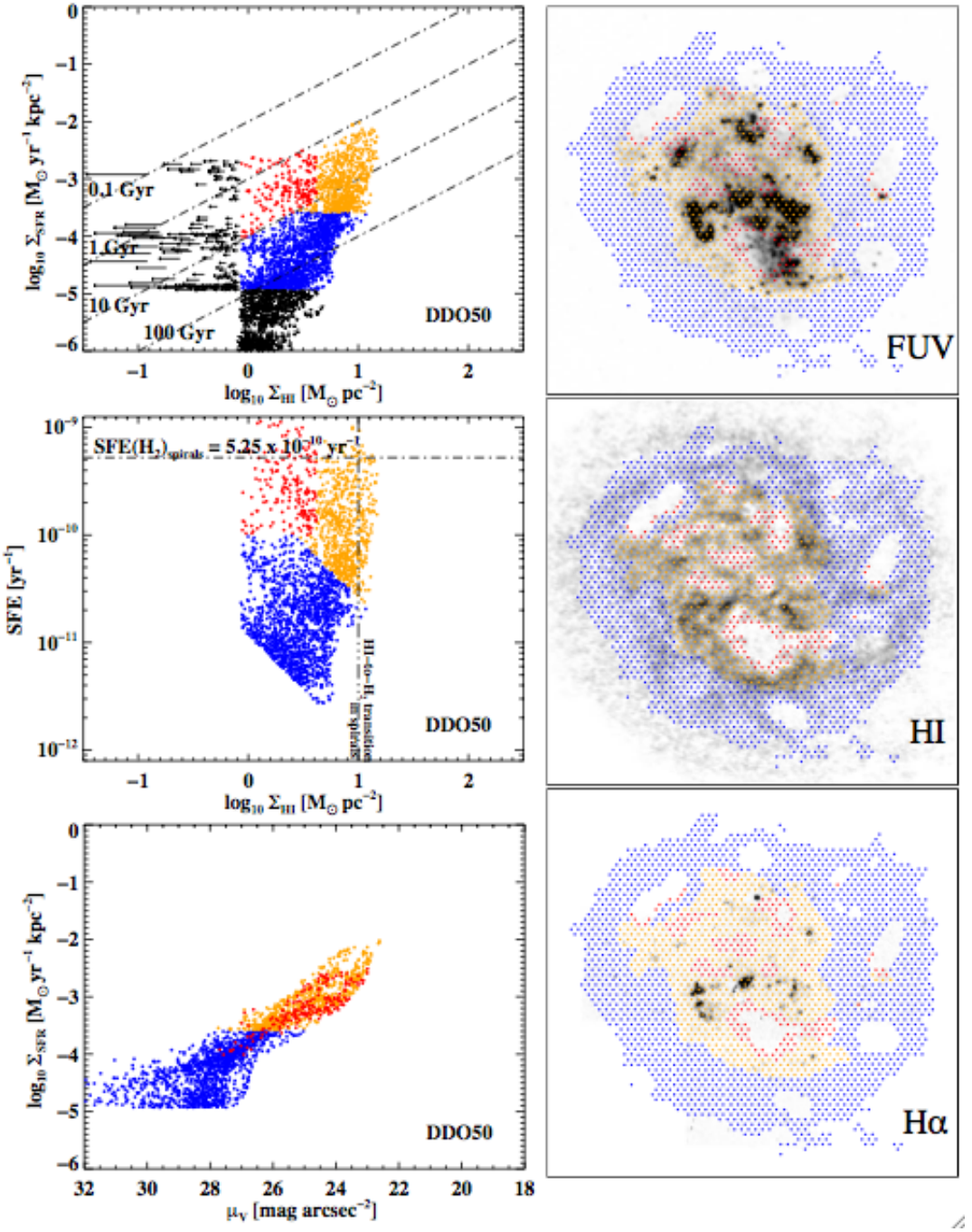

Figure 4.33: DDO 50: In an in depth study of the SF Law, based on the H I distribution map we separate the galaxy into three regions: red for H I shell interiors, orange for high H I surface density regions and blue for the outskirts. Their position is plotted on the FUV (top right), H I (middle right) and Hα (bottom right) maps. We plot the same pixels as in the panels to the right as a SFRD vs. H I surface density plot (top left), SFE vs. H I surface density (middle left), and SFRD vs. V–band surface brightness (bottom left). All points are independent and above a 5σ cutoff level in SFR. The vertical dashed line represents an H I surface density of $10\,M_\odot\,pc^{-2}$. The horizontal dashed line represents constant molecular gas SFE of $5.25\times10^{-10}\,yr^{-1}$. The four diagonal dashed lines in the top left panel represent constant gas depletion times of 0.1 Gyr, 1 Gyr, 10 Gyr, and 100 Gyr.

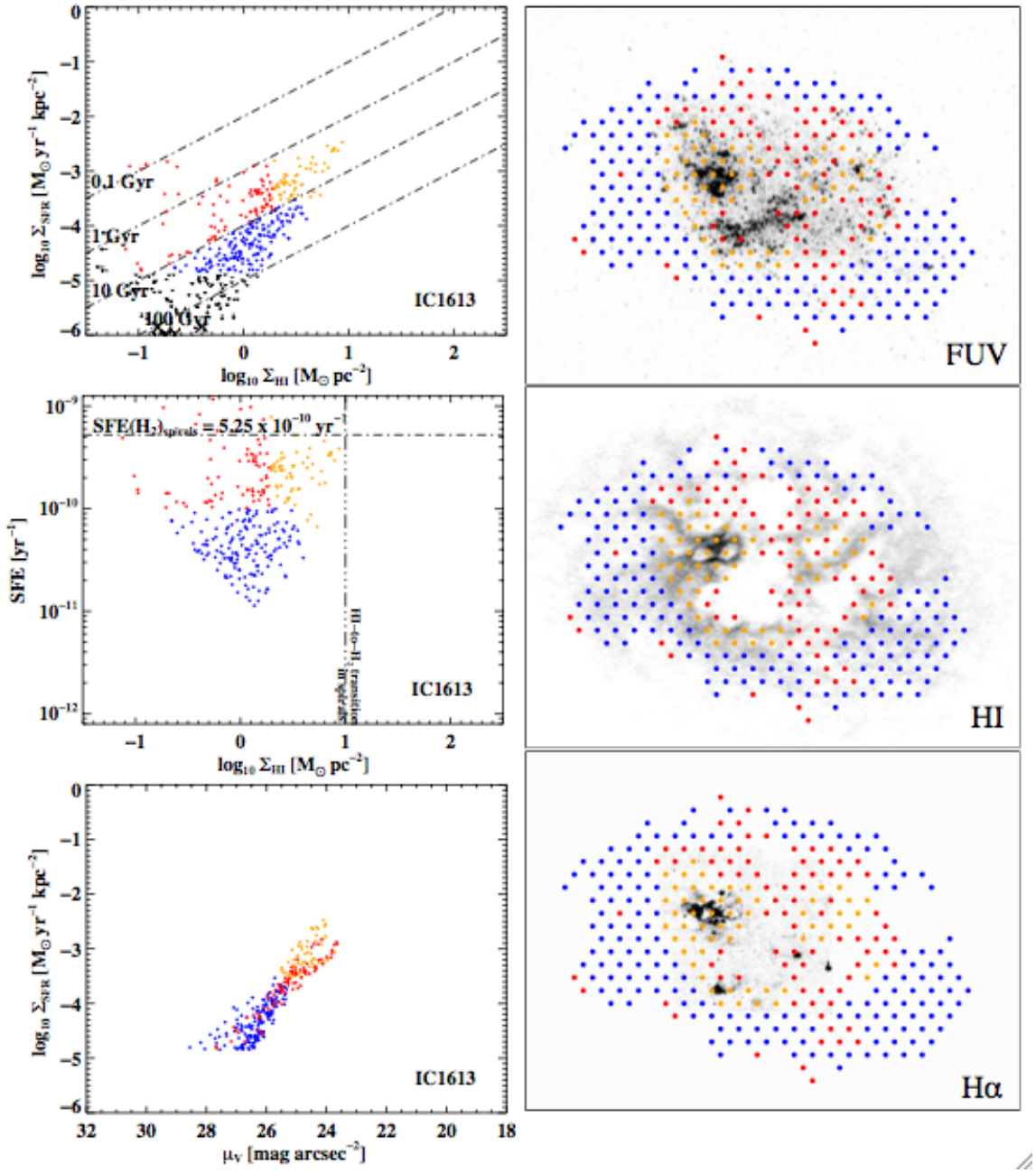

Figure 4.34: IC 1613: In an in depth study of the SF Law, based on the H I distribution map we separate the galaxy into three regions: red for H I shell interiors, orange for high H I surface density regions and blue for the outskirts. Their position is plotted on the FUV (top right), H I (middle right) and Hα (bottom right) maps. We plot the same pixels as in the panels to the right as a SFRD vs. H I surface density plot (top left), SFE vs. H I surface density (middle left), and SFRD vs. V–band surface brightness (bottom left). All points are independent and above a 5σ cutoff level in SFR. The vertical dashed line represents an H I surface density of $10\,M_\odot\,pc^{-2}$. The horizontal dashed line represents constant molecular gas SFE of $5.25\times10^{-10}\,yr^{-1}$. The four diagonal dashed lines in the top left panel represent constant gas depletion times of 0.1 Gyr, 1 Gyr, 10 Gyr, and 100 Gyr.

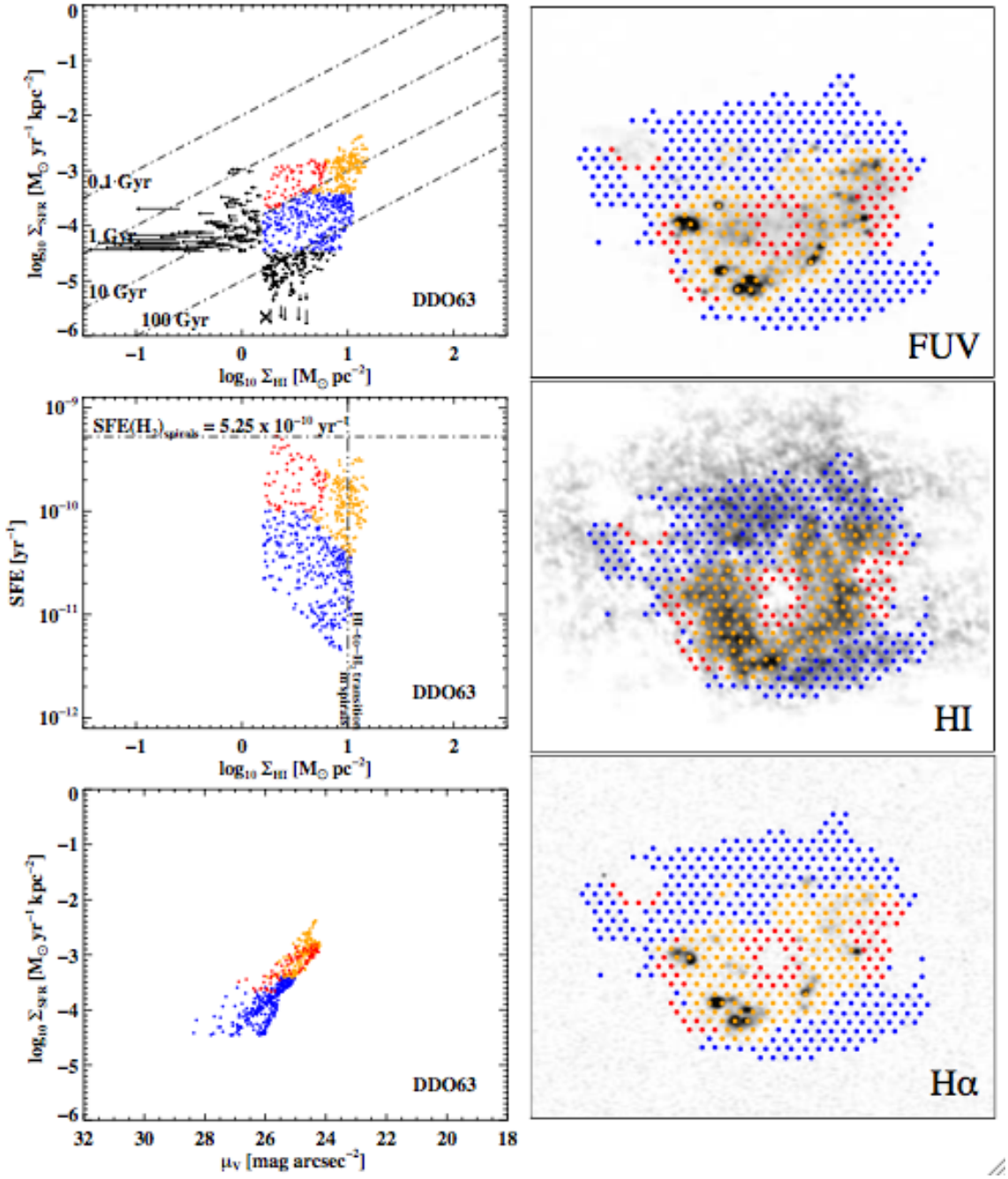

Figure 4.35: DDO 63: In an in depth study of the SF Law, based on the H I distribution map we separate the galaxy into three regions: red for H I shell interiors, orange for high H I surface density regions and blue for the outskirts. Their position is plotted on the FUV (top right), H I (middle right) and Hα (bottom right) maps. We plot the same pixels as in the panels to the right as a SFRD vs. H I surface density plot (top left), SFE vs. H I surface density (middle left), and SFRD vs. V–band surface brightness (bottom left). All points are independent and above a 5σ cutoff level in SFR. The vertical dashed line represents an H I surface density of $10\,M_\odot\,pc^{-2}$. The horizontal dashed line represents constant molecular gas SFE of $5.25\times10^{-10}\,yr^{-1}$. The four diagonal dashed lines in the top left panel represent constant gas depletion times of 0.1 Gyr, 1 Gyr, 10 Gyr, and 100 Gyr.

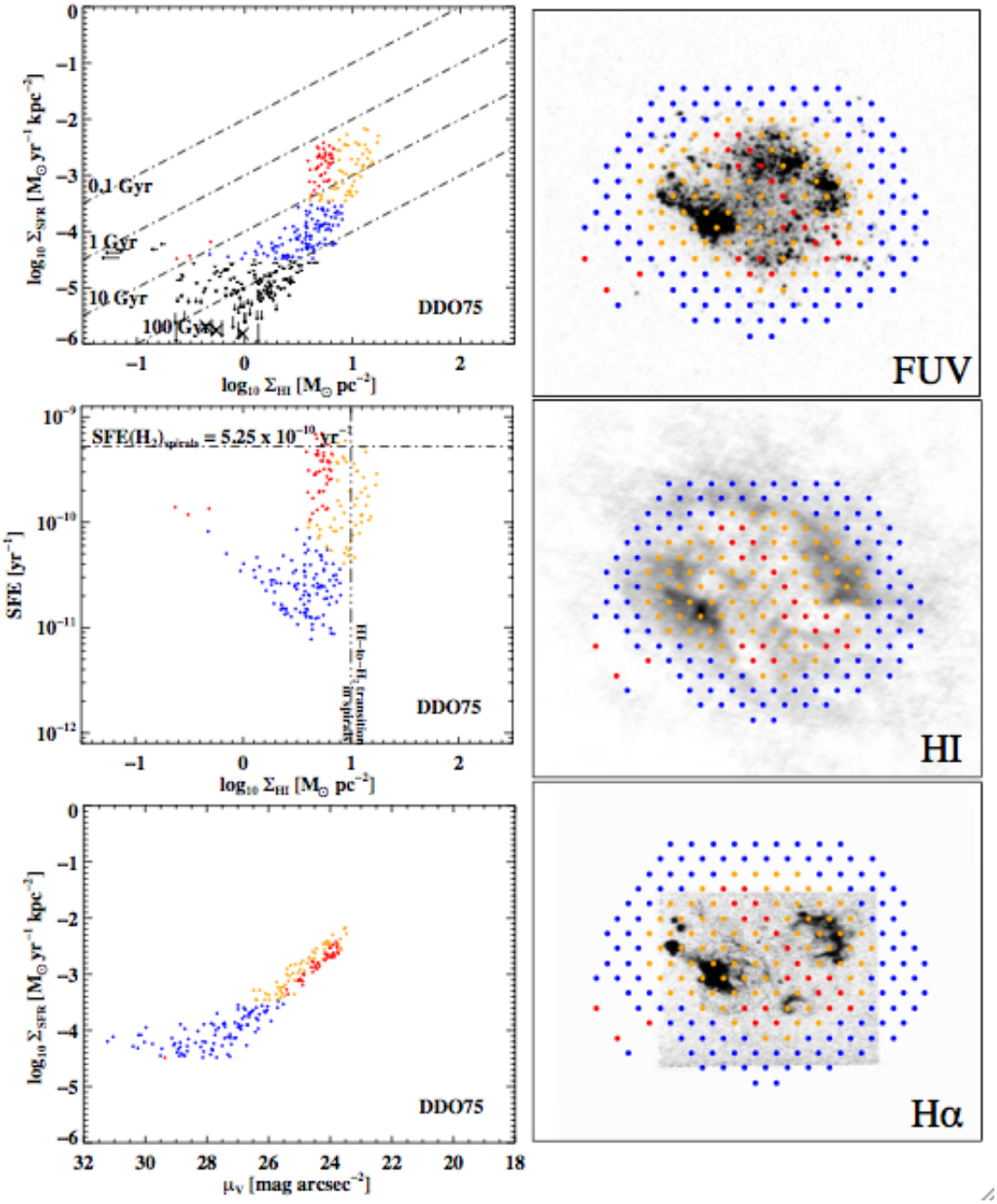

Figure 4.36: DDO 75: In an in depth study of the SF Law, based on the H I distribution map we separate the galaxy into three regions: red for H I shell interiors, orange for high H I surface density regions and blue for the outskirts. Their position is plotted on the FUV (top right), H I (middle right) and Hα (bottom right) maps. We plot the same pixels as in the panels to the right as a SFRD vs. H I surface density plot (top left), SFE vs. H I surface density (middle left), and SFRD vs. V–band surface brightness (bottom left). All points are independent and above a 5σ cutoff level in SFR. The vertical dashed line represents an H I surface density of $10\,M_\odot\,pc^{-2}$. The horizontal dashed line represents constant molecular gas SFE of $5.25\times10^{-10}\,yr^{-1}$. The four diagonal dashed lines in the top left panel represent constant gas depletion times of 0.1 Gyr, 1 Gyr, 10 Gyr, and 100 Gyr.

Table 4.3. Fitted Power-Law Parameters at 400 pc Resolution for six galaxies (Σ_{SFR}–Σ_{HI})

	Before excluding the shell regions			After excluding the shell regions		
Name	Coefficient (A)	Index (N)	Correlation coeff. (r_s)	Coefficient (A)	Index (N)	Correlation coeff. (r_s)
DDO 133	−4.9	2.10	0.78	−5.1	2.21	0.89
NGC 4214*	−4.8	1.93	0.55	−5.2	2.23	0.77
DDO 50*	−5.2	2.39	0.66	−5.4	2.46	0.80
IC 1613	−4.0	1.49	0.61	−4.3	1.91	0.86
DDO 63*	−4.8	1.74	0.49	−5.2	2.03	0.66
DDO 75	−5.0	2.23	0.74	−5.2	2.22	0.86
All Six	-4.88 ± 0.4	1.96±0.2	0.62	-5.2 ± 0.3	2.18±0.2	0.79

Table 4.3: We give for each of the six galaxies showing resolved H I shells the linear fit parameters and the Spearman rank coefficient of the SFRD–H I surface density distribution before (columns 2 to 4) and after (columns 5 to 7) excluding the points representing the H I shell interiors.

If we exclude the points representing the H I shell interiors the correlation improves by 10 to 20%, bringing most of the six galaxies to correlation coefficients of above 0.8 (in DDO 63 the correlation of 0.49 improves to 0.66). Finally, this larger sample of galaxies with extended shells, allows us to estimate the correlation coefficient and the fitted power law parameters for all six galaxies after excluding the pixels corresponding to the H I shells.

As shown in Table 4.3, if we exclude the red points representing the H I shell interiors, the correlation coefficient of all the galaxies taken together improves from 0.62 to 0.79. Although impressive, this improvement should be interpreted carefully; the distribution of the six galaxies may be dominated by galaxies such as DDO 50 and NGC 4214 which bring more points to the total distribution than other galaxies such as IC 1613 and DDO 75.

4.7 The H I to H_2 Transition

In the previous chapter we looked at DDO 168 and DDO 133 and their H I to H_2 transition threshold and found that, although they have similar metallicities, they exhibit different behaviours. While DDO 168 has an H I maximum of $27.7\,M_\odot\,pc^{-2}$, DDO 133 has a maximum less than $10\,M_\odot\,pc^{-2}$. We concluded that metallicity alone could not explain the H I maximum. We come back to this idea here and involve our subsample to see what the H I limits are in dwarfs.

From the 18 galaxies in our subsample, the following 8 galaxies have maxima that are greater than the $10\,M_\odot\,pc^{-2}$ limit found by Bigiel et al. (2008) for spirals: DDO 187, DDO 50, DDO 63, DDO 53, DDO 75, NGC 2366, NGC 4214 and DDO 168. In low metallicity systems, the molecular phase can be described as small CO emitting cores (Madden et al., 1997) embedded in molecular clumps of similar size to the ones found in spiral galaxies, sitting in a dense H I envelope. The neutral gas in the H I envelope will not turn molecular because the interstellar radiation field (ISRF) will not allow it to cool, instead it will play a key role in shielding the newly formed molecules, as dust–shielding loses its dominating role to self–shielding by H_2 and H I. Therefore, the theoretical prediction is that, as metallicity goes down, we will tend to see more dense H I envelopes (Schaye, 2004). Moreover, at subsolar metallicities, Krumholz et al. (2011) predict that the H I to H_2 transition takes place at a metallicity dependent factor of the $10\,M_\odot\,pc^{-2}$ threshold.

Indeed, we see that in almost half of our subsample of low metallicity galaxies we

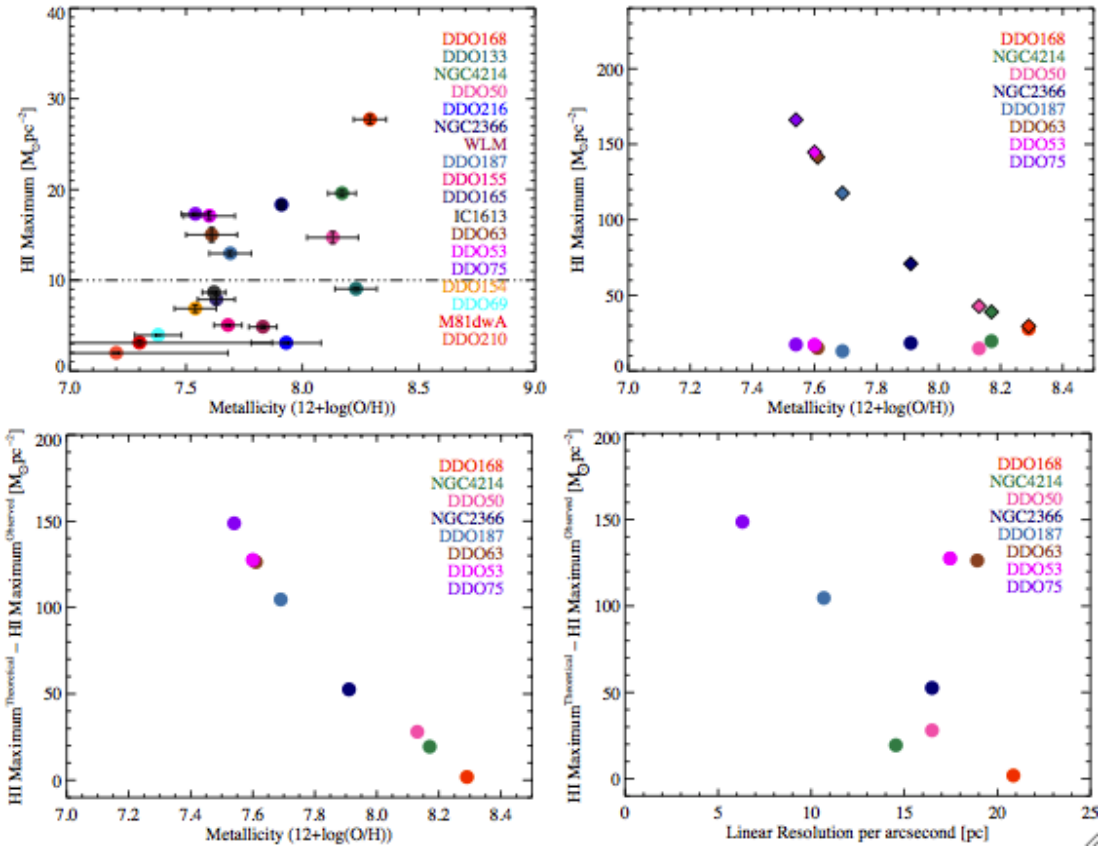

Figure 4.37: Top Left: For all galaxies we plot the H I maximum surface density against metallicity. Top Right: For all galaxies that have an H I maximum surface density higher then 10 $M_{\odot}$ pc^{-2} we plot both observed values (coloured filled circles) and theoretical values based on Krumholz et al. (2011) assuming a clumping factor equal to 1 (coloured filled diamonds) against metallicity. We also show the difference between the theoretically predicted value of the H I maximum surface density and the observed one as a function of metallicity (bottom left) and linear resolution per arcsecond (bottom right). Different colours represent different galaxies.

encounter higher (than in spirals) H I column densities which quite possibly hint at the presence of dense H I envelopes. A legitimate question in this context is why only half of them show this feature if the phenomenon is depending solely on metallicity. It may very well be that the dense H I envelopes are transient structures which form and disperse around the SF event, and, therefore, they would not be observable during the long periods of time between SF episodes.

If we plot (in the left panel of Fig. 4.37) the H I surface density maxima against metallicity, despite the theoretical prediction (Krumholz et al., 2011, 2009), no clear trend emerges. The behaviour of galaxies like DDO 210, DDO 69 and M81dwA can not be attributed to large error bars in the metallicity measurement, but one should

note that all three galaxies seem to have ceased their SF activity. They are known to have gone through SF episodes in the recent past, hence the FUV emission present in these galaxies, but a lack of Hα emission in DDO 210 and M81dwA and a deficit of Hα emission in DDO 69 as they have not formed stars in the past 10 Myr. The galaxy with the highest metallicity, DDO 168 is also the galaxy with the highest H I maximum, whereas DDO 133, the galaxy with a similarly high metallicity is the galaxy with the lowest H I maximum of the group. Consequently, we conclude that metallicity alone cannot explain the H I to H_2 transition and that there must be other factors that come into play.

In low metallicity galaxies, Krumholz et al. (2011) predict that the H I to H_2 transition takes place at $10\,M_\odot\,pc^{-2}/cZ$, where Z is the metallicity and c is a clumping factor ranging from 1 to 5 at resolutions of several hundred parsecs. In a study which applies the theoretical predictions from Krumholz et al. (2009) and Krumholz et al. (2011) to the SMC, Leroy et al. (2011) explain that the clumping factor, c, can be defined as a ratio between the molecular complexes and the gas surface densities. The larger the spatial scale, the more the molecular complexes become unresolved and hence the need for a clumping factor larger than one. However, Leroy et al. (2011) find that changing the clumping parameter does not match the effect of smoothing and explains it as due to a larger than expected part of the H I being locked up as a warm, diffuse component. These results have motivated us to assume for all the galaxies in our sample, all at a linear resolution of 400 pc, a clumping factor of 1.

In the top right panel of Fig. 4.37 we plot both the predicted H I maximum and the observed one as a function of metallicity and find a large discrepancy between points, the only close match being DDO 168. In the bottom panels of the same figure we plot the difference between the predicted and the observed maxima against metallicity and linear resolution per arcsecond and find that the discrepancy between the theoretically predicted value and the observed one is metallicity dependent and not conclusively dependent on resolution. We would have expected a dependence on resolution that would have brought us back to our choice of clumping factor, yet we found that the lower the metallicity the larger the discrepancy between the predicted and the observed values of the maximum. Clearly metallicity plays an important role in driving the H I to H_2 transition. However, it seems to act in complicity with some other hidden parameter which is neither the clumping nor the resolution.

As discussed in Chapter 3, Section 3.2.4.1 the value of the H I surface density

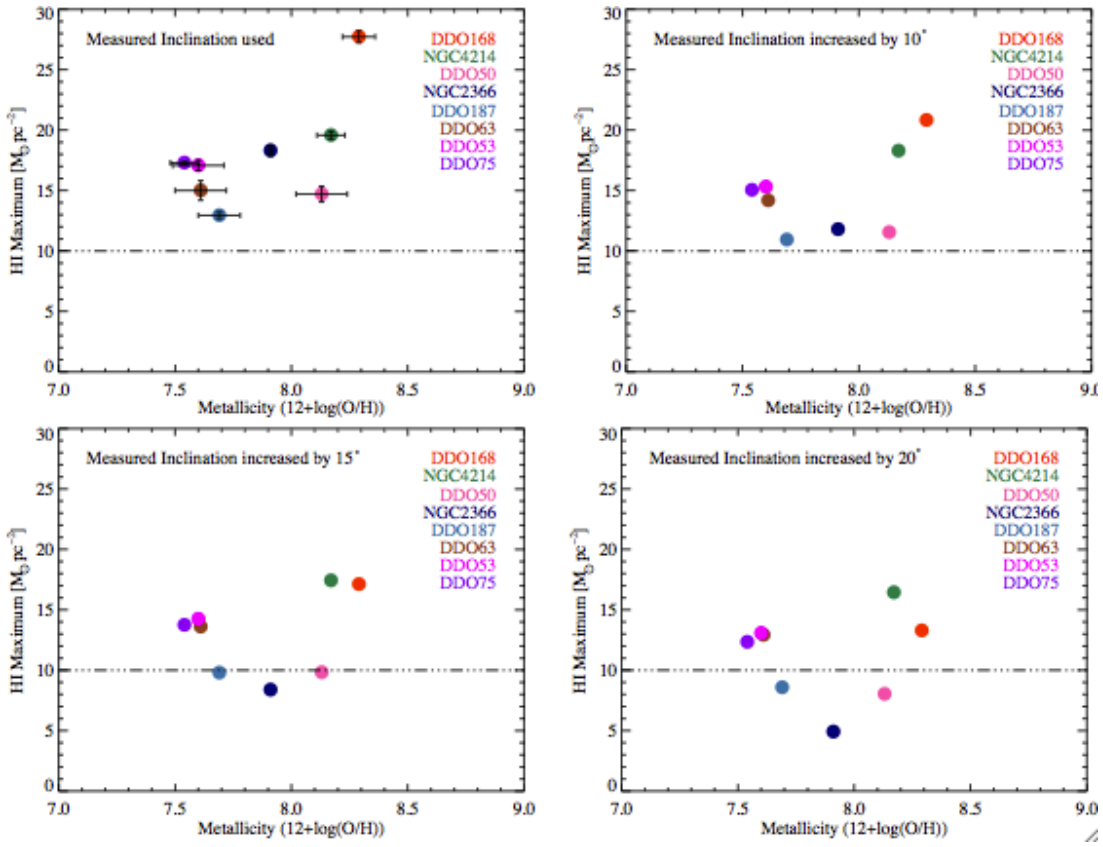

Figure 4.38: Top Left: We plot for all galaxies with H I maximum above 10 $M_\odot$ pc^{-2}, the H I maximum against metallicity when the inclination of the galaxies is changed by 10° (top right), 15° (bottom left) or 20° (bottom right). In the top left panel we show as a reference the H I maximum as a function of metallicity for the measured inclination in galaxies with H I maximum above 10 $M_\odot$ pc^{-2}. Different colours represent different galaxies.

maximum depends to a certain degree on the uncertainty in the inclination measurement. We showed there that in the case of DDO 168 this uncertainty alone cannot bring down the H I surface density maximum to a value below 10 $M_\odot$ pc^{-2}. In Fig. 4.38, for the galaxies in our sample that have H I maxima above 10 $M_\odot$ pc^{-2} we plot the H I maximum vs. metallicity in four different panels and for each panel we vary the inclination correction applied. We find that even when increasing the inclination by 20 °, more than half of the galaxies in the plot still have H I maxima above 10 $M_\odot$ pc^{-2}. Therefore inclination uncertainties alone cannot explain the value of the H I maxima in these galaxies.

Using a sample of 23 dwarf galaxies, Roychowdhury et al. (2011) found that the H I to H_2 transition above the 10 $M_\odot$ pc^{-2} threshold always happens in galaxies where the ratio between the SFRD based on Hα as a SF tracer and the SFRD based

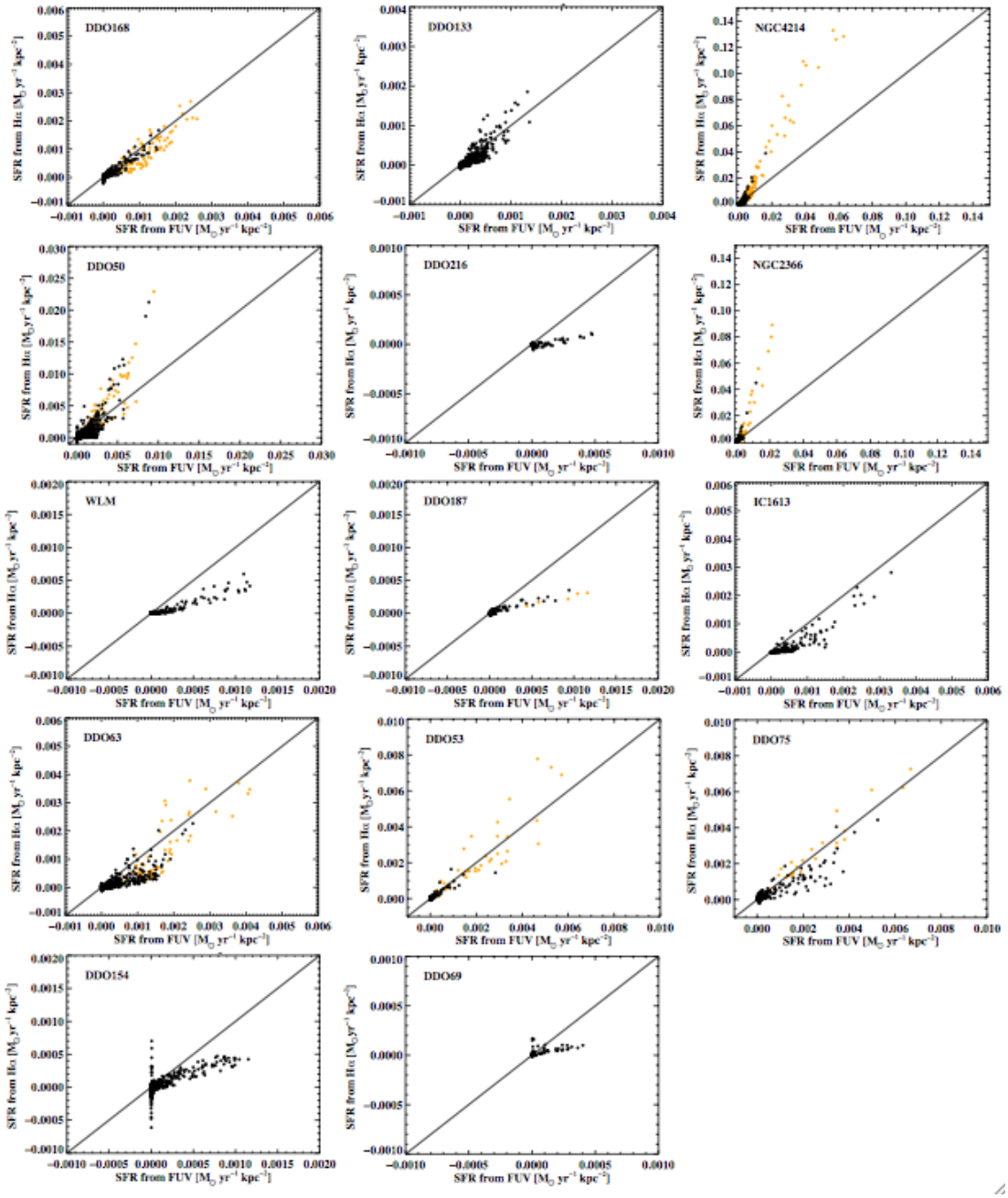

Figure 4.39: We present for all galaxies in our subsample with appropriate ancillary data available, SFRD from FUV–only vs. SFRD based on Hα–only. The orange points represent points that also have an H I surface density higher than $10\,M_{\odot}\,pc^{-2}$. The black continuous line represents a 1:1 relation between the x and y axis.

on FUV as a SF tracer is larger than 1. To test their results in our sample, in Fig. 4.39 we plot the SFRD based on FUV vs. the SFRD based on Hα and highlight in orange all the points that have an H I surface density higher than $10\,M_{\odot}\,pc^{-2}$.

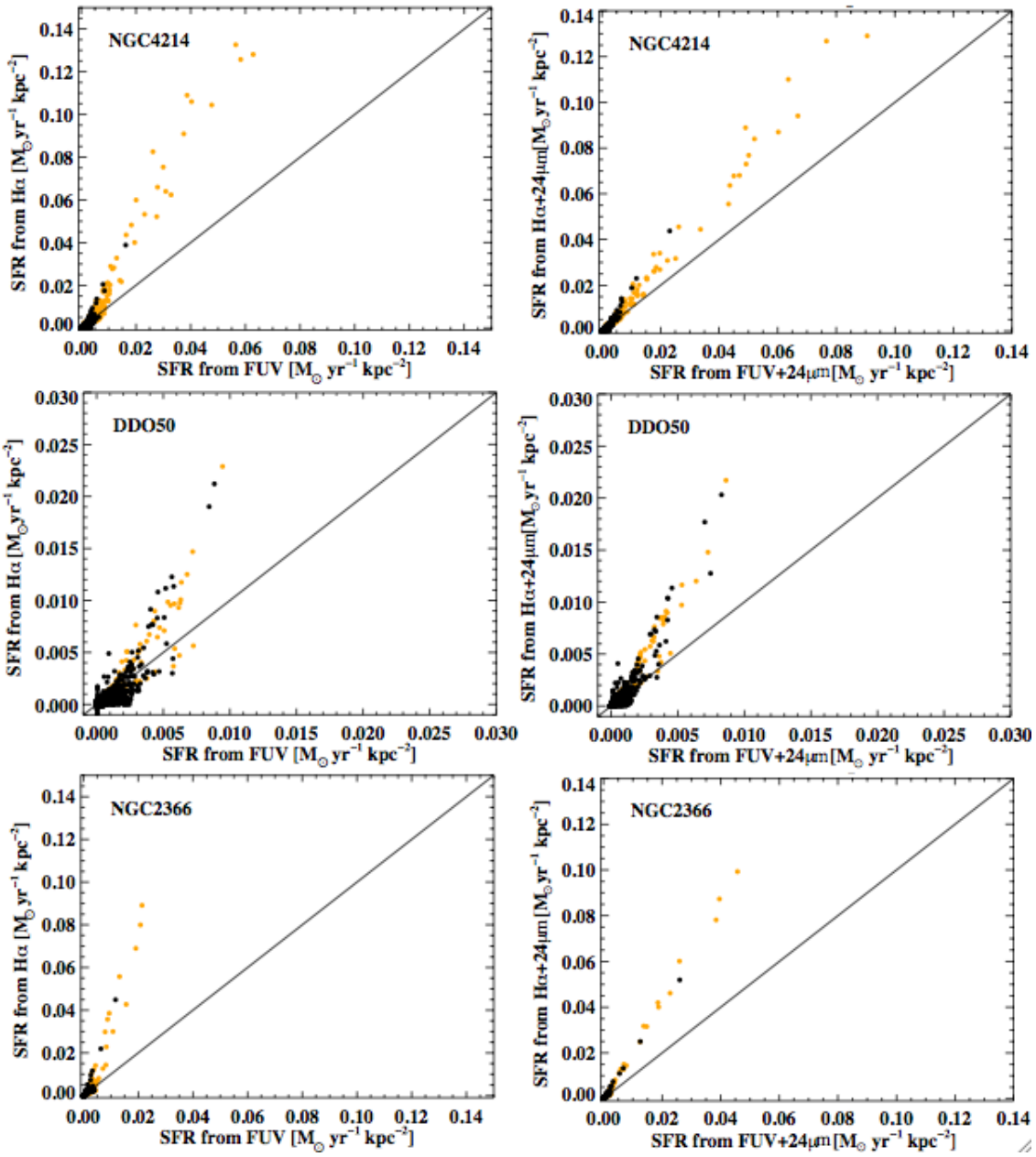

Figure 4.40: To show that the SFRD(Hα) and SFRD(FUV) ratio is influenced by the internal extinction correction applied, for the three galaxies with the most significant 24 μm emission in our subsample: NGC 4214, DDO 50 and NGC 2366, we present SFRD from FUV–only vs. SFRD based on Hα–only (left) and SFRD from FUV+24 μm vs. SFRD based on Hα+24 μm (right). The orange points represent points that also have an H I surface density higher than 10 $M_\odot$ pc^{-2} . The black continuous line represents a 1:1 relation between the x and y axis.

Out of the eight galaxies that have some orange points, in four of them (DDO 168, DDO 63, DDO 53 and DDO 75) the orange points are associated with SFRD(Hα)

and SFRD(FUV) ratios of one, whereas in three of them (NGC4214, DDO 50 and NGC 2366) the ratio of each orange point is above one as predicted by Roychowdhury et al. (2011). Finally, in the case of DDO 187 the orange points have a ratio smaller than one.

However NGC 4214, DDO 50 and NGC 2366 are the more massive galaxies in our subsample and have more dust content which can easily affect their SFRD(Hα) and SFRD(FUV) ratio. In Fig. 4.40, for these three galaxies, we show by comparison SFRD based on FUV vs. the SFRD based on Hα (both with no internal corrections applied) on the left side and the SFRD based on FUV+24 μm vs. the SFRD based on Hα+24 μm on the right side and immediately notice that indeed the SFRD(Hα+24 μm) and SFRD(FUV+24 μm) ratio is smaller than the SFRD(Hα) and SFRD(FUV) ratio, yet still above one.

Also noteworthy is the fact that apart from DDO 187 where the orange points representing areas of H I surface density higher than 10 $M_{\odot}$ pc^{-2} have a ratio smaller than one, all the other galaxies in the subsample follow a similar trend where most of the black points in each galaxy have ratios smaller than one and only orange points have higher than one ratios. In other words only where the H I surface density is above the threshold does the SFRD(Hα) and SFRD(FUV) ratio become one or higher, confirming the Roychowdhury et al. (2011) result.

The behaviour of the orange and the black points hint towards the coexistence of two different regimes in some galaxies, therefore in Fig. 4.41, for those particular galaxies, the H I maximum representing the higher density regime is always plotted against values derived for that regime by integrating or averaging over the area occupied by the orange points. In this way in the top left panel of Fig. 4.41 we compare two different regimes and although unorthodox our method shows that the two regimes share the same relation between the H I maximum and the ratio between SFRD(Hα) and SFRD(FUV) integrated over the region the H I maximum originates from. We find that the higher the SFRD(Hα) and SFRD(FUV) ratio, the higher the H I maximum. However, one galaxy, DDO 168 does not follow the main trend.

A higher SFRD(Hα) and SFRD(FUV) ratio means in fact more very young stars of a few Myrs (as opposed to several hundred Myrs), which intensely emit UV photons and boost up the intensity of the interstellar radiation field (ISRF). According to Blitz & Rosolowsky (2006); Elmegreen (1993), the ISRF emissivity is directly proportional to the stellar mass surface density and hence plays a role in regulating SF (Ostriker et al., 2010). We have already shown in the previous

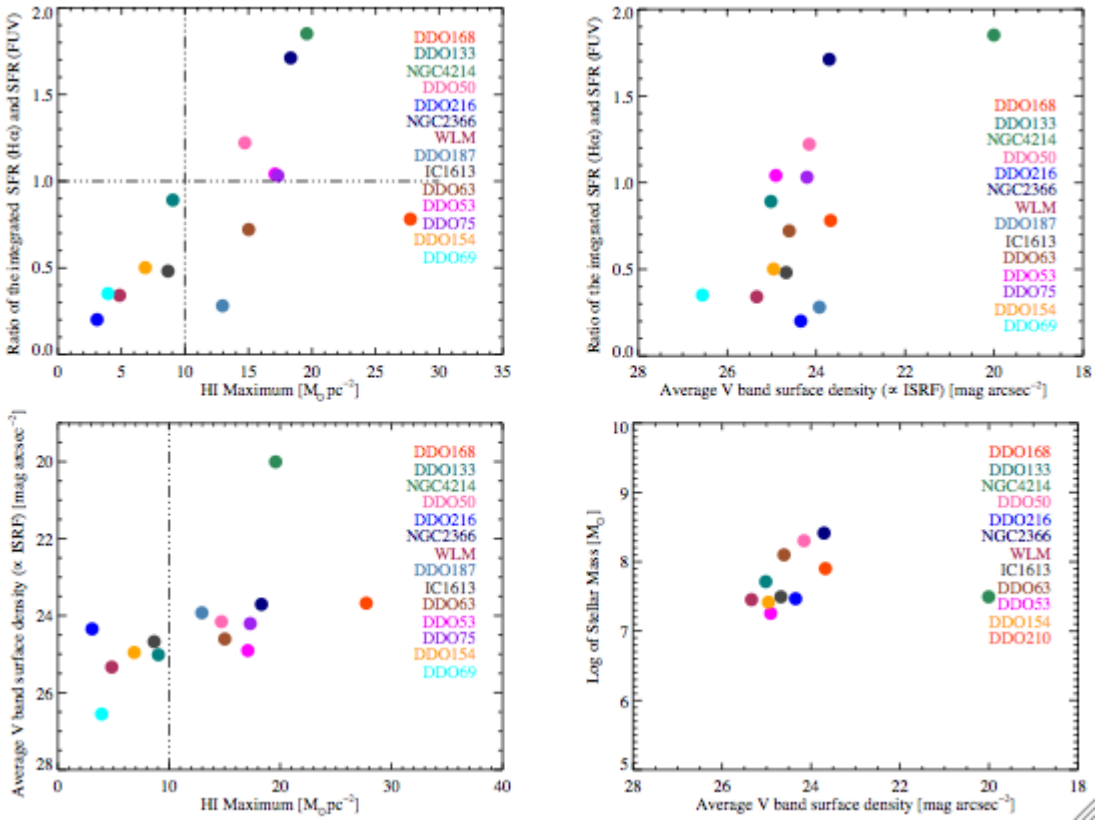

Figure 4.41: We plot for those same galaxies as in Fig. 4.37 the ratio of the integrated star formation rates based on Hα and on FUV vs. the H I maximum (top left) and the ISRF (top right). We also plot the average V–band surface density ($\propto$ ISRF) vs. H I maximum (bottom left) and vs. stellar mass (bottom right). The integrated star formation rates and the average V–band surface density are estimated based on the orange points in Fig. 4.37 for galaxies that have H I maximum higher than $10\,M_{\odot}\,pc^{-2}$ and based on the black points in Fig. 4.37 for all the other galaxies. Different colours represent different galaxies. The vertical dashed line represents an H I surface density of $10\,M_{\odot}\,pc^{-2}$. The horizontal dashed line represents a ratio of the integrated star formation rates based on Hα and on FUV of 1.

chapter that at least in the case of DDO 168 and DDO 133 the V–band surface density and the 3.6 μm band surface density (the core of our stellar surface density measurement) follow the same relation with SFRD. The next section shows this to be true for our whole subsample. Moreover a closer look at bottom right panel of Fig. 4.41, illustrates a tight relation between stellar mass and the average V–band surface density. In conclusion, the average V–band surface density (an average over the region the H I maximum originates from) can indeed be used as a proxy for ISRF emissivity.

Under these assumptions, in the top right panel of Fig. 4.41, we find that the

SFRD(Hα) and SFRD(FUV) ratio is in fact tightly connected to the emissivity of the ISRF. We also find that the higher the ISRF emissivity the higher is the H I maximum (see bottom left panel of Fig. 4.41), a result not at all unexpected if we think that the more UV photons available to dissociate the newly formed molecules the more H I is necessary to self–shield the molecular cloud. Also noteworthy is the exceptionally high ISRF emissivity in NGC 4214, which sets this galaxy apart from the main trend followed by all the other galaxies.

4.8 The Correlation between SFR and the Stars

We have already established in Section 4.3 that for all the galaxies in our sample the SFRD and V–band surface density follow a tight relation. This result not only holds in dwarf galaxies at the higher end of our metallicity range such as DDO 168 and DDO 133 (see previous chapter), but for all galaxies in our sample, confirming the existence of a SFRD with V–band surface density relation at small scales (400 pc resolution element). Such a relation but at larger scales (per galaxy) was previously established by Hunter et al. (1998) and Hunter & Elmegreen (2004). The fact that this relation holds locally as well as globally, suggests that current stars play an active role in driving star formation.

To analyse this relation further, in Fig. 4.42 we change our perspective and look at density contours at 10%, 25%, 50%, 75% and 90% of the pixel–by–pixel distribution of SFRD based on FUV–only vs. V–band surface density overlaid with the radial profile of this distribution (coloured circles). Each black point represents the average within a circular annulus with the width of an H I beam. The coloured cores correspond to the galactocentric radius range of the points participating in the average.

The radial behaviour of the azimuthally averaged profiles follow the pixel–by–pixel distribution (Figs. 4.5 – 4.22) closely. The black continuous line in each panel of Fig. 4.42, represents the linear fit through the data of each galaxy. For the linear regression ($log_{10}\Sigma_{SFR} = A + N\mu_V$) we have used the OLS bisector method, for reasons which have been explained in Section 4.3. The numerical results of the linear fit of the $log_{10}\Sigma_{SFR}$ – μ_V point distribution considering both FUV and Hα as SF tracers for the SFR map are given in Table 4.4. The coefficient A given in Table 4.4 is normalized and it represents the $log_{10}\Sigma_{SFR}$ at $\mu_V = 23\,\mathrm{mag\,arcsec^{-2}}$, the peak V–band intensity for dwarfs. The values for A across the sample are quite

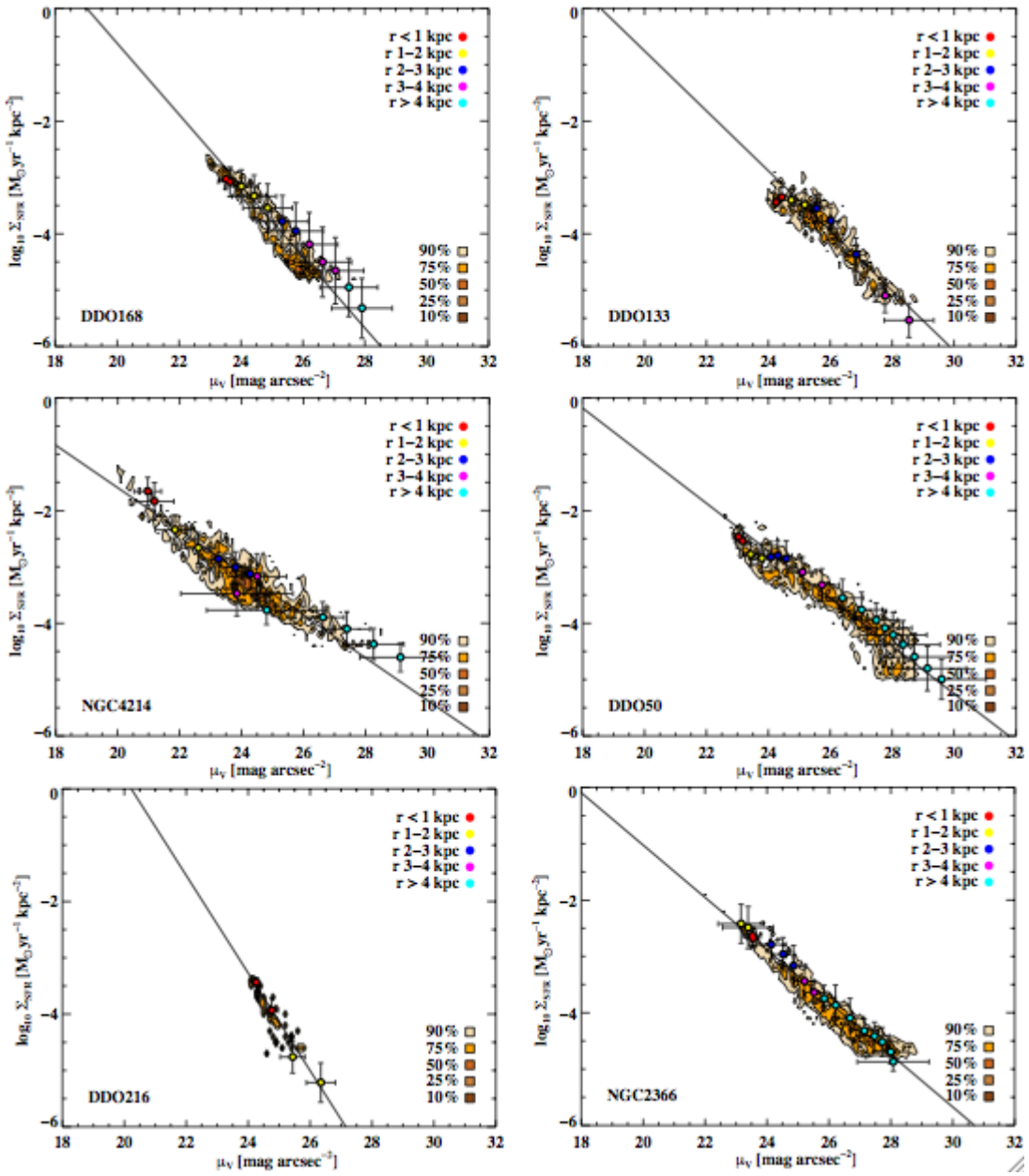

Figure 4.42: We plot for all galaxies in our subsample observed in FUV, density contours at 10%, 25%, 50%, 75% and 90% of the pixel–by–pixel distribution of SFRD based on FUV–only vs. V–band surface density. The colour filled circles show the data plotted in radial bins of a beam size wide their colours representing different radii: red cores for smaller than 1 kpc, yellow cores from 1 to 2 kpc, blue cores from 2 to 3 kpc, magenta cores from 3 to 4 kpc and cyan cores for larger than 4 kpc. All maps used for the above plots have the same linear resolution of 400 pc. All points are independent and above a 5σ cutoff level. The black continuous line represents for each galaxy, a fitted power law through the galaxy's points distribution. The power law parameters are given in Table 4.4

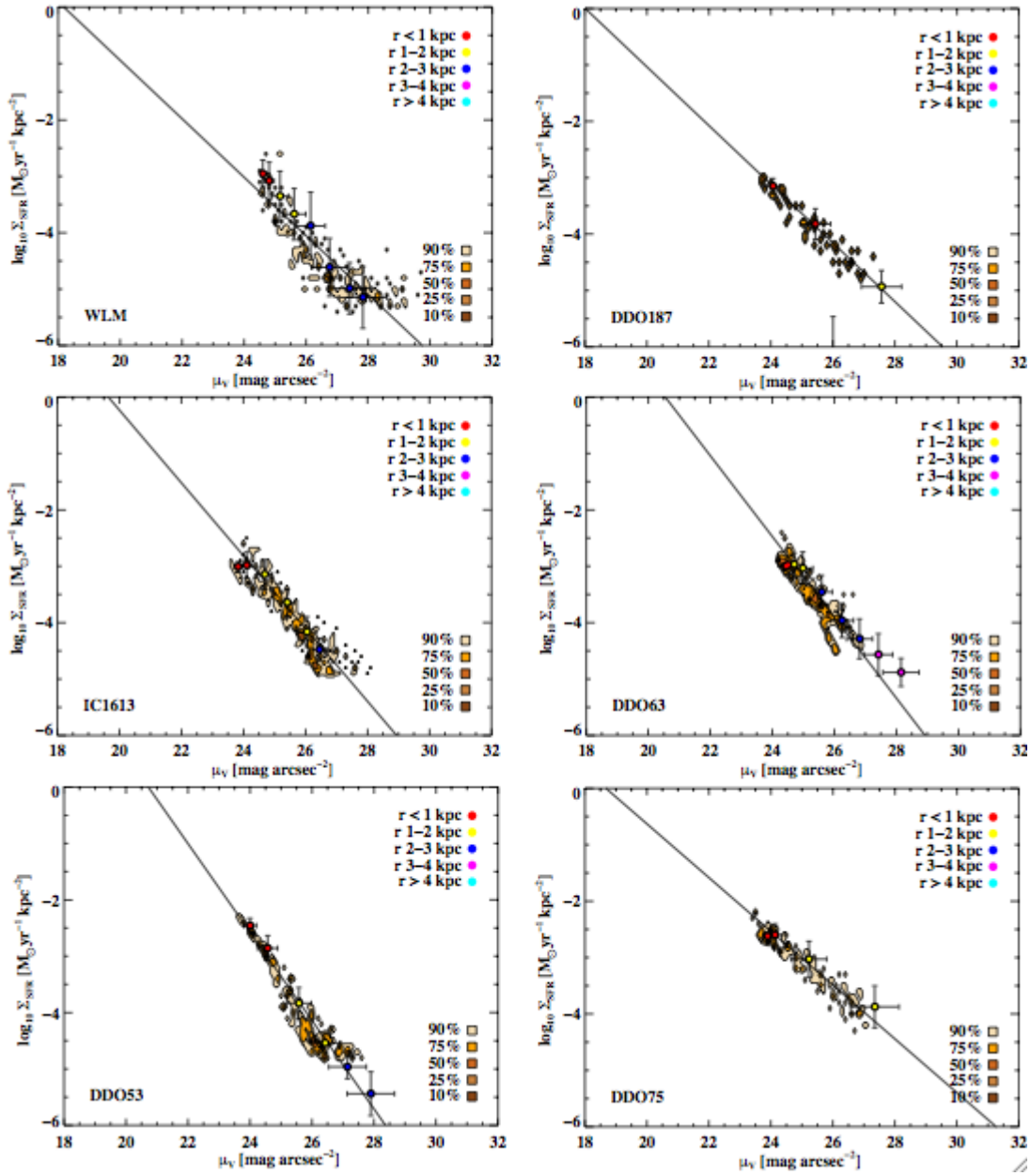

Fig. 4.42 continues ...

consistent, with the exception of DDO 53 and M81dwA which fall further from the mean of the whole subsample or the A coefficient of the distribution of all galaxies together.

At a close inspection of Table 4.4 one quickly notices that the SFRD based on FUV–only shows a higher degree of correlation with the V–band surface density than the SFRD based on Hα does. We remind the reader here that Hα samples young stars from within the past 10 Myr, whereas FUV averages over the past 100 Myr, so

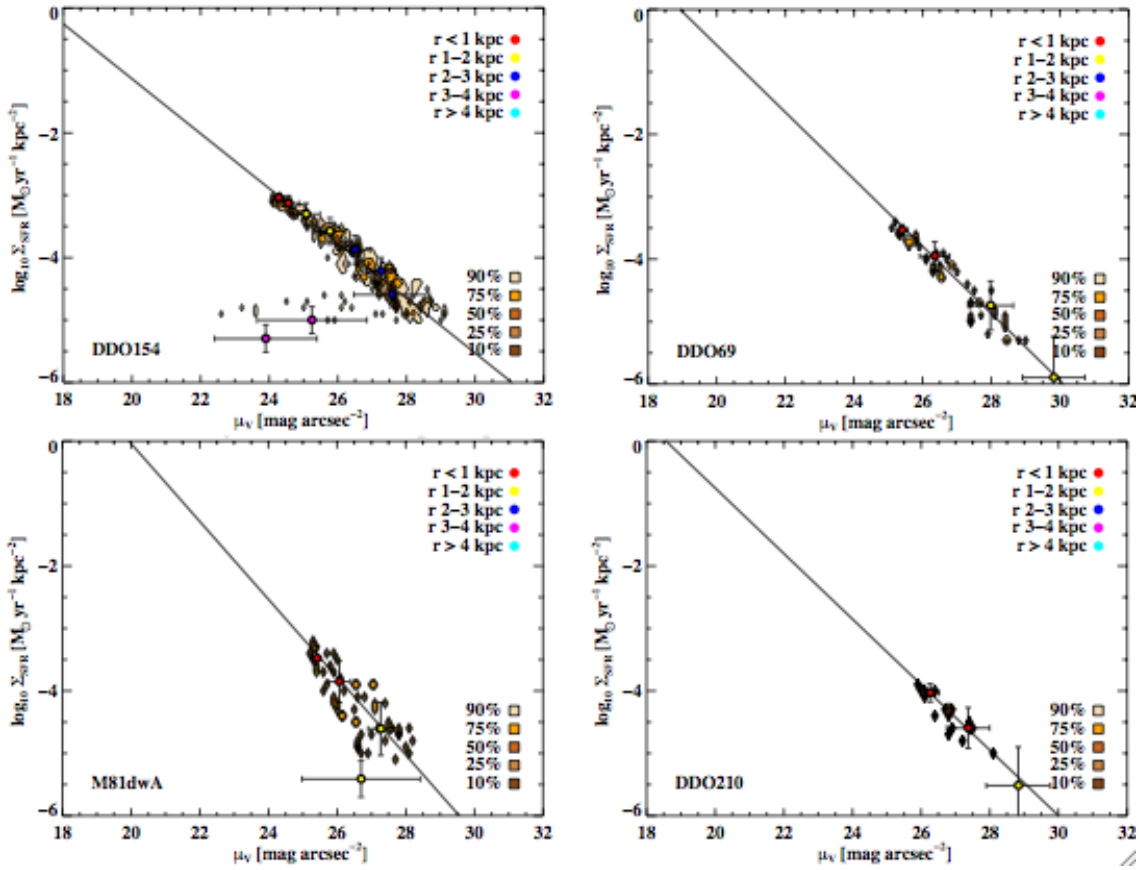

Fig. 4.42 continues ...

FUV is smoothing the SFR over a larger timescale than Hα and this reflects in the differences in the degree of correlation between the SFRD(FUV)–V–band surface density and the SFRD(Hα)–V–band surface density.

To assess whether the higher degree of correlation between SFRD based on FUV–only and V–band surface density is in fact due to a dominating contribution of young stars to the V–band emission we present Fig. 4.43 based on Zhang, H., (private communication). A detailed description on the method used for obtaining the values plotted is given in Zhang et al. (2012). Fig. 4.43 shows that as long as the SFH is more or less constant stars younger than 100 Myr (the timescale of FUV as a SF tracer) or 10 Myr (the timescale of Hα as a SF tracer) do not dominate the V–band emission. Specifically, if the current SFR relative to the average SFR over the lifetime of the galaxy is less than 5, stars younger than 100 Myr contribute less than 50% of the V–band light. In fact, generally for dwarf irregulars, the dominant contribution to the V–band emission is from populations formed in the past 2 Gyr again under the assumption that we are dealing with galaxies with a steady state

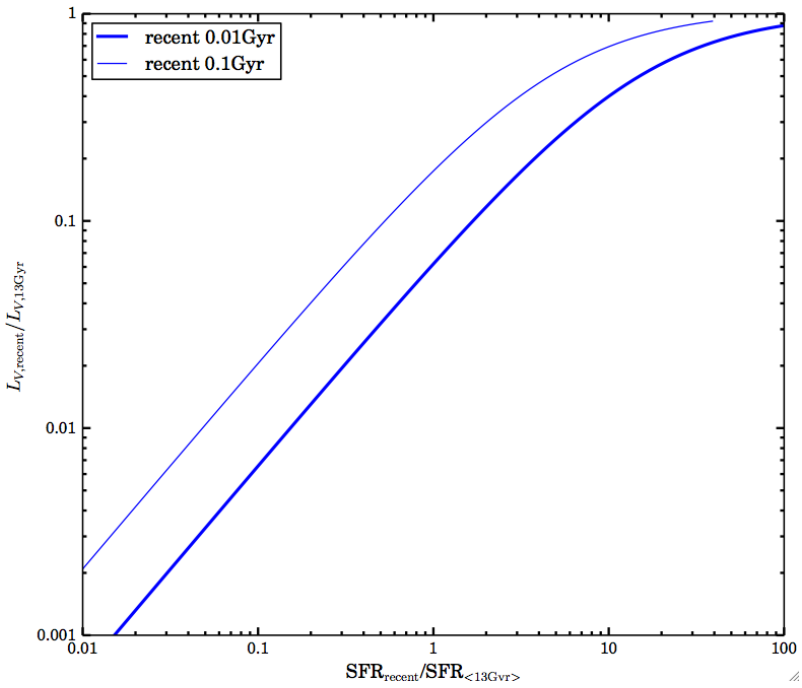

Figure 4.43: We show the fraction of V–band light contributed by stars formed in the past 10 Myrs (thick blue curve) and in the past 100 Myrs (thin blue curve) as a function of the amplitude of the current SFR relative to the average SFR over the lifetime of the galaxy. The figure is from Zhang, H., private communication.

star formation situation rather than starburst galaxies.

For all galaxies in our sample, Zhang et al. (2012) derived the current SFR (recent 100 Myr) relative to the average SFR over the lifetime of the galaxy and those values are mostly under five, the exceptions being three galaxies DDO 168, DDO 75 and M81dwA with values of 6.19, 9.17 and 7.81 respectively. The galaxy with the highest of the latter three values is not the galaxy with the highest degree of correlation between SFRD based on FUV and V–band surface density shown in Table 4.4 as we would have expected to see if the degree of correlation was induced by a more dominant role of younger stars to the V–band emission. Hence, we conclude that SFRD based on FUV–only and V–band surface density are largely independent of each other and their correlation is not due to young stars dominating the V–band.

The degree of correlation between SFRD(FUV) and the V–band surface density ranges between 0.71 in DDO 154 to 0.95 in DDO 187. We have shown that in DDO 168 the SFRD(FUV) and the V–band surface density relation follows the SFRD(FUV) and the K–band surface density and the SFRD(FUV) and the 3.6 μm surface density relations closely.

Table 4.4. Fitted Power-Law Parameters at 400 pc Resolution ($log_{10}\Sigma_{SFR}$–μ_V)

Name	FUV as SF tracer				Hα as SF tracer			
	Coefficient (A) Normalized at $\mu_V = 23$ mag arcsec^{-2}	Index (N)	Cor. coef. (r_s)	rms scatter	Coefficient (A) Normalized at $\mu_V = 23$ mag arcsec^{-2}	Index (N)	Cor. coef. (r_s)	rms scatter
DDO 168	−2.5	−0.63	0.92	0.2	−2.7	−0.61	0.86	0.2
DDO 133	−2.4	−0.53	0.90	0.2	−2.0	−0.66	0.26	0.5
NGC 4214*	−2.9	−0.34	0.90	0.3	−2.5	−0.48	0.74	0.3
DDO 50*	−2.4	−0.43	0.92	0.3	−2.2	−0.44	0.55	0.4
DDO 216	−2.5	−0.87	0.85	0.2	−3.3	−0.72	0.50	0.1
NGC 2366*	−2.3	−0.46	0.92	0.2	−2.0	−0.67	0.85	0.3
WLM	−2.6	−0.52	0.84	0.4	−2.1	−0.84	0.74	0.4
DDO 187	−2.7	−0.49	0.95	0.2	−2.6	−0.30	0.63	0.2

IC 1613	-2.3	-0.65	0.93	0.3	-2.1	-1.03	0.54	0.6
DDO 63*	-2.0	-0.63	0.90	0.2	-1.5	-0.89	0.12	0.5
DDO 53*	-1.7	-0.78	0.92	0.3	-1.5	-0.83	0.89	0.2
DDO 75	-2.1	-0.48	0.95	0.2	-2.2	-0.47	0.45	0.3
DDO 154*	-2.4	-0.43	0.71	0.5	-3.3	-0.17	0.73	0.2
DDO 69	-2.3	-0.55	0.94	0.2	-1.2	-0.84	0.19	0.9
M81dwA*	-1.8	-0.62	0.81	0.3	...	...	...	...
DDO 210	-2.3	-0.52	0.81	0.1	...	...	...	...
All	-2.4 ± 0.4	-0.43 ± 0.03	0.85	...	-2.3 ± 0.5	-0.53 ± 0.02	0.69	...

Table 4.4: We give for each galaxy in our sample observed in FUV the linear fit parameters A normalized at $\mu_V = 23\,\mathrm{mag\,arcsec^{-2}}$ and N ($log_{10}\Sigma_{SFR} = A + N\mu_V$), the rms scatter in the SFRD direction and the Spearman rank coefficient (r_s) of the SFRD–V–band surface density distribution, where the considered SFR map uses both FUV (columns 2 to 5) and Hα (columns 6 to 9) only as SF tracers.

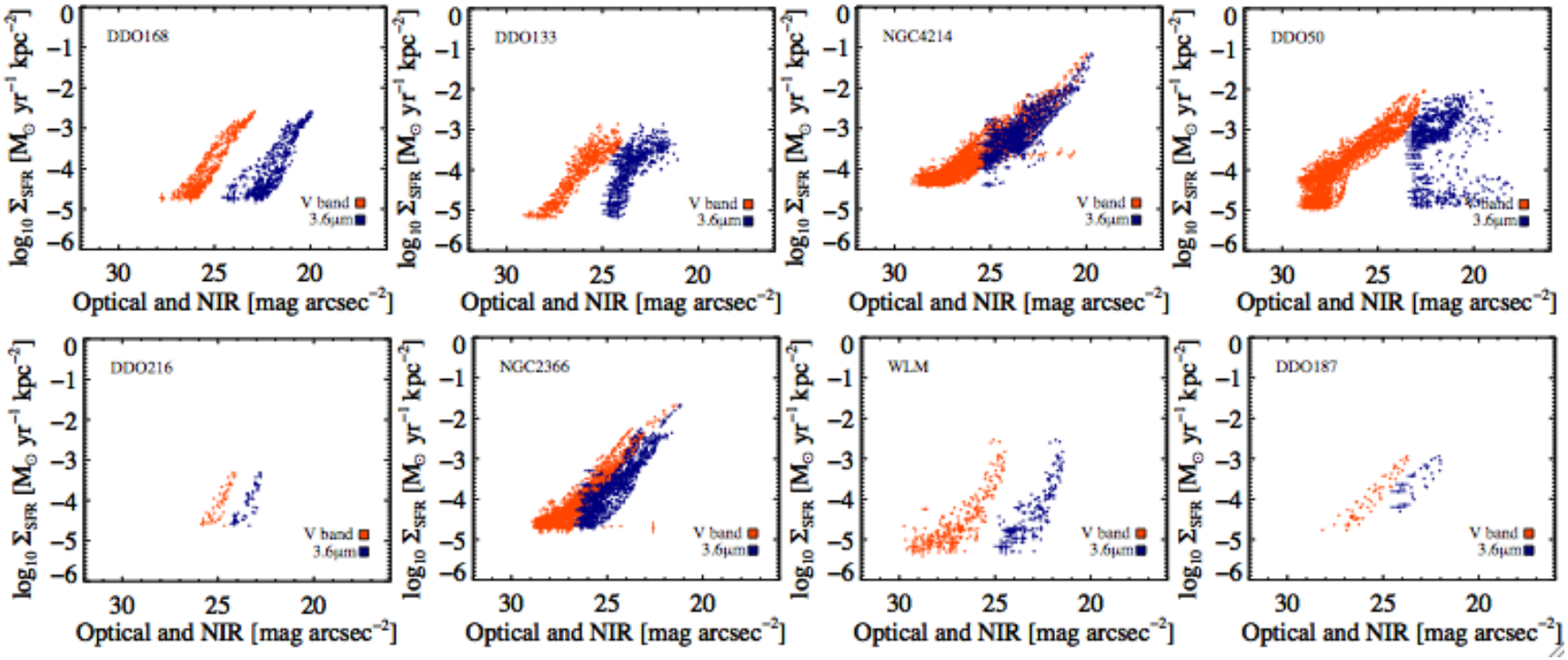

Figure 4.44: We present for all galaxies in our subsample with appropriate ancillary data available, scatter plots of V–band (orange) and 3.6 μm (navy) surface densities vs. SFRD. All maps used for the above plots have the same linear resolution of 400 pc. All points are independent and above a 2σ cutoff level in H I and in V–band surface density maps and 5σ cutoff level in FUV.

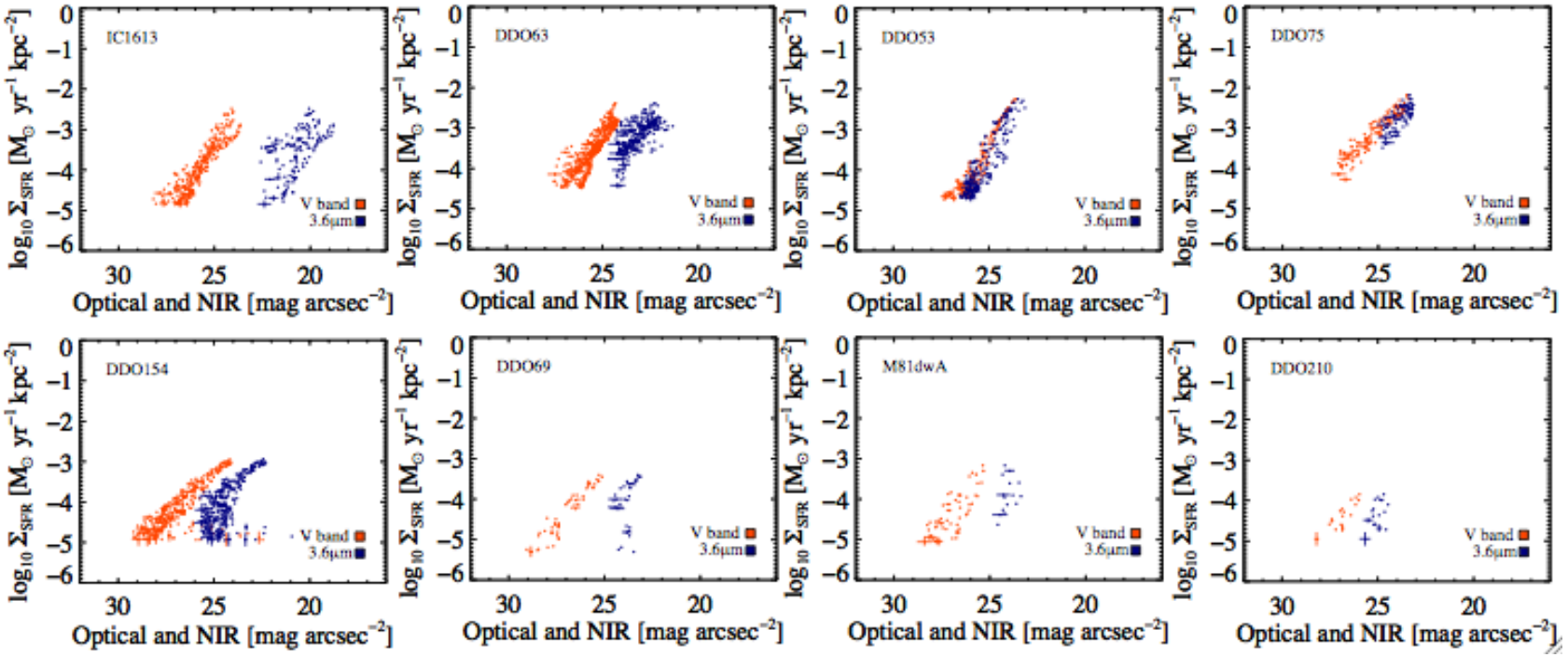

Fig. 4.44 continues ...

We confirm this result for our whole subsample in Fig. 4.44, where we plot SFRD as a function of V–band (orange) and 3.6 μm (navy) surface densities. All galaxies follow the same trend in both optical and near infrared (NIR) bands. Although the trend is the same there is more strength in the correlation with V–band than with the 3.6 μm band. Moreover the 3.6 μm emission is quite shallow and with larger error bars than the V–band so consequently the stellar mass surface density derived from the 3.6 μm band will not relate so neatly with SFRD as V–band does (see top and bottom panels of Fig. 4.45), even though both optical and (NIR) bands sample the same relation.

Rather than looking at individual galaxies, we can also make a single plot where all the independent points of each galaxy contribute to a total distribution of points. As we mentioned in Section 4.3 some of the galaxies in our subsample, due to their small size and distance from us, at 400 pc linear resolution are represented by a small number of points (under 60), therefore when plotting the total distribution of points the small galaxies' contribution would be lost in the sea of points coming from larger galaxies. To avoid this, in Fig. 4.45, we plot the density contours of a per galaxy–weighted total distribution of points. We find in Fig. 4.45 that as a whole, our subsample presents an increasing SFRD and only a mildly increasing SFE with increasing stellar surface density. The Spearman rank correlation coefficient of the SFRD vs. the V–band surface density distribution is 0.85 if the SF tracer used for the SFR map is FUV and 0.69 if the SF tracer used is Hα, suggesting that the two variables SFRD and the V–band surface density are highly correlated.

Having established a SFRD–V–band surface density relation, we are interested in giving it a functional form. To begin with we use the OLS bisector to do a linear fitting through the points distribution derived from all the galaxies in our sample and find that $\Sigma_{SFR} \propto (10^{\mu_V})^{-0.43\pm0.03}$. The azimuthally averaged data follow closely the linear fit shown in Fig. 4.42 as black continuous lines. In Fig. 4.46, we present in the left panel all the radial profiles based on azimuthal averaging from all galaxies with FUV data in our subsample (each galaxy plotted with a different colour) along with the linear (black continuous line). In the right panel of Fig. 4.46 overlaid on the SFRD–V–band surface density point distribution we show the linear fit through the azimuthal averages distribution (black line) and through the total point distribution (red line). The red and black lines overlap reinforces the idea that the radial profiles describe the data very closely and at least in the case of this subsample can be used as proxies for the total distribution.

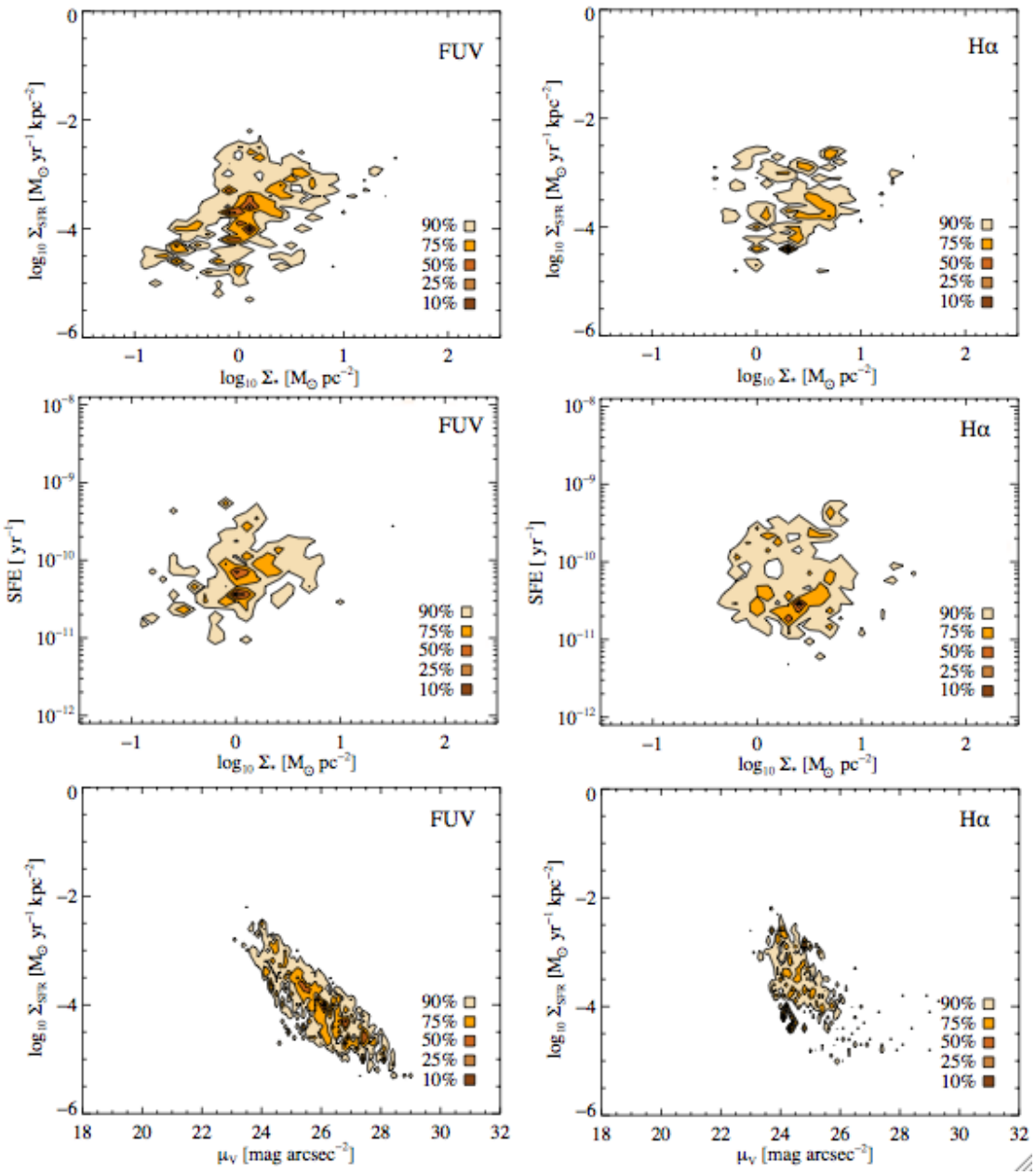

Figure 4.45: We plot for all galaxies in our subsample observed in FUV and Hα respectively, density contours at 10%, 25%, 50%, 75% and 90% of the pixel–by–pixel distribution of: SFRD (top) and SFE (middle) vs. stellar surface density (based on the 3.6 μm *Spitzer* map), SFRD vs. V–band surface density (bottom) plotted separately for two different SF tracers FUV (left) and Hα (right). All maps used for the above plots have the same linear resolution of 400 pc. All points are independent and above a 5σ cutoff level.

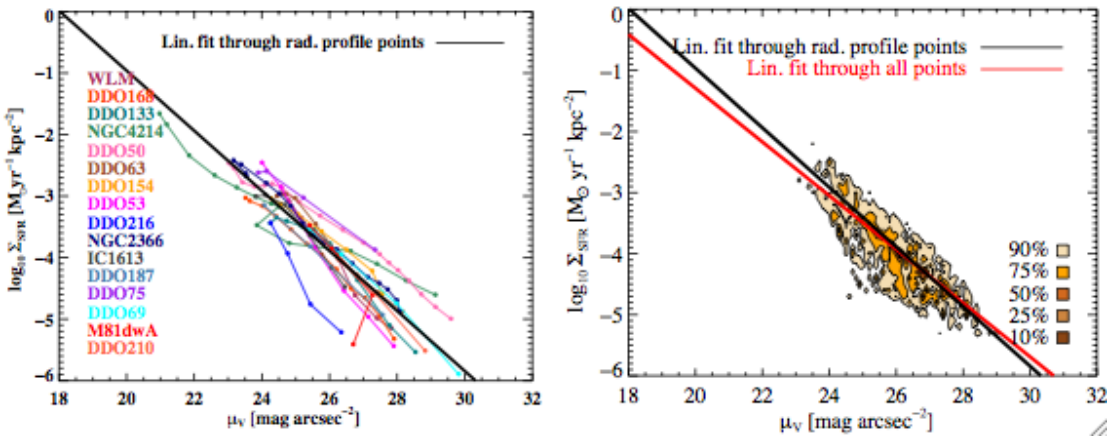

Figure 4.46: In the left panel, for all galaxies in our subsample we compute the radial profiles in both the SFRD (based on FUV–only) and the V–band surface density maps, each point representing an azimuthal average inside two concentric circles at a beam size distance of each other (same points as in Fig. 4.42). Each colour represents a different galaxy. In the right panel we over impose linear and polynomial fits on the density contours at 10%, 25%, 50%, 75% and 90% of the pixel–by–pixel distribution of SFRD vs. V–band surface density. All maps used for these plots have the same linear resolution of 400 pc. All points are independent and above a 5σ cutoff level. The continuous line represents a linear fit through the distribution of radial profile points (black) and through the total points distribution (red) of all galaxies.

In an attempt to better understand the nature of this relation between SFRD and V–band surface density, we computed for each galaxy in our sample the Spearman rank correlation coefficient (see Table 4.4), an indicator of how strong the correlation between the two quantities is. We computed these Spearman rank correlation coefficients for SFRD based on FUV and in Fig. 4.46 we find a high degree of correlation between SFRD(FUV) and V–band surface density. Further, in Fig. 4.47 we plot separately the above mentioned sets of correlation coefficients against quantities like metallicity, H I mass and absolute V–band magnitude and find that the degree of correlation between SFRD and V–band surface density is independent of any of the latter quantities.

As previously mentioned, the relation between the correlation coefficient and other parameters tells us about the SFRD–V–band surface density relation within each galaxy and nothing about whether all galaxies in our sample line up to a common SFRD–V–band surface density relation. This latter relation has been the study of previous paragraphs to the extent of confirming its existence. To relate it to parameters such as metallicity, H I mass, absolute V–band magnitude and

others we studied the index value N of the SFRD–V–band surface density relation in each galaxy as a function of the above mentioned parameters and found nothing conclusive.

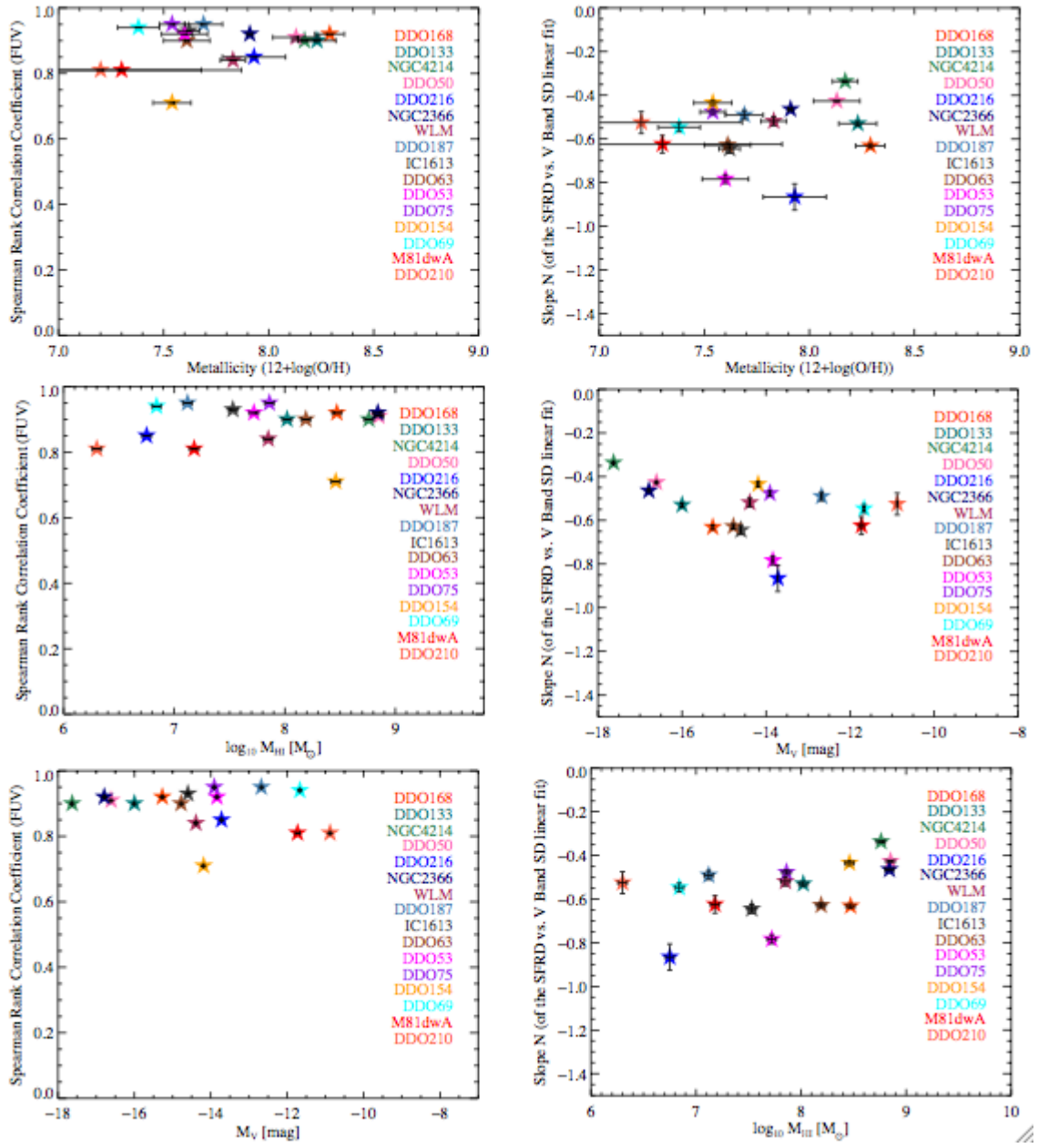

Figure 4.47: We plot for all galaxies in our subsample, the Spearman correlation coefficient (left) and the linear fit slope, N (right) between SFRD and V–band surface density vs. metallicity (top), H I mass (middle) and M_V (bottom). The SFR maps used for the linear fit and the measurement of the correlation coefficient are based on FUV–only as a SF tracer.

4.9 The Relation between SFR and Hydrostatic Pressure

The amount of gas turned molecular, the molecular fraction, at a given radius is determined by hydrostatic pressure. Spergel & Blitz (1992) were the first to point out that the large molecular fraction in the centre of Milky Way is probably due to the high hydrostatic pressure in the Galactic bulge. In fact, Elmegreen (1993) argues that both hydrostatic pressure and the mean interstellar radiation field influence the value of the molecular fraction and hence they theoretically derive the following relation: $f_{mol} \propto P_h^{2.2} j^{-1.1}$, where f_{mol} represents the molecular gas fraction defined as Σ_{H_2}/Σ_g, Σ_g representing the total gas surface density, P_h the hydrostatic pressure and j the ISRF emissivity.

Using a sample of 14 galaxies (mostly spiral galaxies), Blitz & Rosolowsky (2006) calculate R_{mol} (Σ_{H_2}/Σ_{HI}) as a function of pressure on a pixel–by–pixel basis and find that $R_{mol} \propto P_h^{0.92\pm0.07}$. Their result agrees well with the Wong & Blitz (2002) result ($R_{mol} \propto P_h^{0.8}$) which was based on azimuthal averages rather than pixel–by–pixel analysis. Considering that in the low f_{mol} regime, since the total gas surface density is mainly H I surface density, $f_{mol} \approx R_{mol}$, and under the assumptions that $j \propto \Sigma_g \propto \Sigma_*$ and that the velocity dispersion of the stars at any certain radius is dependent of Σ_* at that same radius in the galaxy, so $\sigma_* \propto \Sigma_*^{0.5}$, Blitz & Rosolowsky (2006) argue that their observationally derived result also agrees with the theoretical expression given by Elmegreen (1993). Moreover, Blitz & Rosolowsky (2006) suggests that although on physical grounds R_{mol} should depend on j, "empirically R_{mol} behaves as if it depends on pressure only".

We use the pressure maps created by Hunter et al. (in prep.). These maps were created using the LITTLE THINGS data for quantities such as surface densities and, gas and stars velocity dispersions. The following formulae taken from Elmegreen (1989, 1993) have been used for creating the pressure maps:

$$\mathrm{P_h[K\,cm^{-3}]} = \frac{\pi}{2} G \times \Sigma_{gas}(\Sigma_{gas} + \frac{\sigma_g}{\sigma_*} \times \Sigma_*) \tag{4.1}$$

where P_h is the hydrostatic pressure, Σ_{gas} is the H I gas surface density, Σ_* is the stellar surface density, σ_g is the gas velocity dispersion, σ_* is the stellar velocity dispersion and G is the constant of gravitation. The gas velocity dispersion, σ_g, is the H I velocity dispersion taken from our moment 2 maps, whereas the stellar velocity

dispersion, σ_*, was derived based on the relation between central stellar velocity dispersion and M_B: $log_{10}\sigma_* = -0.15M_B - 1.27$ (Swaters, 1999; Swaters et al., 2003), without taking into consideration the radial dependence of stellar velocity dispersion. The stellar masses, Σ_*, were determined using V–band luminosity (L_V) and the ratio between mass and V–band luminosity (M/L_V) the latter derived by Herrmann et al. (2013) from the relationship between M/L_V ratio and $B-V$. If the surface density maps are in units of atoms cm^{-2} then the equation can be written as:

$$\mathrm{P_h[dyne\,cm^{-2}]} = 2.934e^{-55} \times \Sigma_{gas}(\Sigma_{gas} + \frac{\sigma_g}{\sigma_*} \times \Sigma_*) \tag{4.2}$$

Pressure maps were created for each individual galaxy used in our pixel–by–pixel analysis. We sample the pressure maps at the same 400 pc linear resolution as in the preceding sections, obtaining independent data points above a 2σ cutoff in H I and V–band and above a 5σ cutoff in SFR. The pressure value of the data points is not a random selection from within the 400 pc resolution element but an average of all the valid pressure values within this resolution element. In this manner we obtain all the following figures.

In Fig. 4.48 we show SFRD as a function of the average pressure within the resolution element and find that these two quantities are indeed correlated. Also noteworthy here is the fact that the orange points representing the pixels with an H I surface density higher than 10 $\mathrm{M_\odot\,pc^{-2}}$ hint towards a pressure threshold of $10^{-12.5}$ dyne cm^{-2} achieved and surpassed only in very dense H I areas.

Using the OLS bisector method, we do a linear fitting through the pressure-SFRD distribution of points in each galaxy. The linear fit parameters, the index N, and the coefficient A normalized at $P_h = 10^{-12.5}\,\mathrm{dyne\,cm^{-2}}$, along with the Spearman correlation coefficient and the rms scatter of the fit for both FUV and Hα as SF tracers are given in Table 4.5.

The Spearman rank correlation coefficient is quite high especially for FUV as a SF tracer, an exception being M81dwA that seems completely uncorrelated and DDO 63 that has a degree of correlation under 60%. In general, the index N varies among galaxies from 0.75 to 1.3, with most values around 1. There are three galaxies that lie away from the main trend and those are DDO 210 and DDO 75 with index value N of 0.51 and 0.63 respectively and DDO 154 with an index value N of 2.3. The normalized coefficient A ranges from −3.3 (IC 1613) to −4.7 (DDO 154), most values being around −3.8.

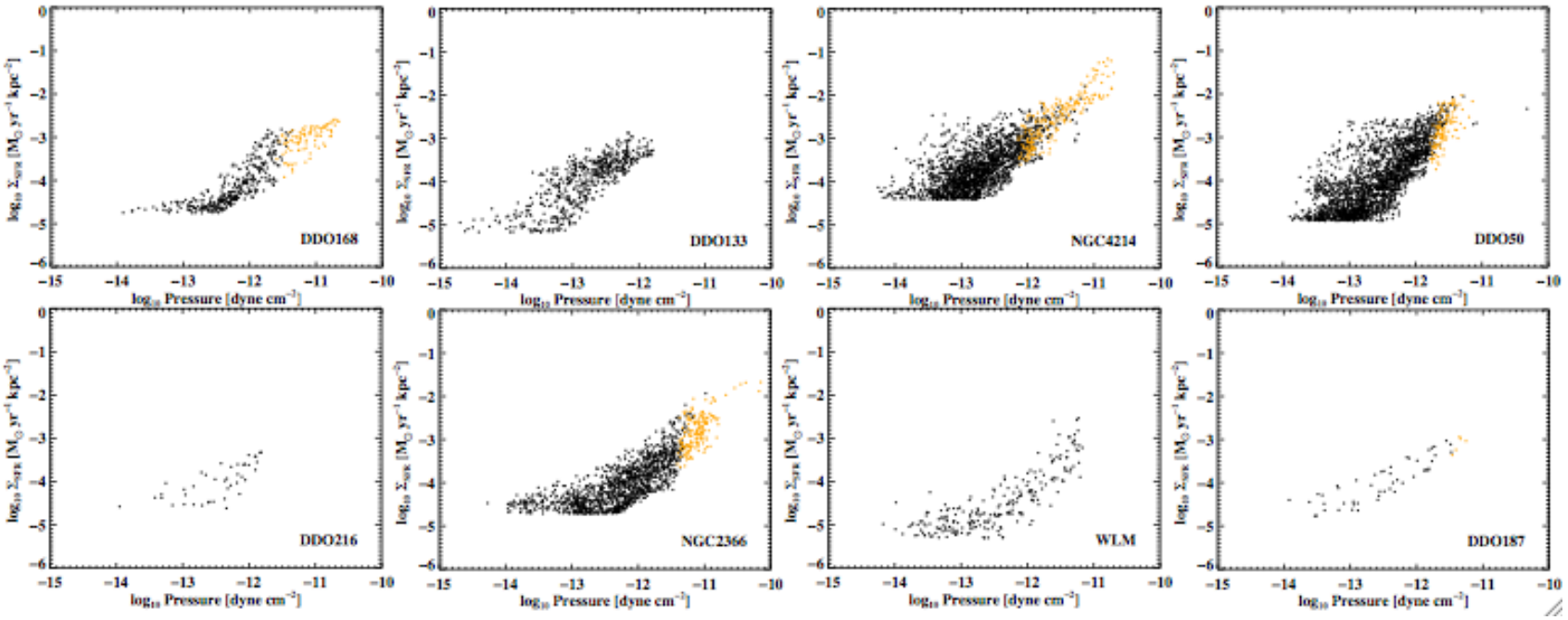

Figure 4.48: We present for all galaxies in our subsample with appropriate ancillary data available, scatter plots of the average pressure within the resolution element vs. SFRD. All SFR maps used have the same linear resolution of 400 pc. All points are independent and above a 2σ cutoff level in HI and 5σ cutoff level in FUV. In orange we show the points with an HI surface density higher than $10\,M_{\odot}\,pc^{-2}$.

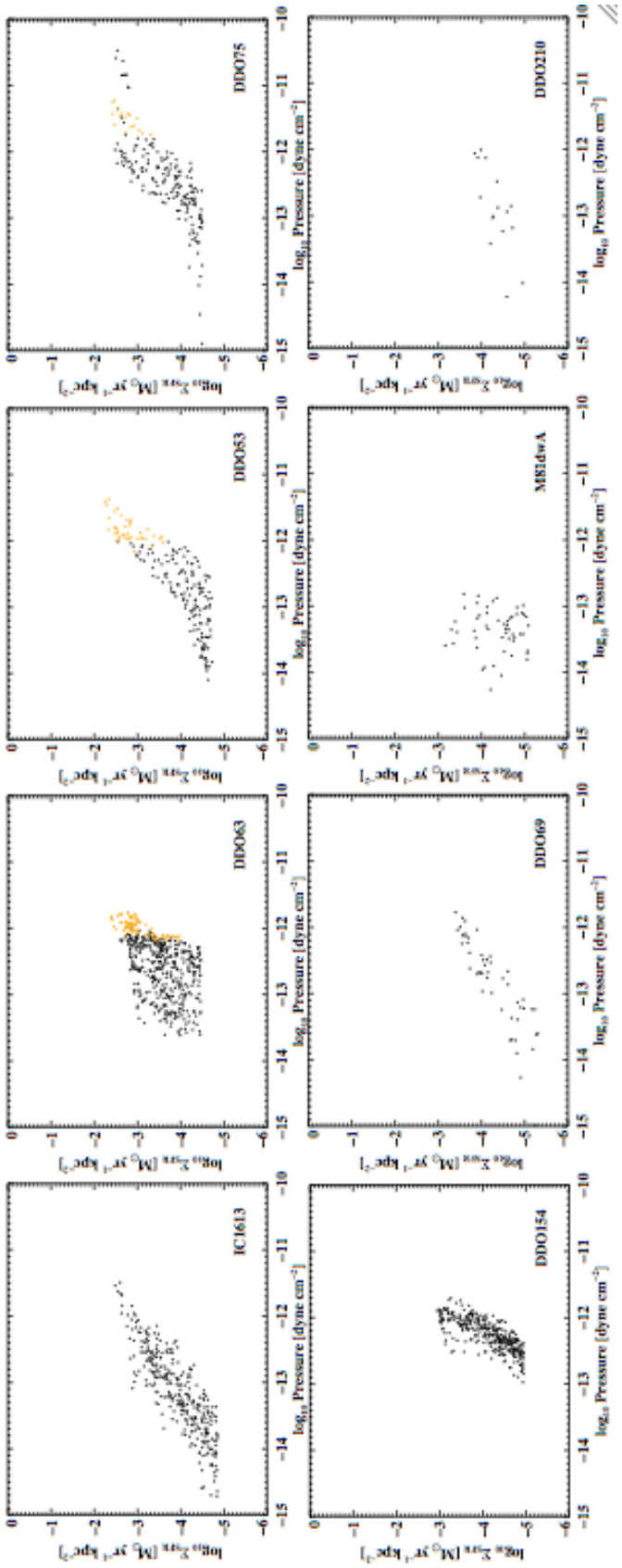

Fig. 4.48 continues ...

Table 4.5. Fitted Power-Law Parameters at 400 pc Resolution (SFRD–P_h)

Name	FUV as SF tracer				Hα as SF tracer			
	Coefficient (A) Normalized at $P_h = 10^{-12.5}$ dyne cm^{-2}	Index (N)	Cor. coef. (r_s)	rms scatter	Coefficient (A) Normalized at $P_h = 10^{-12.5}$ dyne cm^{-2}	Index (N)	Cor. coef. (r_s)	rms scatter
DDO 168	−4.4	1.03	0.92	0.3	−4.0	0.63	0.83	0.4
DDO 133	−3.6	1.05	0.82	0.4	−3.8	0.92	0.78	0.4
NGC 4214*	−3.5	1.02	0.73	0.4	−3.5	1.17	0.78	0.5
DDO 50*	−3.9	1.31	0.76	0.5	−3.8	1.11	0.61	0.6
DDO 216	−4.1	0.80	0.76	0.3	−4.8	1.2	0.65	0.1
NGC 2366*	−4.2	0.93	0.84	0.4	−4.3	0.96	0.85	0.5
WLM	−4.6	0.90	0.80	0.4	−5.3	1.37	0.83	0.4
DDO 187	−3.9	0.75	0.90	0.3	−4.2	0.46	0.66	0.3

IC 1613	-3.3	0.94	0.86	0.3	-3.8	1.51	0.58	0.5
DDO 63*	-3.4	1.11	0.55	0.5	-3.6	1.12	0.60	0.5
DDO 53*	-3.6	1.12	0.87	0.4	-3.7	1.09	0.78	0.5
DDO 75	-3.8	0.63	0.88	0.5	-3.6	0.49	0.75	0.4
DDO 154*	-4.7	2.3	0.78	0.4	-4.3	1.17	0.55	0.5
DDO 69	-3.9	0.85	0.89	0.3	-4.2	0.53	0.47	0.5
M81dwA*	-3.4	1.05	0.05	0.6	...	...	...	...
DDO 210	-4.2	0.51	0.68	0.4	...	...	...	...
All	-3.8 ± 0.6	1.02 ± 0.05	0.64	...	-3.8 ± 0.7	1.05 ± 0.06	0.40	...

Table 4.5: We give for each galaxy in our sample observed in FUV the linear fit parameters A normalized at $P_h = 10^{-12.5}\,\mathrm{dyne\,cm^{-2}}$ and N ($log_{10}\Sigma_{SFR} = A + N log_{10}\Sigma_{P_h}$), the rms scatter in the SFRD direction and the Spearman rank coefficient (r_s) of the SFRD–P_h average pressure per resolution element, where the considered SFR map uses both FUV (columns 2 to 5) and Hα (columns 6 to 9) only as SF tracers.

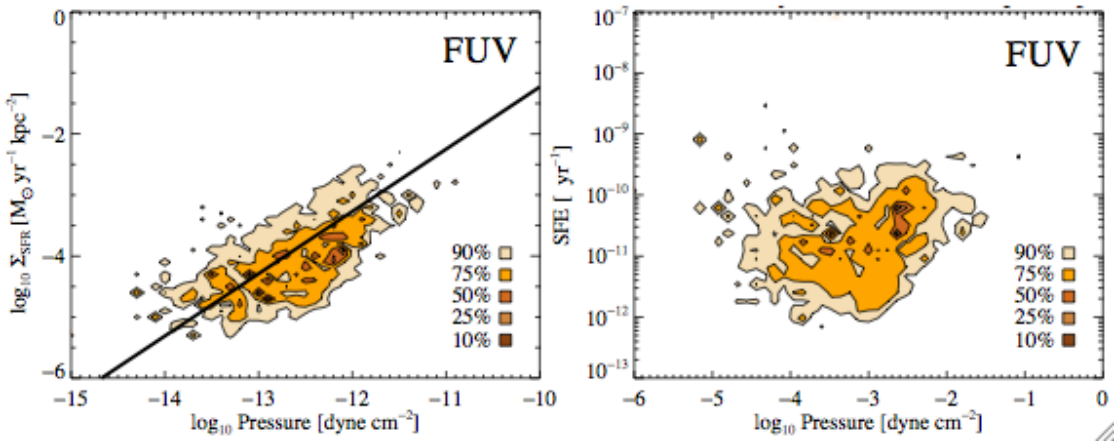

Figure 4.49: We plot for all galaxies in our subsample observed in FUV, density contours at 10%, 25%, 50%, 75% and 90% of the pixel–by–pixel distribution of the average pressure vs. SFRD (left) and SFE(right). All maps used for the above plots have the same linear resolution of 400 pc. All points are independent and above a 5σ cutoff level in FUV. In the top left panel the black continuous line represents a linear fit through the points distribution of all galaxies.

When we use the OLS bisector method to do a linear fitting through the pressure–SFRD points distribution derived from all the galaxies in our sample we find a one to one relation between the SFRD and pressure: $\Sigma_{SFR} \propto P_h^{1.02\pm0.05}$. The error bar on the fit of the total distribution of points is driven by the three galaxies mentioned above as outliers (DDO 154, DDO 75 and DDO 210).

In Fig. 4.49, in two different panels we show single plots where all the independent points of each galaxy contribute to a total distribution of points. To ensure all galaxies contributing to the plot are equally represented we weighted the total distribution of points by galaxy. In the left panel of Fig. 4.49, we present the linear fit through the Pressure–SFRD distribution of points, overlaid on the colour density contours of that same distribution whereas in the right panel we present the colour density contours of the pressure–SFE distribution of points. Fig. 4.49 shows that even for the total distribution of points in all our galaxies the average midplane hydrostatic pressure per resolution element and the SFRD are in a 1:1 relation. However pressure does not seem to influence the SFE defined as the ratio between SFRD and H I surface density. This result is difficult to interpret, knowing that it is hydrostatic pressure that drives the molecular fraction and that molecular gas surface density and SFRD are in a 1:1 relation. Most probably our pressure vs. SFE figure is contaminated by data points with H I surface densities unrelated to SF.

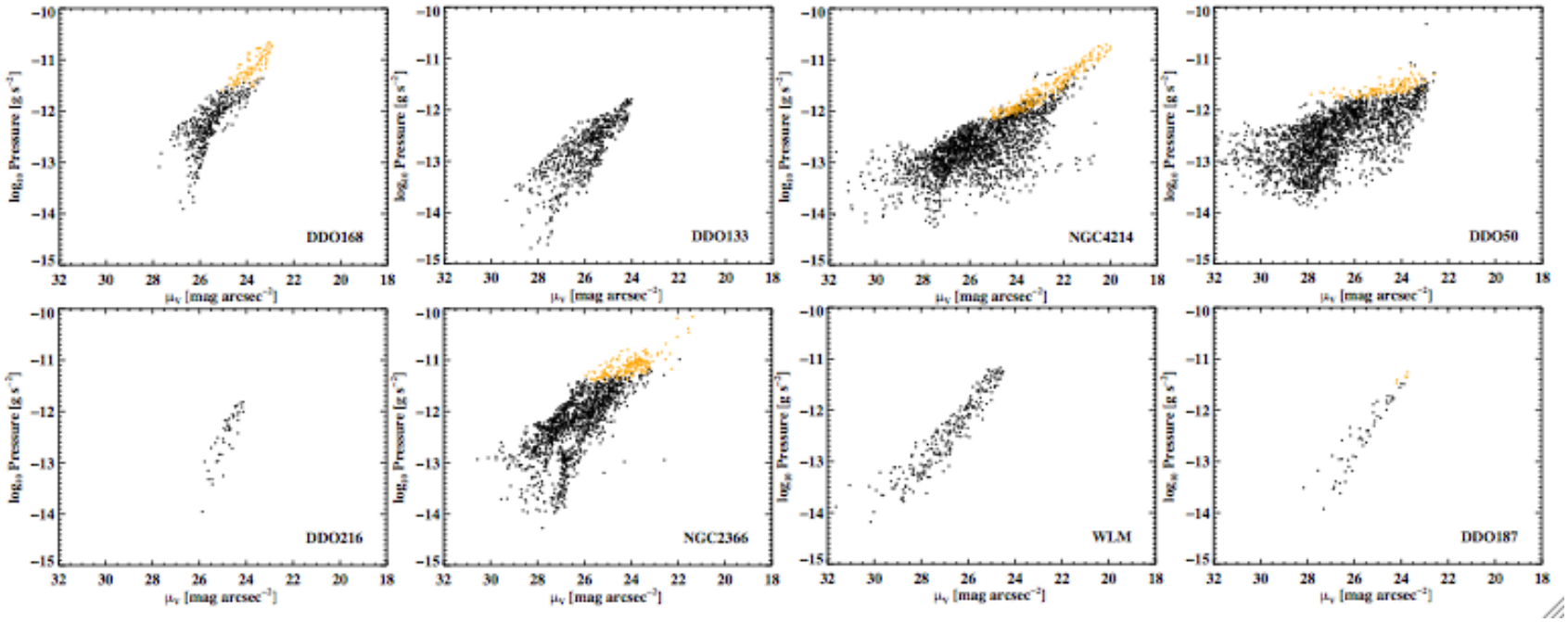

Figure 4.50: We present for all galaxies in our subsample with appropriate ancillary data available, scatter plots of the average pressure within the resolution element vs. V–band surface density. All SFR maps used have the same linear resolution of 400 pc. All points are independent and above a 2σ cutoff level in HI and in em V–band surface density maps. To ease the comparison with previous plots we only show the points that are also above 5σ cutoff level in FUV. In orange we show the points with an HI surface density higher than $10\,M_{\odot}\,pc^{-2}$.

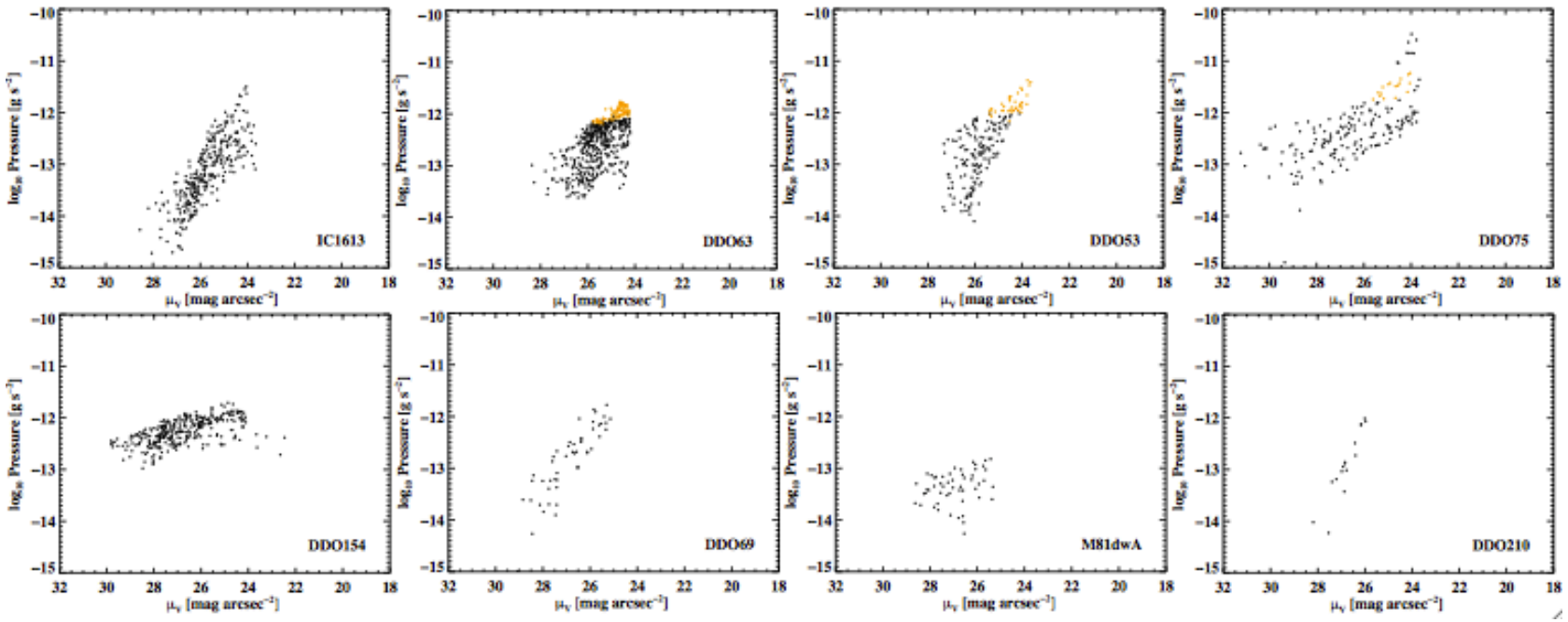

Fig. 4.50 continues ...

The expression of pressure (see Eq. 4.2) already takes into account the contribution of stars as local pressure enhancers through the Σ_* term. We find that there is a correlation between pressure and V–band surface density and we plot this correlation in Fig. 4.50.

In each of our galaxies, when averaged over hundreds of parsecs, 400 pc in our case, the mean H I surface density exceeds the H_2 surface density everywhere, so we find ourselves in the low–pressure regime described by Blitz & Rosolowsky (2006), where the surface density of the GMCs as traced by CO is roughly constant and consequently the dense gas fraction and the SFR of individual GMCs are roughly constant too. Hence in this regime, assuming that the SF occurs in dense molecular gas with a constant SFE, ϵ, Blitz & Rosolowsky (2006) find that $\Sigma_{SFR} = 0.1\,\epsilon\,\Sigma_g(P_h)^{0.92}\,\mathrm{M_\odot\,pc^{-2}\,Gyr^{-1}}$, where Σ_g represents the total surface density of gas. Within the error bars, the 1:1 relation between the average midplane hydrostatic pressure per resolution element and the SFRD we found confirms the Blitz & Rosolowsky (2006) result above.

Blitz & Rosolowsky (2006) have shown that the average pressure per resolution element and the SFRD relation above holds in the low–pressure regime of spiral galaxies and we were able to add to their result the fact that the average pressure per resolution element and the SFRD relation also holds in the more extreme environment of dwarfs. In Fig. 4.51 we investigate how the characteristics of the dwarfs' environment affect the index value N and through it the pressure–SFRD relation. We find that the index value N of the pressure–SFRD relation increases with metallicity and stellar mass. It also shows a milder increase with H I mass and molecular mass. In all panels of Fig. 4.51, DDO 154 stands out as an outlier due to its high index value N of 2.3.

In the bottom two panels of Fig. 4.51 we compare the index value N of the pressure–SFRD relation with the index values N of the V–band surface density–SFRD relation and of the H I surface density–SFRD relation. Whereas the index values N of the pressure–SFRD relation and the V–band surface density–SFRD relation are unrelated, the index values N of the pressure–SFRD relation and the H I surface density–SFRD relation are closely related: the higher the index values N of the pressure–SFRD relation, the higher the index value of the H I surface density–SFRD relation. It is tempting to interpret this close relation as a consequence to the fact that the expression of pressure (see Eq. 4.2) contains a term based on H I surface density and hence the relation of the two N slopes (or index values) is due to the

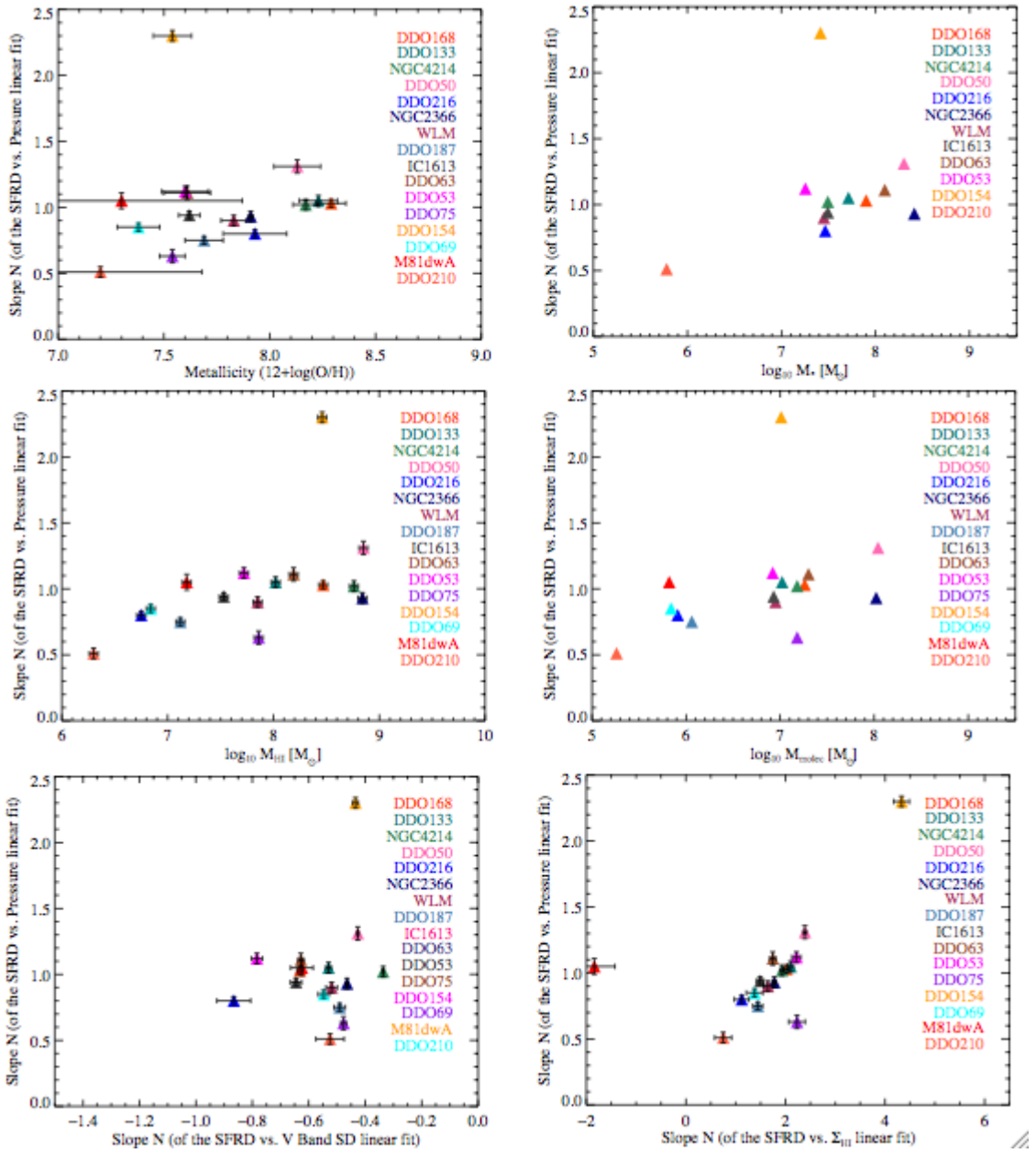

Figure 4.51: We plot for all galaxies in our subsample, the linear fit slope (N) between average pressure per resolution element and SFRD vs. metallicity (top left), stellar mass (top right), H I mass (middle left) and molecular mass (middle right). We also compare the index value N of the pressure–SFRD relation with the index values N of the V–band surface density–SFRD relation (bottom left) and of the H I surface density–SFRD relation (bottom right). The SFR maps used for the linear fit and the measurement of the correlation coefficient are based on FUV–only as a SF tracer. Different colours represent different galaxies.

two values not being independent of each other. In this case however, since stellar surface density is also a term in the expression of pressure, we would have expected a false relation in the bottom left panel of Fig. 4.51 as well, yet the index values N of the pressure–SFRD relation and the V–band surface density–SFRD relation are unrelated.

In conclusion, the main result of this section is that in dwarf galaxies, the average pressure per resolution element and the SFRD are in a 1:1 relation, the same type of a relation as the one between SFRD and molecular gas surface density. In other words, we find that in low metallicity environments the pressure is the main driver of the SFR and the most important ingredient that compensates for the dearth of metals.

Chapter 5
CONCLUSIONS

5.1 Summary & Conclusions

In this thesis I present an analysis of a spatially resolved study of a subsample of the LITTLE THINGS dwarf irregular galaxies. In Chapter 2, I explain the data calibration and how my contribution was of pivotal importance in creating the data calibration pipeline. In the process I calibrated 39% of the galaxies in my subsample and 17% of the entire LT sample. I also describe how I explored the Multi–Scale CLEAN procedure and again developed the prescription that was used for the entire LITTLE THINGS sample. I imaged 78% of the galaxies in my subsample and 34% of the entire LT sample. These efforts have resulted in superb data cubes and maps, despite the multiple problems with the data that surfaced during the upgrade the VLA was undergoing at the time. The data used in this thesis are presented in Chapter 2 and Appendix A. The H I data of LITTLE THINGS were released to the community in 2012 and are described in an accompanying paper (Hunter, Ficut-Vicas, et al. 2012) to which I provided substantial sections.

The thesis then deals with an extensive investigation of SF laws in the low metallicity environment of two dwarf galaxies, DDO 133 and DDO 168, which was fully described and discussed in Chapter 3. We summarise those results as follows:

- We use 24 μm emission maps to evaluate the internal extinction in the two dwarfs and find that $E(B-V) < 0.01$ and no internal extinction correction is

necessary for the SF analysis.

- In both DDO 133 and DDO 168 we find a trend between SFRD and H I surface density. Although not a one–to–one relation, what we find matches previous results in the literature (Bigiel et al., 2010b) in both H I surface density range and SFRD range.

- We are also able to confirm that the relation between SFRD and V band luminosity (Hunter & Elmegreen, 2004) is evident on a local scale of 400 pc in the two galaxies studied and in passbands dominated by older stars. Moreover we find this relation to be tighter than the one between SFRD vs. H I surface density not only globally but also at smaller scales.

- The H I threshold, above which any additional gas column density turns molecular (Bigiel et al., 2008), has a different value in DDO 168 than in spirals. However, when taking into account the lower metallicity of DDO 168, the theoretically predicted (Krumholz et al., 2009) threshold for DDO 168 matches the observed one. In the case of DDO 133, however, although its metallicity is similar to DDO 168, the threshold does not increase beyond the $10\,M_{\odot}\,pc^{-2}$ value appropriate for spirals. We conclude that metallicity alone cannot explain why DDO 133 does not reach to the H I threshold, and that more than one mechanism must be at work.

- At 400 pc resolution DDO 133 shows H I shells as distinct features in the SF plot. While most of the points in the SFRD vs. H I surface density plot follow the same trend as in DDO 168, there is a group of points that stand out as different from the main trend. Considering that in dwarfs the shell sizes can be over 1 kpc, we suggest that disregarding the shell regions when investigating the relation between SFRD and H I surface density may tighten the SFRD–H I surface density relation.

- We discuss the applicability of the molecular gas prediction given by Leroy et al. (2008) to dwarf galaxies and find that as the SFR dependency on molec-

ular gas does not vary with metallicity (Krumholz et al., 2011), we can estimate the amount of molecular gas in both our dwarf galaxies.

Starting from the conclusions of Chapter 3 we extend this in Chapter 4 by testing the results mentioned above in a larger subsample of 18 galaxies. The larger sample also allowed a more in depth study on the behaviour of SF tracers and on internal extinction and their effects on our SF analysis. With the increased number of galaxies in our SF analysis we increased the statistical significance of our fits through the collective data and we were able to look for trends that allow a more accurate description of the SF process and the laws that govern this process in dwarf irregular galaxies. All these results are discussed in Chapter 4 and are summarised here:

- We compare the behaviour of all four considered SF tracers (FUV–only, Hα–only, FUV+24 μm, and Hα+24 μm) within different galaxies in our subsample. We find that, with the exception of NGC 4214, where FUV+24 μm provides an SFR tracer corrected on a pixel–by–pixel basis, all tracers agree on the higher end of the SFRD and H I surface density relation, but FUV–only is the only tracer, except for FUV+24 μm for NGC 4214, able to also sample the lower end of the relation. Under these circumstances we find that the best SF tracer for our sample is the FUV–only.

- Any SFR map derived from hybrid SF tracers (FUV+24 μm or Hα+24 μm) has an increased noise level because of the weak signal–to–noise in the 24 μm maps. A conservative cutoff of 5σ in this kind of SFR map results in sampling only the higher end of the SFRD and H I surface density relation.

- We delve deeper into the subject of internal extinction by adding additional considerations to our method of evaluating the internal extinction based on the 24 μm emission maps. We consider the SMC extinction law in addition to the Milky Way one. We find that in either case the average internal extinction is minimal ($\mathrm{E}(B-V) < 0.02$), with the exception of some SF regions in NGC 4214 or DDO 53. We elected not to correct for internal extinction.

- We use the molecular gas prediction given by Leroy et al. (2008) for dwarf galaxies to estimate the amount of molecular gas in each galaxy of our subsample. Based on these predicted values for molecular gas mass we find that neither the molecular mass nor the molecular fraction are metallicity dependent.

- We confirm the existence of the SFRD vs. H I surface density relation in dwarf galaxies and the linear fit through our data yields a power law index number of 1.87 ± 0.3 similar to the 1.7 value found in the literature (Bigiel et al., 2010b).

- The degree of correlation between the SFRD and the H I surface density does not depend on either metallicity, H I mass or absolute V–band magnitude, the integrated SFR/area from FUV or Hα or the molecular or neutral gas fractions.

- To understand how galaxies in our sample correlate with each other towards a common SFRD vs. the H I surface density relation, we studied the power law index number N and the normalized coefficient A as a function of metallicity, H I mass, integrated SFR, and others and found no conclusive results.

- We find evidence for increasing SFE with SFRD and no clear relation between SFE and H I surface density. The SFE relates to the stellar surface density as traced by 3.6 μm: the higher the stellar density the more efficient the star formation process is in most of the galaxies in our sample.

- Apart from DDO 133, our subsample hosts a set of another five galaxies (NGC 4214, DDO 50, IC 1613, DDO 63 and DDO 75) with resolved H I shells at 400 pc scales represented in the K–S plot by multiple points although within the shell interior we have SFRD values but no H I surface density related to them. We show that excluding these regions when investigating the SFRD vs. H I surface density relation improves the correlation between SFRD and H I surface density by 10% to 20%.

- In our sample, 8 out of 18 galaxies have H I maxima greater than the $10\,M_{\odot}\,pc^{-2}$ threshold found by Bigiel et al. (2008) for spirals. Although Krumholz et al. (2011) predicted that the $10\,M_{\odot}\,pc^{-2}$ threshold increases with decreasing metallicity, the theoretically predicted values do not match the observed H I maxima in any of the 8 galaxies except DDO 168. The discrepancy between the theoretical and the observed values of the H I maxima depends on metallicity and does not conclusively depend on linear resolution.

- Our data show that excepting DDO 187, all galaxies with H I maxima above $10\,M_{\odot}\,pc^{-2}$ are also galaxies with a SFRD(Hα) and SFRD(FUV) ratio higher than one, confirming the results of Roychowdhury et al. (2011). This ratio is higher than that in the galaxies that have more recently gone through a SF event. This suggests that the H I envelopes are transient structures that are observable only near the time of the SF event and would explain why similar metallicity galaxies do not show similar H I maxima. Moreover we find indications that the higher SFRD(Hα) and SFRD(FUV) ratio the stronger the ISRF.

- Working under the assumption that the average V–band surface density in the region of the H I maximum is proportional to the local strength of the ISRF, we find that the higher the ISRF the denser the H I envelopes necessary to shield the molecular cores. Except DDO 69 with the lowest ISRF intensity and NGC 4214 with an exceptionally high ISRF intensity, all galaxies follow the main trend of the ISRF–H I maxima relation.

- We find a tight relation between SFRD and μ_V surface density within our sample, confirming the result in Chapter 3. The relation between SFRD and μ_V surface density is tighter than the SFRD and H I surface density relation. Generally we find that the higher SFR is associated with more stars and more gas. We give a mathematical form to this relation: $\Sigma_{SFR} \propto (10^{\mu_V})^{-0.43\pm0.03}$.

- The relation between SFRD and μ_V surface density formulated above applies to both the interior and the exterior of H I shells, unlike the SFRD and H I surface density relation.

- The degree of correlation between SFRD and μ_V surface density is independent of metallicity, H I mass or absolute V–band magnitude.

- Plotting the power law index number N and the normalized coefficient A of the SFRD vs. μ_V surface density relation, for each galaxy of our sample, as a function of metallicity, H I mass, and absolute V–band magnitude gives no conclusive results.

- To understand how galaxies in our sample correlate with each other towards a common SFRD vs. μ_V surface density relation, we studied the power law index number N and the normalized coefficient A of this relation, for each galaxy of our sample, as a function of metallicity, H I mass, and absolute V–band magnitude and found no conclusive results.

- Within our sample of dwarf galaxies the pressure per resolution element and the SFRD are in a 1:1 linear relation: $\Sigma_{SFR} \propto P_h^{1.02\pm0.05}$. Three galaxies cause most of the scatter in this relation: DDO 154, DDO 75 and DDO 210. Our power law index number for this relation is remarkably close to the one given by Blitz & Rosolowsky (2006) for the low–pressure regimes of spiral galaxies.

- We find that the index value N of the pressure–SFRD relation increases with metallicity and stellar mass. It also shows a milder increase with H I mass and molecular mass.

5.2 Implications

This thesis set out to investigate the existence of the SFRD vs. H I surface density relation in low metallicity environments. Here, the low metallicity environment is represented by a sample of 18 dwarf irregular galaxies with metallicities ranging from 7.2 to 8.29. We remind the reader that according to the latest measurement by

Pereira et al. (2009) the solar metallicity has a value of 8.69 ± 0.05. The existence of such a relation tells us that the dearth of metals is compensated by giving new roles to the H I gas. If in spirals the higher metallicity ensures the conversion from neutral to molecular gas, in dwarf galaxies the neutral gas assumes an additional role apart from that of providing hydrogen atoms: it participates in creating conditions for the creation and survival of molecules. Since in the history of our universe it is known that stars have been forming without the aid of metals, logically this additional role played by the neutral hydrogen is carried through time, until the metal enrichment of a galaxy is enough to take over the H I to H_2 conversion.

The importance of this result lies in the fact that the SFRD vs. H I surface density relation in dwarf galaxies is caused not by the indirect link H I gas – molecular gas – stars, but rather by the additional role the H I surface density is playing in the molecular gas conversion. Hence, in the low metallicity environment of dwarf galaxies one is able to assess this additional role and further understand the way the stars form in extreme environments. Without doubt this additional role evolves in time (from low metal content to enough metal content) and along with it also the SF processes and mechanisms at play in ensuring the creation of the next generation of stars.

This additional role of the H I gas is fully manifested in galaxies with H I to H_2 transition above $10\,M_\odot\,pc^{-2}$. Theoretical results have shown that in low metallicity environments, dust-shielding is replaced by self-shielding so that, as the intensity of the ISRF increases, the H I envelopes protecting the molecular cores will be denser pushing the transition limit to higher values (Ostriker et al., 2010; Schaye, 2004). Under the assumption that the average V–band surface density measured over the region the H I maximum originates from is in fact a proxy for the strength of the ISRF, our study suggests that the ISRF–H I maxima relation indeed exists and we believe this result should be incorporated in any formula predicting the H I to H_2 transition.

Another important result of this thesis is confirming that SFRD and μ_V surface density are related even at small scales. This means that stars play a role in the formation of new generations of stars. Is this also a compensating mechanism acting only in low metallicity environments or is it generally acting in all types of galaxies? This question is the title of a future project. However, the linearity of the SFRD and μ_V surface density relation certainly suggests that stars predict the SFR better than the neutral gas, but not as well as the molecular gas does.

We have also found that in the dwarf galaxies of our sample there is a 1:1 relation between the pressure per resolution element and SFRD. Blitz & Rosolowsky (2006) have found a similar result in the low–pressure regime of spiral galaxies whereas we were able to show that the average pressure per resolution element and the SFRD relation also holds in the more extreme environment of dwarfs. Pressure has always had an important contribution in the SF process, yet in low metallicity environments its role has been brought to a new level.

In extreme environments where there are no spiral arms and no shear to stimulate SF, where the metals, the molecular gas catalysts, are insufficient, the stars still form. As the amount of metals diminishes other components from within the galaxy take over some of the roles played by metals in normal galaxies and "light" switches on...

5.3 Final Act: Have we fulfilled our aims?

Have we fulfilled our aims? We have successfully confirmed the existence of the SFRD and H I surface density relation in dwarf irregular galaxies. We have found that metallicity influences star formation as a threshold, below a certain metallicity the SF processes get re–adapted to compensate for the change in environmental conditions. We found evidence that the intensity of the ISRF is correlated with H I surface density maximum, suggesting that along with metallicity, the ISRF also influences the H I to H_2 transition. We have shown that the tight SFRD and μ_V surface density relation suggests that the old stars play their part in the formation of new stars. We also found that in dwarf irregular galaxies, the SFRD is linked to the average pressure per resolution element through a 1:1 relation.

We sincerely believe our results not only constitute an improvement towards understanding the complex process of star formation, but also have initiated enough new questions to motivate further research in this direction (see Chapter 6).

Chapter 6
FUTURE PROJECTS

6.1 A three dimensional SF analysis where the scale height is accounted for

We stress here the important fact that at its origin the power law between SFR and gas density involved volume densities rather than surface densities (Schmidt, 1959). According to Guibert et al. (1978), the relation between SFRD and gas surface density is equivalent to the relation between SFR and gas volume densities only if the thickness of the gas disk and young star disk are uniform. This assumption largely holds in spiral disk galaxies but is it also true for dwarfs? We now know that the gas scale height is not constant with galactic radius; as a matter of fact, the H I flares in the outskirts of galaxies, so gas density as a function of height follows an exponential distribution (Bagetakos et al., 2011; Banerjee et al., 2011). In the simplest scenario, even with an exponential gas distribution as a function of height, as long as the star formation is perfectly mixed within the H I layer most of the H I will be co-located with the SF layer. However, in the case that the H I layer is much thicker than the SF layer, in other words if a significant difference in the scale height of the two layers exists, then the H I gas density involved in the SF process is being overestimated because when measuring the gas surface density (gas volume "in projection") along the line of sight we probe a longer path which is partly unassociated with the SF process.

The idea of this project is to return to thinking in terms of volume densities and take advantage of the current research regarding H I scale height and use it to put in place a correction that accounts for the exponential gas distribution with height. In this way our star formation analysis gains a third dimension, one where accurate considerations of the scale height allow estimates of volume densities in both SFR and H I directions. Technically, achieving this goal is no trivial matter. Currently, models of the H I density as a function of its scale height exist for dwarf galaxies such as DDO 50, DDO 154 and NGC 2366 from Banerjee et al. (2011). Therefore, in principle, if we also had estimates of the star scale height in these dwarfs we could begin a pilot project towards a three dimensional star formation analysis.

6.2 What drives the scatter in the SFRD vs. H I surface density relation in dwarfs?

In Chapter 4 of this thesis we have shown that, as suggested by Bigiel et al. (2010b, 2011b), in dwarf galaxies the SFRD relates with the H I surface density. This relation however is not without considerable scatter, what is intriguing is that there is more scatter in the SFRD vs. H I surface density relation than in SFRD vs. V–band surface density. A question worthy of a future project is what drives the scatter in the SFRD vs. H I surface density relation. One source of scatter in the relation could be the difference in scale height between the gas layer and the layer where SF takes place. As suggested in Section 6.1, due to the scale height difference the H I surface density might be overestimated by adding along the line of sight H I gas unrelated to star formation. Another source of scatter in the SFRD vs. H I surface density relation is the inclusion of data points which originate from the interior of the H I shells.

Before we start finding the sources of scatter we have to first overcome an important technical problem. Can the scatter be explained by the error bars in the H I and SFR directions? Applying a crude estimate where the error bars in each direction are considered successively rather than at the same time we find that the scatter of the points distribution is no larger than 2σ in both H I and SFR directions at least at a linear scale of 400 pc. Hence, if the error bars are too large, then any other effect (than the uncertainties in the data) driving the scatter will be difficult to identify.

6.3 The contribution of resolved H I shells to the scatter in the SFRD–H I surface density relation for the entire LITTLE THINGS sample

Returning to the subject of multiple components of the SF law we remind the reader that in DDO 133 (see Section 3.3.2) and another 5 galaxies in our subsample (see Section 4.6) we find resolved H I shells at 400 pc scales. When the H I shells are larger than the chosen resolution element of 400 pc, the H I shell interior will be represented in the K–S plot by multiple points although within the shell interior we have SFRD values but no H I surface density related to them. If we want to study in depth the scatter in the SFRD vs H I surface density relation, it is important to take in account all sources of scatter and the data points representing the resolved H I shell regions are themselves a source of scatter.

Some of our LITTLE THINGS collaborators have prepared a catalogue of all the H I holes within the LITTLE THINGS sample (see Simpson et. al., in prep). With such a catalogue at hand we will be able to isolate all the points corresponding to the H I holes larger than our resolution element and exclude them from the SFRD–H I surface density distribution to be able to explore further whether the correlation between points within this distribution improves. Such an endeavour will allow us to improve the power law index number estimates by throughly accounting for this kind of source of scatter in the relation at study. Also, this project will be able to take advantage of the whole LITTLE THINGS sample, which will make our conclusion so much more statistically coherent.

Technically, our analytical method is already in place and has been tested for the subsample discussed in this thesis. What we still need for this project is the complete catalogue of all H I holes within the LITTLE THINGS sample.

6.4 Does the SFRD vs. *V*–band surface density relation hold only in dwarf irregular type galaxies?

We ask the reader to remember that previous observations of dwarf irregulars have shown that in terms of averaged per galaxy quantities, SFR relates with the V–band

surface brightness more than with any other measure (Hunter & Elmegreen, 2004; Hunter et al., 1998; Shi et al., 2011). We have shown in Section 3.3.4 and Section 4.7 that this same tight relation holds on small scales too, in other words SFRD is related to the V–band surface brightness density. This relation has surfaced in dwarf irregular galaxies and it indicates that the presence of stars is important in the star formation process. Most probably stars provide a large proportion of the baryonic matter contributing to the midplane pressure, which in turn enables molecular cloud formation.

As a future project we intend to verify if such a relation exists in spiral galaxies. Shi et al. (2011) found for a sample of 12 spiral galaxies that the SFE and the stellar mass are in a power law relation with an index of 0.48 ± 0.04. Their result suggests that the stars play a role in star formation in spiral galaxies, just as we have shown to be also true for dwarfs. Comparing spirals and dwarf irregulars from this point of view can shed some light into the processes regulating star formation in different types of galaxies.

In order to start such a project we have available V– band maps of a sample of spiral galaxies, complemented of course by FUV and/or Hα maps as a basis for the SFR maps and H I observations from the wonderful data base of the THINGS project. Again the method is already in place and can easily be applied to this new sample of galaxies.

6.5 Understanding the dense H I regime and its relation with the H I to H_2 turnover

Current studies suggest that the molecular fraction is driven by the midplane hydrostatic pressure complemented by ISRF emissivity (Blitz & Rosolowsky, 2004, 2006; Elmegreen, 1993). However, for the purpose of pixel–by–pixel studies, we are still not able to distinguish between the H I gas related to the star formation process and the gas unrelated to star formation. In this context, understanding the transition from H I to H_2 qualitatively as well as quantitatively, becomes essential. Until our molecular gas detection methods are improved such that they are applicable to low metallicity environments, our best guess regarding the molecular content of dwarfs is enclosed into the atomic gas measurements combined with a deeper knowledge of the H I to H_2 transition.

In spiral galaxies the H I to H_2 turnover takes place at $10\,M_\odot\,pc^{-2}$ (Bigiel et al.,

2008; Leroy et al., 2008). In dwarf galaxies, the H I densities can exceed this threshold (Leroy et al., 2011; Roychowdhury et al., 2011) and this phenomenon is justified theoretically by Krumholz et al. (2011, 2009) as caused by the fact that in low metallicity environments, where dust shielding loses its dominant role to self shielding, the H I envelopes have to be denser in order to protect the molecules from dissociating. The authors also gave a mathematical expression to the H I to H_2 turnover.

In Section 3.3.3 and Section 4.7 we compare the empirically predicted (based on Krumholz et al. (2011, 2009)) values for the H I to H_2 turnover with our highest H I surface densities and find that these densities are higher than the predicted turnover suggesting that either the mathematical expression of the turnover needs tuning or the highest H I surface densities in fact represent the molecular regime. Of course, beyond the H I to H_2 turnover point the gas is predominantly molecular, yet small amounts of H I gas at high densities are expected. This project's idea is to study these dense H I regions and fully understand them as they most probably are windows into the molecular regime that due to technical impediments is still difficult to observe in many low metallicity environments.

Technically we would start this project with a sample of 4 dwarf galaxies that our team has observed with both *Herschel* (PDR observations) and *ALMA* (CO observations) which would allow us to properly pinpoint the H I to H_2 turnover and use these values to establish the dense H I regions to study and to compare them with the predicted values for the turnover and fine tune the mathematical formula if necessary.

Bibliography

Allen, R. J., Heaton, H. I., & Kaufman, M. J. 2004, ApJ, 608, 314

Bagetakos, I., Brinks, E., Walter, F., de Blok, W. J. G., Usero, A., Leroy, A. K., Rich, J. W., & Kennicutt, Jr., R. C. 2011, AJ, 141, 23

Banerjee, A., Jog, C. J., Brinks, E., & Bagetakos, I. 2011, MNRAS, 415, 687

Becerra, F., & Escala, A. 2014, ApJ, 786, 56

Begeman, K. G. 1989, A&A, 223, 47

Bhatnagar, S., & Cornwell, T. J. 2004, A&A, 426, 747

Bigiel, F., Leroy, A., Seibert, M., Walter, F., Blitz, L., Thilker, D., & Madore, B. 2010a, ApJL, 720, L31

Bigiel, F., Leroy, A., & Walter, F. 2011a, in IAU Symposium, Vol. 270, Computational Star Formation, ed. J. Alves, B. G. Elmegreen, J. M. Girart, & V. Trimble, 327–334

Bigiel, F., Leroy, A., Walter, F., Blitz, L., Brinks, E., de Blok, W. J. G., & Madore, B. 2010b, AJ, 140, 1194

Bigiel, F., Leroy, A., Walter, F., Brinks, E., de Blok, W. J. G., Madore, B., & Thornley, M. D. 2008, AJ, 136, 2846

Bigiel, F., et al. 2011b, ApJL, 730, L13

Binggeli, B., & Popescu, C. C. 1995, A&A, 298, 63

Binney, J., & Tremaine, S. 2008, Galactic Dynamics: Second Edition (Princeton University Press)

Blanc, G. A., Heiderman, A., Gebhardt, K., Evans, II, N. J., & Adams, J. 2009, ApJ, 704, 842

Blitz, L. 1993, in Protostars and Planets III, ed. E. H. Levy & J. I. Lunine, 125–161

Blitz, L., & Rosolowsky, E. 2004, ApJL, 612, L29

—. 2006, ApJ, 650, 933

Bodenheimer, P., & Sweigart, A. 1968, ApJ, 152, 515

Boissier, S. 2008, in Astronomical Society of the Pacific Conference Series, Vol. 396, Formation and Evolution of Galaxy Disks, ed. J. G. Funes & E. M. Corsini, 133

Boissier, S., et al. 2007, ApJS, 173, 524

Bolatto, A. D., Leroy, A. K., Rosolowsky, E., Walter, F., & Blitz, L. 2008, in IAU Symposium, Vol. 255, IAU Symposium, ed. L. K. Hunt, S. Madden, & R. Schneider, 274–277

Bolatto, A. D., Wolfire, M., & Leroy, A. K. 2013, ARA&A, 51, 207

Bolatto, A. D., et al. 2007, ApJ, 655, 212

—. 2011, ApJ, 741, 12

Bonnor, W. B. 1956, MNRAS, 116, 351

Bosma, A. 1978, PhD thesis, Groningen Univ.

—. 1981, AJ, 86, 1825

Bosma, A. 1996, in Astronomical Society of the Pacific Conference Series, Vol. 91, IAU Colloq. 157: Barred Galaxies, ed. R. Buta, D. A. Crocker, & B. G. Elmegreen, 132

Boss, A. P. 1987, ApJ, 319, 149

Bottema, R. 1993, A&A, 275, 16

Bradamante, F., Matteucci, F., & D'Ercole, A. 1998, A&A, 337, 338

Braun, R., & Walterbos, R. A. M. 1985, A&A, 143, 307

Brinks, E., & Bajaja, E. 1986, A&A, 169, 14

Brinks, E., Braun, R., & Unger, S. W. 1990, in NASA Conference Publication, Vol. 3084, NASA Conference Publication, ed. D. J. Hollenbach & H. A. Thronson, Jr., 221–223

Brinks, E., & Shane, W. W. 1984, Astronomy and Astrophysics Supplement Series, 55, 179

Brinks, E., & Walter, F. 1998, in Magellanic Clouds and Other Dwarf Galaxies, ed. T. Richtler & J. M. Braun, 1–10

Broeils, A. H., & Rhee, M. 1997, A&A, 324, 877

Broeils, A. H., & van Woerden, H. 1994, Astronomy and Astrophysics Supplement Series, 107, 129

Bruzual, G., & Charlot, S. 2003, MNRAS, 344, 1000

Bureau, M., & Carignan, C. 2002, AJ, 123, 1316

Burton, W. B., Elmegreen, B. G., & Genzel, R., eds. 1992, The galactic interstellar medium

Calzetti, D., et al. 2005, ApJ, 633, 871

—. 2007, ApJ, 666, 870

—. 2010, ApJ, 714, 1256

Cardelli, J. A., Clayton, G. C., & Mathis, J. S. 1989, ApJ, 345, 245

Condon, J. J. 1992, ARA&A, 30, 575

Cornwell, T., Braun, R., & Briggs, D. S. 1999, in Astronomical Society of the Pacific Conference Series, Vol. 180, Synthesis Imaging in Radio Astronomy II, ed. G. B. Taylor, C. L. Carilli, & R. A. Perley, 151

Cornwell, T. J. 1983, A&A, 121, 281

—. 2008, IEEE Journal of Selected Topics in Signal Processing, 2, 793

Côté, S., Carignan, C., & Freeman, K. C. 2000, AJ, 120, 3027

Côté, S., Freeman, K. C., & Carignan, C. 1997, in Astronomical Society of the Pacific Conference Series, Vol. 117, Dark and Visible Matter in Galaxies and Cosmological Implications, ed. M. Persic & P. Salucci, 52

Cox, D. P., & Smith, B. W. 1974, ApJL, 189, L105

Crosthwaite, L. P., & Turner, J. L. 2007, AJ, 134, 1827

Dabringhausen, J., & Kroupa, P. 2013, MNRAS, 429, 1858

Dale, D. A., et al. 2009, ApJ, 703, 517

Dame, T. M., Hartmann, D., & Thaddeus, P. 2001, ApJ, 547, 792

Dawson, J. R., McClure-Griffiths, N. M., Wong, T., Dickey, J. M., Hughes, A., Fukui, Y., & Kawamura, A. 2013, ApJ, 763, 56

de Blok, W. J. G., & Walter, F. 2006, AJ, 131, 363

de Blok, W. J. G., Walter, F., Brinks, E., Trachternach, C., Oh, S.-H., & Kennicutt, Jr., R. C. 2008, AJ, 136, 2648

de Jong, T., Klein, U., Wielebinski, R., & Wunderlich, E. 1985, A&A, 147, L6

de Vaucouleurs, G., & Freeman, K. C. 1972, Vistas in Astronomy, 14, 163

Dolphin, A. E., & Hunter, D. A. 1998, AJ, 116, 1275

Dopita, M. A., Mathewson, D. S., & Ford, V. L. 1985, ApJ, 297, 599

Draine, B. T. 2011, Physics of the Interstellar and Intergalactic Medium (Princeton University Press, 2011, ISBN: 978-0-691-12214-4)

Ebert, R. 1955, Zeitschrift fr Astrophysik, 36, 222

Elmegreen, B. G. 1989, ApJ, 338, 178

—. 1993, ApJ, 411, 170

Elmegreen, B. G., & Elmegreen, D. M. 1986, ApJ, 311, 554

Ewen, H. I., & Purcell, E. M. 1951, Nature, 168, 356

Fabbiano, G. 2006, ARA&A, 44, 323

Feldmann, R., & Gnedin, N. Y. 2011, ApJL, 727, L12

Fisher, J. R., & Tully, R. B. 1981, ApJS, 47, 139

Fumagalli, M., Krumholz, M. R., & Hunt, L. K. 2010, ApJ, 722, 919

Galametz, M., Madden, S. C., Galliano, F., Hony, S., Bendo, G. J., & Sauvage, M. 2011, A&A, 532, A56

Gallagher, J. S., et al. 1996, ApJ, 466, 732

Gallagher, III, J. S., & Hunter, D. A. 1984, ARA&A, 22, 37

Galliano, F., et al. 2011, A&A, 536, A88

Gil de Paz, A., et al. 2007, ApJS, 173, 185

Glassgold, A. E., Galli, D., & Padovani, M. 2012, ApJ, 756, 157

Glassgold, A. E., & Langer, W. D. 1973, ApJ, 186, 859

Gnedin, N. Y., & Kravtsov, A. V. 2006, ApJ, 645, 1054

—. 2011, ApJ, 728, 88

Goldsmith, P. F. 2007, in Molecules in Space and Laboratory

Gordon, K. D., & Clayton, G. C. 1998, ApJ, 500, 816

Gordon, K. D., Clayton, G. C., Misselt, K. A., Landolt, A. U., & Wolff, M. J. 2003, ApJ, 594, 279

Greisen, E. W., Spekkens, K., & van Moorsel, G. A. 2009, AJ, 137, 4718

Guibert, J., Lequeux, J., & Viallefond, F. 1978, A&A, 68, 1

Hamajima, K., & Tosa, M. 1975, PASJ, 27, 561

Hartquist, T. W., & Williams, D. A. 1995, The Chemically Controlled Cosmos (Cambridge, UK: Cambridge University Press, 1995)

Hartwick, F. D. A. 1971, ApJ, 163, 431

Heesen, V., Brinks, E., Leroy, A. K., Heald, G., Braun, R., Bigiel, F., & Beck, R. 2014, AJ, 147, 103

Heesen, V., Rau, U., Rupen, M. P., Brinks, E., & Hunter, D. A. 2012, in American Astronomical Society Meeting Abstracts, Vol. 219, American Astronomical Society Meeting Abstracts, 148

Heesen, V., et al. 2015, MNRAS, 447, L1

Helou, G., Soifer, B. T., & Rowan-Robinson, M. 1985, ApJL, 298, L7

Herrmann, K. A., Hunter, D. A., & Elmegreen, B. G. 2013, AJ, 146, 104

Hodge, J. A., Riechers, D., Decarli, R., Walter, F., Carilli, C. L., Daddi, E., & Dannerbauer, H. 2015, ApJL, 798, L18

Hodge, P. W., & Hitchcock, J. L. 1966, PASP, 78, 79

Högbom, J. A. 1974, Astronomy and Astrophysics Supplement Series, 15, 417

Hollenbach, D., & Salpeter, E. E. 1971, ApJ, 163, 155

Hollenbach, D. J., & Tielens, A. G. G. M. 1999, Reviews of Modern Physics, 71, 173

Hollenbach, D. J., Werner, M. W., & Salpeter, E. E. 1971, ApJ, 163, 165

Huchtmeier, W. K., & Richter, O. G. 1986, Astronomy and Astrophysics Supplement Series, 63, 323

Hunter, D. A., & Elmegreen, B. G. 2004, AJ, 128, 2170

—. 2006, ApJS, 162, 49

Hunter, D. A., Elmegreen, B. G., & Baker, A. L. 1998, ApJ, 493, 595

Hunter, D. A., Elmegreen, B. G., & Ludka, B. C. 2010, AJ, 139, 447

Hunter, D. A., Elmegreen, B. G., & van Woerden, H. 2001a, ApJ, 556, 773

Hunter, D. A., Gallagher, J. S., & Rautenkranz, D. 1982, ApJS, 49, 53

Hunter, D. A., & Gallagher, III, J. S. 1985a, AJ, 90, 1789

—. 1985b, ApJS, 58, 533

Hunter, D. A., & Hoffman, L. 1999, AJ, 117, 2789

Hunter, D. A., Rubin, V. C., Swaters, R. A., Sparke, L. S., & Levine, S. E. 2005, ApJ, 634, 281

Hunter, D. A., et al. 2001b, ApJ, 553, 121

—. 2012, AJ, 144, 134

Iglesias-Páramo, J., et al. 2006, ApJS, 164, 38

Isobe, T., Feigelson, E. D., Akritas, M. G., & Babu, G. J. 1990, ApJ, 364, 104

Israel, F. P., Maloney, P. R., Geis, N., Herrmann, F., Madden, S. C., Poglitsch, A., & Stacey, G. J. 1996, ApJ, 465, 738

Jeans, J. H. 1902, Philosophical Transactions of the Royal Society of London Series A, 199, 1

Johns-Krull, C. M. 2007, ApJ, 664, 975

Johnson, M., Hunter, D. A., Oh, S.-H., Zhang, H.-X., Elmegreen, B., Brinks, E., Tollerud, E., & Herrmann, K. 2012, AJ, 144, 152

Jones, A. P., Madden, S. C., Colgan, S. W. J., Geis, N., Haas, M., Maloney, P., Nikola, T., & Poglitsch, A. 1997, in Extragalactic Astronomy in the Infrared, ed. G. A. Mamon, T. X. Thuan, & J. Tran Thanh Van, 101

Jörsäter, S., & van Moorsel, G. A. 1995, AJ, 110, 2037

Kennicutt, R. C., & Evans, N. J. 2012, ARA&A, 50, 531

Kennicutt, Jr., R. C. 1983, ApJ, 272, 54

—. 1988, ApJ, 334, 144

—. 1989, ApJ, 344, 685

—. 1998, ApJ, 498, 541

Kennicutt, Jr., R. C., Lee, J. C., Funes, José G., S. J., Sakai, S., & Akiyama, S. 2008, ApJS, 178, 247

Kennicutt, Jr., R. C., et al. 2003, PASP, 115, 928

—. 2007, ApJ, 671, 333

Kim, C.-G., Ostriker, E. C., & Kim, W.-T. 2013, ApJ, 776, 1

Kitchener, B., Brinks, E., Heesen, V., Hunter, D. A., Zhang, H., Rau, U., Rupen, M. P., & Little Things Collaboration. 2015, in American Astronomical Society Meeting Abstracts, Vol. 225, American Astronomical Society Meeting Abstracts, 248.16

Kroupa, P. 2012, Publications of the Astronomical Society of Australia, 29, 395

Krumholz, M. R. 2012, ApJ, 759, 9

Krumholz, M. R., Leroy, A. K., & McKee, C. F. 2011, ApJ, 731, 25

Krumholz, M. R., & McKee, C. F. 2005, ApJ, 630, 250

Krumholz, M. R., McKee, C. F., & Tumlinson, J. 2009, ApJ, 699, 850

Kuzio de Naray, R., Arsenault, C. A., Spekkens, K., Sellwood, J. A., McDonald, M., Simon, J. D., & Teuben, P. 2012, MNRAS, 427, 2523

Larson, R. B. 1977, in Evolution of Galaxies and Stellar Populations, ed. B. M. Tinsley & R. B. G. Larson, D. Campbell, 97

Lee, J. C., Kennicutt, R. C., Funes, José G., S. J., Sakai, S., & Akiyama, S. 2007, ApJL, 671, L113

Lee, J. C., et al. 2009, ApJ, 706, 599

Legrand, F., Kunth, D., Roy, J.-R., Mas-Hesse, J. M., & Walsh, J. R. 2000, A&A, 355, 891

Leroy, A., Bolatto, A., Stanimirovic, S., Mizuno, N., Israel, F., & Bot, C. 2007a, ApJ, 658, 1027

Leroy, A., Bolatto, A., Walter, F., & Blitz, L. 2006, ApJ, 643, 825

Leroy, A., Bolatto, A. D., Simon, J. D., & Blitz, L. 2005, ApJ, 625, 763

Leroy, A., Cannon, J., Walter, F., Bolatto, A., & Weiss, A. 2007b, ApJ, 663, 990

Leroy, A. K., Walter, F., Brinks, E., Bigiel, F., de Blok, W. J. G., Madore, B., & Thornley, M. D. 2008, AJ, 136, 2782

Leroy, A. K., et al. 2011, ApJ, 737, 12

—. 2012, AJ, 144, 3

Madden, S. C., Geis, N., Genzel, R., Herrmann, F., Jackson, J., Poglitsch, A., Stacey, G. J., & Townes, C. H. 1993, ApJ, 407, 579

Madden, S. C., Poglitsch, A., Geis, N., Stacey, G. J., & Townes, C. H. 1997, ApJ, 483, 200

Madden, S. C., Rémy, A., Galliano, F., Galametz, M., Bendo, G., Cormier, D., Lebouteiller, V., & Hony, S. 2012, in IAU Symposium, ed. R. J. Tuffs & C. C. Popescu, Vol. 284, 141–148

Madore, B. F., van den Bergh, S., & Rogstad, D. H. 1974, ApJ, 191, 317

Maloney, P., & Black, J. H. 1988, ApJ, 325, 389

Maloney, P. R., & Wolfire, M. G. 1997, in IAU Symposium, Vol. 170, IAU Symposium, ed. W. B. Latter, S. J. E. Radford, P. R. Jewell, J. G. Mangum, & J. Bally, 299–301

Martín-Manjón, M. L., Mollá, M., Díaz, A. I., & Terlevich, R. 2012, MNRAS, 420, 1294

Mateo, M. L. 1998, ARA&A, 36, 435

McKee, C. F., & Ostriker, J. P. 1977, ApJ, 218, 148

McQuinn, K. B. W., Skillman, E. D., Cannon, J. M., Dalcanton, J. J., Dolphin, A., Stark, D., & Weisz, D. 2009, ApJ, 695, 561

Melena, N. W., Elmegreen, B. G., Hunter, D. A., & Zernow, L. 2009, AJ, 138, 1203

Meurer, G. R., Thilker, D., Bianchi, L., Ferguson, A., Madore, B., Gil de Paz, A., Hameed, S., & GALEX Science Team. 2004, in Bulletin of the American Astronomical Society, Vol. 36, American Astronomical Society Meeting Abstracts, 1410

Miller, G. E., & Scalo, J. M. 1979, ApJS, 41, 513

Miralda-Escudé, J. 2003, Science, 300, 1904

Momose, R., et al. 2013, ApJL, 772, L13

Murphy, E. J., et al. 2011, ApJ, 737, 67

Myers, P. C. 1995, in Molecular Clouds and Star Formation, ed. C. Yuan & J.-H. You, 47

Neufeld, D. A., Lepp, S., & Melnick, G. J. 1995, ApJS, 100, 132

Oh, S.-H., Brook, C., Governato, F., Brinks, E., Mayer, L., de Blok, W. J. G., Brooks, A., & Walter, F. 2011a, AJ, 142, 24

Oh, S.-H., de Blok, W. J. G., Brinks, E., Walter, F., & Kennicutt, Jr., R. C. 2011b, AJ, 141, 193

Oh, S.-H., de Blok, W. J. G., Walter, F., Brinks, E., & Kennicutt, Jr., R. C. 2008, AJ, 136, 2761

Oh, S.-H., et al. 2015, AJ

O'Halloran, B., et al. 2010, A&A, 518, L58

Onodera, S., et al. 2010, ApJL, 722, L127

Opik, E. J. 1953, Irish Astronomical Journal, 2, 219

Ostriker, E. C., McKee, C. F., & Leroy, A. K. 2010, ApJ, 721, 975

Ott, J., Walter, F., & Brinks, E. 2005a, MNRAS, 358, 1423

—. 2005b, MNRAS, 358, 1453

Palla, F., & Stahler, S. W. 1991, ApJ, 375, 288

Parker, E. N. 1966, ApJ, 145, 811

Pelupessy, F. I., & Papadopoulos, P. P. 2009, ApJ, 707, 954

Pelupessy, F. I., Papadopoulos, P. P., & van der Werf, P. 2006, ApJ, 645, 1024

Pereira, T. M. D., Asplund, M., & Kiselman, D. 2009, A&A, 508, 1403

Pérez-González, P. G., et al. 2006, ApJ, 648, 987

Pina, R. K., & Puetter, R. C. 1993, PASP, 105, 630

Poglitsch, A., Krabbe, A., Madden, S. C., Nikola, T., Geis, N., Johansson, L. E. B., Stacey, G. J., & Sternberg, A. 1995, ApJ, 454, 293

Puetter, R. C. 1995, International Journal of Imaging Systems Technology, 6, 314

Rahman, N., et al. 2012, ApJ, 745, 183

Recchi, S., & Hensler, G. 2004, Astronomische Nachrichten Supplement, 325, 63

Rémy-Ruyer, A., et al. 2013, A&A, 557, A95

Rich, J. W., de Blok, W. J. G., Cornwell, T. J., Brinks, E., Walter, F., Bagetakos, I., & Kennicutt, Jr., R. C. 2008, AJ, 136, 2897

Ricotti, M., Gnedin, N. Y., & Shull, J. M. 2008, ApJ, 685, 21

Roman-Duval, J., et al. 2010, A&A, 518, L74

Rosenberg, J. L., Wu, Y., Le Floc'h, E., Charmandaris, V., Ashby, M. L. N., Houck, J. R., Salzer, J. J., & Willner, S. P. 2008, ApJ, 674, 814

Roychowdhury, S., Chengalur, J. N., Kaisin, S. S., Begum, A., & Karachentsev, I. D. 2011, MNRAS, 414, L55

Safronov, V. S. 1960, Annales d'Astrophysique, 23, 979

Salim, S., et al. 2007, ApJS, 173, 267

Sandstrom, K. M., et al. 2013, ApJ, 777, 5

Sanduleak, N. 1969, AJ, 74, 47

Schaye, J. 2004, ApJ, 609, 667

Schlegel, D. J., Finkbeiner, D. P., & Davis, M. 1998, ApJ, 500, 525

Schmidt, M. 1959, ApJ, 129, 243

—. 1963, ApJ, 137, 758

Schruba, A., Leroy, A. K., Walter, F., Sandstrom, K., & Rosolowsky, E. 2010, ApJ, 722, 1699

Schruba, A., et al. 2011, AJ, 142, 37

Schuster, K. F., Kramer, C., Hitschfeld, M., Garcia-Burillo, S., & Mookerjea, B. 2007, A&A, 461, 143

Schwarz, U. J. 1984, in Indirect Imaging. Measurement and Processing for Indirect Imaging, ed. J. A. Roberts, 255

Shi, Y., Helou, G., Yan, L., Armus, L., Wu, Y., Papovich, C., & Stierwalt, S. 2011, ApJ, 733, 87

Shu, F. H. 1977, ApJ, 214, 488

Simon, J. D., Robishaw, T., & Blitz, L. 2004, in Astronomical Society of the Pacific Conference Series, Vol. 327, Satellites and Tidal Streams, ed. F. Prada, D. Martinez Delgado, & T. J. Mahoney, 32

Slezak, E., Bijaoui, A., & Mars, G. 1990, A&A, 227, 301

Spekkens, K., & Sellwood, J. A. 2007, ApJ, 664, 204

Spergel, D. N., & Blitz, L. 1992, Nature, 357, 665

Springel, V., Frenk, C. S., & White, S. D. M. 2006, Nature, 440, 1137

Springob, C. M., Haynes, M. P., Giovanelli, R., & Kent, B. R. 2005, ApJS, 160, 149

Stahler, S. W. 1988, ApJ, 332, 804

Starck, J. L., Pantin, E., & Murtagh, F. 2002, PASP, 114, 1051

Steer, D. G., Dewdney, P. E., & Ito, M. R. 1984, A&A, 137, 159

Stewart, S. G., & Walter, F. 2000, AJ, 120, 1794

Stewart, S. G., et al. 2000, ApJ, 529, 201

Struck, C., & Smith, D. C. 1999, ApJ, 527, 673

Suwannajak, C., Tan, J. C., & Leroy, A. K. 2014, ApJ, 787, 68

Swaters, R. A. 1999, PhD thesis, Rijksuniversiteit Groningen, (1999)

Swaters, R. A., Madore, B. F., van den Bosch, F. C., & Balcells, M. 2003, ApJ, 583, 732

Swaters, R. A., Sancisi, R., van Albada, T. S., & van der Hulst, J. M. 2011, ApJ, 729, 118

Thilker, D. A., et al. 2007, ApJS, 173, 538

Toomre, A. 1964, ApJ, 139, 1217

Tosa, M., & Hamajima, K. 1975, PASJ, 27, 501

Tosi, M., Greggio, L., Marconi, G., & Focardi, P. 1991, AJ, 102, 951

van de Hulst, H. C. 1945, Ned. tijd. natuurkunde, 11, 210

van den Bergh, S. 1957, Zeitschrift für Astrophysik, 43, 236

—. 1988, PASP, 100, 344

van der Marel, R. P., Alves, D. R., Hardy, E., & Suntzeff, N. B. 2002, AJ, 124, 2639

van der Marel, R. P., & Franx, M. 1993, ApJ, 407, 525

van Dishoeck, E. F., & Blake, G. A. 1998, ARA&A, 36, 317

van Dyk, S. D., Puche, D., & Wong, T. 1998, AJ, 116, 2341

van Zee, L., Maddalena, R. J., Haynes, M. P., Hogg, D. E., & Roberts, M. S. 1997, AJ, 113, 1638

Verdugo, C., Rubio, M., & Bolatto, A. 2011, Boletin de la Asociacion Argentina de Astronomia La Plata Argentina, 54, 247

Wakker, B. P., & Schwarz, U. J. 1988, A&A, 200, 312

Walch, S., Wünsch, R., Burkert, A., Glover, S., & Whitworth, A. 2011, ApJ, 733, 47

Walter, F., Brinks, E., de Blok, W. J. G., Bigiel, F., Kennicutt, R. C., Thornley, M. D., & Leroy, A. 2008, AJ, 136, 2563

Warren, S. R., et al. 2012, ApJ, 757, 84

Weidner, C., Bonnell, I. A., & Zinnecker, H. 2011, in IAU Symposium, Vol. 270, Computational Star Formation, ed. J. Alves, B. G. Elmegreen, J. M. Girart, & V. Trimble, 385–388

Weisz, D. R., Skillman, E. D., Cannon, J. M., Dolphin, A. E., Kennicutt, Jr., R. C., Lee, J., & Walter, F. 2008, ApJ, 689, 160

White, S. D. M., & Rees, M. J. 1978, MNRAS, 183, 341

Wilson, R. W., Jefferts, K. B., & Penzias, A. A. 1970, ApJL, 161, L43

Wolfire, M. G. 2010, Highlights of Astronomy, 15, 409

Wong, T., & Blitz, L. 2002, ApJ, 569, 157

Wong, T., et al. 2013, ApJL, 777, L4

Wyder, T. K., et al. 2007, ApJS, 173, 293

Young, L. M., van Zee, L., Lo, K. Y., Dohm-Palmer, R. C., & Beierle, M. E. 2003, ApJ, 592, 111

Zhang, H.-X., Hunter, D. A., Elmegreen, B. G., Gao, Y., & Schruba, A. 2012, AJ, 143, 47

Zhang, Y., et al. 2013, ApJ, 767, 58

Zwaan, M. A., Briggs, F. H., Sprayberry, D., & Sorar, E. 1997, ApJ, 490, 173

Appendix A
Channel Maps

We present here the H I channel maps of all the galaxies in our subsample in Fig. A.1 to Fig. A.18. These channel maps are based on the robust=0 cubes and the noise levels of these cubes are given in Table 2.4 in units of mJy beam^{-1}, and in the figure captions in K. Note that the beam sizes are indicated in the bottom left corner of the top left panel, however they may be too small to be properly reproduced. All emission channels are shown unless otherwise stated in the figure caption. In the top right of each panel is indicated the heliocentric radial velocity of the H I gas in km s^{-1}. The order in which the channel maps of different galaxies are shown is from the highest to the lowest metallicity.

Glancing through the channel maps one quickly notices the morphological diversity of our subsample. Some galaxies are large in size especially the higher metallicity ones while others are tiny. Some like DDO 50 or IC 1613 impress with large H I shells, whereas others like DDO 69 or M81dwA show a doughnut shape. When looking at the channel maps one notices a wide span in velocity ranges (24 to 121 km s^{-1}). Generally the high velocity ranges correspond to the higher metallicity , higher mass galaxies. The lowest three metallicity galaxies are the ones with the smallest velocity range. Dwarf galaxies are slow rotators, exhibiting a rigid body rotation if at all. Galaxies such as DDO 155, DDO 165, M81dwA, DDO 75, DDO 187 and DDO 69 show no projected circular rotation, which is due to a combination of their intrinsically low rotational speed and orientation with respect to the observer.

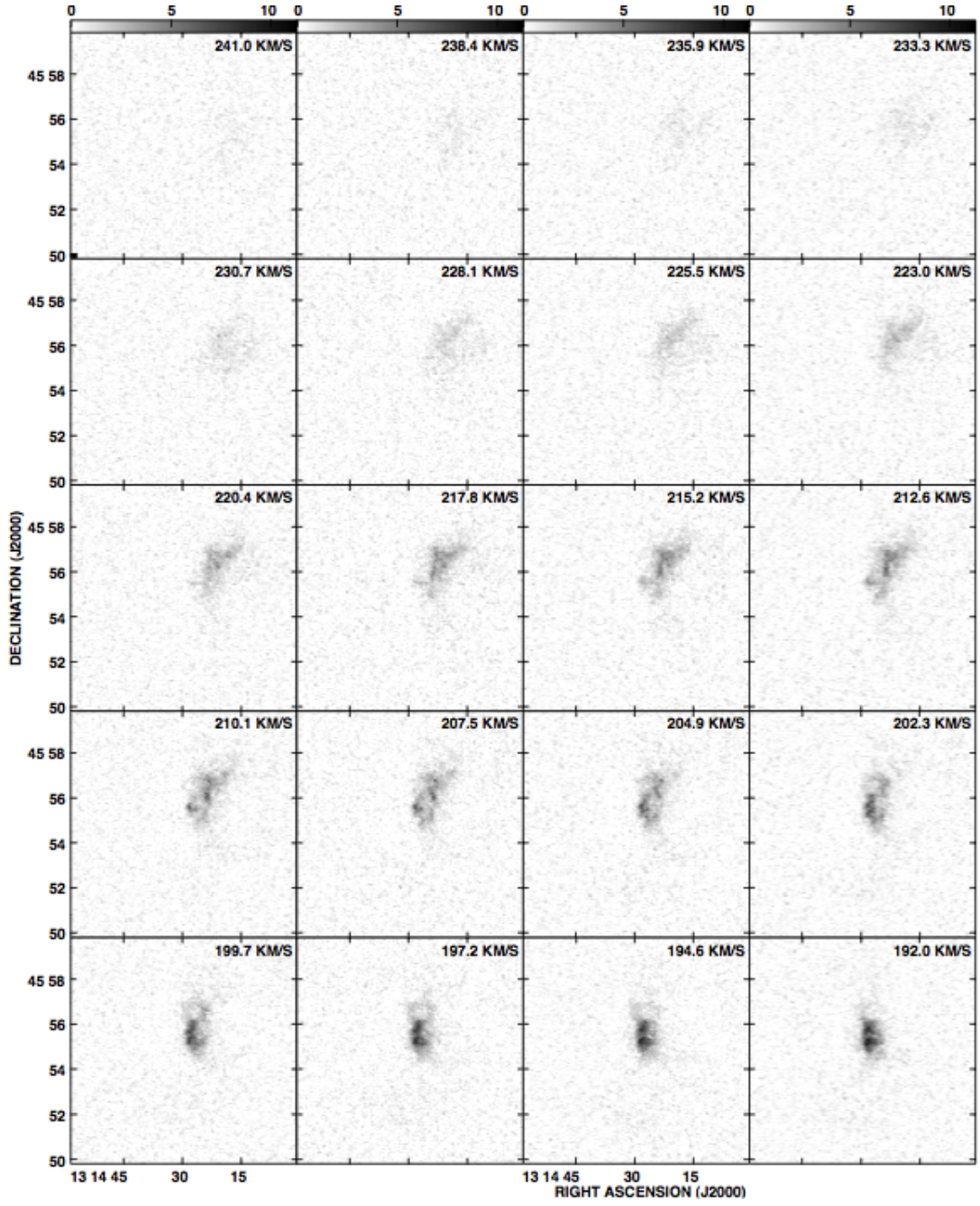

Figure A.1: DDO 168. Channel maps based on the robust weighted cube (Resolution: 7.″8 × 5.″8, σ= 6.8 K). The grey scale range is: 0-150.3 K (0 - 11.3 mJy beam^{-1}). All emission channels are shown. The beam is indicated in the bottom left corner of the top left panel.

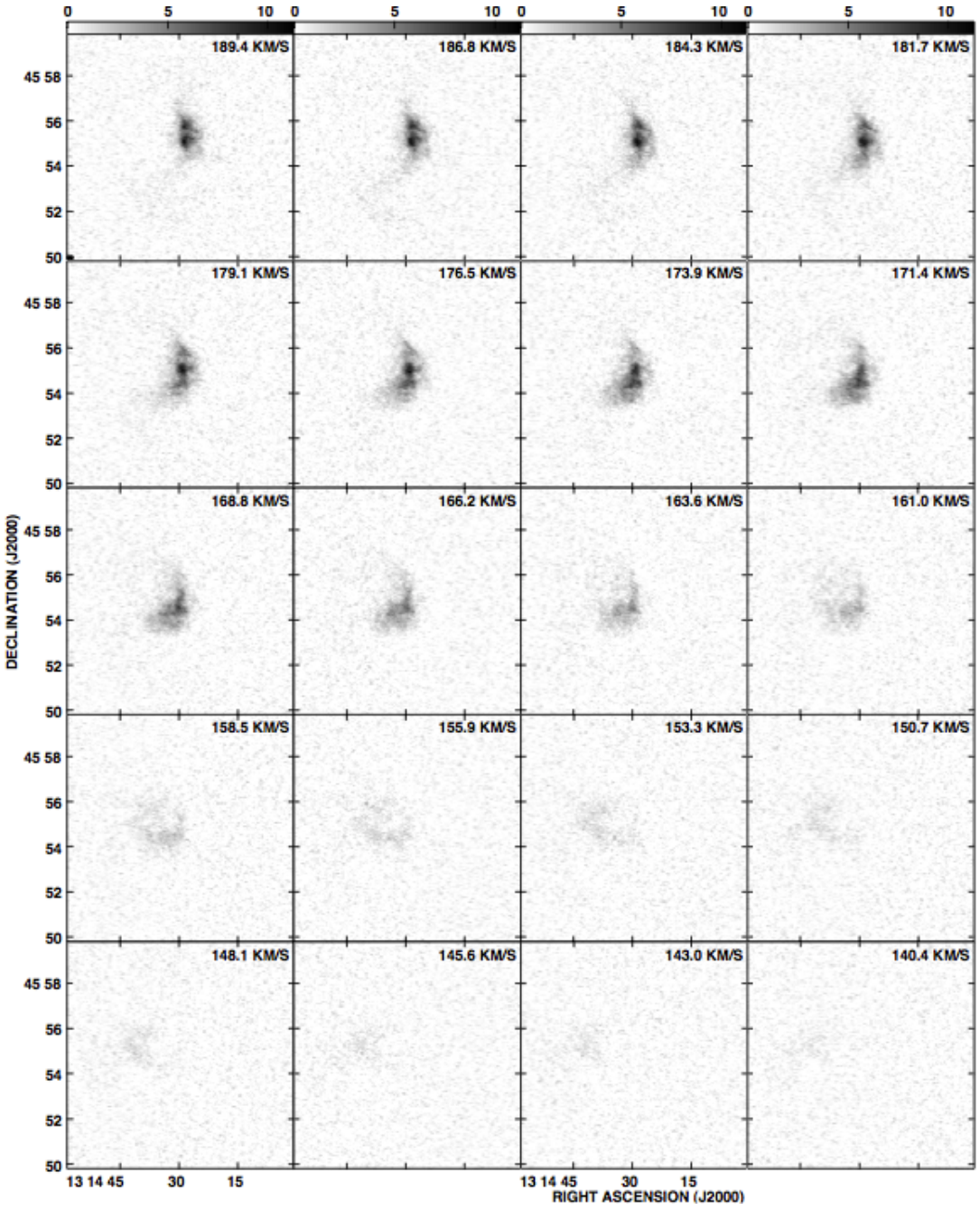

Fig. A.1 continues ...

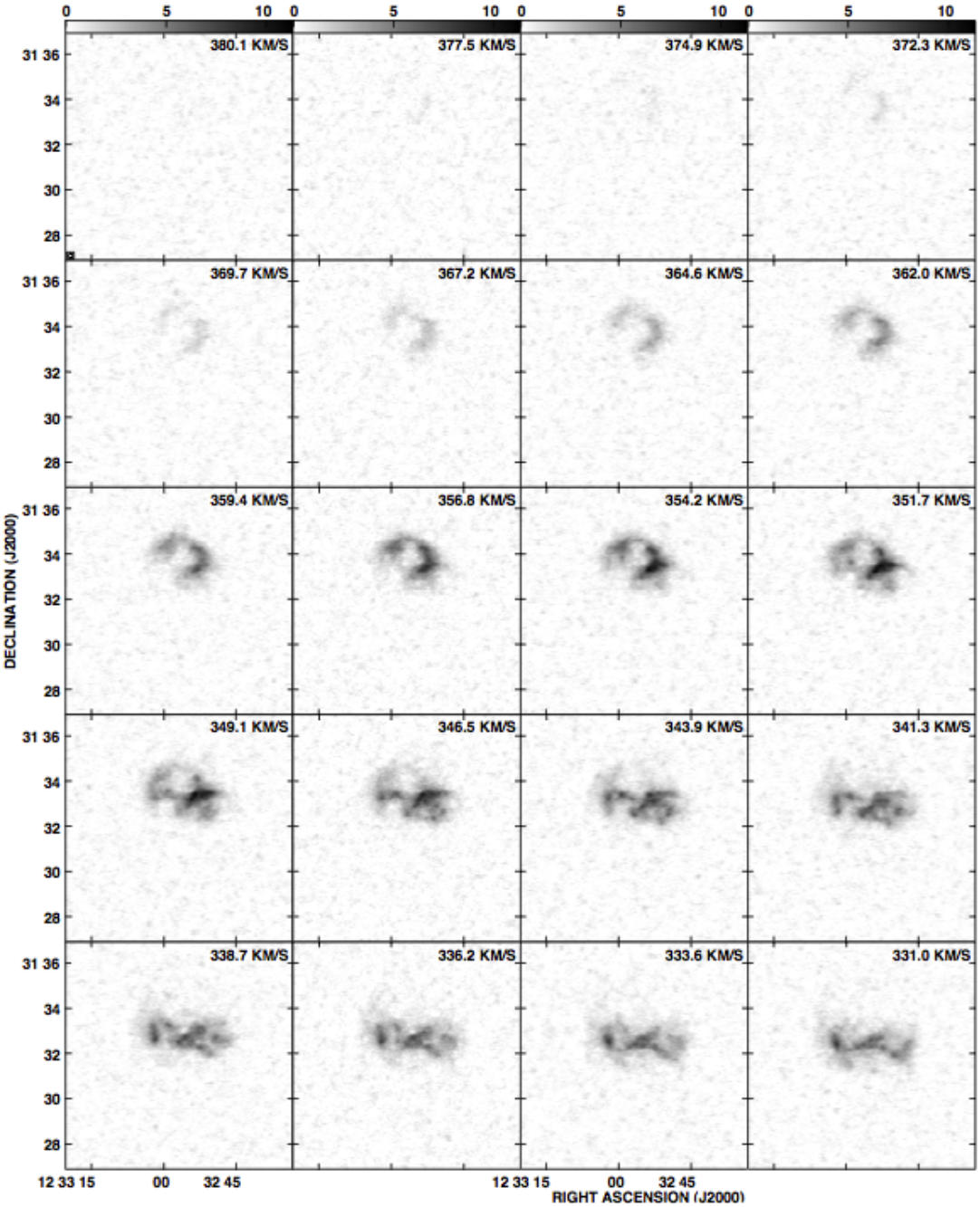

Figure A.2: DDO 133. Channel maps based on the robust weighted cube (Resolution: $12\farcs4 \times 10\farcs8$, σ= 1.7 K). The grey scale range is: 0-51.6 K (0 - 11.3 mJy beam^{-1}). All emission channels are shown. The beam is indicated in the bottom left corner of the top left panel.

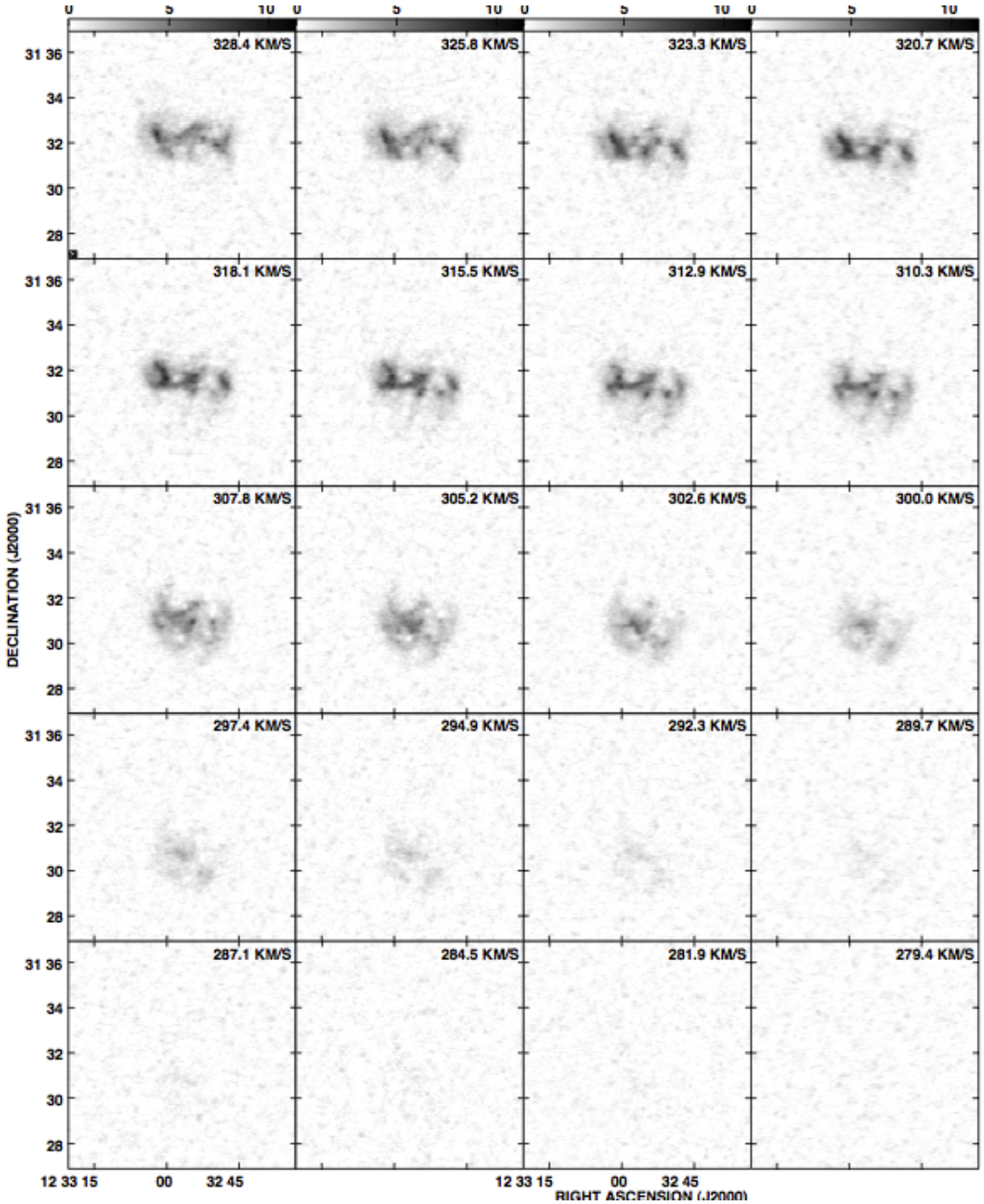

Fig. A.2 continues ...

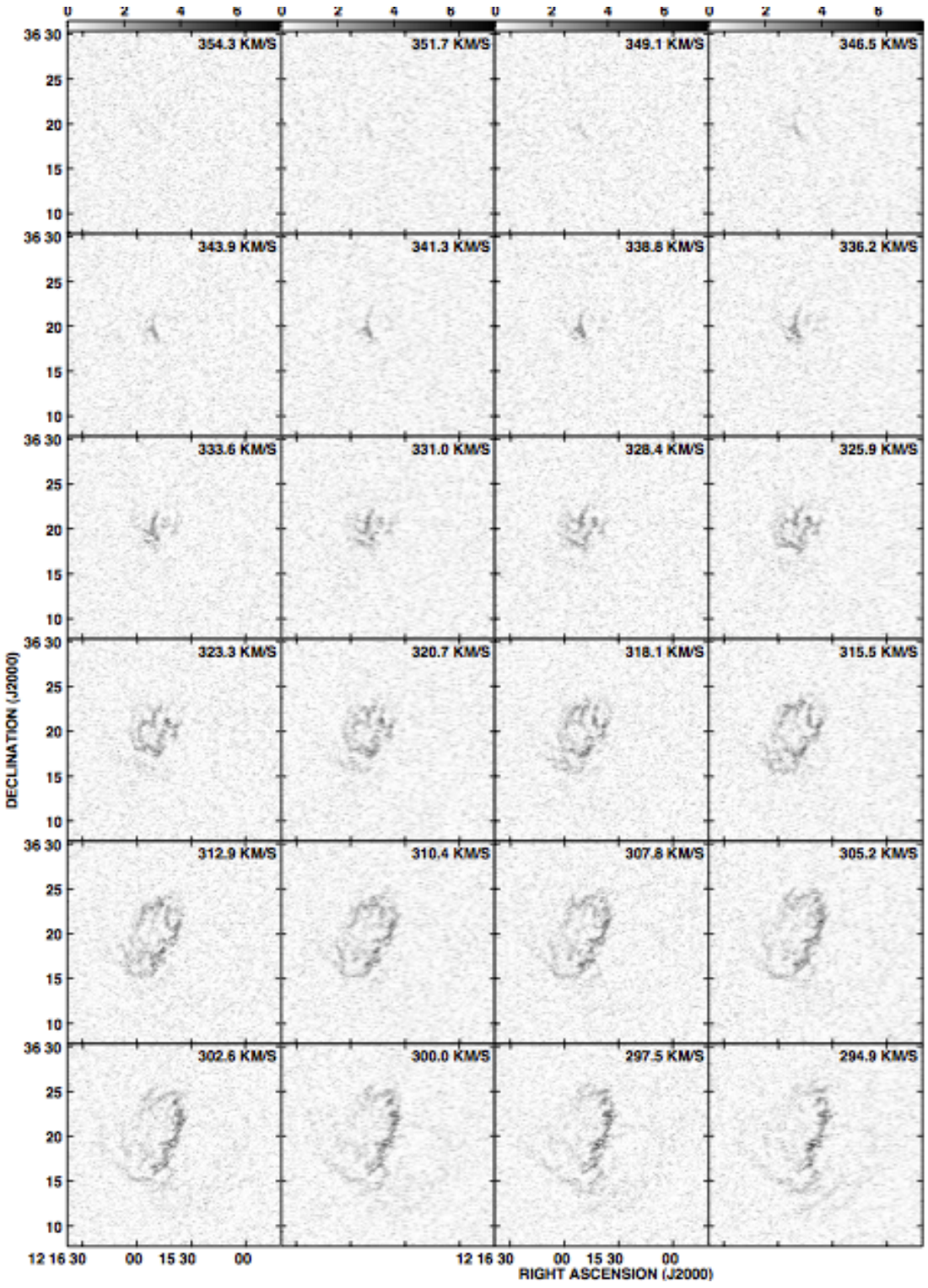

Figure A.3: NGC 4214. Channel maps based on the robust weighted cube (Resolution: $7\farcs6 \times 6\farcs4$, σ= 9.1 K). The grey scale range is: 0-94.4 K (0 - 7.6 mJy beam^{-1}). All emission channels are shown. The beam is indicated in the bottom left corner of the top left panel.

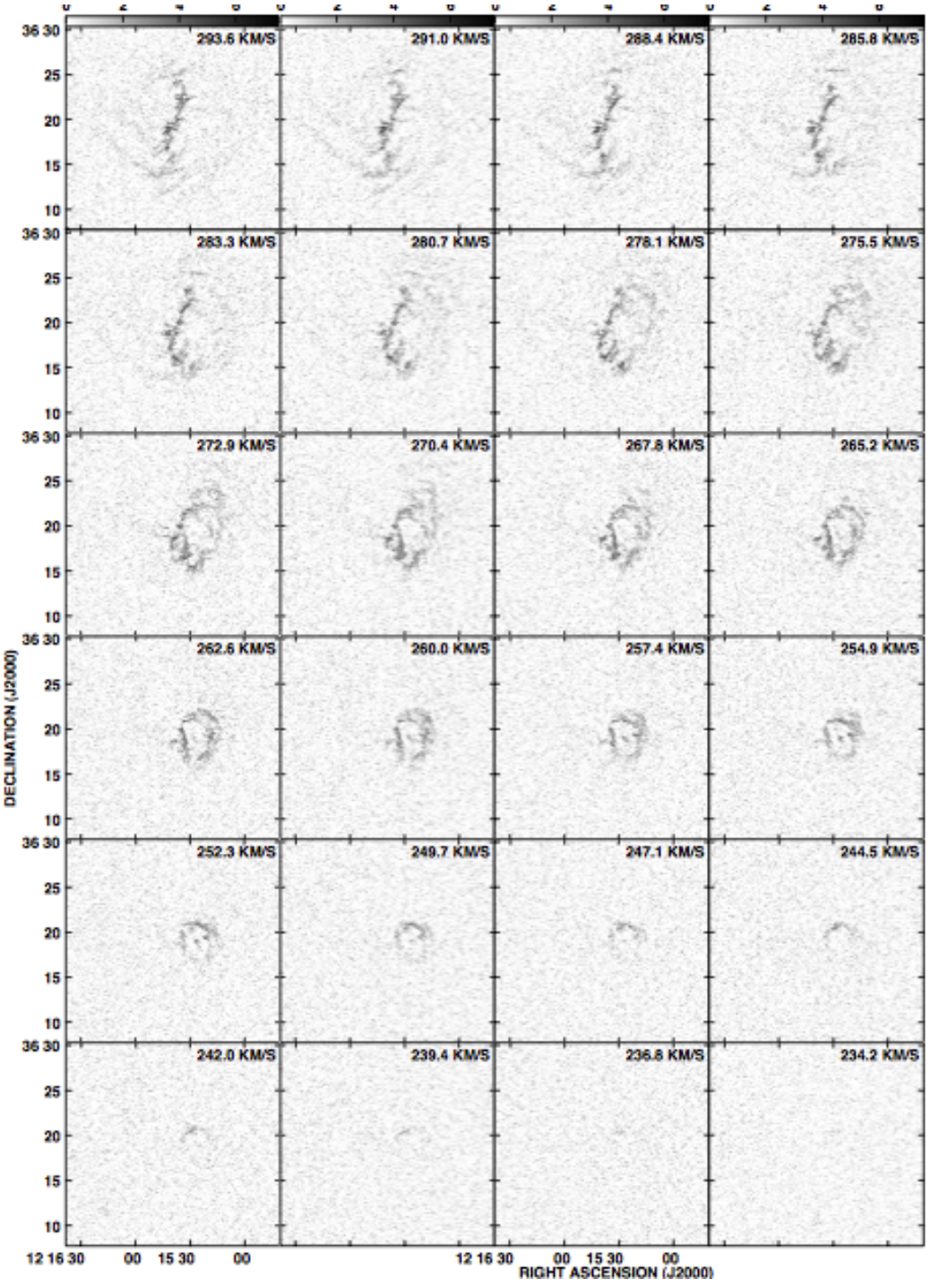

Fig. A.3 continues ...

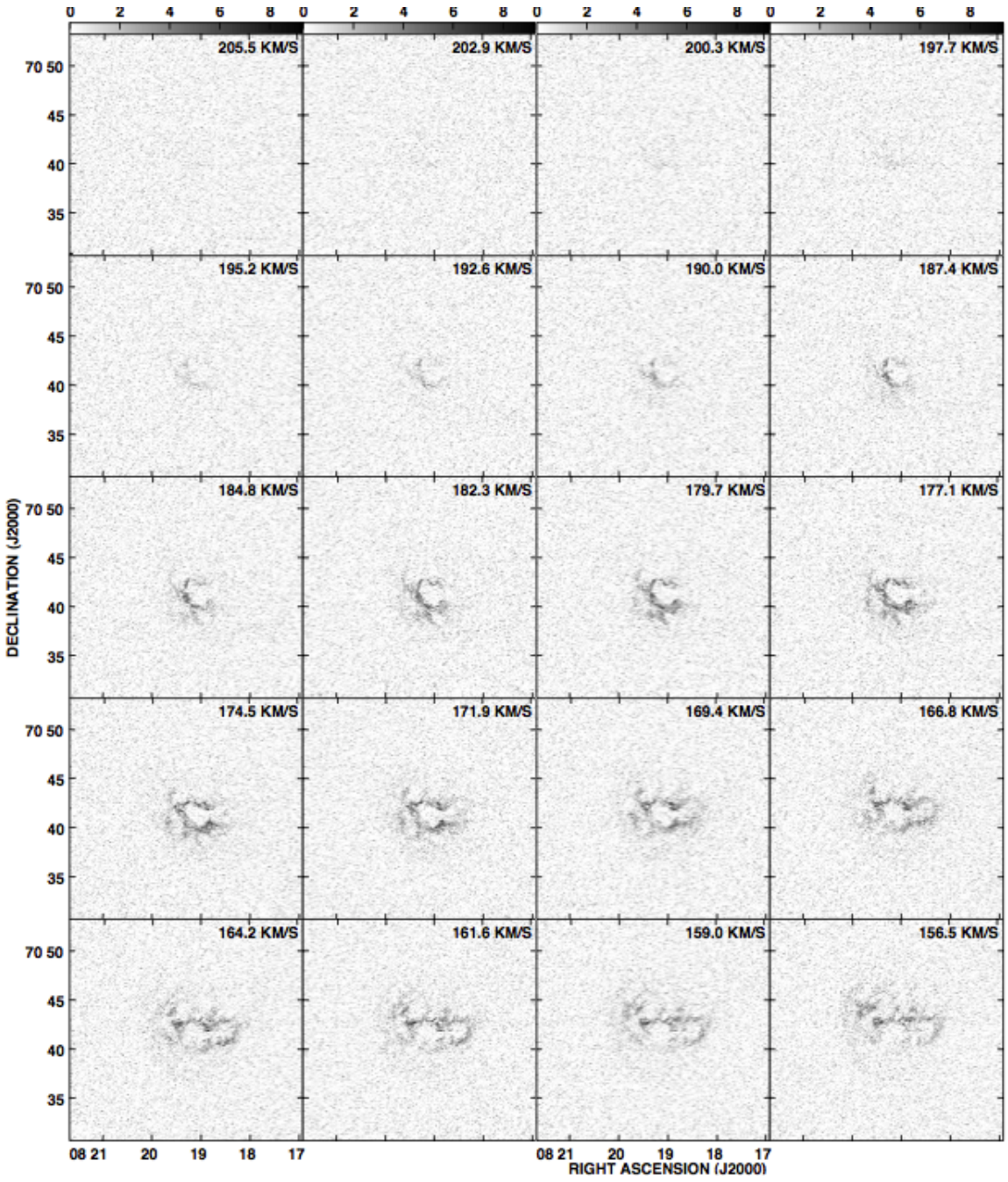

Figure A.4: DDO 50. Channel maps based on the robust weighted cube (Resolution: 7.″0 × 6.″1, σ= 15.2 K). The grey scale range is: 0-132.2 K (0 - 9.3 mJy beam^{-1}). All emission channels are shown. The beam is indicated in the bottom left corner of the top left panel.

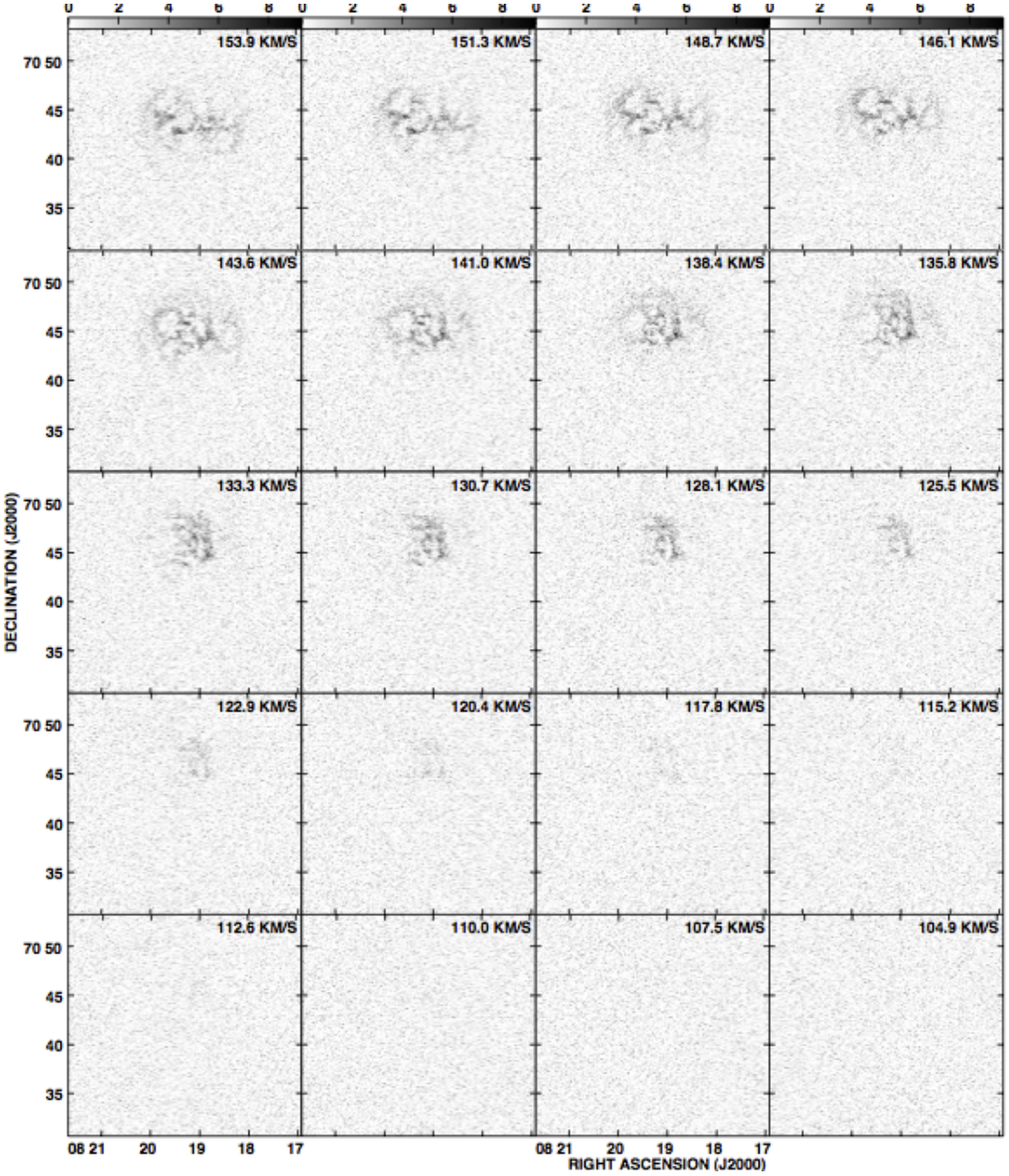

Fig. A.4 continues ...

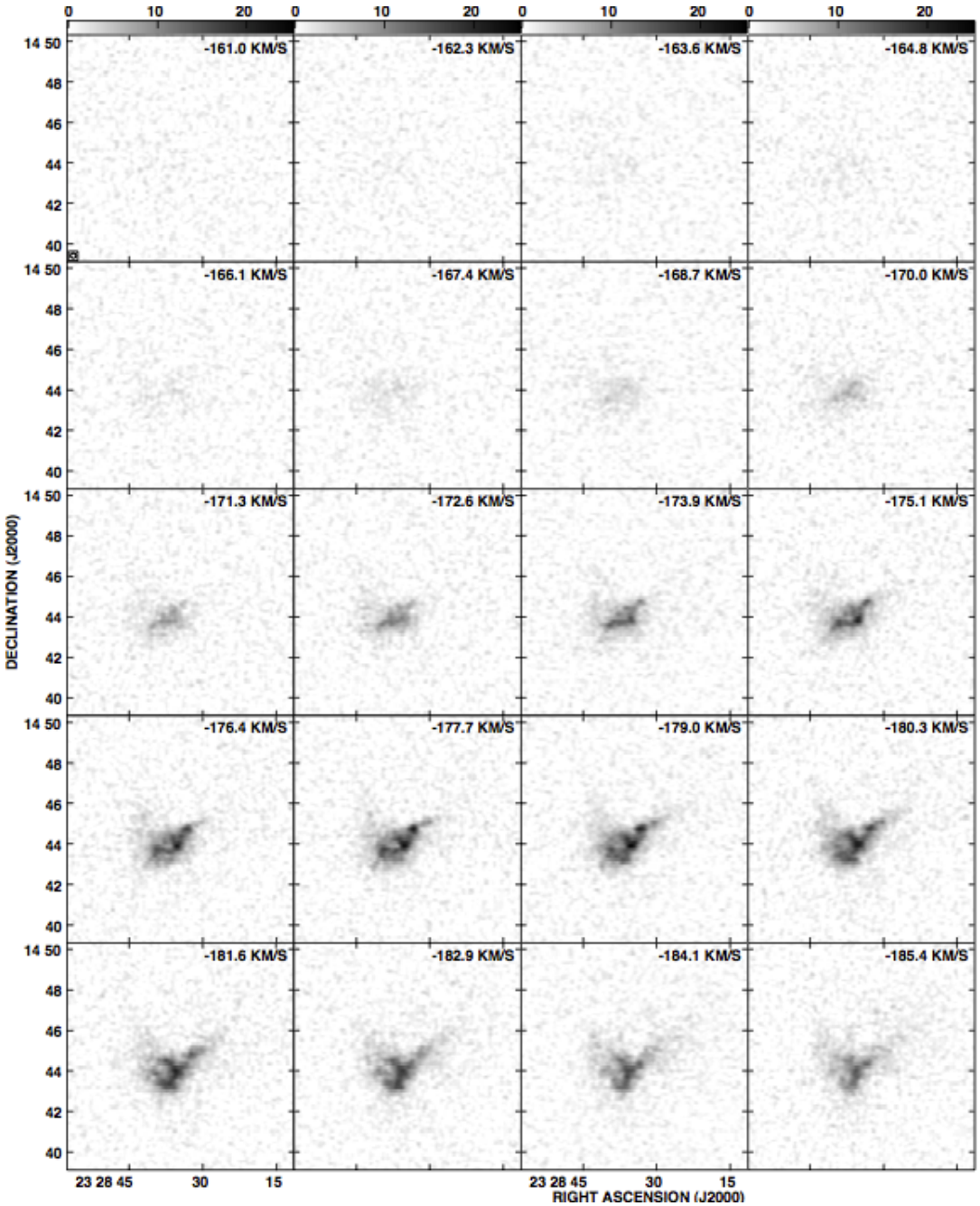

Figure A.5: DDO 216. Channel maps based on the robust weighted cube (Resolution: $16\farcs2 \times 15\farcs4$, σ= 2.3 K). The grey scale range is: 0-61.1 K (0 - 25.2 mJy beam^{-1}). All emission channels are shown. The beam is indicated in the bottom left corner of the top left panel.

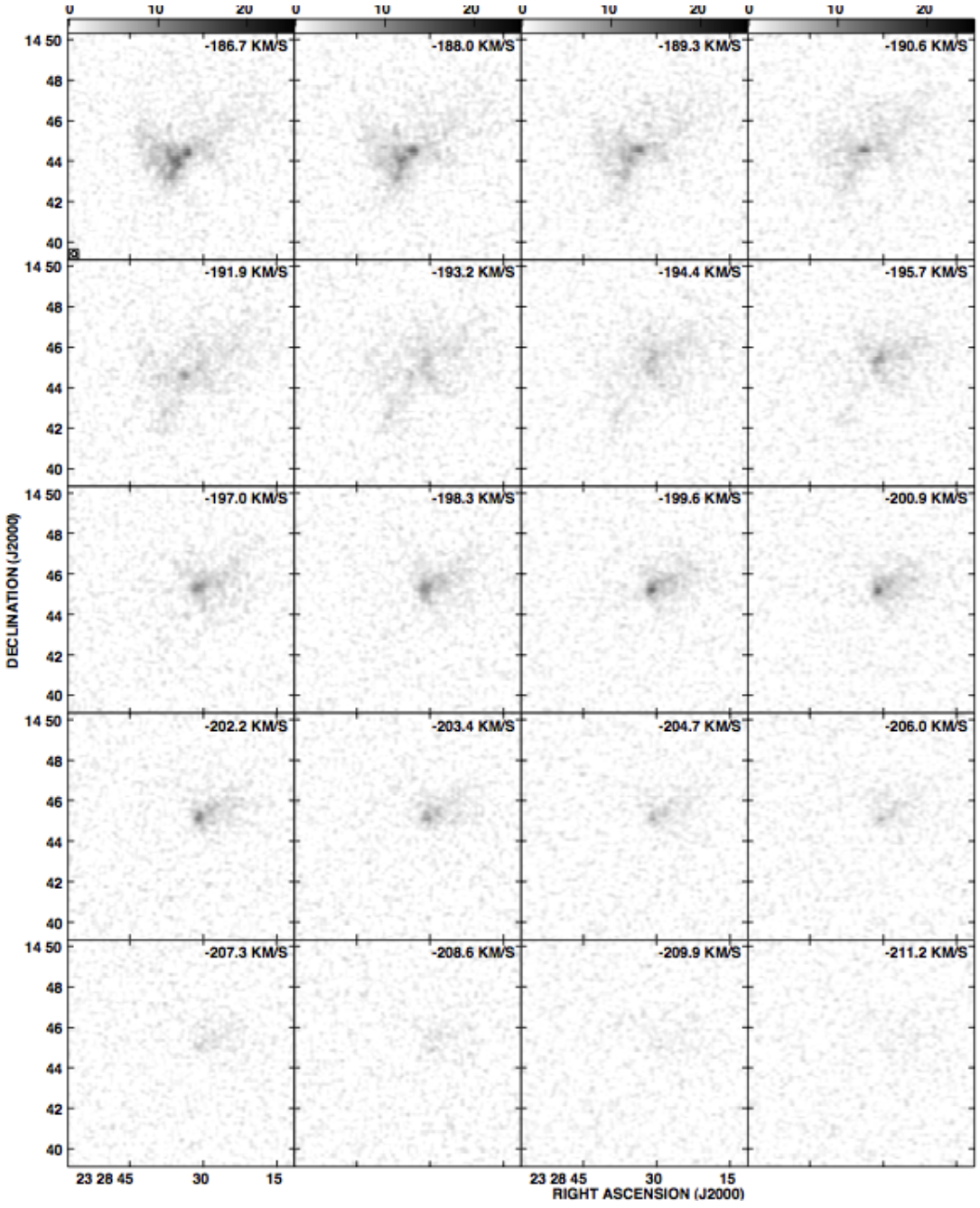

Fig. A.5 continues ...

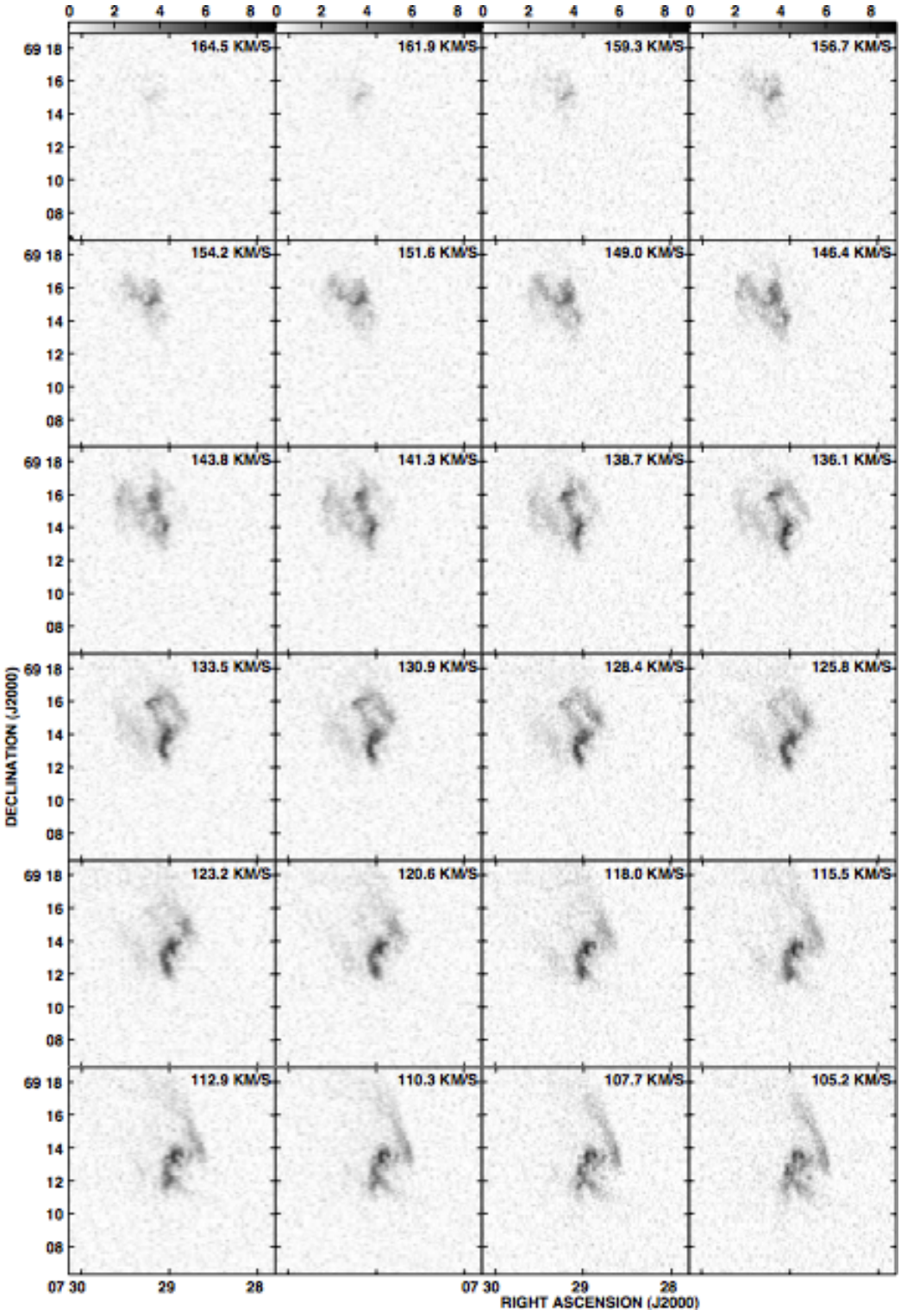

Figure A.6: NGC 2366. Channel maps based on the robust weighted cube (Resolution: $6\farcs9 \times 5\farcs9$, $\sigma = 9.4$ K). The grey scale range is: 0-135.2 K (0 - 9.1 mJy beam^{-1}). All emission channels are shown. The beam is indicated in the bottom left corner of the top left panel.

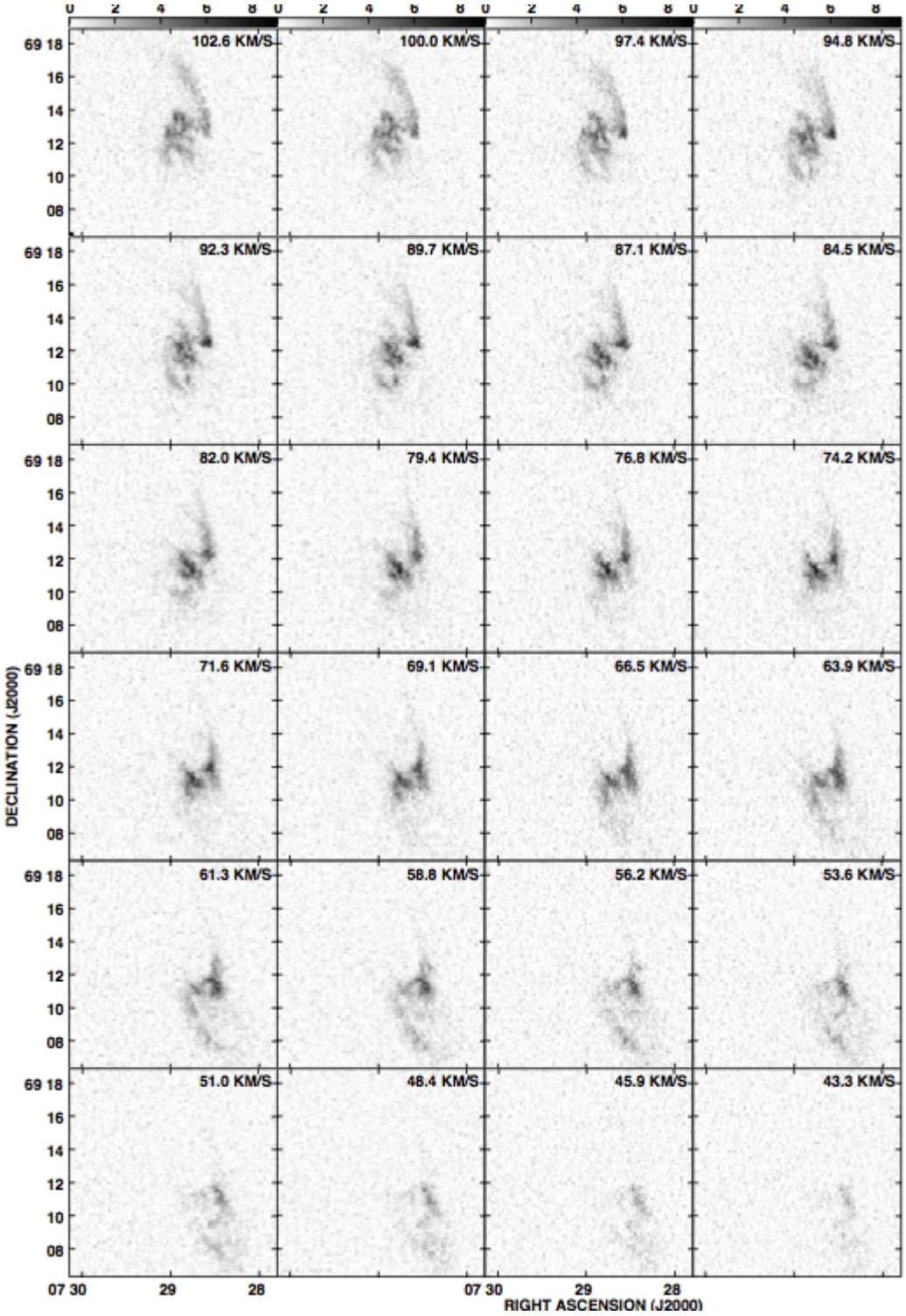

Fig. A.6 continues ...

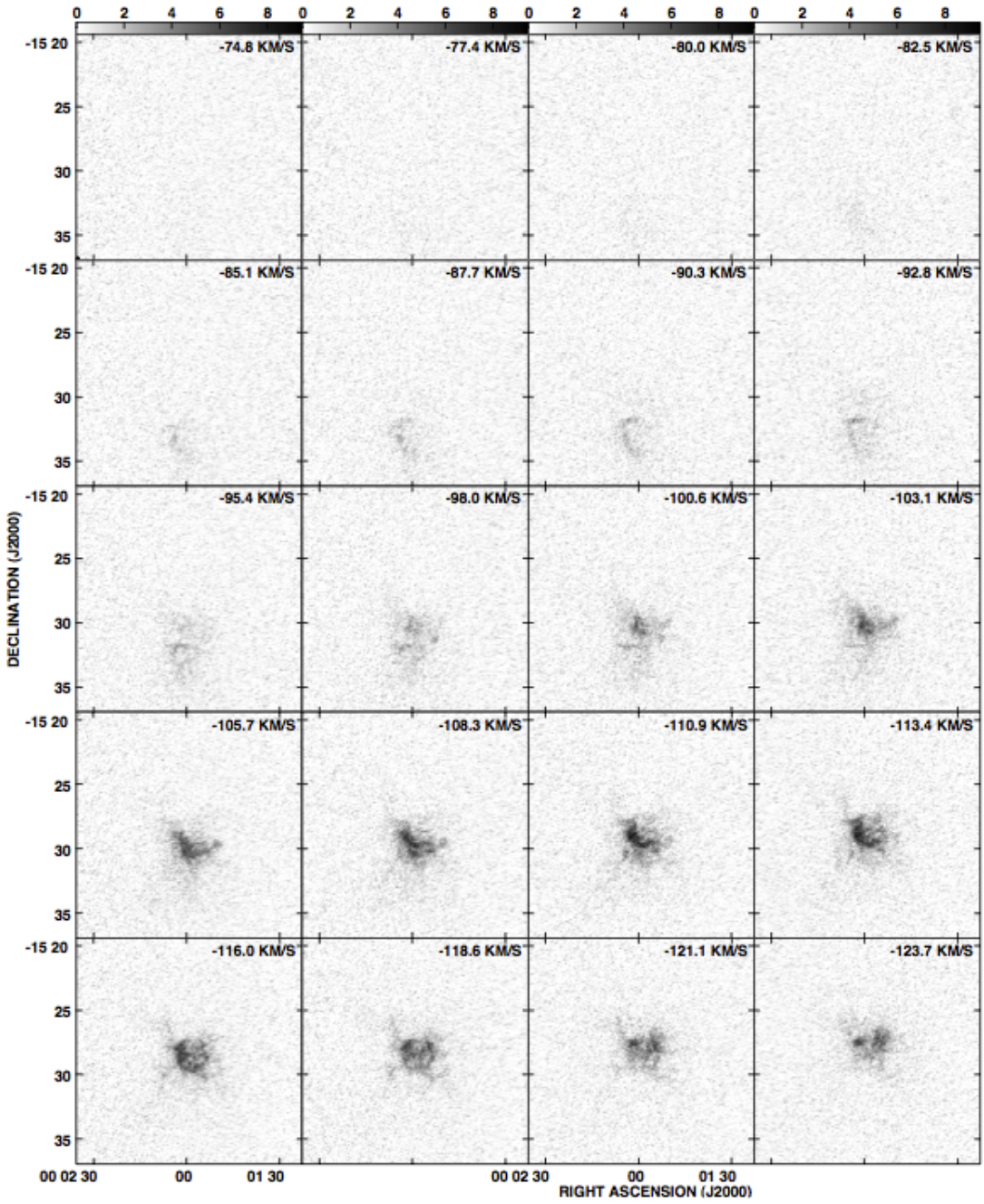

Figure A.7: WLM. Channel maps based on the robust weighted cube (Resolution: $7\farcs6 \times 5\farcs1$, σ= 12.8 K). The grey scale range is: 0-147.9 K (0 - 9.5 mJy beam^{-1}). All emission channels are shown. The beam is indicated in the bottom left corner of the top left panel.

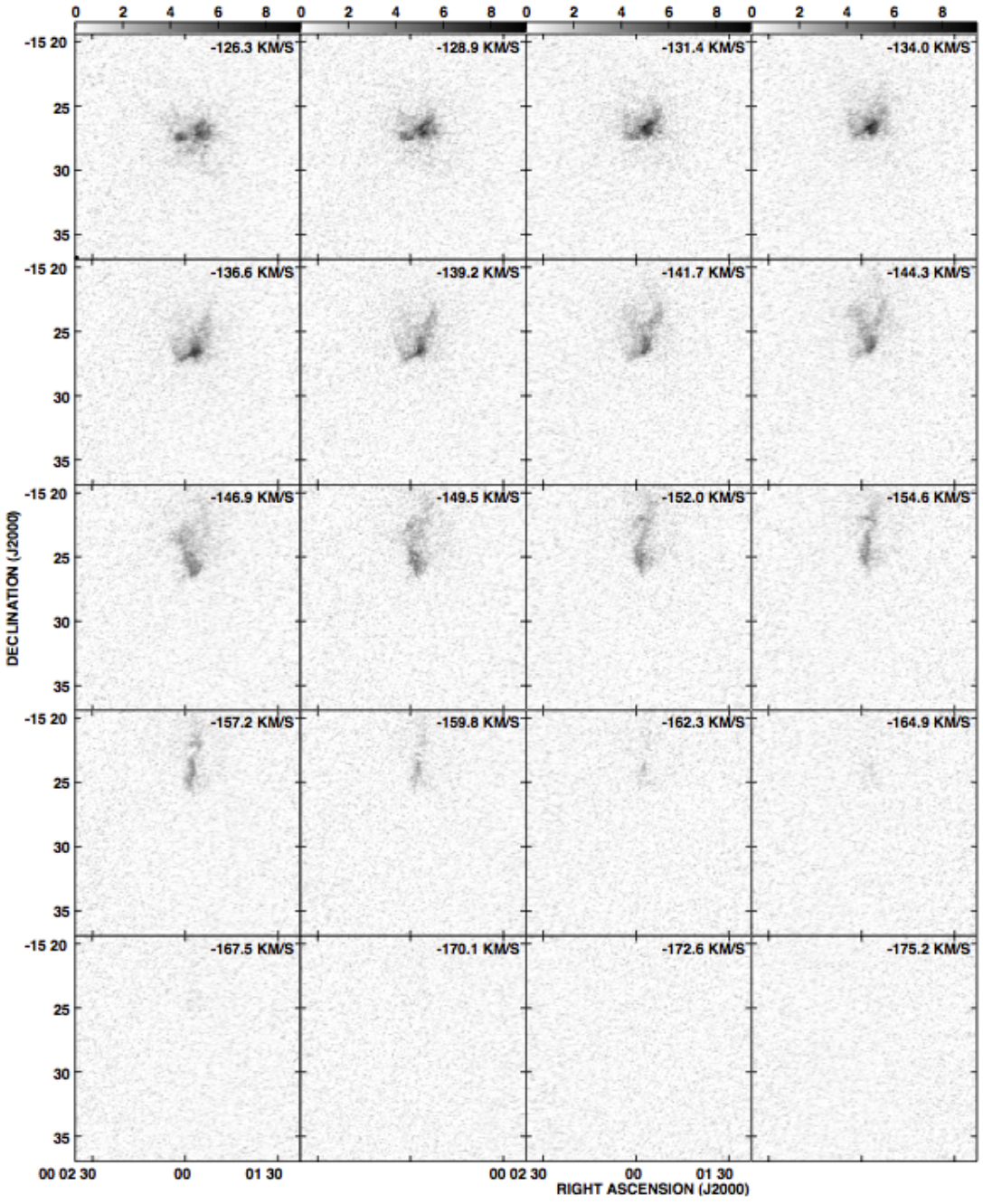

Fig. A.7 continues ...

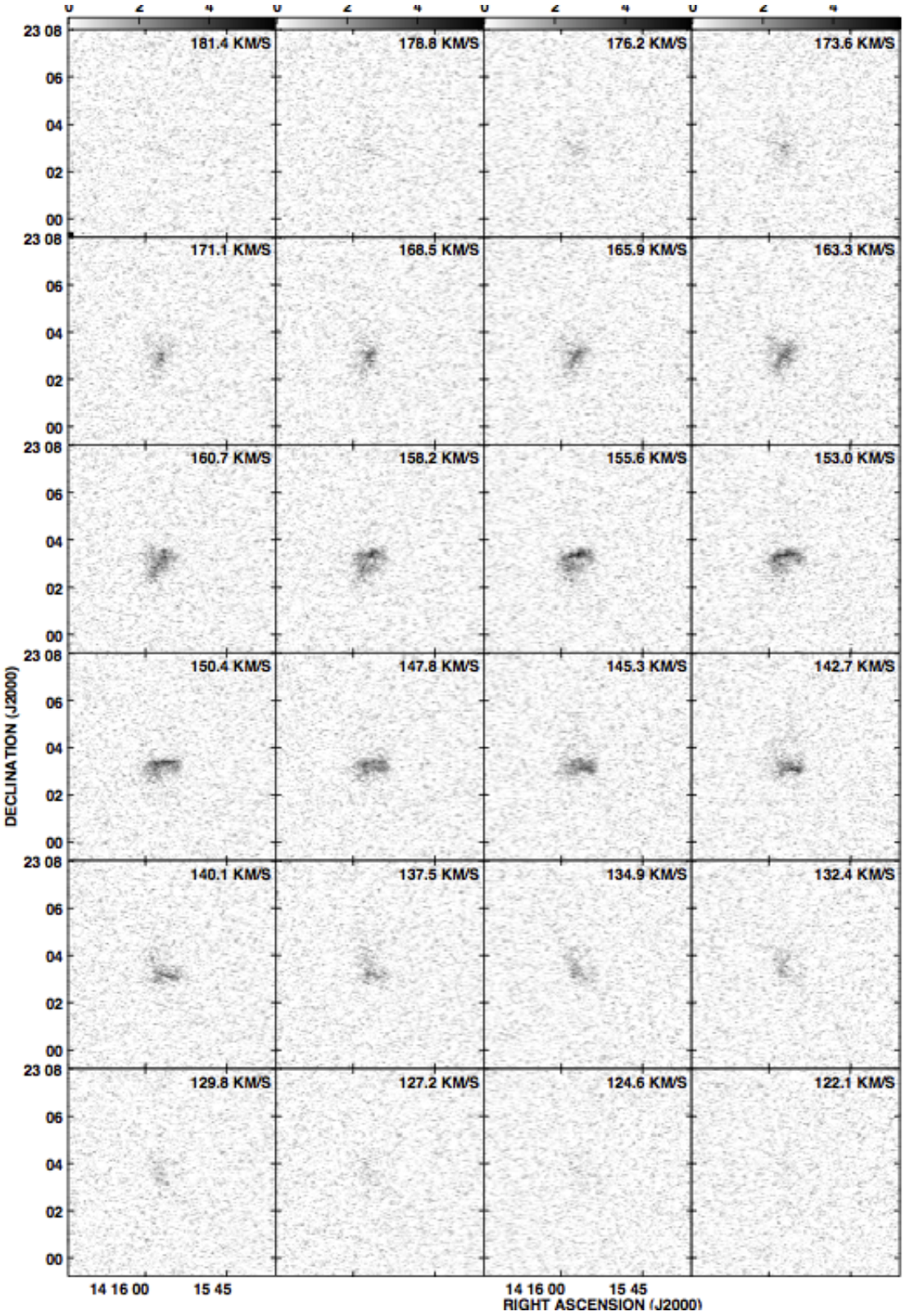

Figure A.8: DDO 187. Channel maps based on the robust weighted cube (Resolution: $6\farcs2 \times 5\farcs5$, σ= 11.0 K). The grey scale range is: 0-104.5 K (0 - 5.879 mJy beam^{-1}). All emission channels are shown. The beam is indicated in the bottom left corner of the top left panel.

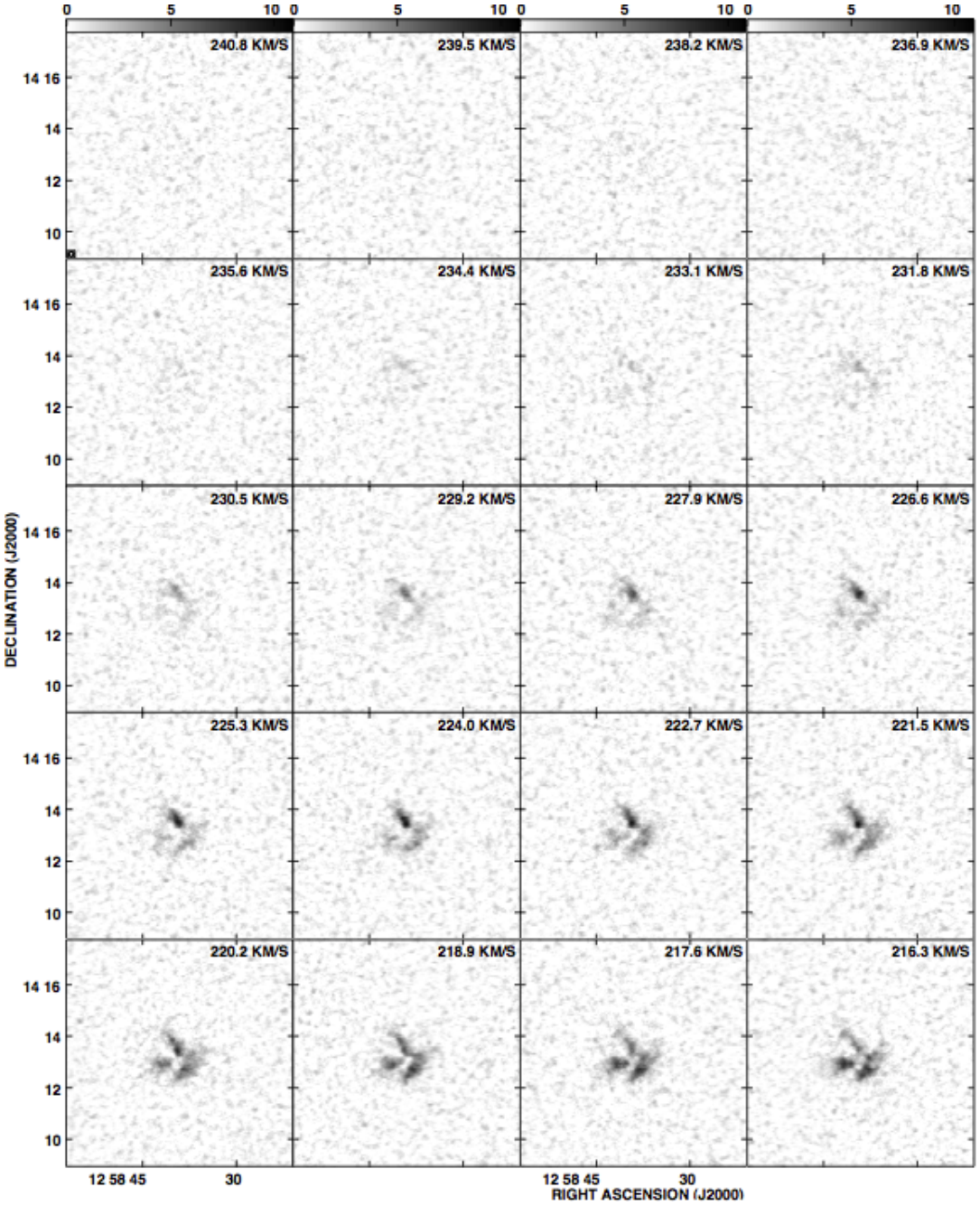

Figure A.9: DDO 155. Channel maps based on the robust weighted cube (Resolution: $11\farcs3 \times 10\farcs1$, σ= 3.5 K). The grey scale range is: 0-57.8 K (0 - 10.9 mJy beam^{-1}). All emission channels are shown. The beam is indicated in the bottom left corner of the top left panel.

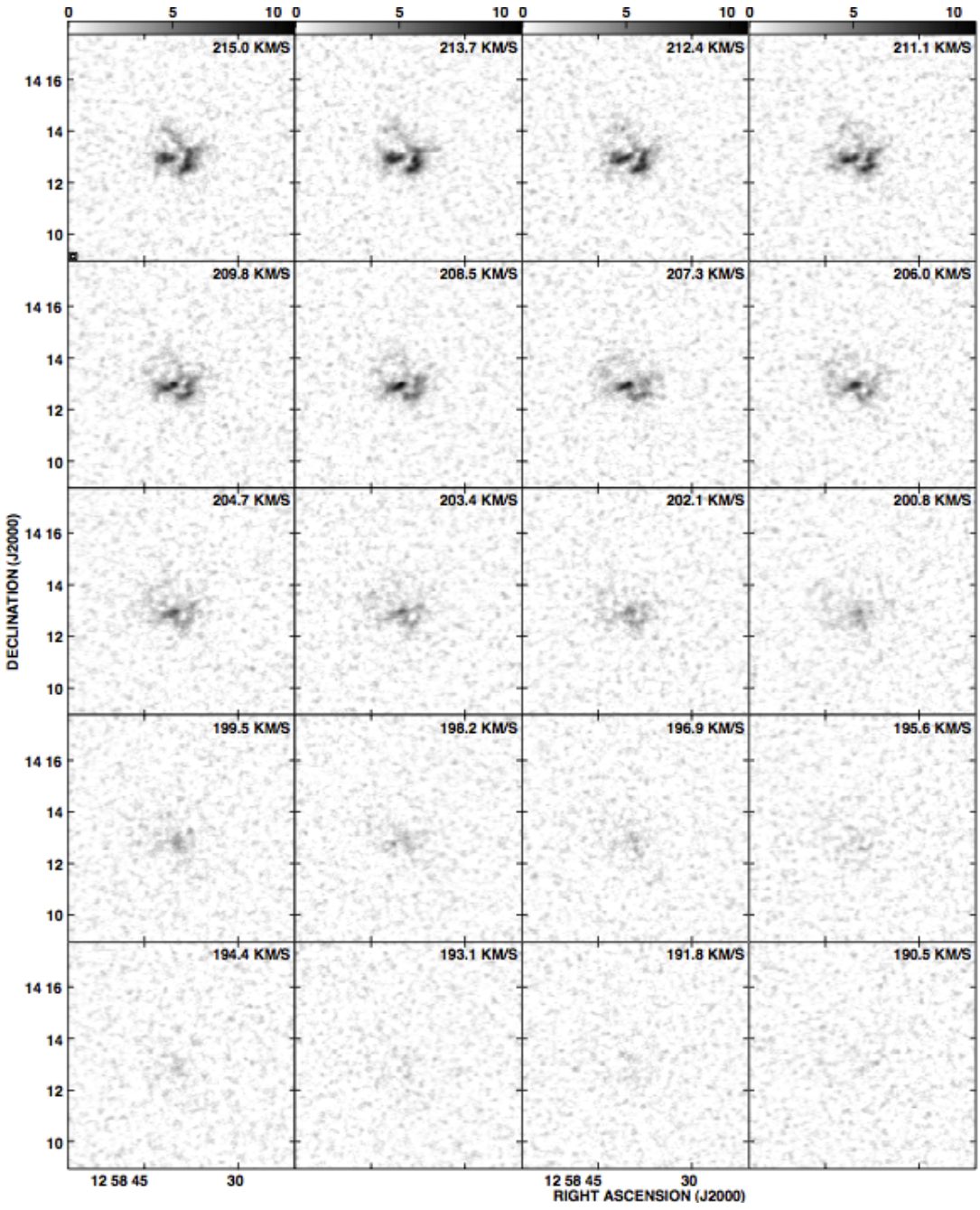

Fig. A.9 continues ...

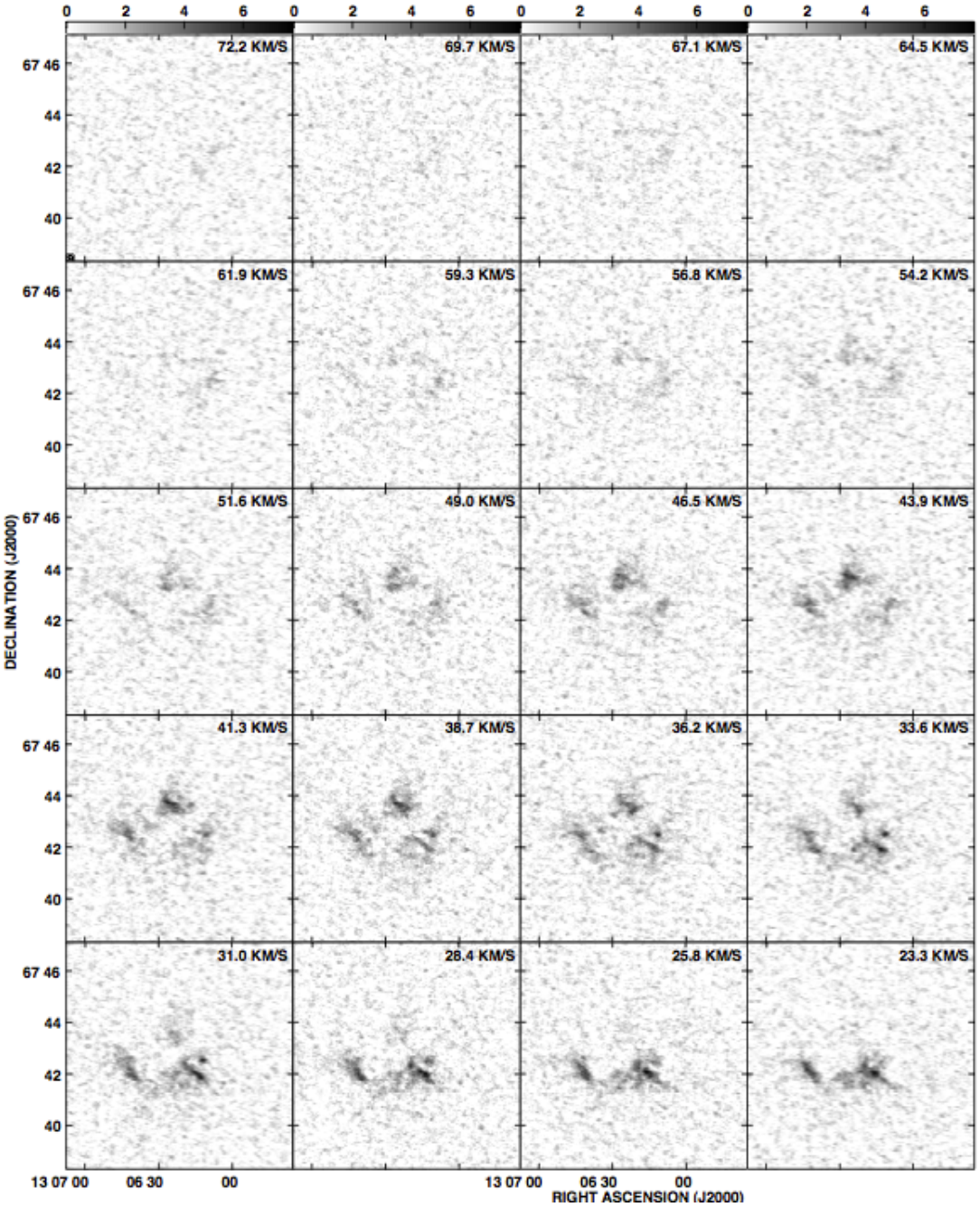

Figure A.10: DDO 165. Channel maps based on the robust weighted cube (Resolution: $10\farcs0 \times 7\farcs6$, σ= 5.1 K). The grey scale range is: 0-61.3 K (0 - 7.686 mJy beam^{-1}). All emission channels are shown. The beam is indicated in the bottom left corner of the top left panel.

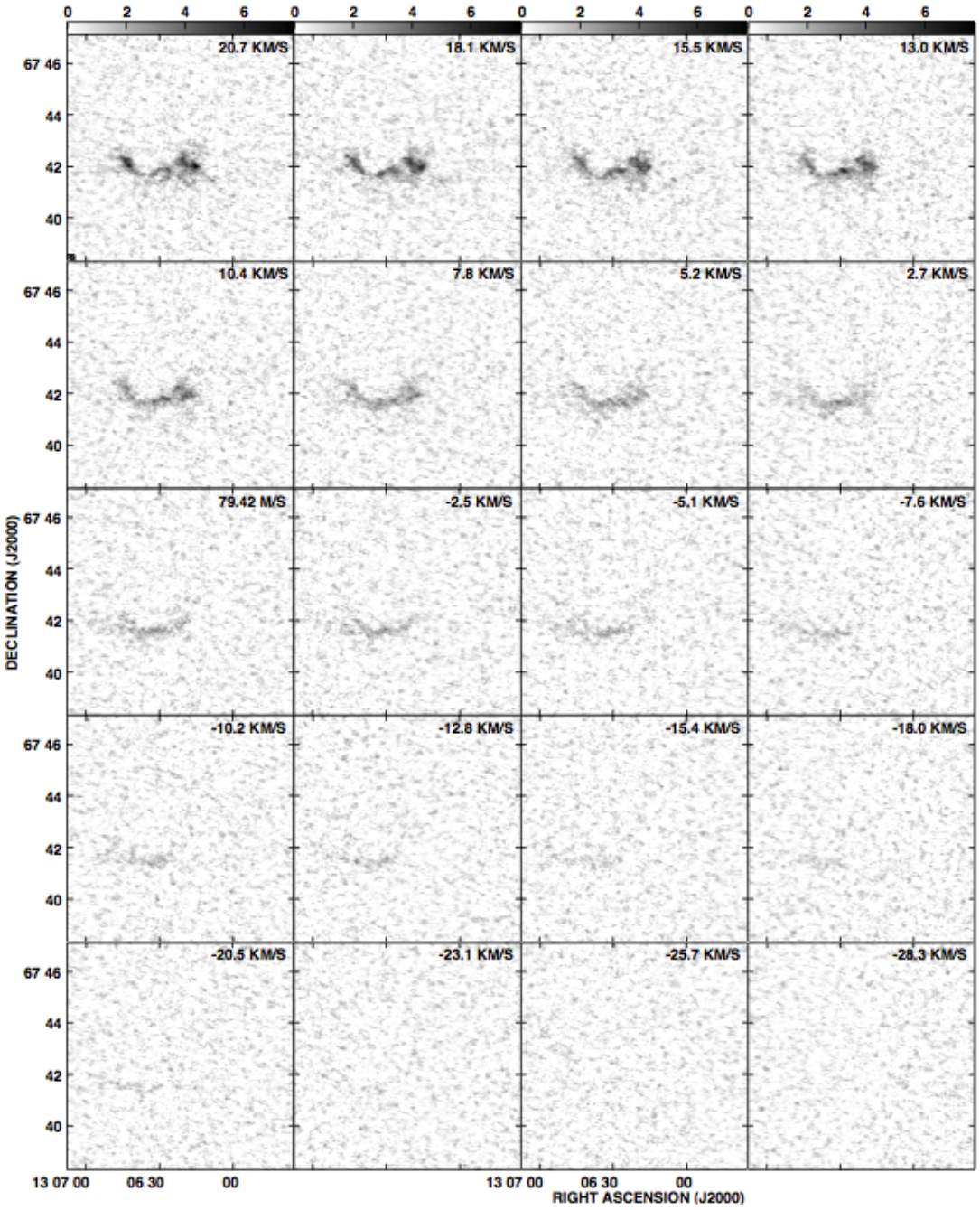

Fig. A.10 continues ...

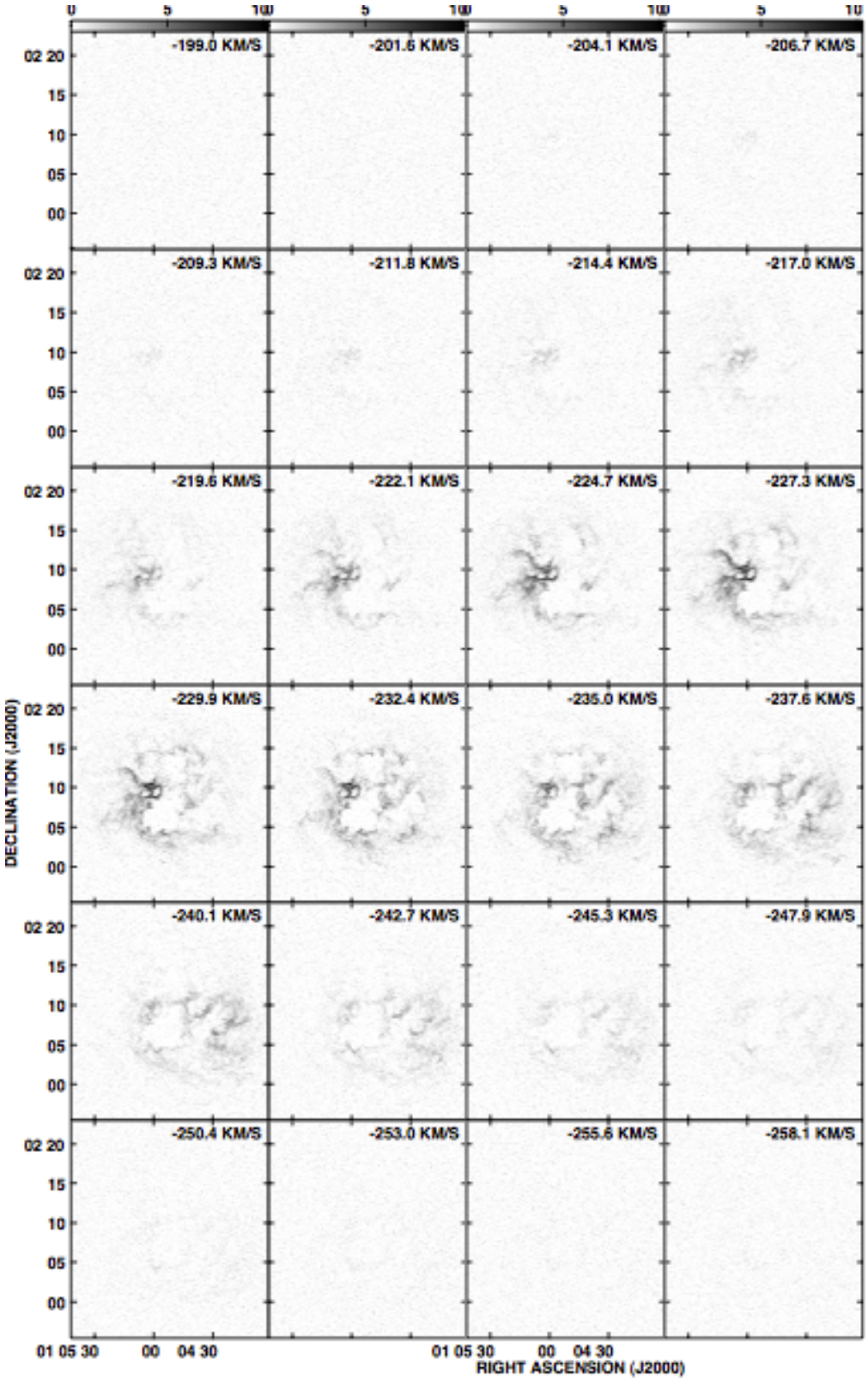

Figure A.11: IC 1613. Channel maps based on the robust weighted cube (Resolution: 7.″7 × 6.″5, σ= 4.5 K). The grey scale range is: 0-124.5 K (0 - 10.3 mJy beam^{-1}). All emission channels are shown. The beam is indicated in the bottom left corner of the top left panel.

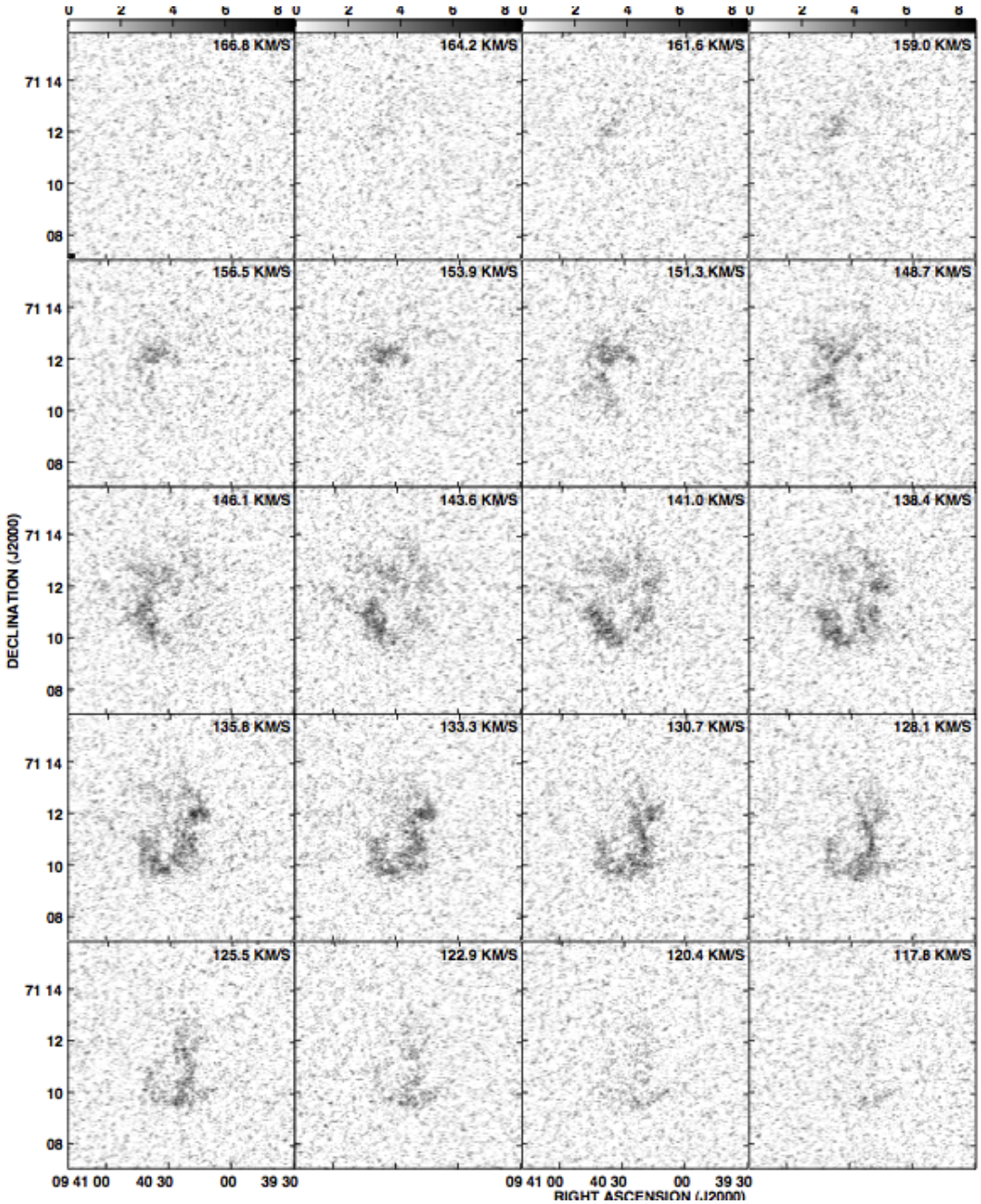

Figure A.12: DDO 63. Channel maps based on the robust weighted cube (Resolution: 7.″8 × 6.″0, σ= 15.4 K). The grey scale range is: 0-91.8 K (0 - 7.1 mJy beam^{-1}). All emission channels are shown. The beam is indicated in the bottom left corner of the top left panel.

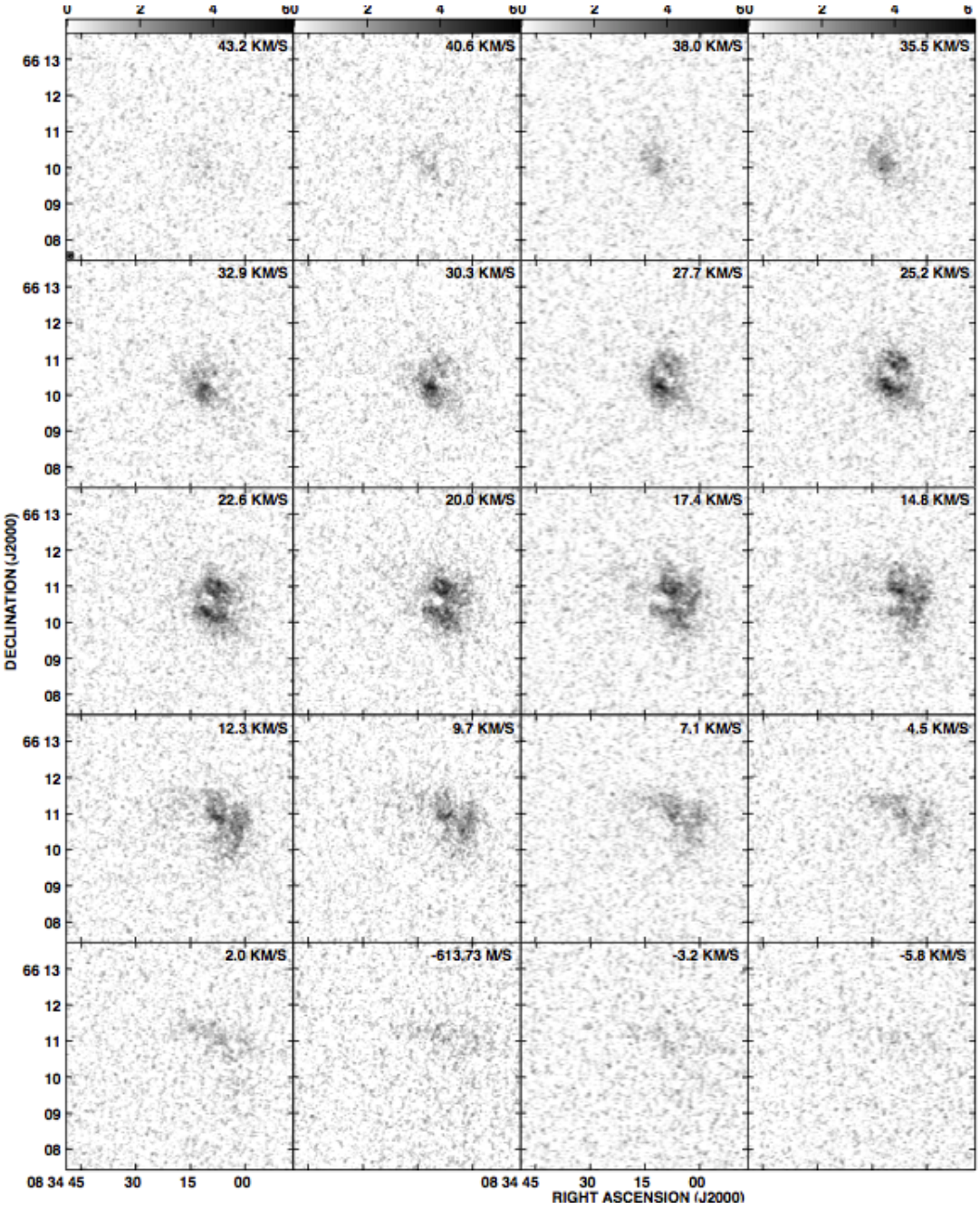

Figure A.13: DDO 53. Channel maps based on the robust weighted cube (Resolution: 6.″3 × 5.″7, σ= 10.1 K). The grey scale range is: 0-104.5 K (0 - 6.2 mJy beam^{-1}). All emission channels are shown. The beam is indicated in the bottom left corner of the top left panel.

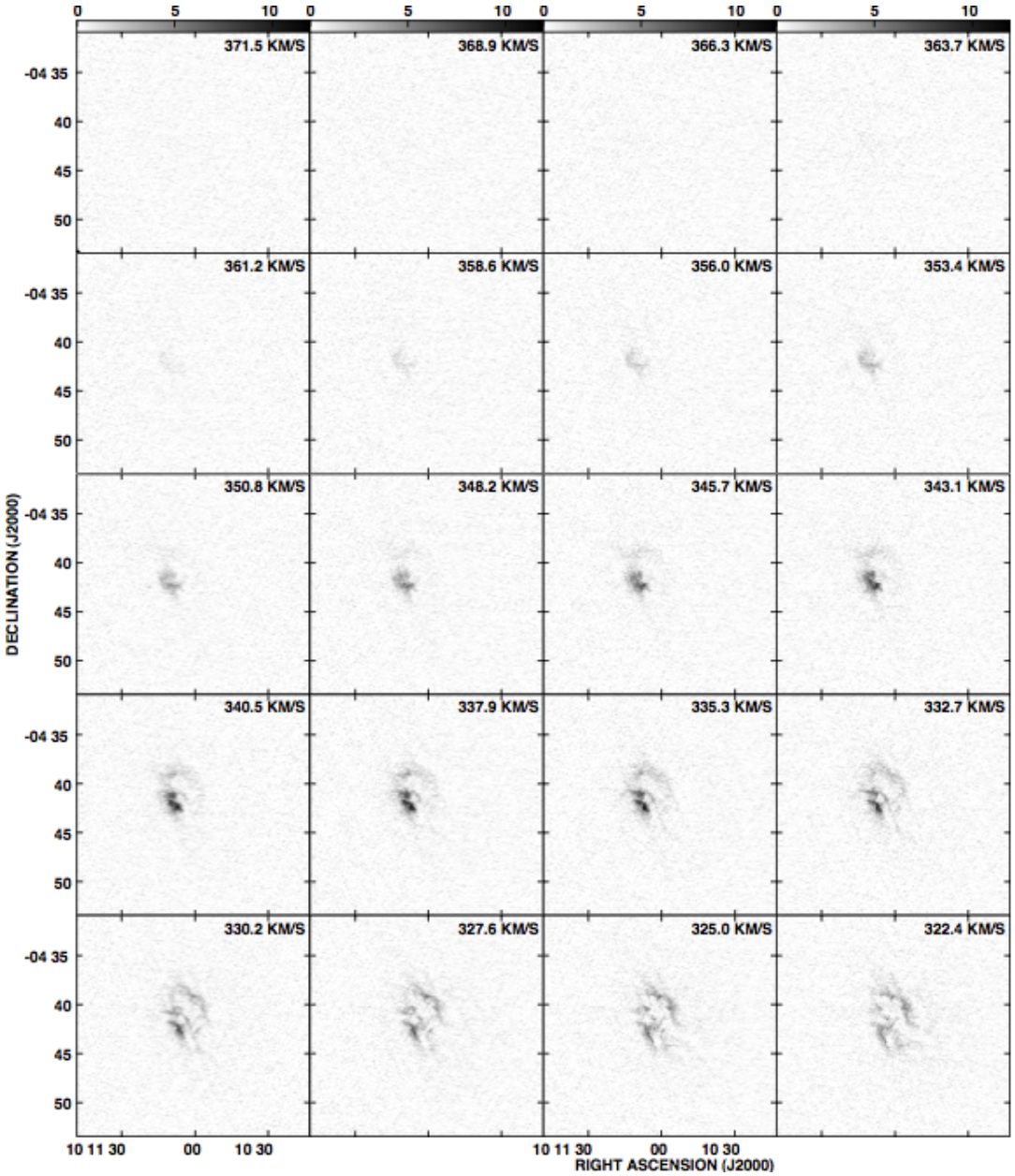

Figure A.14: DDO 75. Channel maps based on the robust weighted cube (Resolution: $7\farcs6 \times 6\farcs5$, σ= 6.3 K). The grey scale range is: 0-146.3 K (0 - 11.9 mJy beam^{-1}). All emission channels are shown. The beam is indicated in the bottom left corner of the top left panel.

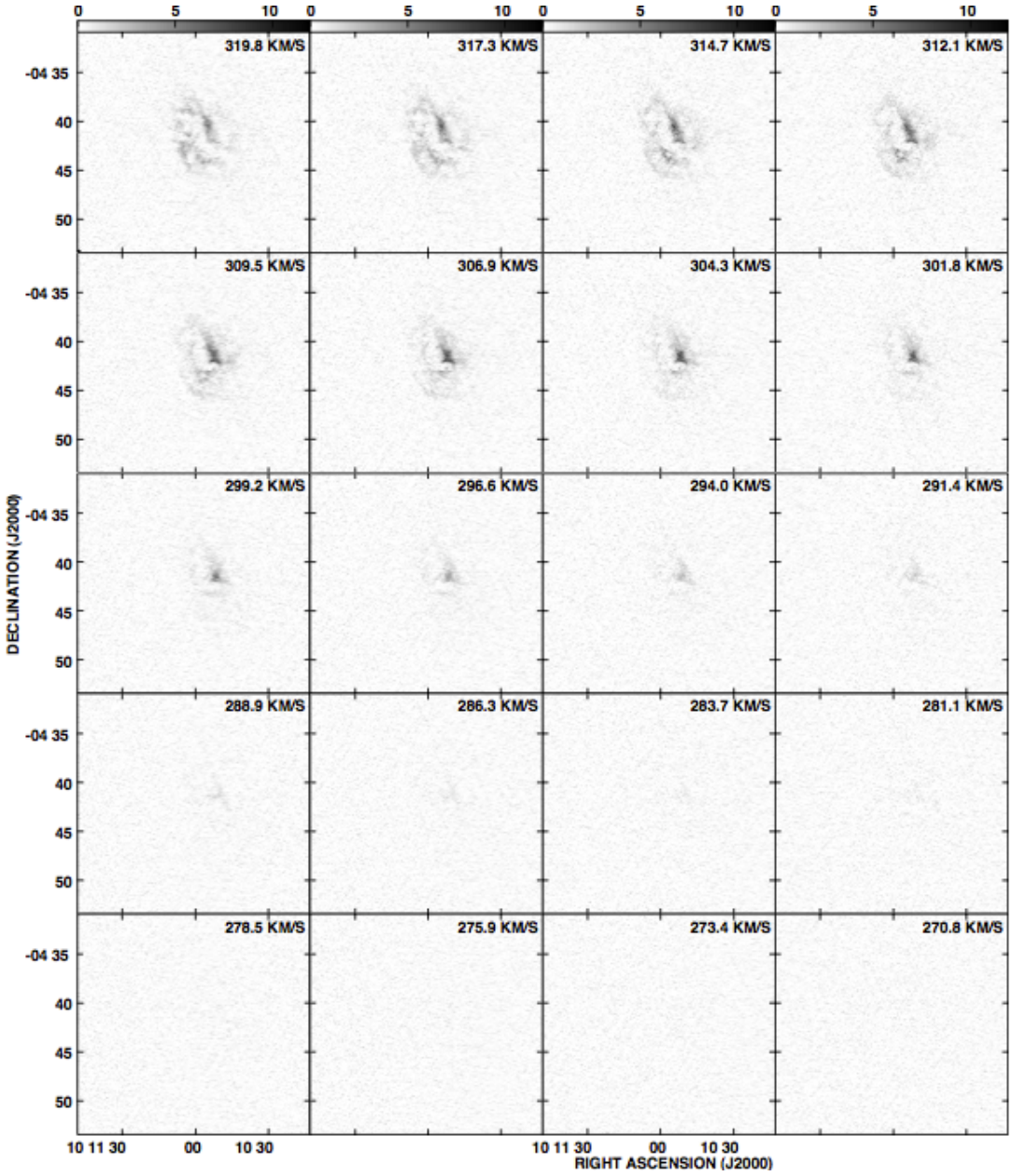

Fig. A.14 continues ...

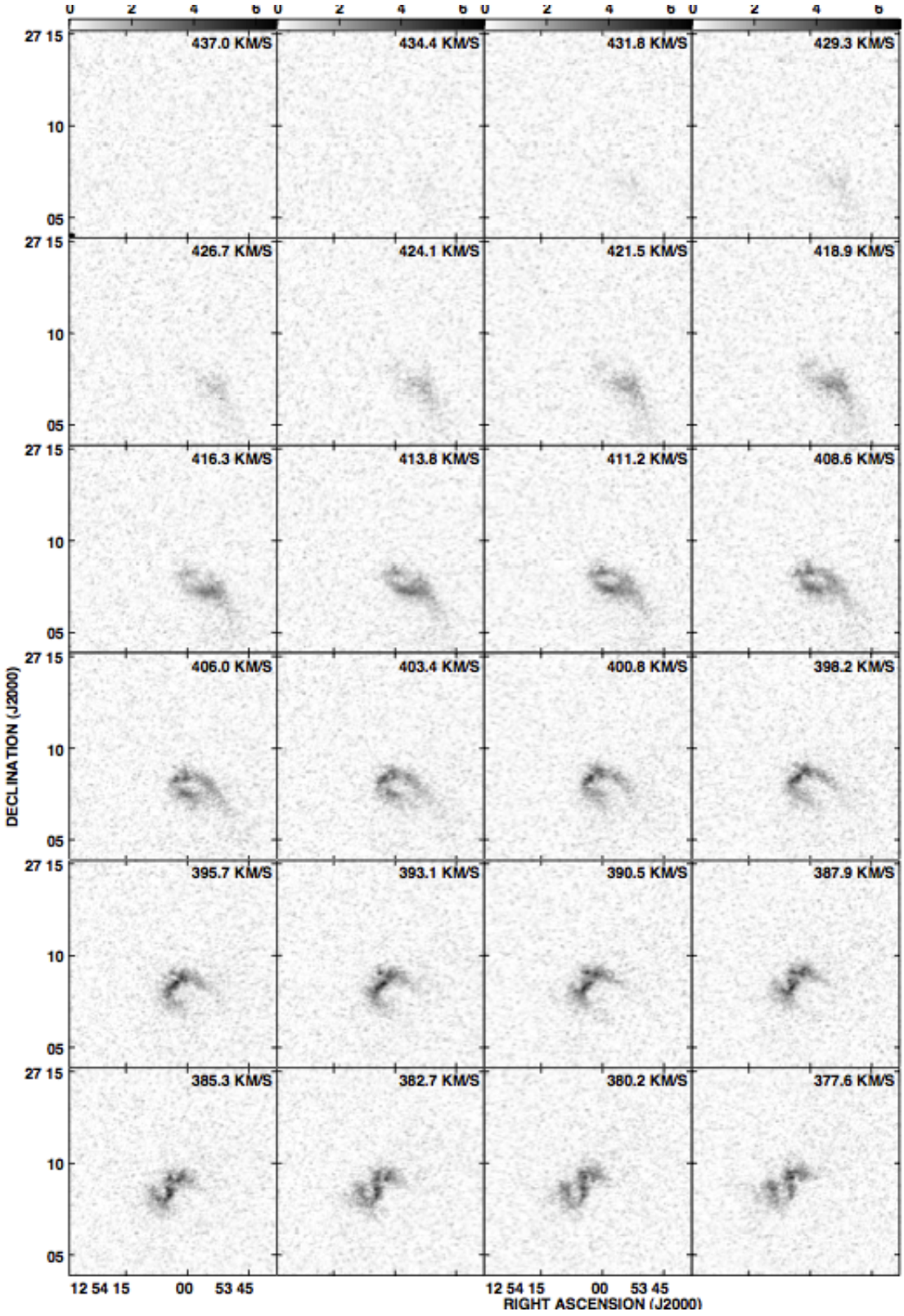

Figure A.15: DDO 154. Channel maps based on the robust weighted cube (Resolution: $7\farcs9 \times 6\farcs3$, σ= 6.6 K). The grey scale range is: 0-81.1 K (0 - 6.7 mJy beam^{-1}). All emission channels are shown. The beam is indicated in the bottom left corner of the top left panel.

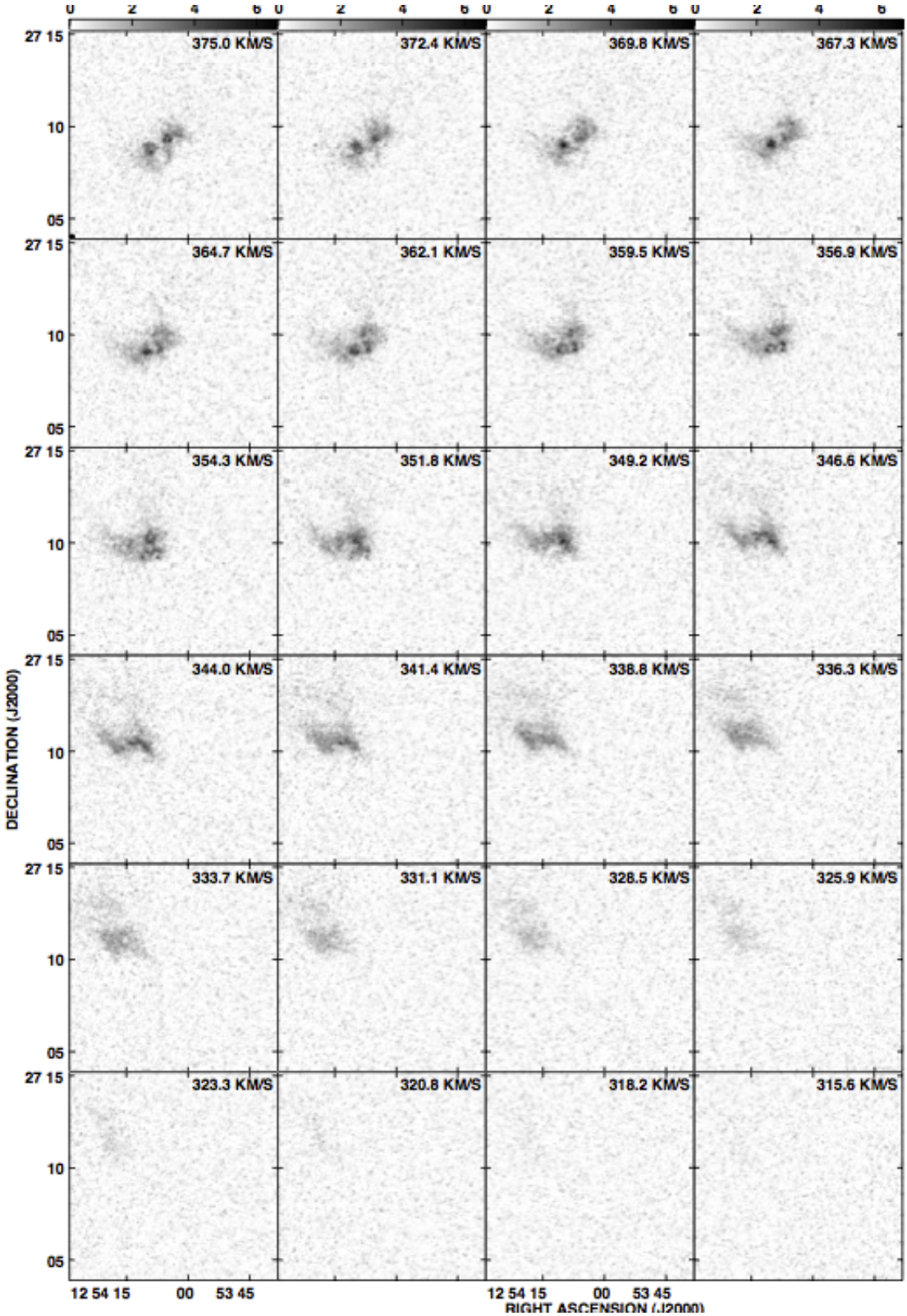

Fig. A.15 continues ...

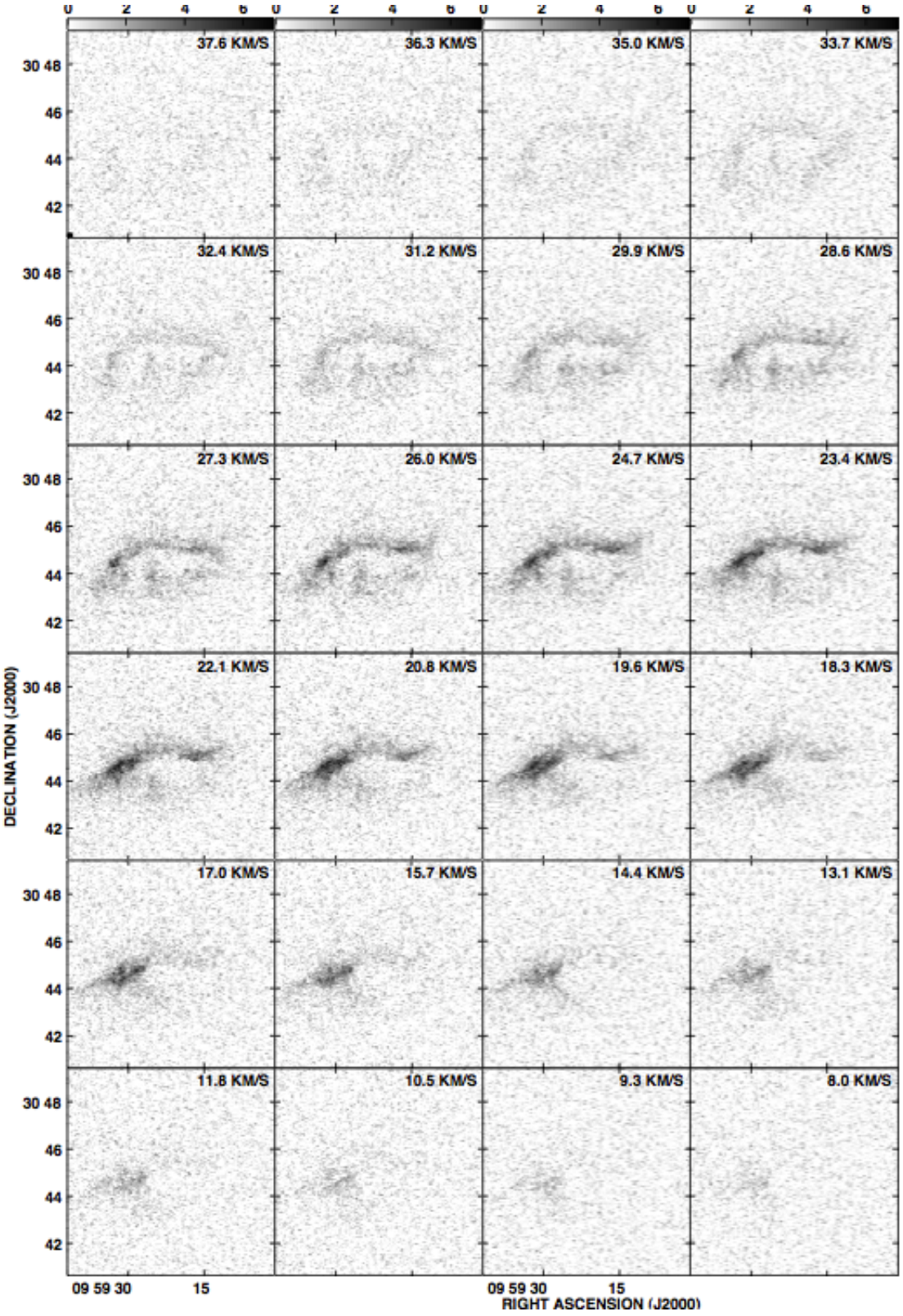

Figure A.16: DDO 69. Channel maps based on the robust weighted cube (Resolution: 5.″8 × 5.″4, σ= 12.8 K). The grey scale range is: 0-167.2 K (0 - 8.6 mJy beam^{-1}). All emission channels are shown. The beam is indicated in the bottom left corner of the top left panel.

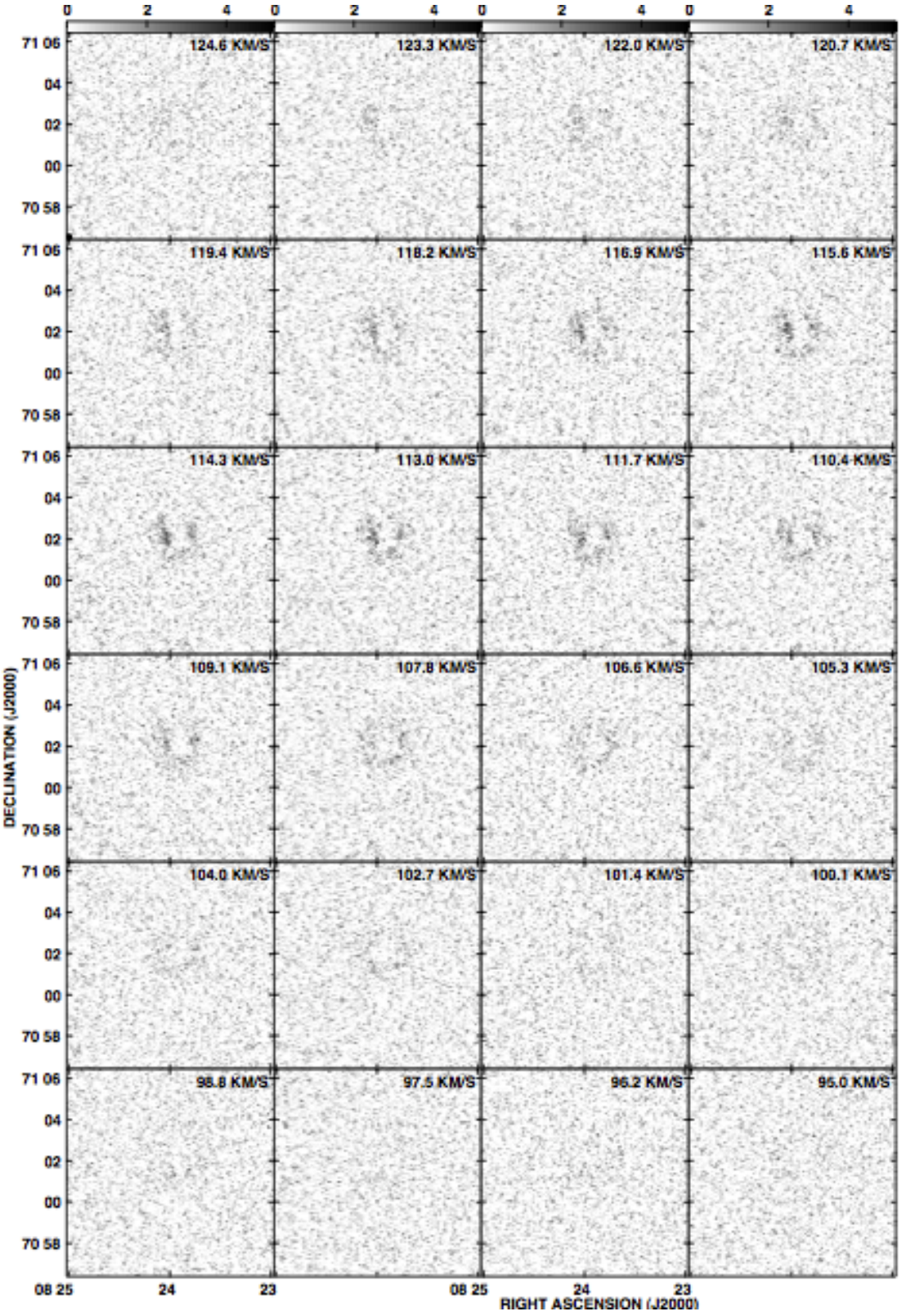

Figure A.17: M81dwA. Channel maps based on the robust weighted cube (Resolution: 7.″8 × 6.″3, σ= 10.4 K). The grey scale range is: 0-63.9 K (0 - 5.2 mJy beam^{-1}). All emission channels are shown. The beam is indicated in the bottom left corner of the top left panel.

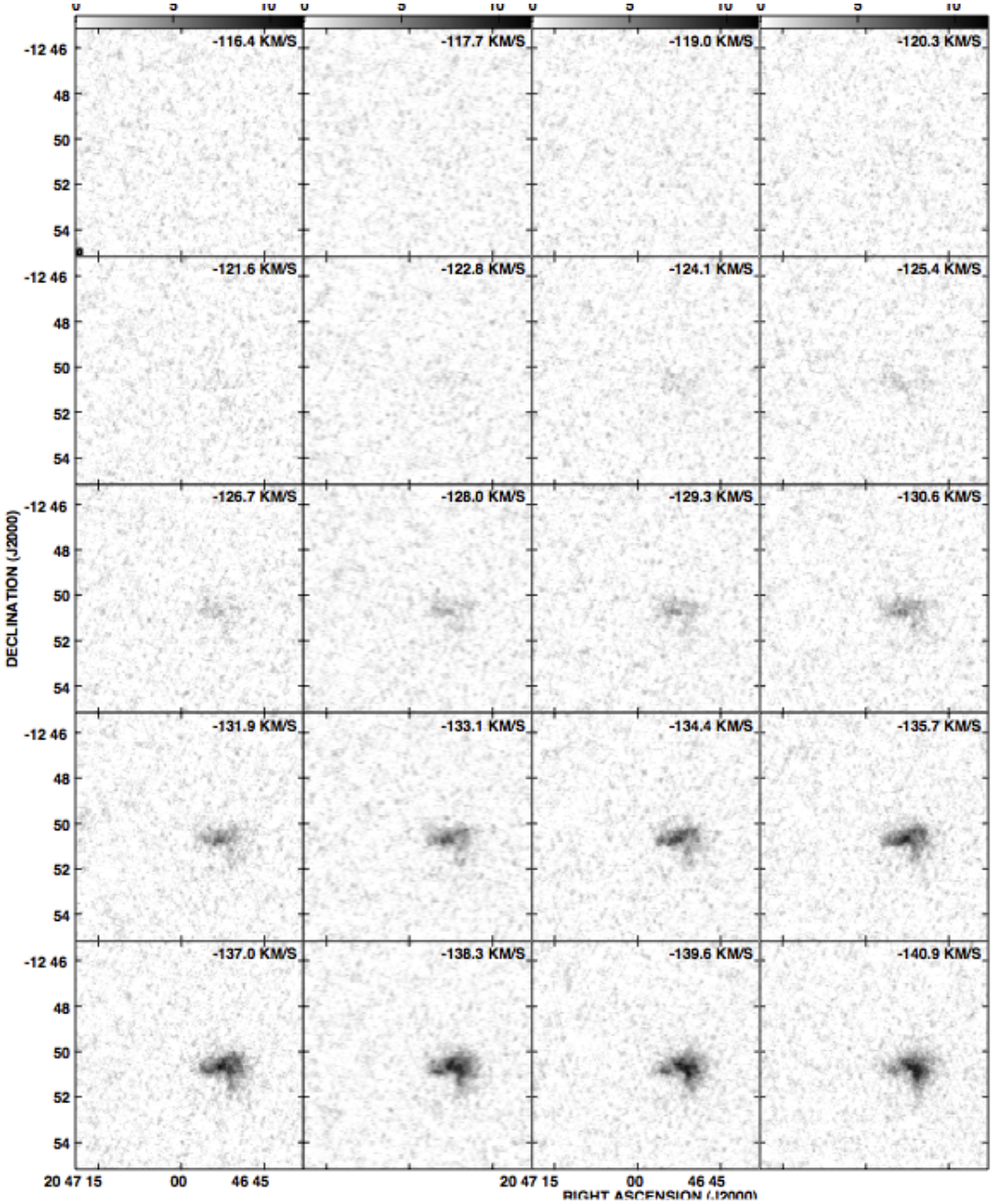

Figure A.18: DDO 210. Channel maps based on the robust weighted cube (Resolution: $11\farcs7 \times 8\farcs6$, σ= 5.2 K). The grey scale range is: 0-70.2 K (0 - 11.7 mJy beam^{-1}). All emission channels are shown. The beam is indicated in the bottom left corner of the top left panel.

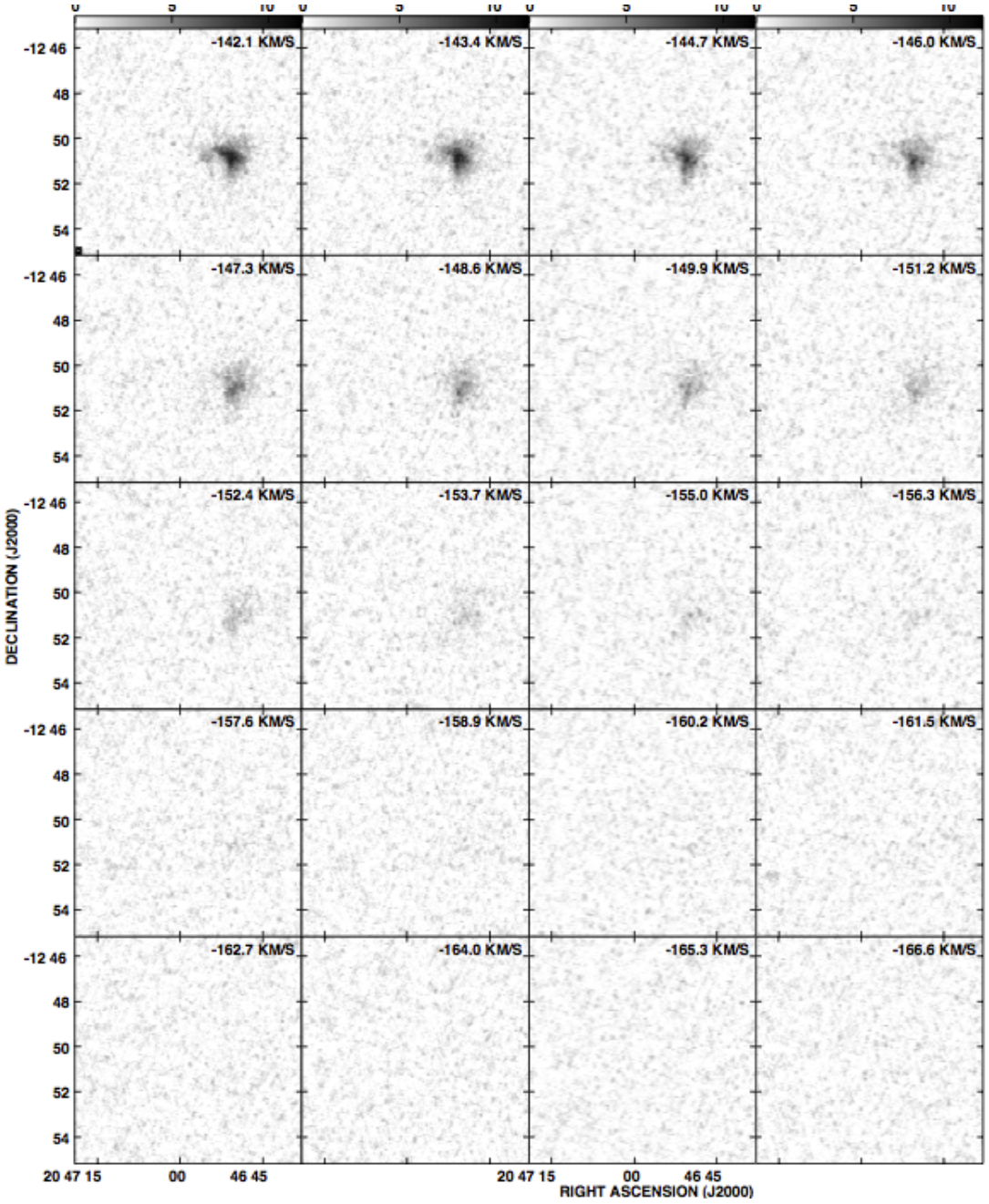

Fig. A.18 continues ...

Appendix B
Internal Extinction Plots

The conversion of FUV and Hα maps into star formation rate (SFR) maps, involves taking into account the need of an internal extinction correction. A fraction of the Hα and the FUV emission is obscured by dust. To account for this obscured emission we need an internal extinction correction. Even in nearby galaxies, internal extinction cannot be measured directly, due to resolution limitations, so any internal extinction corrections rely on measurements done in the Milky Way and more recently in the LMC and SMC, or dust measurements.

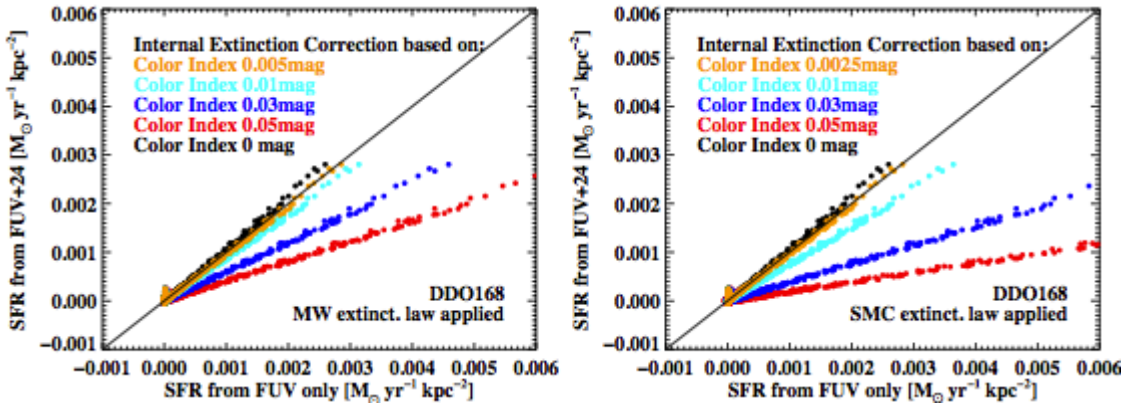

Figure B.1: We present SFRD derived from FUV+24 μm vs. SFRD based on FUV only with a Milky Way extinction law applied (left) and a SMC extinction law applied (right). Different colours represent internal extinction corrections of different colour index values: 0.05 mag (red), 0.03 mag (blue), 0.01 mag (cyan), 0.005 mag (orange) and 0 mag (black). The black continuous line represents a 1:1 relation between the x and y axis.

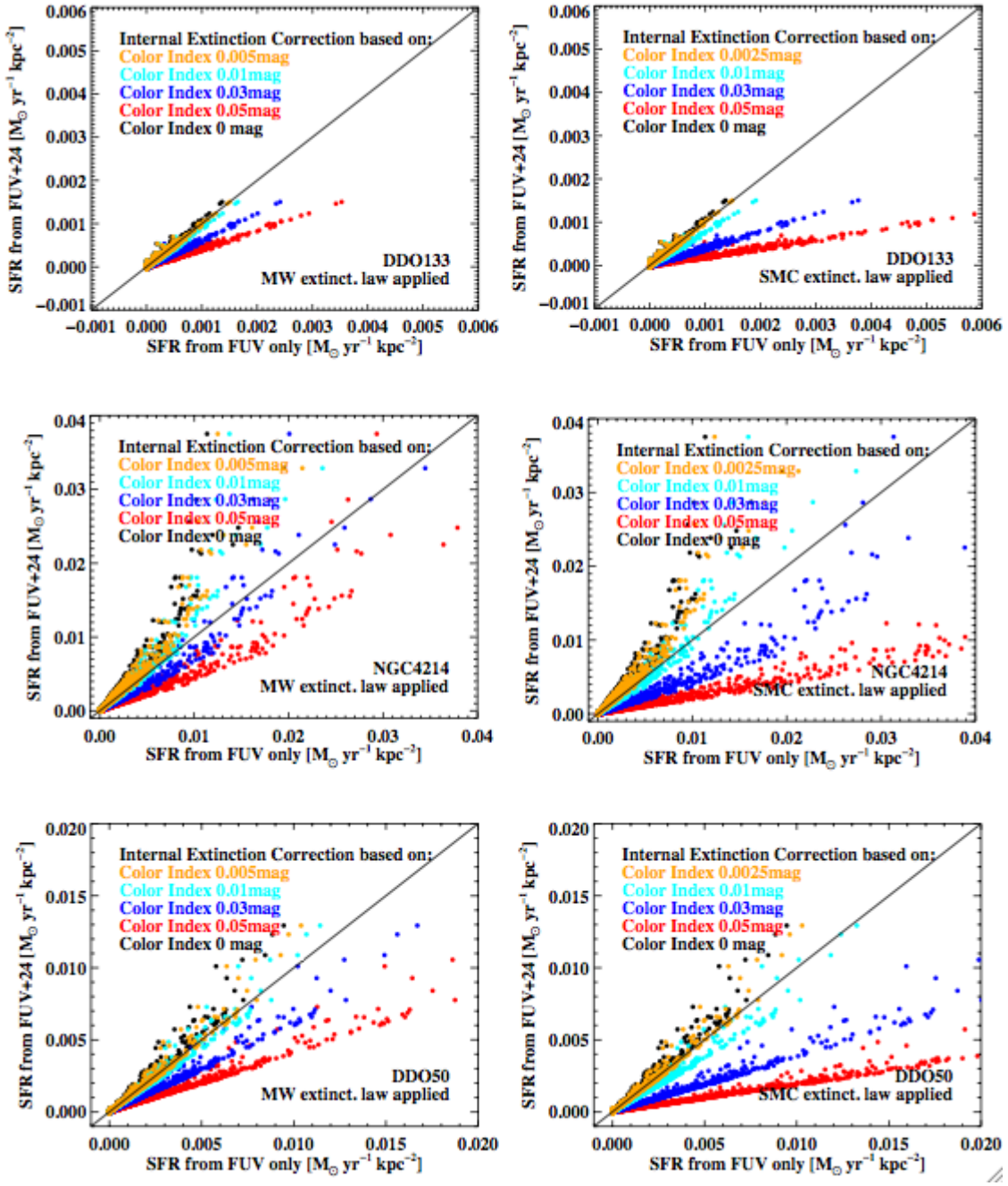

Fig. B.1 continues ...

The internal extinction correction is done by multiplying the FUV and the Hα map by a factor of $10^{A_{FUV}}$ and $10^{A_{H\alpha}}$ respectively. To determine A_{FUV} and $A_{H\alpha}$ we have to assume an extinction law to be applied. For the moment there are only two available either the Milky Way extinction law: A_{FUV}=8.24E$(B-V)$ for FUV

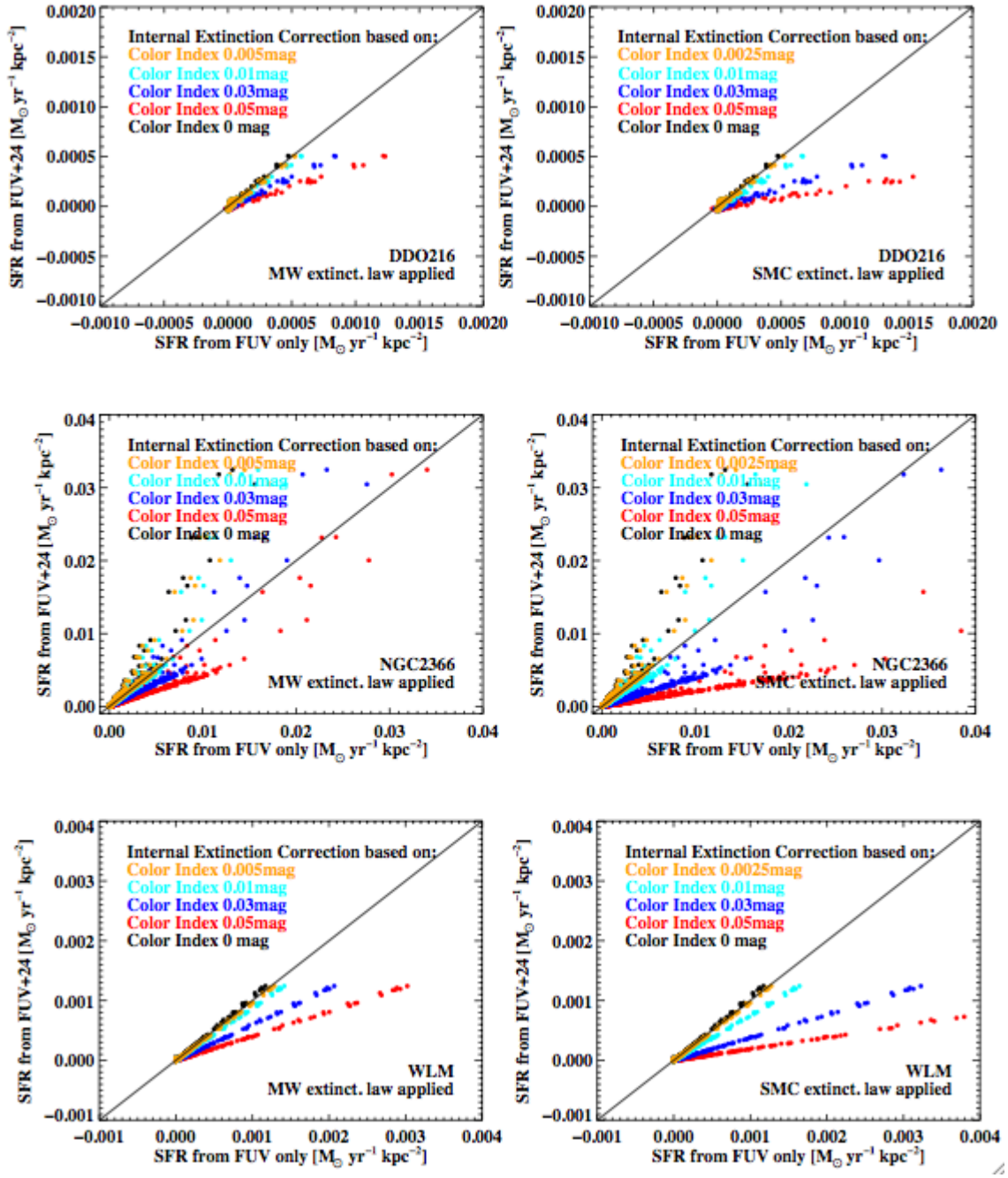

Fig. B.1 continues ...

and $A_{H\alpha}$=2.5E$(B-V)$ for Hα (Cardelli et al., 1989; Leroy et al., 2008; Wyder et al., 2007), or the SMC extinction law: A_{FUV}=14.68E$(B-V)$ for FUV and $A_{H\alpha}$=2.11E$(B-V)$ for Hα (Calzetti et al., 2007; Gordon & Clayton, 1998; Gordon et al., 2003). Having assumed the extinction law, we still need a value for E$(B-V)$, which has not been directly measured for any of our galaxies. Tradition-

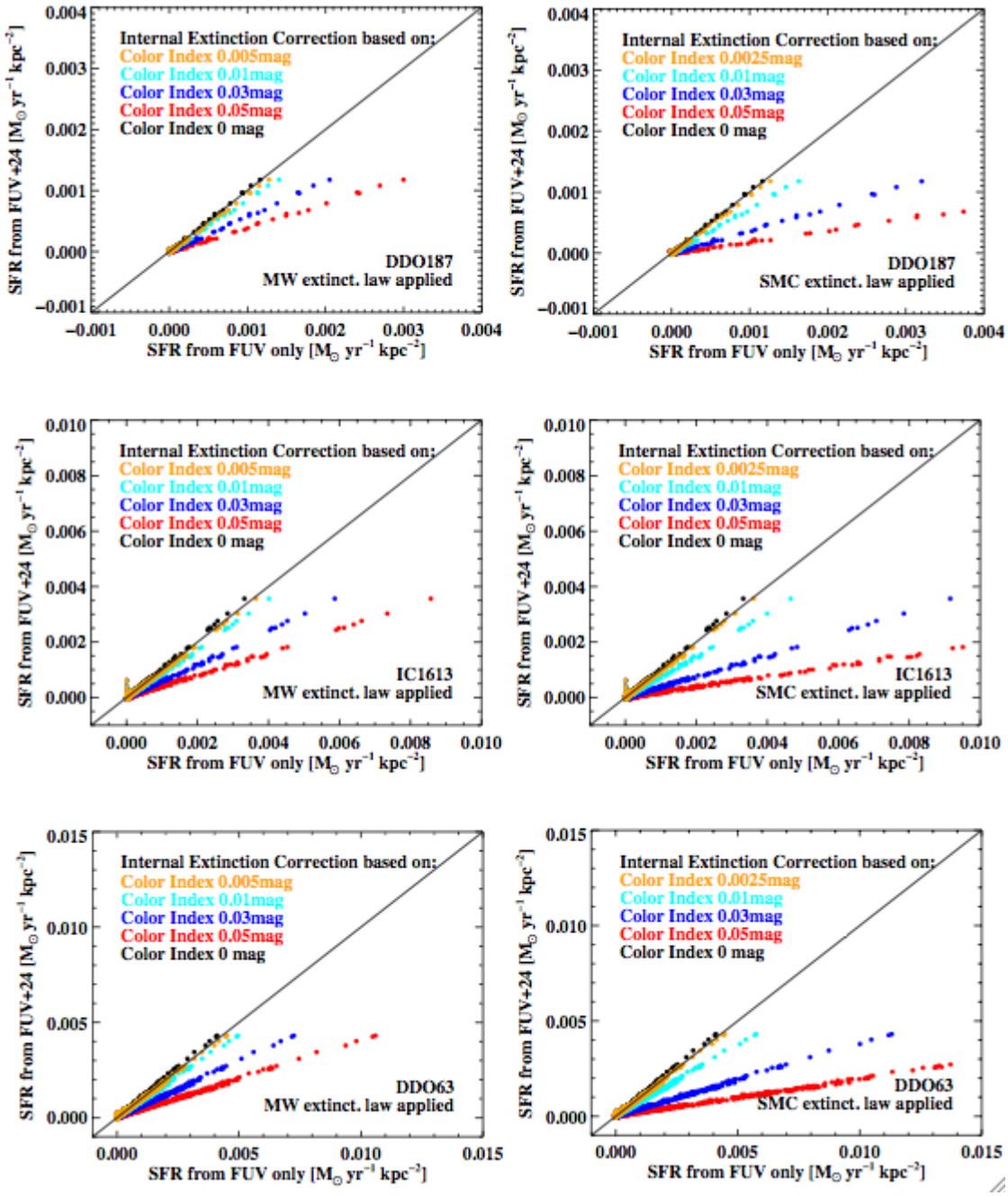

Fig. B.1 continues ...

ally a fixed $E(B-V)$ has been assumed (Cardelli et al., 1989; Leroy et al., 2008; Schlegel et al., 1998). Here we will investigate to what degree that is a reasonable assumption.

Another way of accounting for the obscured emission is using dust observations such as the 24 μm map as the obscured emission is re–radiated by the dust particles

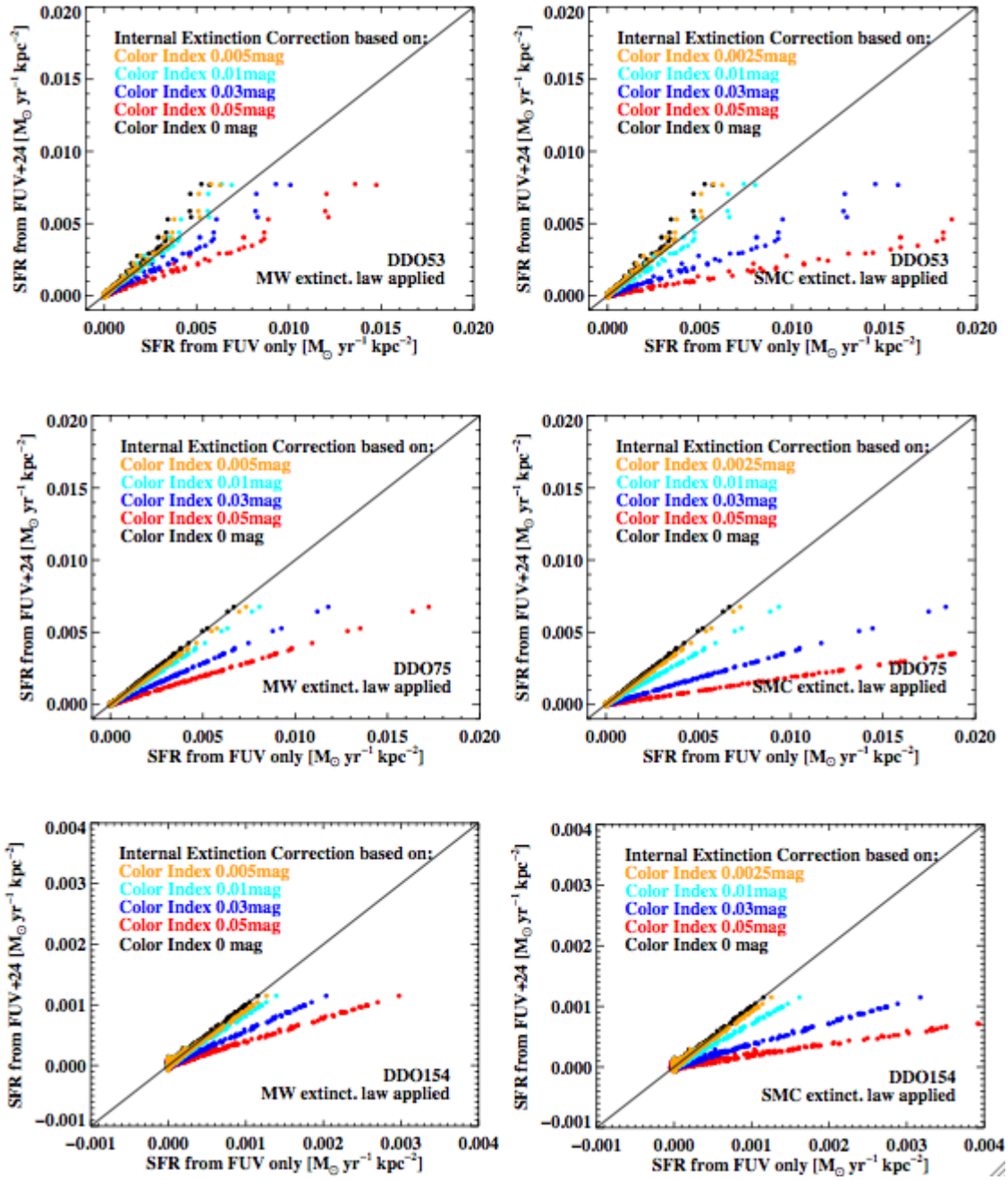

Fig. B.1 continues ...

in the infrared. Knowing that either with a correction as described above applied to the FUV or Hα emission or combined with a 24 μm map either SF tracer map should result in a unique SFR map, we decided to go through the exercise of deducing what E$(B-V)$ value corresponds to each galaxy based on its 24 μm emission, with different assumptions regarding the extinction law to be applied. We present our

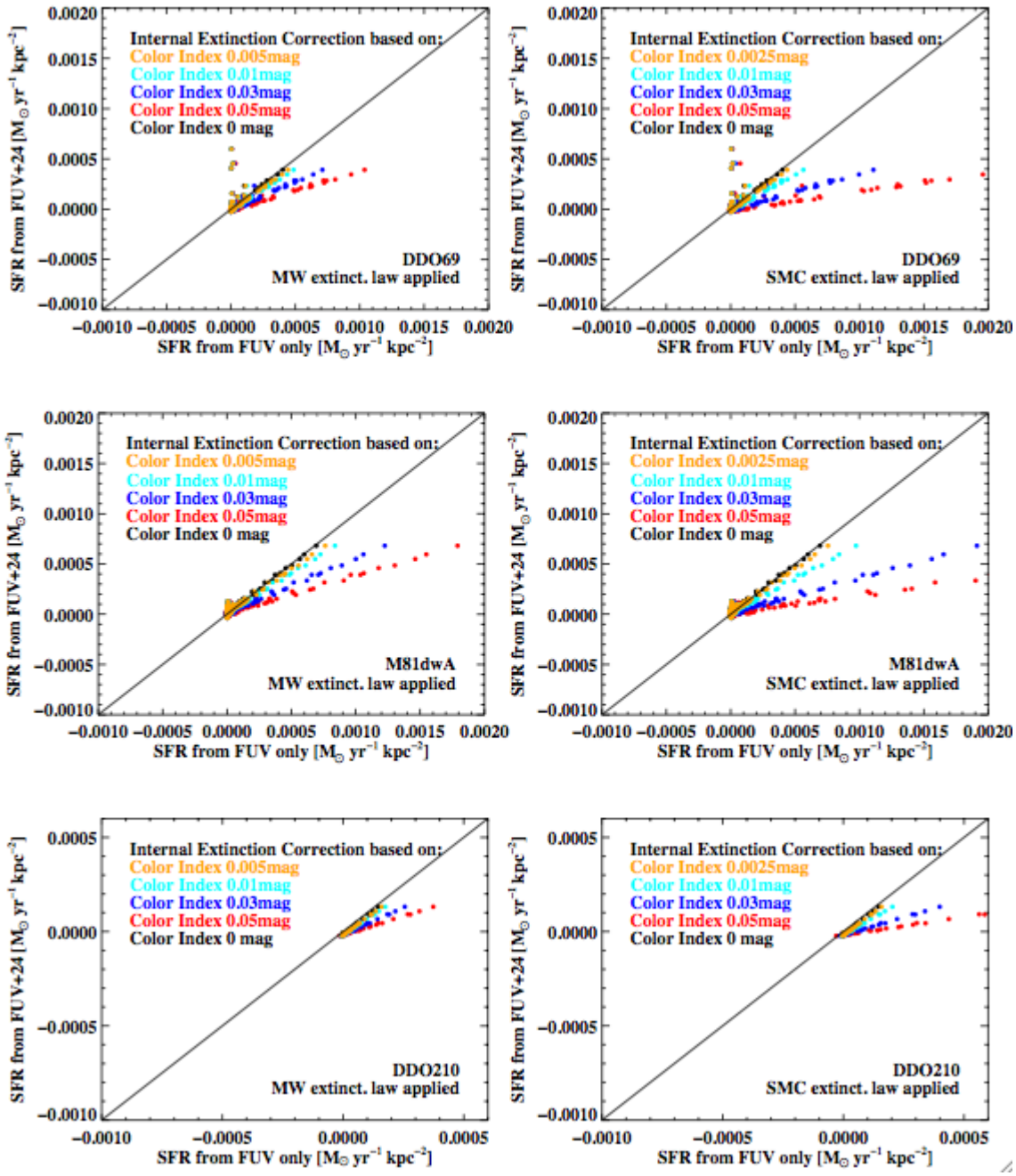

Fig. B.1 continues ...

results for each galaxy in Fig. B.1 which explores FUV as a SF tracer and assumes both the Milky Way extinction law (left) and the SMC extinction law (right).